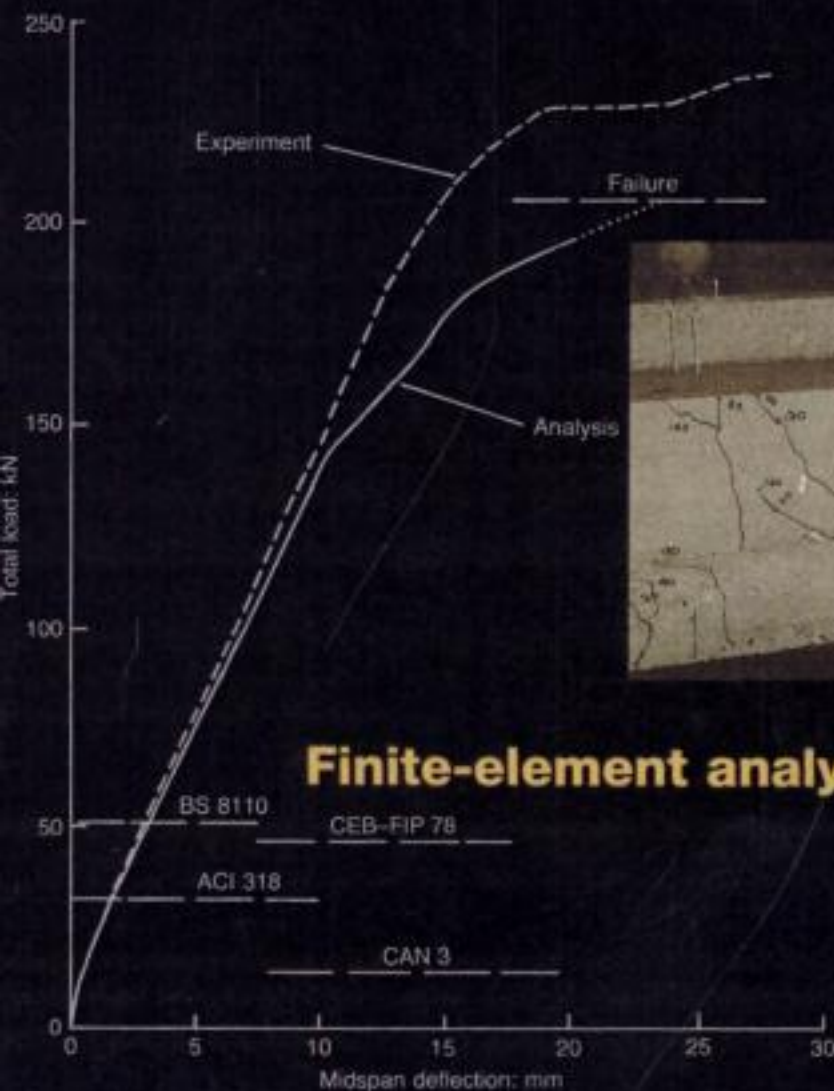


STRUCTURAL CONCRETE



Finite-element analysis for limit-state design

Structural concrete

Finite-element analysis for limit-state design

M. D. Kotsovos and M. N. Pavlović

 Thomas Telford

This One



A1GW-B2R-0G6K

Published by Thomas Telford Publications, Thomas Telford Services Ltd, 1 Heron Quay,
London E14 4JD

First published 1995

Distributors for Thomas Telford books are

USA: American Society of Civil Engineers, Publications Sales Department, 345 East 47th
Street, New York, NY 10017-2398

Japan: Maruzen Co. Ltd, Book Department, 310 Nihonbashi 2-chome, Chuo-ku, Tokyo 103

Australia: DA Books and Journals, 648 Whitehorse Road, Mitcham 3132, Victoria

A catalogue record for this book is available from the British Library

Classification

Availability: Unrestricted

Content: Original analysis

Status: Authors' invited opinion

Users: Structural and civil engineers, researchers

ISBN: 0 7277 2027 9

© M. D. Kotsovos and M. N. Pavlović, 1995

All rights, including translation reserved. Except for fair copying, no part of this publication may be reproduced, stored in a retrieval system or transmitted in any form or by any means, electronic, mechanical, photocopying or otherwise, without the prior written permission of the Publisher: Books, Publications Division, Thomas Telford Services Ltd, Thomas Telford House, 1 Heron Quay, London E14 4JD.

This book is published on the understanding that the author is solely responsible for the statements made and opinions expressed in it and that its publication does not necessarily imply that such statements and/or opinions are or reflect the views or opinions of the publishers.

Typeset by MHL Typesetting, Coventry.

Printed in Great Britain by Redwood Books, Trowbridge, Wiltshire.

Contents

Preface	ix
Introduction	1
1. Material modelling	8
<i>1.1. Experimental data</i>	<i>8</i>
1.1.1. Triaxial data and scatter, 8	
1.1.2. Test methods, 9	
1.1.3. Strength data, 13	
1.1.3.1. Uniaxial tests, 13	
1.1.3.2. Biaxial tests, 18	
1.1.3.3. Triaxial tests, 18	
1.1.3.4. Effect of testing technique on strength data, 19	
1.1.4. Constitutive-relations data, 20	
1.1.5. Choice of testing technique for the generation of material data, 22	
<i>1.2. Behaviour of concrete at failure</i>	<i>23</i>
1.2.1. Uniaxial compression tests, 26	
1.2.1.1. Behaviour of a test specimen under compressive load, 26	
1.2.1.2. Experimental evidence for the brittle nature of concrete, 28	
1.2.2. Triaxial compression tests and the effect of tensile stresses, 37	
1.2.3. Concrete: a brittle fracturing material, 40	
<i>1.3. Fracture processes in concrete</i>	<i>42</i>
1.3.1. The nonlinear behaviour of concrete materials, 42	
1.3.2. Causes of fracture, 43	
1.3.3. Fracture mechanism of concrete, 44	
1.3.3.1. Fracture processes under deviatoric stress, 48	
1.3.3.2. Fracture processes under hydrostatic stress, 53	
1.3.3.3. Fracture processes under generalized stress, 58	
<i>1.4. A mathematical model for concrete materials</i>	<i>58</i>
1.4.1. Constitutive relations for concrete, 59	
1.4.1.1. Experimental data on observed behaviour, 61	
1.4.1.2. Mathematical description of deformational behaviour, 68	
1.4.1.3. The accuracy of the mathematical model for the constitutive relations, 81	
1.4.2. Strength envelopes for concrete, 83	
1.4.2.1. Experimental data on, and mathematical description of, failure surfaces, 83	

1.4.2.2. <u>The accuracy of the mathematical model for the failure surfaces, 96</u>	
1.4.3. <u>Deformational and yield characteristics of the reinforcing steel, 101</u>	
1.5. <i>Failure mechanism in concrete structures</i>	103
1.5.1. <u>A fundamental explanation of failure initiation based on triaxial material behaviour, 103</u>	
1.5.2. <u>Triaxiality and failure initiation by macrocracking: some experimental and analytical evidence, 108</u>	
1.6. <i>A summary of the main characteristic features of concrete materials relevant to finite-element modelling</i>	123
2. <i>Structure modelling</i>	126
2.1. <u><i>The finite-element method</i></u>	<u>126</u>
2.2. <u><i>Nonlinear analysis</i></u>	<u>130</u>
2.3. <u><i>A finite-element program for linear analysis</i></u>	<u>136</u>
2.3.1. <u>Brief description of FINEL, 136</u>	
2.3.2. <u>Finite elements selected, 141</u>	
2.4. <u><i>The nonlinear finite-element model for structural concrete</i></u>	<u>151</u>
2.4.1. <u>Background and scope, 151</u>	
2.4.2. <u>Incremental formulation up to macrocracking, 153</u>	
2.4.2.1. <u>The incremental Newton–Raphson scheme, 153</u>	
2.4.2.2. <u>Incremental strain–displacement relationships, 156</u>	
2.4.2.3. <u>Incremental stress–strain relationships for uncracked concrete, 157</u>	
2.4.2.4. <u>Incremental force–displacement relationships, 158</u>	
2.4.2.5. <u>Residual forces, 160</u>	
2.4.2.6. <u>Convergence and divergence criteria, 162</u>	
2.4.3. <u>Modelling of macrocracking, 164</u>	
2.4.3.1. <u>The nature of structural cracking, 164</u>	
2.4.3.2. <u>The smeared-crack approach, 171</u>	
2.4.3.3. <u>Incremental stress–strain relationships for cracked concrete, 174</u>	
2.4.3.4. <u>The shear-retention factor: its role on the conditioning of stiffness matrices and actual physical evidence, 182</u>	
2.4.4. <u>Description of the reinforcing steel, 185</u>	
2.4.4.1. <u>Incremental relations for the three-node uniaxial element, 185</u>	
2.4.4.2. <u>Concrete–steel interaction, 187</u>	
2.5. <u><i>An overview of material and procedural factors influencing finite-element predictions</i></u>	<u>192</u>
2.6. <u><i>A brief outline of the smeared-model package</i></u>	<u>198</u>

3. Two-dimensional analysis	208
<i>3.1. Introduction</i>	208
<i>3.2. Guidelines for a systematic numerical procedure</i>	209
<i>3.3. Plain concrete structures</i>	214
3.3.1. Various prisms and cylinders under concentrations of load, 214	
3.3.1.1. Prism under concentric strip loading over one-half of each end face, 214	
3.3.1.2. Prism under concentric strip loading over one-quarter of each end face, 216	
3.3.1.3. Prism under eccentric strip loading over one-quarter of each end face, 216	
3.3.1.4. Cylinder under concentric patch loading over one-quarter of each end face, 216	
3.3.1.5. Cylinder under concentric patch loading over one-sixteenth of each end face, 220	
3.3.2. Parametric study of prisms and cylinders under concentrations of load, 222	
3.3.2.1. Scope, 222	
3.3.2.2. Discussion of results, 226	
3.3.2.3. Conclusions, 232	
3.3.3. Parametric study of the effect of boundary conditions on prisms and cylinders under concentrations of load, 232	
3.3.3.1. Scope, 232	
3.3.3.2. Results and discussion, 233	
3.3.3.3. Conclusions, 239	
3.3.4. Hollow sphere under hydrostatic pressure, 243	
<i>3.4. Reinforced concrete structures</i>	244
3.4.1. Beams, 244	
3.4.1.1. Beams with untypical reinforcement details, 245	
3.4.1.2. Phenomenological insight, 248	
3.4.1.3. Beams with and without stirrups under central point load, 271	
3.4.2. Deep beams, 274	
3.4.2.1. Deep beams under two-point loading, 275	
3.4.2.2. Deep beam with web openings and web reinforcement under two-point loading, 277	
3.4.2.3. Deep beam with complex reinforcement subjected to a concentrated load at midspan, 281	
3.4.3. Structural walls, 283	
3.4.3.1. Modelling of test data, 284	
3.4.3.2. Parametric study, 293	
3.4.4. Punching mechanism in slabs, 309	
3.4.4.1. Presentation of results, 311	
3.4.4.2. Validation of analytical predictions, 315	
3.4.4.3. Discussion of results, 316	

3.4.4.4. Conclusions, 325	
3.4.5. Shear panels, 328	
3.4.6. Corbels, 334	
3.4.7. Shells, 336	
3.4.7.1. Sandwich cylinder under external pressure, 337	
3.4.7.2. Dome under central point loading, 343	
3.4.8. Membrane action in flexural members, 343	
3.5. <i>Concluding remarks</i>	344
4. Three-dimensional analysis	347
4.1. <i>Introduction</i>	347
4.2. <i>Some observations on numerical instabilities in the smeared-crack approach</i>	348
4.3. <i>Performance of the three-dimensional finite-element model</i>	361
4.3.1. Objectivity study, 361	
4.3.1.1. Case study 1: PC prism under strip loading, 364	
4.3.1.2. Case study 2: RC beam under two-point loading failing in flexure, 367	
4.3.1.3. Case study 3: RC beam without stirrups under central point loading failing in shear, 374	
4.3.1.4. Tentative recommendations, 385	
4.3.2. Generality study, 386	
4.3.2.1. Case study 4: PC prism under patch loading, 386	
4.3.2.2. Case study 5: RC beam with stirrups under central point loading failing in shear, 389	
4.3.2.3. Case study 6: RC T-beam under four-point loading, 391	
4.3.2.4. Case study 7: RC structural wall failing in flexure, 400	
4.3.2.5. Case study 8: RC slab exhibiting punching failure, 404	
4.3.2.6. Summary of results, 408	
4.4. <i>A comparative study of two-dimensional and three-dimensional analyses by reference to structural walls</i>	412
4.5. <i>Modelling of normal-strength and high-strength reinforced concrete members, with special reference to T-beams</i>	418
4.5.1. Economic modelling of RC T-beams, 418	
4.5.1.1. Modelling using 50 brick elements, 419	
4.5.1.2. Modelling using 40 brick elements, 420	
4.5.1.3. Modelling using 25 brick elements, 423	
4.5.2. Modelling of high-strength RC members, 427	
4.5.2.1. Case study 1: high-strength RC T-beam subjected to four-point loading failing in flexure, 427	
4.5.2.2. Case study 2: high-strength RC T-beam subjected to two-point loading failing in flexure, 433	

- 4.5.2.3. Case study 3: high-strength RC rectangular beam subjected to central point loading failing in shear, 439
- 4.5.2.4. Case study 4: an analytical investigation on the effectiveness of flange reinforcement in HSC members, 445
- 4.5.3. Summary of main conclusions, 452
- 4.6. *Prestressed concrete beams* 453
 - 4.6.1. Modelling of PSC members and scope of the investigation programme, 453
 - 4.6.2. Case study 1: PSC I-beam subjected to two-point loading failing in web-shear, 455
 - 4.6.3. Case study 2: PSC T-beam subjected to two-point loading failing in shear, 461
 - 4.6.4. Case study 3: PSC T-beam subjected to six-point loading failing in shear, 469
 - 4.6.5. Case study 4: PSC T-beam subjected to six-point loading failing in flexure, 473
 - 4.6.6. Case study 5: an analytical investigation of a PSC T-beam made from high-strength concrete subjected to six-point loading failing in flexure, 478
 - 4.6.7. Summary, 482
- 4.7. *The phenomenon of 'size effects' in structural concrete* 483
 - 4.7.1. Background, 483
 - 4.7.2. An analysis of some experimental data and of their FE modelling, 484
 - 4.7.2.1. Case study 1: RC slabs, 485
 - 4.7.2.2. Case study 2: RC beams with stirrups, 486
 - 4.7.2.3. Case study 3: RC beams without stirrups, 487
 - 4.7.2.4. A possible explanation, 488
 - 4.7.3. A numerical experiment, 489
 - 4.7.3.1. Objective, 489
 - 4.7.3.2. Structural forms investigated, 490
 - 4.7.3.3. Results and discussion, 494
 - 4.7.3.4. Summary and tentative conclusions, 501
- 4.8. *Structural brickwork* 502
 - 4.8.1. Shape factors for brick units, 503
 - 4.8.1.1. Background, 503
 - 4.8.1.2. Material testing, 504
 - 4.8.1.3. Structural FE modelling, 506
 - 4.8.1.4. Theoretical results, 509
 - 4.8.1.5. Discussion of the shape-factor formulation in the light of the present material and analytical results, 511
 - 4.8.2. Effect of the number of mortar joints on the strength of a masonry wall, 516

4.8.2.1. Problem formulation, 516	
4.8.2.2. Preliminary study of the effect of FE mesh size, 518	
4.8.2.3. Results and discussion, 519	
4.9. <i>Concluding remarks</i>	524
Appendix A. Octahedral formulation of stresses and strains	528
<i>A.1. Octahedral coordinates</i>	528
<i>A.2. Octahedral stresses</i>	528
<i>A.3. Invariants of the stress tensor and their relation to the octahedral parameters</i>	529
<i>A.4. Octahedral strains</i>	530
<i>A.5. Elastic constitutive relations in terms of octahedral stresses and strains</i>	530
Appendix B. Coordinate transformations	532
<i>B.1. Strain transformations</i>	532
<i>B.2. Stress transformations</i>	533
<i>B.3. Transformations of material properties</i>	533
References	534
Index	544

Preface

Over the last ten years the Authors have steadily conducted a programme of research aimed at rationalizing the analysis and design of structural concrete. This programme of work was preceded by a decade of experimental research at the material level which furnished the key data input for structural considerations, namely the fundamental behaviour of concrete materials under multiaxial stress conditions. Thus, the latter provided the starting point for a comprehensive investigation into the response of concrete structures to loading up to collapse, a study that encompassed the following three basic structural aspects: numerical modelling by the finite-element method; laboratory testing of structural members; and a consistent design methodology. This book is concerned with the first of these three fundamental approaches to structural behaviour and, although some elements of the remaining two aspects will also be mentioned whenever the necessary practical supporting evidence to the theoretical findings might be deemed appropriate, a full outline of the proposed unified design philosophy (comparable in effort — although not in concept — to the current code calculations) will be published separately. The present book, therefore, not only provides the theoretical background of, and justification for, the latter design approach for ultimate strength but also affords a powerful tool for both analysis and design of the more complex structural elements for which hand calculations and/or simplified design rules are not sufficient and which therefore demand a more formal, rigorous and, indeed, sophisticated computational model such as the one — based on nonlinear finite-element analysis — here described.

The Authors are indebted to many colleagues and past research students who, throughout the years, have contributed to the shaping of the present unifying approach to structural-concrete modelling. Among the former, mention must be made of Professors J. Bobrowski and Sir Alan Harris who encouraged the Authors with their salutary — albeit somewhat irreverent — comments on codes of practice, and Dr J.B. Newman who participated in the early research on triaxial testing that led eventually to the material model adopted herein. Mr D. Hitchings kindly provided the linear package FINEL which formed the basis of the program for the nonlinear modelling of concrete structures, and he was particularly generous with his advice on the use of the former. At a time of rapid development in hardware, many useful suggestions for the choice and implementation of the computing equipment were made by

Dr K. Anastasiou. The actual numerical implementation of the finite-element model and its application to specific problems was carried out with the help of the following research collaborators: Dr C. Bédard (two-dimensional modelling); Dr F. González Vidosa (three-dimensional modelling and the study of punching failure in slabs); Dr I.D. Lefas (application of the two-dimensional package to structural walls); Dr S.M. Seraj (application of the three-dimensional package to high-strength concrete members and masonry problems, as well as its extension to prestressed-concrete elements); Dr M. Kinoshita (extension of the present material and finite-element models so as to cater for certain composite-construction problems — a recently developed topic which, although mentioned, is not included in this book). The excellent support provided by the technical staff of the Laboratory of Concrete Structures at Imperial College, headed by R.W. Loveday, P. Jellis and R. Baxter, in the course of both triaxial material testing and structural experiments, is gratefully acknowledged.

Finally, the Authors wish to express their sincere appreciation to the editorial team of Thomas Telford Services Ltd, especially to Linda Schabedly, who patiently and painstakingly guided the editing process throughout, and to Lynne Darnell for the consistency and quality of the figures.

Introduction

The analysis of large, multi-member structures is still carried out almost invariably on the basis of linear elastic theory. It is also this method that is used to check the serviceability requirement in the course of the structure's design. With regard to the key aspect of strength, this design requirement is generally accepted nowadays as being realistic when allowance is made for the post-linear response of the structure. It is for this reason that both national and international codes have tended to encourage even the initial design in accordance with ultimate-strength concepts, the resulting structure then being subject to an elastic check to ascertain its serviceability. However, at present, such an approach is possible only in the course of design of individual members, and is further restricted to simple elements, predominantly those of the beam type.

In the specific instance of structural concrete, the case for bypassing the classical elastic working-stress approach is even stronger than, say, for other construction materials — such as, for example, steel — since the departure from linearity occurs at a relatively early stage. Unlike steel components, however, the attainment of the peak stress at a material level is followed by very rapid unloading and hence the implicit use of plasticity concepts in the ultimate-load design of concrete elements is questionable. Admittedly, such concepts often yield adequate predictions of 'standard' members at the structural level, especially when good design practice has ensured the achievement of the required degree of ductility. Nevertheless, one can find instances where existing methods of analysis and/or design fail to produce an accurate strength estimate even for what appear to be relatively simple element types. In this respect, code guidelines are especially relevant, for — leaving aside the need to observe a more flexible attitude between the use of elastic (or working-stress) calculations and their collapse-load counterparts (especially with regard to the variable relative importance of service and overload conditions) — there is the obvious question of how reliable the more specific code provisions are.¹

That some current code guidelines may be in gross error even in the case of elastic calculations can be illustrated by reference to Fig. 1, which shows the effective-width ratios (B/b) of flat-floor slabs under conditions of sway. The notion that a constant value of B/b is always applicable (0.5 or 1.0, depending on whether the British or American codes are invoked) is seen to be rather an oversimplification which, for the range of practical column sizes (u/a) and aspect ratios (b/a) could lead to errors of several orders

of magnitude, thus invalidating any subsequent lateral-frame type of analysis which, as is well known, is greatly affected by the stiffness of the horizontal member.² It is, therefore, not surprising that even larger errors might be inherent in ultimate-load predictions based on code clauses. For example, Fig. 2 contains the pertinent information on a T-beam for which the actual failure load is several orders of magnitude above those allowed by present code guidelines (for instance, in accordance with current American and British codes for structural concrete, the permissible loads (assuming a partial safety factor of 1) are only 13% and 19% respectively of the experimental value³). Conversely, Fig. 3 illustrates the overestimate of the true strength of a structural wall (the test result stems from reference 4) were this structure to be

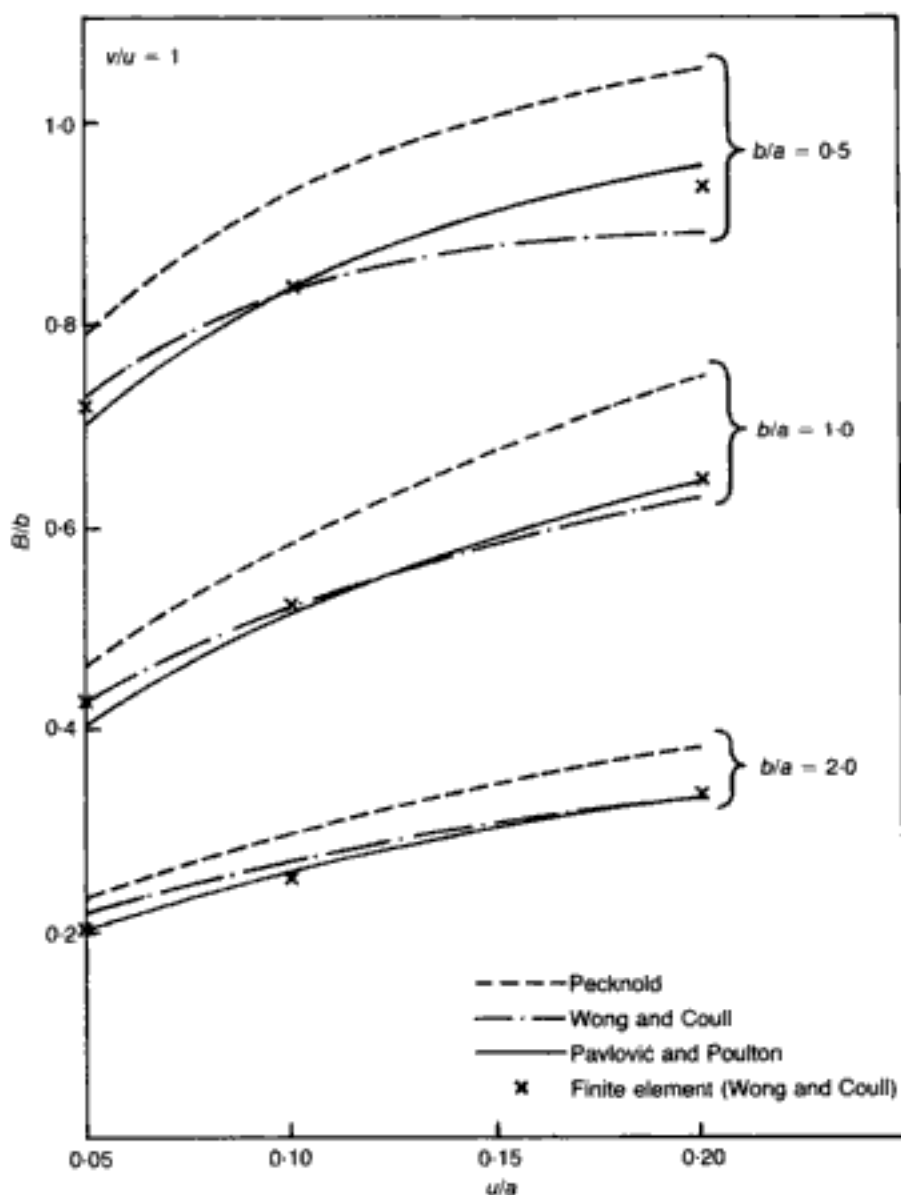


Fig. 1. Comparison of effective-width ratios for (elastic) flat slabs under lateral load for various computational techniques.² British and American code guidelines suggest constant values of 0.5 and 1.0 respectively

designed in accordance with widely accepted code tenets (an exception appears to be the method recommended in reference 5, but the latter, on the other hand, is far too conservative); the potential danger of adhering to these for such a component — particularly in the case of possible overloading such as, for example, seismic action — is evident. (The analytical predictions for both these structural elements are fully discussed in Chapters 3 and 4.)

In the case of ultimate-load predictions, code shortcomings such as the ones illustrated in Figs 2 and 3 arise because design rules are usually based either on empirical tests (which are then expressed in terms of concrete-strength values seen as descriptors of the material type used in these tests rather than as measures of fundamental material properties⁶), or on poor attempts at material modelling (relying here almost invariably on either plasticity or elastic concepts); what is required, clearly, is the need for proper constitutive and failure criteria even in the case of standard structural members. For complex elements, this need for a realistic description of material behaviour becomes more evident still, in particular when a reliable prediction of their failure load and mechanism requires such elements to be modelled as continua. By far the most popular numerical technique for the analysis of continua is, at present, the finite-element (FE) method. Despite the proliferation of FE packages, and the steadily increasing adoption of the technique for the solution of nonlinear structural problems, the FE method has not met, to date, with widespread success in the case of concrete structures. The main problem is the generally acknowledged lack of consistency in results between various structural forms (and, indeed, sometimes between components of the same type but differing in size and/or detailing). Therefore, even if a successful FE model is established for a given structural form, such a success is not automatically guaranteed for other types of structure. It would appear that there are two main reasons for this lack of reliability of the method when applied to concrete members: one of these is a direct consequence of unrealistic material description, as mentioned above; the other is essentially a computational problem that arises as a consequence of numerical instabilities associated with the cracking of concrete.

The present book aims at providing a generally reliable nonlinear FE model for concrete structures. The model attempts to remove the major pitfalls stated earlier; as such, emphasis is placed on the accurate description of material properties for concrete (some of which have long been known but have not been incorporated into structural design thinking^{7,6}) and on the control of potential numerical instabilities. While the resulting computer package has proved useful both as an analysis tool and for obtaining phenomenological insights into actual behaviour of structural concrete, a third dimension will be emphasized in this book, namely

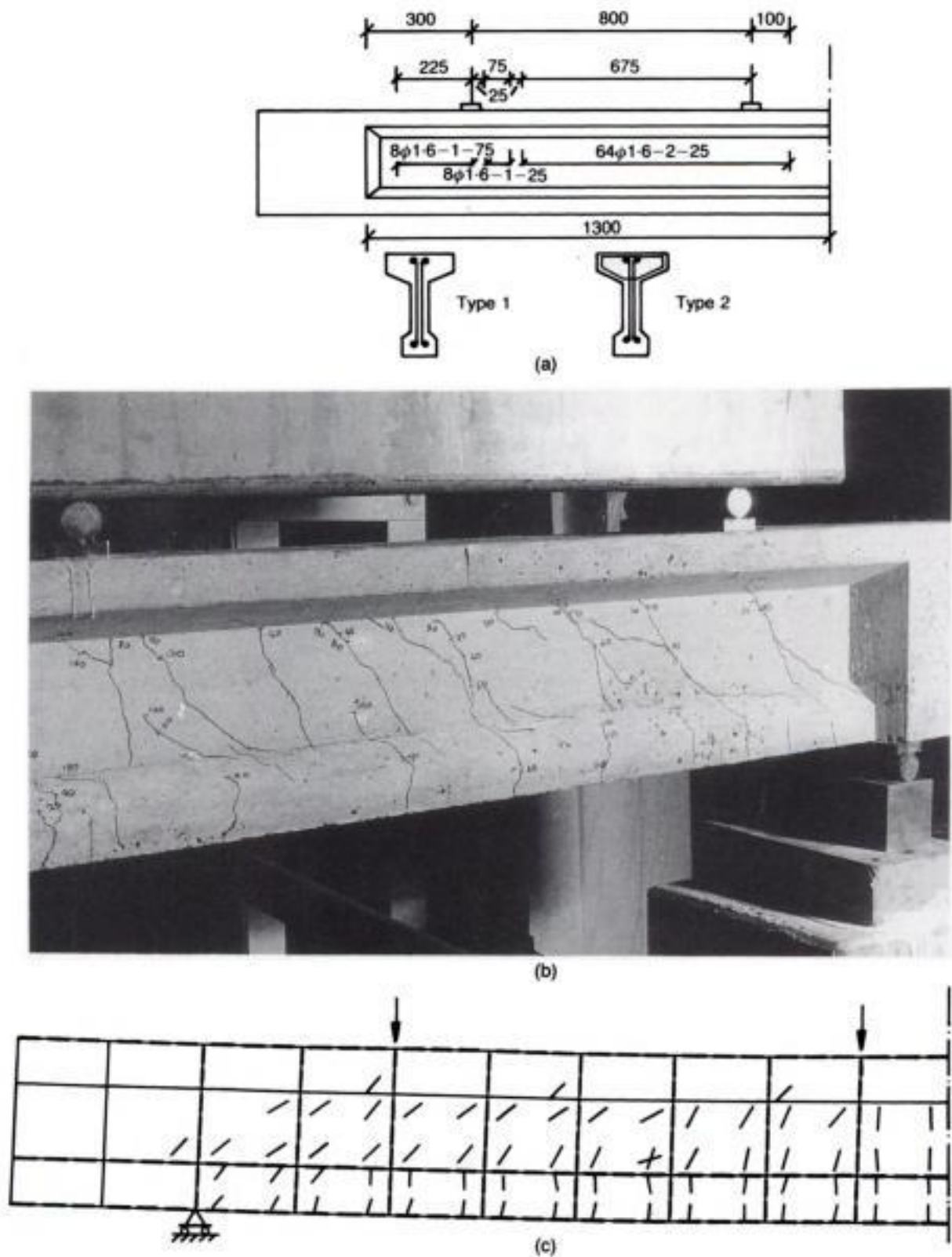


Fig. 2 (above and facing). Predicted and experimental behaviour of a member chosen from a series of T-beam tests:³ (a) design details (all dimensions in mm); (b) experimental crack pattern just prior to failure; (c) analytical crack pattern at failure; (d) load-deflection curves (note the large underestimate by code guidelines of both analytical (FE model) and experimental load-carrying capacities)

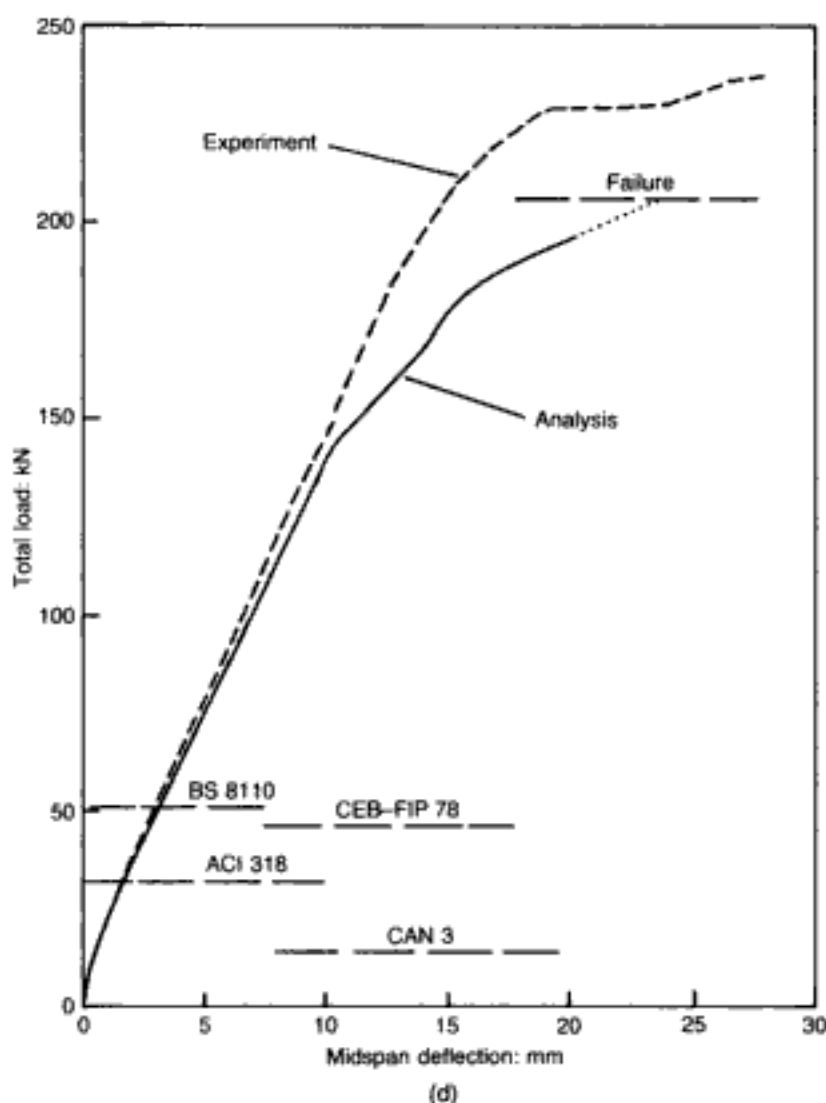


Fig. 2 — continued

the implications of the various results on current design philosophy. For this reason, the FE model will be simplified as far as possible, and this will be achieved by the inclusion in it of only those factors that are considered to play a key role in the response of concrete structures to applied loading, while secondary effects will be neglected. It will be seen that many of these simplifications are consistent with plain engineering 'commonsense' in respect of both design aims and computational efficiency.

The book is divided into four chapters. Chapter 1 presents the material modelling of concrete, while its incorporation, at the structural level, into the FE package is the subject of Chapter 2. The resulting nonlinear FE model is then applied to structures amenable to two-dimensional (2-D) representation (Chapter 3) as well as to the more general three-dimensional (3-D) structural problems (Chapter 4). Throughout the book, a wide range of examples of various structural forms will be studied, and these will be interspersed with relevant experimental evidence against which the accuracy and, indeed, the validity of the modelling are

to be gauged. Thus, existing data — including collapse load, deformational response and fracture processes — will be used to ascertain whether or not the FE package succeeds in giving sensible predictions of both the actual strength of the structure and the failure mechanism that leads to this ultimate load. Since often more detailed information on such mechanisms can be obtained from numerical

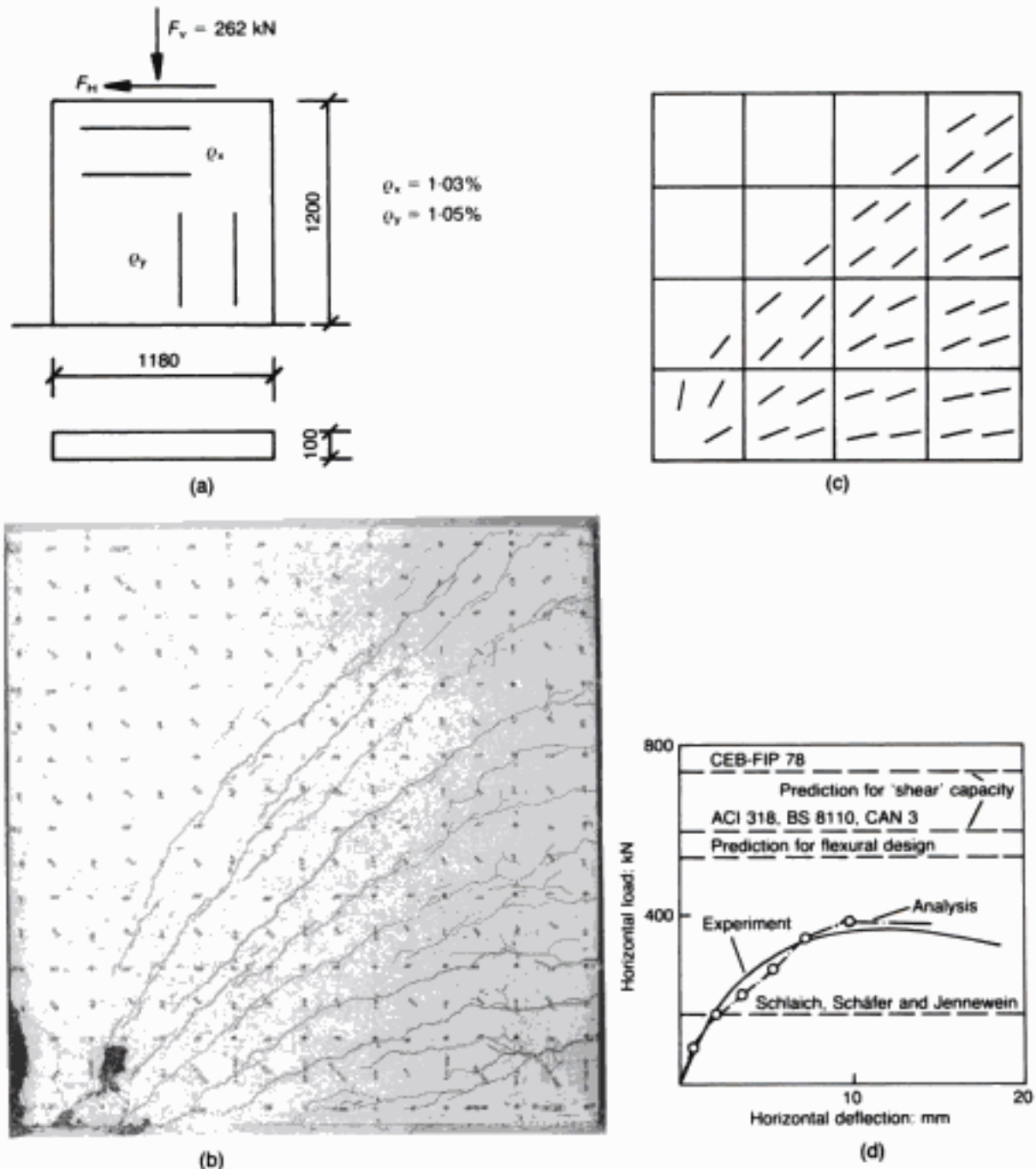


Fig. 3. Predicted and experimental behaviour of a member chosen from a series of structural-wall tests:⁴ (a) design details (all dimensions in mm); (b) experimental crack pattern at failure; (c) analytical crack pattern at failure (photograph provided by courtesy of Dr. J. Maier); (d) load-deflection curves (note the large overestimate by code guidelines of both analytical (FE model) and experimental load-carrying capacities)

modelling than from experimental testing (although the latter must always be resorted to as the ultimate means of checking any theoretical findings — especially if these are at odds with ‘current practice’), it is expected that the former will usually enable inferences to be made with regard to possible design improvements for the structural member in question.

1. Material modelling

1.1. Experimental data

1.1.1. Triaxial data and scatter

Material behaviour is, clearly, an important constituent of the overall input data required for the structural analysis of a continuum. This part of the input, however, is usually fairly straightforward as, for example, in isotropic elasticity or idealized elasto-plastic modelling. Such a cosy picture, however, no longer applies in the case of concrete structures: in these, a proper description of material behaviour turns out to be the key factor to their successful analysis and, moreover, is fraught with difficulties. Two main factors can be identified as the sources of such difficulties. The first of these is the necessity of obtaining triaxial material data, namely the material description should refer to the response of concrete under a generalized (i.e. three-dimensional) state of stress. The reason for this will become apparent throughout the present book but, at this stage, it is sufficient to say that, in a concrete structure, the effect of the smaller stress components need not itself be negligible in relation to that of the main stresses, even though the magnitude of the former could well be very small in comparison with the latter. Such conclusions, of course, are contrary to one's intuition and, indeed, experience with either elastic structures or elasto-plastic metal members (the latter, being usually thin, thus precluding the necessity of three-dimensional (3-D) and, sometimes, even two-dimensional (2-D) analysis). Concrete structures, on the other hand, not only require 2-D or 3-D modelling on account of their massive nature, but their strength is frequently governed by what are often considered to be negligible stresses acting orthogonally to the directions of the main stresses. Therefore, although experimental triaxial test data are both expensive and difficult to attain, it is evident that such information forms the prerequisite to a realistic modelling of concrete behaviour. The second source of difficulties associated with the establishing of actual properties of concrete materials relates to the scatter of available experimental results. Not surprisingly, this apparent discrepancy in the failure envelopes and constitutive relations obtained by the various laboratories and research groups working in this important field raises the question of whether or not a reliable model for concrete is at all possible, such that consistent and repeatable results might be obtained among a set of nominally-identical specimens.

In an attempt to resolve the problem of data scatter, an international cooperative project was set up, with subsequent publication of its findings on strength⁸ and constitutive response.⁹ In the recognition that the large scatter in past studies of the

response and strength of plain concrete under multiaxial stress states could be attributed to two principal factors — namely variation of the materials tested and variation in the test methods themselves — the cooperative study concentrated on eliminating at least the first of these factors. This was achieved through the use, by all participants of the joint programme, of specimens of the same concrete or mortar mix, cast and cured in one laboratory, shipped under controlled conditions and tested at identical age. On the other hand, these specimens were cast in the participants' own moulds and were tested in accordance to the different methods developed previously by the various laboratories. Thus the material-variability factor (which will be discussed later on, in section 1.4) was removed, and attention was focused on the effect of different test methods on the apparent material properties.

1.1.2. Test methods

The differences among test methods are predominantly a function of the specimen boundary conditions as imposed by the various types of loading system used. Typical loading systems, among which all major variants are represented, are shown schematically in Fig. 1.1, and also appear listed in Table 1.1. In this table, the laboratories which participated in the international cooperative programme referred to earlier are identified in column one by means of the following abbreviations: BAM — Bundesanstalt für Materialprüfung, Berlin, Germany; CU — University of Colorado, Boulder, Colorado, USA; ENEL — Ente Nazionale per l'Energia Elettrica, Milan, Italy; ICL — Imperial College of Science, Technology and Medicine, London, UK; NMSU — New Mexico State University, Las Cruces, New Mexico, USA; TUM — Institut für Massivbau, Technical University of Munich, Germany; UCD — University of California at Davis, California, USA. The different loading systems employed in the programme are specified in column two as follows: BR — brush-bearing platens; CYL — cylinder test; DP — dry or unlubricated metal platens; FC — fluid cushion; FP — steel piston—flexible cushion system used by BAM; LP — lubricated metal platens. The main characteristic variables of the different loading systems are as follows.

- (a) *Degree of normal boundary constraint in the direction of the applied load.* Rigid steel platens, causing uniform normal displacements but variable normal stresses, represent one extreme; fluid cushions, which are considered to ensure uniform normal stresses but permit variable normal displacements, provide the other extreme. Both of these limiting systems were represented in the cooperative study, along with various other devices that gave rise to intermediate degrees of normal boundary constraints (see Fig. 1.1).

The degree of constraint in the direction of the applied

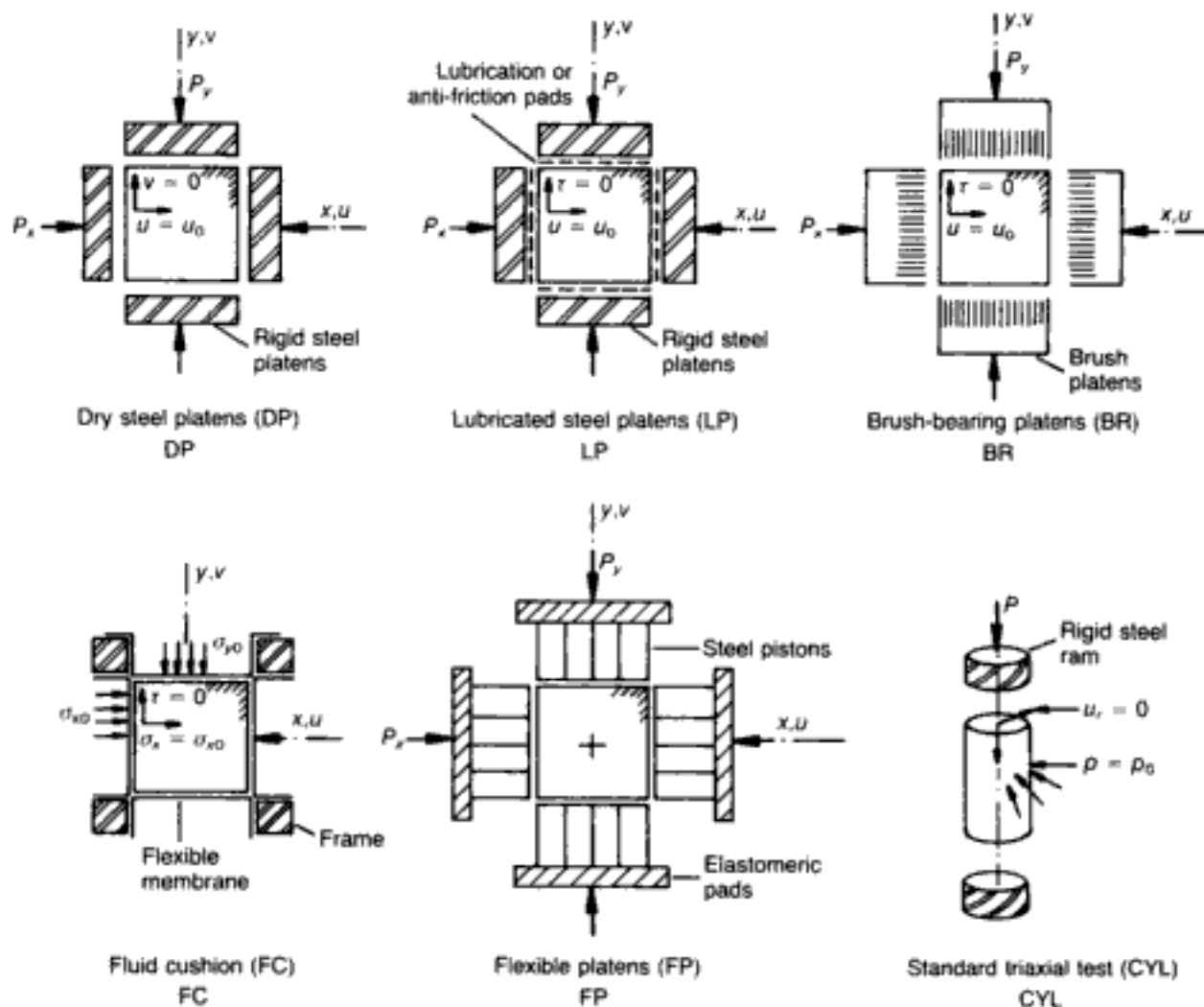


Fig. 1.1. Multiaxial test methods^{8,9}

load will lead to different observed specimen behaviour, especially when non-homogeneous materials — e.g. concrete — are tested. With uniform normal stresses, brittle failure may result when the strength of the weakest portion of the specimen surface is attained. With uniform normal strain, on the other hand, the possibility of stress redistribution may delay failure until the average strength of the specimen is reached.

- (b) *Degree of lateral boundary constraint on the plane of the boundary.* Fluid cushions may be considered sufficiently deformable so as to permit free lateral displacements, with consequent zero shear stresses on the surface. At the other extreme, rigid steel platens without surface lubrication give rise to sufficiently high friction so as to constrain the specimen boundary against lateral displacements, thereby leading to the maximum development of shear stresses on the surface. To reduce this friction, different methods of lubrication or brush-bearing platens are used, thus allowing

Table 1.1. Loading systems^{8,9}

Laboratory*	Boundary condition†	Specimen size	Description	Loading rate
BAM	DP FP	10 cm cubes 10 cm cubes	Unlubricated steel platens Cushion type system with 16 steel pistons 2.5 cm × 2.5 cm on elastomeric pad	Stress rate: Biaxial tests: 0.03 N/mm ² /s Triaxial tests: 0.075 N/mm ² /s
ENEL	DP LP	10 cm cubes 10 cm cubes	Unlubricated steel platens Lubricated steel platens (four polyethylene sheets with molybdenum sulfide grease)	Stress rate: Normally: 0.05 N/mm ² /s Series T8 and T9: 1 N/mm ² /s
	CYL	16 cm × 32 cm cylinders	Axial load through steel platens, confining pressure through membrane	
ICL	LP	10 in × 10 in × 4 in plates	Rigid steel platens with specimen surfaces treated with 'Feb-cure' curing membrane to minimize friction	Strain rate equivalent to 0.25 N/mm ² /s 2.0 ksi/min)
	CYL	4 in × 10 in cylinders	Axial load through steel platens, confining pressure through membrane	
TUM	BR	10 cm cubes	Brush-bearing platens (bristles 4 mm × 4 mm × 95 mm)	Strain rate: Biaxial: 0.003% o/s (0.2% o/min) Triaxial: 0.008–0.017% o/s (0.5%–1.0% o/min)
NMSU	DP LP	3 in cubes	Unlubricated steel platens Lubricated steel platens (two 4 mm polyethylene sheets with axle grease)	Stress rate: 0.35–0.60 N/mm ² /s (3–5 ksi/min)
UCD	DP LP	2 in cubes	Unlubricated aluminum platens Lubricated aluminum platens (one layer grease)	Strain rate: 0.35–0.55 N/mm ² /s (3.0–4.5 ksi/min)
	BR		Brush-bearing platens (bristle dia. 0.025 in, length 5/15 in)	
CU	DP FC	4 in cubes	Unlubricated steel platens Fluid cushion	Stress rate: 0.2 N/mm ² /s (0.2 ksi/min)

*The laboratories which participated in the international cooperative programme are:

BAM: Bundesanstalt für Materialprüfung, Berlin, Germany

CU: University of Colorado, Boulder, Colorado, USA

ENEL: Ente Nazionale per l'Energia Elettrica, Milan, Italy

ICL: Imperial College of Science, Technology and Medicine, London, UK

NMSU: New Mexico State University, Las Cruces, New Mexico, USA

TUM: Institut für Massivbau, Technical University of Munich, Germany

UCD: University of California at Davies, California, USA

†The different loading systems employed in the programme are:

BR: brush-bearing platens

CYL: cylinder test

DP: dry or unlubricated metal platens

FC: fluid cushion

FP: steel piston–flexible cushion system used by BAM

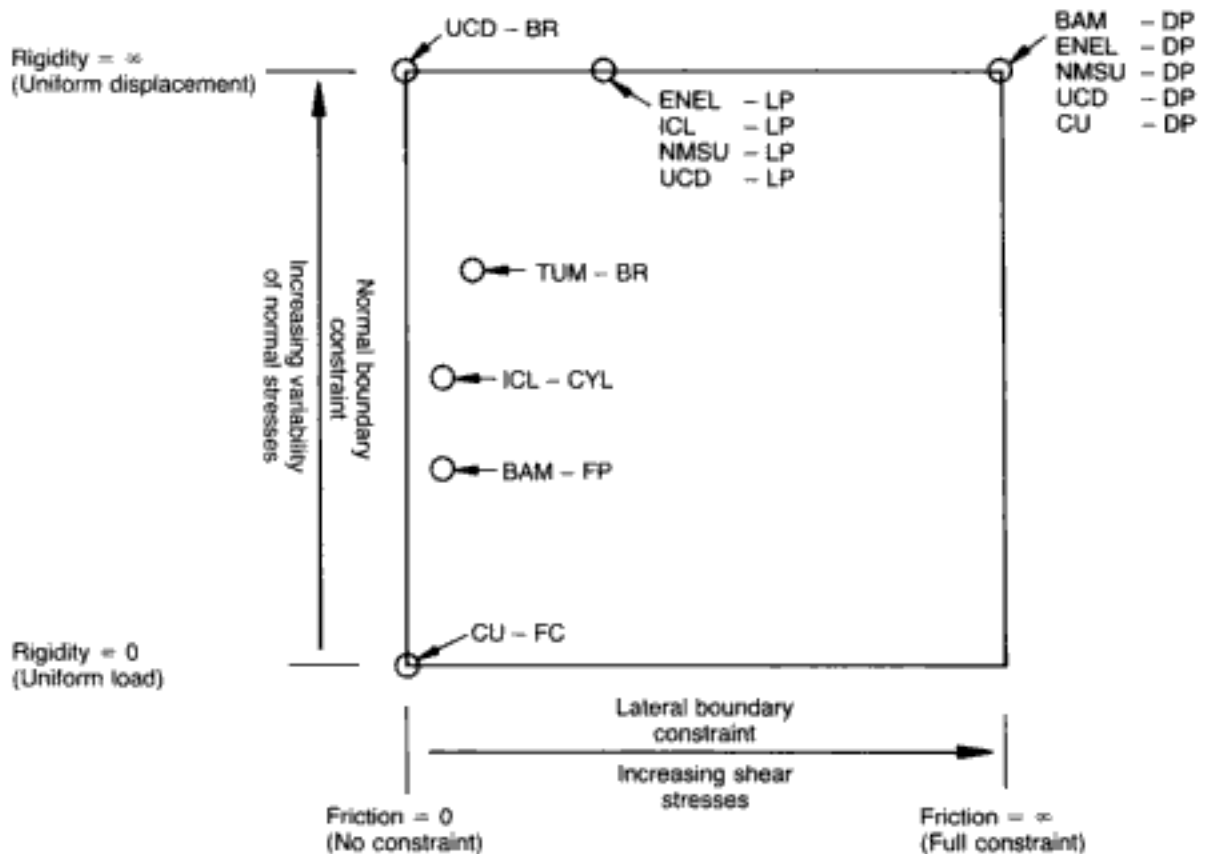
LP: lubricated metal platens

varying amounts of lateral movement to take place. Figure 1.1 depicts the systems used within the cooperative programme, which provided various degrees of lateral boundary constraint.

The actual degree of lateral boundary restraint can also affect the observed specimen behaviour. In the uniaxial compression test, the inward-directed shear stresses at the interface with the horizontal loading platens can result in what is essentially a confining pressure, thus leading to higher strength than would otherwise be obtained. (This is certainly true in the case of short specimens, while for slender cylinders — say, with a height-to-diameter ratio of 2 to 2.5 — such effects become negligible, a point which will be discussed subsequently.) An additional reinforcing effect may occur in biaxial and triaxial tests, when the confining pressure is not applied hydraulically but relies on rigid platens; then, vertical shear stresses transfer part of the vertical load from the specimens to the vertical loading platens (through friction) as a result of the relatively larger stiffness of the latter.

Fig. 1.2. A qualitative representation of boundary restraint conditions imposed by various loading techniques⁸

These observations can be summarized in a plot such as that shown in Fig. 1.2, in which the degree of normal constraint increases along one axis and that of the lateral constraint along



the other. Each test method can be entered qualitatively on such a plot. The actual location of each testing technique within the plot is, of course, open to discussion. For instance, it has been observed in the past that excessive lubrication of cube surfaces can, in fact, lead to outward-directed friction forces because of the squeezing out of lubricant; therefore, such cases should be indicated on the negative side of the axis marked 'lateral boundary constraint'. In the absence of more specific information, however, all lubricated specimens were lumped together as shown.

1.1.3. Strength data

The effect of testing methods on the compressive strength of a typical concrete as established from uniaxial, biaxial and triaxial tests is indicated in Figs 1.3, 1.4 and 1.5 respectively. In all cases, the data represent the mean of at least three values and it is apparent that they are significantly affected by the testing method used to obtain them.

1.1.3.1. Uniaxial tests

In Fig. 1.3, the uniaxial compressive strength is expressed in a dimensionless form by normalization of the strength values obtained in the various tests on cubes (f_{cube}) with respect to the cylinder strength (f_{cyl}) established from control tests. (The standard

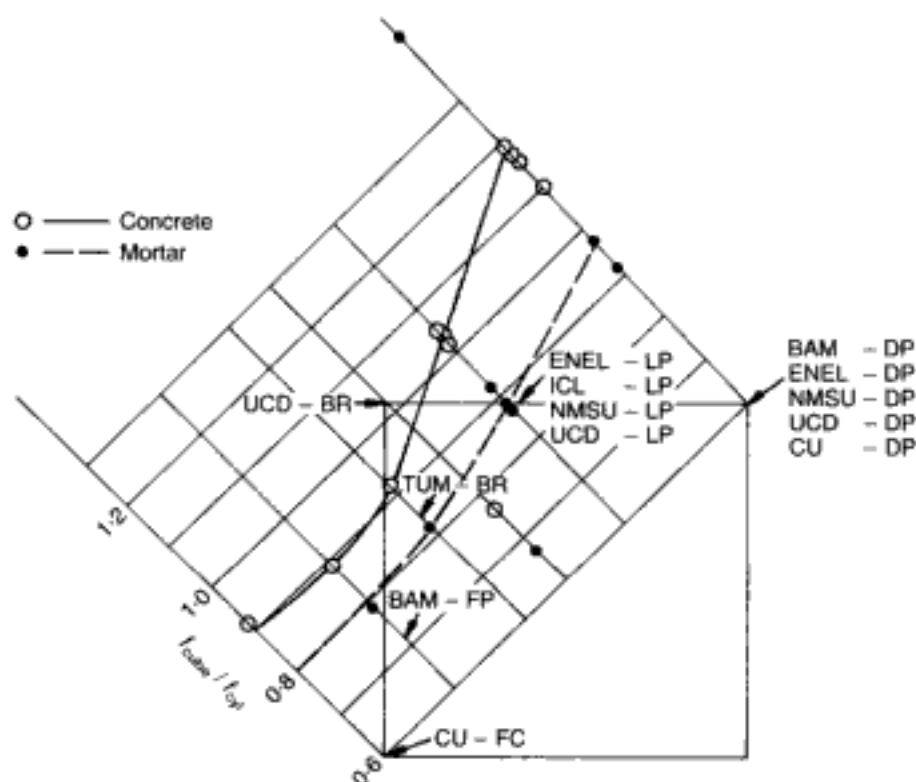


Fig. 1.3. Typical uniaxial strength data. Relation between strength properties (given as the ratio of cube and cylinder strengths) and specimen constraint (the latter, based on the superposition of the qualitative representation of Fig. 1.2, is indicated by the arrow)⁸

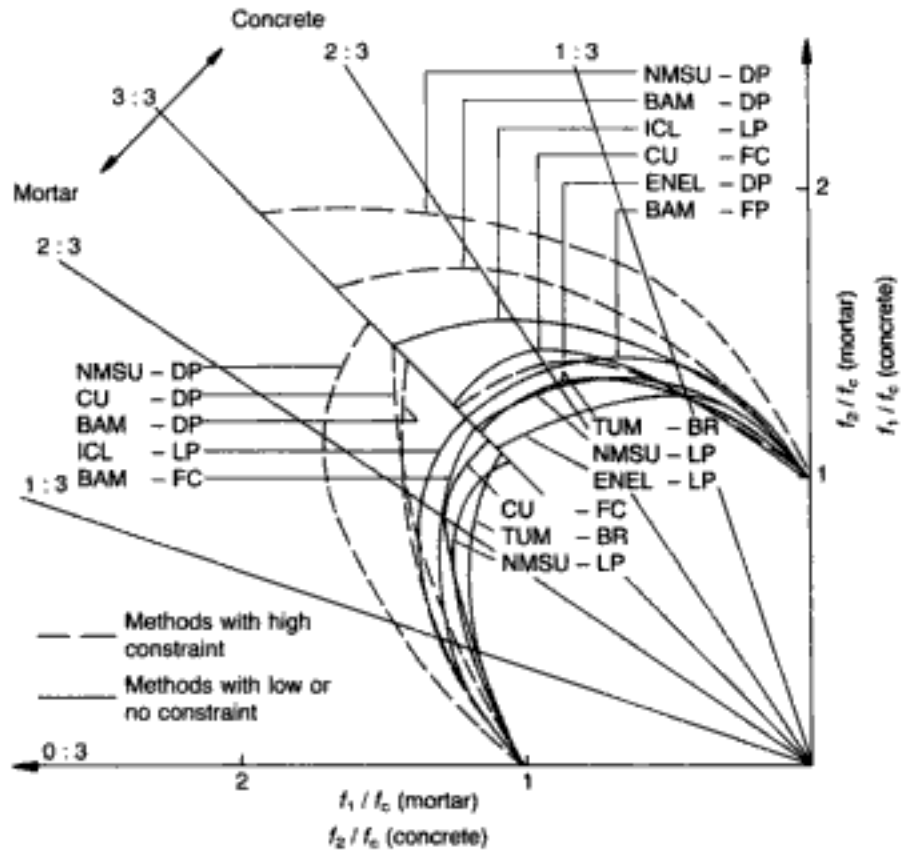


Fig. 1.4. Typical biaxial strength data. Normalized strength envelopes for mortar and concrete⁸

control test refers to a cylinder specimen with height-to-diameter ratio of 2:1 loaded uniaxially by means of rigid platens and with no attempt to reduce the resulting interface friction; experience has shown that, beyond this slenderness ratio, the cylinder strength becomes practically constant (thus, for example, the cylinder test CYL (ICL) uses a ratio of 2.5:1 irrespective of the actual boundary conditions at the loaded edges.) Admittedly, the results depicted in Fig. 1.3 are far from ideal since various factors combine to affect them, such as, for example, the relative sizes of cylinders and cubes, the shapes of the latter (some of these were not actual cubes but slabs/prisms), and especially the large scatter of the results due to some of the test methods used which illustrates how vital it is to ensure that a reliable testing technique be adopted. Nevertheless, the overall trend is correct, and one may even draw some more definite conclusions from this experimental evidence.

Since the height-to-width ratio of the cubes is 1:1, so that their strength is influenced by end conditions, it is evident from Fig. 1.3 that dry platens introduce a significant degree of frictional constraint leading to strength values which are about 17% higher than f_{cyl} . On the other hand, when this latter restraint is nearly eliminated by the use of lubricated platens, the strength values are only marginally above f_{cyl} (by about 3%). Such difference in behaviour suggests that the large lateral restraint on the specimen

produced by the 'dry' platens induces a triaxial state of compressive stress which, as will be discussed later, leads to higher strength; but when this restraint is removed, the reference cylinder strength is attained, irrespective of specimen shape and/or size. Of course, this assumes that the *relative* sizes of cylinder and cube were equivalent. In the tests, however, the size of the control cylinders used was smaller than the various cubes, introducing a size effect arising from the fact that a small concrete specimen is likely to have fewer weak points — and is, therefore, stronger — than a large one. Thus, for instance, as the lubrication could not fully eliminate frictional effects, the uniaxial strength of concrete cube specimens was enhanced, compensating for their inherently weaker nature relative to the smaller cylinders, with the net result that the $f_{\text{cube}}/f_{\text{cyl}}$ ratio approached 1. On the other hand, mortar specimens are less susceptible to boundary restraints,¹⁰ and hence such degree of compensation due to friction for the size effect cannot take place: this explains the value of $f_{\text{cube}}/f_{\text{cyl}} \sim 0.9$ in the case of the LP tests on mortar.

In contrast to the behaviour established by using the testing methods with dry or unlubricated metal platens (DP) and lubricated metal platens (LP), the strength values obtained by means of fluid cushions (FC) and flexible platens (FP) are consistently smaller (by about 10%) than the cylinder strength. A similar conclusion can be reached in the case of the brush-bearing platens (BR), although the actual values appear to depend on the design of the 'brushes' (on average, the loss in strength is of the order of 15%). The lower strength obtained by the methods employing flexible and brush platens may be considered to be attributable to the development of outward-directed friction caused by either the relatively large expansion of the elastomeric pad of the flexible platens or the lateral deflection of the brushes under increasing load (see Fig. 1.1). Such outward-directed friction induces lateral tensile stresses in the specimen which, as will be discussed later, reduce strength.

On the other hand, the lower strength values obtained by using fluid cushions may be explained by the theory of the 'weakest link': failure is considered to occur when the strength of the weakest portion on the surface of the specimen is attained, since the uniform normal boundary stress imposed by the fluid cushions does not allow stress redistribution to take place. However, in contrast to most of the other methods investigated in the cooperative project, it will be seen later that the use of fluid cushions yielded inconsistent results for the triaxial tests. While such inconsistency may be explained in terms of the 'weakest-link' theory, it may also be attributed to secondary testing-procedure effects which may not have been identified by the research workers who developed the technique.

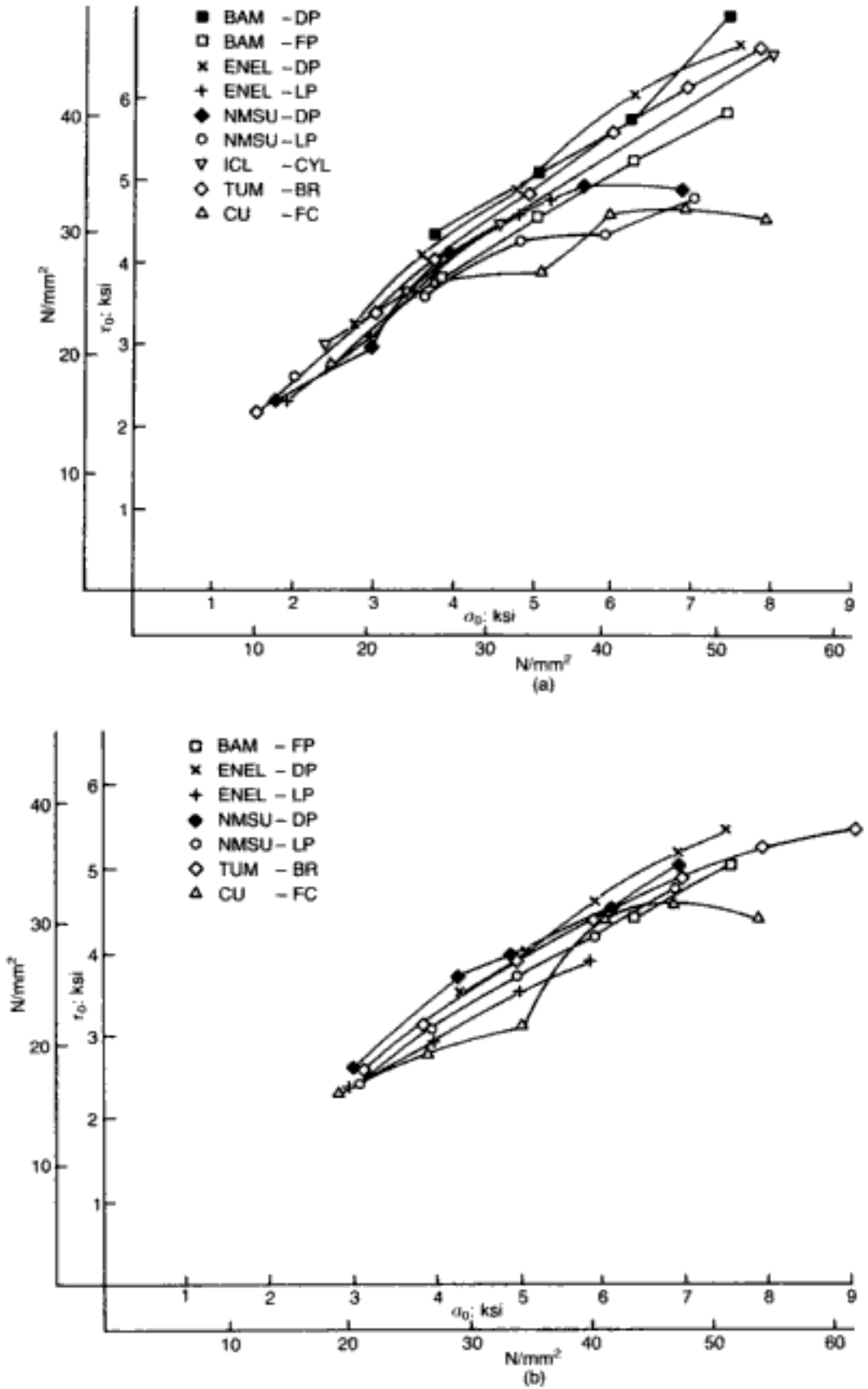


Fig. 1.5. (above and facing). Typical triaxial strength data:⁸ (a) path 1 ($\theta = 60^\circ$); (b) path 2 ($\theta = 30^\circ$); (c) path 3 ($\theta = 0^\circ$); (d) view on octahedral plane $\sigma_0 = 35 \text{ N/mm}^2$

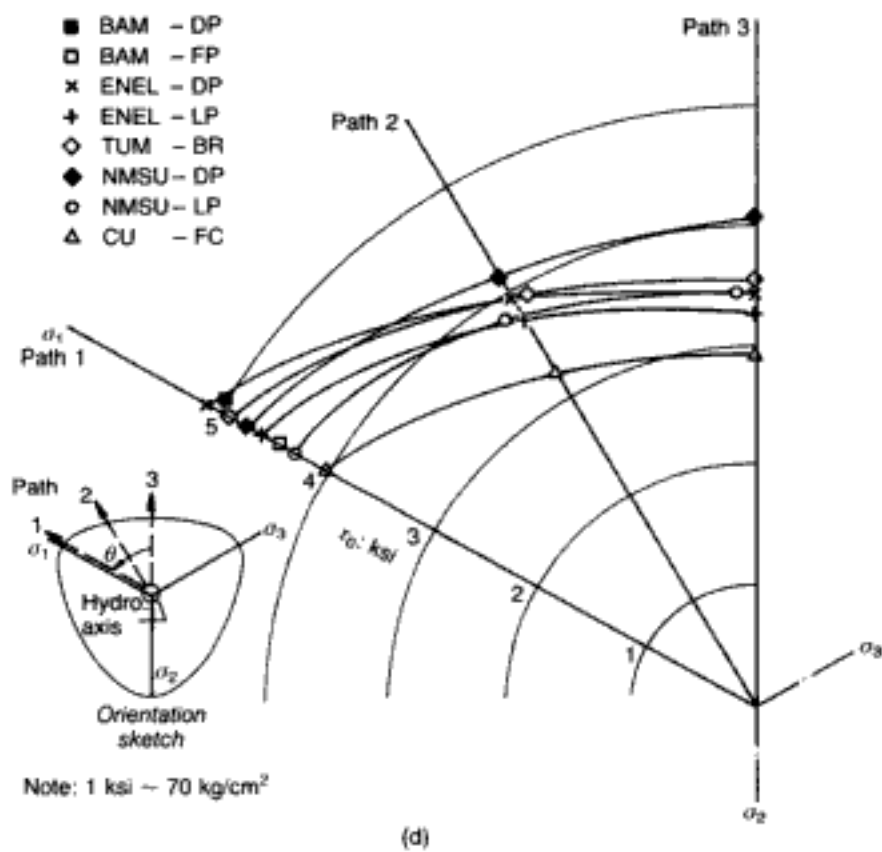
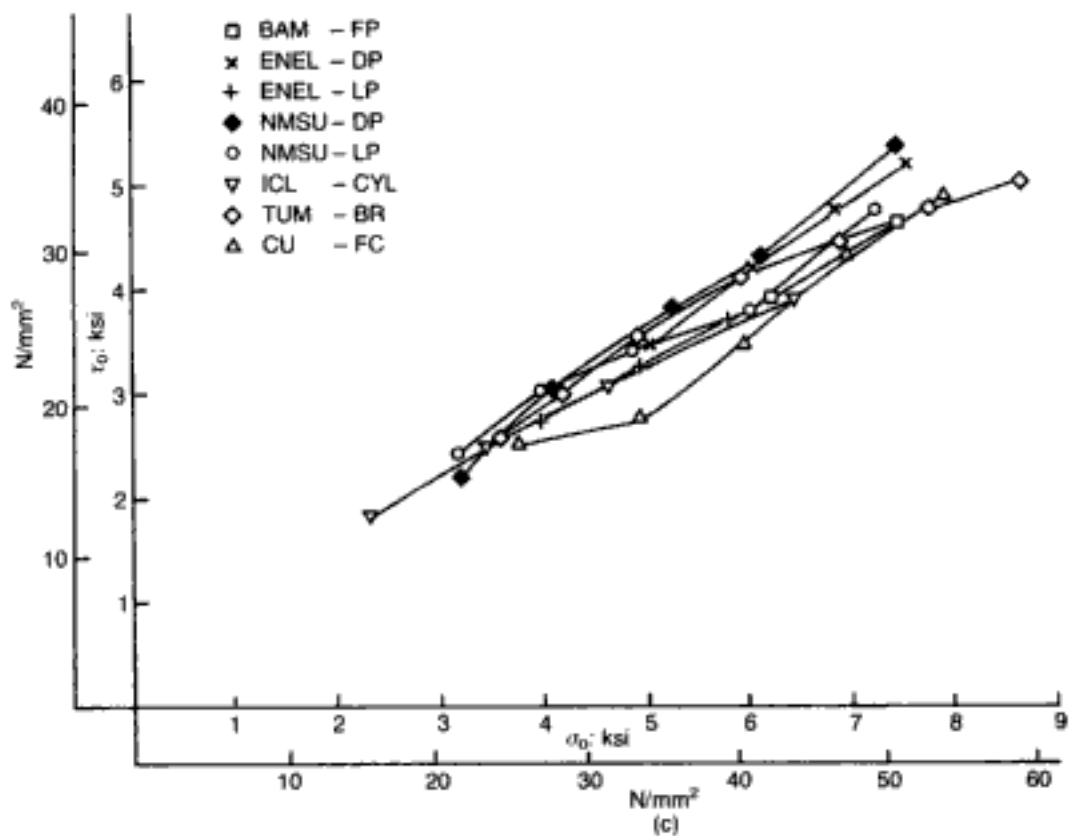


Fig. 1.5 — continued

1.1.3.2. Biaxial tests

Figure 1.4 contains the strength envelopes established from the biaxial tests for the same typical mixes. As for the uniaxial data, the strength values are expressed in a dimensionless form: this is done by dividing the combination of stresses causing failure (f_1, f_2) with the uniaxial compressive strength (f_c). The figure indicates that the dependence of the strength data on the testing method is more pronounced in the case of biaxial stress states. For example, the strength values obtained by using dry platens are significantly larger (in many cases by more than 50%) than those obtained by adopting lubricated platens. Once again, such differences in behaviour can be attributed only to the reduction of the lateral boundary constraint which is achieved by the use of lubricated platens. However, Fig. 1.4 also shows that the strength values obtained by using various types of lubricated platen exhibit significant systematic differences, and this is an indication of the varying degree of effectiveness in reducing lateral boundary restraint which characterizes the different lubricated platens used in the programme. It is interesting to note that the strength envelopes obtained by using flexible platens, brush platens and fluid cushions tend to cluster together around the lower-bound envelopes provided by some of the lubricated-platen results.

1.1.3.3. Triaxial tests

Figure 1.5 shows four views of typical strength envelopes which were constructed by using data obtained from the triaxial tests. The envelopes essentially represent intersections of strength surfaces in stress space with, for example, the plane which includes the space diagonal and one of the principal axes (Fig. 1.5(a)), a plane normal to the space diagonal (Fig. 1.5(d)), etc. All envelopes are expressed in terms of the octahedral normal (σ_0) and shear (τ_0) stresses and the rotational variable (θ). (These parameters will be discussed in more detail later in the chapter and are fully defined in Appendix A. It should be noted, however, that the sense of the angle θ in Fig. 1.5(d) is different from that adopted in Appendix A and, indeed, throughout the rest of the chapter. This is done in order to comply with the way in which the data in reference 8 have been presented. Figure 1.5(d) can be made compatible with the convention used in the remainder of the chapter by noting the six-fold symmetry of the failure surface (see section 1.4.2.1), and that the shorter path 3 represents triaxial 'extension' while the longer path 1 constitutes triaxial 'compression' (these terms will be defined subsequently).) The figures indicate that, as for the cases of uniaxial and biaxial states of stress, the use of lubricated platens yields smaller strength values than those obtained by means of dry platens; however, the differences in strength are not as pronounced as they are for the former cases. It can also be seen that, in contrast to the trends of behaviour

exhibited by the uniaxial and biaxial strength data, the use of flexible platens and brush platens leads to strength values which are not significantly different from those obtained by employing the dry platens and, in some cases, are larger than those resulting from the adoption of lubricated platens. It is also interesting to note that the use of fluid cushions yields a lower-bound strength envelope; however, since, unlike all other envelopes, its shape is distinctly irregular and does not conform with the generally accepted 'convexity rule'¹¹ (this appears to be consistently the case for all three loading paths — see Figs 1.5(a)–1.5(c)), it would appear that the reliability of triaxial data stemming from this technique is somewhat questionable.

1.1.3.4. Effect of testing technique on strength data

A general conclusion that may be drawn from the above discussion is that, although the testing methods used in the programme may induce a wide range of boundary conditions in the direction of the applied load, it would appear that it is the degree of lateral boundary constraint which develops at the interface between specimen and loading platens that has a key effect on strength values. This constraint develops as a result of the incompatible lateral deformation of the specimen and the loading platens, and gives rise to frictional stresses at the specimen boundaries. The frictional stresses cause a complex and indefinable state of stress which can be significantly different from the intended stress conditions.

One of the main objectives in developing a testing method for the investigation of the mechanical properties of concrete is to minimize, if not eliminate, the above frictional stresses and thus to create a definable state of stress in specimens. Although the various techniques used during the international cooperative project covered most methods developed, to that date, for testing concrete under different stress states, no attempt was made at the time to identify those methods which essentially achieve the above objective. What is clear, however, is that those investigations which adopt lubricated platens do appear to provide identifiable stress states. Although such frictionless boundary conditions would seem to be especially important in conducting biaxial tests, while being apparently less critical in the case of triaxial tests, it should be stated that the use of octahedral shear (or deviatoric) and normal (or hydrostatic) stresses for representing strength data has the effect of producing a tight cluster of octahedral failure stresses even when the corresponding set of principal stresses exhibits a wide range of scatter; this is the main reason for the apparent relative insensitivity of the triaxial test data of Fig. 1.5 to testing techniques, and a similar clustering trend would be obtained if the biaxial strength data were replotted in terms of octahedral stresses.⁸

With regard to the most widely employed type of concrete testing,

namely the uniaxial test, the effect of end friction is important for short specimens, but practically disappears when the height-to-width ratio exceeds 2. Thus the standard cylinder test provides reliable uniaxial strength estimates despite the lack of special provisions for eliminating end effects. Moreover, such cylinder geometries that do not fall below an aspect ratio of 2 can also be employed with confidence in the obtainment of triaxial data. It is for this reason that the triaxial cell developed by one of the participants of the cooperative programme (ICL), where dry platens at the cylinder ends are combined with hydraulically-controlled loading on the curved edges, provides a simple and dependable technique for gathering triaxial strength data. (Although the device is capable of reproducing only axisymmetric loading cases, such a limitation does not pose a practical problem for reasons which will be outlined later.)

Finally, it should again be emphasized that the aim of the cooperative project, described in the foregoing, was to investigate the effect of the testing technique on the strength-data scatter. The effect on this scatter of the material-variability factor will be discussed later in the chapter, when the data obtained by means of one of the reliable testing methods are presented.

1.1.4. *Constitutive- relations data*

The stress(σ)—strain(ϵ) relationships for concrete are generally considered to comprise ascending and gradually descending branches. However, in view of the difficulties associated with establishing experimentally the descending branches under generalized stress, the cooperative programme's investigation of the effect of testing methods on deformation has been based on a comparative study of the ascending branches established by using the testing methods described in Table 1. (The relevance of the σ — ϵ characteristics beyond the point of maximum attained strength will be discussed in section 1.2.)

A convenient and widely used method for representing the σ — ϵ data is to express the latter in terms of hydrostatic and deviatoric stress and strain components. In such a form of representation, the deformational behaviour of concrete under any state of stress is defined fully by the hydrostatic stress—volumetric strain, the deviatoric stress—deviatoric strain, and the deviatoric stress—volumetric strain relationships. (It has been established that a hydrostatic stress state has negligible effect on deviatoric strains,¹² as will be discussed more fully in section 1.4.1.) These relationships for the typical concrete investigated in the cooperative project are shown in Figs 1.6, 1.7 and 1.8 respectively. The figures include only such information as was obtained by using the testing methods in which an attempt was made to reduce the lateral boundary constraint; hence, the results derived by means of dry platens do not appear in the figures.

It is evident that, with the exception of the three stress—strain

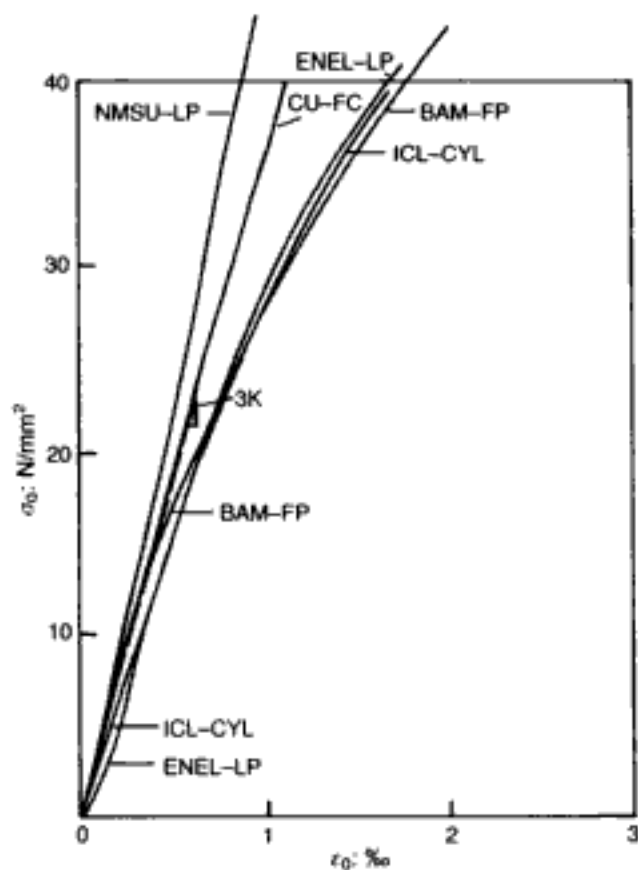


Fig. 1.6. Typical mean volumetric stress-strain curves established from triaxial tests⁹

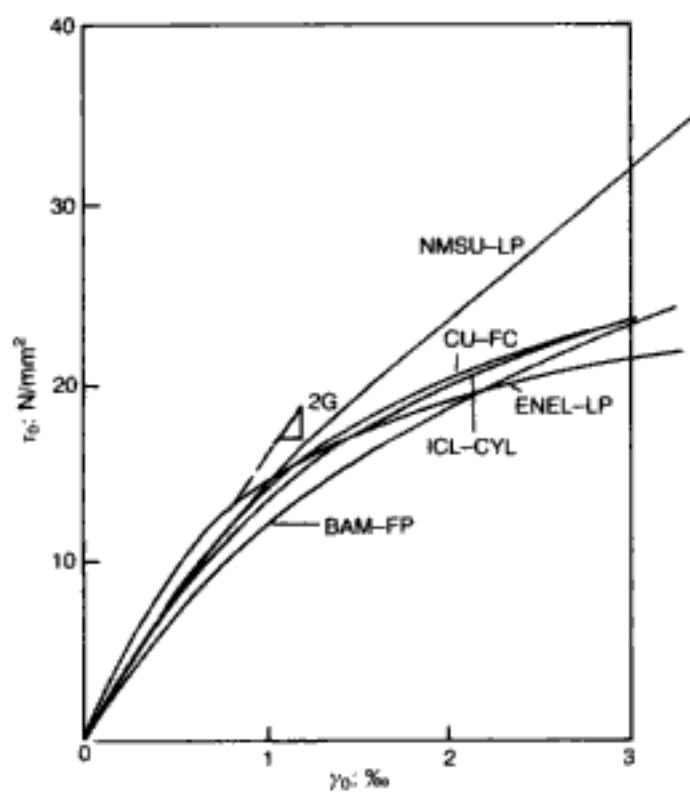


Fig. 1.7. Typical mean deviatoric stress-strain curves established from triaxial tests⁹

relationships obtained by using one type of lubricated platen and the hydrostatic stress–volumetric strain relationships obtained by means of fluid cushions, the constitutive relations stemming from the various tests do not appear to be significantly affected by the type of testing method. Such a result suggests that the different testing techniques which were employed to derive the above relationships (i.e. those using either flexible or lubricated platens, or relying on (slender) cylindrical specimens) are likely to subject the specimens to a *definable* state of stress, thus fulfilling the main objective of a test method. It should be emphasized that this conclusion is valid even though the information presented in Figs 1.6–1.8 has been plotted in terms of octahedral stresses and strains, a choice which was shown earlier (see section 1.1.3.4) to lead to a clustering of results. (One of the advantages of adopting an octahedral stress–strain representation is the applicability of the ensuing relations to express uniaxial, biaxial and triaxial concrete behaviour.⁹)

1.1.5. Choice of testing technique for the generation of material data

A comparison of results stemming from the cooperative project described in the previous sections indicates that much of the scatter in the material data for concrete is a direct result of the variation in test methods. Several of the existing techniques do not always ensure that the actual applied load is that which is intended. On the other hand, the cooperative programme has shown that the testing techniques used by certain research institutions are, in fact, capable of inducing definable states of stress in the specimens.

Among the latter reliable methods of testing, one should mention that used by ICL, which, as stated earlier, employs cylinders with a height-to-diameter ratio of 2.5:1. Its success and relative simplicity in providing realistic data on strength envelopes and

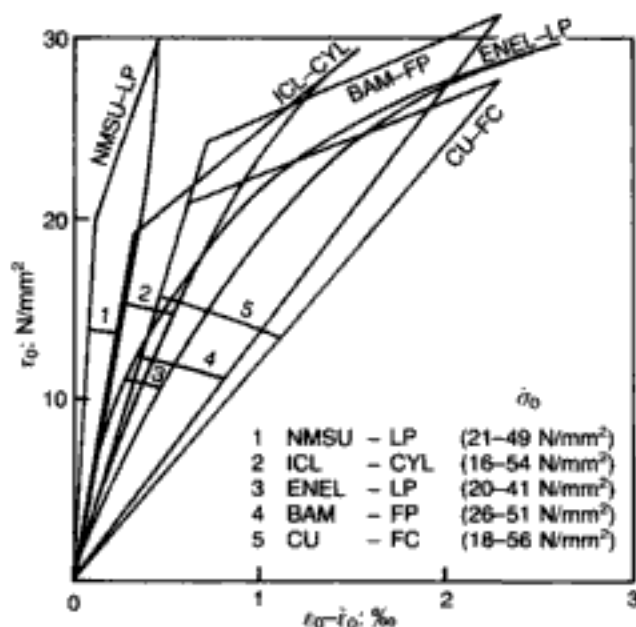


Fig. 1.8. Typical mean deviatoric stress–volumetric strain curves established from triaxial tests⁹

on constitutive relations within the region of the ascending branch, for both uniaxial and triaxial conditions, make it an attractive way of gathering the necessary data for various concrete types under different stress conditions. (The fact that the intermediate stress always coincides with either the maximum or the minimum principal stress value is not, in practical terms, a limitation, for reasons to be discussed later.) This is true despite the presence of dry platens since, as pointed out earlier, the slenderness of the specimen used ensures that the end effects play an insignificant role on strength and on the stress-strain law up to this peak level of sustained load. What happens to the descending branch of the constitutive relations is discussed in the next section.

1.2. Behaviour of concrete at failure

It is a widely held view that, beyond ultimate strength, the load-carrying capacity of concrete under a compressive state of stress is reduced *progressively* with increasing deformation. This view is supported by experimental evidence obtained from tests carried out using techniques which are generally considered to induce definable states of stress in specimens, and hence may be considered to be reliable. Such evidence indicates that the deformational response of specimens under a compressive load exhibits a trend similar to that of a typical uniaxial or triaxial stress-strain set of relationships, of the type shown in Fig. 1.9,^{13,14} each of which consists of an ascending and a *gradually* descending portion. The latter portion is usually referred to as the 'softening' branch and is deemed to indicate a certain degree of ductility at the material level.

However, a characteristic feature of the relationships of Fig. 1.9 is that, for stress levels beyond ultimate strength, the tensile strain increases at a rate which is very much higher than that of the compressive strain.¹⁵ Poisson's ratio values, which describe such behaviour, may vary from a value of approximately 1 at the ultimate strength level to values as large as 10 for stress levels beyond ultimate strength.¹⁴ Now, it should be recalled that an isotropic continuum (which concrete is assumed to be throughout the whole range of testing) cannot exhibit Poisson's ratio values in excess of 0.5. In fact, this is implicit in the design of the testing devices used to obtain the stress-strain relations such as those shown in Fig. 1.9. Therefore, existing testing techniques assume that the deformational behaviour of concrete is compatible with that of a continuous medium up to and beyond the maximum sustained load. There is a historical justification for such an assumption, in the sense that the various test methods were devised originally with the aim of obtaining reasonably accurate estimates of the strength of concrete. In this respect, loading devices such as brush and flexible platens are considered to induce negligible frictional restraint at the specimen-platen interfaces when designed to allow displacements in the direction orthogonal to loading compatible

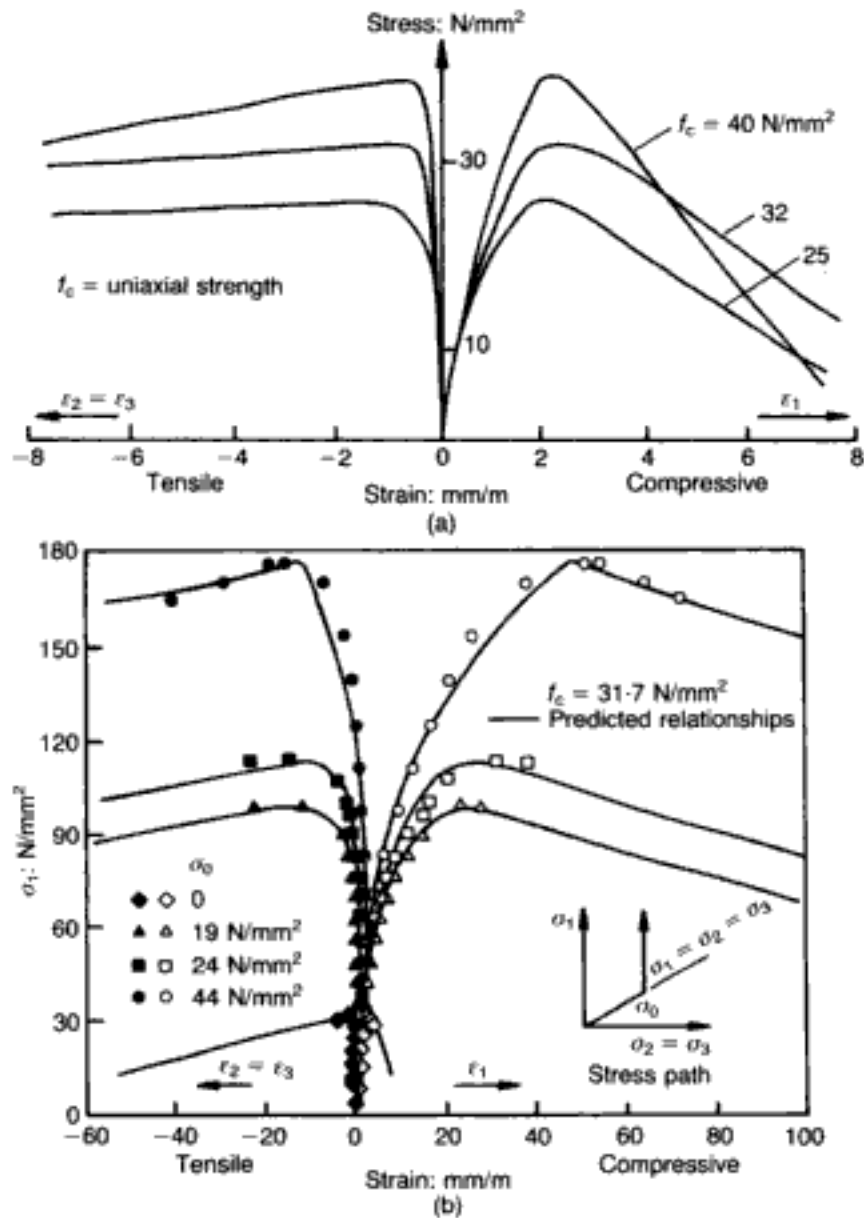


Fig. 1.9. Typical stress-strain relationships for concretes obtained from tests on cylinders.^{13,14} (a) various concretes under uniaxial compression; (b) given concrete (with $f_c = 31.7 \text{ N/mm}^2$) under triaxial compression for various values of hydrostatic stress σ_0

with tensile strains calculated on the basis of Poisson's ratio values up to 0.5. Now, as shown in Fig. 1.10, such values characterize concrete behaviour up to a level close to, but not beyond, ultimate strength. Therefore, it is evident that, as the ultimate load is approached, and Poisson's ratio becomes increasingly large, the concrete specimen is no longer a continuum but is beginning to be affected markedly by internal fracture processes. Despite this, an *average* load-deformation path can still be recorded for the specimen as a whole, and this implies that considerable frictional restraint between platen and specimen must, at these late stages of the deformational response, come into effect.

The importance of frictional forces between specimen and machine has been recognized at least as early as 1882, when Mohr criticized Bauschinger's results of compression tests made with cubic specimens, on the grounds that the friction on the cube

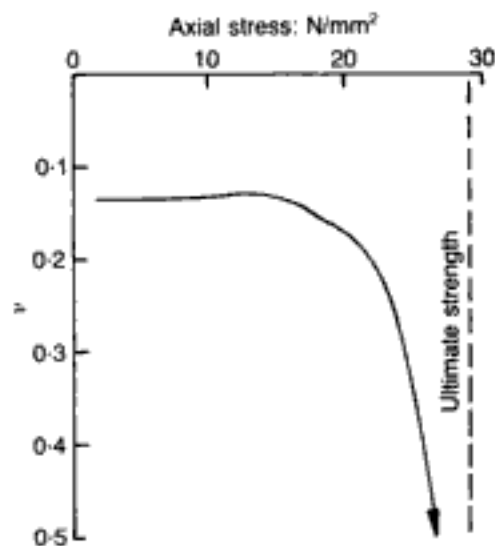


Fig. 1.10. Typical variation of Poisson's ratio with increasing stress obtained from tests on cylinders under uniaxial compression¹⁴

surfaces in contact with the machine test-plates: 'must have a great effect upon the stress distribution so that the results are not those of a simple compression test'.⁷ Similar observations regarding the importance of interface frictional forces were made by Föppl when working with cubic specimens of cement; he explored various ways of reducing such effects, showing that the usual tests of cubic specimens give exaggerated values for the compressive strength of the material.⁷ As mentioned earlier, most of the attempts by subsequent investigators to eliminate frictional effects between specimen and machine were aimed at obtaining realistic *strength* values. In addition to reducing these friction forces to varying extents, experimentalists also increased the aspect ratio of specimens (i.e. the length to cross-sectional dimensions ratio) in order to minimize end effects. As pointed out above, all these measures seem to have been successful in terms of strength-data accuracy (a typical example being the cylinder test mentioned in section 1.1.5). On the other hand, the large deviation of the measured values of Poisson's ratio (i.e. $\nu \gg 1$) from their assumed counterparts (i.e. $\nu < 0.5$ — used to design the experimental set-up that would minimize end restraint) at load levels beyond ultimate strength indicates that the post-ultimate tensile deformation of the specimens in the direction orthogonal to that of the maximum applied compressive load (see Fig. 1.9) is, in fact, significantly affected by the end restraint provided by the testing device, and that the experimental set-up cannot fulfil its objective of eliminating end friction. Clearly, the actual behaviour of a concrete specimen in uniaxial compression as the peak load is approached (and beyond) can be obtained only if the frictional effects are truly eliminated. One such investigation was successfully undertaken in order to assess the effect that reduction — and eventual removal — of the end friction would have on existing uniaxial-compression data on (a) ultimate strength and (b) post-ultimate characteristics.¹⁴ Its findings are outlined in the next section.

1.2.1. Uniaxial compression tests

1.2.1.1. Behaviour of a test specimen under compressive load
 Complete stress–strain relationships for concrete under uniaxial compression have been obtained to date by loading cylinders at a constant rate of displacement through a ‘stiff’ testing machine either by using a loading system capable of releasing almost instantaneously any load in excess of that which can be sustained by the specimen at any time¹⁶ or by loading a steel specimen in parallel with the concrete specimen in a manner such that, as the load-carrying capacity of the concrete beyond ultimate strength is reduced, the concrete–steel system transfers the excess load from the concrete to the steel to maintain the internal equilibrium of the overall system.¹⁷ Such relationships describe the response of the central zone of the cylinders, which is generally accepted to be subjected to a near-uniform *uniaxial* compressive stress in contrast to the complex and *indefinable* compressive stress state imposed on the end zones by frictional restraints resulting from the interaction between specimen and loading device (see Fig. 1.11).

At a load level close to the maximum load-carrying capacity of the specimens, cracks aligned in the direction of loading appear in the central zone, and the maximum load-carrying capacity is reached when the ultimate strength of this zone is attained. At this stage, the end zones remain stressed below their ultimate strength

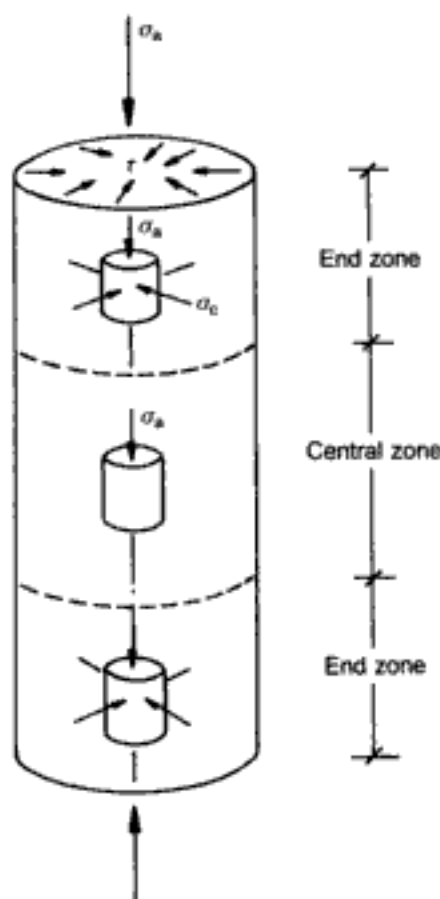


Fig. 1.11. Schematic representation of the effect of boundary frictional restraint (r) on the state of stress within cylinders under uniaxial compression (σ_a)¹⁴

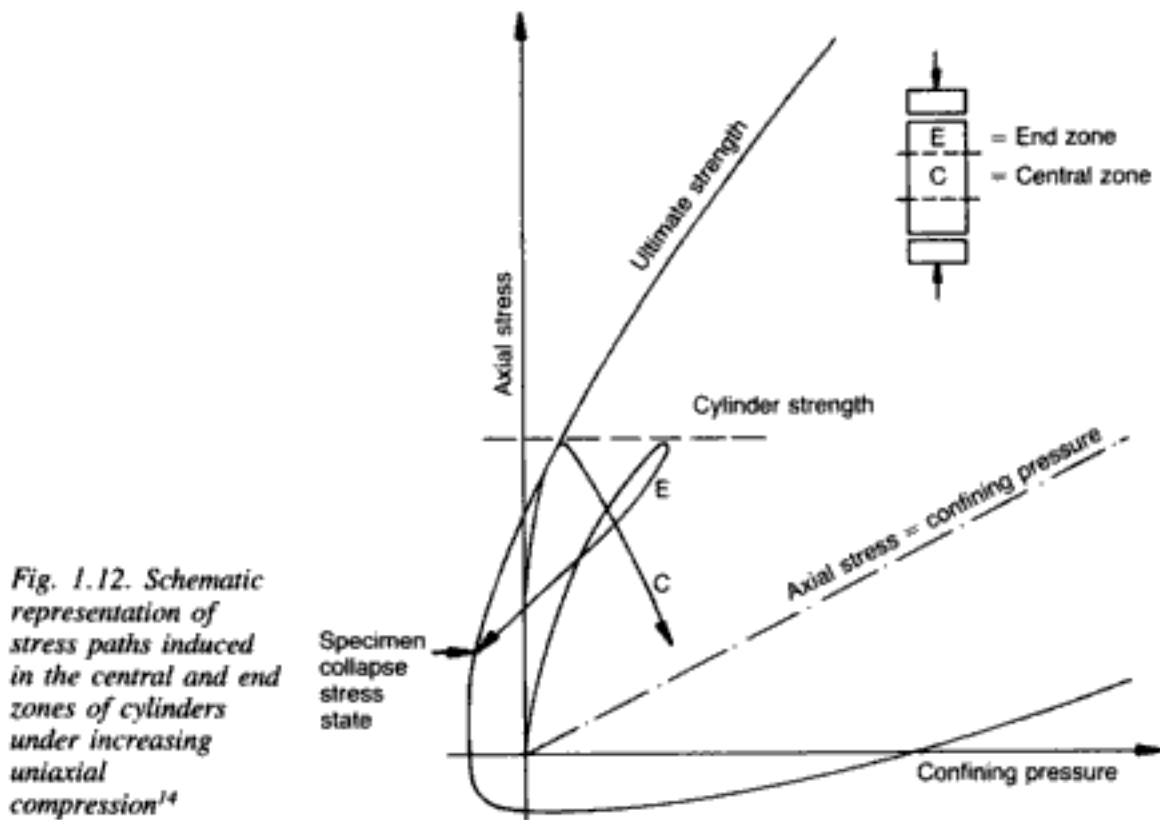


Fig. 1.12. Schematic representation of stress paths induced in the central and end zones of cylinders under increasing uniaxial compression¹⁴

capacity on account of the confining (triaxial) stress state (see Fig. 1.12), without suffering any visible cracking.

The voids caused by the cracks of the central zone result in a dramatic increase of the lateral expansion of the zone which is incompatible with the much smaller lateral expansion of the 'uncracked' end zones. This incompatibility gives rise to *internal* forces acting so as to (a) *restrain* the lateral expansion of the central zone and (b) *increase* the lateral expansion of the end zones (see Fig. 1.13). With increasing deformation, the internal forces acting on the end zones progressively reduce the effects of boundary frictional restraints and eventually create a state of stress in the end zone with at least one of the principal stress components tensile (see Fig. 1.12). When the ultimate strength of the end zones is attained, the cracks of the central portion propagate into the ends of the specimen, and the latter collapse under an applied load which induces, in the end regions, a state of stress similar to that indicated in Fig. 1.12.

It appears from the above, therefore, that the post-ultimate stress-strain relationships obtained from the tests describe behaviour under a *complex and indefinable* state of stress which is clearly induced by the frictional restraint (developing under increasing load) at the specimen-loading device interfaces. It therefore seems that the only reason for the central zone of the specimen to respond as a unit during the post-ultimate stage is the restraining action of the end zones. This suggests that, if the state

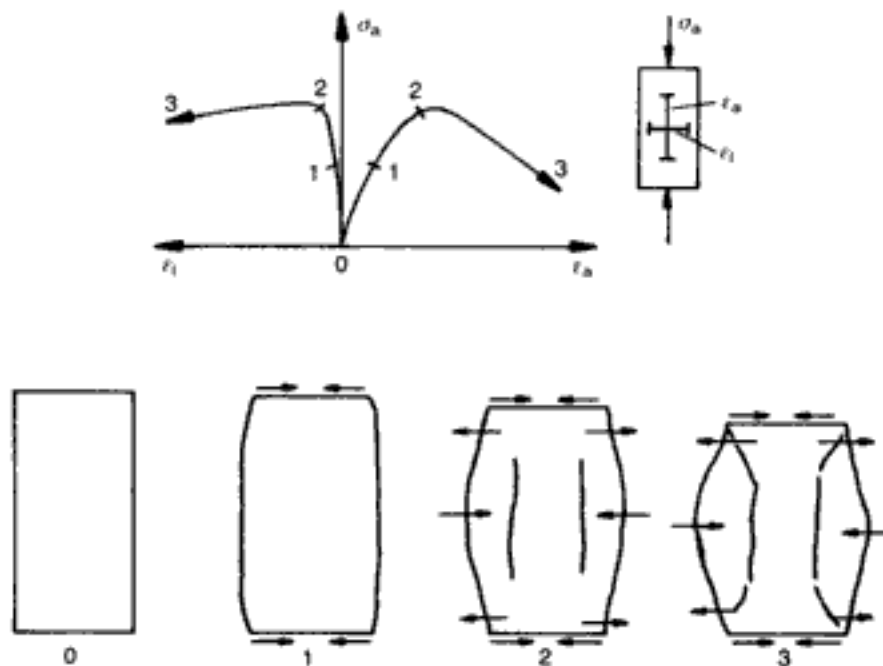


Fig. 1.13. Stages of behaviour of concrete cylinders under increasing uniaxial compression¹⁴

of stress were the same throughout the specimen, no such restraining action would exist and the specimen would completely collapse as a result of the formation of continuous cracks at the ultimate strength level. It is considered realistic to propose, therefore, that concrete suffers a complete and immediate loss of its load-carrying capacity when ultimate strength is exceeded. Clearly, such a proposal implies that, while the end restraints affect the post-ultimate deformational response of concrete specimens, they have little influence on the maximum recorded load level since overall collapse immediately follows the onset of cracking in the central zone.

1.2.1.2. Experimental evidence for the brittle nature of concrete

An unequivocal experimental proof of the validity of the proposed behaviour of concrete can be obtained only by using testing techniques which eliminate completely any frictional restraint on the specimen—testing device interfaces. Although this is unlikely to be achieved by using existing testing techniques, an indication of the effect of frictional restraint on post-ultimate deformation can be obtained from uniaxial compression tests by employing testing devices which induce varying degrees of boundary frictional restraint on the specimens.

For this purpose, an experimental programme was carried out¹⁴ which involved the testing of two types of specimen: 250 mm height \times 100 mm diameter cylinders and 100 mm cubes. Two mixes were used, the strength of which at the time of testing were: for the cylinders, 50.0 N/mm² (Mix 1) and 29.0 N/mm² (Mix 2); for the cubes, 60.0 N/mm² (Mix 1) and 37.7 N/mm² (Mix 2).

The specimens were subjected to varying degrees of frictional restraint across their loaded surfaces. This was achieved by placing various types of 'anti-friction' media between the specimen and hardened steel subsidiary load platens, the latter having a thickness of 25.4 mm and the same cross-sectional dimensions as the nominal cross-section of the specimens tested. Three cylinders and three cubes, from each of the two concrete mixes used, were tested for every one of the following anti-friction media:

- (a) a layer of *synthetic rubber* (neoprene) 0.45 mm thick
- (b) an *MGA pad* consisting of: 0.008 mm thick hardened aluminium steel placed adjacent to the specimen; Moly slip grease (containing 3% MoS₂); and a Melinex polyester film, gauge 100, placed against the steel platen. (The higher-strength concrete specimens were tested by using previously-unused MGA pads; the same pads were then used to test the lower-strength concrete specimens.)
- (c) a *brush platen* developed by splitting a steel platen longitudinally and transversely to form a large number of individual 'bristles'
- (d) no 'anti-friction' medium, i.e. plain steel platens
- (e) in addition to the above techniques, three cylinders made of the higher-strength concrete were subjected to an *active* restraint induced by 'Hi-Torque' hose clamps placed at a distance of 3 mm from the loaded surfaces and tightened by a small torque load of 1000 Nmm.

For the cubes, only the strength was determined, while for the cylinders both strength and deformational response were established. The complete deformational behaviour was measured within the central zone of the cylinders by attaching 60 mm electrical resistance strain gauges in the axial and circumferential directions. Two gauges placed diametrically opposite each other were used for each direction. The overall axial deformation of the specimens was also measured by using linear voltage displacement transducers (LVDTs).

The main results of the tests appear in Figs 1.14–1.19. Figure 1.14 shows the variation of the cube and cylinder strengths (normalized with respect to the cylinder strength obtained from the tests using plain steel platens (f_c)) with the various techniques adopted to reduce frictional restraint. The variation of cylinder strength with the technique used is also shown in Fig. 1.15 which, in addition, includes the corresponding axial and lateral strains and the tangent values of Poisson's ratio. Figures 1.16 and 1.17 show the axial stress–axial strain and load–displacement relationships respectively, obtained from the cylinder tests; for comparison purposes, these relationships are expressed in a normalized form with respect to both the maximum sustained stress (load) and corresponding strain (displacement). The typical

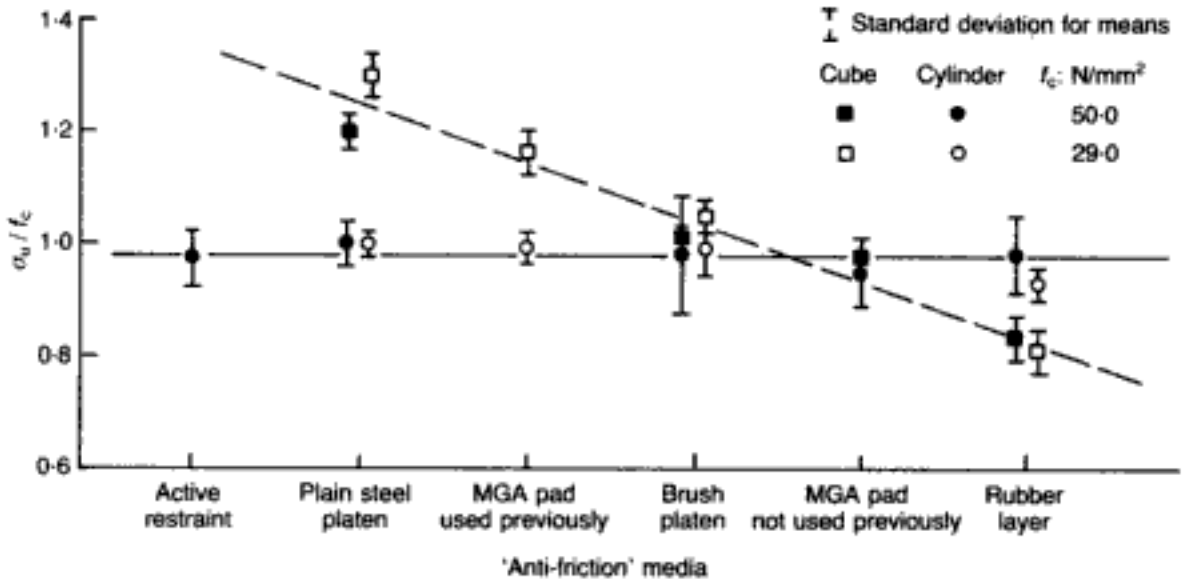


Fig. 1.14. Variation of cube and cylinder normalized strength with the various 'anti-friction' devices adopted¹⁴

deformational response of the cylinders under increasing load established from the strain-gauge measurements is compared with that established from the LVDT measurements in Fig. 1.18. Finally, Fig. 1.19 presents typical fracture modes of the cylinders subjected to the various degrees of boundary frictional restraint imposed by the testing techniques used.

The frictional restraint induced on the specimens by the testing techniques adopted may be quantified in terms of the strength of the cubes tested in compression. Since it is generally accepted that the difference between cube and cylinder strength reflects the influence of significant boundary restraints on the cube, it is considered realistic to accept also that, for a given concrete, the larger this difference, the higher the boundary restraints. On the basis of this argument, Fig. 1.14 shows that the restraint is significantly reduced if increasingly-efficient 'anti-friction' media are employed.

The normalized cylinder-strength data presented in Fig. 1.14 are in agreement with those obtained in a previous investigation,¹⁸ which has shown that the uniaxial compression strength of the cylinders with a height-to-diameter ratio of 2.5 is essentially independent of the frictional-restraint conditions across the loaded surface (a point already stressed in earlier parts of this chapter). It is of interest that the results obtained by using brush platens confirm the findings of similar investigations that have indicated that the use of such platens leads to the cube and cylinder strengths being nearly equal (see reference 14). It may also be interesting to note in Fig. 1.14 that, when a rubber layer is used, the cube strength is smaller than the cylinder strength. This is considered to indicate that, as soon as the load increases to ultimate strength, the rubber layer causes 'tensile' rather than 'compressive' stresses to develop across the loaded surface and that such stresses

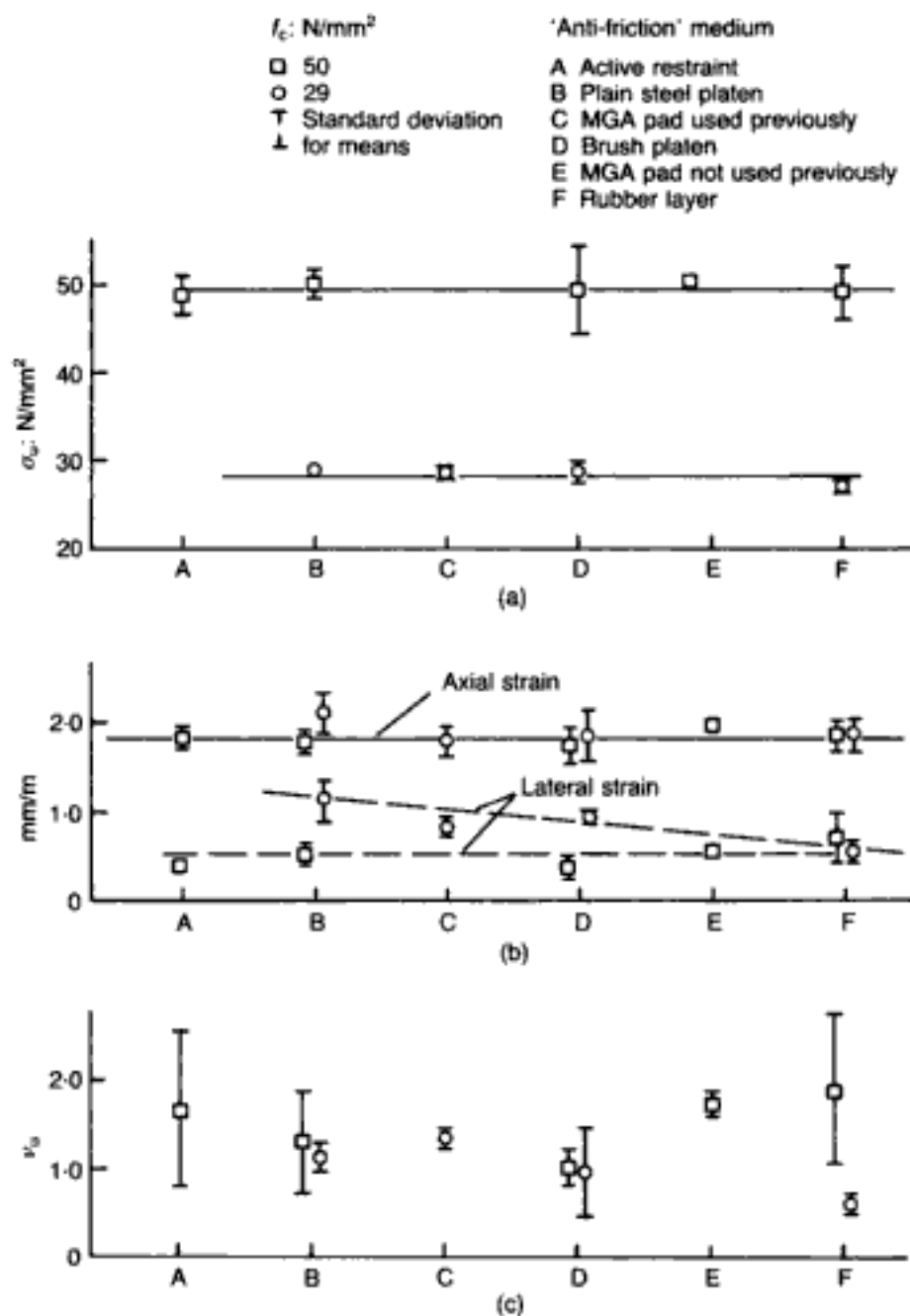


Fig. 1.15. Variation of cylinder-tests' parameters at ultimate load with the various 'anti-friction' devices adopted.¹⁴ (a) strength; (b) axial and lateral strains; (c) Poisson's ratio

produce lateral expansion rather than induce restraint. (However, under stress levels beyond ultimate strength, the capacity of the rubber for lateral expansion is much smaller than that of concrete, and, as a result, the 'tensile' stresses become 'compressive' and thus restrain further lateral expansion of the specimens, which then tend to be held together by friction.)

The cylinder-strength data, from which the normalized values of Fig. 1.14 are derived, are shown in Fig. 1.15 which also includes the corresponding data for axial and lateral strains. The figure indicates that, as for the strength data, the axial-strain values at ultimate strength appear to be essentially independent of the boundary frictional restraint conditions. Furthermore, they are

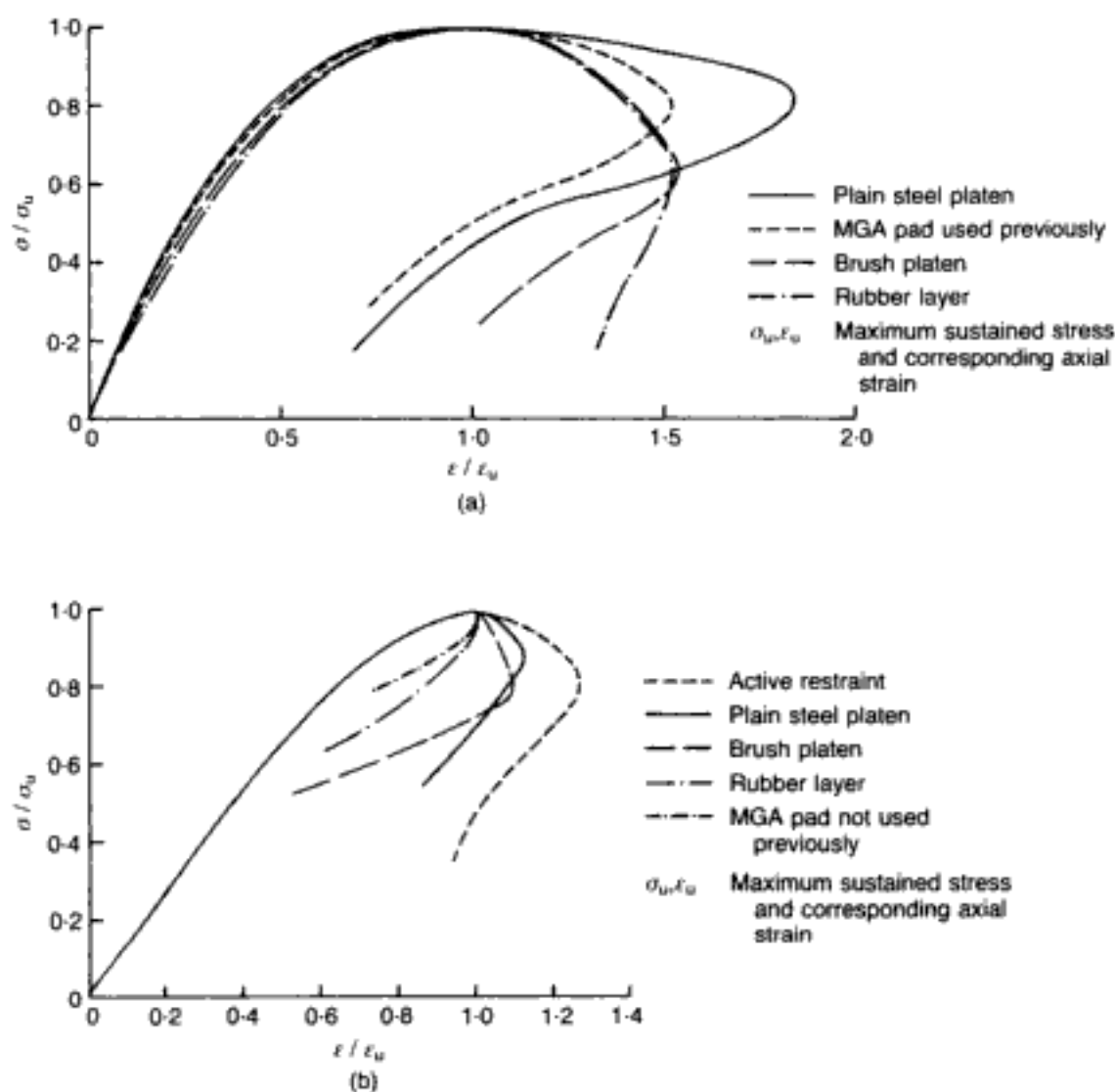


Fig. 1.16. Axial stress-axial strain relationships established from cylinder tests.¹⁴
 (a) $f_c = 29 \text{ N/mm}^2$;
 (b) $f_c = 50 \text{ N/mm}^2$

shown to be independent of the concrete strength. On the other hand, the lateral strains appear to decrease with increasing concrete strength, and while those of the higher concrete strength are also essentially independent of frictional restraint conditions, those of the lower concrete strength specimens seem to decrease with decreasing frictional restraint. (The reason for this difference in behaviour will become apparent later, when the inclination of the post-ultimate branch of the load-displacement relationships for the two types of concrete tested is discussed.)

The tangent values of Poisson's ratio at ultimate strength are shown in Fig. 1.15(c) which indicates that, for all cylinders tested, the values are much greater than 0.5. Such behaviour is compatible with earlier reported experimental information.¹⁵

Figures 1.16 and 1.17 show that, for stress levels up to ultimate strength, the deformational behaviour of the cylinders as established by both strain-gauge and LVDT measurements is practically the same for any of the boundary frictional conditions induced by the

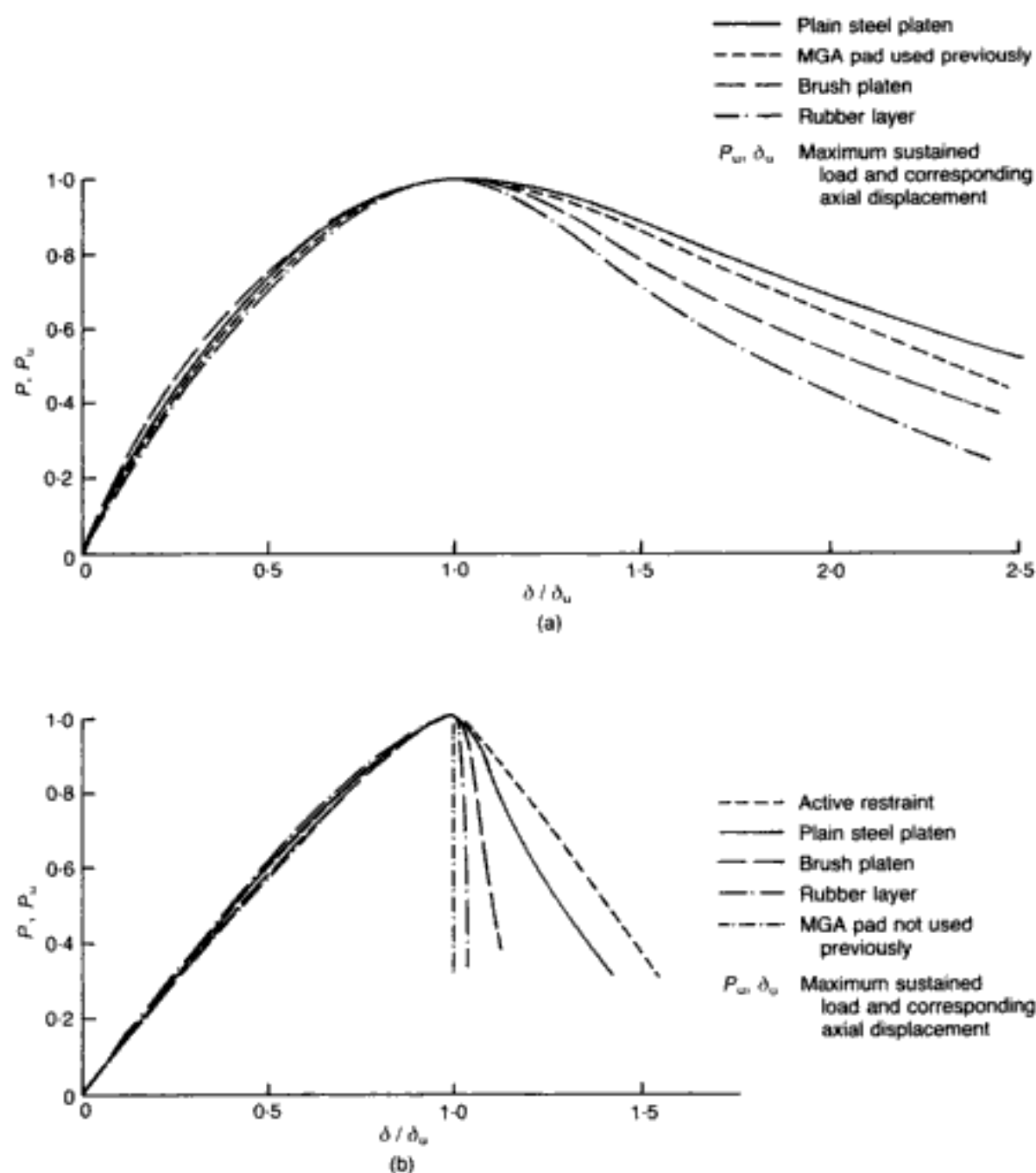


Fig. 1.17. Load-displacement relationships established from cylinder tests:¹⁴
 (a) $f_c = 29 \text{ N/mm}^2$;
 (b) $f_c = 50 \text{ N/mm}^2$

testing techniques adopted. On the other hand, for stress levels beyond ultimate strength, both figures indicate a very pronounced dependency of the specimen response on the frictional-restraint conditions at their boundaries.

However, it is interesting to note that, while the load-displacement relationships of Fig. 1.17 exhibit continuous increase of displacement throughout the whole of the loading path, the stress-strain relationships of Fig. 1.16 show that the post-ultimate strain increases numerically but that the corresponding stresses decrease to a level between approximately 60% and 80% of ultimate strength. At this level the trend reverses and the strain decreases

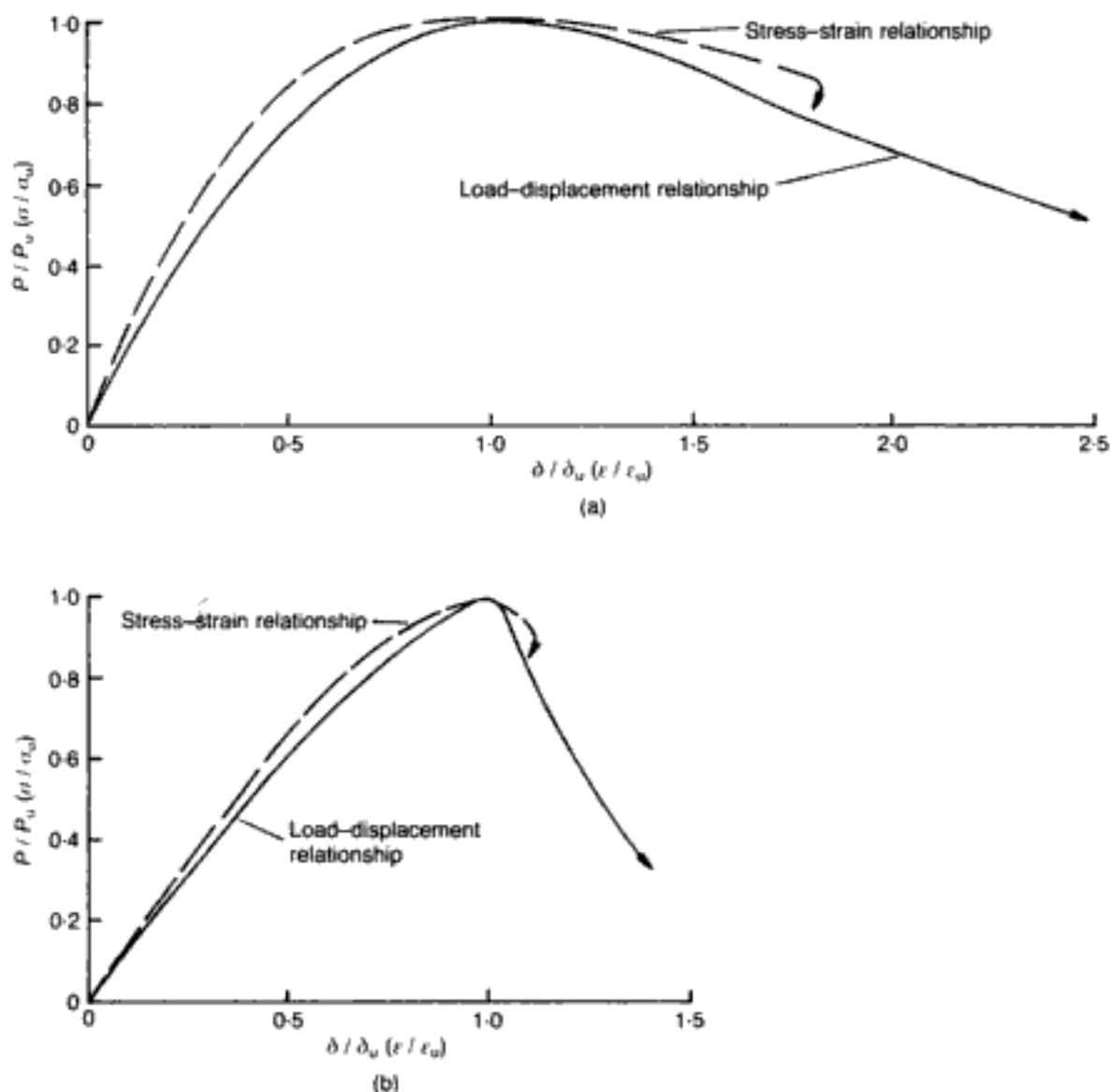


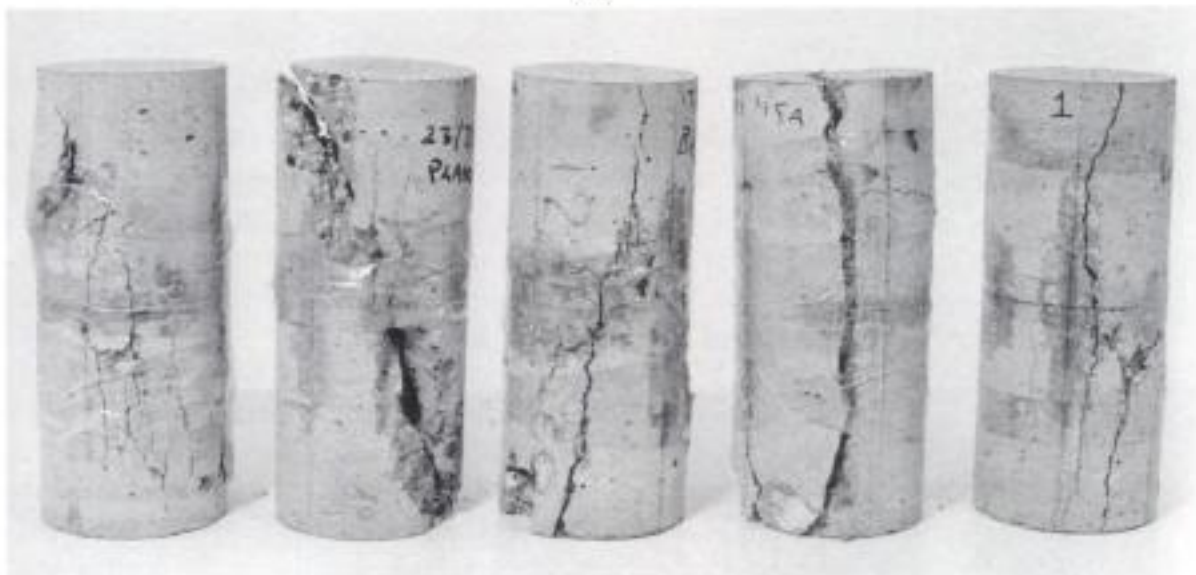
Fig. 1.18. Deformation response of cylinders under uniaxial compression established from strain-gauge and LVDT measurements:¹⁴
 (a) $f_c = 29 \text{ N/mm}^2$;
 (b) $f_c = 50 \text{ N/mm}^2$

continuously to complete disruption of the specimens. This late change of trend in behaviour in the characteristics of Fig. 1.16 is considered to reflect the effect on deformation of the occurrence of continuous axial cracks which subdivide the specimen in such a way that the applied load is predominantly supported by the core rather than the outer layers of the specimen, as indicated in Fig. 1.20 (see also stage 3 in Fig. 1.13). As a result, the stresses within the outer layers decrease and this causes an 'elastic recovery' (in fact, the outer layers are no longer load-carrying) which is not typical of the overall specimen behaviour since it does not reflect the deformational response of the (ungauged) *core* of the specimen.

It can also be seen that, before the above 'elastic recovery' (i.e. unloading) occurs, the relationships of Fig. 1.16 exhibit trends of post-ultimate behaviour similar to those of the relationships of Fig. 1.17. There are, however, quantitative differences, demonstrated in Fig. 1.18, which reflect the fact that, while the strain-



(a)



(b)

Fig. 1.19. Typical fracture modes of cylinders (standard size 10 in \times 4 in/25.4 cm \times 10.2 cm).¹⁴ 'Anti-friction' media used from left to right: (a) for lower-strength cylinders: plain-steel platen, brush platen, MGA pad, rubber; (b) for higher-strength cylinders: active restraint, plain-steel platen, brush platen, MGA pad, rubber layer

gauge measurements describe essentially the deformational response of the central zone of the specimen (see Fig. 1.11), the displacement measurements describe the overall response of the specimen—loading system. It can be shown, however, that, as the loading frame becomes stiffer, the displacement measurements become more representative of the specimen behaviour.¹⁶ The

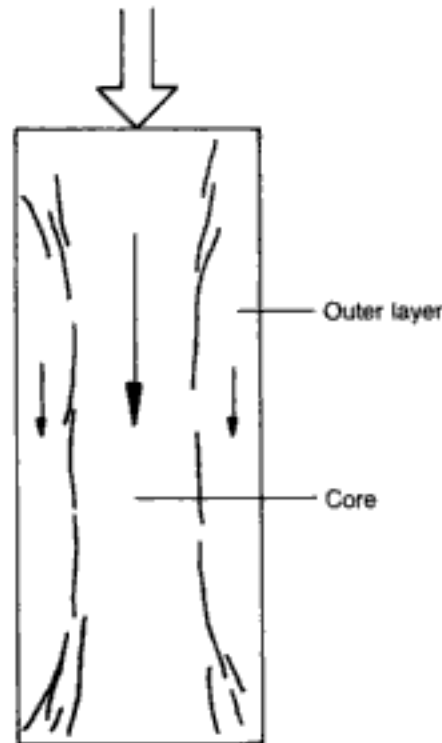


Fig. 1.20. Distribution of post-ultimate load-carrying capacity of cylinders¹⁴

relatively good correlation of the relationships shown in Fig. 1.18 may be taken as an indication that, through the use of the relatively stiff loading frame, the loading-system effects on the displacement measurements have been minimized to the extent that the resulting load–displacement relationships of Fig. 1.17 provide a realistic description of the specimen behaviour.

Figure 1.17 indicates that, for all the boundary conditions investigated, the inclination of the post-ultimate branch of the relationships obtained for the lower concrete-strength cylinders appears to be less steep than that of the relationships obtained for the higher concrete-strength cylinders. This difference in behaviour is considered to reflect the difference in size of the central zone of the specimens within which continuous longitudinal cracks appear when the maximum load-carrying capacity of the specimens is approached (see Fig. 1.13). For the higher concrete-strength specimens, the size of the above zone was observed to be substantially larger than that of the lower concrete-strength specimens, indicating a more dynamic type of crack propagation for the former as against the relatively gradual extension of the cracking exhibited by the latter; as a result, the size and restraining effect on lateral expansion of the end zones was smaller. Furthermore, it was also observed that cracking of the higher concrete-strength specimens always extended in both directions with increasing deformations (see Fig. 1.19), thus reducing further the size and the restraining action of *both* end zones. In contrast,

for the lower concrete-strength cylinders, cracking extended in one direction only and, as a result, the size and restraining action of at least one of the end zones was maintained throughout the whole length of the post-ultimate branch (see Fig. 1.19).

However, a characteristic feature of the relationships shown in Fig. 1.17 is that, for both concretes used, their descending portion becomes significantly steeper as the frictional restraint decreases. In fact, for the higher concrete-strength cylinders, the reduction of boundary frictional restraint achieved by some of the testing techniques adopted was sufficient to cause complete breakdown on the specimens as soon as ultimate strength was exceeded. Such trends of behaviour appear to support the proposal that, if the boundary frictional restraints are completely eliminated, the post-ultimate behaviour of the specimens will be characterized by a complete and immediate loss of load-carrying capacity. At the same time, and as mentioned earlier, it is evident that the secondary effects due to interface friction at the ends of a cylinder having a height-to-diameter ratio of 2.5 are unimportant up to about the maximum sustained load, so that the uniaxial concrete strength is practically independent of the boundary restraint provided by the testing device.

It is important to stress that, even though the above conclusion regarding the brittle nature of concrete materials when tested uniaxially in compression has been reached on the basis of a particular experimental study,¹⁴ such a view is supported by the findings of a number of other investigators. In these, however, one rarely — if ever — finds an unambiguous statement that the post-ultimate deformation branch is attributable wholly to the interaction between specimen and loading platens, and is not a characteristic of the material (e.g. see reference 19). Instead, such a belief (whether explicit or implicit) in the existence of the strain-softening regime of concrete is still widespread, despite evidence to the contrary, and it is often found even among those workers whose results lend support to the view that concrete suffers an abrupt and total loss of load-carrying capacity as soon as its peak strength is attained.

1.2.2. Triaxial compression tests and the effect of tensile stresses

In the preceding section, it was argued that a specimen of concrete under truly uniaxial compression does not exhibit a post-ultimate load-deformation branch. Since concrete in a structure is generally under the action of a multiaxial stress state, it is important to ascertain whether or not the mode of failure of the material remains brittle when subjected to these more complex loading conditions.

Considerable insight into the type of failure exhibited by concrete under multiaxial compression has been obtained by means of tests on concrete cylinders with a height-to-diameter ratio of 2.5 which have been subjected to an axial compression (σ_a) and a lateral

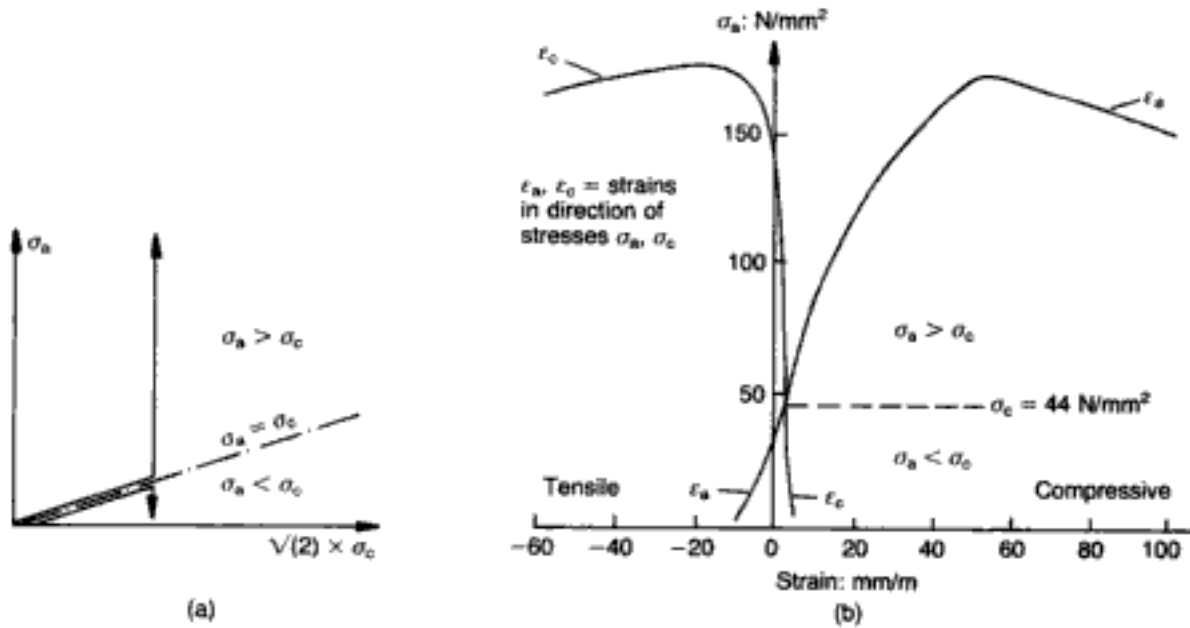


Fig. 1.21. Triaxial compression tests on cylinders.¹³ (a) stress paths used; (b) typical stress-strain relationships obtained from 'compression' and 'extension' tests on cylinders with $f_c = 31.7 \text{ N/mm}^2$

confining pressure (σ_c).^{20,13} These actions were combined in such a way that the state of stress within the specimen was either $\sigma_a > \sigma_c$ (triaxial 'compression') or $\sigma_a < \sigma_c$ (triaxial 'extension'). The axial compression was applied by using a loading method similar to that employed for uniaxial testing (i.e. no attempt was made to reduce the friction at the ends of the cylinder), while the confining pressure was hydrostatic (with the result that the curved surface of the specimen was essentially friction-free). In all tests, the entire specimens were subjected initially to a given hydrostatic pressure and then the axial compression was either increased (triaxial 'compression') or decreased (triaxial 'extension') to failure (see Fig. 1.21(a)).

Typical stress-strain relationships obtained from the above tests are shown in Fig. 1.21(b) which indicates that, while under triaxial 'compression' concrete exhibited a gradual reduction of load-carrying capacity for stress levels beyond ultimate strength, under triaxial 'extension' concrete suffered an immediate and complete loss of load-carrying capacity. This difference in material behaviour is considered to reflect the effect of frictional restraint on the fracture processes of the specimens. According to the fracture mechanism of uniaxially-tested concrete (discussed in section 1.2.1), under triaxial 'compression' crack propagation occurs in the axial direction and, therefore, when cracking spreads in the end zones of the specimen, the frictional restraint will affect the specimen behaviour as for the uniaxial case. On the other hand, under triaxial 'extension' crack propagation takes place in the lateral direction (i.e. perpendicular to the cylinder's axis) and hence the fracture processes that occur in the central zone of the specimen

are not affected by the frictional restraint that exists at the specimen–platen interfaces.

The above findings strongly suggest that a truly ‘unrestrained’ specimen of concrete under arbitrary (but compressive) stress conditions would suffer a complete loss of load-carrying capacity on attaining its maximum strength. Therefore, it seems reasonable to postulate that brittle failure is a characteristic of concrete behaviour at a material level under any state of three-dimensional compression.

The effect of tensile stresses on the post-ultimate behaviour of concrete remains to be considered. The case when a cylinder is acted upon by confining circumferential pressure σ_c and an axial tension σ_a may be considered to be an extrapolation of the triaxial ‘extension’ case discussed above. In fact, such a specimen would be expected to exhibit an even more explosive type of failure than the case when σ_a is compressive. By reference to the particular instance of uniaxial compression, a similar lack of strain softening may be anticipated when σ_a is compressive while σ_c is tensile, provided that frictional end effects are eliminated. Finally, it seems unlikely that the presence of a fully tensile set of principal stresses will lead to an increase in ductility in the material. On the contrary, such a stress combination in concrete represents an inherently brittle system, despite gradually-descending post-ultimate branches proposed by some investigators, as the latter strain softening, far from being a characteristic of the material, is a direct result of the control of crack propagation imposed by the machine in the course of tensile testing. In this respect, it is significant that strain-softening branches in direct tensile tests can be observed only if the stiffness of the testing machine is steeper than the steepest portion of the falling branch; otherwise, a sudden failure is deemed to occur.²¹ Evidently, the interaction between such testing machines and the specimen, which dictates the fracture processes in the material, has no relevance for concrete within a structure, as the latter is surrounded by material having the same (if plain concrete) or similar (if reinforced concrete) stiffness.

Typical failed cylinders for the various triaxial-test types just described, showing the relevant fracture mechanisms, may be seen in Figs 1.22 and 1.23. For triaxial ‘compression’ (see Fig. 1.22),^{10,6} where the principal stress is maintained compressive or is increased in compression, failure — under low values of volumetric stress — can be observed to occur along planes parallel to the maximum compressive stress in a manner similar to uniaxial compression. For larger values of volumetric stress, on the other hand, the failure planes become less distinct as the behaviour — although still brittle, since failure coincides with the peak of the stress–strain curve — becomes more ‘ductile’ in the sense that larger strains now occur. The use of a conventional hydraulic



Fig. 1.22. Typical concrete specimens (for four mix types) after failure under triaxial 'compression', with confining pressure increasing from left to right (all standard-size cylinders 10 in \times 4 in/25.4 cm \times 10.2 cm)¹⁰

1.2.3. Concrete: a brittle fracturing material

coaxial cell to apply the loads gives rise to 'bulged' profiles of specimens under high confining pressures, allied to the considerable shortening in the axial direction.⁶ In contrast, for the 'extension' or compression-compression-tension (C-C-T) test types (Fig. 1.23),^{20,6} failure occurs abruptly on planes orthogonal to the minimum compressive stress. (In decreasing the axial stress to failure, the latter occurs in a 'tensile mode' under a resultant axial stress which may be either compressive (triaxial 'extension') or tensile (C-C-T, or triaxial 'tension'), depending on the value of the maximum confining pressure in the test.)

The test results discussed in previous sections shed considerable doubt over the validity of the current widely accepted view that a gradually-decreasing post-ultimate load-carrying capacity for

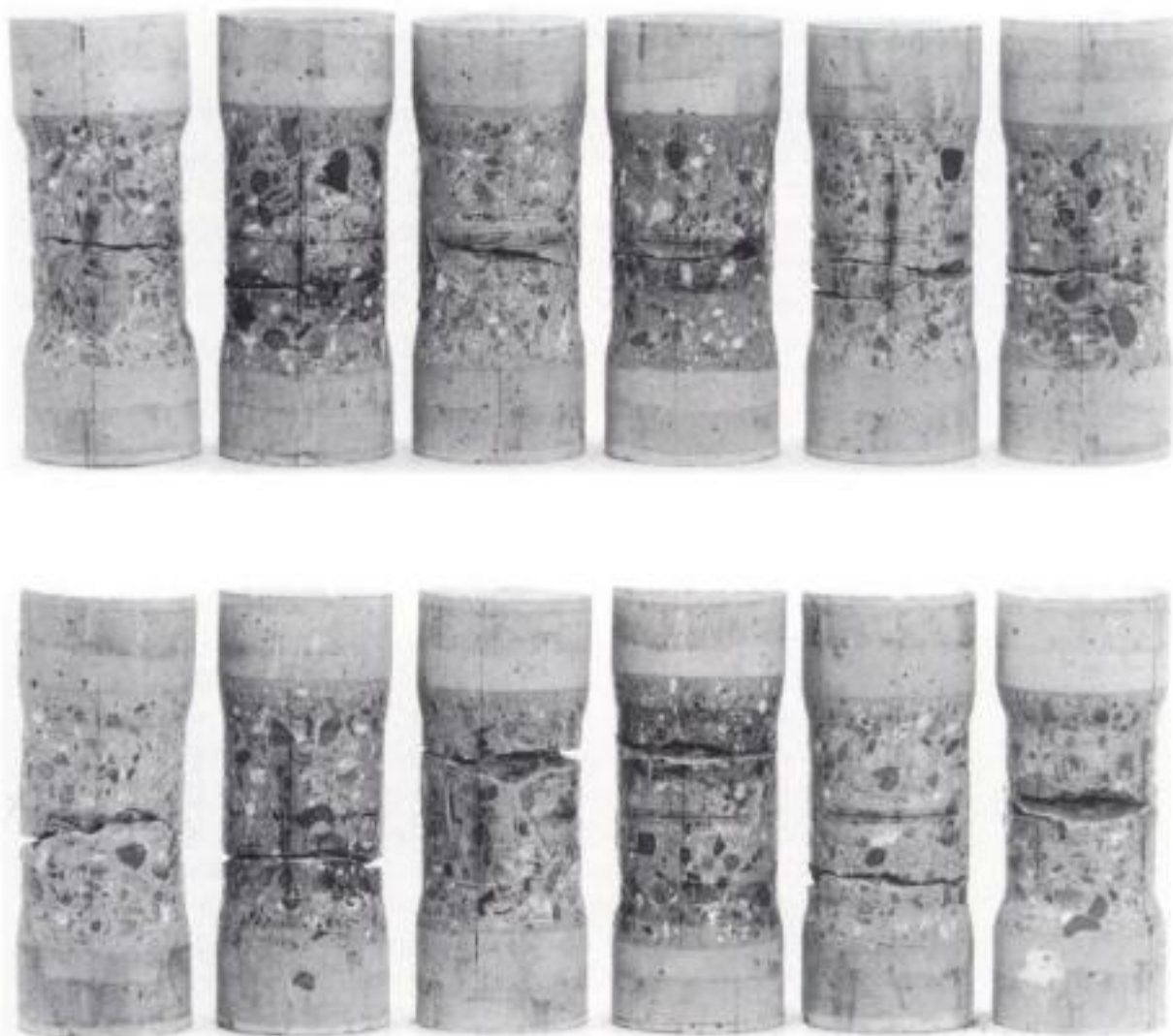


Fig. 1.23. Typical concrete specimens (for a given mix) after failure under triaxial 'extension' and C-C-T (all standard-size cylinders 10 in \times 4 in/25.4 cm \times 10.2 cm)²⁰

concrete is an essential part of the mechanism of stress redistribution within reinforced concrete structures under increasing load. The validity of this view has, for a long time, been considered self-evident and in recent years a significant amount of research work has been concentrated on the development of testing apparatus capable of yielding stress-strain relationships which exhibit a gradually-descending post-ultimate portion. Although such research has reached the stage when the shape of stress-strain relationships exhibiting 'softening' is readily obtainable, the results of the work presently described indicate that the time has come to reappraise existing testing methods in an attempt to establish to what extent the obtained relationships really represent the behaviour of an element of concrete *in a structure*.

The experimental evidence presented in the preceding sections points unequivocally to the conclusion that plain concrete exhibits a sudden mode of failure under both uniaxial and the more general triaxial stress states. Such a brittle nature at the material level,

however, is not incompatible with the fact that, when properly designed, a concrete structure or member can exhibit a ductile type of failure.

Ductility at the structural level is often due to the fact that material failure occurs locally and in a gradual manner, thus allowing stress redistribution to take place. Another obvious source of ductility is the presence of steel reinforcement. However, there is a more fundamental explanation as to why structural concrete is capable of failing in a ductile fashion, and this concerns the interaction of various elements of concrete within the structure.^{22,23} This interaction gives rise to complex (triaxial) stress states which result in at least some of the principal stresses being very large: individually, these may be well in excess of the uniaxial strength of concrete but, when taken together, they represent a stress system below the *triaxial* strength of the material. Such large stresses are associated with large local strains which allow the formation of what one might term local 'hinges' that account for overall member ductility. This point will become evident later in the chapter, once the triaxial strength of concrete has been presented and the characteristic failure mechanism in a structure discussed.

In view of the above, it should be clear that, even though not consistent with the notion of concrete as a brittle material, plasticity concepts may often be used at a structural level, although they do not always guarantee the correct failure-mechanism and/or ultimate-load prediction. In the latter instances, the reason does not lie so much in the brittle nature of concrete. After all, Heyman²⁴ has shown how, for brittle masonry structures, plasticity concepts can be applied. However, the stresses in the latter type of structure are very low and failure occurs through the formation of a mechanism. Concrete structures, in contrast, tend to be subject — albeit locally — to high triaxial stresses as their ultimate load is approached, and it is these large stresses which cause the strains necessary to produce ductile behaviour. Therefore, the latter is compatible with the brittle failure that occurs at the material level, and is not due to the existence of a strain-softening branch that is often argued to be necessary in order to explain the observed ductility of structural concrete.

1.3. Fracture processes in concrete

1.3.1. *The nonlinear behaviour of concrete materials*

The response of concrete at a material level is characterized by a distinctly nonlinear behaviour. Such a characteristic is already evident in the early portion of the stress—strain relations, becoming more pronounced as the ultimate strength is approached. If nonlinear computer-based techniques are to be employed to analyse rigorously the response of concrete structures to the imposed loading conditions, information must be expressed in a mathematical form suitable for use with such techniques. Before this is done, however, the origin and nature of material nonlinearities should be properly understood.

The nonlinear properties of concrete are generally accepted to reflect the fracture processes which occur under stress, and hence a knowledge of these processes provides a suitable basis for the mathematical description of concrete nonlinearity.²⁵ The term fracture process is used to denote the structural changes which a brittle material undergoes under increasing stress; in concrete, these structural changes are considered to be primarily those caused by cracking. A fracture mechanism (i.e. the law or group of laws which controls the above fracture processes) for concrete, valid under any state of stress and which can be used to predict observed deformational behaviour, may be postulated on the basis of theoretical considerations regarding the extension of a crack within a brittle medium (which, as shown in section 1.2, concrete is). This fracture mechanism forms the basis for an analysis of experimental triaxial stress-strain data which will lead to the mathematical description of the deformational behaviour of concrete under static short-term loading conditions. Before such an analytical description is presented, it is helpful to give, in a unified form, the complete *qualitative* description of the structural changes of concrete under any type of increasing stress.

1.3.2. Causes of fracture

It is generally accepted that the cause of fracture and failure of concrete is the proliferation of flaws or microcracks which exist within the body of the material even before the application of load. These flaws are attributable to a number of causes; the main ones are:

- (a) discontinuities in the cement paste matrix resulting from its complex morphology (such flaws range in size from a number of ångström units at the gel-lattice level, to several microns (or above) for isolated or continuous capillary pores)
- (b) voids caused by shrinkage or thermal movements due to incompatibility between the properties of the various phases present in concrete
- (c) discontinuities at the boundary between the aggregate particles and the paste or mortar matrix caused by segregation
- (d) voids present in concrete as a result of incomplete compaction.

The above pre-existing flaws can be considered as randomly distributed and oriented within the material and to exhibit a range of shapes and sizes.

The stress and strain applied to the boundary of an element of a composite material, such as concrete, generates a strain field within the material which is dependent on the distribution of the component phases (i.e. aggregate particles and cement-paste matrix), and the size, shape and distribution of flaws. Local strain

concentrations, therefore, develop throughout the material as a result of the incompatible deformation of the constituent phases. Such strain concentrations are further intensified to far higher orders of magnitude owing to the presence of flaws, particularly those with high aspect ratios.²⁶ It is primarily these flaws that are considered to be the potential sources of any load-induced cracking.

1.3.3. Fracture mechanism of concrete

The existence of a flaw or microcrack within a *brittle elastic material* under stress disturbs the stress and strain field around the microcrack and causes *high*, predominantly *tensile*, stress and strain concentrations (and thus strain-energy concentrations) within small regions near the microcrack tips. The energy capacity of these small regions must have a limit dependent on the material properties which, if exceeded, results in spontaneous crack extension²⁶ due to the initiation of branches. This process is followed by stable propagation of these branches, eventually becoming unstable and leading to ultimate collapse.^{10,20} The above crack extension and propagation processes have been found to occur in the direction of the *maximum principal compressive stress* applied to the boundaries of a specimen (or orthogonal to the direction of the maximum principal tensile stress)^{27,28} and takes place in order to release any excessive strain energy fed within the material by external loads. (The cracking can be visualized by reference to a series of parallel planes of fracture containing the largest and intermediate principal compressive stresses, the planes extending along the former (i.e. maximum) stress direction as cracking propagates.)

For a tensile stress field, crack extension is insufficient to reduce the strain-energy concentrations to a level that can be contained within small regions near the crack tips. As a result, the fracture process is unstable in that crack extension continues to complete disruption even if the load is maintained constant.

On the other hand, for a predominantly compressive stress field, the strain energy which is released during the fracture process reduces the strain-energy concentrations to a level below the energy capacity of the material in the vicinity of the crack tips and, as a result, the crack ceases to extend. Crack extension is resumed when energy fed into the material by external loads tends to increase again the strain-energy concentrations to values above the capacity of the local energy-storing regions. The fracture process, therefore, occurs in discrete steps, and is stable since crack extension ceases when the load is maintained constant. Eventually, however, further increases in load lead to the stage when no more energy can be stored within the material; any additional energy induced by the applied load is released immediately by crack extension which, in turn, reduces further the energy capacity of the system and creates a state of instability.²⁹

The energy release which occurs during the above fracture processes results in a reduction of the stress and strain

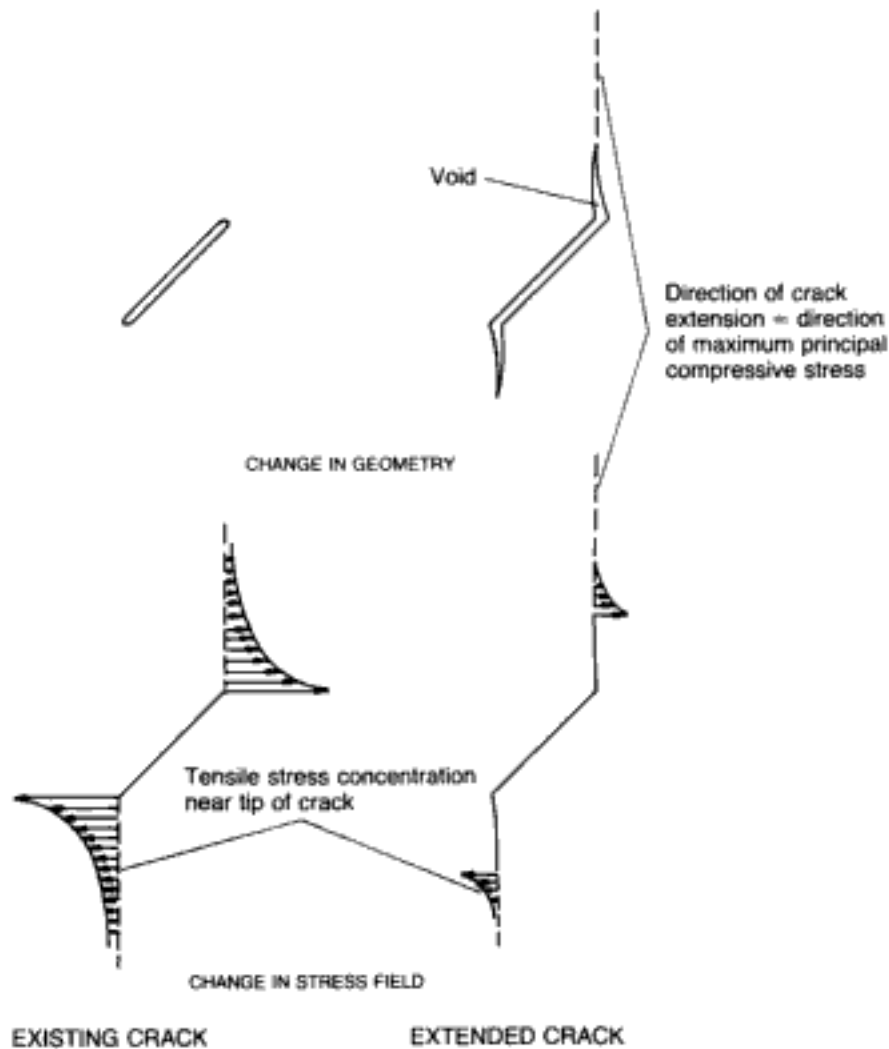


Fig. 1.24. Schematic representation of changes in crack geometry and stress field associated with crack extension²⁹

concentrations which exist near the crack tips orthogonal to the path of crack extension. Furthermore, these fracture processes create voids within the material (see Fig. 1.24). The reduction of these high tensile stress and strain concentrations tends to cause a contraction of the material in the direction normal to the crack-extension path, while void formation tends to cause an extension. The overall effect on deformation, therefore, will be either a contraction or an extension, depending on whether the effect of reduction of the tensile stress and strain concentrations or the effect of void formation predominates.

Based on the research of previous investigators, which has been concerned with the study of the fracture processes of concrete at both the microscopic and the phenomenological levels, it has been postulated that the fracture mechanism of this material is qualitatively similar to the fracture mechanism described above. The salient features stemming from the work of these investigators may be summarized as shown in Table 1.2.^{10,25} (It should be noted that the deformational behaviour denoted in the table by the term 'quasi-elastic' and 'plastic' could be described more accurately as nonlinearly elastic and inelastic (i.e. exhibiting permanent

Table 1.2. Failure processes occurring when concrete is subjected to load^{10,25}

Observed material behaviour under increasing stress	Deduced changes in internal structure	Deduced changes in deformational behaviour	Approximate stress level	Influencing characteristics
Presence of cracks detected microscopically and from X-rays	Pre-existing cracks		Prior to load	Shrinkage, thermal effects, etc.
<i>From structural investigations:</i> Bond cracking and matrix cracking increases depending on spacing of particles of aggregate, with cracking aligned in direction of maximum compressive stress as load increases		Quasi-elastic behaviour	30–40% ultimate	Spacing of particles for a given mix, etc.
<i>From phenomenological investigations:</i> Decrease in ultrasonic pulse velocity, start of significant acoustic emissions, measurable void formation	Start of localized stable cracking	Plastic behaviour	45–90% ultimate	Method of detection, type of aggregate, type of specimen, state of stress, rate of loading, curing conditions, and level decreases with increase with w/c ratio; increase in volume fraction of aggregate; decrease in age; decreasing roughness and angularity of aggregate
<i>From structural investigations:</i> Formation of continuous crack patterns through matrix and around aggregate particles	Start of continuous cracking		70–90% ultimate	Spacing of aggregate particles for a given mix
<i>From phenomenological investigations:</i> Increase in volume, marked increase in acoustic emission, and change in stress-strain relationship	Unstable behaviour caused by reduction in number of load paths due to cracking (leading to complete disruption)		70–90% ultimate	As for localized stable cracking (detected phenomenologically)

deformation upon unloading) respectively.) A feature of the fracture process being discussed is that its mechanism is specific, in the sense that, as mentioned previously, crack extension occurs in the direction of the 'applied' maximum principal compressive stress, and affects predominantly the deformation in the direction orthogonal to the crack-extension paths, while the effect on deformation along these paths is negligible. Clearly, it is implicitly assumed here that the many microcracks that exist within concrete under stress extend in a mode *qualitatively similar* to that of a single microcrack within a stressed brittle medium. Such a postulate is reasonable, but it must be borne in mind that, in a heterogeneous material such as concrete, the crack extension paths will be orientated in the direction of the *local* rather than the 'applied' maximum principal compressive stress. Owing to this heterogeneous and complex nature of concrete, the direction of *local* principal stresses is indefinable, and hence the orientation of fracture paths is difficult, if not impossible, to establish. Nevertheless, it seems realistic to assume that, under a deviator stress (i.e. any stress state which is not purely hydrostatic), the directions of most of these *local* maximum principal compressive stresses practically coincide with the direction of the 'applied' maximum principal compressive stress. This is supported by a comprehensive investigation of the fracture processes of concrete specimens subjected to near-uniform states of multiaxial stress,^{10,20,30} which has indicated that the fracture processes which lead to ultimate collapse of the material are, indeed, those that occur in the direction of the maximum applied compressive (principal) stress. Therefore, it would appear that, for concrete under deviator stress, the effect of the fracture processes on deformation may be reflected in the relationship between the deformation of the material in the direction of the 'applied' maximum principal compressive stress and the deformation in the orthogonal direction under increasing stress; such a relationship could thus form the basis for the investigation of the fracture processes of concrete under increasing load. On the other hand, it is found that hydrostatic stress states are associated with an essentially random orientation of fracture processes.

In view of the above, it is convenient to classify the fracture processes of concrete into the following two categories.

Category A: processes with a unique orientation. These are easily definable since the propagation path coincides with the direction of the 'applied' maximum principal compressive stress. Such fracture processes may occur under any type of non-hydrostatic state of stress but they are unlikely to take place under pure hydrostatic stress.

Category B: processes with a 'random' orientation (in the sense that the propagation direction is indefinable). Such fracture

processes may occur under any stress state but they are considered to be reduced to a minimum under a pure deviatoric stress.

It follows from the above considerations, therefore, that a deviatoric stress state causes predominantly the fracture processes of category A, whereas a hydrostatic stress causes only the fracture processes of category B. A detailed description of these two categories of fracture processes is given below.

1.3.3.1. Fracture processes under deviatoric stress

It is assumed here that, under a deviatoric state of stress, the principal directions of both *local* and *applied* states of stress coincide. For this reason, no distinction is made in the following between local and applied stress states.

The various stages of the fracture processes. Comprehensive investigations into the behaviour of concrete under multiaxial stress^{10,20} have indicated that there are at least four stages in the process of crack proliferation under increasing stress. These are as follows.

Stage 1. When the load is first applied, microcracks additional to those pre-existing in the material may be formed at isolated points where the tensile stress concentrations due to the incompatible deformations of the aggregate and cement-paste phases are highest. During this stage, the microcracks do not propagate but remain stable.

Stage 2. As the load is increased, high tensile strain concentrations gradually develop near the tips of the microcracks as a result of the microcrack geometry and/or orientation. The stage is reached, therefore, when the initially stable microcracks begin to initiate branches in the direction of the maximum principal compressive stress. This branching process tends to relieve the strain concentrations and, once strain redistribution has occurred, the individual crack configurations remain stable during further increases of applied stress. Although this process may produce voids, the reduction of strain concentrations along the crack branches is such that it results in contraction of the material in localized zones near the crack tips which, in turn, causes the rate of increase of the tensile strain in the direction at right angles to that of branching to be reduced with respect to the rate of increase of the strain in the direction of branching. The start of such deformational behaviour has been termed *local fracture initiation* (LFI) and is considered to mark the start of the branching-initiation process.

Stage 3. When the load is increased to a higher level, a stage is reached at which the branched cracks start to propagate.

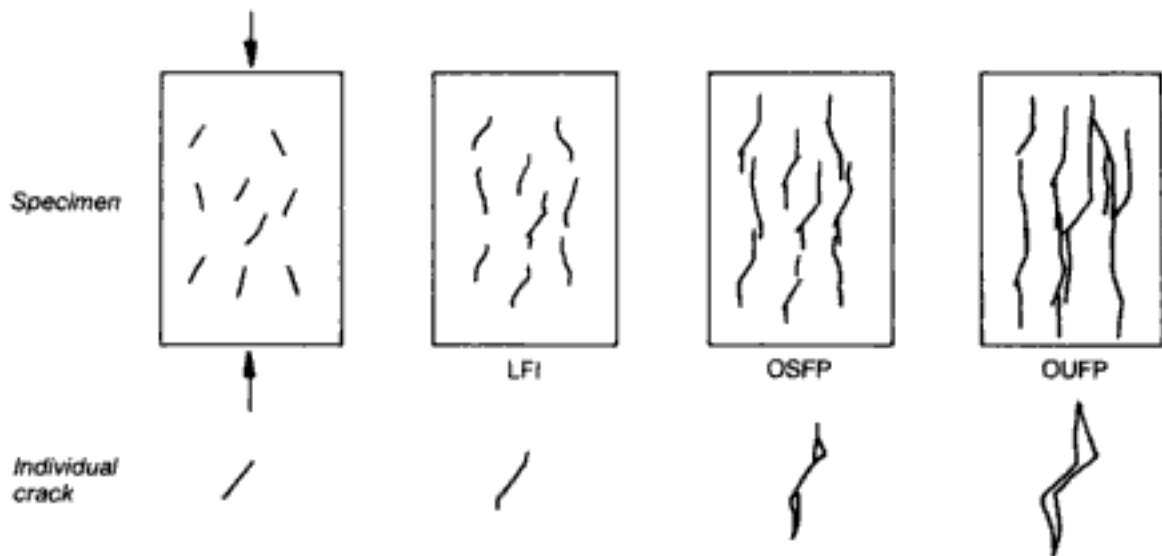


Fig. 1.25. Stages in the process of crack extension and propagation for concrete under compressive stress¹³

During this crack-propagation stage, each crack of the system extends in a relatively stable manner, in that, if the applied load is held constant, the process ceases. Although the relief of strain concentrations continues during this process, void formation is such that it causes the *rate of increase* of the strain at right angles to the direction of branching to increase with respect to the rate of increase of the strain in the direction of branching. The start of such deformational behaviour is considered to mark the start of the stable crack-propagation process and has been termed *onset of stable fracture propagation* (OSFP).

Stage 4. The degree of cracking eventually reaches a more severe level, after which the crack system becomes unstable and failure occurs even if the load remains constant. The start of this stage has been termed *onset of unstable fracture propagation* (OUFP). Under compressive stress states, this level is easily defined since it coincides with the level at which the overall volume of the material becomes a minimum. Under predominantly tensile stress states, it is marked by a rapid increase in the overall volume of the material and can be detected as described elsewhere.²⁰

The above four stages of crack extension and propagation are illustrated schematically in Fig. 1.25 by reference to concrete under compressive stress. Such a representation may be thought of as possibly corresponding to a uniaxial cylinder test in which the frictional effects between specimen and platens have been removed, or to the central portion of such a specimen if the end effects are present.

A simplified qualitative description of microcracking and macrocracking processes: critical levels of concrete behaviour. It is important to emphasize that the above four stages of the fracture

process are not all as clearly defined as might have been implied by the subdivision adopted. In particular, there is no easily detectable limit separating the local and essentially random process of stage 1 from the aligned cracking of stage 2. However, an analysis of triaxial stress-strain data can lead to a detection of reasonably distinct levels of change in the behaviour under increasing stress. As noted earlier, these levels are considered to represent the start of the stages within which crack branching (LFI), stable crack propagation (OSFP), and unstable crack propagation (OUFP) occur. (It is interesting to note that it has not been possible to detect the LFI level under triaxial 'compression' (C-C-C) of cylinder specimens when the maximum principal compressive stress is applied axially so that $\sigma_a > \sigma_c$. However, an indication of this level may be obtained by using the LFI levels detected under triaxial 'extension' (C-C-C but with the maximum principal stress applied laterally, i.e. $\sigma_a < \sigma_c$) and triaxial 'tension' (C-C-T, i.e. σ_a tensile) — see reference 29.)

The above considerations suggest that, in attempting to establish failure criteria for concrete, three critical levels might be considered. The significance of these levels will depend on the damaging effect which the ensuing fracture process has on the structure of the material. Since branching-crack initiation appears to induce stabilization of the material owing to the resulting relief of the stress concentrations (and, as intimated above, it is not always readily detectable), the OSFP and OUFP levels could be considered suitable for use as bases for lower-bound and upper-bound failure criteria in conformity with the limit-state requirements of serviceability and ultimate strength. The validity of this consideration is supported by experimental evidence which has indicated a very close correlation between: (a) the OSFP level and the 'fatigue strength' of concrete, i.e. that level below which concrete does not suffer distress under repeated applications of load; and (b) the OUFP level and the 'long-term strength' of concrete, i.e. that level below which concrete does not collapse under sustained load.

For structural purposes, however, the number of repeated loadings at the OSFP level which are required to cause fatigue failure of concrete is considered to be impractically high. For this reason, it seems that it is mainly the OUFP level which is relevant in structural applications where the governing criterion is that of static strength. In this respect, it is found convenient to simplify the cracking processes conceptually by considering these to consist of two major stages, which occur at the microscopic and macroscopic levels of observation respectively. Accordingly, the first of these can be denoted generically by the term microcracking, and encompasses stages 1 to 3 (inclusive) described above. Microcracking can be said to be the underlying cause of the nonlinear behaviour at the material level and thus determines the

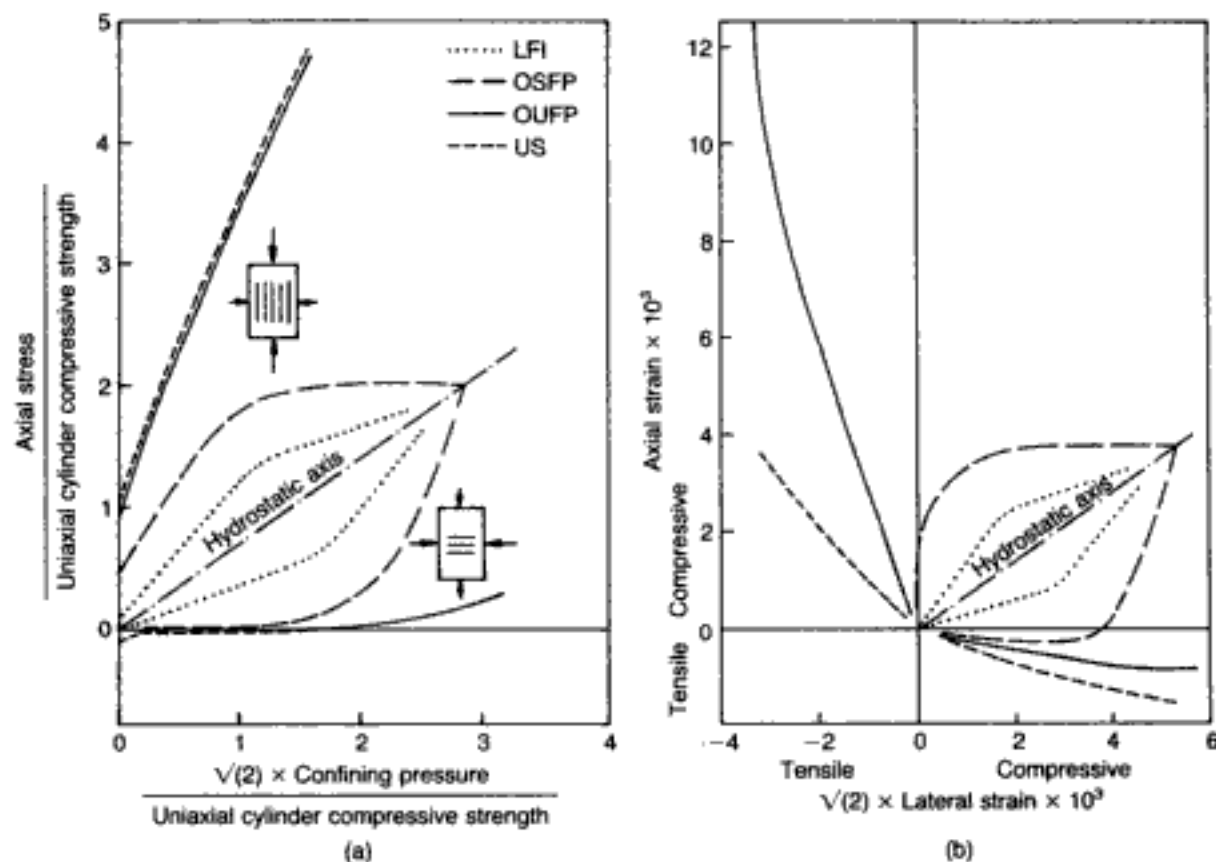


Fig. 1.26. Typical LFI, OSFP, OUFP and US envelopes for concrete (with $f_c = 46.9 \text{ N/mm}^2$) subjected to axisymmetric triaxial stress states using the stress path 3 defined in Fig. 1.27.^{13,25,29,30}

(a) stress space;
(b) strain space

constitutive relations of concrete. One way of describing it would be as a static process in the sense that crack extension stops when the load is maintained constant. The second major stage in the fracture process is that of macrocracking, which coincides with stage 4 discussed earlier. In contrast to microcracking, macrocracking indicates material failure in localized regions within a structure and is a dynamic phenomenon in that crack extension continues even if the load is maintained constant. It stops when equilibrium, which is disturbed by material failure in the region of the macrocrack, is re-established through stress redistribution (elsewhere) in the structure. Due to material breakdown, macrocracking causes local discontinuities in the original geometry of a structure. Clearly, unlike microcracking, macrocracking affects concrete at the *structure level* and hence defines the *failure criterion* (or the failure 'envelope') of concrete.

Failure envelopes. Figure 1.26 shows typical variations in stress and strain space of LFI, OSFP, OUFP and ultimate strength (US). (The actual values correspond to a concrete with $f_c = 46.9 \text{ N/mm}^2$ subject to axisymmetric triaxial conditions^{13,25,29,30} in which the stress path 3^{25,31} depicted in Fig. 1.27 was followed.) The figure indicates that the OSFP forms a closed envelope in both stress and strain space. It may also be noted that, in both strain space and the wholly compressive portion of the stress space, the OSFP envelope is nearly symmetrical about the hydrostatic axis.

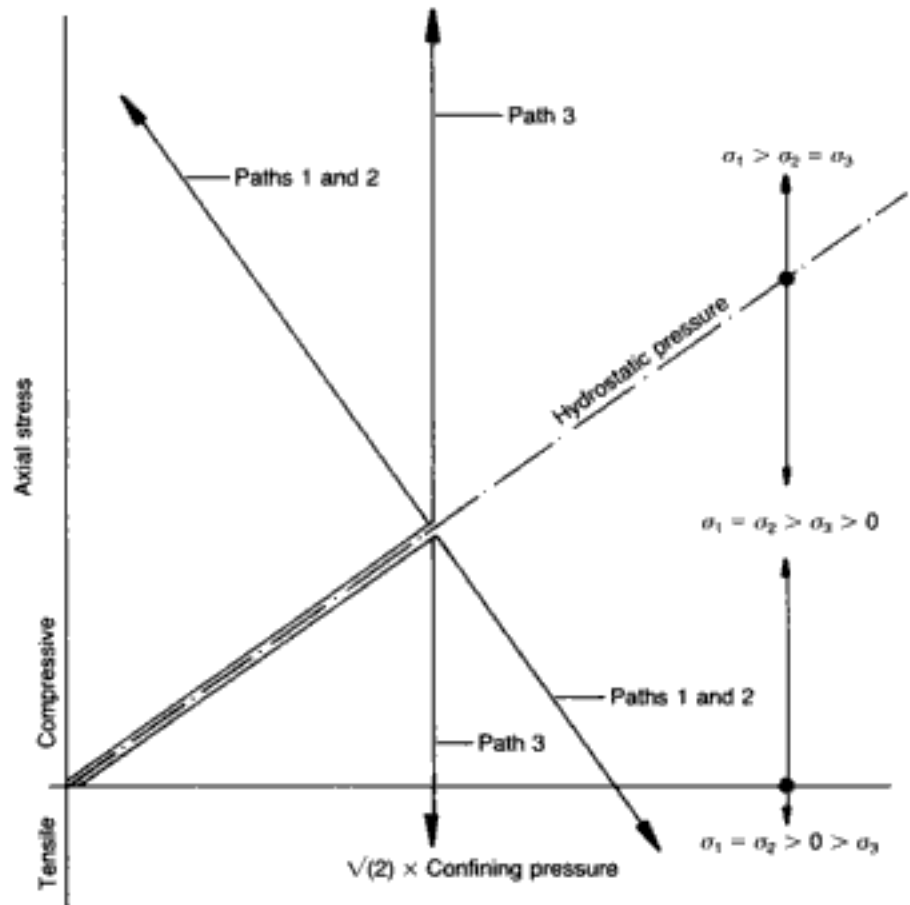


Fig. 1.27. Schematic representation of various stress paths used in the triaxial testing of concrete cylinders^{25,31}

Such behaviour implies that, for stress and strain states enclosed by the envelope, the material may be considered isotropic. Since the orientation of crack branching under a triaxial 'compression' state of stress is perpendicular to that under triaxial 'extension' or C-C-T (see the schematic sketches in Fig. 1.26(a)), such isotropic behaviour indicates that the fracture process up to the OSFP level causes insignificant disruption in the structure of the material. In view of this isotropy, it is possible that the LFI envelope within the triaxial 'compression' zone may be represented by the reflection of the LFI envelope in the triaxial 'extension' and C-C-T zones with respect to the hydrostatic axis, as shown in the figure.

In contrast to the LFI and OSFP envelopes, the OUFPP and US envelopes are open-ended for the range of stresses used in the tests, and are non-symmetrical with respect to the hydrostatic axis. This latter observation suggests that, for stress and strain states outside the OSFP envelope, the material becomes anisotropic, because crack extension occurs along a particular direction dictated by the maximum principal compressive stress. However, allowing for the scatter of results that is encountered in processing the deformational stress-strain data within the OUFPP envelopes for a wide variety of concrete mixes (this scatter will be discussed in section 1.4), it seems reasonable to postulate that the description of the stress-strain relations may be approximated by means of

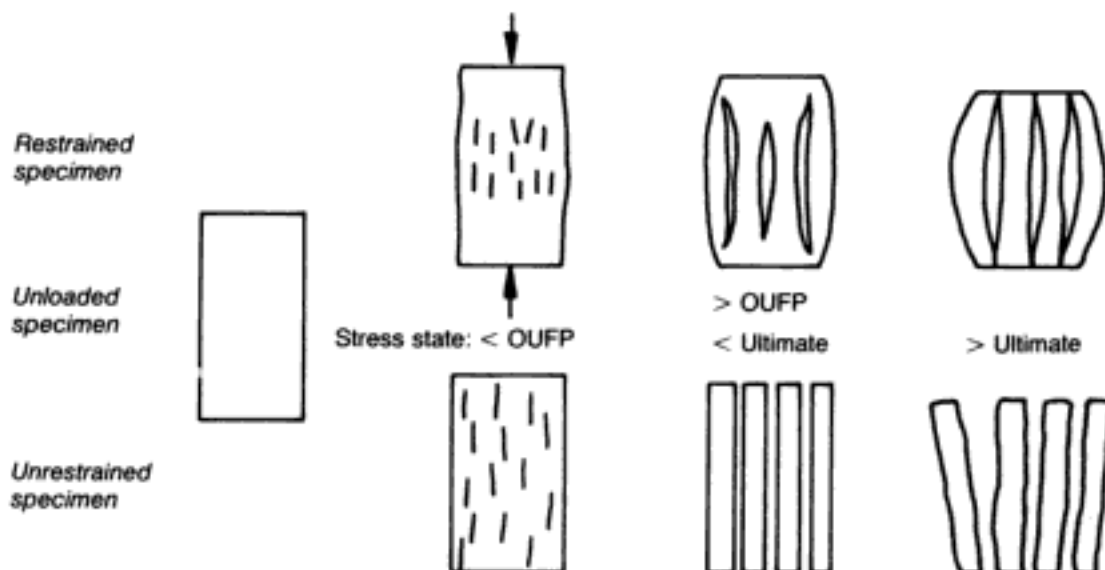


Fig. 1.28. Schematic representation of the fracture processes for restrained and unrestrained concrete specimens under increasing compressive stress¹³

an isotropic model up to the OUFP level corresponding to macrocracking. Moreover, it is found that the OUFP stress level forms a surface in stress space similar in shape and size with that of the ultimate-strength surface. As the strength of the concrete increases, the two surfaces become practically identical, but even for lower-strength concrete these surfaces are quite close to each other.²⁰ Therefore, it seems reasonable to consider the OUFP and US levels as being essentially the same, at least for practical purposes. This may be represented schematically, as in Fig. 1.28, by reference to both restrained and unrestrained concrete specimens under uniaxial compression.

1.3.3.2. Fracture processes under hydrostatic stress

This section can be summarized as follows.

Description of the fracture processes. Except for the 'random' orientation (which, as a result of its local character, cannot be measured), the fracture processes under hydrostatic stress may be considered qualitatively similar to those described by the stages 1 to 3 of the fracture processes under deviatoric stress. Owing to this 'random' orientation, a characteristic feature of these processes is that they increase the likelihood that a crack will be situated in the path along which a potential crack may propagate under some future applied state of stress. The former crack will act as a crack-propagation 'inhibitor' which will tend to increase the energy required to start the crack-propagation process.³² The number of such crack 'inhibitors' will increase with the level of applied stress, and it is considered realistic to assume that the crack extension and propagation processes will eventually diminish under hydrostatic stress. Furthermore, under such a state of stress the fracture processes described above are considered capable of reducing the internal stress and strain concentrations to such small

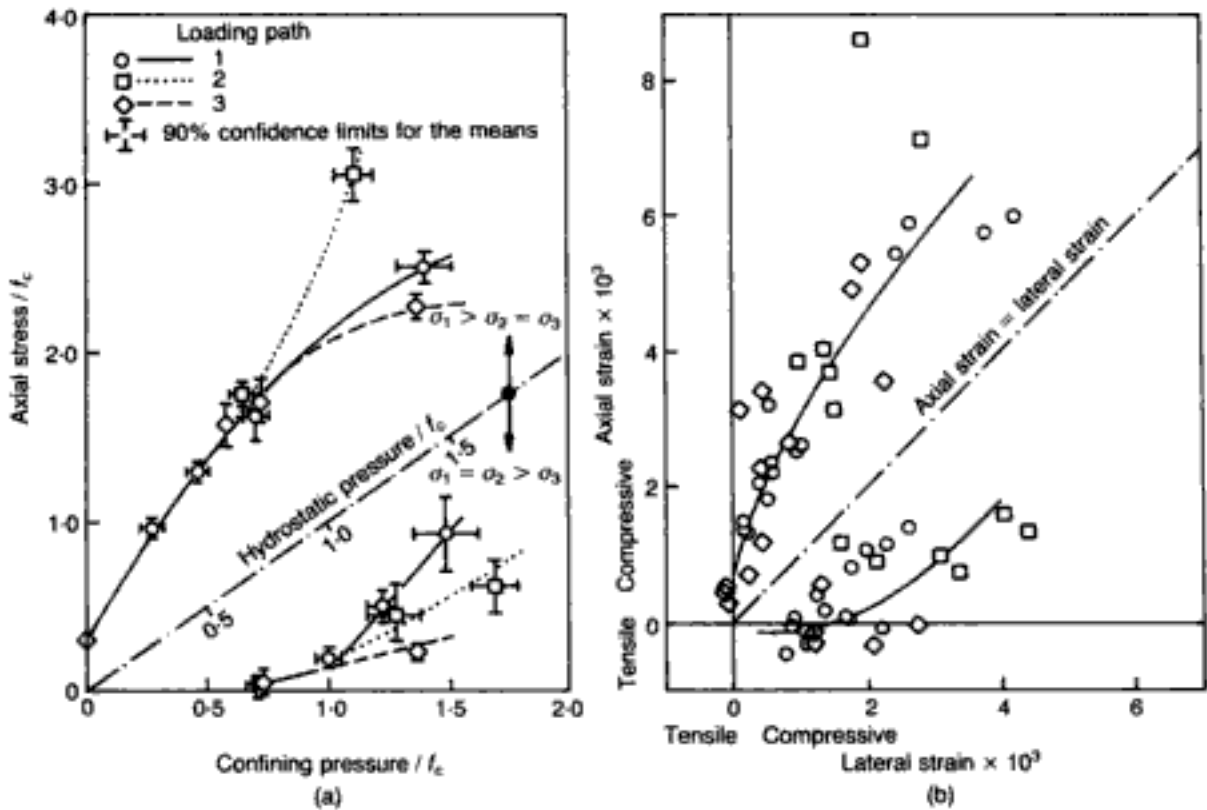


Fig. 1.29. Typical OSFP envelopes ($f_c = 31.7 \text{ N/mm}^2$):^{25,31}
 (a) stress space;
 (b) strain space

values that a very high load, well outside the capacity of currently-used testing machines, will be required to restart a fracture process which will lead to ultimate collapse of the material.

The application of hydrostatic stresses, which cause a reduction in stress concentrations, increases the isotropy of concrete at the macroscopic level. Under such conditions, concrete can withstand very high hydrostatic loading (as mentioned above, considerably outside the capacity of current testing machines), a well-known feature of isotropic media.

Effect of fracture processes on failure envelopes. Figures 1.29–1.31 show the failure envelopes obtained from the tests on a typical concrete with $f_c = 31.7 \text{ N/mm}^2$ subjected to various stress paths (see Fig. 1.27) comprising both *hydrostatic* and subsequent *deviatoric* portions. Path 2 is similar to path 1 except that, after applying the required hydrostatic pressure, the latter is maintained constant until the rate of increase of deformation through 'creep' has reduced to a negligible value (as compared with the rate of deformation under increasing deviatoric load as assessed from the results of previous tests using path 1). This path has been investigated for values of hydrostatic pressure higher than $0.7f_c$ since, for lower values, 'creep' under hydrostatic pressure is so small that the path coincides with path 1.

The figures indicate that the stress path has a similar effect on all envelopes but this effect appears to be smaller for OUPF and US, particularly within the $\sigma_1 = \sigma_2 > \sigma_3$ region where it seems

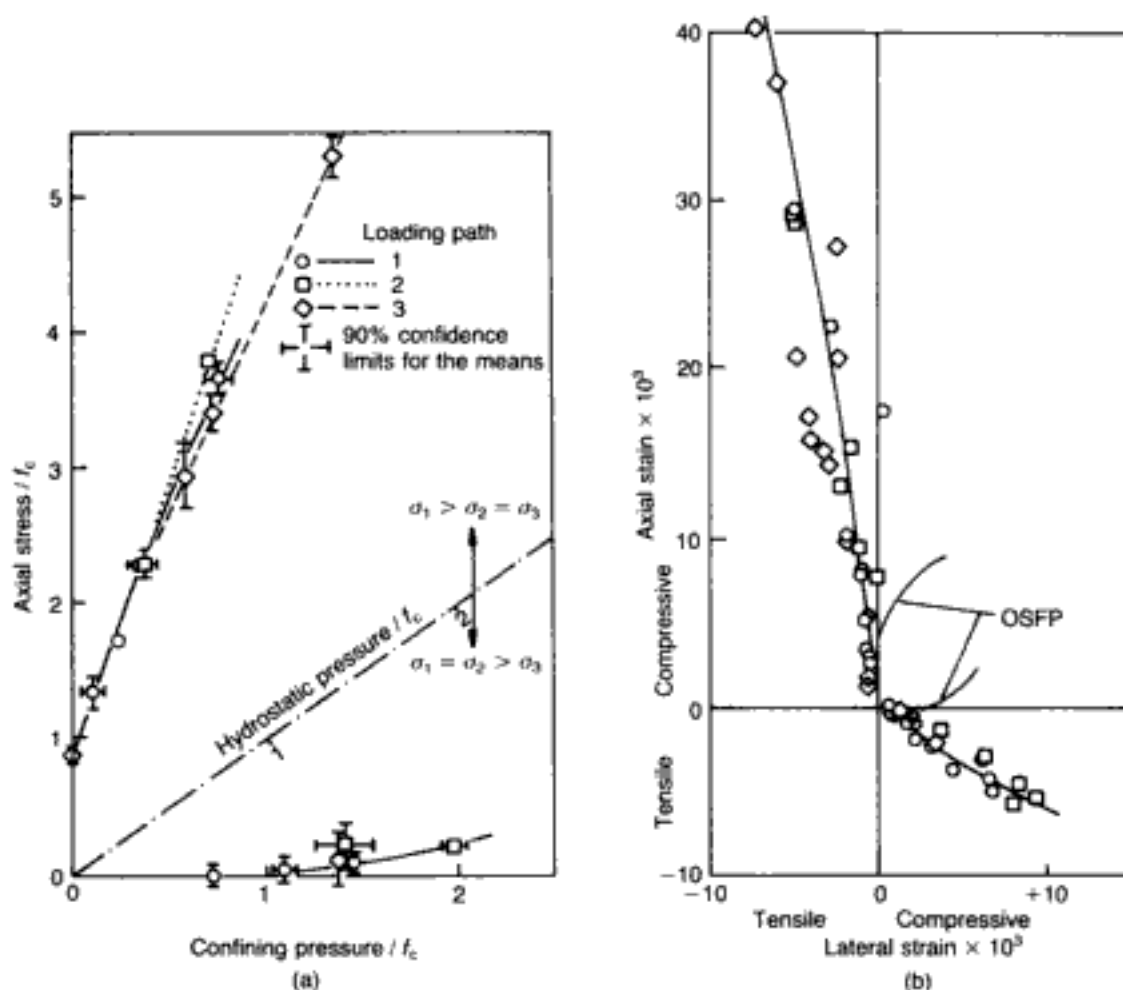


Fig. 1.30. Typical OUFP envelopes ($f_c = 31.7 \text{ N/mm}^2$);^{25,31}
 (a) stress space;
 (b) strain space

to be insignificant. For values of the hydrostatic component of the stress states at OSFP, OUFP and US up to approximately $0.8 f_c$, the envelopes are unaffected by stress path and therefore can be expressed by a single envelope. For higher values of the hydrostatic component the envelopes appear to be stress-path dependent, such that, for a given hydrostatic level, OSFP, OUFP and US occur under deviatoric stress levels which increase with the type of stress path, varying in the order 3, 1, 2 for $\sigma_1 > \sigma_2 = \sigma_3$ and 1, 2, 3 for $\sigma_1 = \sigma_2 > \sigma_3$. It is clear that the deviatoric stress levels increase by both increasing the maximum value of the pure hydrostatic stress of the test and sustaining this value until the rate of deformation becomes negligible in comparison with that occurring under the subsequent deviatoric stress. Such behaviour has been attributed to the fracture processes of 'random' orientation which occur under hydrostatic stress and, in particular, to the delaying effect which the crack propagation 'inhibitors' have on the fracture processes that occur under the deviatoric portions of the stress path. The number of such 'inhibitors' increases as a result of both increasing and sustaining the maximum value of the hydrostatic stress of the test, and this causes the failure envelopes to expand in stress space.

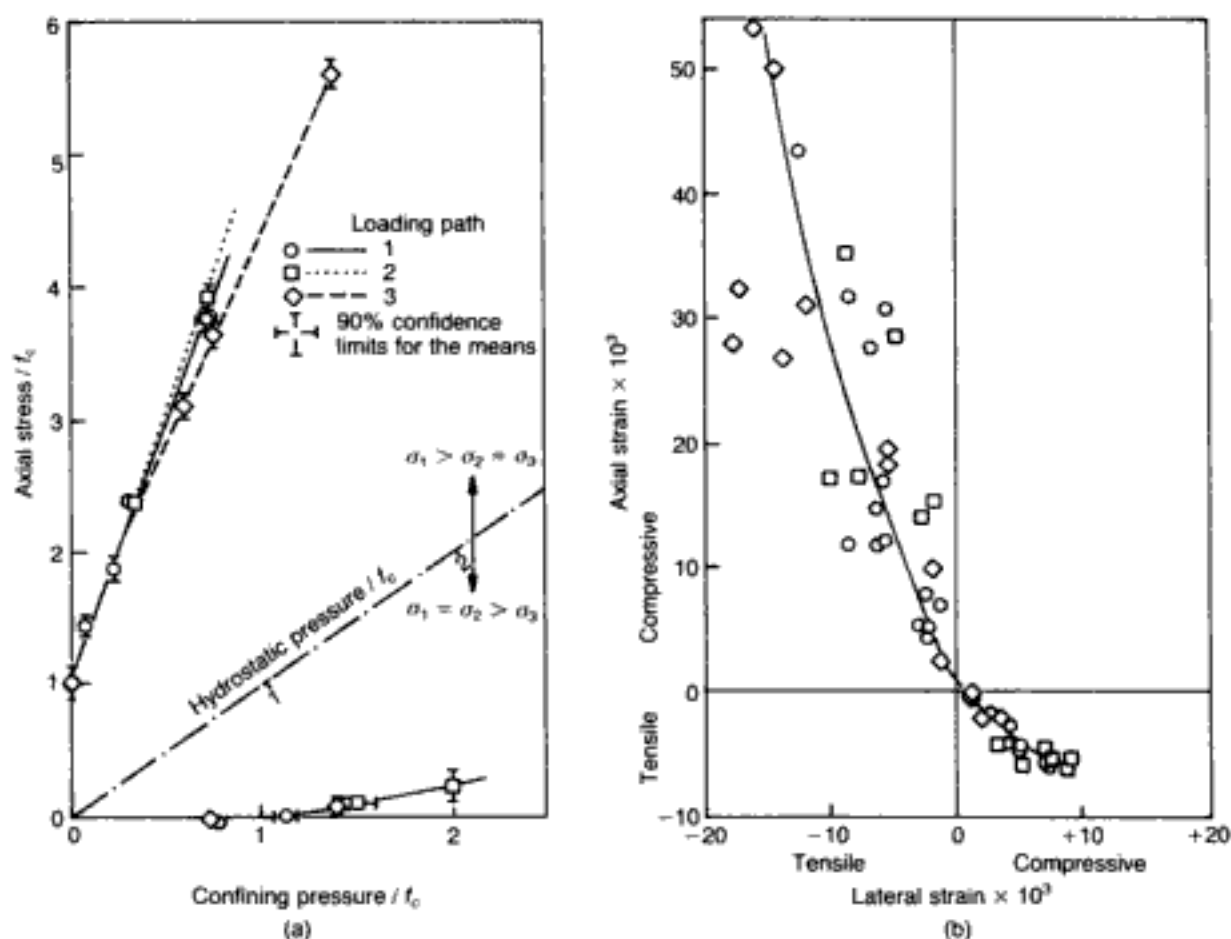
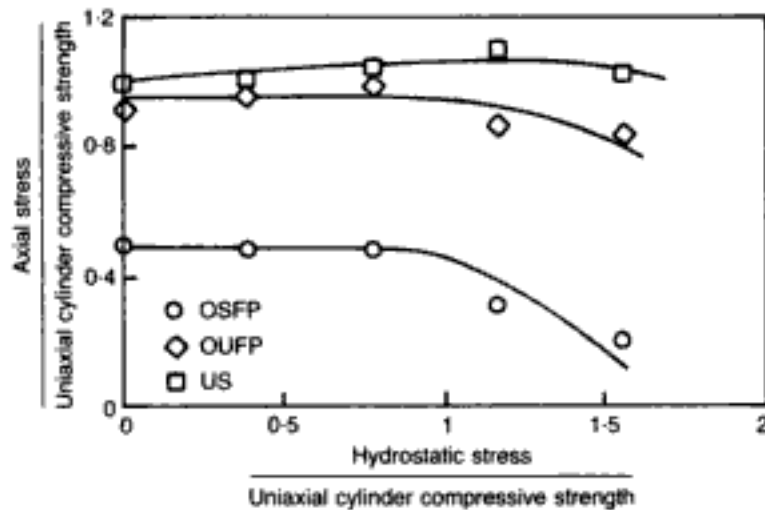


Fig. 1.31. Typical US envelopes ($f_c = 31.7 \text{ N/mm}^2$):^{25,31}
 (a) stress space;
 (b) strain space

It should be noted, however, that the above qualitative observations regarding the effect of the stress path on the various envelopes should not obscure the key fact that the variability of the data in strain space is such that it is difficult to establish any path effects on the failure envelopes, i.e. the experimental scatter swamps any path-dependency effects even at high values of the hydrostatic-stress component. Moreover, the available results for the OUF and US envelopes seem to indicate that, if any significant stress-path influence does occur, this can take place only at stress levels that are unlikely to be realized in ordinary structural-concrete applications. It can be concluded, therefore, that, for practical purposes, it is sufficiently accurate to neglect the effect of stress path on: (a) the ultimate strength envelope (as noted in section 1.3.3.1, the latter can be taken to be practically identical to the corresponding OUF envelope); (b) the stress-strain relations (since, allowing for data scatter, the strains are — like the stresses — effectively independent of stress path).

The above conclusions are both confirmed and extended by some tests on cylinders in which the stress path consisted of the following three stages: increasing the hydrostatic pressure to a given value; decreasing the hydrostatic pressure to zero; and applying an axial compressive stress to failure.²⁹ Such an approach provides some

Fig. 1.32. Variation of stress level at OSFP, OUFP and US with hydrostatic stress obtained from typical uniaxial compression tests on concrete (with $f_c = 47 \text{ N/mm}^2$) which has been subjected to previous hydrostatic loading²⁹



information on the changes in the material caused by previous histories of hydrostatic loading. Figure 1.32 shows the variation, with the maximum value of the hydrostatic stress of the test, of the stress levels at OSFP, OUFP and US obtained under subsequent uniaxial compression. This figure indicates that the above stress levels vary slightly up to a value of the hydrostatic stress of approximately $0.8f_c$, beyond which they begin decreasing with increasing hydrostatic stress. If it is assumed that the fracture processes that occur under the hydrostatic portion of the stress path are related to the maximum value of the applied hydrostatic stress, the above variation reflects the effect of these fracture processes on the fracture processes that occur under the subsequently-applied uniaxial compression.

As already mentioned, in a heterogeneous material such as concrete, the principal directions of the local stress fields that develop within the material when subjected to hydrostatic stress are indefinable and the cracking paths are of random orientation. Such cracking tends to create a more uniform stress and strain distribution within the material, because high stress and strain concentrations are relieved, and when situated in the path along which a crack is likely to propagate, tends also to inhibit such crack propagation. These effects may, in fact, cause the slight increase of the stress levels at OUFP and US with increase of hydrostatic stress up to about $0.8f_c$, as well as the increase in stress difference between OUFP and US which may be attributable to the delaying effect of the above fracture process on the unstable material behaviour above OUFP — see Fig. 1.32. However, the figure suggests that, for values of hydrostatic stress higher than $0.8f_c$, the fracture processes under hydrostatic stress reduce the energy capacity of the material and thus the stress levels at OSFP, OUFP and US decrease with increasing hydrostatic stress. Nevertheless, any decrease in OUFP and, especially, US, appear to be quite small even up to the limit of available results (i.e.

hydrostatic stress of around $1.5f_c$), particularly in view of the ever-present material-data scatter.

1.3.3.3. Fracture processes under generalized stress

Since any generalized state of stress can be decomposed into a hydrostatic and a deviatoric component, it would be expected that, under such a stress state, both types of fracture process discussed above would occur concurrently.

The crack extension and propagation processes caused by the deviatoric component are considered to be those fracture processes which will eventually lead to ultimate collapse of the material. On the other hand, the fracture processes caused by the hydrostatic component will act as 'inhibitors' of the previous type of fracture process. Such an effect will tend to reduce the rate of the crack propagation processes caused by the deviatoric component, and thus increase the stress level required to cause ultimate failure, as is evident, for example, by reference to the OUF and US envelopes for paths 1 and 2, which lie outside those for path 3 (the latter having a smaller hydrostatic-stress component since, in Figs 1.29–31, the hydrostatic stress corresponding to any given data point is obtained by a projection onto the hydrostatic axis that is either perpendicular to it (stress paths 1 and 2) or parallel to the axial-stress axis (stress path 3)). However, as mentioned earlier, such path-dependency is small and, for practical purposes, can be ignored.

1.4. A mathematical model for concrete materials

Comprehensive models of the behaviour of concrete under load derived to date have, almost invariably, been based on continuum-mechanics theories such as those of plasticity, elastoplasticity, viscoplasticity, etc. (see, for example, references 33–36). However, the use of such theories has led to complex analytical formulations which, in most cases, are dependent on the inclusion of a large number of functions and parameters. These functions and parameters are invariably evaluated by fitting the analytical expressions to experimental data; thus the validity of the model predictions appears to depend primarily on the validity of the data used rather than on the choice of a particular theory. As a result, certain features of the models may be of questionable validity, especially the prediction of post-ultimate behaviour (which is heavily dependent on testing techniques, as discussed earlier) and of the cyclic response (for which experimental information is sparse).

As explained earlier in this chapter, a model that defines material behaviour (under generalized stress) up to a peak level is sufficient for the description of the deformational response of concrete, and, in view of the brittle nature of the material, this peak level can itself form the basis for the failure criterion. Furthermore, in accordance with the concepts associated with the fracture processes

outlined in the previous section, it is possible to arrive at mathematical descriptions for both the constitutive law and the failure criterion for concrete. As made clear in section 1.3.3.1, the ensuing analytical expressions for these two key material characteristics correspond to the phenomenological observations associated with the processes which were termed, generically, microcracking and macrocracking respectively. Such expressions will be presented in this section, alongside the deformation and yield criteria for the reinforcing steel. It should be emphasized that all mathematical relations for the concrete are based purely on experimental evidence obtained from triaxial test data, while those for steel, for which there is little room for variation and/or disagreement, follow the recommendations of codes of practice.

1.4.1. Constitutive relations for concrete

This section is concerned with deformational properties and it describes an attempt to express mathematically the ascending portion of the stress-strain curve for concrete when subjected to short-term static loading conditions. The mathematical description of the deformational behaviour is based on an analysis of experimental data on the behaviour of concrete under multiaxial stress (both biaxial and triaxial) which were obtained at Imperial College by adopting the testing methods mentioned in section 1.1.5 (see also reference 37), and using a range of concretes with uniaxial cylinder compressive strength (f_c) varying from about 15 N/mm² to about 65 N/mm².^{20,38} In this analysis, use is made of the assumption that the nonlinear material behaviour is dictated mainly by structural changes. These structural changes occur in the form of fracture initiation and propagation processes which have the following two opposing effects on the material deformation.

Effect A. Cracking causes a reduction of the high, predominantly tensile stress concentrations existing near the crack tips. This reduction in tensile stress can be assumed to be equivalent to the application of a compressive stress which tends to *reduce* the volume of concrete.

Effect B. Cracking produces voids which tend to *increase* the volume of material.

It was shown in section 1.3.3.1 that, depending on the combined effects of A and B on deformation, the cracking processes could be described qualitatively by reference to four stages. For present purposes, such a description may be simplified by dividing these fracture processes into three stages, which are shown schematically in Fig. 1.33. These can broadly be described as follows.

Stage I. In Stage I, effect A is significant while effect B is insignificant since cracking is localized. As a result, the volume decreases.

Stage II. In Stage II, effects A and B are significant, but effect A is greater than effect B and thus the volume continues

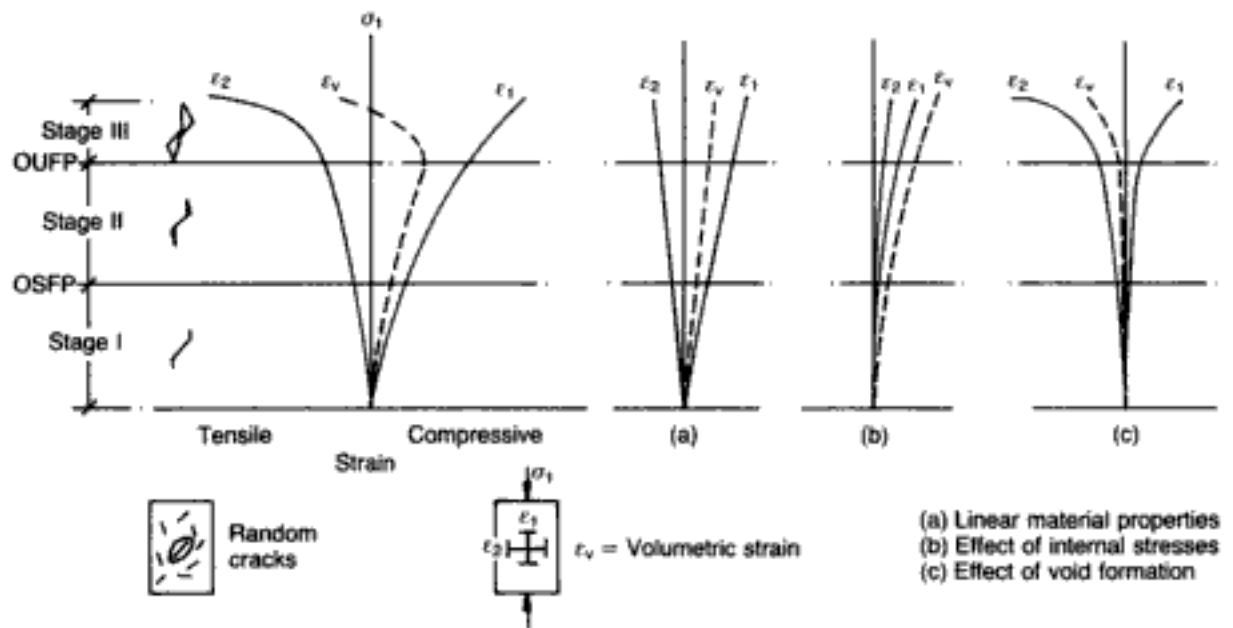


Fig. 1.33. Stages of fracture processes and their effect on the stress-strain relationships of concrete³⁸

to decrease. The beginning of this stage was previously termed the OSFP level, at which the rate of increase of the strain ϵ_2 begins to exceed the rate of increase of the strain ϵ_1 , even though ϵ_1 still exceeds ϵ_2 .

Stage III. In Stage III, both effects A and B are significant, but effect B is greater than effect A and this causes the volume to increase. The beginning of this stage was previously termed the OUF level and can be defined easily since it corresponds to the level at which the volume of the material becomes a minimum (i.e. beyond the OUF, ϵ_2 soon exceeds ϵ_1).

On the basis of the above considerations, therefore, it is evident that the deformational behaviour of concrete at all three stages may be decomposed into the following three components:

- a 'linear' component throughout, dictated by the material characteristics and unaffected by the above fracture processes
- a nonlinear component expressing the effect of the internal stresses caused by the fracture processes
- a nonlinear component expressing the effect of void formation.

To quantify the above components using experimental stress-strain data appears to be an impossible task since the data describe overall material behaviour. Nevertheless, it is clear that their combined effects result in two broad regimes of (overall) nonlinearity. The first of these, which forms the subject of the present section and relates to the constitutive relations up to the OUF level, is governed primarily by a combination of (a) and

(b). Therefore, although microcracking does cause some increase in the volume of the material owing to void formation, its predominant effect is to release the high tensile stresses at the crack tips which, as noted above, is statically equivalent to the application of an *internal* compressive state of stress that reduces the volume of concrete. Therefore, it is the latter effect (i.e. effect A) which is considered to be the underlying cause of the nonlinear behaviour up to the minimum-volume level. This first regime of nonlinearity (namely stages I and II in Fig. 1.33), which is of a 'mild' nature, may be described mathematically by means of the concept of internal compressive stress state described above. Before this is done, however, it is necessary to discuss briefly in terms of suitable parameters the experimental data on the deformational behaviour of concrete during both loading and unloading.

1.4.1.1. *Experimental data on observed behaviour*

These can be summarized as follows.

Deformational behaviour during loading. The generalized stress-strain relationships for the experimental data corresponding to the ascending branch of concrete materials are expressed most conveniently by decomposing each state of stress and strain into hydrostatic and deviatoric components, i.e. in the form of normal and shear octahedral stresses (σ_0 , τ_0) and strains (ϵ_0 , γ_0) respectively. (For a definition of these octahedral parameters, see Appendix A.) In this form of representation, the deformational behaviour of concrete up to the minimum-volume level under increasing stress (behaviour under decreasing stress is discussed later) can be described completely by reference to the strains produced upon the application, in turn, of hydrostatic and deviatoric components of stress.

The results of tests indicate that the deformational behaviour of concrete under hydrostatic stress σ_0 can be fully described by the variation of the hydrostatic (volumetric) strain $\epsilon_{0(h)}$ with σ_0 , since the accompanying deviatoric strain $\gamma_{0(h)}$ has been found to be insignificant.^{12,9} (The subscript h serves as a reminder that the octahedral strains result from the application of a pure hydrostatic stress state.) These $\sigma_0 - \gamma_{0(h)}$ relationships depend only on the uniaxial strength f_c of the particular concrete, and typical results are shown as data points in Fig. 1.34. It is evident that the variation of $\epsilon_{0(h)}$ with σ_0 is distinctly nonlinear. Such nonlinear behaviour is considered to reflect the dependence of volumetric strains on internal stresses resulting from redistributions that occur as a result of changes in the structure of the material when subjected to an externally-applied hydrostatic stress. It would be expected that internal stresses can be decomposed into hydrostatic and deviatoric components, but the fact that the distortion of the material under a pure applied hydrostatic stress σ_0 has been found to be

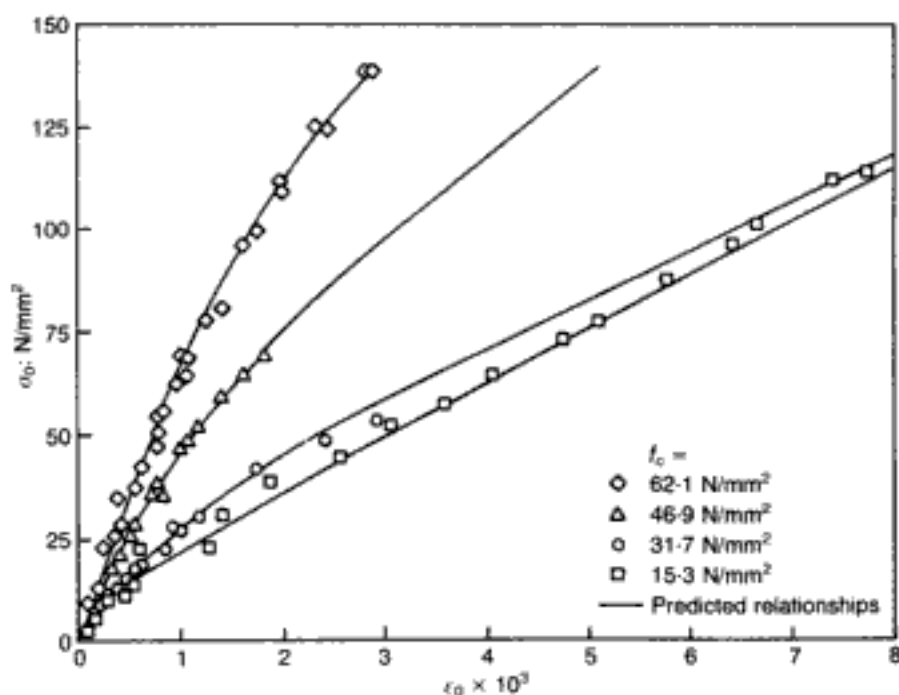


Fig. 1.34. Typical experimental $\sigma_0 - \epsilon_{0(h)}$ relationships for various concretes³⁸

insignificant (i.e. $\gamma_{0(h)} = 0$) indicates that the deviatoric component of the internal stress is negligible, and this may be attributed to the random orientation of the structural changes that concrete undergoes under external hydrostatic stress. Furthermore, it has also been found that specimens subjected to various levels of uniaxial compression below the failure level, when unloaded and then reloaded hydrostatically, exhibit a stress-strain relationship which is essentially the same as that exhibited by specimens under increasing hydrostatic stress without any previous (deviatoric) loading history.¹⁰ In view of this experimental evidence, it appears realistic to consider that the volumetric strain $\epsilon_{0(h)}$ of concrete due to the hydrostatic component σ_0 of the applied state of stress is independent of the value of the applied deviatoric component τ_0 , and hence $\epsilon_{0(h)}$ may be expressed in terms of σ_0 only. Finally, it should be pointed out that, since this variation of $\epsilon_{0(h)}$ with σ_0 indicates consolidation of the material that occurs at a progressively increasing rate, the hydrostatic component of internal stresses must be compressive and is considered to represent the reduction of high tensile-stress concentrations that occur near the crack tips as a result of crack extension; such a view is clearly consistent with the fracture mechanism of concrete under increasing stress discussed previously in the description of component (b) of the deformational behaviour which governs nonlinearity up to the OUF level.

The application of an external deviatoric stress τ_0 gives rise to both volumetric and deviatoric (shear) strains. Therefore, the deformational response of concrete under increasing deviatoric stress is defined by both $\tau_0 - \gamma_{0(d)}$ and $\tau_0 - \epsilon_{0(d)}$ relationships. (The subscript d indicates that the octahedral strains are due to

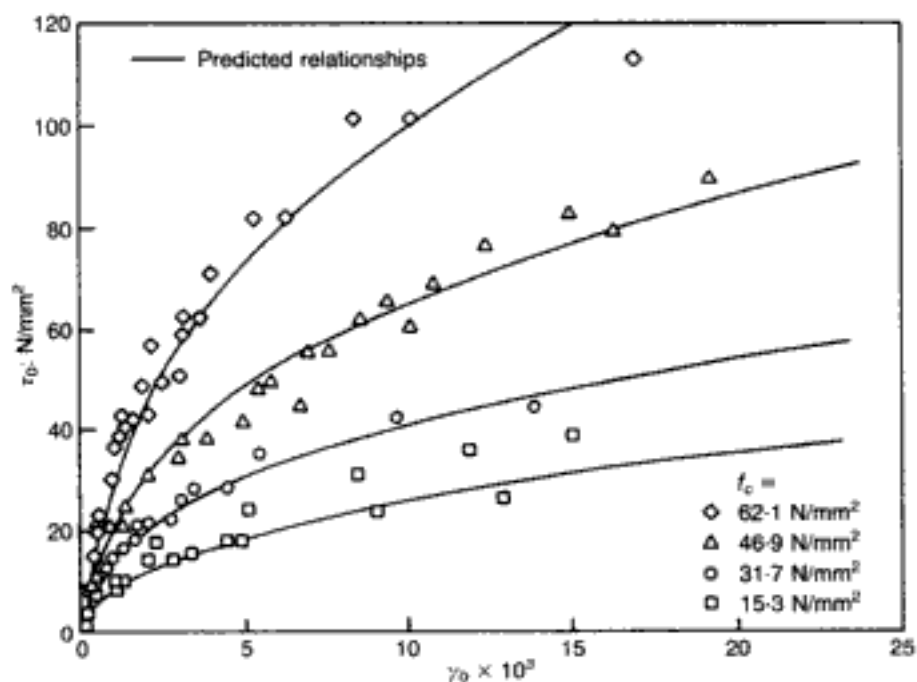


Fig. 1.35. Typical experimental $\tau_0 - \gamma_{0(d)}$ relationships for various concretes³⁸

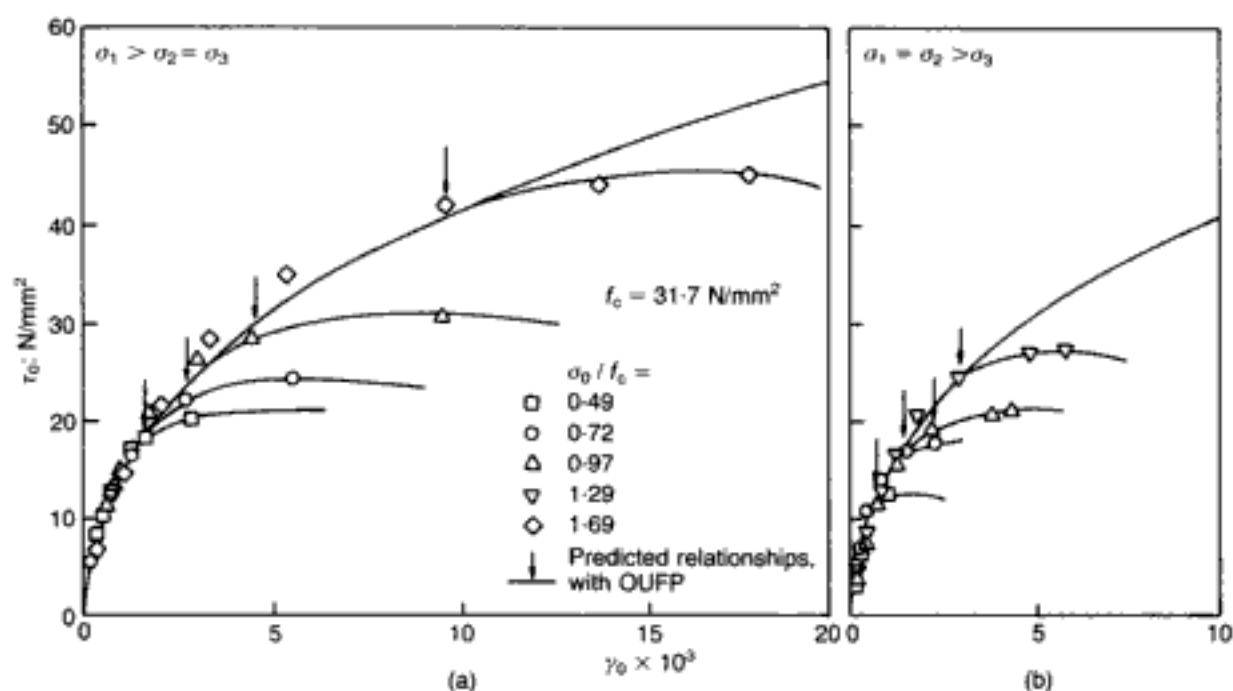


Fig. 1.36. Typical experimental $\tau_0 - \gamma_{0(d)}$ relationships for concrete (with $f_c = 31.7$ N/mm²) for two possible stress paths:³⁸ (a) $\sigma_1 > \sigma_2 = \sigma_3$; (b) $\sigma_1 = \sigma_2 > \sigma_3$

a pure deviatoric stress state.) Typical experimental results for the $\tau_0 - \gamma_{0(d)}$ relations for various concretes are shown as data points in Fig. 1.35. In addition, data points for both the $\tau_0 - \gamma_{0(d)}$ and $\tau_0 - \epsilon_{0(d)}$ characteristics appear in Figs 1.36 and 1.37 respectively for two possible stress paths ($\sigma_1 > \sigma_2 = \sigma_3$ (triaxial 'compression') and $\sigma_1 = \sigma_2 > \sigma_3$ (triaxial 'extension')). It is evident that both sets of relationships are essentially independent of stress path, indicating that the influence of the direction of τ_0 (i.e. rotational angle θ — see Appendix A) on the octahedral (or deviatoric) planes (i.e. the planes orthogonal to the stress-space

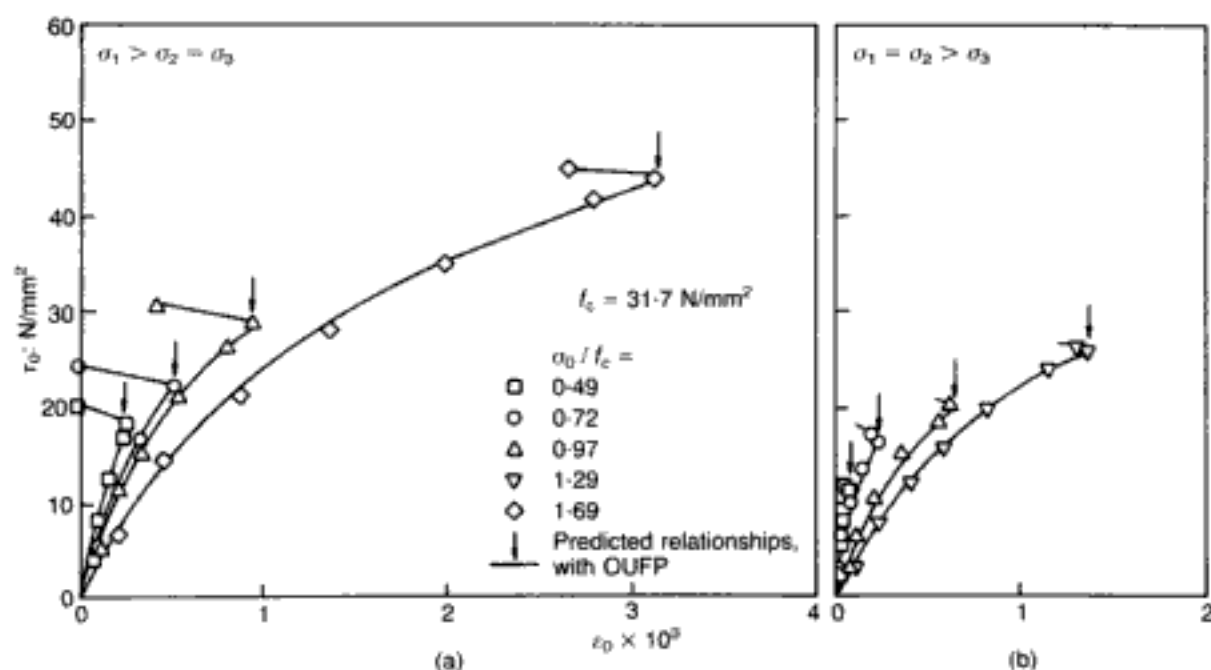


Fig. 1.37. Typical experimental $\tau_0 - \epsilon_{0(d)}$ relationships for concrete (with $f_c = 31.7 \text{ N/mm}^2$) for two possible stress paths:³⁸ (a) $\sigma_1 > \sigma_2 = \sigma_3$; (b) $\sigma_1 = \sigma_2 > \sigma_3$.

diagonal at various levels of σ_0) is negligible and that any stress-induced anisotropy is insignificant and can be ignored for practical purposes.

Additional confirmation of path independency (but concentrating now only on the $\tau_0 - \gamma_{0(d)}$ relations) is provided by the results gathered in the international cooperative project mentioned earlier in the chapter, and which was based on the use of a common concrete mix by all participants.⁹ These findings appear in Fig. 1.38 in the form of three curves that correspond to the different stress paths followed. (The stress paths denoted as 1 and 3 correspond to the triaxial 'compression' and 'extension' respectively, while 2 refers to the additional case of constant

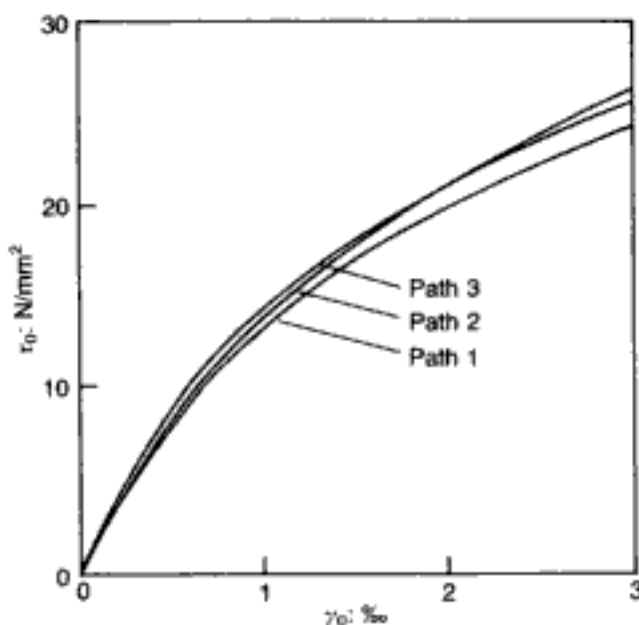


Fig. 1.38. Deviatoric stress-strain curves obtained from triaxial tests using different loading paths⁹

intermediate principal stress.) Mean curves were obtained for each participant's test series and for each path, and these, in turn, averaged as shown in the mean $\tau_0 - \gamma_{0(d)}$ curves of Fig. 1.38. It is obvious that these mean curves for the three paths coincide sufficiently closely so that the differences may be attributed to random effects, a conclusion confirmed by the fact that, among the various test series, there was no clear-cut ordering of stiffnesses for the different paths.

Such path independency of the relations $\tau_0 - \gamma_{0(d)}$ and $\tau - \epsilon_{0(d)}$ with respect to the direction of τ_0 on the deviatoric plane defined for any given σ_0 is an important and very useful property of concrete materials, as it simplifies considerably the mathematical model to be derived subsequently. However, it leads next to the question of whether or not the two relations between τ_0 and the strains it produces are in fact affected by the magnitude of σ_0 itself. It turns out that, as in the case of the $\sigma_0 - \epsilon_{0(h)}$ relationships, the $\tau_0 - \gamma_{0(d)}$ characteristic has also been found to be essentially unique, i.e. for a given concrete (defined by f_c), γ_0 is dependent on τ_0 only and not on the level of σ_0 . This is implicit in Fig. 1.35 but may be seen more clearly by reference to Fig. 1.36 where, for a given f_c , a single curve describes the $\tau_0 - \gamma_{0(d)}$ relationship up to the OUFP level, i.e. up to about the peak of the ascending branch that defines the range of material properties relevant for purposes of structural applications. Therefore, the fact that, beyond the minimum-volume level, where the predominant effect on deformation is void formation (which is considered to cause the much faster rate of increase of $\gamma_{0(d)}$ with τ_0), the $\tau - \gamma_{0(d)}$ characteristic does become dependent on the value of σ_0 has no bearing on the material model. Further evidence of the independence of the $\tau_0 - \gamma_{0(d)}$ relations with respect to the location of octahedral planes is provided by some of the results of the various test series of the international cooperative project.⁹ The triaxial load history followed in a number of these tests allowed stress deviation within various octahedral planes of mean normal stress varying from about $0.5f_c$ to almost $2.0f_c$. Deviatoric stress-strain curves were plotted for all these octahedral planes and the results are shown in Fig. 1.39. Here, deviations were imposed within different octahedral planes ranging from $\sigma_0 = 0.55f_c$ ($= 17.6 \text{ N/mm}^2$) to $\sigma_0 = 1.75f_c$ ($= 56.3 \text{ N/mm}^2$). Each individual curve in Fig. 1.39 represents the mean of several tests along each of these paths. It is clear that the curves are very closely bunched, with no systematic ordering according to σ_0 . Other test series gave entirely similar results, especially as regards the very small random scatter of curves, thus confirming that the $\tau_0 - \gamma_{0(d)}$ relations are independent of σ_0 .

The $\tau_0 - \epsilon_{0(d)}$ characteristics, on the other hand, are a function of both f_c and σ_0 , as is clear by reference to Fig. 1.37. (It should be noted that the sharp deviations from the smooth curves on

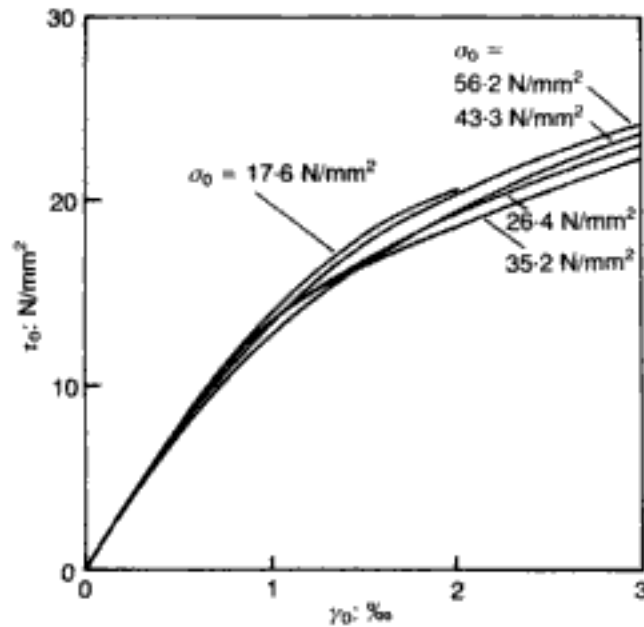


Fig. 1.39. Deviatoric stress-strain curves for different octahedral planes⁹

reaching the OUF_P level are of no relevance to the mathematical model.) Such characteristics, therefore, appear to represent the only form of interaction (i.e. coupling) between the hydrostatic and deviatoric components of the stress and strain states. As for the $\sigma_0 - \epsilon_{0(h)}$ relationships, the nonlinearity of $\tau_0 - \gamma_{0(d)}$ and $\tau_0 - \epsilon_{0(d)}$ is due primarily to the dependence of $\gamma_{0(d)}$ and $\epsilon_{0(d)}$ on the internal stress redistributions that take place when an externally-applied deviatoric stress is imposed. While the nonlinear variation of $\gamma_{0(d)}$ with τ_0 may be regarded as being caused by the deviatoric component of internal stresses, the nonlinearity of $\epsilon_{0(d)}$ with τ_0 is considered to be dictated by the effect of the hydrostatic component of the internal stresses on the deformation of the material when subjected to applied deviatoric stress. The fact that $\epsilon_{0(d)}$ increases (i.e. volume of specimen decreases) at an increasing rate implies that, as in the case of the $\sigma_0 - \epsilon_{0(h)}$ relationship, the hydrostatic component of internal stresses (under external deviatoric stress) is compressive and may also be considered to represent the reduction of the high tensile stress concentrations that occur near the crack tips as a result of crack extension.

Deformational behaviour during unloading. An indication of the stress-strain behaviour of concrete during unloading may be given by uniaxial and triaxial experimental data obtained from cyclic tests.^{10,20,39,40} The hysteresis loop exhibited by such data during the first cycle is so small that the same linear stress-strain relationship may be used to describe in a realistic way concrete behaviour during both unloading and subsequent reloading up to the maximum stress level experienced previously by the material (see Fig. 1.40). Figure 1.40 indicates that this linear relationship has an essentially constant inclination and its distance from the origin of the monotonically increasing stress-strain curve increases

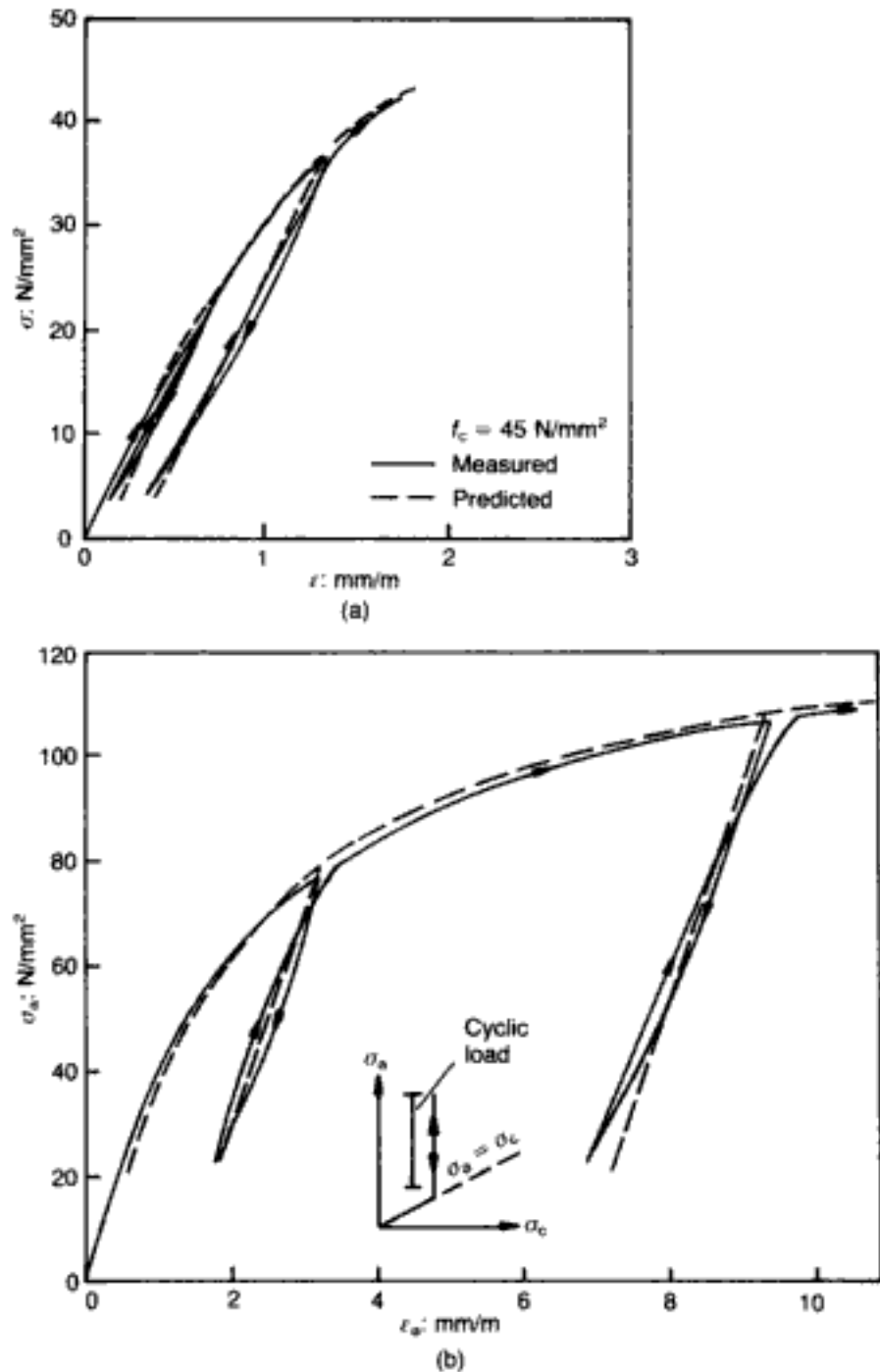


Fig. 1.40. Measured and predicted stress-strain behaviour during loading and unloading/reloading for a typical concrete (with $f_c = 45 \text{ N/mm}^2$) under (a) uniaxial and (b) triaxial compression⁴⁰

with the maximum stress level of the cyclic load. For stress levels beyond this maximum stress, concrete response is described by the monotonically increasing stress-strain relationships discussed in the preceding section.

The above simple behaviour upon unloading may readily be understood by reference to the internal fracture processes that were used earlier to explain the causes of the observed behaviour under increasing stress. During unloading, these fracture processes cease and, as a result, concrete behaviour is then essentially elastic. Only when the maximum stress level previously experienced by the material is exceeded can fracture be resumed.

1.4.1.2. *Mathematical description of deformational behaviour*

The aim of the present section is to incorporate the salient phenomenological features and related experimental data outlined in the preceding section into an analytical material model in a form suitable for use in the nonlinear finite-element (FE) analysis of concrete structures. This can be done in several ways, and three possible approaches will be described in detail. The first of these will be most familiar to structural engineers used to dealing with a given number of material 'constants' that are required for defining the stress-strain relationships. The second approach is conceptually ideal in expressing the fracture processes associated with microcracking and the internal stresses which arise therefrom. For purposes of computer implementation, however, the third approach has been found to be most convenient (although such a standpoint is, arguably, a matter of personal taste); this is an eclectic procedure, combining the philosophies of the first two methods as needed. It should be evident that, whatever the formulation used to arrive at a suitable mathematical model, the key analytical ingredient is effectively a curve-fitting process based on reliably established experimental data of the kind discussed throughout this chapter.

The three-moduli approach. As is well known, in the case of linearly-elastic material behaviour in three dimensions, the six components of stress are related to their strain counterparts by the generalized law of Hooke involving a maximum of 21 independent constants. Material isotropy reduces the number of these constants to 2, which may be expressed in several (clearly interdependent) ways, such as by means of Lamé's expressions or by the use of Young's modulus E and Poisson's ratio ν . For present purposes, where the octahedral representation of stresses and strains is adopted, perfect isotropy permits the decoupling of volume changes and distortional (i.e. shape) changes, with the two natural material constants becoming the bulk modulus K and the shear modulus G , as given by the following expressions (see Appendix A)

$$K = \frac{\sigma_0}{3\epsilon_0} = \frac{E}{3(1-2\nu)} \quad (1.1)$$

$$G = \frac{\tau_0}{2\gamma_0} = \frac{E}{2(1+\nu)} \quad (1.2)$$

Since these parameters are constant for linearly-elastic materials, it follows that both the octahedral normal and shear stress-strain (straight-line) curves are unique, as they are independent of stress magnitudes and stress ratios in the uniaxial, biaxial, and triaxial ranges.

In the case of nonlinear materials, parameters akin to relations (1.1) and (1.2) may still be employed, but then K and G are

functions of the stress and strain levels in the material. For example, the following definitions could be used

$$K_s(\epsilon_0) = \frac{\sigma_0(\epsilon_0)}{3\epsilon_0} \quad (1.3)$$

$$G_s(\gamma_0) = \frac{\tau_0(\gamma_0)}{2\gamma_0} \quad (1.4)$$

where the subscript *s* indicates that the secant-modulus approach has been adopted. Now, it was argued in section 1.3.3 that, up to about the OUF_P level, concrete may be approximated by an isotropic model. Thus, expressions such as (1.3) and (1.4) can be used to describe the ascending branch of the stress-strain relations for concrete, or, more specifically, the $\sigma_0 - \epsilon_{0(h)}$ and $\tau_0 - \gamma_{0(d)}$ characteristics respectively. Such an approach, however, is not sufficient on account of the presence of the coupling between stress deviation and volume change. Owing to this $\tau_0 - \epsilon_{0(d)}$ characteristic, a third material modulus is needed, and a coupling modulus *H* has been proposed,⁹ defined as

$$H_s = \frac{\tau_0}{\epsilon_{0(d)}} \quad (1.5)$$

Therefore, the total octahedral strains resulting from the application of an external stress state (σ_0, τ_0) may be written as

$$\epsilon_0 = \epsilon_{0(h)} + \epsilon_{0(d)} = \frac{\sigma_0}{3K_s} + \frac{\tau_0}{H_s} \quad (1.6)$$

$$\gamma_0 = \gamma_{0(d)} = \frac{\tau_0}{2G_s} \quad (1.7)$$

It is evident that the presence of the second term on the right-hand side of expression (1.6) implies that the assumption of isotropy in concrete at the material macrolevel may be used only in an approximate sense. Unlike a truly isotropic material, for which the principal stress and strain axes coincide, the coupling effect in concrete leads to the schematic representation of Fig. 1.41, and the requirement for a third modulus for what may be described more accurately as quasi-isotropic behaviour. While data on the moduli K_s and G_s associated with true isotropy will be presented later, it may be of interest to include here some information on the additional modulus that has emerged from the international cooperative project in which various testing techniques were used.⁹ This cooperative work produced, among other data, a number of relations and, although these allow only a superficial estimate of H_s to be achieved, it is worth exhibiting here the main trend of results. If a straight-line relation between $\tau_0 - \epsilon_{0(d)}$ is assumed (clearly an approximation — see, for example, Fig. 1.37), H_s will be a parameter that varies only with hydrostatic pressure

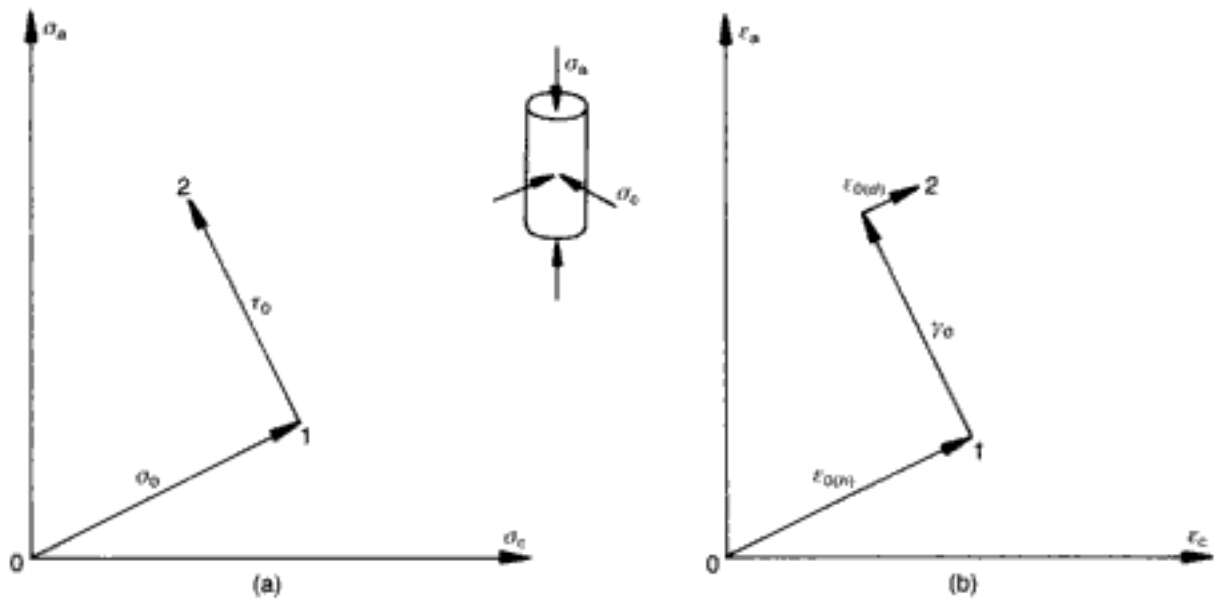


Fig. 1.41. Schematic representation of the coupling effect between stress deviation τ_0 and volume change $\epsilon_{0(d)}$: (a) stress path followed; (b) resulting strains

σ_0 . In order to assess this variation, the mean $\tau_0 - \epsilon_{0(d)}$ curves of all triaxial series considered were plotted individually and their moduli determined. These were then plotted against σ_0 and are shown as data points in Fig. 1.42 (the solid curve refers to the resulting approximate mean $H_s - \sigma_0$ characteristic). It is evident that the coupling effect tends to become very slight at low values of σ_0 , as indicated by the corresponding high values of H_s .

The internal-stress approach. Consider a typical ascending branch of the stress-strain relations of concrete, such as that represented

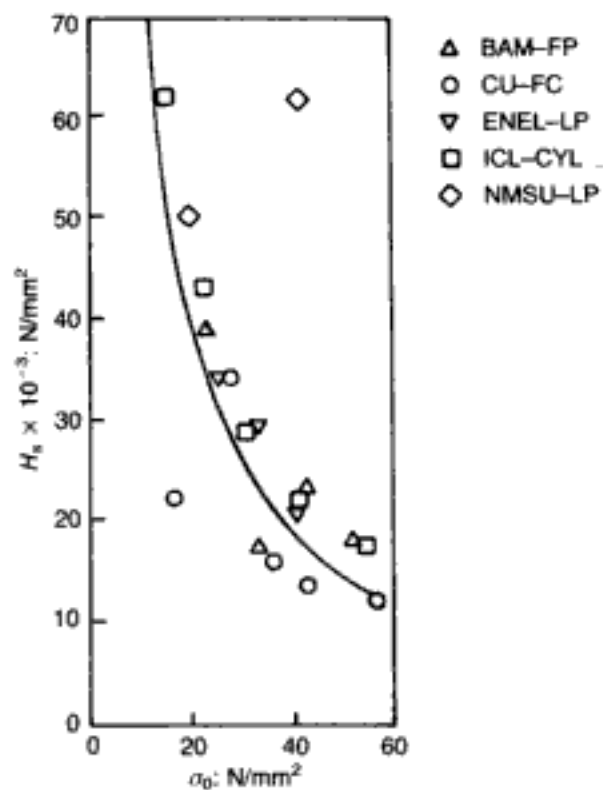
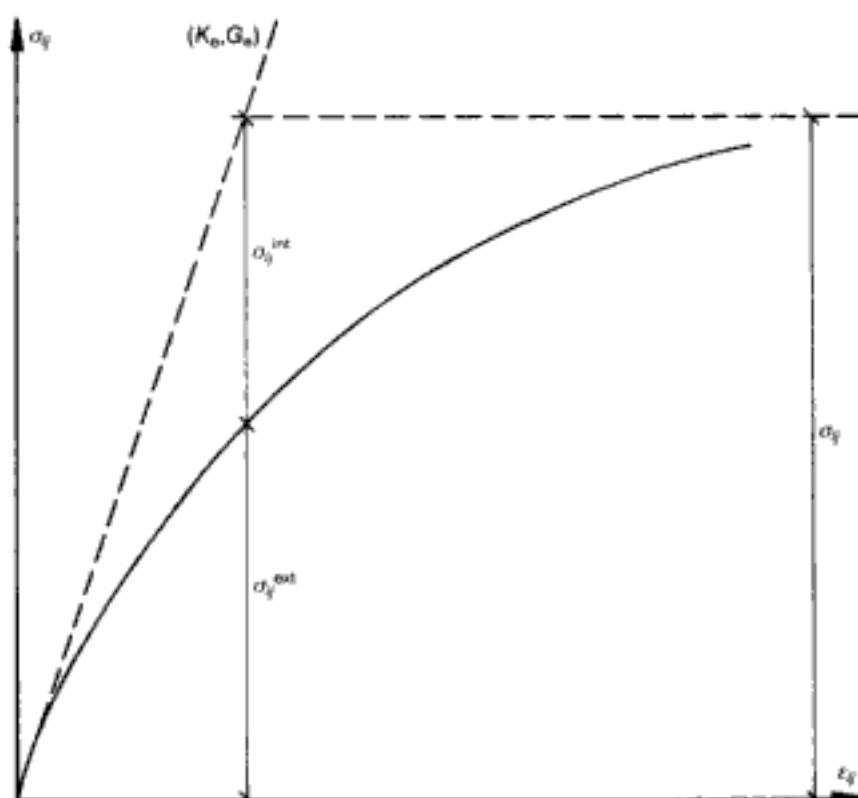


Fig. 1.42. Coupling modulus versus octahedral normal stress⁹

Fig. 1.43. The internal-stress concept used to account for the nonlinear constitutive relations of concrete materials



by the curve of Fig. 1.43. (The tensorial notation and convention adopted for the stresses and the strains is used here in a generic sense; the main specific application of Fig. 1.43 and associated equations (1.8) — see below — concerns, of course, octahedral stress–strain characteristics.) As explained already, the nonlinearity of such a stress–strain relationship is governed essentially by the fracture processes identified with microcracking and which may be viewed as being equivalent to the application of an internal compressive state of stress. It follows, therefore, that, once the departure from linearity is established and quantified, it can be thought of as the overall effect of these internal stresses at the structural level. Then, the use of this internal state of stress, in conjunction with the initial elastic moduli K_e , G_e or E_e , ν_e (tangent to the curve at the origin), is sufficient to describe fully the nonlinear constitutive characteristic(s). In this way, the knowledge of the internal stress state throughout the ascending range of the stress–strain relations enables the nonlinear response of concrete to be expressed analytically by using linear material properties, namely the two moduli associated with isotropic behaviour.⁴⁰ Thus, when σ_{ij} refers to a stress related to the state of strain by constant material properties, the generalized form of Hooke's law may be written as

$$\epsilon_{ij} = - \frac{\nu_e}{E_e} \sigma_{kk} \delta_{ij} + \frac{(1 + \nu_e)}{E_e} \sigma_{ij} \quad (1.8a)$$

or, equivalently,

$$\epsilon_{ij} = - \frac{(3K_e - 2G_e)}{18K_e G_e} \sigma_{kk} \delta_{ij} + \frac{1}{2G_e} \sigma_{ij} \quad (1.8b)$$

in which the tensorial summation convention is implicit (as is the well-known meaning of Kronecker's delta), so that $\sigma_{kk} = 3\sigma_0$ and $2\epsilon_{ij} = \gamma_{ij}$. By decomposing the total strains ϵ_{ij} and stresses σ_{ij} into their hydrostatic components, $\epsilon_0 = \epsilon_{kk}/3$ and $\sigma_0 = \sigma_{kk}/3$, and deviatoric components, $e_{ij} = \epsilon_{ij} - \epsilon_0 \delta_{ij}$ and $s_{ij} = \sigma_{ij} - \sigma_0 \delta_{ij}$, the following simple alternative expression for Hooke's law in its generalized form is obtained

$$\epsilon_{ij} = \epsilon_0 \delta_{ij} + e_{ij} = \frac{\sigma_0}{3K_e} \delta_{ij} + \frac{s_{ij}}{2G_e} \quad (1.8c)$$

For any of the above expressions (1.8) to be applicable to concrete behaviour, it is evident that the following equation must hold

$$\sigma_{ij} = \sigma_{ij}^{\text{ext}} + \sigma_{ij}^{\text{int}} \quad (1.9)$$

where the superscripts ext and int refer to the external (applied) and internal (microcracking) stress states respectively. The strain component due to σ_{ij}^{ext} is recoverable during unloading whereas that due to σ_{ij}^{int} is permanent and equivalent to the strain state caused by the maximum level of σ_{ij}^{int} previously experienced by the material. The elastic recovery can be evaluated from any of the equations (1.8) by setting $\sigma_{ij}^{\text{int}} = 0$.⁴⁰ However, the use of equations (1.8) for the evaluation of the strain state corresponding to a given stress level requires a quantitative description of: the elastic constants K_e and G_e ; the internal state of stress σ_{ij}^{int} ; a criterion defining loading and unloading; and a criterion defining the variation in stress space of the external state of stress causing failure. Qualitative descriptions of the first three of the above items are presented in the following, while the failure criterion will be given in section 1.4.2.

The elastic moduli K_e and G_e (in N/mm^2) corresponding to the initial properties (i.e. those for $\sigma_{ij}^{\text{ext}} = 0$) of the stress-strain curves for concrete may be expressed as follows⁴⁰

$$K_e = 11000 + 3 \cdot 2 f_c^2 \quad (1.10)$$

$$G_e = 9224 + 136 f_c + 3296 * 10^{-15} f_c^{8 \cdot 273} \quad (1.11)$$

where the uniaxial cylinder compressive strength f_c is also expressed in N/mm^2 .

Equations (1.10) and (1.11) are valid for values of f_c in the range 15–65 N/mm^2 . Outside this range, K_e and G_e remain constant and equal to their values for $f_c = 15 \text{ N}/\text{mm}^2$ and $f_c = 65 \text{ N}/\text{mm}^2$; this is also true for all the other parameters to be defined subsequently (namely b, A, d, C, k, l, m, n). (Such approximations are based on the observations that, beyond $f_c \sim$

65 N/mm², any parameter variations flatten out to nearly constant values, while below $f_c \sim 15$ N/mm², the relevant characteristics for the latter f_c value represent sufficiently accurate averages for the scatter of results in this low concrete-strength range.)

By decomposing each state of stress and strain into a hydrostatic and a deviatoric component, the internal stress state may be quantified by using experimental data similar to those shown in Figs 1.34–1.37. A regression analysis of $\sigma_0 - \epsilon_{0(h)}$ data (see Fig. 1.34) has led to the following analytical expression for the relationship between external stress and resulting strain⁴⁰

$$\epsilon_{0(h)} = \frac{\sigma_0 + 3aK_c\sigma_0^b}{3K_c} \quad \text{for } \sigma_0/f_c \leq 2 \quad (1.12a)$$

$$\epsilon_{0(h)} = \frac{\sigma_0 + 3abK_c(2f_c)^{b-1}\sigma_0 + 3a(1-b)K_c(2f_c)^b}{3K_c} \quad \text{for } \sigma_0/f_c > 2 \quad (1.12b)$$

where K_c is given by equation (1.10), while a and b are parameters that depend on the material properties and can be evaluated by regression analysis. The relation for b may be expressed in the following form

$$b = 2.0 + 1.81 * 10^{-8} f_c^{4.461} \quad (1.13)$$

A regression analysis for a is not actually carried out at this stage, since this parameter is later absorbed into another one (A), as will be seen below. In keeping with the notion that the nonlinear variation of $\epsilon_{0(h)}$ with σ_0 , as expressed by equation (1.12a), is to be attributed to internal stresses caused by the fracture processes that occur under increasing hydrostatic stress, it is useful to recall the description in section 1.3.3.1 of these processes, which take the form of microcracks that are randomly distributed and oriented. When the microcracks are situated in the path along which a potential crack is likely to propagate, they will tend to increase the energy required to start the process and therefore act as crack 'inhibitors'. Since the number of such crack-propagation inhibitors will increase with the level of hydrostatic stress, it is realistic to assume that this type of fracture process diminishes progressively with increasing stress and that, therefore, the cause of the nonlinearity of the $\sigma_0 - \epsilon_0$ relationship should eventually cease to exist. Such considerations are supported by experimental evidence which shows that, for hydrostatic stress levels higher than $2f_c$, the $\sigma_0 - \epsilon_0$ relationship becomes linear (see, for example, the curve for $f_c = 15.3$ N/mm² in Fig. 1.34). The validity of equation (1.12a), therefore, is assumed to extend up to $\sigma_0 = 2f_c$. For higher values, a linear variation of σ_0 with ϵ_0 may be expressed by the tangent of equation (1.12a) at $\sigma_0 = 2f_c$, and this is what equation (1.12b) refers to.

For equations (1.12) to be compatible with the first term of the

right-hand side of equation (1.8c), the hydrostatic component of the internal state of stress ($\sigma_{0(i)}^{\text{int}} \equiv \sigma_{ih}$) resulting from the external hydrostatic stress ($\sigma_0^{\text{ext}} \equiv \sigma_0$) must be

$$\frac{\sigma_{ih}}{f_c} = A \left(\frac{\sigma_0}{f_c} \right)^b \quad \text{for } \frac{\sigma_0}{f_c} \leq 2 \quad (1.14a)$$

$$\frac{\sigma_{ih}}{f_c} = 2^{b-1} Ab \left(\frac{\sigma_0}{f_c} \right) + 2^b A(1-b) \quad \text{for } \frac{\sigma_0}{f_c} > 2 \quad (1.14b)$$

where

$$A = 3aK_c f_c^{b-1} \quad (1.15)$$

with a regression analysis of experimental data yielding the following expressions for A (which now incorporates — and defines — a)

$$A = 0.516 \quad \text{for } f_c \leq 31.7 \quad (1.16a)$$

$$A = \frac{0.516}{1 + 0.0027(f_c - 31.7)^{2.397}} \quad \text{for } f_c > 31.7 \quad (1.16b)$$

As discussed previously, the deviatoric component of the internal stress state under applied σ_0 is insignificant since the measured deviatoric strain under external hydrostatic stress has been found to be negligible. It appears, therefore, that equations (1.14) describe completely the internal stress state which develops within concrete when it is subjected to increasing external hydrostatic stress. On the other hand, while an *external hydrostatic stress* gives rise to an internal stress state which is also purely *hydrostatic*, the internal stress state which develops within concrete under *external deviatoric stress* consists of both a *hydrostatic* and a *deviatoric* component.

The deviatoric component ($\tau_{0(d)}^{\text{int}} \equiv \tau_{id}$) of the internal stress state that develops as a result of an externally-applied deviatoric stress can be quantified on the basis of an analytical description of $\tau_0 - \gamma_0$ data similar to those shown in Fig. 1.35. Such an analytical description may take the form⁴⁰

$$\gamma_0 = \frac{\tau_0 + 2cG_e \tau_0^d}{2G_e} \quad (1.17)$$

where G_e is given by equation (1.11), while c and d are material parameters. A regression analysis for d yields the following expressions

$$d = 2.12 + 0.0183f_c \quad \text{for } f_c \leq 31.7 \quad (1.18a)$$

$$d = 2.7 \quad \text{for } f_c > 31.7 \quad (1.18b)$$

As before, when the parameter a was discussed, there is no need at this stage to perform a regression analysis for c , as the latter is to be absorbed into another parameter (C). Now, for equation

(1.17) to be compatible with the second term of the right-hand side of equation (1.8c), τ_{id} must be

$$\frac{\tau_{id}}{f_c} = C \left(\frac{\tau_0}{f_c} \right)^d \quad (1.19)$$

where

$$C = 2cG_c f_c^{d-1} \quad (1.20)$$

With C both incorporating and defining the parameter c , all that remains to be done is to perform a regression analysis on the experimental data for the $\tau_0 - \gamma_{0(d)}$ relations. This yields the following expressions

$$C = 3.573 \quad \text{for } f_c \leq 31.7 \quad (1.21a)$$

$$C = \frac{3.573}{1 + 0.0134(f_c - 31.7)^{1.414}} \quad \text{for } f_c > 31.7 \quad (1.21b)$$

The hydrostatic component ($\sigma_{0(d)}^{\text{int}} \equiv \sigma_{id}$) of the internal stress state resulting from an external deviatoric stress is considered to be the fundamental cause of the volumetric response ($\epsilon_{0(d)}$) of concrete under deviatoric stress. Nominal values of σ_{id} for a given concrete may easily be obtained by using $\tau_0 - \epsilon_{0(d)}$ and $\sigma_0 - \epsilon_{0(h)}$ relationships such as those shown in Figs 1.37 and 1.34 respectively. For a value of the volumetric strain $\epsilon_{0(d)}$ corresponding to a given level of applied stress (σ_0, τ_0) (see Fig. 1.37), a value of hydrostatic stress — which may be considered to represent a nominal value for σ_{id} — can be obtained from the $\sigma_0 - \epsilon_{0(h)}$ relationship of Fig. 1.34. In this way, the $\tau_0 - \epsilon_{0(d)}$ relationships of Fig. 1.37 can be transformed into $\sigma_{id} - \tau_0$ relationships such as those shown, for example, in Fig. 1.44. This procedure⁴¹ is illustrated schematically in Fig. 1.45. A regression analysis of experimental data similar to those shown in Fig. 1.44 has led to the following analytical expression for σ_{id} ⁴⁰

$$\frac{\sigma_{id}}{f_c} = M \left(\frac{\tau_0}{f_c} \right)^n \quad (1.22)$$

where

$$M = \frac{k}{1 + l \left(\frac{\sigma_0}{f_c} \right)^m} \quad (1.23)$$

and k, l, m, n are material parameters which may be expressed in terms of f_c as follows

$$k = \frac{4.0}{1 + 1.087(f_c - 15.0)^{0.23}} \quad (1.24)$$

$$l = 0.222 + 0.01086f_c - 0.000122f_c^2 \quad (1.25)$$

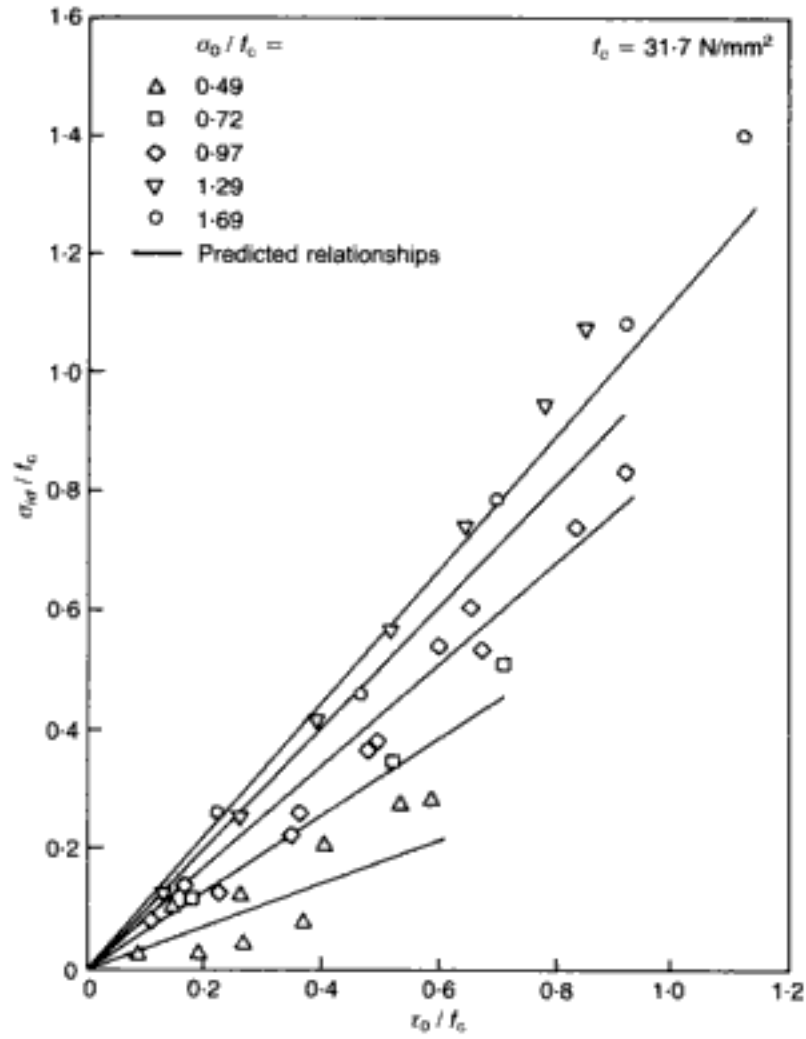


Fig. 1.44. Variation of σ_{wd} with τ_0 for various σ_0 , for a typical concrete (with $f_c = 31.7 \text{ N/mm}^2$)^{38,40,41}

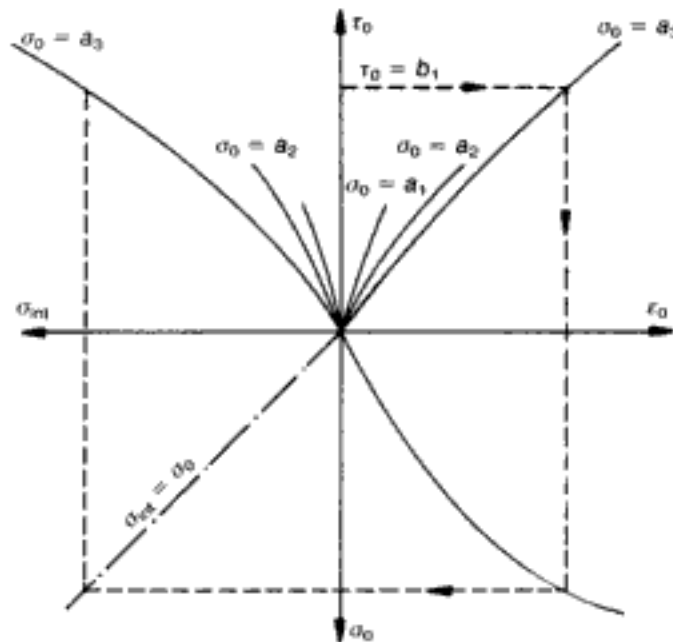


Fig. 1.45. Schematic representation of the approach used to evaluate σ_{wd} for a given combination of σ_0 and τ_0 ⁴¹

$$m = -2.415 \quad \text{for } f_c \leq 31.7 \quad (1.26a)$$

$$m = -3.531 + 0.0352f_c \quad \text{for } f_c > 31.7 \quad (1.26b)$$

$$n = 1.0 \quad \text{for } f_c \leq 31.7 \quad (1.27a)$$

$$n = 0.3124 + 0.0217f_c \quad \text{for } f_c > 31.7 \quad (1.27b)$$

It is evident that, up to a uniaxial cylinder strength of 31.7 N/mm², the relationships between σ_{id} and τ_0 are always linear (since $n = 1$), as is clear, for example, by reference to Fig. 1.44. For higher values of f_c , $n \neq 1$, and hence such relationships become nonlinear.

It should be noted that the coupling between stress deviation and volume change, expressed in terms of σ_{id} , has been carried out in a manner which, although referring to the latter parameter as an internal stress, in fact treats σ_{id} as an external stress. This is clear if it is recalled that σ_{id} is eventually obtained from the $\sigma_0 - \epsilon_{0(h)}$ relationship (see, for example, Fig. 1.45), so that $\sigma_{id} = \sigma_0$ refers to the σ_{ij}^{ext} (and not the σ_{ij}^{int}) component (see Fig. 1.43). Therefore, while σ_{ih} and τ_{id} are indeed internal stresses (compatible with the generic definition (1.9)), σ_{id} is an *equivalent* external stress required to produce the actual $\epsilon_{0(d)}$. While it would be an easy matter to express the coupling by means of a truly internal stress (as was done for σ_{ih} and τ_{id}), it turns out to be more convenient — from a computational viewpoint — to follow the present approach, as will be shown subsequently.

Finally, a criterion that defines loading and unloading may also be expressed in terms of the internal-stress concept. As discussed above, the internal stress state which develops within concrete under loading consists of three components, namely σ_{ih} , τ_{id} , and σ_{id} (the latter coupling parameter is expressed as an equivalent external stress), defined by equations (1.14), (1.19), and (1.22) respectively. These equations indicate that, while σ_{ih} and τ_{id} occur independently of each other under increasing external hydrostatic and deviatoric stresses respectively, σ_{id} occurs under combined external hydrostatic and deviatoric stress and represents the fundamental cause of all observed interaction between the hydrostatic and deviatoric components of the external stresses and corresponding strains. (Although σ_{id} is caused primarily by the deviatoric component of the applied stress (τ_0) — see expression (1.22) — its actual value is also governed by the relevant octahedral plane defined by the hydrostatic component of the applied stress, as indicated by the ‘constant’ M (expression (1.23)).) In view of the above, loading, defined as any change of the external stress state that results in an increase of the level of the internal stresses, may be classified as follows.

- (a) *Hydrostatic loading.* This occurs when the current external σ_0 exceeds any previous external σ_0 , thus resulting in an increase of σ_{ih} .

- (b) *Deviatoric loading.* This occurs when the current external τ_0 exceeds any previous external τ_0 , thus resulting in an increase of τ_{id} .
- (c) *Combined loading.* This occurs when the current combination of external σ_0 and τ_0 results in a σ_{id} larger than any previous σ_{id} . This loading may occur when at least one of (a) and (b) is true.

On the basis of the above, unloading occurs when any of (a), (b), or (c) is not true. Furthermore, it is implied that various combinations of loading and unloading may take place simultaneously.

The combined approach. The combined approach is based on the use of two variable mechanical properties — namely the moduli K and G — which account for the nonlinearities in the $\sigma_0 - \epsilon_{0(h)}$ and $\tau_0 - \gamma_{0(d)}$ relationships respectively, combined with the use of the σ_{id} variable that accounts for the coupling effect $\tau_0 - \epsilon_{0(d)}$. It will be recalled that, although based on the internal-stress concept, the latter parameter was expressed earlier as an equivalent external stress: the reason for this is that the coupling effect may then be allowed for by simply adding σ_{id} to the externally-applied hydrostatic stress. Such an approach enables the total octahedral strains ((1.6) and (1.7)) caused by an arbitrary, externally-applied stress state (σ_0, τ_0) to be rewritten as follows

$$\epsilon_0 = \epsilon_{0(h)} + \epsilon_{0(d)} = \frac{\sigma_0 + \sigma_{id}}{3K_s} \quad (1.6a)$$

$$\gamma_0 = \gamma_{0(d)} = \frac{\tau_0}{2G_s} \quad (1.7)$$

In this way, the three-moduli approach has now been modified by the replacement of the third modulus (H_s) by an equivalent superimposed stress state (σ_{id}) based on the internal-stress concept.

While $\sigma_{id}(\sigma_0, \tau_0, f_c)$ accounts for the coupling between τ_0 and $\epsilon_{0(d)}$, $K_s(\sigma_0, f_c)$ and $G_s(\tau_0, f_c)$ are secant bulk and shear moduli respectively should such a coupling not exist (i.e. they are obtained by ignoring σ_{id}). It was shown earlier how curve fitting of experimental uniaxial, biaxial, and triaxial data has enabled expression (1.22) for σ_{id} to be derived. Similarly, a regression analysis of experimental information has led to expressions (1.12) and (1.17), and it is from these that $K_s = (1/3)(\sigma_0/\epsilon_0)$ and $G_s = (1/2)(\tau_0/\gamma_0)$, respectively, can easily be derived in the following form

$$\frac{K_s}{K_c} = \frac{1}{1 + A \left(\frac{\sigma_0}{f_c} \right)^{b-1}} \quad \text{for } \frac{\sigma_0}{f_c} \leq 2 \quad (1.28a)$$

$$\frac{K_s}{K_e} = \frac{1}{1 + 2^{b-1}Ab - 2^b(b-1)A\left(\frac{\sigma_0}{f_c}\right)^{-1}} \quad \text{for } \frac{\sigma_0}{f_c} > 2 \quad (1.28b)$$

$$\frac{G_s}{G_e} = \frac{1}{1 + C\left(\frac{\tau_0}{f_c}\right)^{d-1}} \quad (1.29)$$

In an analogous manner, the tangent bulk and shear moduli (again, neglecting σ_{id}) which relate stress and strain increments, $K_t = (1/3)(d\sigma_0/d\epsilon_0)$ and $G_t = (1/2)(d\tau_0/d\gamma_0)$, may readily be obtained by differentiation of expressions (1.12) and (1.17) respectively. The result is

$$\frac{K_t}{K_e} = \frac{1}{1 + bA\left(\frac{\sigma_0}{f_c}\right)^{b-1}} \quad \text{for } \frac{\sigma_0}{f_c} \leq 2 \quad (1.30a)$$

$$\frac{K_t}{K_e} = \frac{1}{1 + 2^{b-1}Ab} \quad \text{for } \frac{\sigma_0}{f_c} > 2 \quad (1.30b)$$

$$\frac{G_t}{G_e} = \frac{1}{1 + dC\left(\frac{\tau_0}{f_c}\right)^{d-1}} \quad (1.31)$$

The above formulae for the secant and tangent moduli are illustrated in Figs 1.46 and 1.47 by reference to a particular concrete ($f_c = 31.7 \text{ N/mm}^2$). (It should be noted that, in the case of G , the experimental data shown cover both triaxial-'compression' and triaxial-'extension' cases.)

Since σ_{id} is a pure hydrostatic correction, expressions (1.6a)

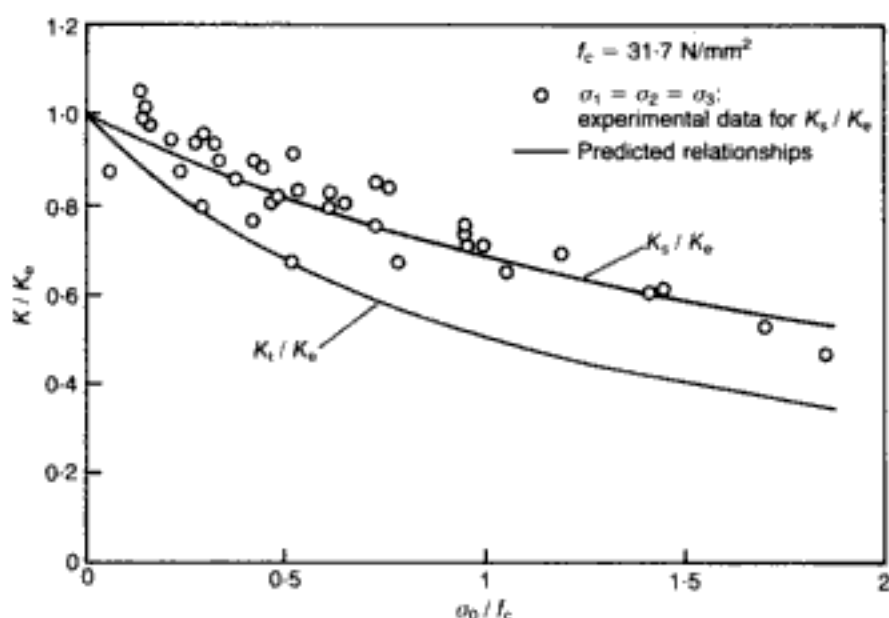


Fig. 1.46. Typical variation of the bulk moduli (K_s , K_t) with σ_0 for a given concrete (with $f_c = 31.7 \text{ N/mm}^2$)^{38,41}

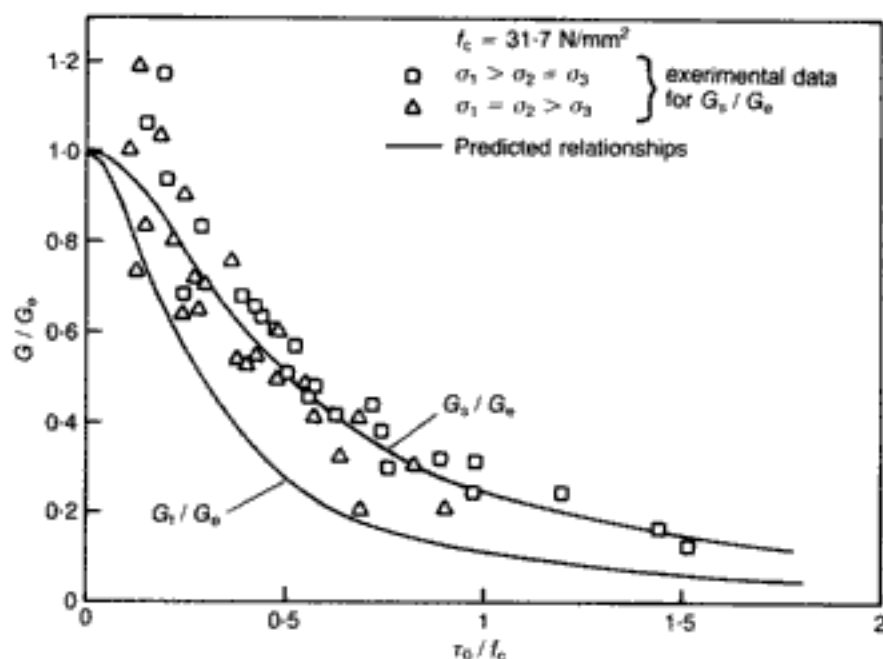


Fig. 1.47. Typical variation of the shear moduli (G_s , G_t) with τ_0 for a given concrete (with $f_c = 31.7 \text{ N/mm}^2$)^{38,41}

and (1.7) are equivalent to the following relations in global coordinate directions

$$\epsilon_{ij} = \frac{\sigma_{ij} + \sigma_{id}\delta_{ij}}{2G_s} - \frac{3\nu_s}{E_s}(\sigma_0 + \sigma_{id})\delta_{ij} \quad (1.32)$$

where $E_s(\sigma_0, \tau_0, f_c)$ and $\nu_s(\sigma_0, \tau_0, f_c)$ are the secant Young's modulus and Poisson's ratio respectively, derived from K_s and G_s by the following standard formulae of linear elasticity (obtained through the use of (1.1) and (1.2))

$$E = \frac{9KG}{3K+G} \quad (1.33)$$

$$\nu = \frac{3K-2G}{6K+2G} \quad (1.34)$$

Expression (1.32) is obtained by noting that the two terms of the strain tensor $\epsilon_{ij} = \epsilon_0\delta_{ij} + e_{ij}$ (see (1.8c)) must be dealt with separately when the constitutive relations are introduced in this tensor relation. Thus, while the model does not impose any deviation from nonlinear elasticity with regard to the second term (i.e. $e_{ij} = (\sigma_{ij} - \sigma_0\delta_{ij})/(2G_s)$), the first term does involve the correction σ_{id} to the actual, applied σ_0 (i.e. $\epsilon_0\delta_{ij} = (\sigma_0 + \sigma_{id})\delta_{ij}/(3K_s)$).

Expressions (1.32) form the basis for calculating global strains from global stresses. The actual procedure reduces to the following steps.

- The octahedral stresses (σ_0, τ_0) are calculated either from the principal stresses ($\sigma_1, \sigma_2, \sigma_3$) — computed previously on the basis of the global stresses σ_{ij} , i.e.

$(\sigma_x, \sigma_y, \sigma_z, \tau_{xy}, \tau_{xz}, \tau_{yz})$ — or directly from the first and second stress invariants expressed in terms of σ_{ij} . (See Appendix A.)

- K_s, G_s and E_s, ν_s are calculated.
- The hydrostatic correction (i.e. coupling stress) σ_{id} is calculated.
- Global strains ϵ_{ij} are calculated.

It is clear that the computation of global strain increments from global stress increments follows the same procedure, but with the material 'constants' now defined in terms of tangent values K_t, G_t and E_t, ν_t .

1.4.1.3. The accuracy of the mathematical model for the constitutive relations

As explained in section 1.4.1, the cracking processes up to failure are governed, broadly, by the following two (opposing) effects: a reduction in the predominantly tensile stress concentrations near the crack tips (leading to volume reduction), and a production of voids (leading to volume increase). The proposed constitutive model is based on the description of the first of these effects, through the use of the mechanical properties (K_s, G_s) and the coupling parameter σ_{id} . On the other hand, the effect of void formation has been ignored in the stress–strain expressions thus derived.

The conceptual accuracy of the model may be judged by reference to Fig. 1.48, which shows some triaxial data for a particular concrete. Three degrees of refinement in the constitutive modelling were applied in turn, and their relative success in mimicking the experimental information can be seen from the resulting curves. First, only the mechanical properties are taken into account, and it is evident that such limited means cannot provide an accurate description of the behaviour beyond the case of pure hydrostatic stress states. Once the stress path departs from this state (at $\sigma_0 = 35 \text{ N/mm}^2$ in Fig. 1.48), the effect of σ_0 requires that σ_{id} (in addition, of course, to G_s) should also be accounted for. Therefore, for general stress states the inclusion of the coupling effect is necessary for a good correlation between model and experimental data to be achieved up to the OUFP level. At this point, the effect of void formation begins to play an increasingly important role and must be given due consideration if the stress–strain paths beyond the OUFP level are to be reproduced (as in Fig. 1.48, where curve III is based on the inclusion of void formation in the constitutive model³⁸). However, as noted in section 1.3.3.1, the OUFP level may be taken to coincide — for all practical purposes — with the US level, so that a sufficiently accurate description of the constitutive relations up to failure is attained by the inclusion of the effect of the internal stresses (i.e. mechanical properties and coupling characteristics)

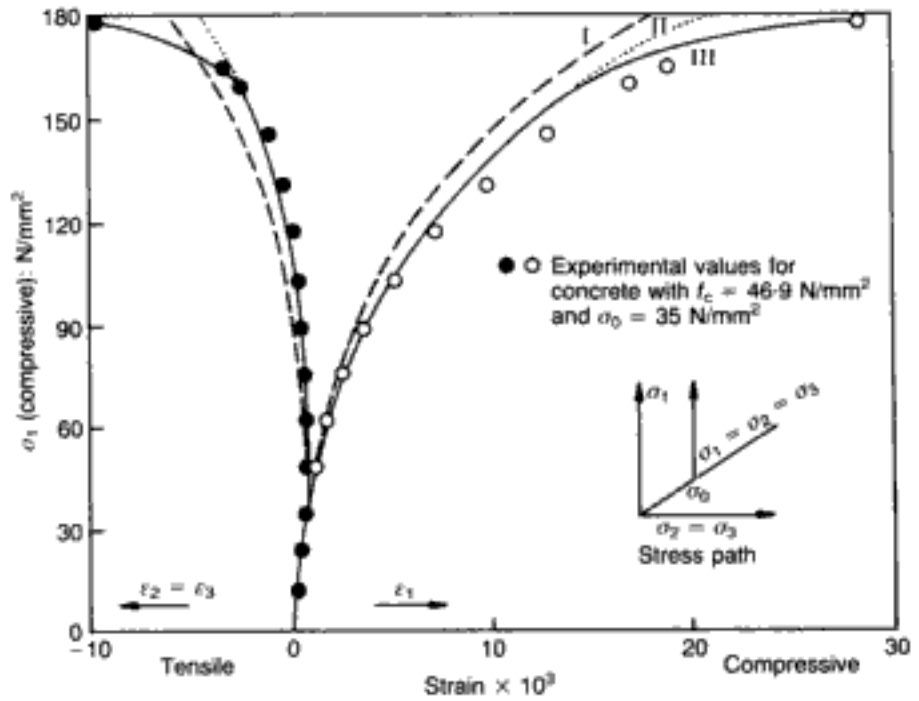


Fig. 1.48. Typical stress-strain relations under triaxial stress predicted by the model for a given concrete (with $f_c = 46.9 \text{ N/mm}^2$):⁵⁸ (I) including mechanical properties of the model only; (II) including mechanical properties and effects of internal stresses only; (III) including mechanical properties and effects of internal stresses and void formation

while the effect of void formation on deformation is disregarded altogether.

The actual accuracy of the model with respect to a large — and varied — body of available experimental data may be seen by reference to Figs 1.34–1.37, 1.42, 1.44, and 1.46–1.47: in most of these the predictions of the adopted model appear as solid lines. It is evident that the proposed mathematical expressions derived on the basis of ‘best fit’ to experimental data provide a very satisfactory description of the deformation of concrete at a material level, whether individual tests or combined data from more than one test (e.g. Fig. 1.47) are considered. Further comparisons between the model and experimental results stemming from specimens tested at Imperial College under triaxial stress conditions appear in Figs 1.49 and 1.50 which refer to triaxial-‘compression’ and triaxial-‘extension’ loading paths respectively; once again, a close fit of the predicted relationships with most of the data is apparent, suggesting that the proposed mathematical model is adequate for all stress paths. The mathematical stress-strain relationships are also in good agreement with the results of biaxial (and uniaxial) stress conditions, as can be seen by reference to Fig. 1.51, which is based on the experimental values obtained at the Technical University of Munich.⁴² (Although carried out well before the international cooperative project aimed at elucidating

the effect of testing procedures which was described earlier in the chapter,⁹ the Munich tests represent reliable experimental data in the same way as the tests performed subsequently at Imperial College: unlike the Imperial College results, however, which use sequential paths and a near-uniform stress state applied by the loading system through the adoption of cylinders with a height-to-width ratio of 2.5, the Munich tests were based on a proportional stress path and the application of a near-uniform state of strain on the specimens through brush-bearing platens; the close correlation between predicted and experimental relationships indicates that the effect of testing conditions on the material deformation in the Munich experiments is also insignificant for practical purposes.) Finally, in addition to the special case $\sigma_2/\sigma_1 = 0$ forming part of the more general biaxial-compression data of Fig. 1.51 for $f_c = 31.7 \text{ N/mm}^2$, Fig. 1.52 shows the model's close fit to experimental values of uniaxial compression for a much wider range of concrete strengths.⁴¹ Up to $f_c = 40 \text{ N/mm}^2$, these experimental values refer to given data points,¹⁵ while for $f_c > 40 \text{ N/mm}^2$ they are seen to correlate very closely with empirical relationships between the applied stress and the corresponding strain in the direction of loading proposed elsewhere.⁴³

In assessing the model's accuracy, the sheer impossibility of fully reproducing experimental data should also be borne in mind, even when comparing results of tests on concrete specimens stemming from a common mix and performed by means of the same apparatus. This scatter of results due to material variability (within a given mix) is illustrated in Figs 1.53(a)–1.53(d),^{20,29} which show the typical range of relevant values for a concrete mix tested triaxially at four values of confining pressure (three specimens were used for each of these confining-pressure values). Such degree of scatter, which is also representative of typical uniaxial and biaxial stress–strain relationships, indicates clearly that further refinement of the mathematical model and/or its component parameters would not be justified.

1.4.2. Strength envelopes for concrete

1.4.2.1. Experimental data on, and mathematical description of, failure surfaces

The use of nonlinear computer-based methods for the analysis of concrete structures subjected to complex stress states requires that both the strength and the deformational properties of concrete should be expressed in a suitable form. The deformational properties have been the subject of the previous section in which a mathematical description of the stress–strain behaviour of the material under generalized stress was outlined. The present section complements the above constitutive properties and is concerned with the mathematical description of the strength properties of concrete.⁴⁴ Such a mathematical description is considered essential, since most of the strength criteria proposed to date for

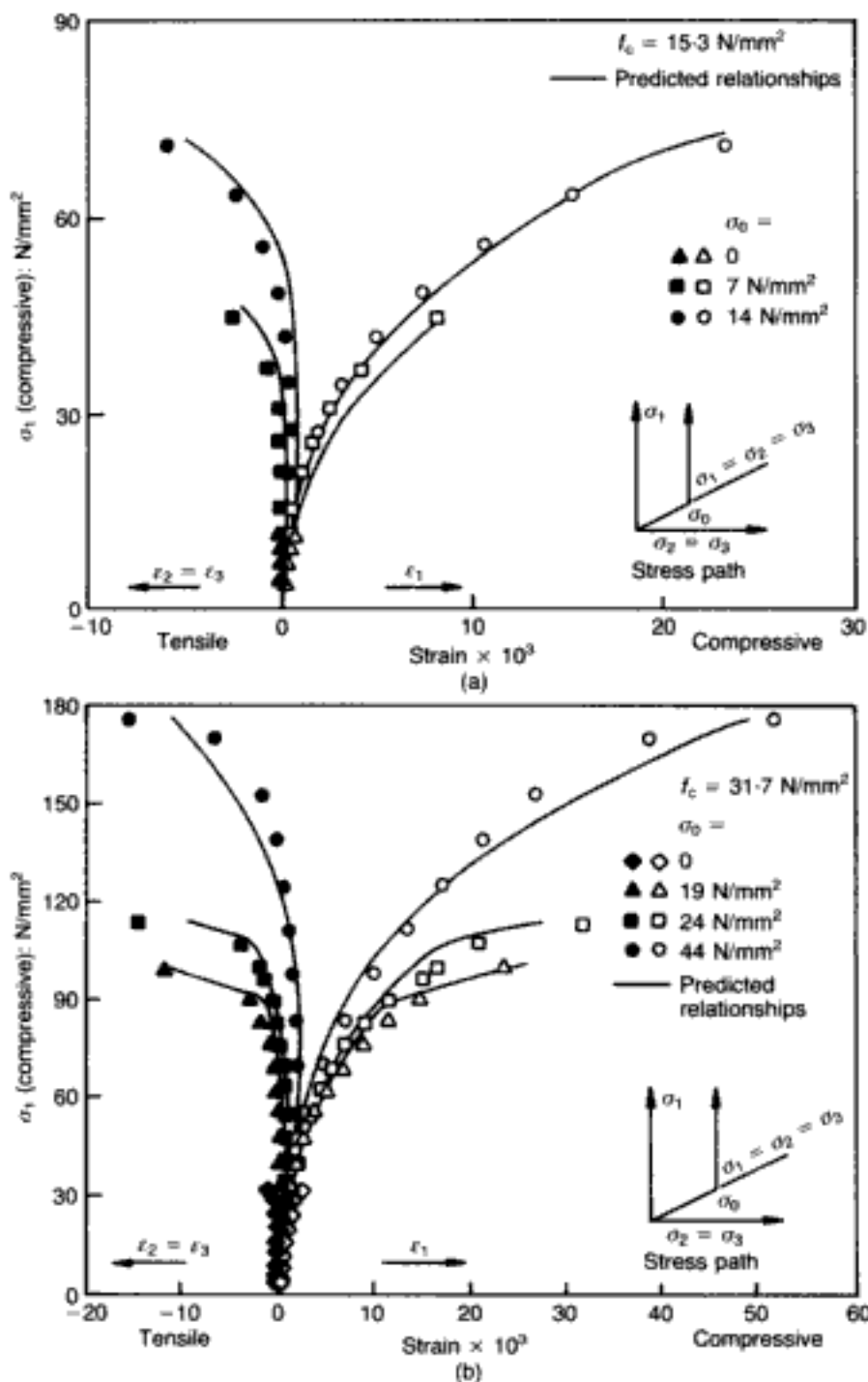


Fig. 1.49 (right and facing). Stress-strain relationships for various concretes under stress states $\sigma_1 > \sigma_2 = \sigma_3$ (triaxial 'compression'):³⁸
 (a) $f_c = 15.3 \text{ N/mm}^2$;
 (b) $f_c = 31.7 \text{ N/mm}^2$;
 (c) $f_c = 46.9 \text{ N/mm}^2$;
 (d) $f_c = 62.1 \text{ N/mm}^2$

use in practical structural design (e.g. references 30, and 45–47) have not been expressed in a suitable form for computer applications. Furthermore, certain criteria⁴⁵ have been formulated in such a way that the convexity principle¹¹ does not hold, whereas the formulation of others has been based on the oversimplified assumptions that the effect of the intermediate principal stress on the strength properties is negligible⁴⁶ or that concrete behaves elastically up to a limiting principal tensile strain which defines ultimate strength and is regarded as a material constant.⁴⁷

The derivation of mathematical expressions given here is based on an analysis of strength data obtained in the course of

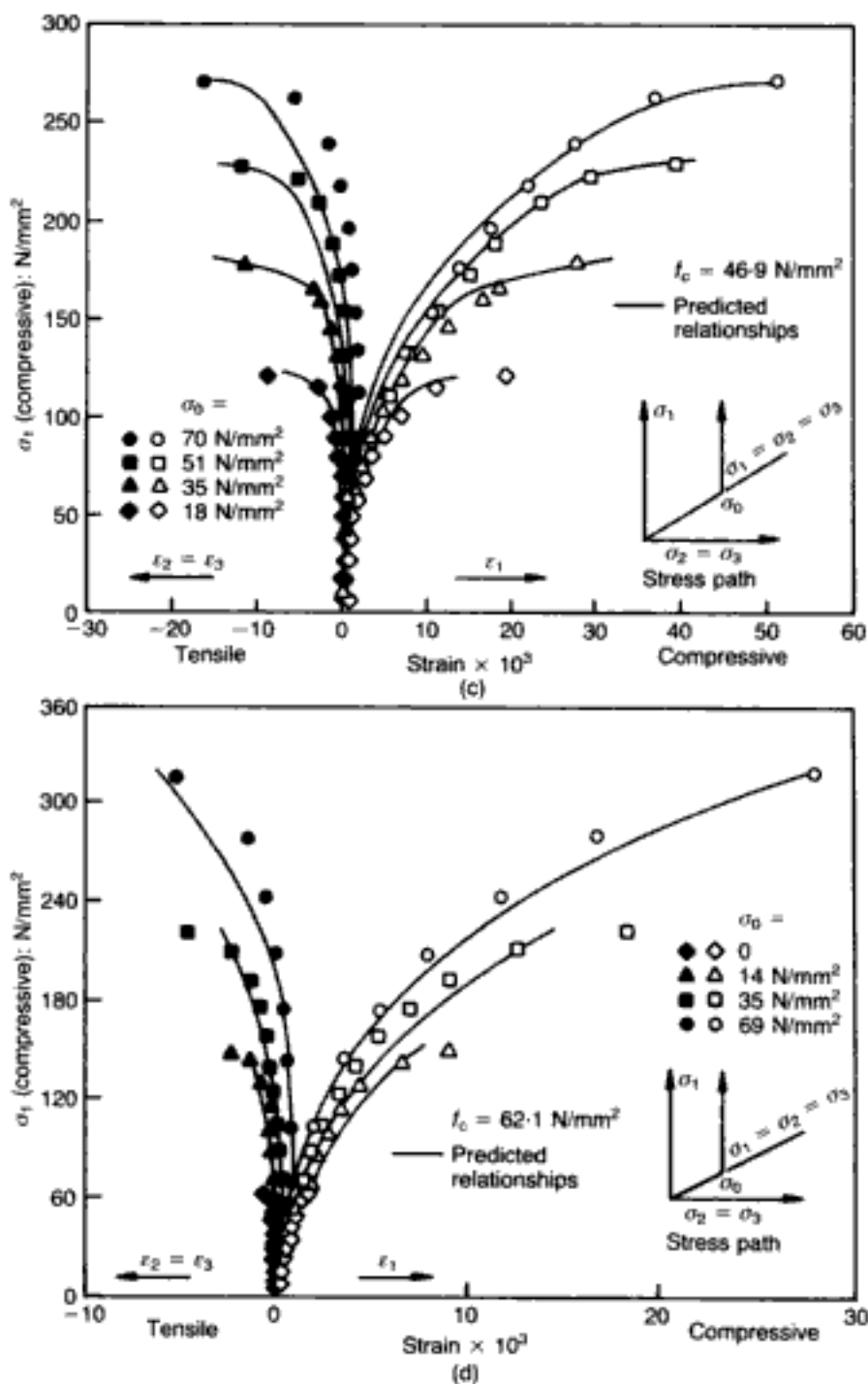


Fig. 1.49 — continued

investigations of the behaviour of concrete under multiaxial stress states carried out at Imperial College and described elsewhere.^{10,20,48,44} The testing techniques used to obtain these data (see section 1.1.5 and reference 37) have been validated by comparing them with those obtained in the international cooperative programme of research into the effect of testing techniques and apparatus on the behaviour of concrete under biaxial and triaxial stress states described previously.^{8,9}

As in the case of the constitutive relations, a mathematical description of the strength envelope of concrete, which is governed by combinations of maximum stresses that define a given failure

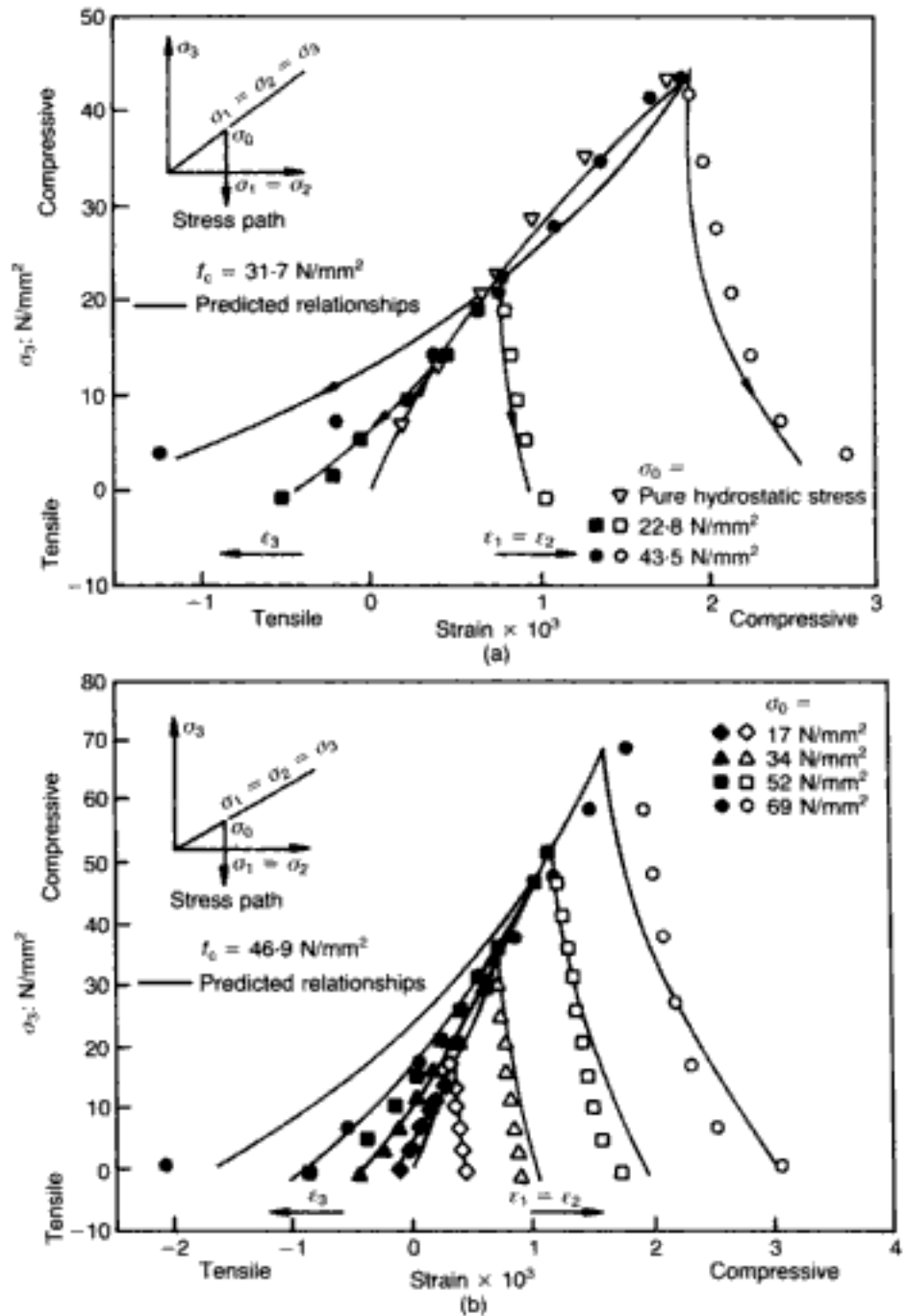


Fig. 1.50 (right and facing). Stress-strain relationships for various concretes under stress states $\sigma_1 = \sigma_2 > \sigma_3$ (triaxial 'extension').³⁸
 (a) $f_c = 31.7 \text{ N/mm}^2$;
 (b) $f_c = 46.9 \text{ N/mm}^2$;
 (c) $f_c = 62.1 \text{ N/mm}^2$

criterion, is most readily formulated in terms of hydrostatic and deviatoric components acting on the octahedral plane. Therefore, it is convenient to define the stress space by the orthogonal coordinate system $(\sigma_1, \sigma_2, \sigma_3)$ of principal stresses. (The convention that compressive stresses are positive will be adopted.) Then, viewing the coordinate system and the octahedral (or deviatoric) plane from the hydrostatic axis, which intersects this plane at right angles, it is easy to see that the stress space can be divided into six regions, within which the following conditions are satisfied

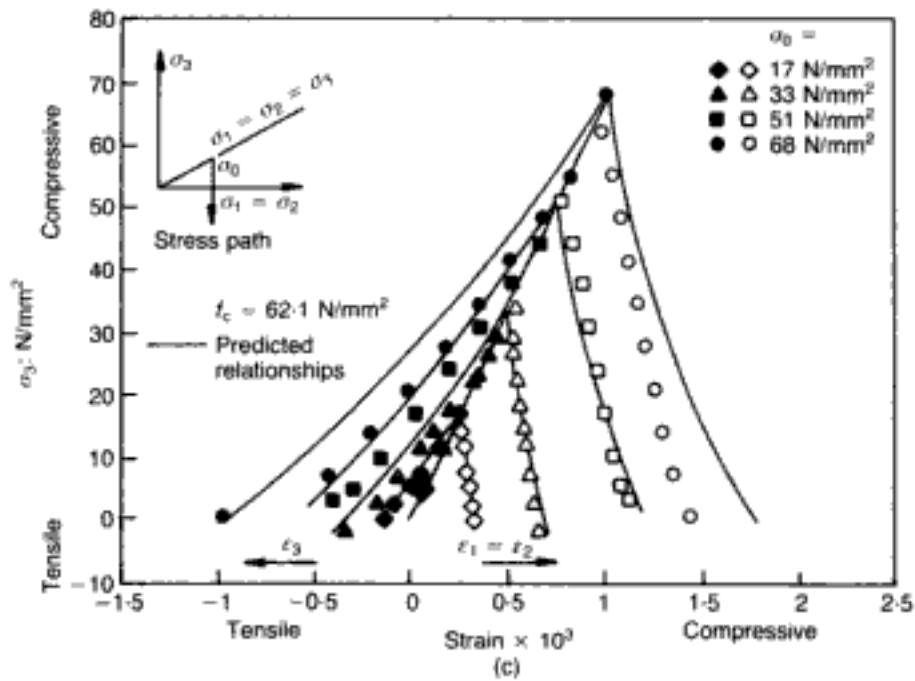


Fig. 1.50 — continued

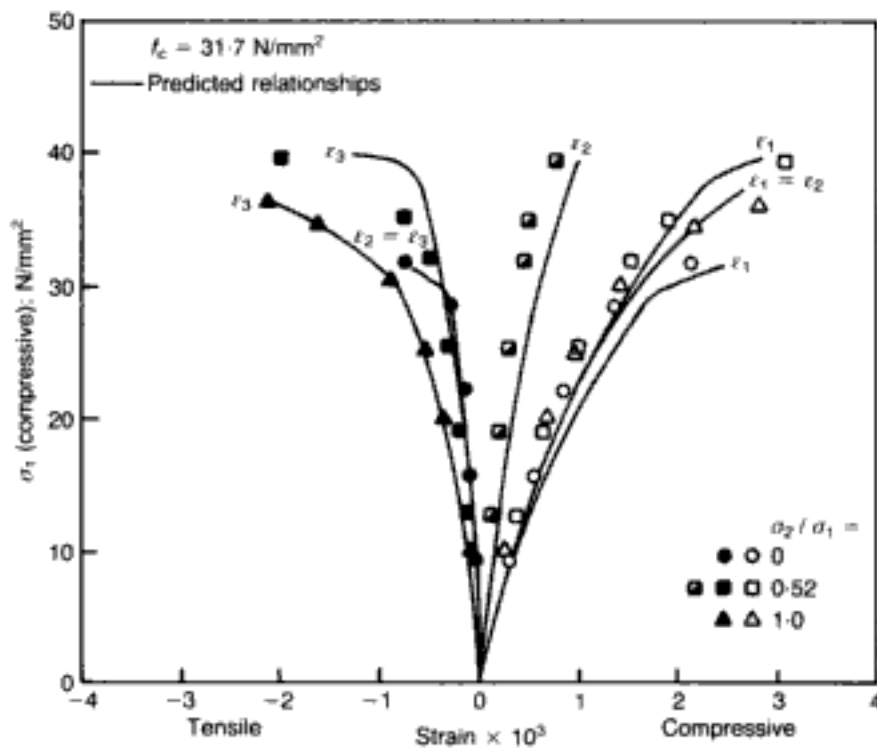


Fig. 1.51. Stress—strain relationships under biaxial (and uniaxial) compression for a typical concrete (with $f_c = 31.7$ N/mm²)^{38,42}

region 1: $\sigma_1 \geq \sigma_2 \geq \sigma_3$ (1.35a)

region 2: $\sigma_1 \geq \sigma_3 \geq \sigma_2$ (1.35b)

region 3: $\sigma_2 \geq \sigma_1 \geq \sigma_3$ (1.35c)

region 4: $\sigma_2 \geq \sigma_3 \geq \sigma_1$ (1.35d)

region 5: $\sigma_3 \geq \sigma_1 \geq \sigma_2$ (1.35e)

region 6: $\sigma_3 \geq \sigma_2 \geq \sigma_1$ (1.35f)

These regions are shown clearly in Fig. 1.54.

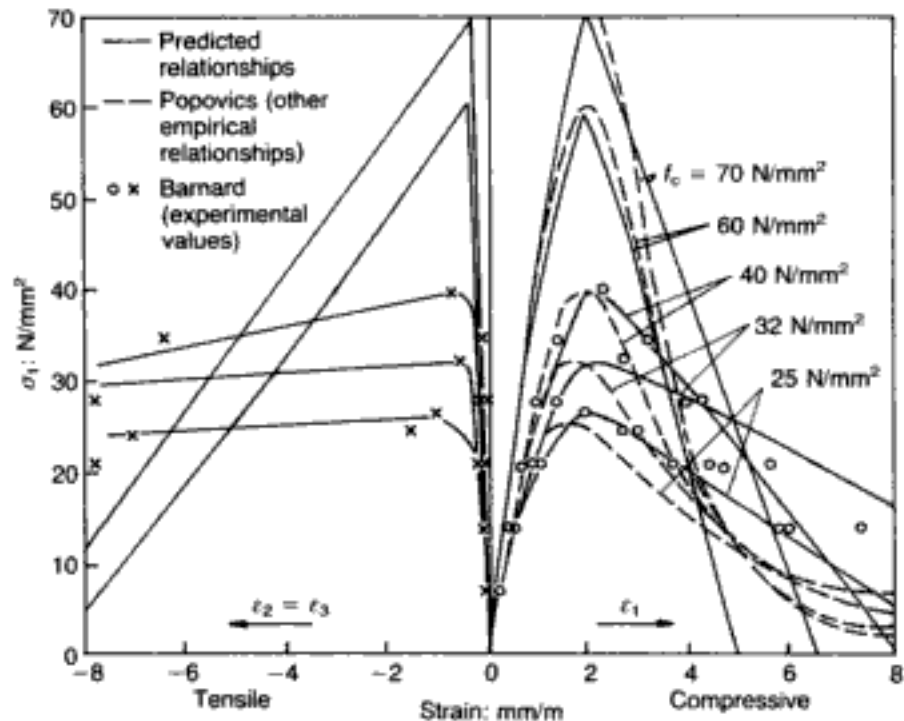


Fig. 1.52. Stress-strain relationships for various concretes under uniaxial compression⁴¹

The transformation of the orthogonal coordinate system $(\sigma_1, \sigma_2, \sigma_3)$ into the cylindrical coordinate system $(z = \sqrt{3}\sigma_0, r = \sqrt{3}\tau_0, \theta)$ has been outlined in Appendix A. Accordingly, z is related to the hydrostatic stress that coincides with the space diagonal $\sigma_1 = \sigma_2 = \sigma_3$, while the radius r is similarly related to the magnitude of the deviatoric stress component, the rotational variable θ defining the latter's orientation on the octahedral plane. (Clearly, the hydrostatic and deviatoric stresses are obtained by contracting the (z, r) coordinates by a constant factor of $\sqrt{3}$.) With these preliminaries, the strength envelope may be described by reference to both coordinate systems, and this is shown in Fig. 1.54. The resulting ultimate-strength variation obeys the convexity principle usually associated with failure surfaces,¹¹ and is open in compression since concrete can sustain increasing values of deviatoric stress for increasing hydrostatic compressive stress levels, i.e. cross-sections of the strength envelope (perpendicular to the z axis) become larger as σ_0 increases.

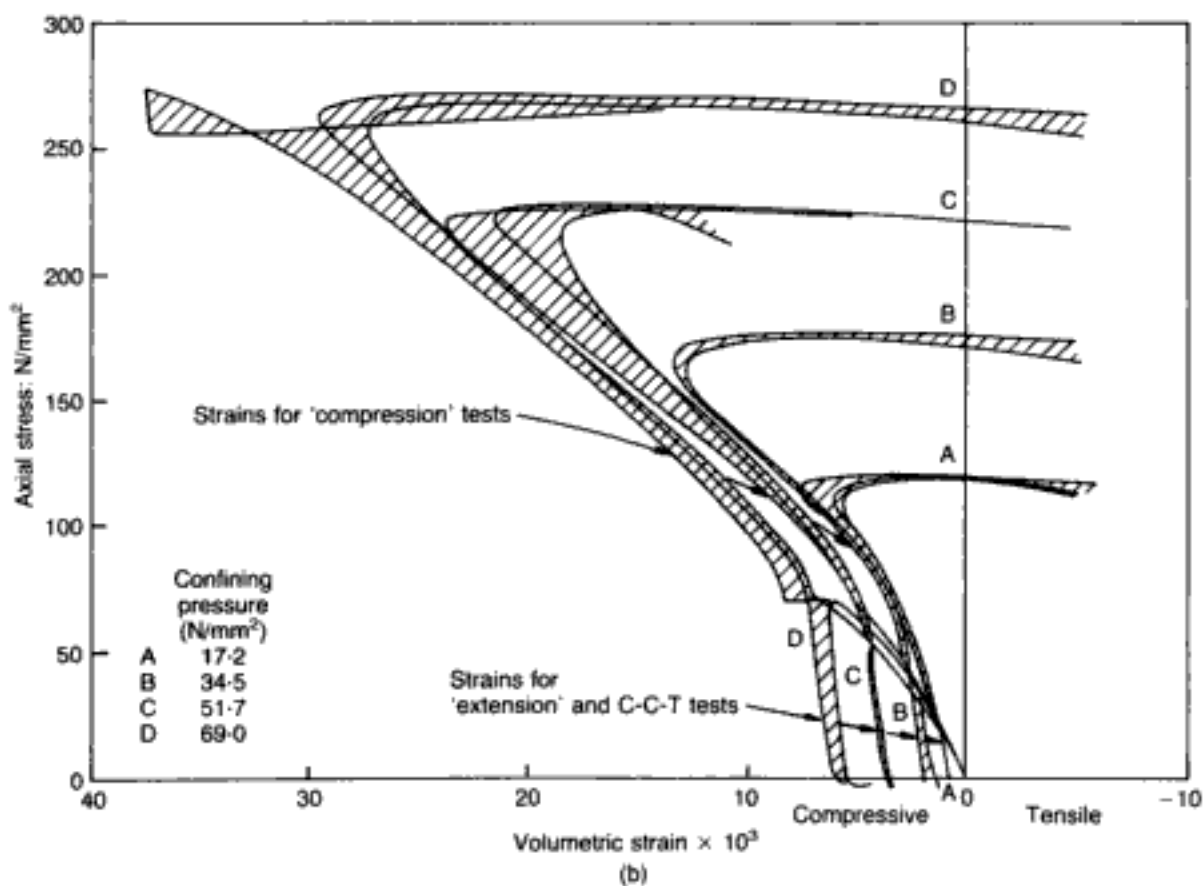
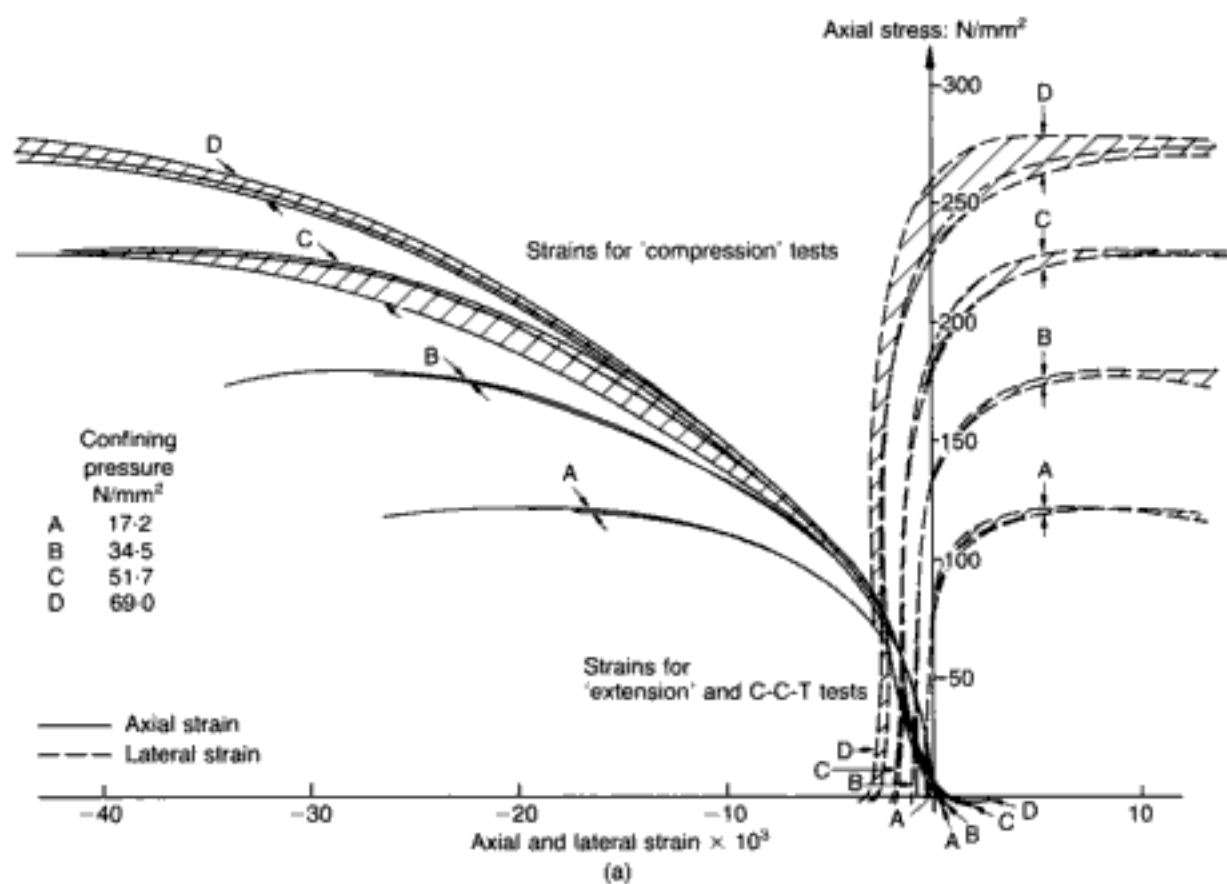
If isotropic material behaviour is assumed, the ultimate-strength surface possesses a six-fold symmetry about the space diagonal $\sigma_1 = \sigma_2 = \sigma_3$. Therefore, it follows that only one-sixth of the closed curve defining the failure boundary on a deviatoric plane (Fig. 1.54(b)) is required for its definition. Now, experimental data are readily obtainable for τ_{0e} and τ_{0c} (the factor $\sqrt{3}$ will henceforth be dropped, i.e. the deviatoric plane will be shrunk to the curve τ_{0u} rather than $\sqrt{3}\tau_{0u}$). These values correspond to axisymmetric stress states easily imposed in a triaxial test. Thus, τ_{0e} (for $\theta = 0^\circ$) is obtained by setting $\sigma_1 = \sigma_2 > \sigma_3$ (triaxial 'extension') while τ_{0c} (for $\theta = 60^\circ$) follows by setting $\sigma_1 > \sigma_2 = \sigma_3$

(triaxial 'compression'). In this way, τ_{0e} and τ_{0c} values can be determined for various levels of hydrostatic stress σ_0 . For each σ_0 , the value of τ_{0u} for any θ intermediate between 0° and 60° may be interpolated between the values of τ_{0u} at 0° and 60° by means of the following expression⁴⁹

$$\tau_{0u} = \frac{2\tau_{0c}(\tau_{0c}^2 - \tau_{0e}^2)\cos\theta + \tau_{0c}(2\tau_{0e} - \tau_{0c})\sqrt{4(\tau_{0c}^2 - \tau_{0e}^2)\cos^2\theta + 5\tau_{0e}^2 - 4\tau_{0c}\tau_{0e}}}{4(\tau_{0c}^2 - \tau_{0e}^2)\cos^2\theta + (\tau_{0c} - 2\tau_{0e})^2} \quad (1.36)$$

This expression describes a smooth convex curve with tangents perpendicular to the directions of τ_{0e} and τ_{0c} at $\theta = 0^\circ$ and $\theta = 60^\circ$ respectively (see Fig. 1.54). Therefore, it follows that a full description of the strength surface may be established once the variations of τ_{0e} and τ_{0c} with σ_0 are determined.

Figure 1.55 shows such variations of τ_{0e} and τ_{0c} . These combinations of octahedral stresses (σ_0, τ_0) at the ultimate-strength level, which appear normalized with respect to the uniaxial cylinder compressive strength f_c , were obtained from triaxial tests carried out at Imperial College on a wide range of concretes (with f_c varying approximately between 15 N/mm² and 65 N/mm²) subjected to the axisymmetric stress states $\sigma_1 > \sigma_2 = \sigma_3 > 0$ (triaxial 'compression'), $\sigma_1 = \sigma_2 > \sigma_3 > 0$ (triaxial 'extension'), and $\sigma_1 = \sigma_2 > 0 > \sigma_3$ (triaxial 'tension' C-C-T). Full details of these tests can be found elsewhere.^{30,8} Figure 1.55 indicates that, for the portion of the stress space investigated, the ultimate-strength envelopes are essentially independent of f_c , i.e. the type of concrete. Furthermore, since the stress-path effects on ultimate strength have been found small enough to be regarded as insignificant for practical purposes,⁴⁴ the two envelopes of Fig. 1.55 are considered to describe adequately the strength of most ordinary concretes likely to be encountered in practice when these are subjected to axisymmetric stress states. This lack of influence of loading history for both stress-strain relations and the ultimate-strength envelope was discussed in section 1.3.3.2, where it was argued that the unsystematic variability of the relevant data is larger than the scatter due to path-dependency. Figure 1.56 shows the justification for such an argument in the case of failure data: it is evident that the scatter of ultimate stresses for concrete of a given f_c for different loading paths is smaller than the scatter of ultimate values for concretes of different f_c but following a given loading path.⁴⁰ A similar justification for adopting the OUF_P level as the failure limit (as opposed to the slightly higher maximum sustained stress level — see section 1.3.3.1) may be seen by reference to Fig. 1.57, which shows that the unsystematic variation of the maximum stress level for various concretes far exceeds the deviation between OUF_P and US level for a given concrete.⁴⁰



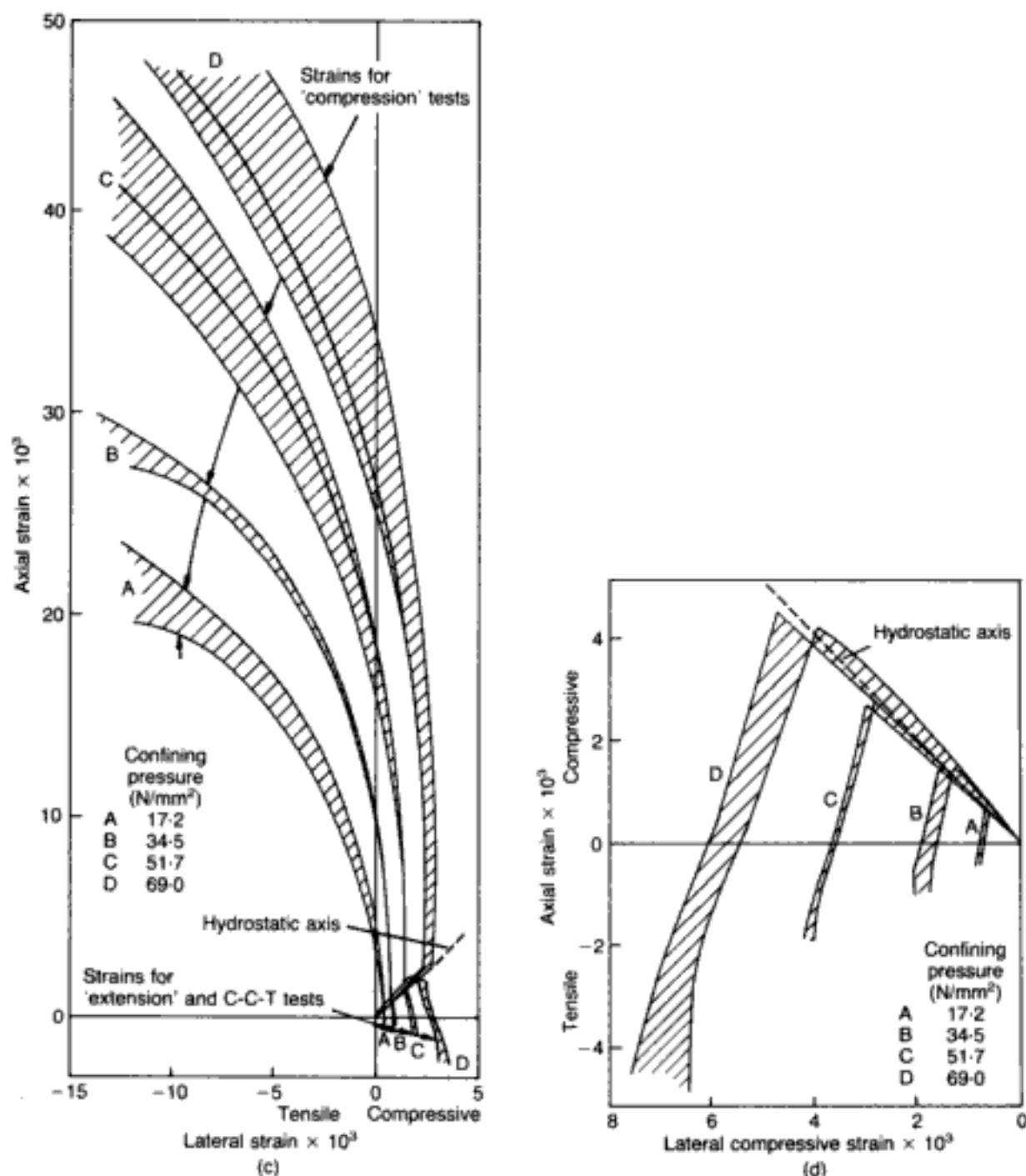


Fig. 1.53 (facing and above). Typical scatter in (triaxial) constitutive material data for a given concrete (with $f_c = 46.9 \text{ N/mm}^2$) tested under various levels of maximum confining pressure.^{20,29} (a) variation of axial and lateral strains with total axial stress for triaxial 'compression', triaxial 'extension' and C-C-T tests; (b) variation of volumetric strain with total axial stress for triaxial 'compression', triaxial 'extension' and C-C-T tests; (c) variation of lateral strain with axial strain for triaxial 'compression', triaxial 'extension' and C-C-T tests; (d) variation of lateral strain with axial strain for triaxial 'extension' and C-C-T tests

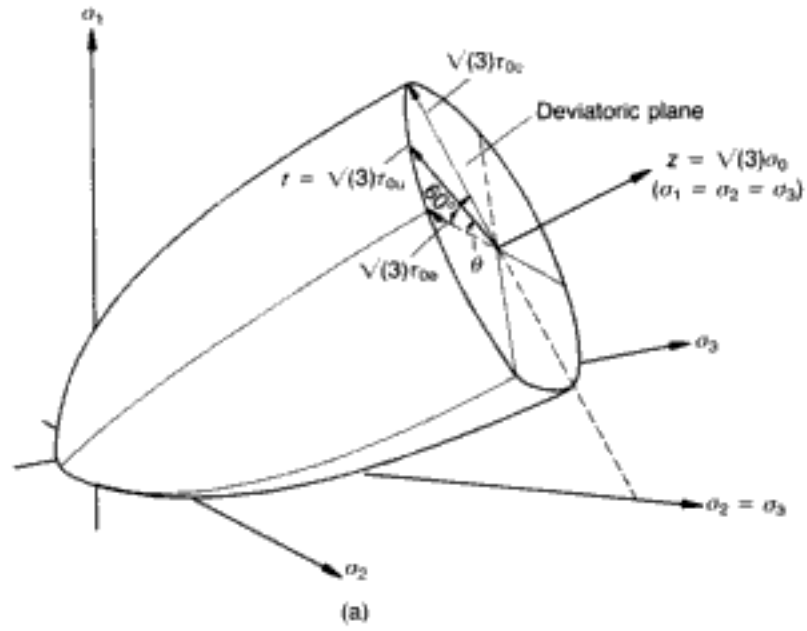


Fig. 1.54. Schematic representation of the ultimate-strength surface.⁴⁴ (a) general view in stress space; (b) typical cross-section of the strength envelope coinciding with a deviatoric plane (i.e. a plane of constant σ_0 , viewed along the axis $\sigma_1 = \sigma_2 = \sigma_3$)

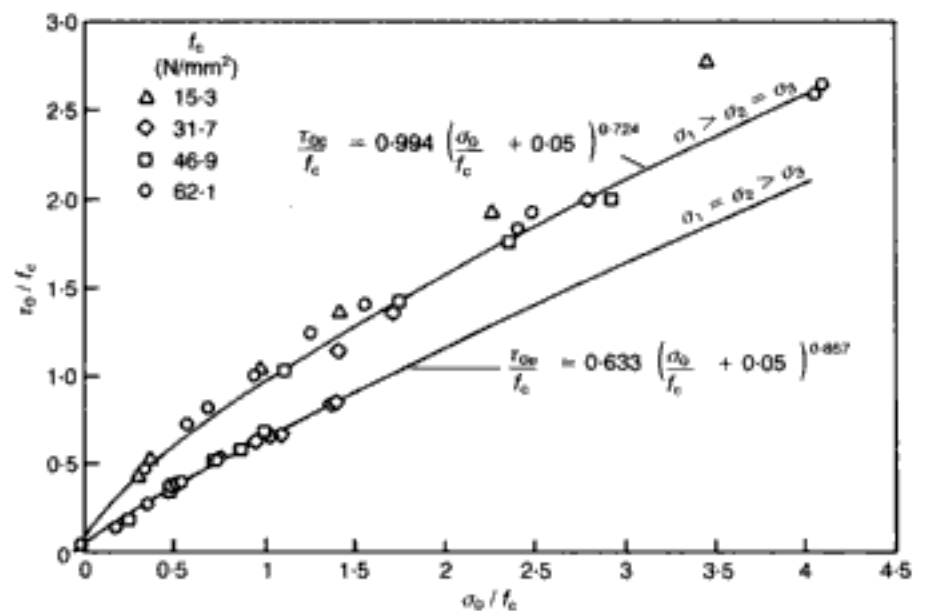


Fig. 1.55. Combinations of octahedral stresses at ultimate strength for concrete under triaxial 'compression' and triaxial 'extension'⁴⁴

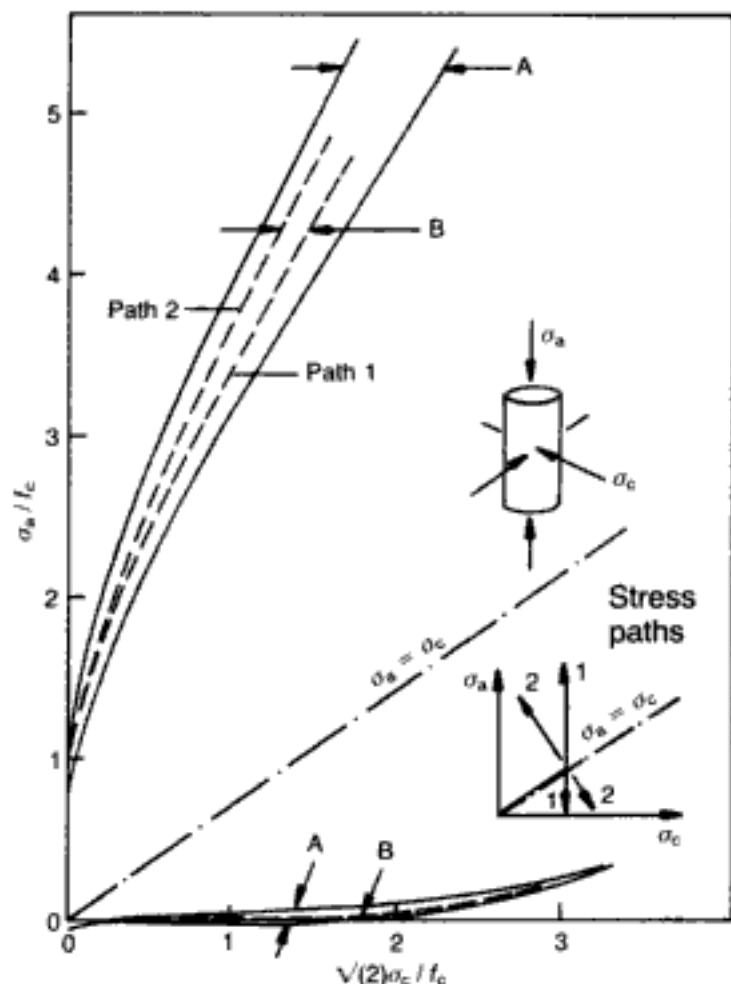


Fig. 1.56. A. Unsystematic variability of 'failure' data obtained from tests using stress path 1 for concretes with f_c varying between approximately 15 N/mm^2 and 65 N/mm^2 ; B. Stress-path effect on 'failure' data for a typical concrete (with $f_c = 31.7 \text{ N/mm}^2$)⁴⁰

A mathematical description of the two strength envelopes in Fig. 1.55 may be obtained by fitting curves to the experimental data. Such an approach leads to the following expressions

$$\frac{\tau_{0c}}{f_c} = 0.944 \left(\frac{\sigma_0}{f_c} + 0.05 \right)^{0.724} \quad (1.37a)$$

$$\frac{\tau_{0e}}{f_c} = 0.633 \left(\frac{\sigma_0}{f_c} + 0.05 \right)^{0.857} \quad (1.37b)$$

Equations (1.37) represent two open-ended convex envelopes the slopes of which tend to become equal to that of the space diagonal as σ_0 tends to infinity. These expressions, together with equation (1.36), define an ultimate-strength surface which conforms with generally accepted shape requirements such as six-fold symmetry and convexity with respect to the space diagonal, open-ended shape which tends to become cylindrical as σ_0 tends to infinity, etc.⁵⁰ A three-dimensional view of this ultimate-strength surface is shown in Fig. 1.58.

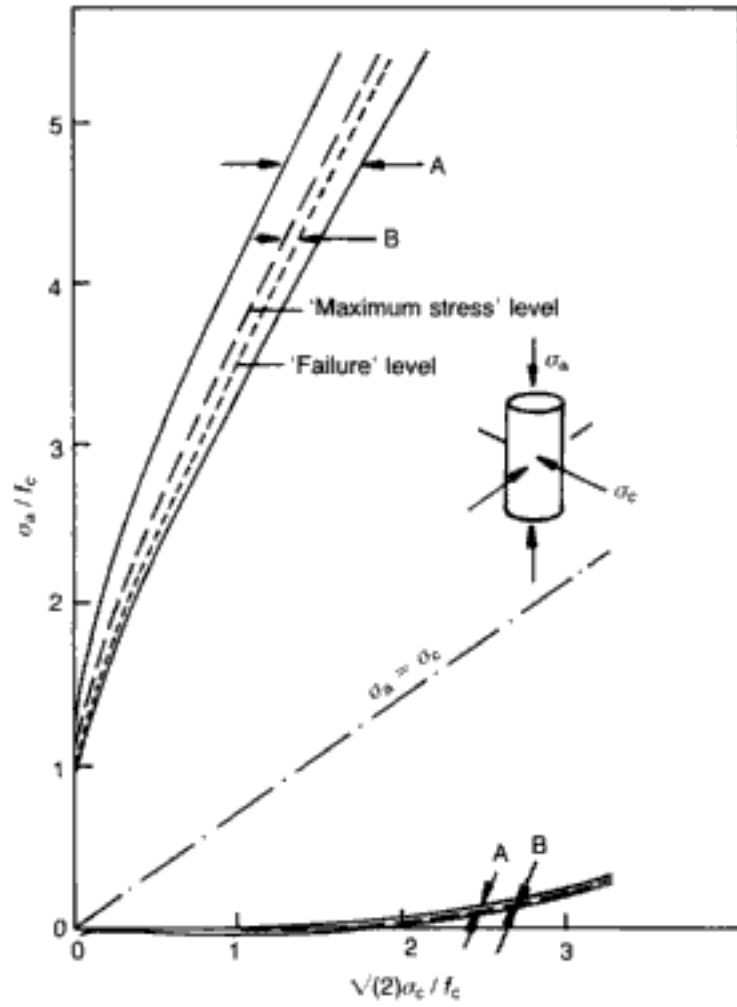


Fig. 1.57. A. Unsystematic variability of 'maximum stress' level exhibited by concretes with f_c varying between approximately 15 N/mm^2 and 65 N/mm^2 ; B. Deviation of 'failure' level from 'maximum stress' level for a typical concrete (with $f_c = 47 \text{ N/mm}^2$)⁴⁰

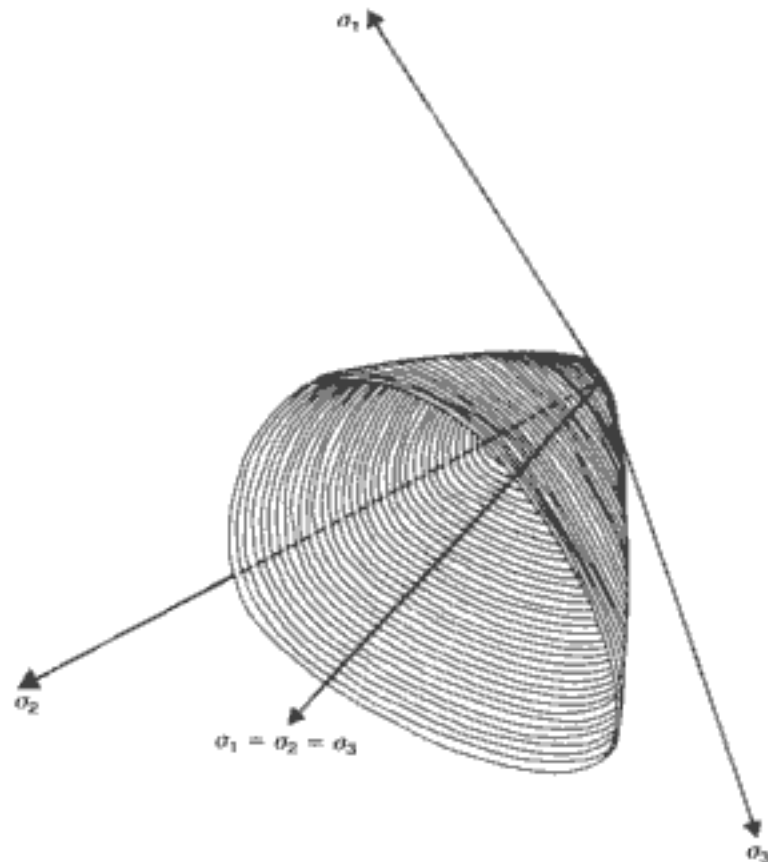


Fig. 1.58. Three-dimensional view of the predicted ultimate-strength surface⁴⁴

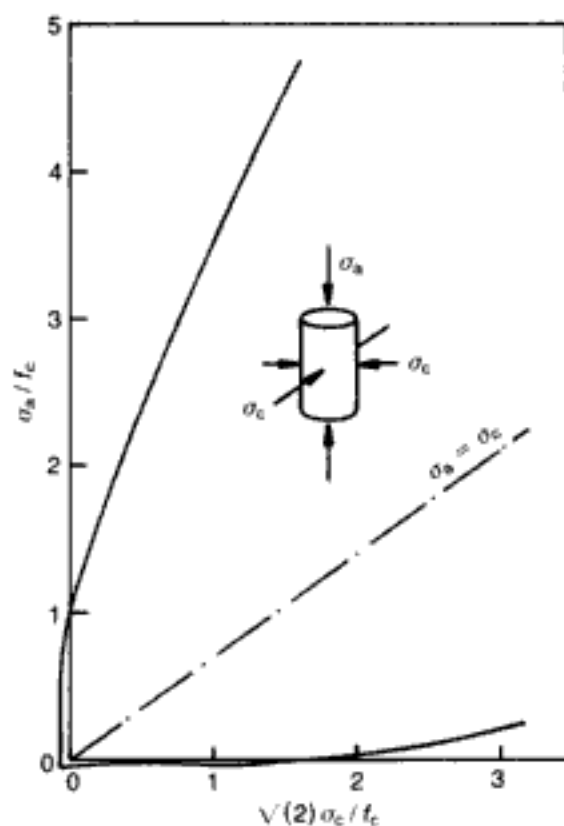


Fig. 1.59. Complete ultimate-strength envelope for concrete under axisymmetric stress⁵¹

It will be noticed that the validity of expressions (1.37) is limited by the constraint that tensile hydrostatic stress states cannot exceed 5% of the uniaxial cylinder compressive strength f_c . This leads to consideration of the question of what experimental data there are for states of stress in which at least two of the principal stresses are tensile, and how the model describes the failure envelopes under such conditions. Experimental evidence of this type is very scarce and, moreover, is invariably associated with large scatter. Under such circumstances, the model smoothly extrapolates the C-C-T portion of the failure surface into regions where more than one principal stress is tensile. A typical cross-section of the failure envelope is shown in Fig. 1.59 (corresponding to the axisymmetric case),⁵¹ and the result is a smooth surface in the 'tension' region which provides a conservative estimate to a parameter that is subject to a very large degree of unsystematic variability, and which, furthermore, represents a small absolute order of magnitude (relative to other stress values) in the stress space. (It is also important to recall the well-known fact that the testing of brittle materials in tension is usually more problematic than the determination of their compressive properties; this was stressed already by Föppl⁷ and is still largely relevant today.)

On the basis of expressions (1.36) and (1.37), checks may be carried out to ascertain whether a state of stress lies inside or outside the failure envelope. The actual procedure consists of the following steps.

- The octahedral stresses and the rotational variable (σ_0 , τ_0 , θ) are calculated either from the principal stresses (σ_1 , σ_2 , σ_3) — computed previously on the basis of the global stresses σ_{ij} , i.e. (σ_x , σ_y , σ_z , τ_{xy} , τ_{xz} , τ_{yz}) — or directly from the first, second, and third stress invariants expressed in terms of σ_{ij} (see Appendix A).
- The ultimate deviatoric stresses at $\theta = 0^\circ$ and 60° (i.e. τ_{0e} and τ_{0c} , respectively) are calculated for the existing state of hydrostatic stress σ_0 .
- The ultimate deviatoric stress τ_{0u} for the existing rotational angle θ is calculated on the basis of the interpolation formula defined by (τ_{0e} , τ_{0c} , θ).
- The values of τ_0 and τ_{0u} are compared; if $\tau_0 > \tau_{0u}$, the state of stress lies outside the failure envelope.

1.4.2.2. *The accuracy of the mathematical model for the failure surfaces*

It is important to assess the accuracy of the proposed model by comparing the predictions with a wider body of experimental data than that which provided the basis for the derivation of the mathematical expressions. This was done in section 1.4.1.3 for the stress-strain relations, and a similar exercise is carried out in the present section for the strength envelopes of concrete.

The intersections of the predicted ultimate-strength surface with the planes $\sigma_1 = 0$, $\sigma_2 = 0$, $\sigma_3 = 0$ represent the ultimate-strength envelopes for concrete under biaxial stress. Figures 1.60(a)–1.60(c) show the biaxial strength envelopes (normalized with respect to f_c) for concrete under compression-compression (C-C), compression-tension (C-T) and tension-tension (T-T), respectively, as predicted by the proposed general expressions. The figures also include most of the experimental data published up to the end of 1973.⁴⁵ Figure 1.61 shows the biaxial strength envelope predicted for concrete under C-C, together with experimental data obtained in the international cooperative project described towards the beginning of the chapter.⁸

The larger scatter of the data shown in all of the above figures is evident. In the case of C-C and C-T, the mathematical model is seen to provide a fair average to such scatter. On the other hand, the model gives a lower bound for the T-T case, in an attempt to ensure a conservative estimate of a parameter which is especially sensitive to the method of testing used; hence, even though the uniaxial tensile strength of concrete is often taken to be of the order of 10% of f_c , such a figure is halved in the present model.

As explained earlier in this chapter, the wide variation of the experimental data shown in all the above figures has been attributed mainly to the different testing techniques used and, in particular, to the degree of frictional restraint at the platen-specimen interfaces.⁸ Now, it is generally accepted that one of the most

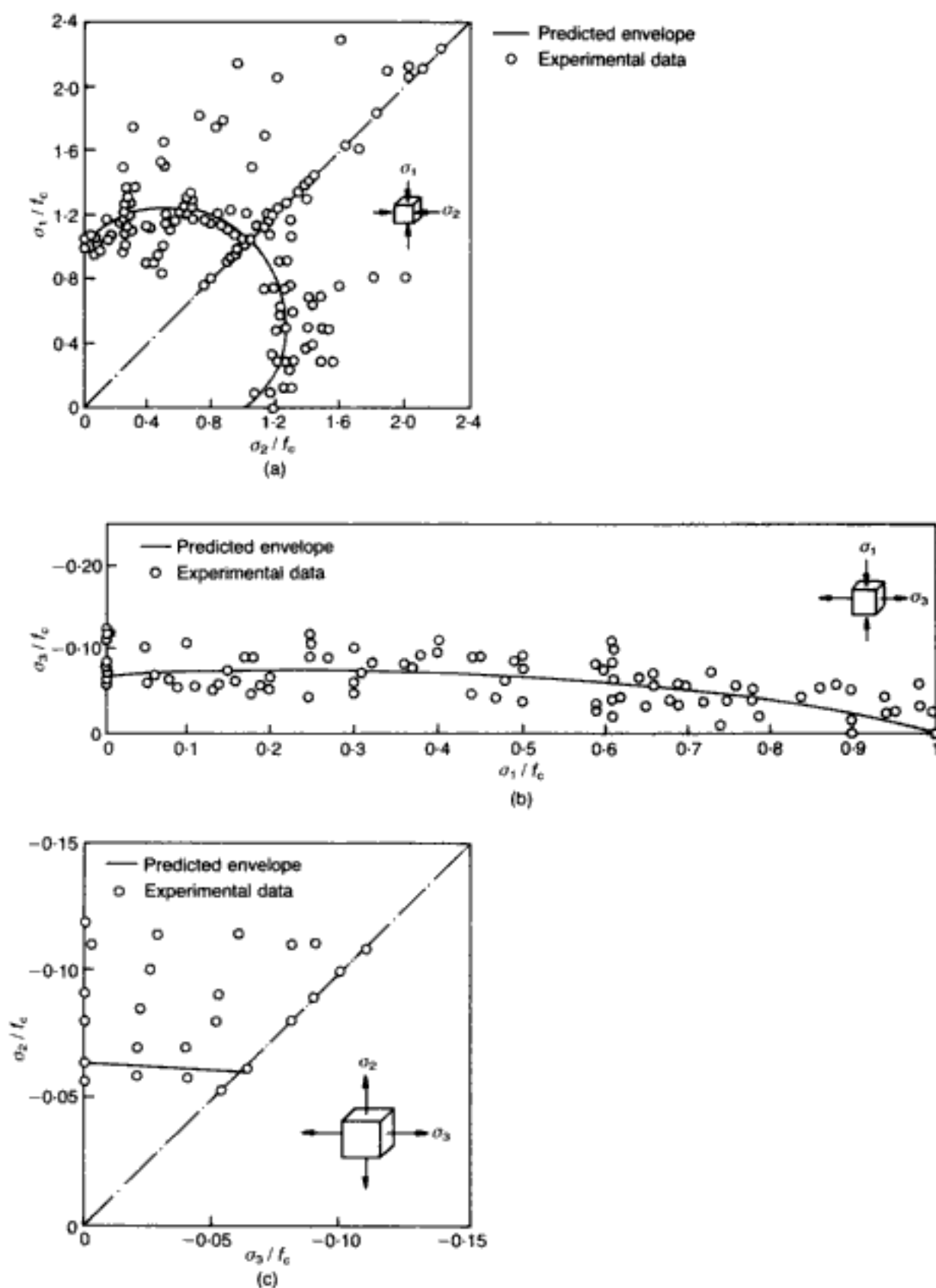


Fig. 1.60. Predicted biaxial strength envelopes for concrete with experimental values published up to 1973 (see reference 45) (it should be noted that the convention $\sigma_1 > \sigma_2 > \sigma_3$, where compression is positive, has been adopted):⁴⁴ (a) compression-compression; (b) compression-tension; (c) tension-tension

efficient ways of minimizing this frictional restraint is by loading through 'brush' platens, and it is by using such a loading system that the biaxial strength envelope shown in Fig. 1.62 has been obtained.⁴² Figure 1.62 also includes the predicted envelope and it is significant that a close correlation between predicted and experimental envelopes is now attained.

So far, the accuracy of the proposed strength envelope has been assessed by comparison of the mathematical prediction with

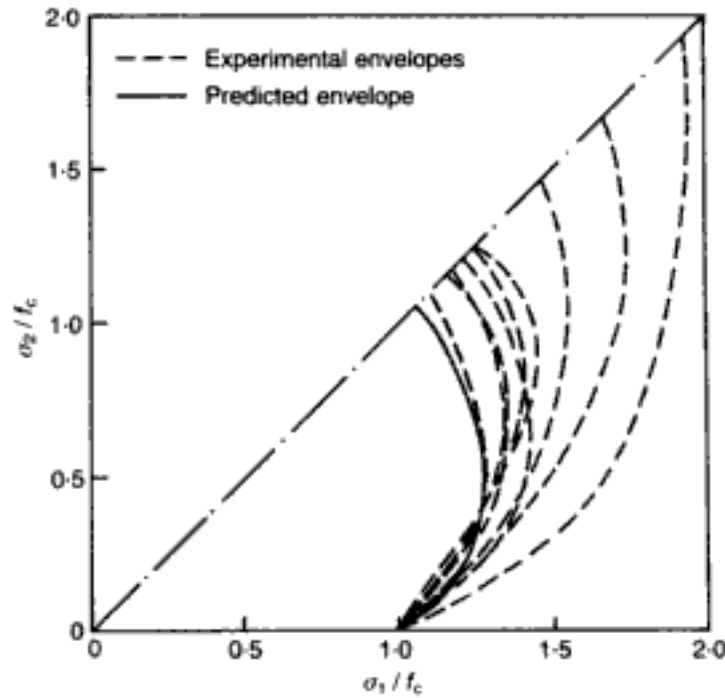


Fig. 1.61. Predicted biaxial strength envelope for concrete under compression-compression with experimental values published between 1973 and 1978 (see reference 8)⁴⁴

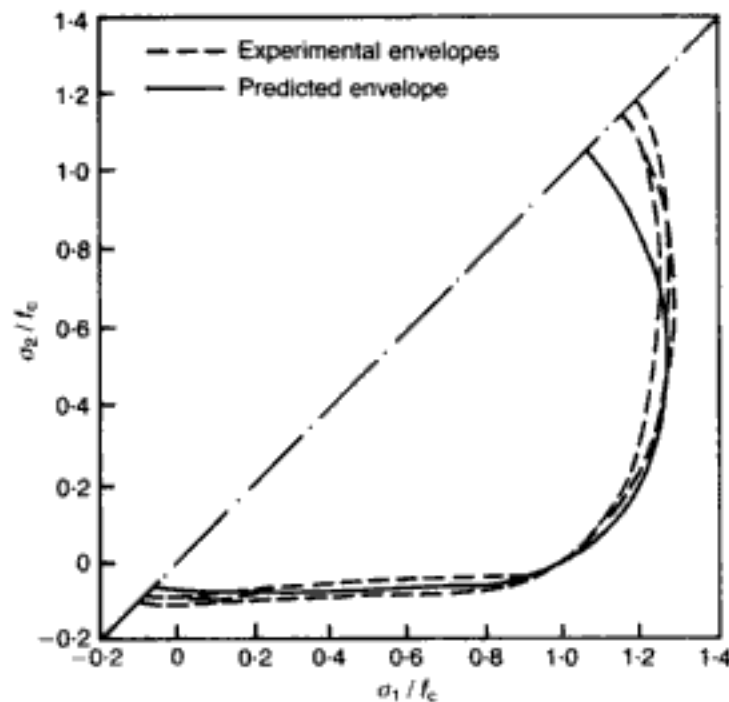


Fig. 1.62. Predicted biaxial strength envelope for concrete with experimental envelopes obtained in tests for which 'brush' platens were used (see reference 42)⁴⁴

available experimental data obtained under biaxial-loading conditions. Next, results from triaxial tests are considered. Figures 1.63(a)–1.63(c) show the strength envelopes, expressed in terms of normalized principal stresses, predicted by the proposed expressions for concrete under various triaxial axisymmetric stress

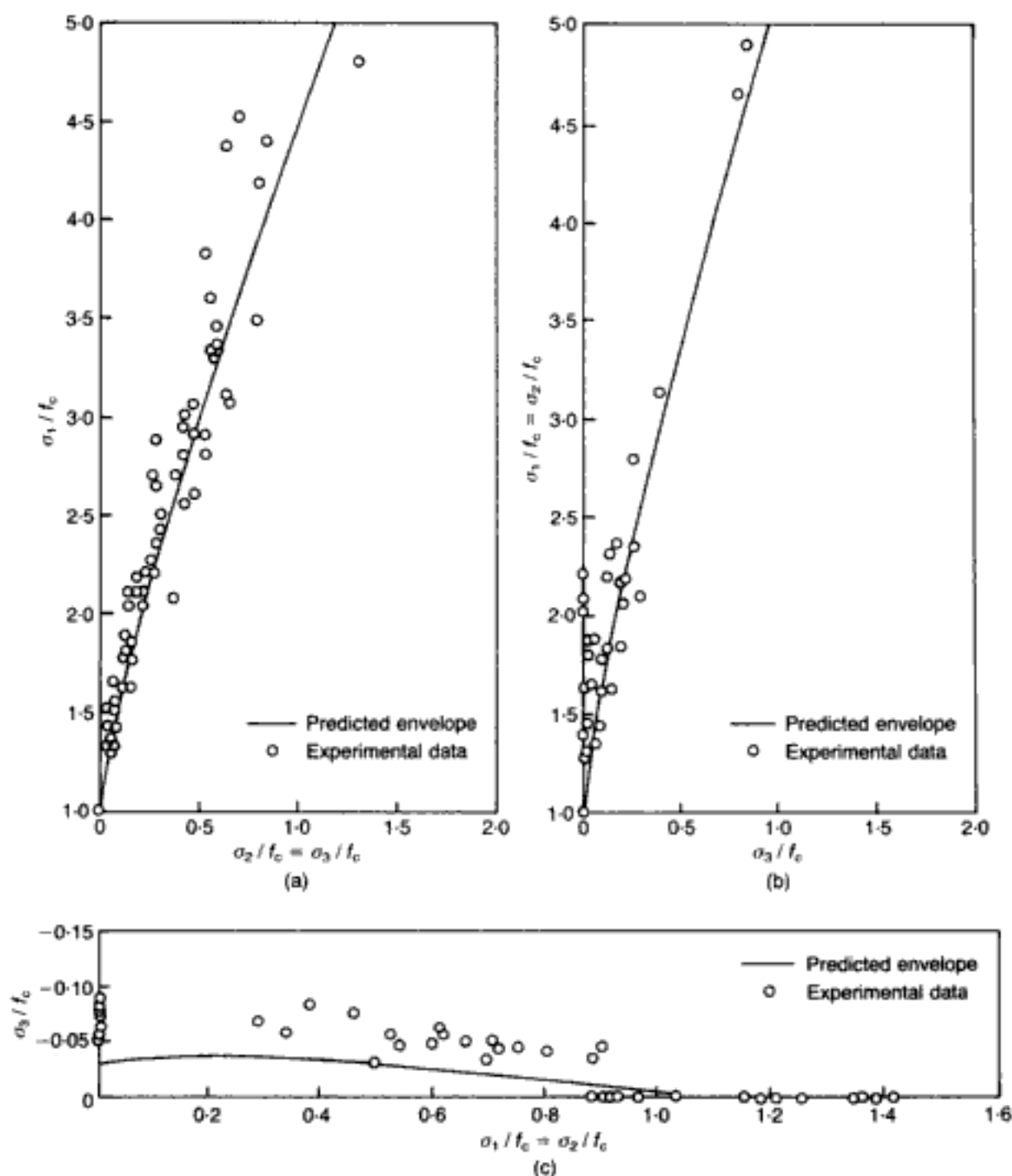


Fig. 1.63. Predicted triaxial strength envelopes for concrete under axisymmetric stress states with experimental values published up to 1973 (see reference 45).⁴⁴ (a) $\sigma_1 > \sigma_2 = \sigma_3 > 0$ (triaxial 'compression'); (b) $\sigma_1 = \sigma_2 > \sigma_3 > 0$ (triaxial 'extension'); (c) $\sigma_1 = \sigma_2 > 0 > \sigma_3$ (triaxial 'tension')

states, together with experimental values corresponding to data published up to the end of 1973.⁴⁵ Figures 1.64(a) and 1.64(b) show the same envelopes corresponding to Figs 1.63(a) and 1.63(b) respectively, but now expressed in terms of octahedral stresses (and for a given concrete), together with experimental values obtained in the international cooperative project.⁸

The octahedral strength envelope predicted by the proposed expressions for $\theta = 30^\circ$ is shown in Fig. 1.65, while Fig. 1.66 depicts the intersection of the ultimate-strength surface with the deviatoric plane $\sigma_0 = 34.5 \text{ N/mm}^2$. Both these figures include experimental values obtained in the international cooperative project.⁸ As for the other triaxial data, the proposed analytical expressions are seen to give a satisfactory fit to experimental results.

In conclusion, the suggested ultimate-strength surface appears to provide a simple generalized mathematical representation of failure in concretes under any type of short-term loading condition.

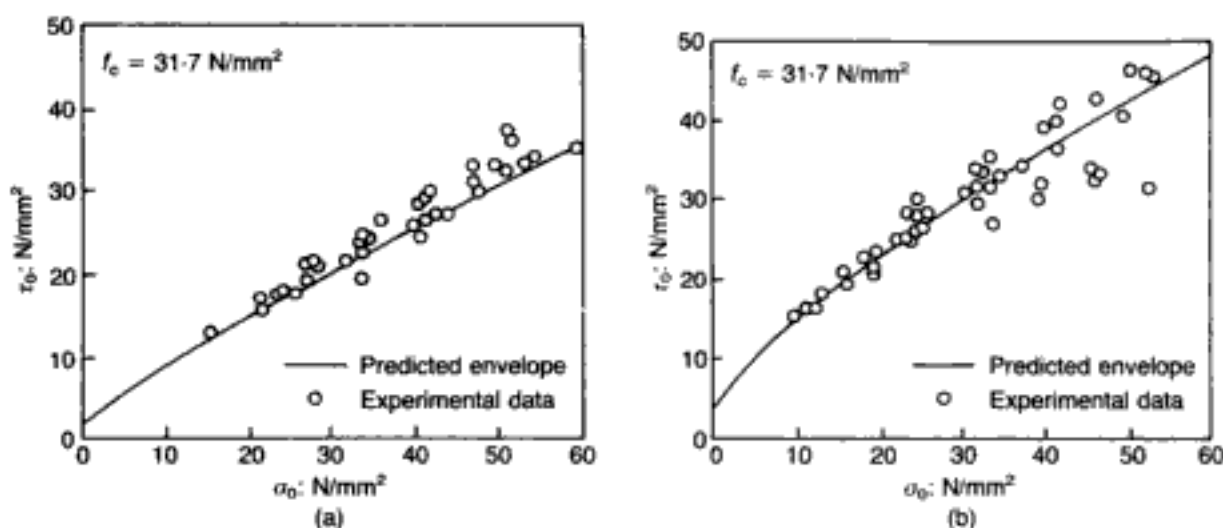
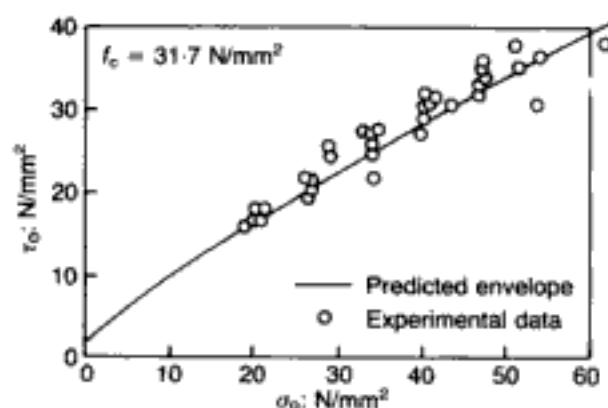
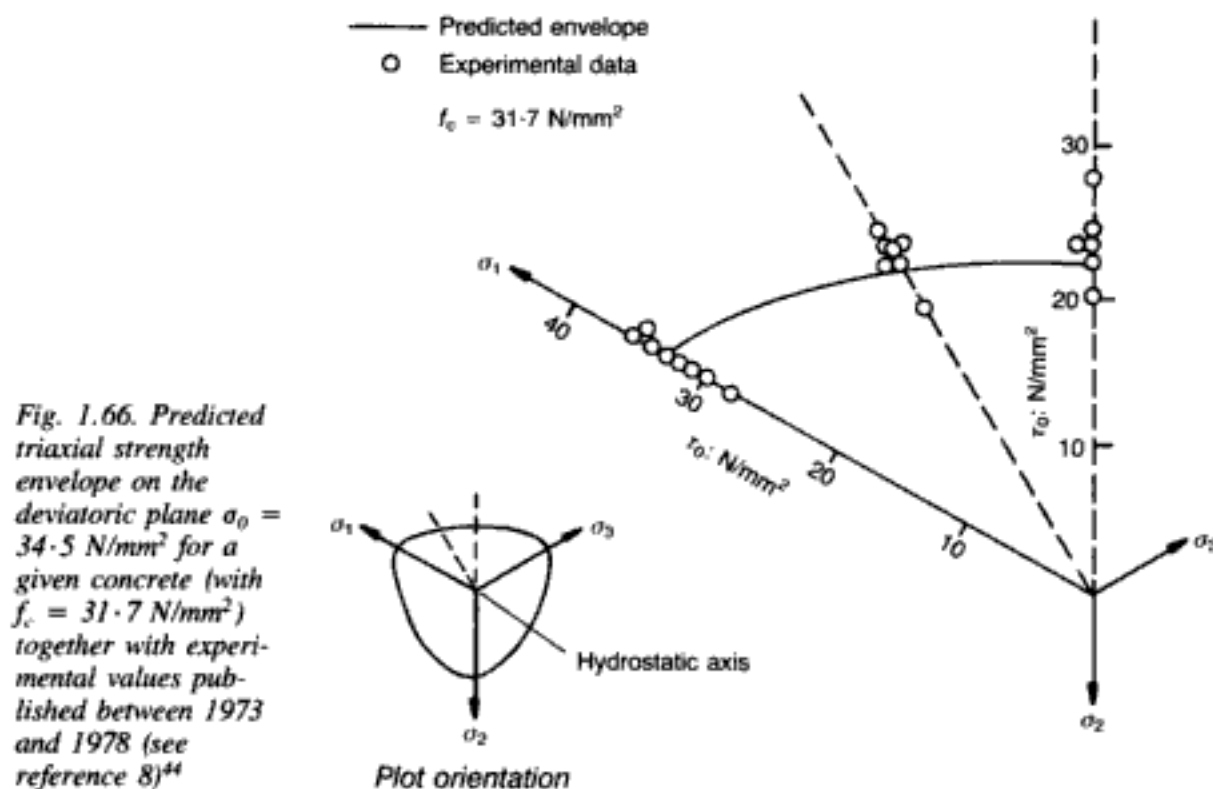


Fig. 1.64. Predicted triaxial combinations of octahedral stresses at ultimate strength for a given concrete (with $f_c = 31.7 \text{ N/mm}^2$) together with experimental values published between 1973 and 1978 (see reference 8):⁴⁴ (a) $\theta = 60^\circ$ (triaxial 'compression'); (b) $\theta = 0^\circ$ (triaxial 'extension')

Fig. 1.65. Predicted combinations of octahedral stresses at ultimate strength for a given concrete (with $f_c = 31.7 \text{ N/mm}^2$) under triaxial stress states with $\theta = 30^\circ$ together with experimental values published between 1973 and 1978 (see reference 8)⁴⁴





The surface conforms with generally accepted shape requirements and has been found to produce a close fit for most biaxial and triaxial strength data published to date.

1.4.3. Deformational and yield characteristics of the reinforcing steel

The deformation and strength of reinforcing steel bars are adequately described by reference to their uniaxial properties. (Therefore, as will be seen in later chapters, the reinforcement is almost invariably modelled by means of line finite elements possessing stiffness along their longitudinal axes only.) Such material modelling is compatible with the negligible importance attached to the effect of the so-called dowel action in shear-transfer mechanisms, as explained elsewhere.^{51,52}

Figures 1.67 and 1.68 show the trilinear diagrams adopted for the stress-strain characteristic of steel bars up to and including their plastification. The first of these was used in the two-dimensional (2-D) version of the FE model, which was developed when the 1972 *Code of practice for the structural use of concrete* (CP 110) was in force.⁵³ Such a diagram, intended primarily for mild-steel reinforcement, broadly follows this code's recommendations but the third branch of the characteristic is given a small slope (instead of being horizontal, as in the code) in order to avoid the numerical difficulties that would result if an abrupt stiffness change to $E = 0$ were to occur.⁵⁴

The diagram corresponding to Fig. 1.68, on the other hand, was adopted in the three-dimensional (3-D) version of the FE model, this having been developed after the 1985 *Code of practice for*

Fig. 1.67. Constitutive and strength relationships for steel (2-D FE package)⁵⁴

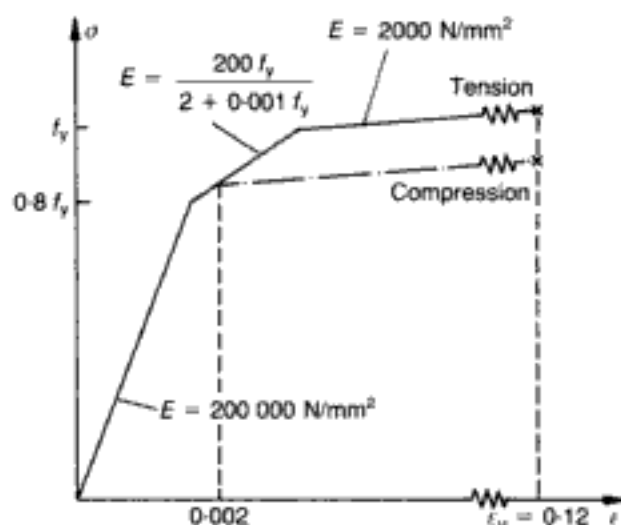
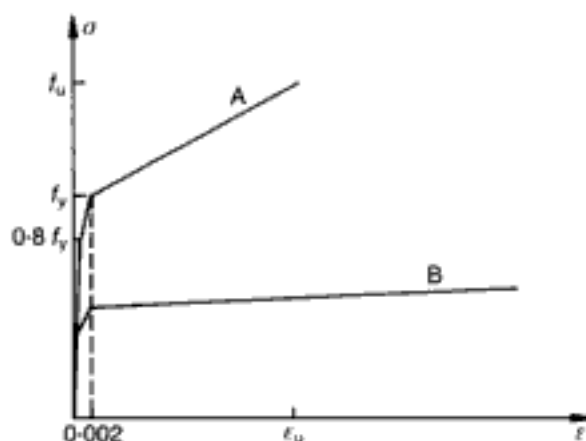


Fig. 1.68. Constitutive and strength relationships for steel (3-D FE package):
 A. high-yield steel;
 B. mild steel (Note: for purposes of clarity, only the salient features for the A characteristics are marked on the vertical axis)



structural concrete (BS 8110) became operative.⁵⁵ The influence of the latter version of the code can be seen, for example, in the fact that high-strength steels are equally catered for and, also, in the lack of differentiation between tension and compression reinforcement.

As one would expect, the choice between Figs 1.67 and 1.68 usually has negligible effect on structural behaviour predicted by the FE model. In both cases, the first two branches of the characteristic are completely defined once f_y (the yield stress in N/mm^2) is specified. The third branch has a much smaller effect on the behaviour of a structure and hence is either given a small nominal slope ($\sim 1\%$ of initial slope) and a cut-off ultimate strain $\epsilon_u = 0.12$ (2-D model), or it requires the specification of the maximum, i.e. ultimate, stress f_u and the corresponding ultimate strain ϵ_u (for the 3-D model). (Since f_u and ϵ_u are rarely reported for mild steel, the 3-D version of the model automatically assumes $f_u = 1.15f_y$ and $\epsilon_u = 0.12$ for such steels.⁵⁶)

It should be stressed that, although a bilinear diagram might appear to be more suitable in the case of mild steels (and is, in fact, recommended by the 1985 code), it turns out to be very

convenient to predict earlier yielding of the steel (i.e. the second branch) in the course of numerical analysis. This avoids the uncertainty of (single) yielding detected in the last and non-converged load step of the analysis and, furthermore, clearly helps to differentiate ductile from brittle predictions.

1.5. Failure mechanism in concrete structures

1.5.1. A fundamental explanation of failure initiation based on triaxial material behaviour

The description of the salient characteristics of concrete at the material level has been presented in the preceding sections in sufficient detail to enable these properties to be implemented in an FE model for the analysis of arbitrary plain and reinforced concrete (RC) structures. Before this is done, however, it is possible to anticipate the typical mode of failure initiation in such structures by means of a simple reasoning based on two key features of concrete materials. These two fundamental characteristics of concrete⁵⁷ are shown schematically in Fig. 1.69, which summarizes much of the earlier discussion on material behaviour.

As is well known, concrete is weak in tension and strong in compression. Its primary purpose in an RC structural member is to sustain compressive forces, while steel reinforcement is used to cater for tensile actions with concrete providing protection to it. Therefore, since the structural role of concrete is concerned primarily with compressive stress states, the present discussion relates to its strength and deformational response under such conditions. Now, information on the strength and deformational properties of concrete is usually obtained by testing cylinder or prism specimens *under uniaxial compression*. Although typical stress–strain curves stemming from such tests have been shown in the earlier part of this chapter, it is useful to refer to Fig. 1.69(a) which depicts, in a generic sense, one further set of such curves. The figure serves as a reminder that, in addition to the strain in the direction of the loading (which usually constitutes the main — if not the sole — item of interest in current design thinking), the uniaxial test also provides information on the strain perpendicular to this direction. Furthermore, a typical plot of volumetric-strain variation appears in the figure. A characteristic feature of the curves in Fig. 1.69(a) is that they comprise ascending and gradually descending branches. However, despite the prominence given to the latter in design, it was explained in section 1.2.1.2 how experimental evidence shows quite conclusively that, unlike the ascending branch, the descending branch does not represent actual material behaviour: rather, it merely describes secondary testing-procedure effects resulting from the interaction between testing machine and specimen. This is an important observation concerning the behaviour of concrete at the material level, as the lack of strain softening, i.e. post-ultimate branch, justifies its being referred to as a brittle material. On the other hand, it turns out that considerations of the behaviour of concrete at the structural level make the actual post-ultimate response of

the material irrelevant for, even if the latter were to exist, failure of concrete in a structure invariably occurs before the attainment of its ultimate compressive stress. The case for such a statement may be argued along the following lines.

Perhaps the most significant feature of concrete behaviour is the abrupt increase of the rate of lateral expansion a uniaxial test specimen undergoes when the load exceeds a level close to, but not beyond, the peak stress. Such a feature was noted already in

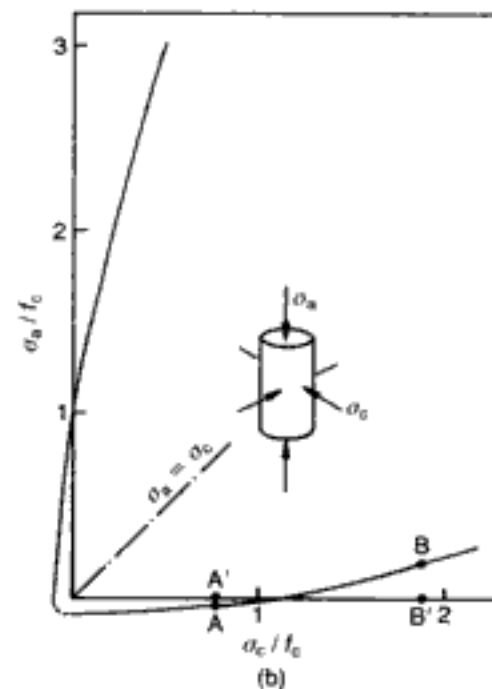
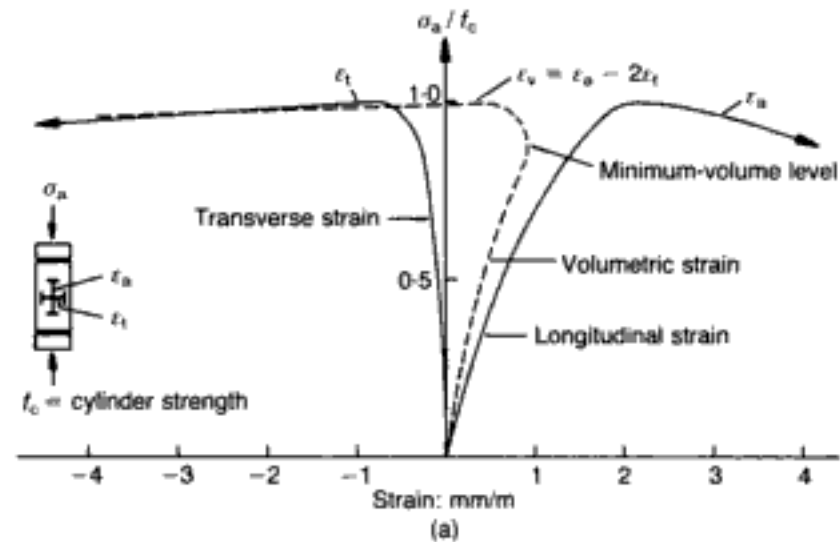


Fig. 1.69. The two key characteristics of triaxial behaviour of concrete materials that govern the fundamental failure mechanism of structural concrete:⁵⁷ (a) typical stress-strain curves obtained from tests on cylinders under uniaxial compression (note the rapid increase of tensile strains orthogonal to the direction of principal stress once the OUF level is exceeded); (b) typical failure envelope of concrete under axisymmetric triaxial stress (note the large effect of even relatively small secondary stresses σ_c on the load-carrying capacity σ_a)

section 1.2 (see, for example, Figs 1.9(a) and 1.13), and the relevant stress level may be identified as the minimum-volume level (see Fig. 1.69(a)) which marks the beginning of a dramatic volume dilation that, in the absence of any frictional restraint at the interface between the ends of the specimen and the steel platens, is considered to lead rapidly to failure even if the load remains constant. This is why the stress at which concrete begins to expand is associated with a process governed essentially by void formation, and is termed the OUPF level which, for all practical purposes, may be equated to the failure load, as explained in section 1.3.3.1. It is important to emphasize here that the rapid expansion at the minimum-volume level, with the tensile strain at right angles to the direction of maximum compressive stress soon exceeding the magnitude of the compressive strain, is a feature of both uniaxial and the more general triaxial compressive behaviour (see Figs 1.9(a) and 1.9(b) respectively).

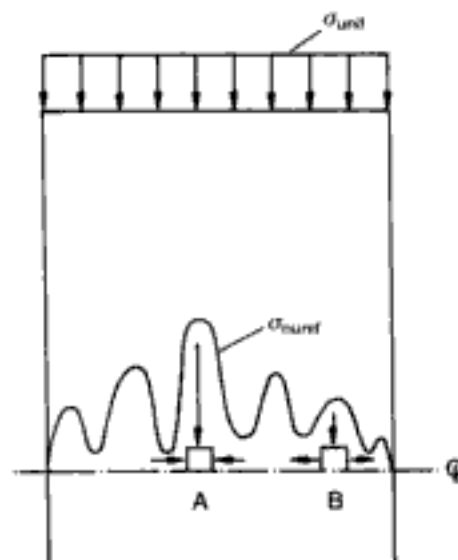
The other key feature of concrete behaviour relates to the major role played by even relatively small (secondary) stresses when the true bearing strength of the material is being assessed. This may be illustrated by reference to Fig. 1.69(b), in which is indicated schematically the variation of the peak axial compressive stress sustained by cylinders under various levels of confining pressure. It is interesting to note that a small confining pressure of about 10% of the uniaxial cylinder compressive strength f_c is sufficient to increase the load-carrying capacity of the specimen by as much as 50%. On the other hand, a small lateral tensile stress of about 5% of f_c is sufficient to reduce the cylinder strength by the same amount. Such behaviour implies that the presence of small secondary stresses that develop within a structural member in the region of the path along which compressive forces are transmitted to the supports should have a significant effect on the load-carrying capacity of the member: compressive stresses should increase it considerably while tensile stresses should — dramatically — have the opposite effect.

While well known, the above two fundamental characteristics of concrete at a material level (summarized in Fig. 1.69) are rarely (if ever) mentioned; more important still from a design viewpoint, their implications for the behaviour of concrete in a structure do not appear yet to have been fully appreciated in terms of failure mechanisms resulting from the interaction of concrete elements in RC structures. In order to appreciate that such interactive behaviour is unavoidable irrespective of the type of structure and/or loading conditions, it is useful to recall that, owing to the heterogeneous nature of concrete, the stress conditions within a concrete structure or member can never be uniform even under uniform boundary conditions. As a result, even for the case of a cylinder subjected to uniform uniaxial compression, the development of triaxial stress conditions is inevitable on account

of the setting up of secondary stresses that are essential for maintaining compatibility of deformation within the structure (see Fig. 1.70). Under service loading conditions, the secondary stresses are negligible and can be ignored for design purposes. However, as the load increases, volume dilation occurs in a localized region where the stress conditions are the first to reach the minimum-volume level. Concrete dilation is restrained by the surrounding concrete and this is equivalent to the application of a confining pressure which, as Fig. 1.69(b) indicates, should increase the strength of the dilating region. At the same time, the dilating region induces tensile stresses in the adjacent concrete and, on the basis of the information shown in Fig. 1.69(b), these should reduce the strength of concrete.

The preceding reasoning for the failure of a specimen under nominally uniform stress conditions is even more evident in the general case of arbitrary structural systems in which there is always a localized region in compression where the OUFPL level is exceeded before it is exceeded in surrounding regions (which are also in compression). As a result, the rate of tensile strain will increase abruptly in this region, thus inducing tensile stresses in the adjacent concrete. Concurrently, equilibrium requires that the surrounding concrete should restrain the expansion of the localized region. While this extra restraint further increases the strength of the localized region, the tensile stresses eventually turn the state of stress in the surrounding concrete into a state of stress with at least one of the principal stress components tensile and thus reduce the strength. Therefore, it is always the concrete surrounding the localized region of wholly compressive stresses that fails first, since its state of stress now has at least one tensile principal stress component.

Fig. 1.70. Schematic representation of the non-uniform stress distribution σ_{unif} due to material heterogeneity within a concrete cylinder under uniform compressive stress σ_{unif} (A: element under triaxial compression; B: element under compression/tension)⁵⁷



It appears, therefore, that, owing to the interaction of the concrete elements within a structure, failure is unlikely to occur in regions where the compressive stress is largest. Instead, failure should occur in adjacent regions, where the compressive stresses may be significantly smaller, owing to the presence of small secondary tensile stresses that develop as discussed above. Such a failure mechanism indicates that concrete invariably fails in tension, and that a concrete structure collapses before the (usually triaxial) ultimate strength of concrete in compression is exceeded anywhere within the structure. This notion that the concrete in the 'critical' zones of compression always fails by 'splitting' — never by 'crushing' — contrasts with widely-held views that form the basis of current analysis and design methods for RC structures. Thus, most design procedures have been developed on the assumption that it is sufficient to rely almost entirely on uniaxial stress-strain characteristics for the description of concrete behaviour. This assumption may be justified by the fact that structural members are usually designed to carry stresses mainly in one particular direction, with the stresses that develop in the orthogonal directions being small enough to be assumed negligible for any practical purpose. However, such reasoning underestimates the considerable effect that small stresses have on the load-carrying capacity and on the deformational response of concrete beyond the in-service conditions. The ignoring of these small stresses in design necessarily means that their actual effect on structural behaviour is normally attributed to other causes that are expressed in the form of — as it turns out, erroneous — design assumptions. The following example will suffice to illustrate this. It is often pointed out that the strains recorded in the compressive zone of beams indicate that these are well in excess of that value that corresponds to the peak stress in a uniaxial cylinder or prism test. As a result, the argument is put forward that strain softening must be present since such large strains are observed only in the region of the descending branch of the uniaxial test. However, the true explanation lies in the fact that such regions are always subject to a state of triaxial compression, and this means that, although the peak stress has not been exceeded, the associated triaxial strains are much larger than their uniaxial-test counterparts around the OUF_P level. Thus, for instance, an axial strain of around 8 mm/m marks practically the end of the descending branch for a concrete of $f_c \sim 32 \text{ N/mm}^2$ in accordance with an ordinary (i.e. uniaxial) cylinder test (Fig. 1.9(a)); when subjected to a hydrostatic stress $\sigma_0 = 24 \text{ N/mm}^2$, the axial strain for the same concrete prior to the attainment of the descending branch is about three times this value, and becomes much higher still with increasing confinement σ_0 (Fig. 1.9(b)).

1.5.2. Triaxiality and failure initiation by macro-cracking: some experimental and analytical evidence

The behaviour of structural concrete outlined in the preceding section has been predicted by analysis and verified by experiment.^{13,22,51,57} The inevitable triaxiality conditions in zones usually (misguidedly) deemed to be critical on account of large compressive action, and the associated failure initiation by tensile stresses adjacent to such zones will become evident throughout the various problems of later chapters tackled by means of FE modelling. Nevertheless, it is instructive to devote the present section to a preliminary illustration of the basic mechanism that governs the ultimate-load conditions in a concrete member.

Consider an RC beam designed in accordance with typical current regulations based on the ultimate-strength philosophy. The stress-strain characteristics of concrete in compression are considered to be adequately described by the deformational response of concrete specimens such as prisms or cylinders under uniaxial compression; thus, the ensuing stress distribution in the compressive zone of a cross-section at the ultimate limit state, as proposed, for example, by BS 8110,^{55,58} exhibits a shape similar to that shown in Fig. 1.71(a). The figure indicates that the longitudinal stress increases with the distance from the neutral axis up to a maximum value and then remains constant. Such a shape of stress distribution has been arrived at on the basis of both safety considerations and the widely-held view that the stress-strain relationship of concrete in compression consists of both an ascending and a gradually descending portion, as illustrated in Fig. 1.71(b). (In fact, the stress block in Fig. 1.71(a) is based on the simplification that, beyond the peak stress, perfect plasticity may be assumed up to a strain of 0.0035; however, alternative stress blocks may also be used, either involving further simplification such as full plasticity leading to a rectangular stress block⁵⁵ or derived by allowing for strain softening between peak stress and a strain of 0.0035 so that the shape of the stress block is curved throughout.⁵⁸) The portion beyond the ultimate (i.e. peak) stress in Fig. 1.71(b) defines the post-ultimate stress capacity of the material which, as indicated in Fig. 1.71(a), is generally considered to make a major contribution to the maximum load-carrying capacity of the beam. It will be noticed that the principal reasoning behind the stress block adopted for design purposes is based on the large compressive strains (in excess of 0.0035) measured on the top surface of an RC beam at its ultimate limit state, such strains being almost twice the value of the compressive strain ϵ_u at the peak-stress level under uniaxial compression. (Typically, ϵ_u is of the order of 0.002 — see Fig. 1.71(b).)

That the above design procedure is not borne out by experimental evidence can be shown by reference to the results obtained from a test series of three simply supported rectangular RC beams subjected to flexure under two-point loading.²² The details of a typical beam are shown in Fig. 1.72, with the central portion under

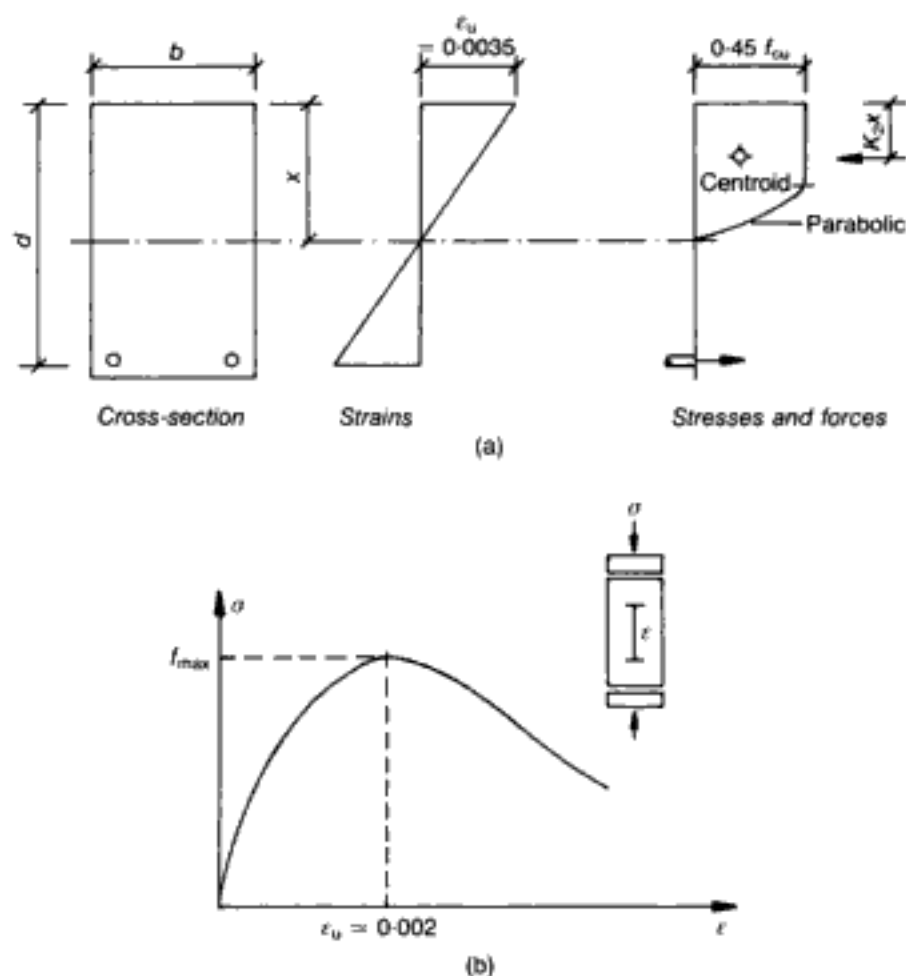


Fig. 1.71. Characteristic design of a beam cross-section for ultimate-load conditions.²² (a) stress and strain distribution proposed by BS 8110 (Part 1) for a critical section at failure (f_{cu} = characteristic or cube strength); (b) typical stress-strain relationships for concrete under uniaxial compression used to derive (a) ($f_{max} = f_c$ for cylinders; $f_{max} = f_{cu}$ for cubes)

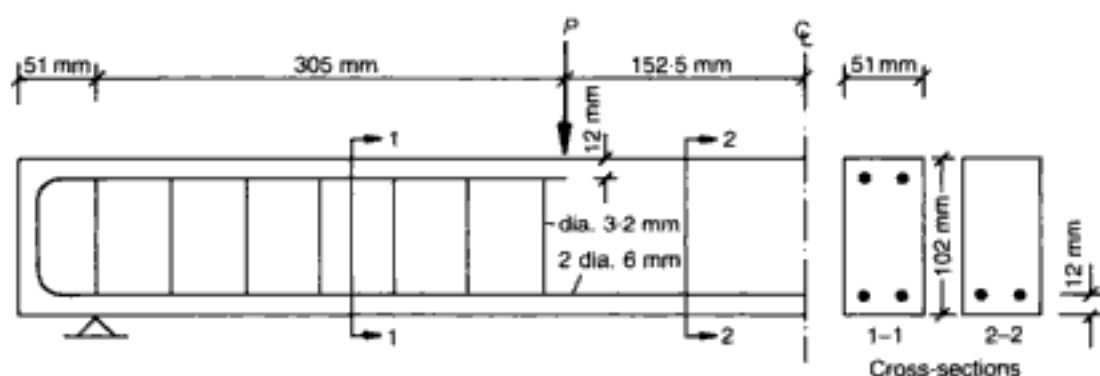


Fig. 1.72. RC beams under two-point loading.²² beam details

pure flexure constituting one-third of the span. The tension reinforcement consisted of two 6 mm diameter bars with a yield load of 11.8 kN. The bars were bent back at the ends of the beams so as to provide compression reinforcement along the whole length of the shear spans. Compression and tension reinforcement along

each shear span were linked by seven 3.2 mm diameter stirrups. Neither compression reinforcement nor stirrups were provided in the central portion of the beams. As a result of the above reinforcement arrangement all beams failed in flexure rather than shear, although the shear span-to-effective depth ratio was around 3. The beams, together with control specimens, were cured under damp hessian at 20° C for seven days and then stored in the laboratory atmosphere (20° C and 40% relative humidity (RH)) for about two months, until tested. The cube and cylinder strengths at the time of testing were $f_{cu} = 43.4 \text{ N/mm}^2$ and $f_c = 37.8 \text{ N/mm}^2$ respectively. Besides the load measurement, the deformational response was recorded by using both 20 mm long electrical resistance strain gauges and linear voltage displacement transducers. The strain gauges were placed on the top and side surfaces of the beams in the longitudinal and the transverse directions as shown in Fig. 1.73. The figure also indicates the position of the LVDTs which were used to measure deflection at midspan and at the loaded cross-sections. Finally, the stress-strain characteristics in uniaxial compression for the concrete used in the investigation are depicted in Fig. 1.74.

In presenting the salient results of the test series of beams, it is convenient to begin by showing the relationships between longitudinal (i.e. along the beam axis) and transverse (i.e. across the beam width) strains, as measured on the top surface of the girders. The relevant information is summarized in Figs 1.75(a) and 1.75(b) which refer to the strains recorded at the critical sections (i.e. throughout the middle third of the beam span) and within the shear spans respectively. Also plotted on these figures is the relationship between longitudinal and transverse strains derived on the basis of the uniaxial material characteristic of Fig. 1.74 (or, equivalently, on the basis of the cylinder strength f_c , through the ensuing mathematical constitutive relations). Now, if the uniaxial-compression stress-strain characteristics of Fig. 1.74 were to provide a realistic prediction of concrete behaviour in the compressive zone of the beams tested in flexure, then the relationships between longitudinal and transverse strains measured on the top surface of the beams would be expected to be compatible with their counterparts derived on the basis of the cylinder test; furthermore, longitudinal macrocracks ought to appear on the top surface of the beams, as indicated in Fig. 1.74, where typical crack patterns of axially-compressed concrete cylinders around (B-C) and beyond (C-D) ultimate strength are depicted schematically. It is apparent from Fig. 1.75(a), however, that, for the region of cross-sections including a primary flexural crack, only the portion of the deformational relationship based on the uniaxial cylinder test up to the OUF level can provide a realistic description of the beam behaviour. Beyond this minimum-volume level, there is a dramatic deviation of the cylinder strains from the beam

Fig. 1.73. RC beams under two-point loading:²² beam instrumentation

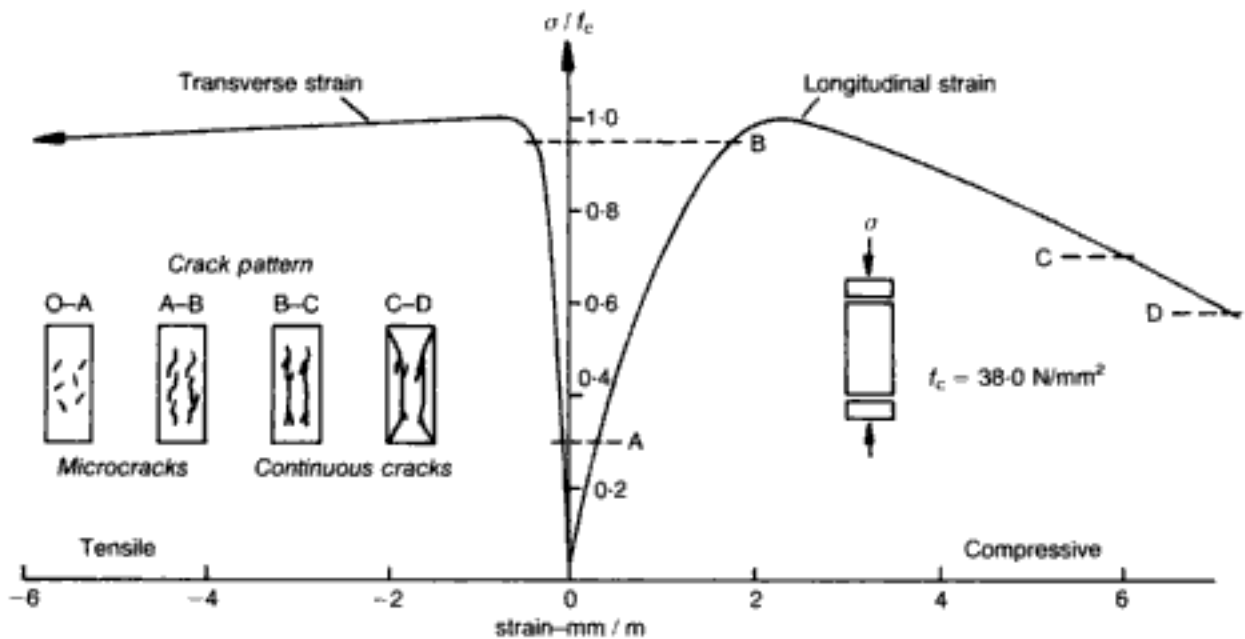
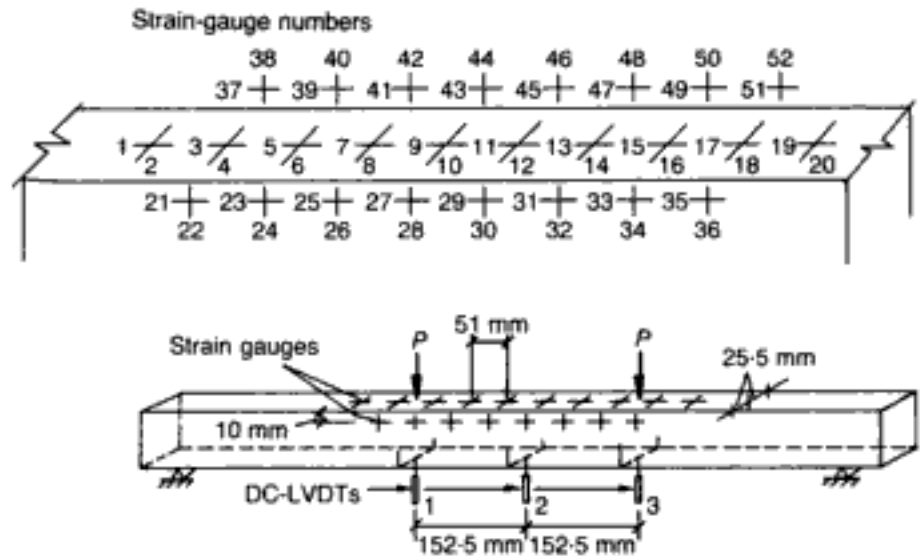


Fig. 1.74. RC beams under two-point loading:²² stress-strain relationships under uniaxial compression for the concrete mix used

relationships. Not only does such behaviour support the view that the post-peak branch of the deformational response of a cylinder in compression does not describe material response but, more importantly for present purposes, clearly proves that, while uniaxial stress-strain data may be useful prior to the attainment of the peak stress, they are insufficient to describe the behaviour once this maximum-stress level is approached. On the other hand, while Fig. 1.75(a) demonstrates the striking incompatibility between cylinder specimen and structural member beyond compressive strains larger than about 0.002 (which, as noted earlier, corresponds to ϵ_u , the strain at the f_c (or f_{cu}) level — see Figs 1.71 and 1.74), Fig. 1.75(b) shows that the relationships between longitudinal and transverse strains measured on the top surface within the shear span of the beams are adequately described by

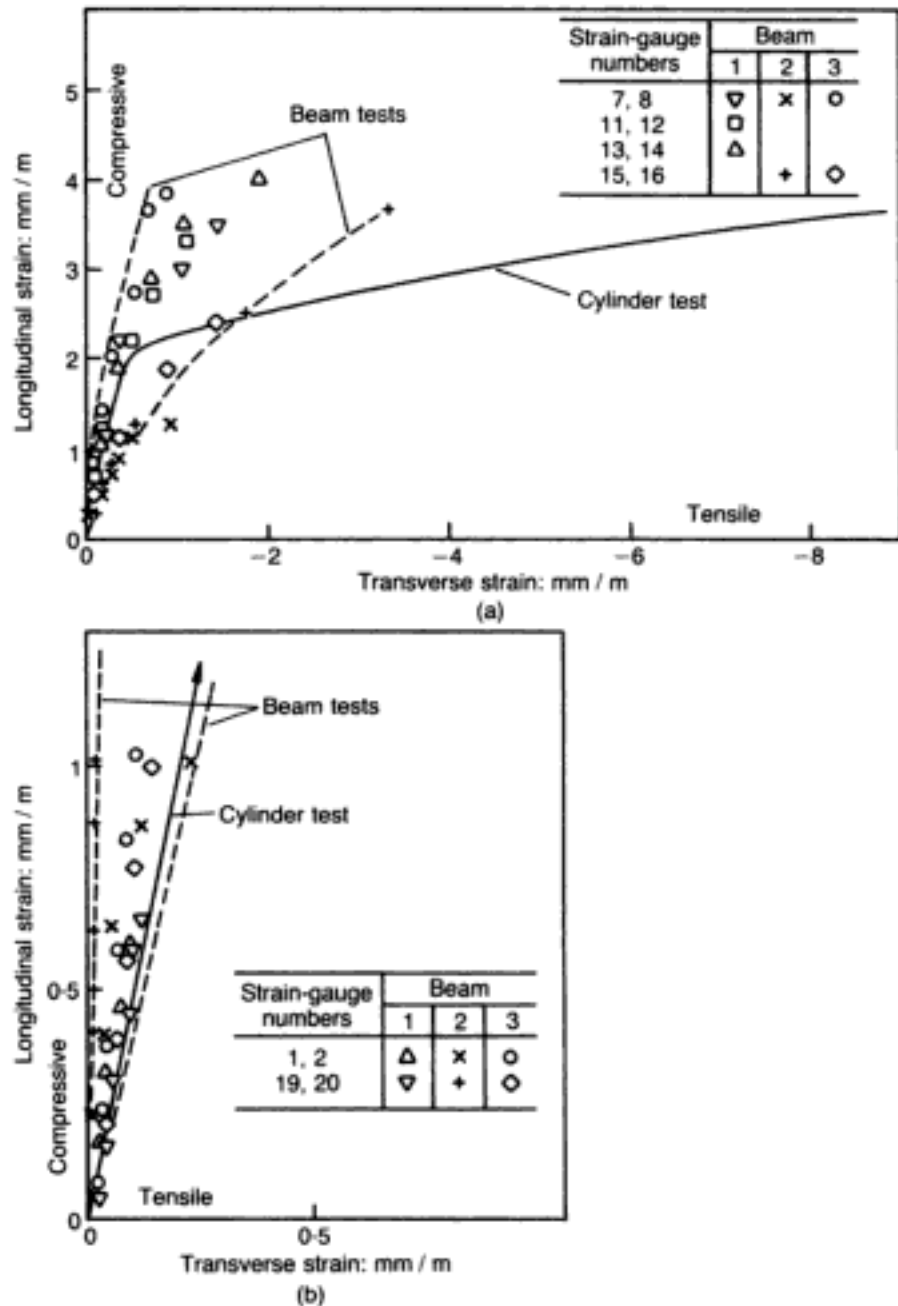


Fig. 1.75. Relationships between longitudinal and transverse strains measured on the top surface of the RC beams under two-point loading (for strain-gauge locations, see Fig. 1.73):²² (a) at critical sections; (b) within the shear spans

the longitudinal strain—transverse strain relationship of concrete under uniaxial compression. It should be noted, however, that the relationships of Fig. 1.75(b) correspond to stress levels well below ultimate strength.

An indication of the causes of behaviour described by the relationships of Figs 1.75(a) and 1.75(b) may be seen by reference to Fig. 1.76, which shows the change in shape of the transverse deformation profile of the top surface of beam 1 (but typical of all beams) with load increasing to failure. The characteristic feature of these profiles is that, within the 'critical' central portion of the beam, they all exhibit large local tensile strain concentrations which develop in the compressive regions of the cross-sections where the primary flexural cracks, that eventually cause collapse, occur.

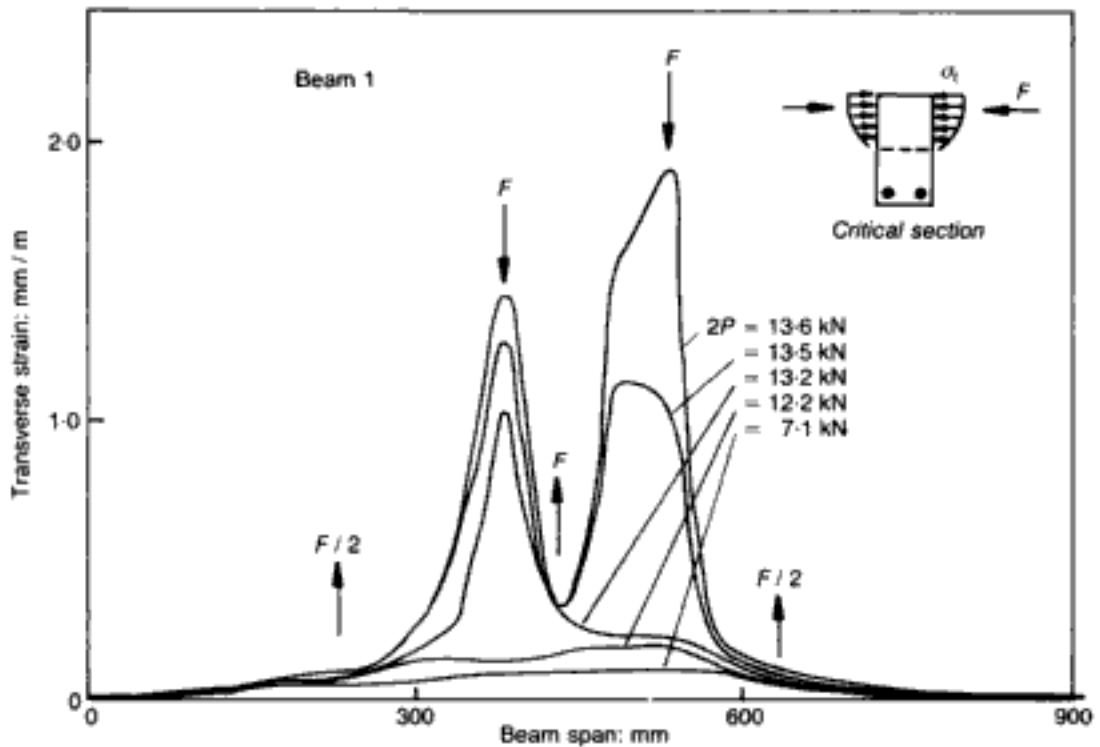
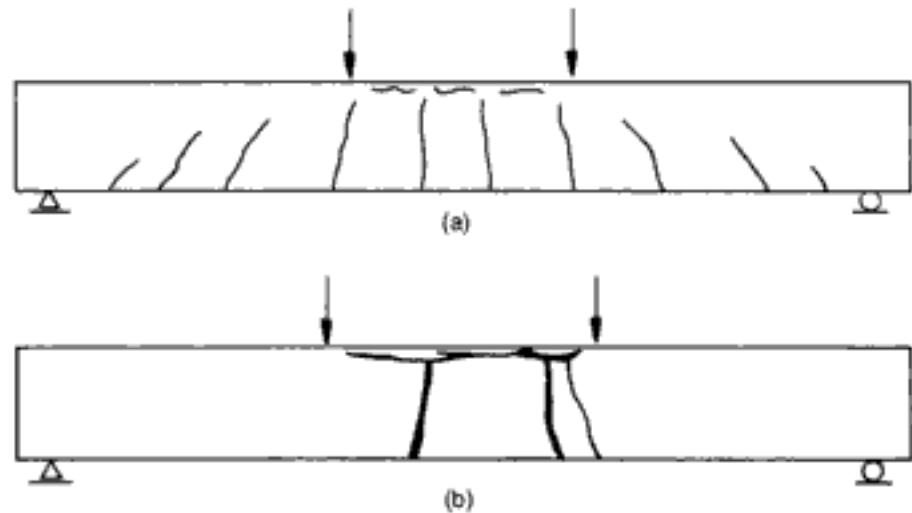


Fig. 1.76. Typical variation of transverse deformation profile of loaded face of RC beams under two-point loading with increasing total load ($2P$) and schematic representation of resulting forces (F) and stresses (σ_c)²²

Although small strain concentrations may develop in these regions at early load stages before the occurrence of any visible cracking, they become large only when the ultimate limit state is approached and visible flexural cracks appear in the tension zones of the beams. Such a large and sudden increase in transverse expansion near the ultimate load is indicative of volume expansion and shows quite clearly that, even in the absence of stirrups, a triaxial state of stress can be developed in localized regions within the compressive zone. The local transverse expansion is restrained by concrete in adjacent regions (as indicated by the resultant compression forces F in Fig. 1.76), a restraint equivalent to a confining pressure that will later be shown as being equivalent to at least 10% of f_c ; hence, as Fig. 1.69(b) indicates, the compressive region in the plane of a main flexural crack is afforded a considerable increase in strength so that failure is not initiated there. Concurrently, the expanding concrete induces tensile stresses in adjacent regions (these are indicated by the resultant tension forces F and $F/2$ in Fig. 1.76), and this gives rise to a compression/tension state of stress. Such a stress state reduces the strength of concrete in the longitudinal direction and collapse occurs as a result of horizontal splitting of the compressive zone in regions between primary flexural cracks, as illustrated schematically in Fig. 1.77(a). Concrete crushing, which is widely considered to be the cause of flexural failure, thus appears to be a *post-failure* phenomenon, that occurs in the compression zone of cross-sections containing a primary flexural crack resulting from a loss of restraint provided previously by the adjacent concrete.

Fig. 1.77. Typical failure mode of RC beams in flexure: (a) schematic representation of failure mechanism at collapse;⁵⁷ (b) observed failure of tested beams following collapse²²



It may be concluded from the above, therefore, that the large compressive and tensile strains measured on the top surface of the central portion of the beams should be attributed to a *multiaxial* rather than uniaxial state of stress. A further indication that these large strains cannot be due to post-ultimate stress-strain characteristics is the lack of any *visible* longitudinal cracking on the top surface for load levels even near the maximum load-carrying capacity of the beams. As shown in Fig. 1.74, such cracks characterize the post-ultimate strength behaviour of concrete under compressive states of stress. Visible cracks occur predominantly on planes parallel to the top surface *at the moment* of final collapse. The typical view of the beam once the collapse of a member has taken place is depicted in Fig. 1.77(b), where the pair of main flexural cracks observed correspond to the peak tensile strain concentrations recorded experimentally in beam 1 (see Fig. 1.76).

It is interesting to note that the results described so far do not contradict the view expressed throughout this chapter that concrete in compression suffers a complete and immediate loss of load-carrying capacity when ultimate strength is exceeded. The implication of the results of the beam tests is that, in the absence of a post-ultimate gradually falling branch of the stress-strain relationships of concrete in compression, the large compressive strains which characterize RC structures exhibiting 'ductile' behaviour under increasing load (i.e. behaviour characterized by load-deflection relationships exhibiting trends similar to those shown in Fig. 1.78 for the under-reinforced members tested) are due to a complex multiaxial compressive state of stress which exists in any real structure at its ultimate limit state. Such stress states may be caused by secondary restraints imposed on concrete by steel reinforcement, boundary conditions, surrounding concrete, etc. The significance of these restraints is, in most cases, not understood or simply ignored. It may thus be concluded that the ultimate strength of concrete in localized regions exhibits significant

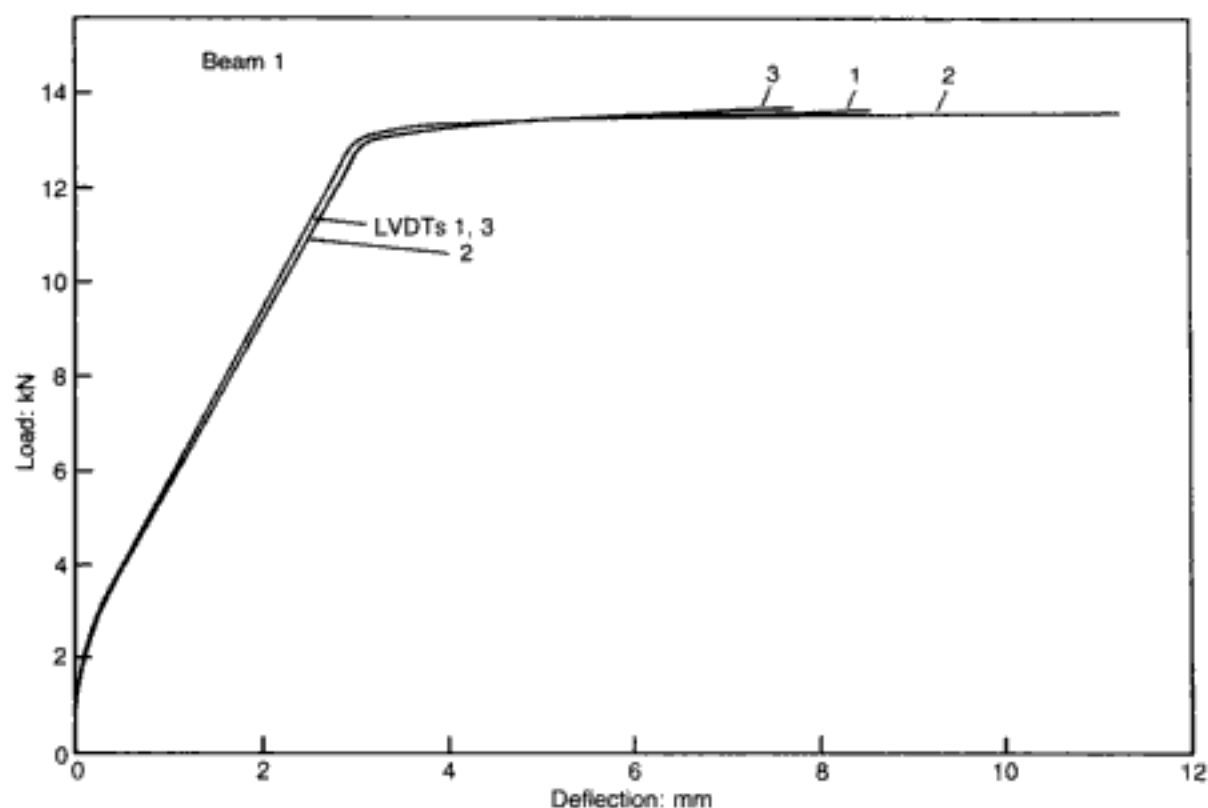
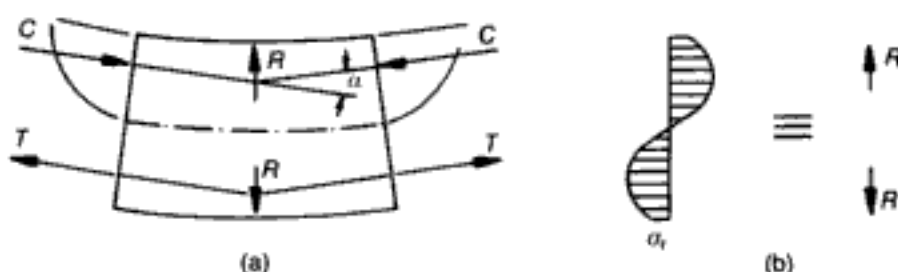


Fig. 1.78. Typical load-deflection curves of RC beams under two-point loading (for LVDT's locations, see Fig. 1.73)²²

variations dependent on the local *triaxial* compressive state of stress within the compressive zone of an RC structure or member. The higher the triaxial ultimate strength of concrete at a critical cross-section, the larger the corresponding compressive and tensile strains. The 'ductility' of the structure, therefore, seems to be dependent on the true (i.e. triaxial) ultimate strength of concrete at critical cross-sections rather than on stress redistributions attributable to post-ultimate material stress-strain characteristics, even if the latter were assumed to exist.

There remains to explore the state of compressive triaxial stresses compatible with the deformations and strains measured in the beams tested. In addition to the main longitudinal (σ_l) and the secondary transverse (σ_t) stresses, another set of secondary actions also exists, namely the radial stresses (σ_r) acting vertically. Clearly, vertical stresses must exist at, and in the vicinity of, the point loads, but the radial stresses referred to are additional to these and are more relevant for present purposes. These radial stresses are associated with the radial stress resultant (R) which develops within the deformed beam as a result of the inclination of the compressive (C) and tensile (T) stress resultants acting in the longitudinal direction. The above stress resultants are shown schematically in Fig. 1.79, which indicates that, even the loaded face (which is generally assumed to be under plane-stress conditions), is subjected to a radial stress resultant. As long as the beam exhibits near-elastic behaviour, the radial stresses corresponding to the radial stress resultant are small in magnitude since they are distributed over

Fig. 1.79. Schematic representation of radial actions due to deflected shape of RC beams.²² (a) forces (R); (b) stresses (σ_r)



the whole length of the central portion of the beam. However, when the central portion of the member starts to develop large deflections (see Fig. 1.78) as a result of the formation of a 'plastic' zone caused by a critical flexure crack, the radial stresses become significant in magnitude since they tend to become localized and to concentrate over the plastic zone.⁵⁹ For load levels close to the maximum load-carrying capacity of the beam, the mean value of the above radial stresses may be estimated — albeit roughly — as follows. If the inclination of the longitudinal compressive and tensile stress resultants is defined by the angle of discontinuity α resulting from the inelastic deformation of the 'plastic' zone (Fig. 1.79), then

$$R = C \sin \alpha = T \sin \alpha \quad (1.38)$$

Now, T is approximately equal to the total yield force of the reinforcement, i.e. $T = 2 * 11\,800 = 23\,600$ N (see earlier details), whereas an approximate value for α may be obtained by the ratio

$$\frac{\alpha}{2} = \frac{\text{maximum mid-point deflection}}{\text{half-span of beam}} \quad (1.39)$$

For a value of the maximum mid-point deflection approximately equal to 10 mm (see Fig. 1.78) equation (1.39) gives $\alpha \sim 4.4 * 10^{-2}$ rad which, when substituted in equation (1.38), results in $R \sim 1000$ N. Finally, assuming that the length of the 'plastic' zone is 5 mm, a nominal value for the radial stresses (approximating the section width to ~ 50 mm) is: $\sigma_r \sim 1000 / (5 * 50) \sim 4$ N/mm². Hence, $\sigma_r \sim 0.1 * f_c$ since, as noted previously, $f_c \sim 38$ N/mm².

The order of magnitude of the transverse stresses σ_t may be assessed by reference to the estimate obtained for σ_r . Consider Fig. 1.80, which shows the variation on the critical section of the average strains measured in the loading direction on the side faces of the beams with the transverse strains measured on the loaded surface. It is interesting to note from the figure that the strains measured on the side faces are slightly larger than those measured on the loaded face. This is considered as an indication that the average value of the stresses restraining the transverse expansion of the critical section should be at least as large as that of the radial stresses, i.e. $\sigma_t > 0.1 * f_c$. The transverse and radial stresses,

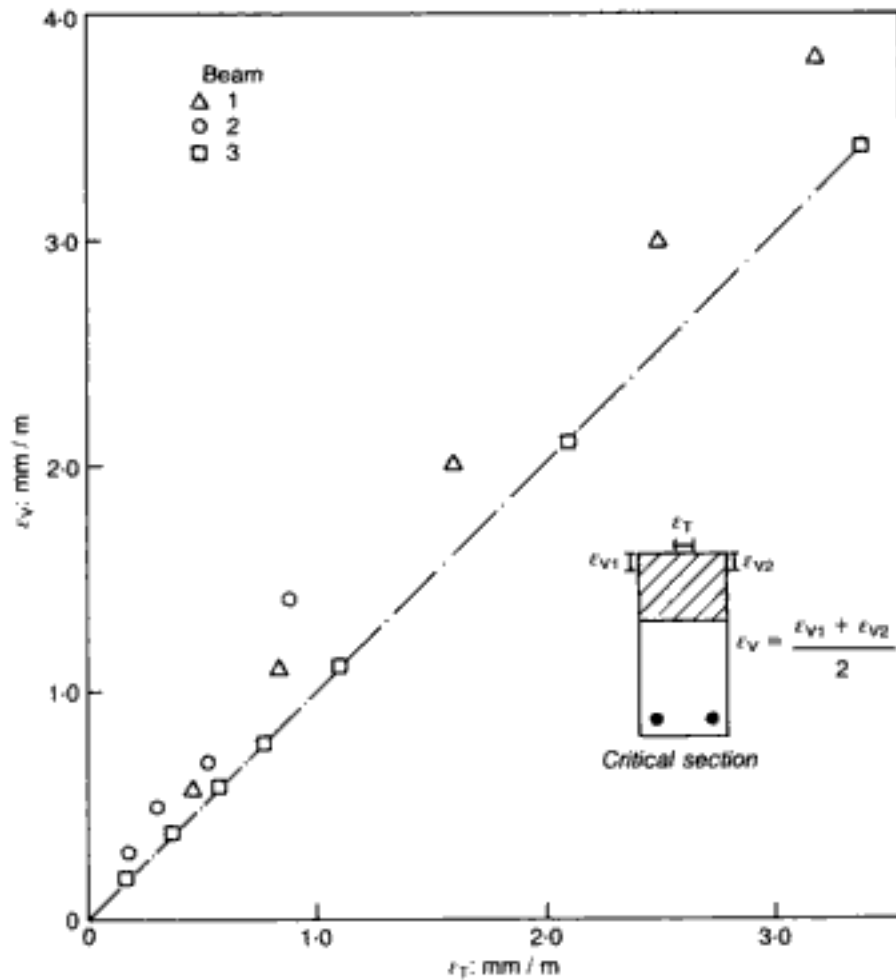


Fig. 1.80. Relationships, with increasing load, between transverse and vertical strains at critical sections of the RC beams under two-point loading²²

therefore, combined with the longitudinal stresses give rise to a complex multiaxial compressive state of stress in the regions of the large tensile strain concentrations within the compressive zone of the beams. Under such a three-dimensional stress state, concrete can sustain both stresses and strains which can be considerably larger than those obtained in uniaxial material tests that form the basis of most current structural design.

How large are the main stresses σ_1 ? These would be expected to be at least 50% in excess of f_c because, as pointed out in section 1.5.1, Fig. 1.69(b) suggests that an axisymmetric confining pressure of about 10% of f_c boosts the actual strength by about one-half of its original value. That this is indeed the case may be seen by reference to Fig. 1.81(a), which shows the resultant tension (T) and compression (C) force resultants at a critical section of a beam. Since only an order-of-magnitude estimate of σ_1 is required, average stress values may be used and hence it is sufficiently accurate to adopt a rectangular stress block. Now, earlier calculations for beam 1 gave $T=C=23\,600\text{ N}$ (i.e. ductile failure), while the ultimate load $P=6800\text{ N}$ combined with a rounded-off value of the shear span of about 300 mm leads to the maximum-sustained bending moment of $\sim 6800 \times 300 \sim 2\,040\,000\text{ N mm}$. The lever arm then follows at $z=2\,040\,000/23\,600 \sim 86.5$

mm, enabling the depth of the stress block to be estimated at $x = 2 * (90 - 86.5) \sim 7$ mm. As before, the beam width may be approximated to 50 mm so that the compressive-zone stresses $\sigma_1 \sim 23\,600 / (50 * 7) \sim 67$ N/mm², i.e. the average value of the longitudinal stress at a critical section is 75% above f_c and, clearly, some of the actual local stresses will be even higher than this figure.

On the basis of the assumed distribution of secondary (i.e. 'confining') stresses σ_1 and σ_r (see Figs 1.76 and 1.79), it could be argued that the degree of triaxiality varies throughout the depth of the compressive zone in the manner shown in Fig. 1.81(b), with the longitudinal stresses σ_1 increasing from the neutral plane up to a maximum value (where the confinement is greatest) and then gradually decreasing to a smaller value at the loaded face. If so, it might be suggested that, neglecting the inevitable stress variations across the beam width, which only a proper three-dimensional

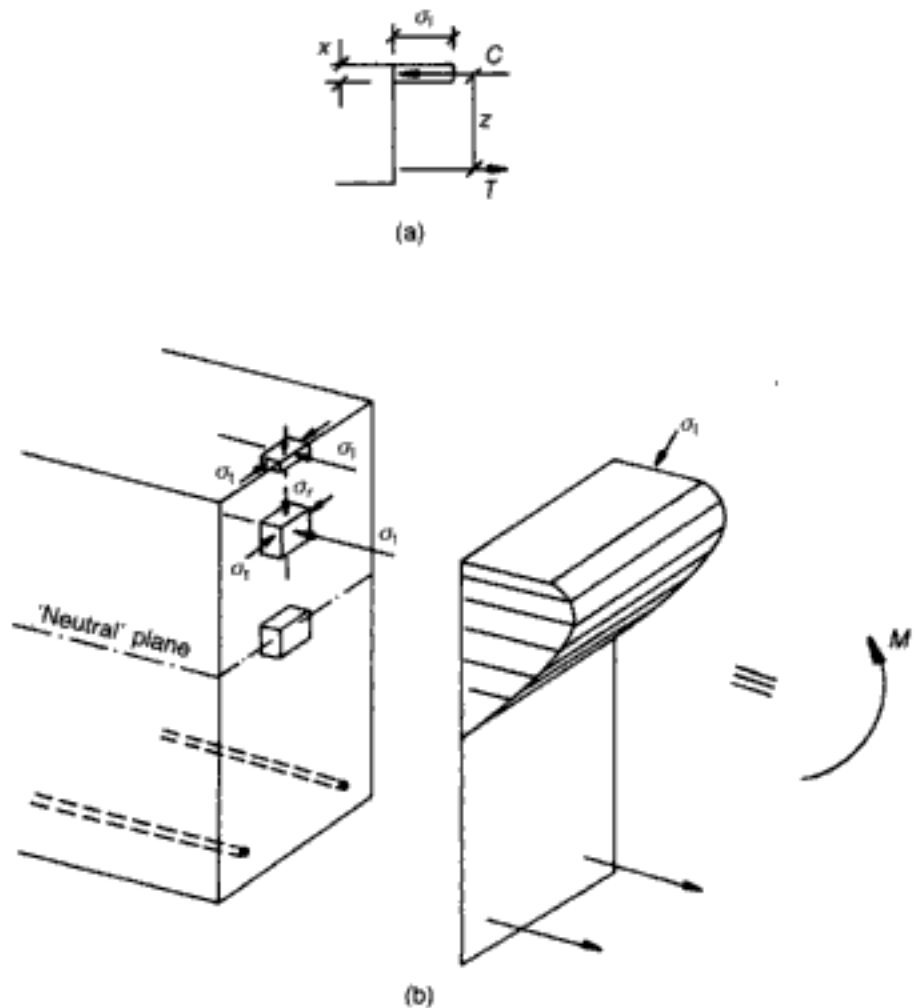


Fig. 1.81. Longitudinal stresses σ_1 in the critical compressive zone of the RC beams under two-point loading at failure: (a) assessment of average σ_1 based on measured values of ultimate tensile force resultant and bending moment;⁵⁷ (b) likely shape of σ_1 distribution predicted on the basis of triaxial behaviour²²

analysis could reveal, the shape of the σ_1 distribution is not unlike that of the generally accepted stress-block shape derived on the basis of a uniaxial stress–strain relationship possessing a gradually descending post-ultimate branch which, as discussed earlier, is used by current design procedures recommended by codes of practice. However, the preceding study shows beyond doubt that, while both the large strains required for ductility and the shape of the stress block might appear as admitting the postulate that uniaxial material properties are applicable at a structural level, such a postulate does not accord with the actual mechanism of failure in a structure and, furthermore, leads to massive underestimates of the true stresses and transverse tensile strains under ultimate conditions. (In view of the latter, it is obvious that the various refinements in the shapes of the stress blocks — see the discussion at the start of the present section — are totally unjustified, so that the simplest stress-block shape (i.e. rectangular) might as well be used in ordinary design calculations.) Therefore, the main conclusion to be drawn from the preceding study is that the importance of triaxiality in elucidating what triggers the collapse of a structure and the sensitivity of triaxial failure envelopes to even small degrees of confinement make it mandatory to incorporate multiaxial material descriptions in any FE model aimed at accurate predictions of ultimate behaviour at the structural level.

The triaxiality in the previous study was provided by concrete itself: namely the compressive region of concrete where volume dilation was reached first was restrained by the surrounding concrete. As already mentioned previously, such ‘secondary’ (but extremely significant) restraints on concrete could also be imposed by other agents such as, for example, steel reinforcement. As an illustration of the latter case, a simplified description of the effect of hoop reinforcement on the strength and deformation of what, in the absence of such reinforcement, is essentially a plain concrete (PC) cylinder under uniform compression will now be presented. The results stem from an FE analysis¹³ of the type that will be described fully in later chapters, in which the constitutive relations and failure criteria have been implemented. The hoop reinforcement is simulated by means of a spring support having a stiffness equivalent to the stiffness of the actual reinforcement. The results obtained from the FE analysis of this structural configuration (shown in Fig. 1.82(a)) are depicted in Figs 1.82(b)–1.82(d). Figure 1.82(b) illustrates how the load-carrying capacity of concrete increases with decreasing spacing of the hoop reinforcement. The cause of such behaviour may be seen by reference to Fig. 1.82(c), which shows the effect of hoop-reinforcement spacing on the stress path to which concrete under increasing load is subjected. Figure 1.82(c) also includes the ultimate-strength envelope for plain concrete and indicates that the confining pressure (σ_c) induced by the restraint which the hoop reinforcement imposes on the

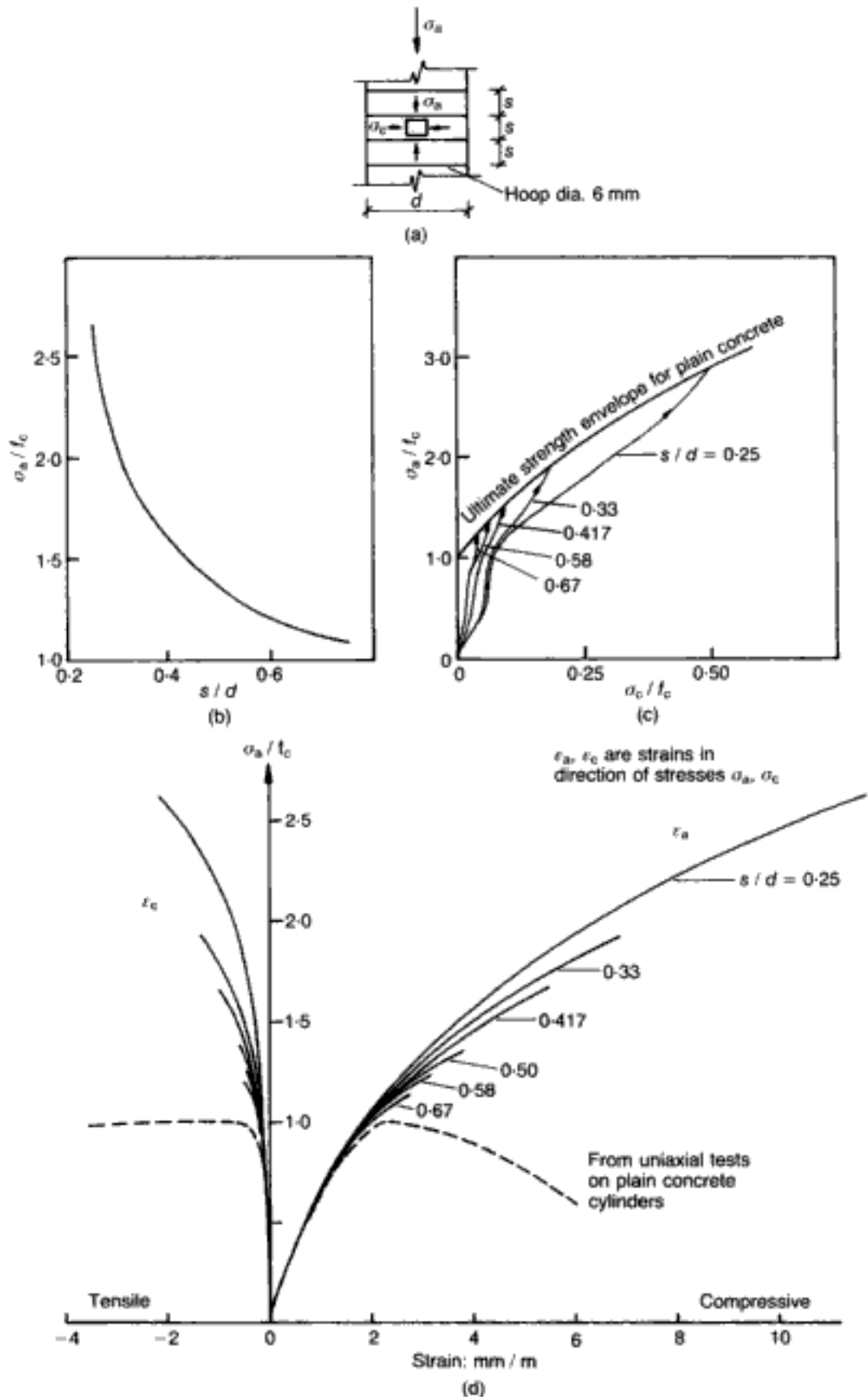


Fig. 1.82. Effect of hoop reinforcement on the strength and deformational response of a PC cylinder:¹³ (a) structural form investigated; (b) relationship between strength and reinforcement spacing; (c) effect of reinforcement spacing on strength and stress path; (d) stress-strain relationships

transverse expansion of concrete with increasing applied axial load increases with decreasing spacing of the reinforcement so that a higher axial stress (σ_a) is required for the ultimate-strength level to be exceeded. Finally, Fig. 1.82(d) shows the variations of axial and lateral strains with increasing axial stress for various values of reinforcement spacing. The stress-strain relationships obtained from tests on plain concrete under uniaxial compression are also shown in the figure for purposes of comparison. It should be noted that, for values of the reinforcement spacing up to about 50% of the diameter of the concrete member, the axial compressive strains corresponding at ultimate strength are comparable to, or higher than, the maximum axial strain exhibited by plain concrete under uniaxial compression.

In previous discussion, it was pointed out that, while a proper allowance for triaxial compression in regions usually considered as critical was a prerequisite in any formal modelling of a structure, it was, in fact, the surrounding concrete which initiates failure, as triaxial compression in the region being restrained is followed eventually by a state of stress in the adjacent zone (which does the restraining) with at least one principal-stress component being tensile. Therefore, it is this latter location, where failure is invariably triggered, which is truly critical. While this will become quite apparent in subsequent chapters describing various FE analyses, it is useful to conclude this section with an illustration of the typical failure mechanism in a concrete structure. This will be done by reference to the problem of a PC cylinder subjected to axisymmetric patch end-loading, as depicted in Fig. 1.83(a). Owing to symmetry, only one-eighth of the structure needs to be analysed, and the results^{13,60} appear in Figs 1.83(b) and 1.83(c), with circumferential cracks denoted by short straight lines, while the regions of radial cracking are indicated by patterns of (mutually) orthogonal dashes. Characteristically, the analysis predicts cracking will occur in regions subjected to a state of stress with at least one of the principal stress components tensile. For the example under investigation, the most critical state of stress is that which initiates cracking in the region marked B in Fig. 1.83(b). With increasing load, this cracking propagates only into other regions subjected to similar states of stress, i.e. with at least one of the principal stress components tensile, up to the formation of the crack pattern corresponding to the collapse stage (see Fig. 1.83(c)). Figure 1.83 also shows that region A, which is subjected to a wholly compressive state of stress, reduces progressively in size as the applied load increases above the level which causes crack initiation. This is due to the redistribution which transforms the state of stress at the periphery of region A from a wholly compressive state of stress (within the strength envelope) to a state of stress in which at least one of the principal stress components is tensile. When the strength of concrete under this latter state of stress is exceeded,

cracking occurs and the size of region A (where failure still does not occur) is reduced further (see Fig. 1.83(c)). Therefore, throughout the whole analysis, the strength of concrete in compression is not exceeded at any point in the member, so that collapse of the structure eventually occurs *before* the strength of concrete in region A is exceeded.

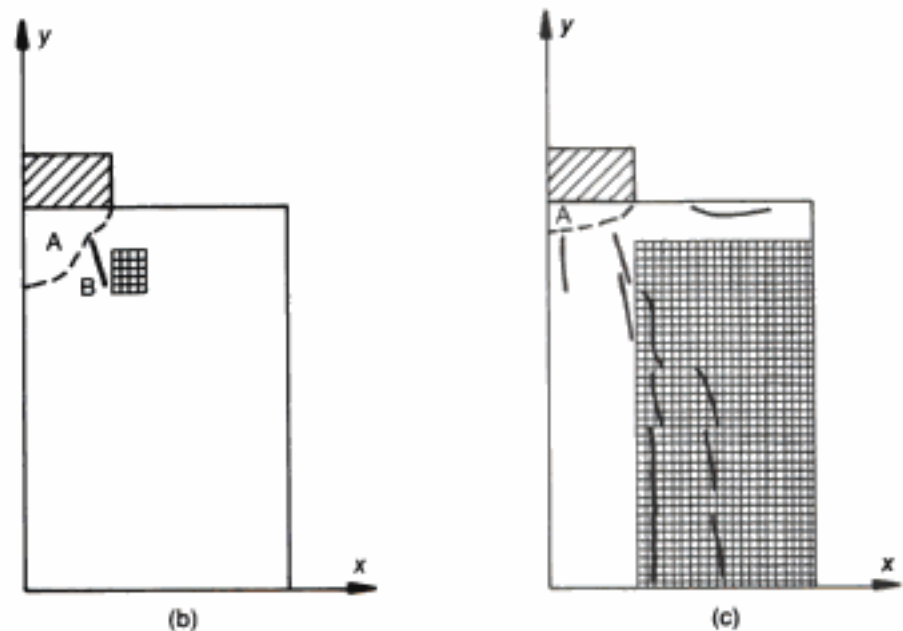
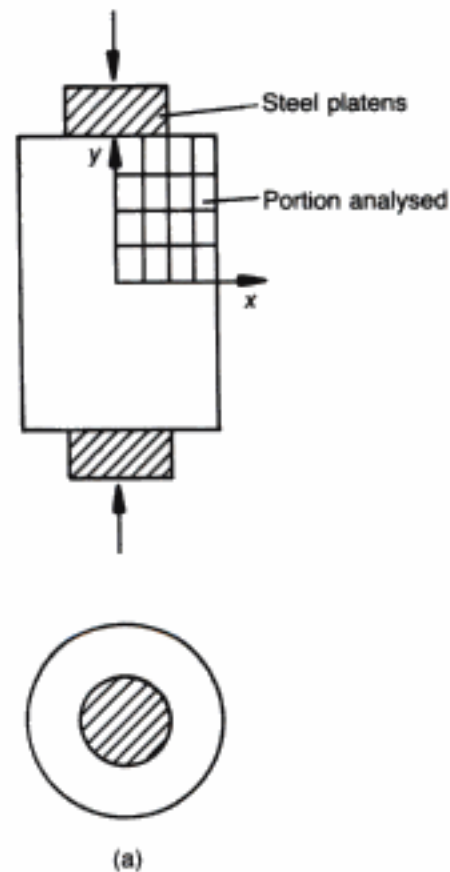


Fig. 1.83.
Characteristic failure mechanism of a PC cylinder under axisymmetric patch load:^{13,60} (a) elevation and plan views of the cylinder, showing portion actually analysed; (b) typical crack pattern at the initiation of cracking; (c) typical crack pattern at collapse

1.6. A summary of the main characteristic features of concrete materials relevant to finite-element modelling

This chapter has been devoted to a detailed description of the various characteristics of concrete materials with reference to both phenomenological causes and the resulting effects which are of direct relevance to the behaviour of a structural-concrete member. Before embarking upon the FE modelling of such components, it is useful to summarize very briefly the main findings of this chapter as regards the salient features of concrete.

Much of the experimental data on concrete properties may turn out to be unreliable on account of the interaction between test machine and tested specimen. A simple technique that is both sound and consistent is provided by the ordinary uniaxial-compression cylinder test. The key parameter obtained from such a test is the cylinder strength in uniaxial compression, f_c . This is the single input variable required by the proposed model for concrete materials subjected to arbitrary multiaxial stress conditions. Thus, both the constitutive relationships and the strength envelopes for concrete under uniaxial, biaxial or triaxial stress states are fully and unequivocally determined (irrespective of the stress path followed) upon specification of f_c . Such a parameter is readily available in everyday engineering practice, and this is in marked contrast with the parameters required by other, more complex models of concrete for which the number of variables may be large, their determination difficult and the ensuing values of doubtful validity. Many such 'theories' are no more than curve-fitting exercises for a particular set of experimental data and, hence, it is not surprising that, besides the inherent awkwardness, their accuracy is usually limited to the particular circumstances and/or structural form for which they were originally derived, more general problems necessitating the adjustment of parameters or the use of altogether new models for concrete behaviour. The model being proposed here, on the other hand, is applicable to all structural forms under any (static) loading and/or boundary conditions, the generality of its predictions being consistent with the fact that a comprehensive description of concrete response — all the way to failure — is provided by the simple uniaxial-strength parameter f_c , which could not possibly be the subject of controversy.

While the ascending branch of the stress-strain curve of a cylinder under uniaxial and/or triaxial stress states provides a realistic description of material behaviour, the descending branch is a direct consequence of the frictional interaction between specimen and the loading device. If the latter frictional forces were to be completely removed, concrete would suffer an immediate loss of carrying capacity on reaching its peak stress. This suggests that, at the material level, concrete is brittle and that a full description of its response is embodied in the stress-strain characteristics up to the maximum sustained stress. Such characteristics represent the complex processes of fracture initiation

and extension. The overall effect of these may be approximated in a simple manner by describing the ascending portion of the stress-strain relations as one due to progressive microcracking that can be explained with the aid of the 'internal compressive stress' concept, the latter being equivalent to the release of tensile-stress concentrations at the tips of (usually barely — if at all — visible) cracks. Clearly, this process is associated predominantly with volume decrease, and minimum volume is reached at the so-called OUF level. From this point onwards, volume dilation begins as a result of void formation and the peak stress is quickly reached. Since the OUF and the maximum-stress levels are very close to each other, the former may be considered to mark, for all practical purposes, failure of the brittle material, with the formation of (now visible) primary cracks. Just as the nonlinear constitutive relations up to the OUF level are associated with microcracking, the OUF limit itself may be used to define the strength surface associated with macrocracking. The quasi-isotropy of concrete permits the description of the stress-strain relations in terms of the two isotropic material parameters as well as a third 'constant' which accounts for coupling between deviatoric stress and ensuing hydrostatic strain. Strength envelopes indicate that failure is essentially a function of deviatoric stresses and that permissible values of these increase with the level of hydrostatic stress.

The need to use the proposed constitutive laws prior to attaining the ultimate-load level is evident in the relatively early departure from linearity exhibited by the stress-strain relations. Even more important is the need to employ the triaxial strength envelopes which allow for the very considerable (local) triaxial strength (usually well in excess of f_c) in the 'critical' regions of a structural component (even when the latter might be considered to approximate quasi-uniaxial conditions). Although such triaxial effects have long been known (for example, they were noted, among others, by Föppl⁷), their use in design has remained largely unexploited, despite the evidence that they govern the actual failure mechanism in structural concrete. In the case of nonlinear FE analysis of concrete structures, due allowance of triaxiality — through the constitutive laws and strength criteria proposed above — is an essential prerequisite if the true failure mechanism is to be identified and an accurate ultimate-load estimate obtained. With regard to the mechanism that triggers failure, one constantly finds that this is governed by the combined effects of sudden volume expansion around the OUF level and the very significant enhancement/deterioration in strength due to secondary compressive/tensile stresses. These cause the so-called critical regions, where maximum compressive-stress conditions are reached first, to gain further in strength so that the failure envelope (in compression) is never exceeded in those regions. Concurrently,

adjacent zones are subjected eventually to a combination of compression-tension, and it is in these zones where failure actually begins by 'splitting', not 'crushing'. It would appear, therefore, that it is sufficient for a failure criterion to describe only those failure conditions in which the state of stress has at least one of the principal stress components tensile, thus bypassing altogether fully compressive stress states. This, of course, is not actually done in the FE model used, as it would clearly constitute a case of prejudging — if not imposing — the failure mechanism in a structure; rather, all possible failure criteria are allowed for, although, as will be seen in subsequent chapters, results invariably confirm that concrete in 'critical' compressive zones always fails in tension, never in compression.

2. Structure modelling

2.1. The finite-element method

The FE approach to structural analysis is used so widely nowadays — both in practice and for research — that a detailed treatment of it in the present work — where the technique is employed merely as a numerical tool — would be superfluous. Instead, only the briefest of general outlines will be given here, mainly in order to fix ideas and notation, and the ensuing condensed summary will form the starting point to the subject of interest, namely the nonlinear finite-element analysis (NLFEA) of concrete structures.

As is often remarked, much of the popularity of the FE method (FEM) stems from its ready visualization and obvious physical interpretation. Thus, the modelling of a continuum by discretizing it into a finite number of components or elements has both a mathematical and a physical counterpart in the solution of actual discrete problems such as, for example, frameworks, where nodes connect standard units (i.e. simple elements, the behaviour of which may be deduced once the relevant parameters — usually displacements — at their end nodes have been determined). In the case of a continuum, however, the implicit assumption is usually made that, in order to attain the exact solution, the discretization process should be extended *ad infinitum*, although, for engineering purposes, a finite degree of subdivision will eventually be sufficiently accurate. In this respect, the FEM may well be compared with its analytical analogue, the Ritz technique, where the assumed fields must be admissible and, also, complete.

By far the most popular FE approach in structural problems is based on assumed displacement fields. Consider an individual FE, having a given number of nodal points along its boundaries. Then the (continuous) displacement field within the element, \mathbf{u} (where the components of \mathbf{u} depend on the dimensions of the problem), is deemed to be obtainable by interpolating between (i.e. by operating on) the relevant nodal parameter \mathbf{d} (such as displacements and, possibly, their derivatives at these locations). In matrix form

$$\mathbf{u} = [\mathbf{N}] \mathbf{d} \quad (2.1)$$

where $[\mathbf{N}]$ is the matrix of shape functions relating the continuous field \mathbf{u} to the discrete set \mathbf{d} . The shape functions represent the approximating interpolation to the actual function within the element (i.e. between nodes), with the known nodal values \mathbf{d} providing the basis for the interpolation even though the vector \mathbf{d} itself will usually constitute also an approximation to the true values at the nodes. The number of parameters that define a given interpolating function must match the number of nodal degrees of freedom

(DOF). As an example, consider a straight beam FE of length l which spans between nodes 1 (coordinate $x=0$) and 2 ($x=l$). Under the assumption of a predominantly flexural response, the displacement field consists of a single variable, namely the transverse displacement w . It is usual to represent the interpolating functions by polynomials. For the beam FE under consideration, the cubic polynomial

$$w = c_1 + c_2x + c_3x^2 + c_4x^3 \quad (2.2)$$

consists of four parametric constants, and hence four nodal DOF are required, i.e. two at each of the end nodes 1 and 2. It is customary to take displacements (w_1, w_2) and slopes ($dw_1/dx=\theta_1, dw_2/dx=\theta_2$) as the four nodal DOF. Then the vectors \mathbf{u} and \mathbf{d} are given by

$$\mathbf{u} = w \quad (2.3)$$

$$\mathbf{d} = \begin{bmatrix} w_1 \\ \theta_1 \\ w_2 \\ \theta_2 \end{bmatrix} \quad (2.4)$$

Clearly, the constants $c_1 - c_4$ must be adjusted so that the relevant nodal parameter(s) in \mathbf{d} are obtained on specification of the coordinates of the given node. This is achieved by the following 1×4 shape-function matrix

$$[\mathbf{N}] = [N_1 \ N_2 \ N_3 \ N_4] \quad (2.5a)$$

where

$$N_1 = 1 - \frac{3x^2}{l^2} + \frac{2x^3}{l^3}; \quad N_2 = x - \frac{2x^2}{l} + \frac{x^3}{l^2};$$

$$N_3 = \frac{3x^2}{l^2} - \frac{2x^3}{l^3}; \quad N_4 = -\frac{x^2}{l} + \frac{x^3}{l^2} \quad (2.5b)$$

It should be evident that, since (2.1) is valid for all \mathbf{d} , the N corresponding to a given node is unity at that node and zero at all the other nodes. (It should be noted that, in the case of N_2 and N_4 , these must be differentiated before the preceding check, which refers, obviously, to dimensionally compatible variables, is applied; however, in all subsequent FE formulations, relevant to the modelling of concrete structures, no such mixture of nodal-variable types will arise as these consist exclusively of displacements.)

Once the displacement field \mathbf{u} has been obtained throughout a given FE, the vector of strains, ϵ , follows upon operating on \mathbf{u} by means of a suitable linear operator $[\mathbf{L}]$, i.e.

$$\epsilon = [\mathbf{L}] \mathbf{u} \quad (2.6a)$$

and, through the use of (2.1)

$$\epsilon = [\mathbf{B}] \mathbf{d} \quad (2.6b)$$

where

$$[\mathbf{B}] = [\mathbf{L}] [\mathbf{N}] \quad (2.7)$$

i.e. $[\mathbf{B}]$ is made up of differentials of the shape functions contained in $[\mathbf{N}]$. For instance, in the previous beam example, the generalized strain is simply the curvature, i.e. $\epsilon \approx -d^2w/dx^2$. Alternatively, if 2-D problems of plane elasticity are considered, where \mathbf{u} consists of two variables, so that

$$\mathbf{u} = \begin{bmatrix} u \\ v \end{bmatrix} \quad (2.8)$$

the strain vector would be given by

$$\epsilon = \begin{bmatrix} \epsilon_x \\ \epsilon_y \\ \gamma_{xy} \end{bmatrix} = \begin{bmatrix} \partial u / \partial x \\ \partial v / \partial y \\ \partial u / \partial y + \partial v / \partial x \end{bmatrix} = \begin{bmatrix} \partial / \partial x & 0 \\ 0 & \partial / \partial y \\ \partial / \partial y & \partial / \partial x \end{bmatrix} \begin{bmatrix} u \\ v \end{bmatrix} \quad (2.9)$$

with the 3×2 matrix in (2.9) defining $[\mathbf{L}]$ for this particular problem type.

Finally, the stress state σ in the FE may be obtained upon specification of the matrix of constitutive relations, $[\mathbf{D}]$, which links stresses and strains. In general form

$$\sigma = [\mathbf{D}] (\epsilon - \epsilon_0) + \sigma_0 \quad (2.10)$$

where, for the sake of completeness, the vectors of initial strains (ϵ_0) and stresses (σ_0) have been included, although these are seldom considered. For the beam example, $[\mathbf{D}] = E I$, i.e. the flexural rigidity, while in the instance of the plane-stress case in 2-D elasticity, (2.10) reduces (ignoring ϵ_0 and σ_0) to

$$\begin{bmatrix} \sigma_x \\ \sigma_y \\ \tau_{xy} \end{bmatrix} = \frac{E}{1-\nu^2} \begin{bmatrix} 1 & \nu & 0 \\ \nu & 1 & 0 \\ 0 & 0 & (1-\nu)/2 \end{bmatrix} \begin{bmatrix} \epsilon_x \\ \epsilon_y \\ \gamma_{xy} \end{bmatrix} \quad (2.11)$$

The computation of the stresses directly from the nodal parameters \mathbf{d} may be written as

$$\sigma = [\mathbf{D}] [\mathbf{B}] \mathbf{d} \quad (2.12)$$

where, for numerical purposes, it is worth noting that $[\mathbf{D}] ([\mathbf{B}] \mathbf{d})$ requires fewer operations than $([\mathbf{D}] [\mathbf{B}]) \mathbf{d}$.

The equilibrium of an FE subject to nodal actions \mathbf{p}_n , as well as loads \mathbf{p}_e which are distributed throughout the element, may be tackled by means of virtual-work considerations or through the principle of minimum potential energy. By adopting the former

approach, the application of a set of virtual displacements $\delta \mathbf{d}$ at the nodes will produce element displacements

$$\delta \mathbf{u} = [\mathbf{N}] \delta \mathbf{d} \quad (2.13)$$

and internal strains

$$\delta \boldsymbol{\epsilon} = [\mathbf{B}] \delta \mathbf{d} \quad (2.14)$$

W_i , the internal work done by the stresses through the volume V of the element, is then

$$W_i = \int_V \delta \boldsymbol{\epsilon}^T \boldsymbol{\sigma} dV \quad (2.15)$$

while W_e , the external work done by the nodal actions and distributed forces, amounts to

$$W_e = \delta \mathbf{d}^T \mathbf{p}_n + \int_V \delta \mathbf{u}^T \mathbf{p}_e dV \quad (2.16)$$

On equating W_i and W_e , and recalling that the result must hold for all values of $\delta \mathbf{d}^T$, the following is obtained

$$\left(\int_V [\mathbf{B}]^T [\mathbf{D}] [\mathbf{B}] dV \right) \mathbf{d} = \mathbf{p}_n + \int_V [\mathbf{N}]^T \mathbf{p}_e dV \quad (2.17)$$

where relations (2.13) and (2.14) have been used. The last term in (2.17) shows that any distributed — and/or concentrated (if present) — loading that is not acting directly at the nodes must be converted to nodal actions in a 'work-equivalent' manner through the use of the shape-function matrix; such 'consistent' nodal forces may then be added to \mathbf{p}_n and the combined result, i.e. the total nodal actions, will be denoted simply by \mathbf{p} . As a final preliminary, the definition of the stiffness matrix for the element is

$$[\mathbf{k}] = \int_V [\mathbf{B}]^T [\mathbf{D}] [\mathbf{B}] dV \quad (2.18)$$

so that the equilibrium statement sought becomes

$$[\mathbf{k}] \mathbf{d} = \mathbf{p} \quad (2.19)$$

Evidently, since there is a one-to-one correspondence between the respective DOF that make up \mathbf{d} and \mathbf{p} , $[\mathbf{k}]$ is always a square matrix.

So far, it has been assumed implicitly that \mathbf{d} is known so that the computation of \mathbf{u} , $\boldsymbol{\epsilon}$, and $\boldsymbol{\sigma}$ can proceed. The determination of the kinematic nodal DOF requires the analysis of the whole structure, modelled by the full assemblage of FEs. Such an analysis is based on the so-called stiffness or displacement method, which requires the solution of the system of linear equations

$$[\mathbf{K}] \mathbf{d} = \mathbf{f} \quad (2.20)$$

where \mathbf{d} is now understood to represent all the generalized nodal displacements to be determined, while \mathbf{f} consists of the vector of generalized forces acting on these nodes, which is obtained by

summing the contributions of all elements at every node. Similarly, the structure stiffness matrix $[K]$ is assembled by adding the contributions of the various element stiffness matrices $[k]$; this process is based on the node numbering at the structural level (rather than that of the individual elements) and on the structure or global coordinate system (hence element stiffness matrices derived in a local coordinate system must be transformed to the structure axes — this is achieved by the relevant transformation matrices made up of the direction cosines defining the relative orientation between the two coordinate systems or, as in the case of the isoparametric elements to be described in section 2.3.2, through the use of the Jacobian matrix linking the derivatives of $[N]$ with respect to the two sets of coordinates). Once $[K]$ has been assembled, it constitutes a singular matrix since, at that stage, the structure being modelled is free to undergo any combination of rigid-body movements; the singularity disappears on specification of the relevant boundary conditions, and this is equivalent to the removal of the rows and columns corresponding to the unknown reactions and the associated known (usually zero) displacements respectively.

Since the superposition of the k -matrices results in the overlapping of the stiffnesses of only those elements meeting at the common node(s), the resulting $[K]$ is sparse, and, with suitable nodal numbering, also 'banded', i.e. the non-zero coefficients cluster around the diagonal. Moreover, on account of the linearity of the problems being considered, stiffness matrices are symmetric. All these properties are used to advantage in achieving an efficient method of solution to the set of equations defined in (2.20).

On the basis of the foregoing, it is evident that the approximation inherent in the discretization process described by (2.20) is subject to automatic enforcement of both equilibrium and compatibility at the nodes, and that, in addition, compatibility is also satisfied within each element. On the other hand, compatibility may or may not be satisfied at the non-nodal element junctions, depending on the type of FE adopted. Furthermore, exact equilibrium is usually not attained within elements, nor across their common boundaries. However, provided that certain basic convergence criteria are met, mesh refinement will gradually reduce these local equilibrium violations and, if incompatible elements are used, the effects of such inter-element continuity breakdowns. For a full description of such convergence requirements and, indeed, for further background to the FE method in general, the reader is referred to standard texts on the subject (for example, references 61–63).

2.2. Nonlinear analysis

The preceding section has dealt with the general problem of the FE discretization process for an arbitrary linear system. Thus, linearity was assumed to apply at the three levels of statics (equilibrium equations written in the initial, undeformed geometry,

as displacements are assumed to be small), kinematics (linearized strain–displacement compatibility equations, as strains are also taken to be small), and constitutive relations (Hooke's law or its generalized version deemed to be applicable). Such linearization assumptions lead directly to a mathematical model possessing the following desirable features: uniqueness of solution, use of superposition, and, most important perhaps, the ready availability of efficient programs for the solving of linear systems of equations based on well-established mathematical tools and algorithms. Although nature tends to be distinctly nonlinear — often highly so — it turns out that a large number of structural-engineering problems may be tackled on the basis of linearly-elastic concepts, at least for purposes of achieving an adequate level of performance under ordinary 'working' or 'serviceability' conditions. On the other hand, the understanding of ultimate-load conditions or, indeed, the more rational and/or economic design of structures necessitates the consideration of nonlinear effects: this is especially true in the case of structural-concrete problems. Unlike linear analyses, nonlinear systems cannot be solved directly but rely on various iterative or 'search' techniques; all of these, however, are based invariably on repeated solutions of linear systems until convergence is achieved. Owing to the possibility of non-uniqueness, care must be exercised — often by appeal to physical reasoning — in order to ensure that the converged solution attained is actually the correct one.

The analysis of a nonlinear structural system, which has been discretized in accordance with the stiffness formulation, still proceeds through the solution of the set of equations (2.20), but now the stiffness matrix is a function of the load/displacement level. For convenience, this will be denoted by the statement $[\mathbf{K}] = [\mathbf{K}(d)]$. In what follows, only the briefest of outlines on the main iterative procedures for nonlinear problems will be presented, with priority of choice given eventually to incremental methods. Discussion will be restricted to 'softening' structures, where this term is now used to denote systems for which the f – d path is 'convex', in the sense that the stiffness decreases with increasing f , as in the case of structural concrete where a steady degradation of stiffness occurs as the load is augmented; 'hardening' or 'concave' systems (i.e. exhibiting a steady increase of stiffness with loading) — which may require different iteration strategies — need not be considered for present purposes.

It is useful to begin with a concise description of the main numerical devices for attaining the solution at a given load level in a single series of iterations, without regard to the previous f – d path, i.e. non-incrementally; subsequently, it will become evident that the incremental techniques are based essentially on identical principles. Perhaps the most basic solution type is that of 'direct iteration' (also known as 'functional iteration' or 'successive

substitution/approximation'). In this method, successive solutions are performed, each iteration making use of the previous solution for the unknown(s) d to predict the improved, current value of $[K(d)]$

$$d_{n+1} = [K(d_n)]^{-1}f; \quad n = 0, 1, 2, 3, \dots \quad (2.21)$$

The initial guess is usually taken to be $d_0 = 0$, and the process is deemed to have converged when $d_{n+1} - d_n = 0$. It will be found convenient to illustrate this method (and, also, subsequent ones) graphically by reference to the one-dimensional case (i.e. f, d constitute a single-DOF system), although, clearly, the same type of iterative behaviour extends to multi-DOF systems. Figure 2.1 shows the implementation of direct iteration in the search for the solution corresponding to the load level f in the given nonlinear response $f-d$, with the initial guess taken as $d_0 = 0$. It can be seen that the unknowns are the displacements, the secant slope being used in each iteration. This 'secant modulus' or 'variable stiffness' approach tends to be expensive since $[K]$ must be revised and a new set of linear equations solved for each iteration. Furthermore, symmetry in the matrix of coefficients need not necessarily result when direct iteration is employed,⁶¹ and this means that the more efficient algorithms, based on the fact that $[K]$ for linear problems is symmetrical, may not always be applicable. Another drawback of the scheme is that its convergence is not guaranteed and cannot be predicted *a priori*. In addition, as the number of DOF increases, coupling of stiffness terms might lead to instability of the iterative technique.⁶⁴

A more sophisticated process of iteration is the well-known Newton-Raphson (NR) method. This can be outlined as follows. Unless convergence has occurred, $[K]d = f$ will not be satisfied

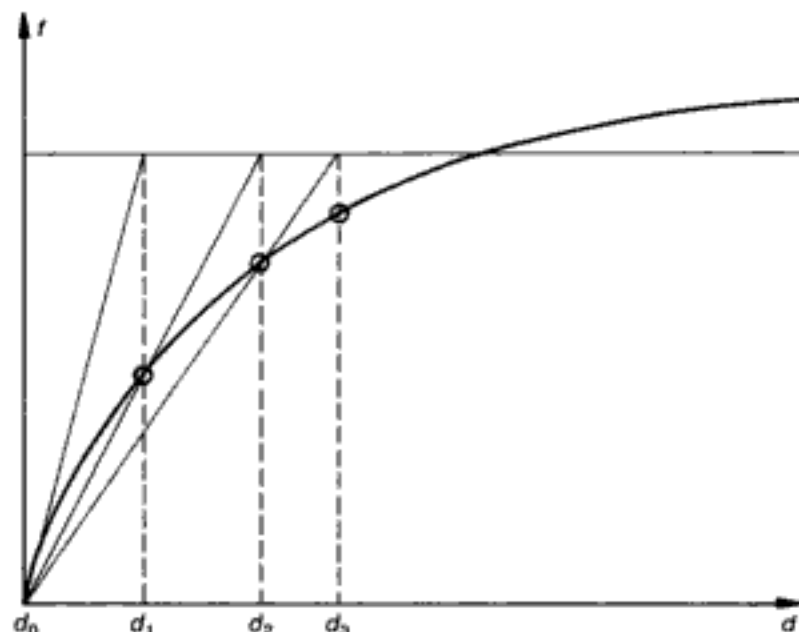


Fig. 2.1. Direct-iteration method

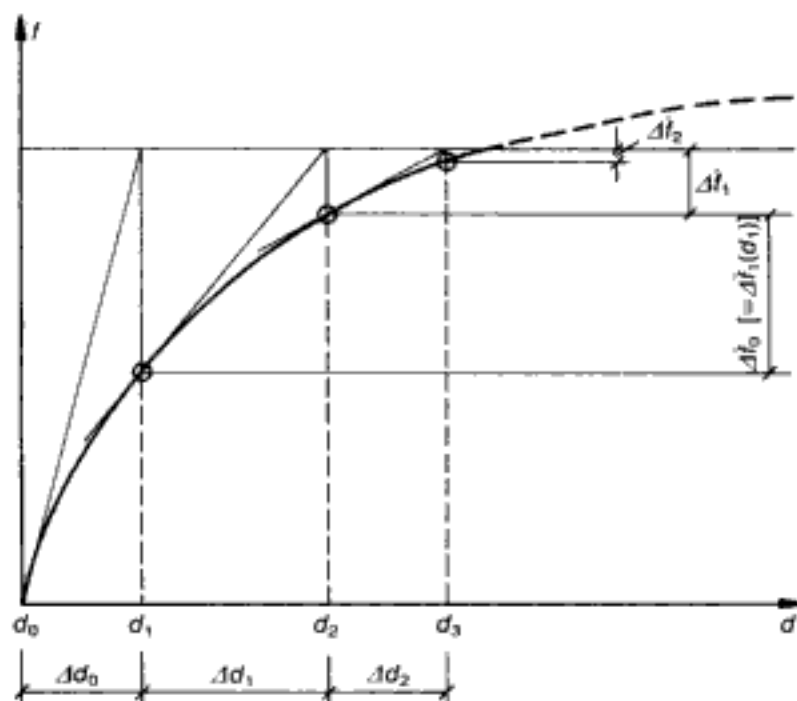


Fig. 2.2. Newton-Raphson method

at any stage of the iteration, and hence a system of residual forces $\Delta \bar{f}$ can be assumed to exist, so that

$$\Delta \bar{f} = f - [\mathbf{K}]d \quad (2.22)$$

i.e. $\Delta \bar{f}$ may be viewed as a measure of the system's current departure from the required state of equilibrium. Now, a better approximation exists at

$$d_{n+1} = d_n + \Delta d_n; \quad n = 0, 1, 2, 3, \dots \quad (2.23)$$

where the NR approximation for the increment or correction Δd_n may be written as

$$\Delta d_n = [\mathbf{K}_t(d_n)]^{-1} \Delta \bar{f}(d_n); \quad n = 0, 1, 2, 3, \dots \quad (2.24)$$

and where the subscript in $[\mathbf{K}]$ indicates that the latter is the tangential stiffness matrix. With increasing number of iterations n , convergence is achieved as $\Delta \bar{f}$ and/or $\Delta d \rightarrow \mathbf{0}$. The process is shown schematically in Fig. 2.2 for a single-DOF system, with initial guess d_0 ($= 0$ here) leading to Δf_0 which, in turn, yields the correction Δd_0 so that $d_1 = d_0 + \Delta d_0$ becomes an improved approximation, and so on. In this figure, the slopes of the $f-d$ characteristic at the locations corresponding to the various d_n are the 1-D counterparts of the tangential stiffness matrix $[\mathbf{K}_t]$ used in multiple-DOF problems, as can readily be seen by invoking the well-known argument whereby Taylor's series are curtailed beyond the first derivative.^{62,62} (For a version of the NR technique in which the matrix of coefficients linking $\Delta \bar{f}$ and Δd is not symmetric, see reference 64; $[\mathbf{K}_t]$, on the other hand, is always symmetric, and hence conforms to those equation-solving

algorithms that make use of this property.) In general, the NR or 'tangential stiffness' method converges more rapidly and exhibits superior stability than the direct-iteration scheme. Again, however, there is no guarantee of convergence, especially if the initial guess is not close to the actual solution and/or combinations of 'convex' and 'concave' characteristics are encountered throughout the region of iteration. As for the direct-iteration process, the NR technique is demanding computationally, since each iteration requires the assembly of the updated matrix $[K_t]$ and the concomitant linear-equation solving.

Instead of tackling a new system of equations for each iteration, the following approximation could be made

$$[K_t(d_n)] \sim [K_t(d_0)] \quad (2.25)$$

so that

$$\Delta d_n = [K_t(d_0)]^{-1} \Delta \bar{f}(d_n); \quad n = 0, 1, 2, 3, \dots \quad (2.26)$$

throughout the entire search process. This algorithm is known as the 'initial/constant stiffness' method, and also as the 'modified Newton-Raphson' approach; its schematic illustration is depicted in Fig. 2.3 for the 1-D case (with $d_0 \neq 0$). The tangential stiffness matrix corresponding to the initial guess is assembled only once and, on reduction or factorization of the set of equations and the storing of the result, solutions required in subsequent iterative cycles can be obtained at a much reduced computational effort. This significant saving in computing cost per iteration, however, is countered by a lower rate of convergence when compared with the formal NR algorithm. Once again, although convergence is

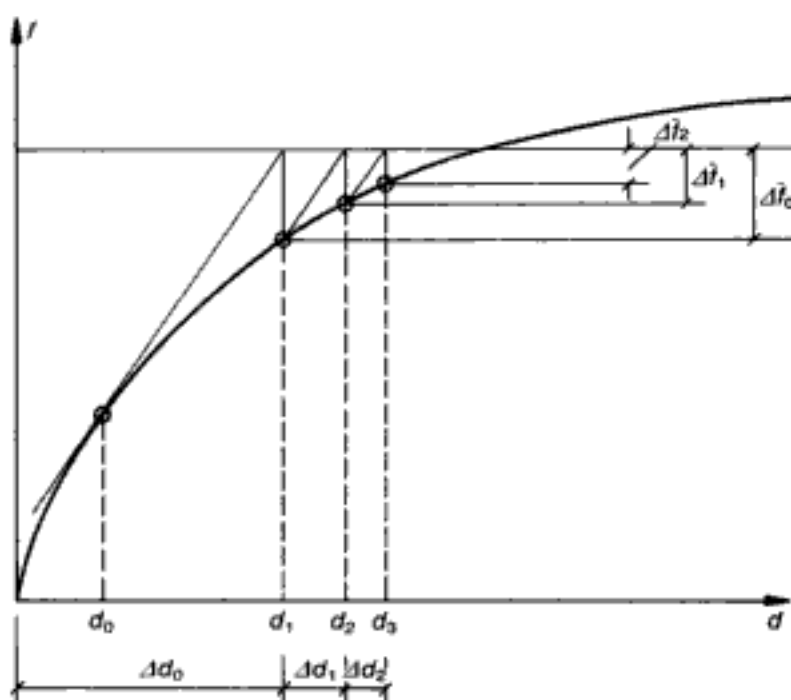


Fig. 2.3. Modified Newton-Raphson method

usually achieved, this cannot be guaranteed for all cases, and sometimes divergence may be encountered in situations where the more rapidly converging NR technique is successful. The relative economics and convergence rates of the initial and tangential stiffness methods depend on the degree and type of nonlinearity of the system considered. The optimum algorithm is usually obtained by combining both methods so that $[\mathbf{K}]$ is updated to $[\mathbf{K}_t]$ only occasionally during iterations.

As stressed repeatedly in the preceding paragraphs, none of the previous methods, in which the unknowns were the total displacements \mathbf{d} , converges in all cases. Only *incremental* procedures, where the unknowns are the changes $\Delta\mathbf{d}$ due to increments in loading $\Delta\mathbf{f}$, can provide some assurance on convergence. Furthermore, such methods enable a full study of the load–deformation behaviour of a structure to be made; besides its obvious usefulness, the complete knowledge of the f – d characteristic followed at the structural level becomes mandatory when the solution is dependent, not only on the current displacements, but also on the previous loading history. Evidently, with sufficiently small increments, convergence may be ensured and the local linearization at each iterative step becomes fully justified. Then the NR method suggests itself as a natural iterative technique (its incremental version being termed the ‘generalized Newton–Raphson’ method), with the initial value now always taken as $\mathbf{d}_0 = \mathbf{0}$. A possible general algorithm might be

$$[\mathbf{K}_t(\mathbf{d}_n)] \Delta\mathbf{d}_n = \Delta\mathbf{f}_n + \Delta\bar{\mathbf{f}}_{n-1}; \quad n = 0, 1, 2, 3, \dots \quad (2.27)$$

where $\Delta\mathbf{f}_n$ represents the increment in the actual load, while $\Delta\bar{\mathbf{f}}_n$ stands for the residual out-of-balance forces from the previous load step. This is often referred to as the ‘incremental with one-step NR correction’, and is illustrated for the 1-D case in Fig. 2.4 by means of the dashed lines and crosses. It is evident that, despite the fact that the single residual-force corrections result in effective load increments (Δf_0 ; $\Delta f_1 + \Delta\bar{f}_0$; $\Delta f_2 + \Delta\bar{f}_1$; etc), a small (usually cumulative) drift from the true solution path occurs. On the other hand, when $\Delta\bar{\mathbf{f}} = \mathbf{0}$ in (2.27), the algorithm becomes in essence the matrix counterpart of Euler’s numerical method for the solution of a differential equation; as can be seen by the path indicated by the dotted lines and squares in Fig. 2.4, the cumulative drift now becomes larger in this purely incremental algorithm without corrections. At the other extreme, by setting $\Delta\mathbf{f} = \mathbf{0}$ in (2.27), the formal NR method (in its incremental form) is recovered, namely sufficient iterations are performed for each load increment in order to converge to the actual solution before the next external-load increment is applied. Obviously, any degree of transition between the extremes $\Delta\bar{\mathbf{f}} = \mathbf{0}$ and $\Delta\mathbf{f} = \mathbf{0}$ could be specified: for example, many small external-load increments with few iterations in each, or fewer but larger external-load steps

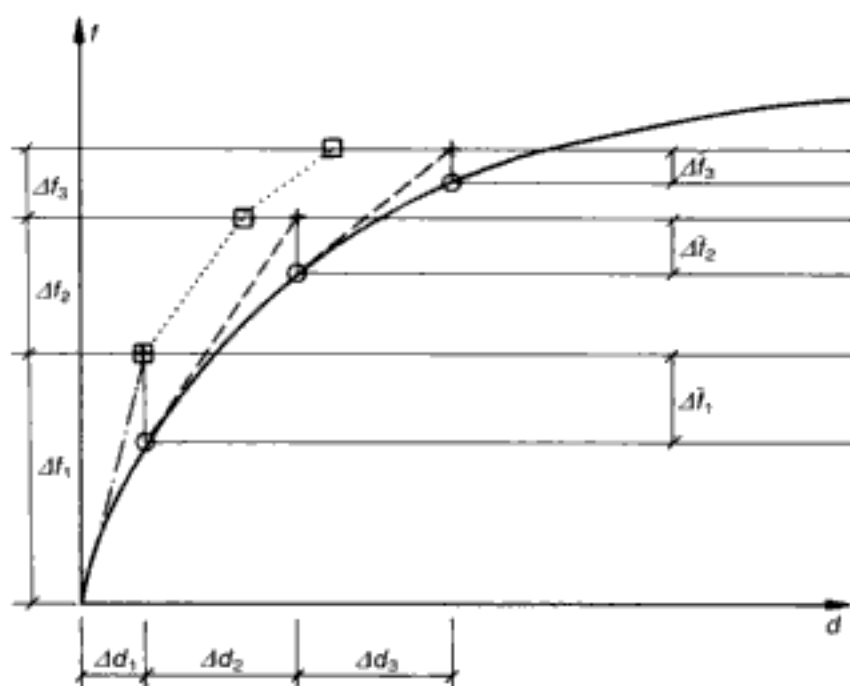


Fig. 2.4. Incremental with one-step Newton-Raphson correction

coupled with a substantial number of corrective iterations for each of them. For overall economy, any such gradations may be combined with the constant-stiffness iteration algorithm.

Reliable algorithms for the nonlinear analysis of concrete structures by means of the FEM should employ incremental techniques. On the basis of the preceding outline, a summary of the three most widely used versions associated with the incremental NR method (INRM) is contained in Fig. 2.5. (It should be noted that all plots refer to a given load step or increment.) Whether on their own, in combination, or slightly amended, they will be found to constitute the backbone of the iterative-search process in the present work.

2.3. A finite-element program for linear analysis

As pointed out in section 2.2, a nonlinear analysis is carried out through a sequence of linear analyses. The latter require the availability of a standard FE package, and one such system, FINEL, was adopted for the present work. In outlining this program, a broad description of its main features will be given, followed by a somewhat more detailed background on the actual FEs selected.

2.3.1. Brief description of FINEL

FINEL is a computer program for the engineering analysis of field problems. Based on the FEM, it was conceived originally by Hitchings^{65,66} and further developed subsequently so as to cater for the needs of analysts and designers working either in an industrial environment (thus requiring a tool that is both reliable and simple to use) or in a research capacity (hence needing a flexible and versatile program base on which new ideas may be implemented). The 'standard' version of FINEL enables users to undertake various types of FE modelling, the main being linear elastic stress analysis (both static and dynamic), transient and

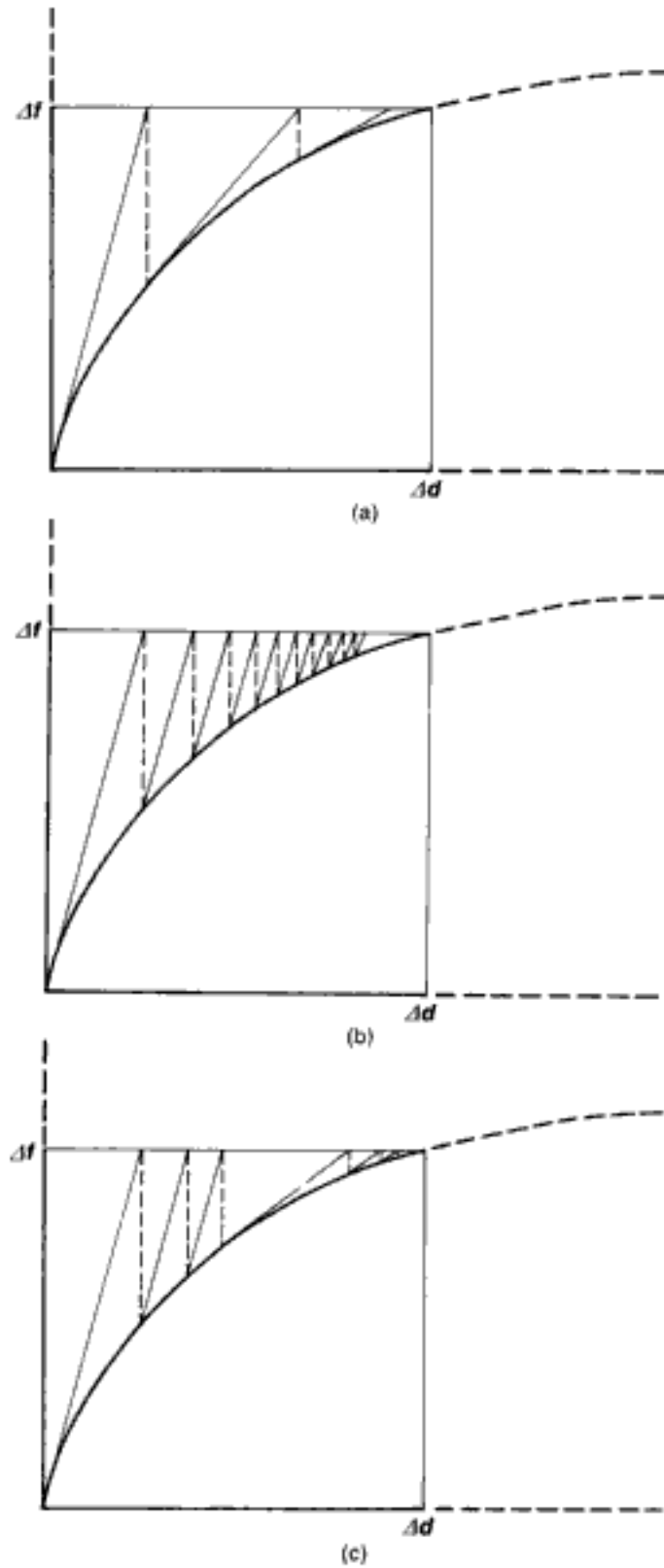


Fig. 2.5. Incremental Newton-Raphson methods (INRMs): (a) pure INRM; (b) modified INRM; (c) mixed INRM

steady-state heat-conduction problems, and certain nonlinear structural calculations including plasticity and large-deformation effects. Each of these options is coupled with an extensive library of different FE types and the more common loadings, as well as mesh-generation and plotting facilities.

The key feature of FINEL is its highly modular structure. This is in keeping with the very nature of the FEM itself, where a sequence of discrete, practically independent and unrelated, steps or routines is followed. More importantly, for present purposes, the modular form of the program enables the development of existing modules and/or the addition of new ones, thus modifying FINEL so as to suit the requirements of any particular problem. After the input data have been read, the sequential execution of the different modules, each representing a discrete aspect of the FEM, is controlled by a central executive section; there is no direct communication between modules, as shown in Fig. 2.6(a). Of present relevance is the standard elastic stress analysis of structures subjected to static loading, and performed on the basis of assumed displacement-field FEs. Its modules may be summarized as follows:

1. GRID: Element and mesh generation; specification of the material properties.
2. RENU: Renumbering of the nodes of the structure to optimize the semi-band width of the set of equations.
3. EDIT: Editions of data depending on nodal numbering.
4. ASMB: Numerical integration of the element stiffness matrices $[k]$ and assembly of the structure stiffness matrix $[K]$.
5. BNCN: Specification of the boundary conditions, i.e. the restrained degree-of-freedom vector.
6. CHOL: Factorization of the structure stiffness matrix (Choleski's method).
7. LOAD: Specification of the external-load vector.
8. SLVE: Calculation of nodal displacements (Choleski's method).
9. STRS: Calculation of strains and stresses.

At the next lower hierarchical level within the program, the modular form of the system consists of a series of FINEL libraries. Of particular interest for current purposes are the element library, containing all the various FE types available in FINEL, and the load library. The latter comprises some of the more commonly encountered loadings applied to a portion of a continuum element. They include, for example, uniform and trapezoidal pressure distributions so as to enable the calculation of equivalent nodal loads to be carried out in accordance with the second term on the right-hand side of (2.17). Each library has a library executive programme associated with it, which can be called by any of the modules; this executive then calls the required entry from the relevant library, as shown schematically in Fig. 2.6(b).

Control information and a small number of data items are transferred between the FINEL executive and any given module by way of different common areas defined within the system in such a way that they contain logically related groups of information

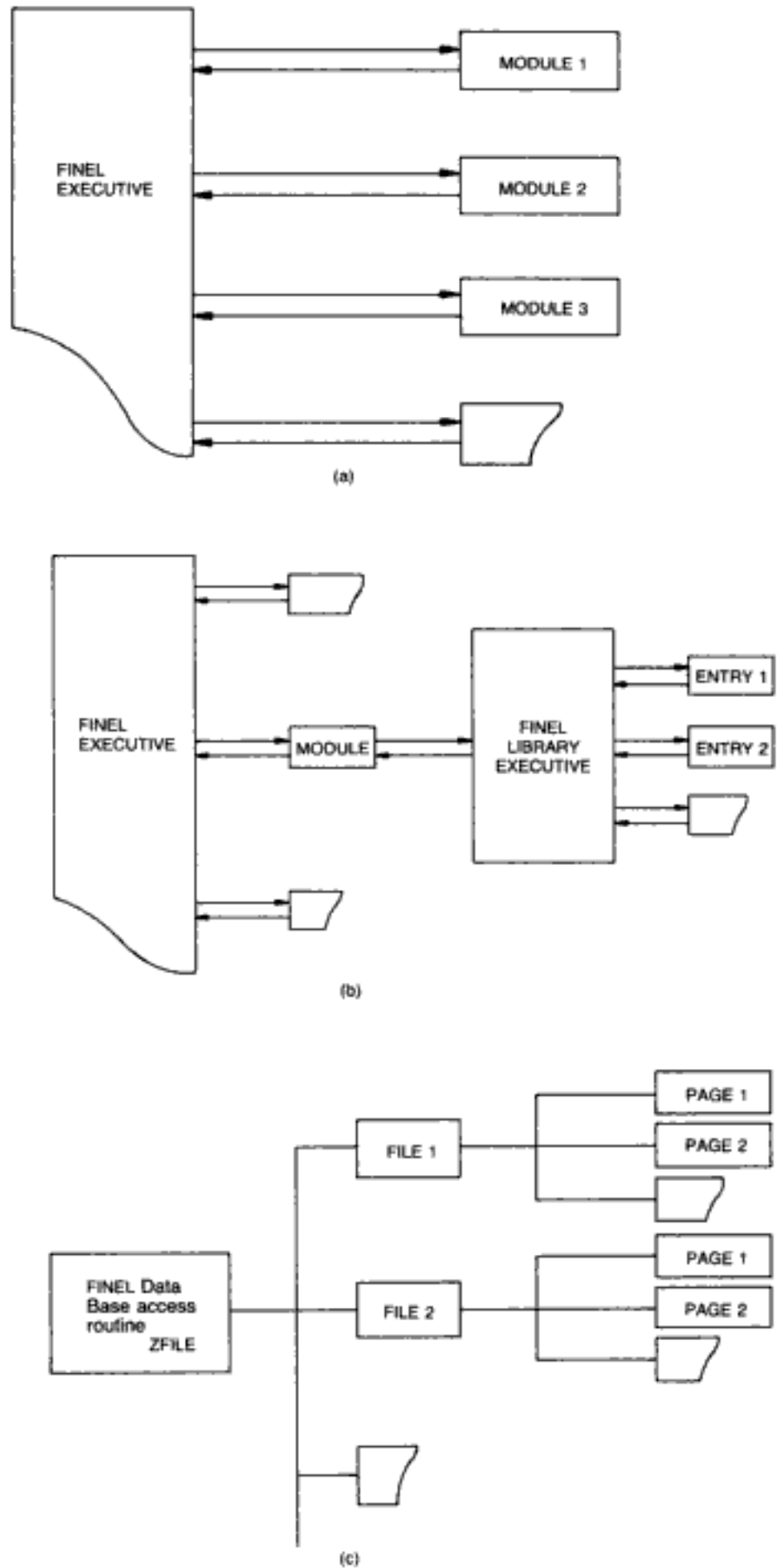


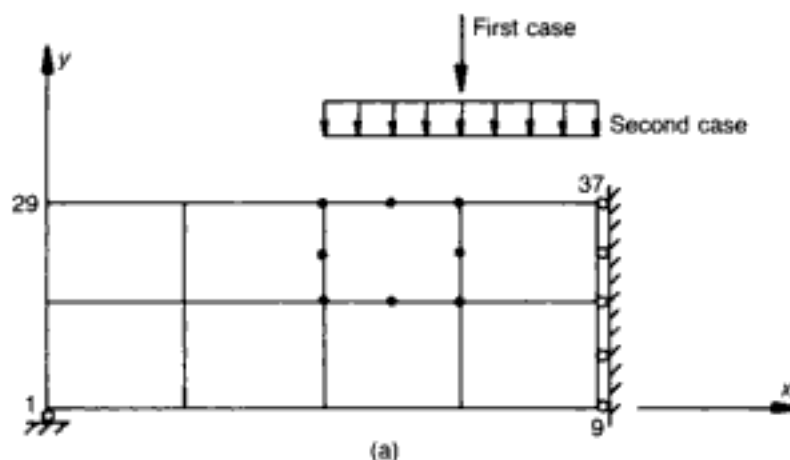
Fig. 2.6. Basic structure of FINEL.⁶⁶
 (a) modular form; (b) internal organization;
 (c) ZFILE

(e.g. control variables relating to input/output). However, any large arrays generated by a module (e.g. the coefficients of the stiffness matrix) are not returned to the FINEL executive; instead, for these to be communicated to other modules, they have to be stored in the ZFILE, which is the main database in the FINEL system. This very large-capacity storage device is an unformatted direct-access file which enables data generated at any stage/module of the analysis to be stored or retrieved as required in subsequent stages/modules. It is through this database that continuity is achieved throughout the execution process. The ZFILE is particularly useful in nonlinear analysis where large sets of data are created repeatedly; moreover, the fact that the database remains available even after execution has been completed permits the post-processing and plotting of the data generated during each run. The FINEL database is arranged as a two-level system containing 30 files, each file consisting of 500 pages, where a page may be of any length (see Fig. 2.6(c)); some files are earmarked for storing particular sets of data while others are free for arbitrary usage. A typical call to ZFILE would be

CALL ZFILE (VAR, NVAR, IFILE, IPAGE, MODE)

where VAR is the array to be read/written, NVAR is the length of the array, IFILE and IPAGE are the dummy file and page on the ZFILE, and MODE specifies input/output in single/double precision.

Figure 2.7 shows a simple example and the input file, in FINEL's fixed format, required to run it. The beam with hinge and roller supports is to be analysed for two loading conditions. The (linear) stress-analysis option is specified, with its various modules (listed earlier) implicit. The whole beam is described initially as a single region defined by its four corners, and then the element type (PM08) is chosen, this being a quadrilateral eight-noded unit, with its thickness set to 50. Specification of the material properties (E , ν) follows, as well as instructions for the subdivision of the initial region into a 4×2 mesh. After the structure coordinates have been generated (nodes 1–37), the boundary conditions are imposed by fixing the relevant degrees of freedom, and the loading on the member is applied (downward point load at node 35). Finally, nodal displacements are automatically solved for, and the analysis is completed upon calculation of the stresses and strains. This example illustrates the simplicity of the standard FINEL in routine stress analysis. It also illustrates its versatility. Therefore, while the initial list of modules is fixed by the specified type of analysis, it is possible to loop around this list by means of executive commands in the input file. For instance, the card RE-E LOAD in Fig. 2.7(b) causes the execution to return to the loading module, so as to calculate a second loading case (uniform load — EPRS — applied on the top edges of elements 7 and 8). It is evident that such simple



```

ANALYSIS STRESS
*
*   simply supported beam under two loading cases
*
*
*   mesh generation
*
REGIONAL COORDINATES 0.  0.  500.  0.
                    0.  90.  500.  90.
ELEMENT PM08      50.
MATERIAL STIFFNESS 40000.  0.2
REGION SQUAD      1  2  3  4      4  2
*
*   boundary conditions and first loading case
*
COORDINATES GENERATED
FIXE DISPLACEMENT 1  2      9  1      14  1
                  23  1      28  1      37  1
LOAD POINT      -5000.  35  2
*
*   second loading case
*
END STRS
RE-E LOAD
LOAD EPRS      20.  0.  7  8  1  4
END JOB

```

Fig. 2.7. Example of application of FINEL to static (linear) stress analysis:
(a) FE discretization;
(b) FINEL's input file

re-entry facility is extremely useful for purposes of extending the program so as to cater for applied-load increments and residual-force iterations in nonlinear analysis.

2.3.2. Finite elements selected

Throughout this book, two broad types of analysis will be implemented, namely two-dimensional and three-dimensional. For this reason, the same general subdivision is extended to the FE types chosen as the basis for such analyses. However, since all the elements used are of the curved, isoparametric type with three nodes along the various edges — arguably, the most widely-employed FEs in current practice — much of the essential discussion pertaining to their salient features is common to all of them, as will become evident in the brief outline that follows. (For a more detailed general background, see, for example, reference 61; with regard to the advantages of the isoparametric formulation

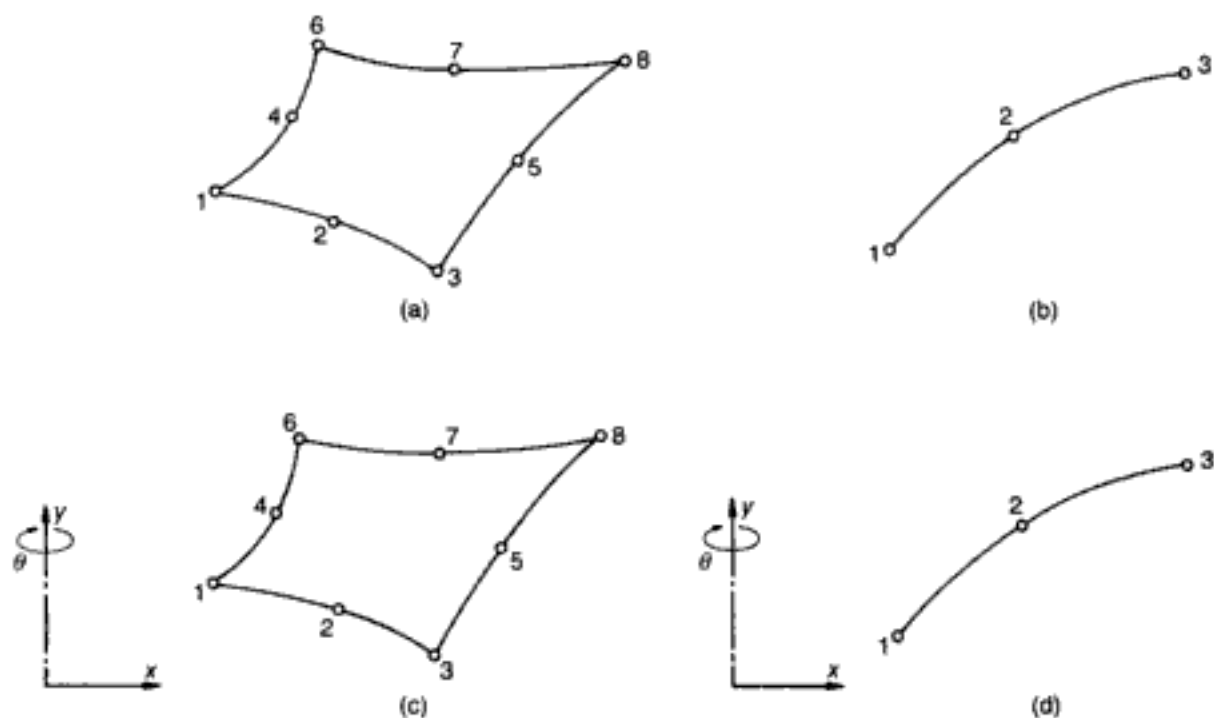


Fig. 2.8. Isoparametric finite elements used in two-dimensional analysis:⁶⁶ (a) PM08; (b) KM03; (c) PX08; (d) KX03

in respect to nonlinear concrete modelling in particular, a good summary may be found in reference 67.)

The isoparametric FEs used in 2-D and 3-D analyses appear in Figs 2.8 and 2.9 respectively, FINEL's convention being adopted to identify each of them. Figures 2.8(a) and 2.8(b) refer to plane-stress analysis, which is built around the eight-node serendipity membrane plate element (PM08) for concrete and the three-node Lagrangian bar element (KM03) for steel reinforcement, all nodes exhibiting two DOF (displacements) for movement in the x - y plane containing the elements. The out-of-plane dimensions of both elements are defined upon specification of the appropriate thickness (PM08) or cross-sectional area (KM03). While PM08 yields the three stress components σ_x , σ_y , τ_{xy} (similarly for the related strains, in addition to ϵ_z), KM03 possesses axial — but no transverse — stiffness so it can only accommodate a direct-stress/strain component along its length. Axisymmetric problems are tackled by means of elements PX08 (concrete) and KX03 (steel) which, when viewed in the x - y plane (Figs 2.8(c) and 2.8(d) respectively), are essentially the same as their plane-stress counterparts. These axisymmetric elements represent serendipity thick-shell (PX08) and Lagrangian membrane (KX03) formulations, and are considered to consist of one-radian slices. The relevant stresses ensuing from the analysis are σ_x , σ_y , τ_{xy} , σ_z (hoop direction) for PX08 (and, clearly, the four related strains), axial and hoop stresses/strains for KX03.

Solid brick elements are the basis for the modelling of concrete, with three DOF (displacements) at each node, the full stress and strain tensors being given in the output. The main brick element

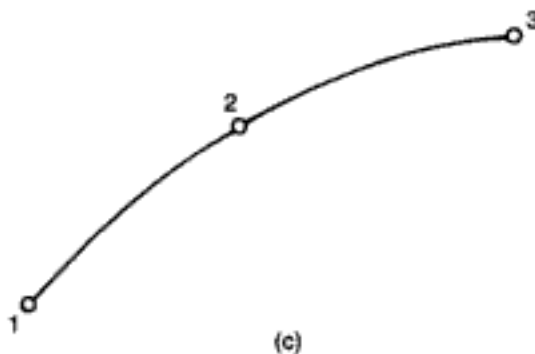
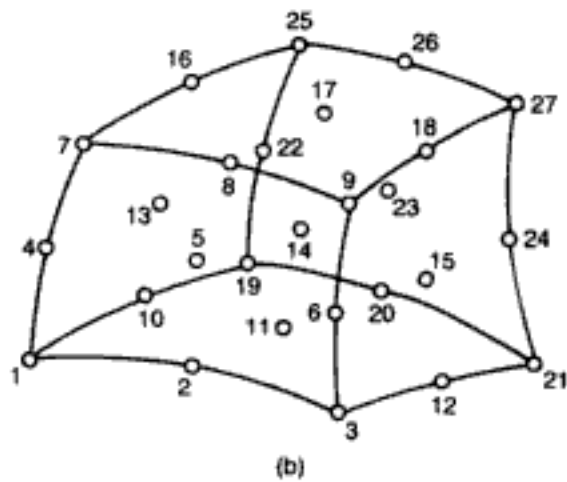
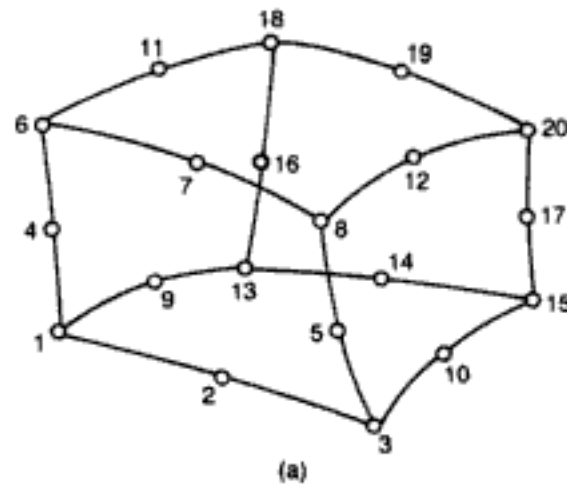


Fig. 2.9. Isoparametric finite elements used in three-dimensional analysis.⁶⁶ (a) HX20; (b) HX27; (c) LM03

is the 20-node serendipity unit HX20 shown in Fig. 2.9(a). In addition, the 27-node Lagrangian element HX27 has been used sometimes, despite the additional 21 DOF required by the insertion of one central and six mid-face nodes (Fig. 2.9(b)). Steel reinforcement is assumed to consist of line elements, which are modelled by means of the three-node FE bar of Fig. 2.9(c) (LM03), with specified cross-sectional area. Such an element now has a total of nine displacement DOF, although its stiffness is still limited to axial properties only, so that the bar admits solely direct stresses/strains along its length on account of its total lack of bending rigidity.

A natural choice for the shape, or interpolating, functions in the case of elements with three-noded edges — a feature common to all of the above FEs — is of the polynomial type that yields a quadratic variation of displacement(s) along these edges. Such shapes usually take the form of the well-established serendipity or Lagrangian formulations on the basis of which the elements in Figs 2.8 and 2.9 are derived. The adoption of second-order polynomials ensures displacement continuity between adjacent elements since a parabola is uniquely defined by three points, in this case the three (common) nodes along the inter-element boundary. A direct consequence of this is that the strains, which, for all the elements under consideration are functions of the first derivatives of displacements (as, for example, in the 2-D case given by (2.9)), always remain finite at the interface between elements, thus satisfying the usual convergence criteria. In addition to this consideration of C_0 -continuity, the quadratic family of elements provides a good balance between accuracy (with an obvious improvement over linear-element formulations) and complexity (as the number of DOF per element is well below those of higher-order models, especially in 3-D problems). Furthermore, the quadratic interpolation functions provide the basis for the curved shapes of the elements in Figs 2.8 and 2.9, that enables the ready modelling of arbitrary geometric contours through the isoparametric formulation, some of the relevant features of which will be summarized subsequently. Before these are discussed, however, it is useful to illustrate the type of shape functions used for some of the elements adopted. In so doing, it may be helpful to imagine that the various 1-D, 2-D and 3-D units have been temporarily 'straightened' (thus consisting of lines, rectangles and cubes respectively) although, as implied above, the same shape functions will also be applied later to their curved counterparts.

The interpolation functions $[N]$ of the various elements are given in terms of local, element coordinates, and it is usual practice to make the latter dimensionless. These natural or intrinsic coordinates have origins at the centre of the element, attaining values of ± 1 at its ends (end nodes in 1-D, mid-edge nodes in 2-D, mid-facets in 3-D). Such local coordinates are to be denoted by ξ , η , ζ (or ξ_i) in contrast to the global or structure coordinates x , y , z (or x_i). The various N s may be checked — and, in fact, are often actually constructed — by recalling that a given N_i that refers to node i is equal to unity at that node and zero at all other nodes. The following three examples (in increasing dimensional order) will help to illustrate the general approach usually adopted.

Consider first the bar (now line) element with its origin at the central node bisecting the element. The intrinsic coordinate ξ runs along its axis and the Lagrangian interpolation functions may be written in terms of it as follows

corner nodes ($\xi_1 = \pm 1$):

$$N_1 = \frac{1}{2}\xi (\xi_1 + \xi) \quad (2.28a)$$

mid-side node ($\xi_1 = 0$):

$$N_1 = 1 - \xi^2 \quad (2.28b)$$

where, as stated already, the subscript 1 defines the node in question. Turning now to a 2-D example, the eight-node serendipity element is described in terms of the intrinsic coordinates located at the centre of the (now rectangular) unit. Its interpolation functions are

corner nodes ($\xi_1 = \pm 1, \eta_1 = \pm 1$):

$$N_1 = \frac{1}{4}(1 + \xi\xi_1)(1 + \eta\eta_1)(\xi\xi_1 + \eta\eta_1 - 1) \quad (2.29a)$$

mid-side nodes ($\xi_1 = 0, \eta_1 = \pm 1; \xi_1 = \pm 1, \eta_1 = 0$):

$$N_1 = \frac{1}{2}(1 - \xi^2)(1 + \eta\eta_1), \quad \text{for } \xi_1 = 0 \quad (2.29b)$$

$$N_1 = \frac{1}{2}(1 - \eta^2)(1 + \xi\xi_1), \quad \text{for } \eta_1 = 0 \quad (2.29c)$$

Finally, the shape functions for the 20-node serendipity element (now a cube) will be used as a basis of a 3-D example, with the intrinsic coordinate system ξ, η, ζ emanating from the centre of the unit

corner nodes ($\xi_1 = \pm 1, \eta_1 = \pm 1, \zeta_1 = \pm 1$):

$$N_1 = \frac{1}{8}(1 + \xi\xi_1)(1 + \eta\eta_1)(1 + \zeta\zeta_1) \quad (2.30a)$$

$$(\xi\xi_1 + \eta\eta_1 + \zeta\zeta_1 - 2)$$

mid-side nodes ($\xi_1 = 0, \eta_1 = \pm 1, \zeta_1 = \pm 1; \xi_1 = \pm 1, \eta_1 = 0, \zeta_1 = \pm 1; \xi_1 = \pm 1, \eta_1 = \pm 1, \zeta_1 = 0$):

$$N_1 = \frac{1}{4}(1 - \xi^2)(1 + \eta\eta_1)(1 + \zeta\zeta_1), \quad \text{for } \xi_1 = 0 \quad (2.30b)$$

$$N_1 = \frac{1}{4}(1 - \eta^2)(1 + \xi\xi_1)(1 + \zeta\zeta_1), \quad \text{for } \eta_1 = 0 \quad (2.30c)$$

$$N_1 = \frac{1}{4}(1 - \zeta^2)(1 + \xi\xi_1)(1 + \eta\eta_1), \quad \text{for } \zeta_1 = 0 \quad (2.30d)$$

Some of the typical quadratic shape functions for the relevant elements with three-noded edges have now been presented, and the way in which those straight-edged units can be distorted so as to produce the types of FEs sketched in Figs 2.8 and 2.9 may next be considered. Such a distortion of straight-edged elements

through mapping to produce FEs with curved boundaries that will fit more easily complex problem geometries, and thus allow coarser meshes for the same degree of accuracy, may be formulated in several ways. In general, the local (straight) coordinates become a set of curvilinear coordinates when mapped onto a global (Cartesian) set of coordinates, the type and degree of distortion depending on the shape functions chosen to establish such a coordinate transformation. Of particular interest is the case when the shape functions $[N]$ adopted as the interpolation functions for the relevant parameter in the FE analysis are also used as the shape functions for the mapping transformation of coordinate geometries. Such an isoparametric formulation is especially advantageous for the elements with three-noded sides based on quadratic interpolation functions, since the resulting parabolic distortions of the edges (as in Figs 2.8 and 2.9) are usually sufficient for practical purposes. In addition, displacement continuity at inter-element boundaries of the parent units also ensures the continuity of the distorted elements, while the choice of the mid-side locations for the non-corner edge nodes for the FEs of Figs 2.8 and 2.9 automatically guarantees uniqueness, i.e. one-to-one mapping.

At this stage, it must be borne in mind that, in the course of FE computations, element stiffness matrices and related load vectors (as defined by the first and last terms of expression (2.17)) must be evaluated in the form of integrals involving quantities that are to be operated upon with respect to global axes x_i : for example, $[B]$ involves first derivatives of $[N]$ with respect to $x/y/z$ (in the present work $[L]$ — see (2.7) — always consists of first derivatives of the type illustrated earlier for the 2-D case — see (2.9) — and readily extendible not only to the 3-D unit but also to the 1-D element, as the latter possesses no bending stiffness); similarly, the infinitesimal volume dV throughout which the integration is performed is given by $dx dy dz$. On the other hand, the N_i s are defined in terms of local (now curvilinear) coordinates ξ_i , and hence a transformation is required between global and local derivatives; and, similarly, the integral itself must be computed through the use of local coordinates, so that a further transformation is needed to obtain the correct scale factor, with the concomitant change of integration limits.

The transformation involving first derivatives of N_i can be derived by invoking the chain rule for partial differentiation. This will be illustrated by reference to the general 3-D case which, clearly, also encompasses its simpler 2-D and 1-D counterparts. In matrix form, the required expression is

$$\begin{bmatrix} \partial N_i / \partial \xi \\ \partial N_i / \partial \eta \\ \partial N_i / \partial \zeta \end{bmatrix} = \begin{bmatrix} \partial x / \partial \xi & \partial y / \partial \xi & \partial z / \partial \xi \\ \partial x / \partial \eta & \partial y / \partial \eta & \partial z / \partial \eta \\ \partial x / \partial \zeta & \partial y / \partial \zeta & \partial z / \partial \zeta \end{bmatrix} \begin{bmatrix} \partial N_i / \partial x \\ \partial N_i / \partial y \\ \partial N_i / \partial z \end{bmatrix} \quad (2.31)$$

To determine the constituent elements of the square Jacobian matrix linking the vectors $\partial N_i/\partial \xi_i$ and $\partial N_i/\partial x_i$, use is made of the shape functions relating the two sets of coordinates x_i and ξ_i . Since the isoparametric formulation has been adopted, in which both displacements and coordinates are interpolated on the basis of their respective nodal parameters by the same shape functions N_i (i.e. $u = [N] d$, $x (\equiv x_i) = [N] c$ where c is the vector of (global) nodal coordinates), it follows that $x_i = N_i x_{iI}$, where the summation convention (i.e. sum over all the element's nodes) applies, x_{iI} being the i^{th} global coordinate (x , y or z) at node I . The Jacobian matrix may then be computed directly through

$$\begin{aligned}
 [\mathbf{J}] &= \begin{bmatrix} \partial N_1/\partial \xi & \partial N_2/\partial \xi & \partial N_3/\partial \xi & - & - \\ \partial N_1/\partial \eta & \partial N_2/\partial \eta & \partial N_3/\partial \eta & - & - \\ \partial N_1/\partial \zeta & \partial N_2/\partial \zeta & \partial N_3/\partial \zeta & - & - \end{bmatrix} \begin{bmatrix} x_1 & y_1 & z_1 \\ x_2 & y_2 & z_2 \\ x_3 & y_3 & z_3 \\ - & - & - \\ - & - & - \end{bmatrix} = \\
 & \begin{bmatrix} \Sigma(\partial N_i/\partial \xi)x_i & \Sigma(\partial N_i/\partial \xi)y_i & \Sigma(\partial N_i/\partial \xi)z_i \\ \Sigma(\partial N_i/\partial \eta)x_i & \Sigma(\partial N_i/\partial \eta)y_i & \Sigma(\partial N_i/\partial \eta)z_i \\ \Sigma(\partial N_i/\partial \zeta)x_i & \Sigma(\partial N_i/\partial \zeta)y_i & \Sigma(\partial N_i/\partial \zeta)z_i \end{bmatrix} \quad (2.32)
 \end{aligned}$$

where, in the last expression, the Σ may be left out provided that the repeated index is still understood to imply summation. The vector $\partial N_i/\partial \xi_i$ on the left-hand side in (2.31) being also readily obtainable, the required vector $\partial N_i/\partial x_i$ of derivatives with respect to global coordinates is finally obtained by inverting $[\mathbf{J}]$ and multiplying the result by the array $\partial N_i/\partial \xi_i$.

The second coordinate transformation, pertaining to the region of integration, involves a scaling factor between the two coordinate systems which may readily be shown to be simply the determinant of $[\mathbf{J}]$ — usually referred to plainly as the 'Jacobian' (see, for example, references 61 and 68). Thus, for the general 3-D case

$$dV = dx \, dy \, dz = (\det[\mathbf{J}]) \, d\xi \, d\eta \, d\zeta \quad (2.33)$$

and, considering, for example, the computation of its element stiffness matrix, the following can be written

$$[\mathbf{k}] = \int_{-1}^1 \int_{-1}^1 \int_{-1}^1 [\mathbf{B}]^T [\mathbf{D}] [\mathbf{B}] (\det[\mathbf{J}]) \, d\xi \, d\eta \, d\zeta \quad (2.34)$$

Clearly, 2-D and 1-D elements will be, essentially, of the same form while, obviously, consisting of double and single integrals respectively.

Integrals such as those forming the basis of the element-stiffness computations are often too complex to be calculated exactly by analytical means. This is particularly true in the case of the more sophisticated curved elements stemming from the isoparametric

formulation, so that resort must be made to numerical-integration techniques (just as the inverse of $[\mathbf{J}]$ is also calculated numerically in such problems). In these methods, the function being integrated (F) is evaluated at a finite number of points within the element, and each of these values is multiplied by the length of the interval associated with that F value, which length may be thought of as an adequate weighting factor W ; the sum of all the products WF constitutes an approximation to, and in certain instances actually coincides with, the true value of the integral. With specific reference to the intrinsic coordinates and integration limits associated with the isoparametric formulation, 1-D, 2-D and 3-D integrals may therefore be expressed as follows

$$I_1 = \int_{-1}^1 F(\xi) d\xi = \sum_i W_i F(\xi_i) \quad (2.35a)$$

$$I_2 = \int_{-1}^1 \int_{-1}^1 F(\xi, \eta) d\xi d\eta = \sum_i \sum_j W_i W_j F(\xi_i, \eta_j) \quad (2.35b)$$

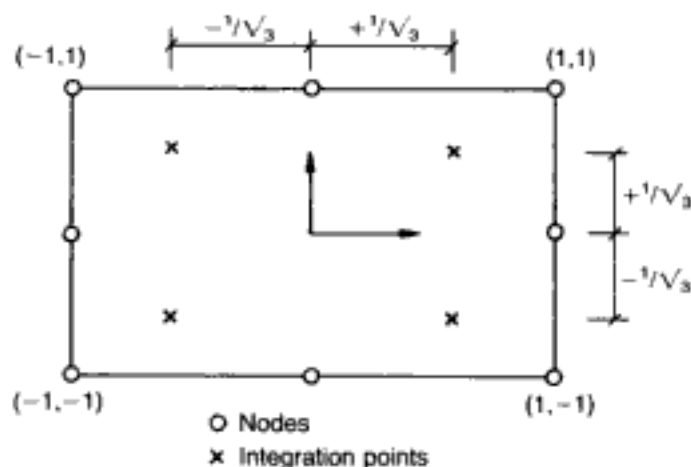
$$\begin{aligned} I_3 &= \int_{-1}^1 \int_{-1}^1 \int_{-1}^1 F(\xi, \eta, \zeta) d\xi d\eta d\zeta \\ &= \sum_i \sum_j \sum_k W_i W_j W_k F(\xi_i, \eta_j, \zeta_k) \end{aligned} \quad (2.35c)$$

where the number of points (i.e. range(s) of i , j and k) are usually the same in all directions (and are symmetrically located with respect to the origin). When the above are applied to an integrand matrix — as, for example, in (2.34) — it should be borne in mind that each coefficient of $[\mathbf{B}]^T [\mathbf{D}] [\mathbf{B}]$ ($\det [\mathbf{J}]$) must be integrated in turn through the relevant formula given in (2.35); the resultant I defines the single coefficient k_{ij} in $[\mathbf{k}]$.

For a given number of points at which F is evaluated, Gauss's method of numerical integration or quadrature provides the best degree of accuracy. These optimal sampling-point locations and their respective weighting coefficients are readily available in tabulated form for various integration orders n , all data being specified to a substantial number of significant figures as required for precision purposes (see, for instance, references 61 and 62). As an example, the locations of the four points associated with the 2×2 integration algorithm for the eight-node quadratic element are shown in Fig. 2.10.

Numerically integrated matrices obviously depend on the order of integration adopted. Accordingly, different numbers of sampling points will produce different stiffness matrices, and the question thus arises as to the optimum — or at least an adequate — quadrature rule. Although such a choice varies from problem to problem — and can be ascertained only through numerical experimentation — a general guideline is that as low an order of

Fig. 2.10. Locations of integration points corresponding to a 2×2 rule inside a typical 8-node quadratic element (with all coordinates shown normalized)



integration is usually desirable provided that it does not lead to numerical instability. Several arguments may be adduced in favour of low-order integration. First, there is the computation time, which is quite considerable as its order of magnitude can be comparable to that of equation solving. The consideration is of special significance in nonlinear work, where element stiffness matrices are usually constantly updated. Bearing in mind that numerical integration is proportional to the square of the number of DOF in the element times the number of sampling points, it is clear that the change from a 2-point to a 3-point rule will more than approximately double — in 2-D cases — and triple — in 3-D problems — the integration cost. Another advantage of low-order quadrature algorithms is that these result generally in a softening of the element, thus counteracting the overly stiff nature inherent in FEs derived on the basis of displacement or stiffness formulations. A third favourable characteristic associated with fewer sampling points refers to the locations at which stresses are computed. It is well known that calculations of stresses along edges or faces of the element tend to be inaccurate, especially at the nodes. This is particularly true of the quadratic C_0 elements used in the present work. It turns out that the optimal locations at which stresses should be calculated coincide with the Gauss points in the interior of the element (if required, stresses at edges/faces or nodes may then be extrapolated from the values obtained at Gauss points). Now, the use of low-order or 'reduced' integration has often been found to provide not only superior answers to those attained by means of 'full' (i.e. higher-order) integration but also the optimum locations for stress computation. For example, such a behaviour is exhibited by serendipity elements where 2×2 integration tends to improve the predictions of the 3×3 rule and, in addition, the stress-sampling locations corresponding to the 4-point quadrature happen to be best irrespective of which of the two integration rules is used.

The above advocacy of low-order integration algorithms must

be tempered with the requirement that it should not give rise to numerical-instability problems. Such difficulties stem from the possible presence of kinematic mechanisms which, as is well known, lead to, and are detectable by, singular systems of equations or, in the present context, result in stiffness-matrix singularity. The cause of these singularities is traceable to zero-energy deformation modes, associated with certain patterns of nodal displacements compatible with a strain field which is zero at all sampling points. Now, it is obvious that, as the number of such quadrature points decreases, the likelihood of occurrence of zero-energy modes becomes greater. In fact, it can be argued that, if the number of independent linear relations, between the nodal unknowns, that are available at all the integrating points is below the number of these nodal parameters, the stiffness matrix will be singular.⁶¹ (The independent relations may be obtained by multiplying the number of strain components per quadrature point times the number of such points; the unknowns are simply the number of DOF per node times the number of nodes, minus those DOF which have been eliminated through the imposition of kinematic restraints.) To show that singularities will definitely not occur is not so easy and, therefore, while the condition that the total number of strains should be larger than the total number of DOF is a requirement for an element/system to be well behaved, it is always advisable to conduct the eigenvalue test so as to determine the actual number of zero-energy modes.⁶² As the eigenvalue test is usually performed on the full stiffness matrix of a given element, i.e. without imposing the necessary nodal restraints necessary to prevent rigid-body motions, a proper element formulation should yield the correct number of mechanisms associated with this type of translation and rotation in space (i.e. three and six mechanisms for 2-D and 3-D elements respectively); any additional mechanisms reveal the presence of zero-energy modes connected with low-order numerical-integration rules.

Reference may be made to some of the quadratic elements used in the present work in order to illustrate the above points. For example, the 2-D serendipity element, with two DOF per node, possesses $2 \times 8 = 16$ DOF when totally unrestrained in its plane. Adopting the 2×2 i.e. 4-point integration rule, with three strains per quadrature location, yields $3 \times 4 = 12$ independent relations. Therefore, it may be concluded that, even if the minimum number of restraints needed to prevent 2-D rigid-body motion were imposed (so that the number of nodal DOF became 13), the element stiffness matrix would still be singular. By increasing the quadrature order to the 3×3 or 9-point integration rule, the number of independent relations augments to $3 \times 9 = 27$, i.e. well in excess of the nodal DOF. Similar conclusions are reached if, for instance, 3-D elements are considered, as may be seen by reference to the serendipity brick element. This element possesses $3 \times 20 = 60$ nodal DOF

and this is well in excess of the 48 independent linear relations stemming from the adoption of the $2 \times 2 \times 2$ or 8-point integration rule (now, with six strains per sampling point); once again, the resulting matrix singularity cannot be removed even if the six kinematic constraints preventing rigid-body motion in space were to be present. On the other hand, a $3 \times 3 \times 3$ or 27-point integration order yields $6 \times 27 = 162$ strain relations, so that zero-energy modes are unlikely, and this is confirmed by the presence of the correct number of mechanisms (six) in the stiffness matrix of the (unrestrained) element (as against 12 mechanisms for the $2 \times 2 \times 2$ quadrature).

From the previous examples, it becomes clear why integration orders for the quadratic elements of Figs 2.8 and 2.9 are often referred to as 'full integration' when 3 (1-D), 3×3 (2-D) and/or $3 \times 3 \times 3$ (3-D) quadrature rules are used, whereas the terms 'reduced integration' or 'under-integration' are employed to denote the cases where 2 (1-D), 2×2 (2-D) and/or $2 \times 2 \times 2$ (3-D) quadrature rules are relied upon. Some of the advantages of adopting the latter low-order algorithm having been outlined previously, it is clear that under-integration is used widely despite the zero-energy mode singularities exhibited by the *individual* elements. This is because the model of a structure consists of several elements so that the total number of strain relations increases in direct proportion to the number of units used in the mesh, while the increase in DOF is relatively slower as more and more nodes become shared as new elements are added. Thus, for example, a 2-D structure made up of two serendipity elements possesses 23 DOF once the three rigid-body constraints are imposed, and — unlike the single-element case — this number is now exceeded by that of available strains even if a 2×2 rule is adopted. However, care must always be exercised when choosing, at the outset of an analysis, reduced-integration techniques, and this is particularly relevant in nonlinear problems of the type considered here, where gradual cracking may give rise to drastic stiffness changes within the element(s) concerned. Not surprisingly, therefore, decisions to under-integrate should be explored with due caution and this is why such questions will be given appropriate prominence in later sections.

2.4. The nonlinear finite-element model for structural concrete

2.4.1. Background and scope

On the basis of the readily-adjustable modular scheme provided by FINEL and the quadratic-type FEs chosen from its library, the nonlinear numerical modelling of concrete structures may now be outlined. Such modelling consists largely of careful implementation of nonlinearities through the gradual updating of element stiffness matrices which, in turn, are essentially described by the matrices **[B]** and **[D]**. Since the dimensions of ordinary concrete members are such that large displacements are usually prevented throughout most — if not the whole of — the loading regime (so that

equilibrium may be formulated in the original configuration), and, in addition, strains being small enough to allow linearized compatibility relations to be adopted, geometric nonlinearities are ignored in the present formulation. This simplifies the modelling quite considerably, the matrix $[B]$ remaining constant throughout the analysis. Therefore, consideration need be given only to material behaviour, as the predominant source of nonlinearity, the latter being introduced through reformulations of the constitutive matrix $[D]$.

In describing the way in which the nonlinear characteristics of concrete are dealt with in the program, the distinction made in Chapter 1 between microcracking and macrocracking phenomena becomes particularly useful. The gradual and mild nature of the former behaviour, described through the constitutive relations of concrete, makes it relatively easy to implement, in contrast to the sudden occurrence and strong type of nonlinearity associated with the latter regime, in which 'structural' cracking takes place once the failure criterion for the material is exceeded. Thus, macrocracking is generally more difficult to model and its explosive nature may lead to convergence problems. This is why the strategy adopted to describe such cracking will receive separate treatment, and will follow the general outline of the incremental formulation of nonlinear concrete behaviour prior to the reaching of the OUPF level which marks the onset of the macrocracking regime.

The overall strategy to be discussed in the next three sections (two dealing with the modelling of concrete, the third devoted to a brief description of the reinforcing steel) will be illustrated by reference to the more general, 3-D problem. However, it should be pointed out that actual analyses are carried out by means of two distinct — although, obviously, very related — computer packages. The first of these to be developed was aimed exclusively at 2-D (plane-stress or axisymmetric) structures.⁵⁴ Later on, when the basic concepts were extended to 3-D problems, some of the strategies were changed, mainly with a view to improving efficiency, convergence and/or numerical stability,⁵⁶ such changes either being necessary in the 3-D context or simply stemming from a natural maturing process built on the experience acquired through the development and use of the 2-D package. Clearly, then, although the general outline of the overall strategy will be provided by reference to the 3-D package, it will also be useful to point out — whenever necessary — those few key instances where the formulations differ, either on account of the specific nature of the 2-D model or because the given feature illustrates the improvement attained by the relevant change introduced in the 3-D model. In addition, mention will also be made of 2-D results when these provide the numerical evidence for certain important strategies which have been incorporated automatically into the 3-D program.

2.4.2. Incremental formulation up to macrocracking

2.4.2.1. The incremental Newton–Raphson scheme

The essence of the nonlinear FE procedure is the incremental Newton–Raphson method (INRM) described previously. Irrespective of the updating strategy adopted, its basic formulation may be summarized in flow-chart form as depicted in Fig. 2.11.

The external-load vector is applied in load steps Δf_e (typically, $\Delta f_e \approx 5\text{--}10\%$ of the estimated failure load), to which the unbalanced nodal forces (i.e. the vector of residual forces, Δf_r)

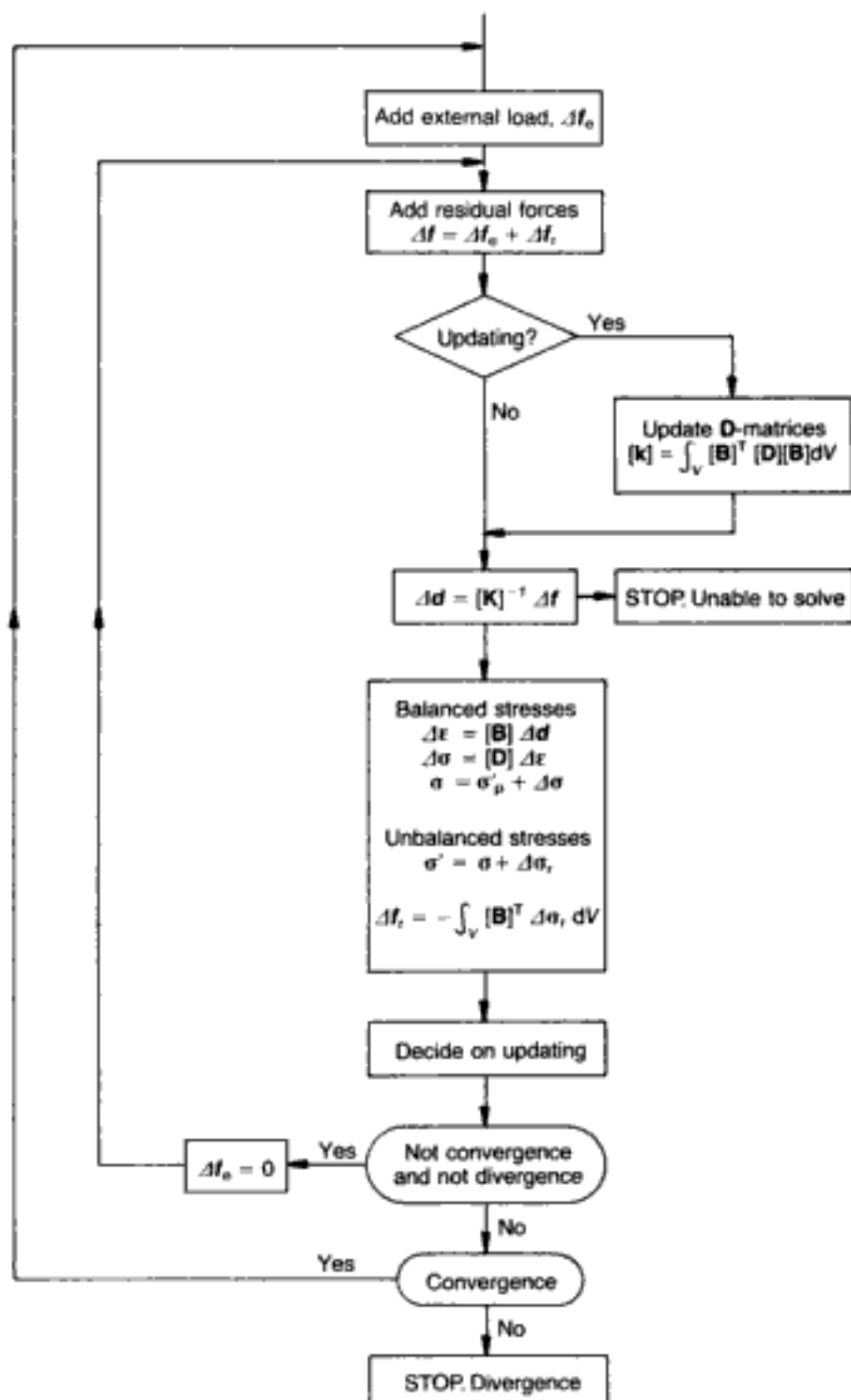


Fig. 2.11. Basic flow-chart for the nonlinear FE analysis based on the incremental Newton–Raphson method

of the previous iteration must be added. Then, a decision on whether or not to update the various \mathbf{D} -matrices — and, hence, the incremental stiffness matrices $[\mathbf{k}]$ — is made. If the current iteration is an updating iteration, the result is an update of the incremental stiffness matrix of the structure (usually known as the tangent \mathbf{K} -matrix — see section 2.2). It should be noted that, although the incremental \mathbf{K} -matrix may be the tangent \mathbf{K} -matrix, it is not necessary to use fully-tangent properties; in fact, any \mathbf{K} -matrix derived from initial secant or tangent properties can be used. In the present work, whenever updating of the \mathbf{K} -matrix is required, the matrix is only quasi-tangent because it is more convenient to use simply the material tangent moduli which, it will be recalled (see section 1.4.1.2, expressions (1.30) and (1.31)), neglect σ_{id} , so that the true constitutive law is not actually implemented. If the system of equations can be solved, the increments of the nodal-displacement vector $\Delta \mathbf{d}$ are obtained, from which the new increments in strains ($\Delta \epsilon$) and stresses ($\Delta \sigma$) at all Gauss points are calculated through the matrices $[\mathbf{B}]$ and $[\mathbf{D}]$ respectively; thus, the total (cumulative) strains (ϵ) and stresses (σ) may be ascertained. The new total stresses are now balanced, i.e. they satisfy, at this stage, equilibrium (namely, $\int [\mathbf{B}]^T \sigma dV = f_i = f_e$, where f_i is the set of (nodal) internal forces), but, in general, they are not compatible with the actual material stress-strain relationships (unless, of course, convergence has been obtained). Therefore, these equilibrated stresses are corrected so as to satisfy the constitutive equations (at this point, obviously, the coupling effect σ_{id} must formally be taken into account), and this requires the additional stress increments $\Delta \sigma_r$, which lead to the total stresses σ' that are now unbalanced (as equilibrium is no longer satisfied since $\int [\mathbf{B}]^T \sigma' dV = f_i \neq f_e$). These corrective stresses $\Delta \sigma_r$ create new residual or unbalanced forces Δf_r which are applied to the structure in the next iteration in order to re-establish equilibrium conditions. If unbalanced forces do not satisfy convergence criteria, the external load is kept constant and further iterations are carried out; otherwise a new external load increment is applied and the whole procedure repeated. There are only two possible reasons for stopping the analysis: unrealistic solutions to the set of equations (e.g. owing to ill-conditioning), or divergence of residual forces. It should be stressed at this point that the preceding outline, as well as much of the subsequent material in the present section (2.4.2) devoted to the microcracking regime is, clearly, also relevant in the presence of macrocracking, although, as stated earlier, the specific features of the latter regime will be covered in detail in section 2.4.3.

An essential requirement of any nonlinear package is the ability to store intermediate results which are then used to obtain more accurate values as the iterative solution proceeds and convergence criteria are eventually met. The need for such a storage facility

is even more apparent when an incremental procedure is being implemented. Such a procedure imposes on the structure under consideration additional external loading when the iterative solution has converged at a given load level, thus enabling the program to follow automatically a monotonic loading path up to overall failure. It is clear that further storage is necessary here in order to follow the structural response at each external-load level, which implies storing strains, stresses, displacements and cracking/yielding information. The storage of such vast quantities of data might, at first, appear somewhat wasteful, in the sense that, once a given external-load increment has achieved convergence, information on previous load steps could be dispensed with; however, the retention of the data pertaining to the whole of the analysis is useful for post-processing purposes such as, for example, plotting and, more generally, the capacity for studying in detail and at leisure the various parameters at given solution stages. While the necessary storage additions and accompanying programming strategies are beyond the scope of the present discussion, the relevant background may be found in references 54 and 56.

So far, no specific choice of updating strategy has been mentioned, all INRMs sharing the common layout of Fig. 2.11, as mentioned previously. However, this question of updating technique must be addressed when certain aspects associated with the convergence and efficiency of the adopted algorithm are being considered. Although the rates of convergence of the modified and mixed INRMs are slower than that corresponding to the pure INRMs (see Fig. 2.5), the former methods usually economize on computer time since they cut down on the high cost of the numerical integration of stiffness matrices. Furthermore, if instead of the set of equations being solved by iterative methods, a single reduction or decomposition of the stiffness matrix is carried out (see section 2.3.1), then the former methods (i.e. modified and mixed INRMs) also save in the number of factorizations of the **K**-matrix of the structure. Now, it must be stressed at this point that the analysis of concrete structures has two sources of high localized nonlinearities which make the above reasoning about efficiency of secondary importance: cracking of concrete and yielding of steel at given Gauss points. These, however, will be discussed later (for concrete, see section 2.4.3) and, before their occurrence, the solution searches corresponding to the microcracking regime associated with a much milder form of nonlinearity may follow safely the mixed INRM in which the stiffness matrix is reformulated or updated only periodically. This combination of the pure and modified INRMs represents a sensible compromise between the high convergence of the former and the low cost of the latter.^{54,67}

To summarize, therefore, the incorporation, in the solution strategy, of the constitutive relationships throughout the micro-

cracking regime consists, very broadly, of the following three specific steps, which are carried out at each integration point:

- At each iteration, a check is made that the state of stress lies within the failure envelope.
- At each iteration, the state of stress corresponding to the state of strain generated by the FE solution is corrected so that the constitutive laws are satisfied.
- When the updating of the stiffness matrix is required, the concrete material properties K_c , G_c , and hence E_c , ν_c , which correspond to the actual state of stress, are obtained.

In order to outline more fully the overall FE procedure described in Fig. 2.11, the formulation of the **B**-, **D**- and **k**-matrices needs to be discussed in some detail, as well as the residual-force implementation and the criteria adopted for convergence and divergence. Such aspects are dealt with in the subsequent five sections and, whenever relevant, this will be done, in generic form, by reference to the 3-D brick element.

2.4.2.2. Incremental strain–displacement relationships

The incremental version of relations (2.1) that link the 3-D displacement field and the nodal displacements is given by

$$\Delta \mathbf{u} = [\mathbf{N}] \Delta \mathbf{d} \quad (2.36)$$

where $\Delta \mathbf{u} = (\Delta u_x, \Delta u_y, \Delta u_z)$ are increments of displacements, $\Delta \mathbf{d} = (\dots, \Delta d_{x1}, \Delta d_{y1}, \Delta d_{z1}, \dots)$ are increments of nodal displacements, and $[\mathbf{N}]$ is the matrix of shape functions. By reference to brick elements, (2.36) may be written as

$$\begin{bmatrix} \Delta u_x \\ \Delta u_y \\ \Delta u_z \end{bmatrix} = \begin{bmatrix} N_1 & 0 & 0 \\ \dots & 0 & N_1 & 0 & \dots \\ 0 & 0 & N_1 \end{bmatrix} \begin{bmatrix} \Delta d_{x1} \\ \Delta d_{y1} \\ \Delta d_{z1} \\ \vdots \\ \vdots \\ \vdots \end{bmatrix} \quad (2.37)$$

in which N_1 is the shape function of the 1th node.

The vector of strains $\epsilon(\epsilon_x, \epsilon_y, \epsilon_z, \gamma_{xy}, \gamma_{xz}, \gamma_{yz})$ is defined on the assumptions of the linear theory of elasticity.⁶⁹ Accordingly, the relevant expressions are

$$\epsilon_x = \frac{\partial u_x}{\partial x} \quad (2.38a)$$

$$\epsilon_y = \frac{\partial u_y}{\partial y} \quad (2.38b)$$

$$\epsilon_z = \frac{\partial u_z}{\partial z} \quad (2.38c)$$

$$\gamma_{xy} = \frac{\partial u_x}{\partial y} + \frac{\partial u_y}{\partial x} \quad (2.38d)$$

$$\gamma_{xz} = \frac{\partial u_x}{\partial z} + \frac{\partial u_z}{\partial x} \quad (2.38e)$$

$$\gamma_{yz} = \frac{\partial u_y}{\partial z} + \frac{\partial u_z}{\partial y} \quad (2.38f)$$

where the (engineering) strain definitions adopted differ from those corresponding to the components of the strain tensor ϵ_{ij} ($=\frac{1}{2}(\partial u_i/\partial x_j + \partial u_j/\partial x_i)$). By reference to (2.6b), the incremental strain-nodal displacement relations are

$$\Delta \epsilon = [\mathbf{B}] \Delta d \quad (2.39)$$

which, in 3-D problems, is obtained by combining (2.37) and (2.38), the result being

$$\begin{bmatrix} \Delta \epsilon_x \\ \Delta \epsilon_y \\ \Delta \epsilon_z \\ \Delta \gamma_{xy} \\ \Delta \gamma_{xz} \\ \Delta \gamma_{yz} \end{bmatrix} = \begin{bmatrix} b_{x1} & 0 & 0 \\ 0 & b_{y1} & 0 \\ 0 & 0 & b_{z1} \\ \dots & b_{y1} & b_{x1} & 0 & \dots \\ b_{z1} & 0 & b_{x1} \\ 0 & b_{z1} & b_{y1} \end{bmatrix} \begin{bmatrix} \cdot \\ \cdot \\ \Delta d_{x1} \\ \Delta d_{y1} \\ \Delta d_{z1} \\ \cdot \\ \cdot \\ \cdot \end{bmatrix} \quad (2.40)$$

where b_{x1} , b_{y1} , b_{z1} ($=\partial N_1/\partial x$, $\partial N_1/\partial y$, $\partial N_1/\partial z$) are functions of x , y , z . These derivatives completely define the 6×3 block of the \mathbf{B} -matrix corresponding to the contribution of the displacements of node I to the strain increments at a given point within the element. Since, as pointed out earlier, the analysis does not include geometrical nonlinearities, such derivatives remain constant throughout the analysis. Therefore, they are calculated for all Gauss points only once (at the first iteration of the analysis). Their calculation, in terms of the local coordinates and the ensuing Jacobian matrix, has already been explained in section 2.3.2.

2.4.2.3. Incremental stress-strain relationships for uncracked concrete

The increments of stresses and strains are related by the \mathbf{D} -matrix adopted. By reference to (2.10), and neglecting initial strains and/or

stresses, its incremental counterpart is simply

$$\Delta\sigma = [\mathbf{D}]\Delta\epsilon \quad (2.41)$$

For uncracked-concrete Gauss points, the \mathbf{D} -matrix may be calculated by reference to a linearly-elastic isotropic material which is usually described in the following concise form

$$\sigma_{ij} = 2G\epsilon_{ij} + 3\mu\epsilon_0\delta_{ij} \quad (2.42)$$

where G and μ are the shear and Lamé's moduli, the former being given by (1.2) while the latter is also related to E and ν by the expression

$$\mu = \frac{\nu E}{(1+\nu)(1-2\nu)} \quad (2.43)$$

On the basis of (2.42), therefore, the incremental constitutive relations (2.41) for uncracked concrete may be written as

$$\begin{bmatrix} \Delta\sigma_x \\ \Delta\sigma_y \\ \Delta\sigma_z \\ \Delta\tau_{xy} \\ \Delta\tau_{xz} \\ \Delta\tau_{yz} \end{bmatrix} = \begin{bmatrix} 2G+\mu & \mu & \mu & 0 & 0 & 0 \\ \mu & 2G+\mu & \mu & 0 & 0 & 0 \\ \mu & \mu & 2G+\mu & 0 & 0 & 0 \\ 0 & 0 & 0 & G & 0 & 0 \\ 0 & 0 & 0 & 0 & G & 0 \\ 0 & 0 & 0 & 0 & 0 & G \end{bmatrix} \begin{bmatrix} \Delta\epsilon_x \\ \Delta\epsilon_y \\ \Delta\epsilon_z \\ \Delta\gamma_{xy} \\ \Delta\gamma_{xz} \\ \Delta\gamma_{yz} \end{bmatrix} \quad (2.44)$$

where $(\Delta\sigma_x, \Delta\sigma_y, \Delta\sigma_z, \Delta\tau_{xy}, \Delta\tau_{xz}, \Delta\tau_{yz})$ are the increments of direct and shear stresses in global coordinates, while G and μ are derived from the tangent shear and bulk moduli described in section 1.4.1.2 (i.e. expressions (1.30) and (1.31)). Clearly, the coefficients of the \mathbf{D} -matrix are functions of the state of stress (i.e. $G(\tau_0), \mu(\sigma_0, \tau_0)$), but, at the same time, it is worth noting that the constitutive matrix is isotropic throughout the microcracking regime and, hence, invariant with respect to any set of orthogonal axes.

Although the \mathbf{D} -matrices for cracked Gauss points will be described in detail in section 2.4.3, it is convenient to note at this stage that they are anisotropic and that they will be defined with respect to cracked directions. Thus, all their coefficients in global coordinates will, in general, be non-zero, since cracked non-isotropic \mathbf{D} -matrices require a transformation from local to global directions (see Appendix B for such a transformation). However, it is evident that axes transformations do not affect the \mathbf{D} -matrix in the present case of isotropic behaviour before macrocracking.

2.4.2.4. Incremental force-displacement relationships

The incremental stiffness matrix of an element connects the increments of nodal forces and nodal displacements. The relevant

expression may readily be written down by reference to either (2.19) or (2.20) which relate total displacements and forces up to a given stage of loading, the result being

$$\Delta f = [k] \Delta d \quad (2.45)$$

with the expression for $[k]$ given by (2.18). As explained previously, this k -matrix is calculated in global directions by numerical integration and, hence, may be written as

$$[k] = \sum_{i=1}^n ((B)_i^T [D]_i [B]_i J_i) w_i \quad (2.46)$$

where J_i and w_i are the Jacobian and the weight of the i^{th} Gauss point respectively, and n is the total number of Gauss points in the element. As was the case with the coefficients of the B -matrix, Jacobians do not change throughout the analysis and, hence, they are calculated only at the first iteration. Furthermore, as $[k]$ is symmetric, it is necessary to calculate only the coefficients of its upper (or lower) triangle.

While $[k]$ can be calculated directly from expression (2.46) without reference to the actual B - and D -matrices, it is worth noting that the expressions for its coefficients can be computed more efficiently by taking into account any special features (such as, for example, sparsity) of the relevant B - and D -matrices. This will be discussed briefly below, as it leads to efficient procedures for the numerical calculation of $[k]$, and also prepares the ground for the discussion (in section 2.4.3) of the effect of the smeared representation of cracking on the conditioning of stiffness matrices.

Expression (2.46) can split into blocks of 3×3 coefficients relating to the DOF of pairs of nodes. Let $[k]^{IJ}$ be one such 3×3 block relating to the DOF of nodes I and J

$$[k] = \begin{array}{cc} & \begin{array}{cc} \text{node I} & \text{node J} \end{array} \\ \begin{array}{c} \text{node I} \\ \text{node J} \end{array} & \begin{bmatrix} \cdot & \cdot & \cdot & \cdot & \cdot \\ \cdot & [k]^{II} & \cdot & [k]^{IJ} & \cdot \\ \cdot & \cdot & \cdot & \cdot & \cdot \\ \cdot & [k]^{JI} & \cdot & [k]^{JJ} & \cdot \\ \cdot & \cdot & \cdot & \cdot & \cdot \end{bmatrix} \end{array} \quad (2.47)$$

This $[k]^{IJ}$ block is equal to $\sum_{i=1}^n [k]_i^{IJ}$, where $[k]_i^{IJ}$ is the contribution of the i^{th} Gauss point to such a block. For the brick elements adopted herein, and for the general case of cracked Gauss points, this contribution is given by the following expression

$$[k]_i^{IJ} = w_i J_i \begin{bmatrix} b_{xI} & 0 & 0 & b_{yI} & b_{zI} & 0 \\ 0 & b_{yI} & 0 & b_{xI} & 0 & b_{zI} \\ 0 & 0 & b_{zI} & 0 & b_{xI} & b_{yI} \end{bmatrix}_I$$

$$\begin{bmatrix}
 d_{11} & d_{12} & d_{13} & d_{14} & d_{15} & d_{16} \\
 & d_{22} & d_{23} & d_{24} & d_{25} & d_{26} \\
 & & d_{33} & d_{34} & d_{35} & d_{36} \\
 & & & d_{44} & d_{45} & d_{46} \\
 \text{symmetric} & & & & d_{55} & d_{56} \\
 & & & & & d_{66}
 \end{bmatrix}_i \quad \begin{bmatrix}
 b_{xj} & 0 & 0 \\
 0 & b_{yj} & 0 \\
 0 & 0 & b_{zj} \\
 b_{yj} & b_{zj} & 0 \\
 b_{zj} & 0 & b_{xj} \\
 0 & b_{zj} & b_{yj}
 \end{bmatrix}_j \quad (2.48)$$

The sparsity of the **B**-matrix is evident: half of its coefficients are zero and placed at known positions. Thus, the number of computations may be reduced quite significantly once all the multiplications involving zero terms are identified and left out of subsequent numerical operations. The **D**-matrix in (2.48) is not sparse, as it refers to the general case of a cracked Gauss point expressed in terms of global coordinates. On the other hand, uncracked Gauss points are described by (2.44) and, for such isotropic conditions, further reduction of computing effort is clearly possible. Various ways of achieving such computational savings for both isotropic and anisotropic material descriptions have been explored in reference 56, with subsequent implementation in the computer program as appropriate.

2.4.2.5. Residual forces

In accordance with the present FE model, the nonlinear force-displacement relationships at the structural level arise exclusively as a result of the nonlinearities in the stress-strain expressions. The iterative procedure required to follow these nonlinear $\sigma-\epsilon$ laws relies on the residual-forces method, by means of which stress corrections (at the material level) of balanced stresses cause the appearance of equivalent unbalanced nodal forces that must be applied in the next iteration in order to re-establish the equilibrium conditions for the overall structure. This may be summarized through the following expression, in which the equivalence between external and internal forces is implicit

$$f_c = \int [\mathbf{B}]^T \sigma' dV + \int [\mathbf{B}]^T (\sigma - \sigma') dV \quad (2.49)$$

where σ and σ' are balanced and unbalanced stresses respectively; and the first term denotes unbalanced (internal) forces (but satisfying the constitutive relations) while the second term re-establishes overall equilibrium conditions (but causing, in turn, lack of compatibility between stresses and strains). Therefore, the residual forces are given by

$$\Delta f_r = - \int [\mathbf{B}]^T (\sigma' - \sigma) dV = f_c - \int [\mathbf{B}]^T \sigma' dV \quad (2.50)$$

where, it should be recalled, the last term represents nodal internal forces.

When the constitutive laws are expressed in the form $\sigma = \sigma(\epsilon)$, as is the case for cracked Gauss points (to be discussed in section

Fig. 2.12. Stress correction, by the standard initial-stress technique, that achieves the satisfaction of the constitutive law but disturbs the equilibrium of the previously balanced stresses σ

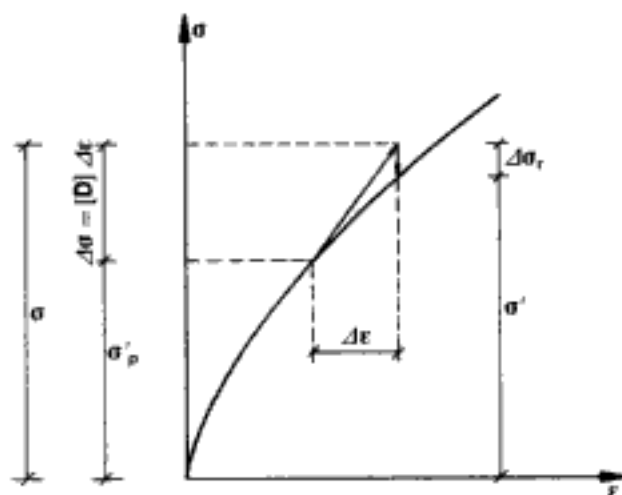
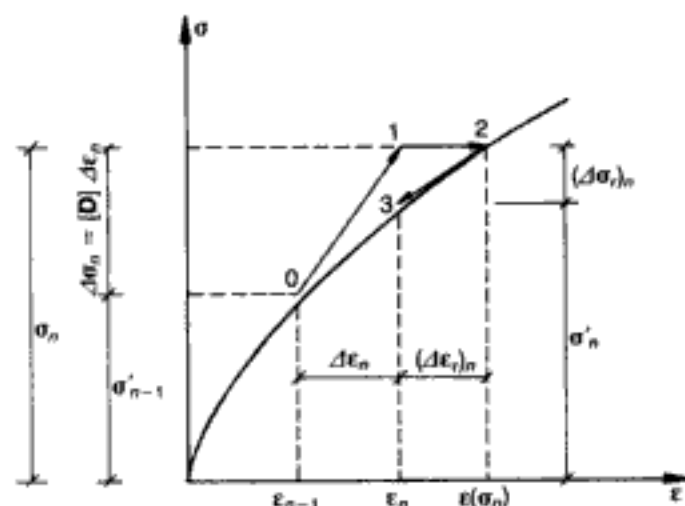


Fig. 2.13. Stress correction, by the initial-strain technique, used for uncracked concrete points (for cracked concrete points, and for all steel Gauss points, refer to Fig. 2.12)



2.4.3) and, also, for steel Gauss points both before and after yielding, unbalanced stresses are worked out in accordance with such laws in the standard manner shown in Fig. 2.12. The residual stresses are given by the components of $\Delta\sigma_r = \sigma' - \sigma$ and must be checked (together with residual forces and, possibly, other criteria) for convergence.

The stress correction for uncracked Gauss points, on the other hand, follows an initial-strain technique, since the constitutive law (for uncracked concrete) is given in the form $\epsilon = \epsilon(\sigma)$ (see expressions (1.32) in section 1.4.1.2). Figure 2.13 summarizes schematically the implemented initial-strain technique for uncracked concrete points. First, increments of strains (and, then, the total strains) are computed from increments of nodal displacements (subscripts other than r indicate the iteration number)

$$\Delta\epsilon_n = [\mathbf{B}]\Delta d_n \quad (2.51a)$$

$$\epsilon_n = \epsilon_{n-1} + \Delta\epsilon_n \quad (2.51b)$$

Balanced stresses are next computed using the \mathbf{D} -matrix incorporated into the set of equations

$$\sigma_n = \sigma_{n-1} + [\mathbf{D}]\Delta\epsilon_n \quad (2.52)$$

These balanced stresses are corrected by the following expression (see Fig. 2.13)

$$\sigma'_n = \sigma_n - [\mathbf{D}(\sigma_n)] \{ \epsilon(\sigma_n) - \epsilon_n \} \quad (2.53)$$

where $[\mathbf{D}(\sigma_n)]$ and $\epsilon(\sigma_n)$ are, respectively, the tangent \mathbf{D} -matrix given by (2.44) and strains, both of these being in accordance with the constitutive law corresponding to the balanced stress level. The components of $(\Delta\epsilon_r)_n = \epsilon(\sigma_n) - \epsilon_n$ are residual strains that have to be checked for convergence. It is worth noting that this initial-strain technique converges very quickly in practice owing to the mild nature of the uncracked material nonlinearities. (Clearly, while the standard initial-stress method of Fig. 2.12 involves the satisfaction of the material law at the end of every iteration, the initial-strain technique satisfies neither equilibrium nor the material law at the end of an iteration unless, of course, convergence has taken place.)

Once stresses are corrected at a given Gauss point, the numerical integration of (2.50) leads to the following contribution to the residual-forces vector

$$\begin{bmatrix} (\Delta f_x)_r \\ (\Delta f_y)_r \\ (\Delta f_z)_r \end{bmatrix}_I = -w_l J_l \begin{bmatrix} b_{xl} & 0 & 0 & b_{yl} & b_{zl} & 0 \\ 0 & b_{yl} & 0 & b_{xl} & 0 & b_{zl} \\ 0 & 0 & b_{zl} & 0 & b_{xl} & b_{yl} \end{bmatrix}_i \begin{bmatrix} (\Delta\sigma_x)_r \\ (\Delta\sigma_y)_r \\ (\Delta\sigma_z)_r \\ (\Delta\tau_{xy})_r \\ (\Delta\tau_{xz})_r \\ (\Delta\tau_{yz})_r \end{bmatrix}_i \quad (2.54)$$

In the above expression, $[(\Delta f_x)_r, (\Delta f_y)_r, (\Delta f_z)_r]_I$ are the residual forces at node I caused by a stress correction $[(\Delta\sigma_x)_r, (\Delta\sigma_y)_r, (\Delta\sigma_z)_r, (\Delta\tau_{xy})_r, (\Delta\tau_{xz})_r, (\Delta\tau_{yz})_r]$ at the i^{th} Gauss point.

2.4.2.6. Convergence and divergence criteria

The convergence of solutions obtained by iterative procedures can be checked in terms of one or more vector increments of various parameters, the norms or elements of which must all be smaller than certain prescribed values. The parameters in question include quantities such as displacements, residual forces, residual stresses and residual strains.⁷⁰ In practice, only one of these vector increments is checked, since all of them are interrelated. Displacement and force criteria are usually preferred to stress and strain criteria. With regard to nonlinear analyses of structural concrete, it would appear that force criteria have mostly been used.^{67,71-74}

In the earlier part of the work,⁵⁴ the two residual-stress criteria

$$\max_i |\Delta\sigma_r(i)| < 0.1 \text{ N/mm}^2 \quad (2.55a)$$

$$\max_i |\Delta\sigma_r(i)| < 0.01 |\sigma_r(i)| \quad (2.55b)$$

were adopted in recognition of the fact that a single criterion might prove unrealistic for the whole of the loading path. Thus, for example, while (2.55a) can ensure a reasonable level of accuracy in the early load steps, at more advanced stages of the loading such a residual-stress value might become impractical to achieve, especially as failure is approached, when the numerical solution tends to become unstable. This is why the second convergence criterion — (2.55b) — based on residual stresses given as percentages of total-stress values, is more attractive as one nears ultimate-load conditions, and is in keeping with the notion of accepting a larger force imbalance as the total load increases.⁷⁵ Clearly, the satisfaction, at each Gauss point, of either of the criteria defined by (2.55) is sufficient for convergence.

In subsequent work,⁵⁶ several additional convergence criteria were studied, of which the following were implemented in the nonlinear procedure. First, a maximum residual strain of 2.5 mm/m, or less than 0.5% of the total strain, was adopted for uncracked concrete, which was found to be slightly more restrictive than the stress criteria adopted earlier (i.e. (2.55) above). In addition, once cracking was implemented, it was prescribed that no concrete Gauss points should exceed the failure envelope, with a maximum residual stress of 0.1 N/mm² set as the limit at cracked Gauss points. The latter stress criterion was also adopted for steel Gauss points, and for these any change from one linear branch to another was treated as a lack of convergence requiring further iterations. Now, it was found that these various convergence criteria are usually met on specification of the following (additional) residual-force criterion

$$\max_i |\Delta f_r(i)| < 0.001 |\Delta F| \quad (2.56)$$

where $|\Delta F|$ is the applied load step (between 5–10% of the ultimate experimental load). This last condition is a very restrictive requirement indeed when compared with other reported criteria (see, for example, references 67, 71–74 mentioned previously). However, all the above criteria were kept (including (2.56)) in order to avoid convergence in certain situations, such as concrete Gauss points being outside the failure envelope ('cracking' criterion) or new yielding of the steel ('yield' criterion), as may occur with less restrictive convergence criteria. Nevertheless, it should be said that residual forces become negligible as soon as material properties are updated, and no new cracking and/or yield occur.

The incremental process stops either because of divergence of residual forces, which is taken to have occurred when

$$\max_i |\Delta f_r(i)| > 100 |F| \quad (2.57)$$

where $|F|$ is the total external load, or because the system of equations cannot be solved as, with extensive cracking, the

degradation of the stiffness matrix of the structure leads to a non-positive or ill-conditioned $[K]$. The former divergence criterion — (2.57) — is very tolerant and thus rarely fulfilled. Hence, most runs stop when $[K]$ becomes sufficiently degraded. As a consequence, all ultimate-load predictions refer to the maximum sustained load (MSL) in the analysis, which corresponds to the last *converged* load step.

2.4.3. Modelling of macrocracking

The presence of macrocracking or 'structural' cracks is unavoidable in most reinforced concrete (RC) structures, and hence codes of practice generally take this into account. For example, BS 8110^{55,58} suggests a maximum crack width of 0.3 mm for reinforced concrete (Part 1 — thus removing the earlier distinction between normal exposure (0.3 mm) and exposure to particularly aggressive environments (>0.004 times the nominal cover to the main reinforcement) present in CP 110⁵³), whereas for prestressed concrete members (Part 2) this limit is set at 0.1 mm for components exposed to particularly aggressive environments and 0.2 mm for all other units. As an instance, typical load–deflection curves from tests on flexural beams exhibit a distinct nonlinear behaviour attributed to the onset of (macro)cracking at load levels as low as 10–20% of the structural failure level.⁷⁶ Accordingly, macroscopic cracks are not only present in most RC structures, but they are usually also present during most of the loading history. It is not an exaggeration, therefore, to say that macrocracking represents the key feature in the nonlinear behaviour of structural concrete, governing its failure mechanism. As a result, the successful numerical treatment of cracking — the predominant nonlinear effect — is an obvious prerequisite for a reliable FE model. In what follows, a description of crack representation will be outlined, while the gradual (or otherwise) implementation of crack propagation — which may give rise to very serious problems of numerical stability — will be discussed in Chapters 3 and 4.

2.4.3.1. The nature of structural cracking

As explained in Chapter 1, the behaviour of concrete is dictated by the fracture processes that the material undergoes under increasing load. These fracture processes first take the form of microscopic cracks (some of which exist within the material even before the application of the load) that extend in the plane of the maximum and intermediate compressive stresses, and propagate in the direction parallel to the maximum principal compressive stress (or in the direction orthogonal to the maximum principal tensile stress). Such microcracks develop in a stable manner up to the OUF_P stress level (their effect on deformation, up to this point, being accounted for by the adopted constitutive relations), which, for practical purposes, can be taken as the failure stress envelope. Once this level is reached, the microscopic cracks link to form a limited number of macroscopic cracks: cracking now

becomes an unstable process and concrete suffers a noticeable loss of material continuity (macrocracking) in the direction orthogonal to the maximum principal tensile (or minimum principal compressive) stress, which leads to a sudden collapse of concrete specimens unless the fracture process is somehow restrained. In this respect, it is worth recalling the fully-brittle nature of concrete once the OUF_P level has been reached. As demonstrated experimentally (see section 1.2.1.2), the strain-softening branches observed in compressive tests arise as a result of friction between loading platens and concrete specimens, so that, if friction is eliminated, a complete loss of load-carrying capacity becomes the most realistic description for concrete behaviour in compression. Similarly, with regard to the post-ultimate behaviour of concrete in tension, it has been shown that strain-softening branches can be observed only in tests where the stiffness of the testing machine is steeper than the steepest portion of the falling branch — otherwise, a sudden failure is deemed to occur. Such testing machines impose large restraints to the fracture processes of concrete that are unlikely to hold for concrete within a structure.

The above observations are summarized schematically with reference to a typical uniaxial $\sigma - \epsilon$ curve (but equally valid for more general — biaxial or triaxial — conditions). Figure 2.14(a) represents such a characteristic in compression, the rising portion covering the various levels of microcracking, while A marks the peak load level (defined by the ultimate surface envelope) at which (macro)cracking occurs. Beyond A, the loss in stiffness properties of the material is immediate and complete. A similar model is applicable to the material characteristic in tension (Fig. 2.14(b)). (The linearity of the stress-strain relationships in tension may be explained by the fact that controlled crack propagation (microcracking) up to the OUF_P level (which practically coincides with macrocracking) can occur only under compressive stress states. In the case of tensile stresses, *any* cracking implies failure and, hence, since nonlinearity reflects microcracking fracture processes, the $\sigma - \epsilon$ relationships for tension should be essentially linear up to failure (i.e. the start of microcracking and macrocracking coincide). This may be argued further on the basis that any departures from linearity as a result of other causes (e.g. time effects) in the case of tension are much less pronounced than in compression. Finally, any attempt at refining the linear model should be tempered by the large scatter inherent in tensile-test results.) Despite the realistic description of both compressive and tensile behaviour at the material level, however, it is only the latter characteristic that is of relevance in a concrete *structure* beyond peak-stress levels. As explained in section 1.5, the peak level in compression is never attained within a structure as tensile failure precedes it (with consequent redistribution of stresses) in adjacent regions. Therefore, although the true zero-stiffness model beyond A in Fig. 2.14(a) will be adopted in the present work, even the

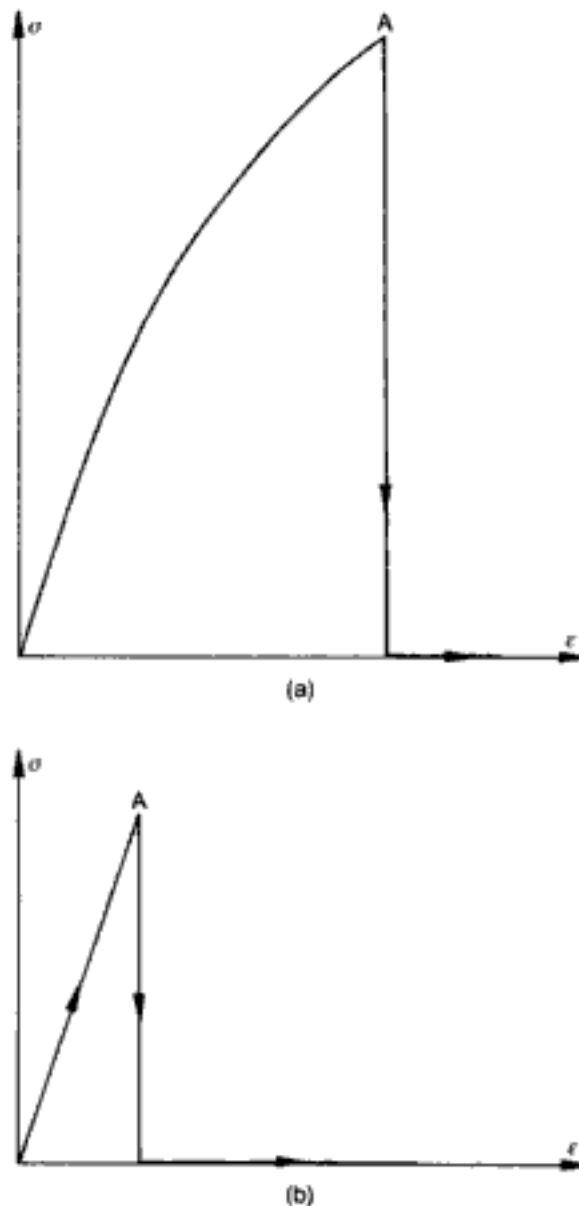


Fig. 2.14. Schematic representation of a typical stress-strain curve for concrete: (a) in compression; (b) in tension (i.e. in the direction orthogonal to the first crack)

inclusion of (the non-existing) strain softening in compression would not influence the analytical prediction of structural members, as will be seen by reference to the examples of Chapters 3 and 4. Conversely, results will generally be affected by the chosen post-ultimate characteristic in tension, and it must be stressed here that the sudden unloading in Fig. 2.14(b), which is to be used henceforth, is in marked contrast with most current modelling approaches which tend to assume a gradual unloading (usually linear), i.e. strain softening in tension, in marked disregard of proven experimental evidence on the one hand, and the difficulties inherent in tensile-test data interpretations on the other.

Figure 2.14(b) refers to the stiffness characteristics in the direction orthogonal to a crack. With regard to the stiffness of cracked concrete in the direction parallel to macrocracks, it is a common hypothesis in analyses to assume that concrete keeps its uncracked stiffness in those directions (such as, for example, that

defined by the ascending regions in Fig. 2.14). Although a certain decay may be expected, it can be shown that the remains of specimens subjected to triaxial tests exhibit uniaxial $\sigma - \epsilon$ relations similar to those of uncracked specimens. Therefore, it appears realistic to assume that concrete between cracks *in a structure* retains its uncracked stiffness in the direction parallel to the cracks.

Some comments with respect to the stress combinations causing failure at a given point/region within a structure may be made by reference to Fig. 2.15. Since cracking causes unloading of the tensile stresses that existed before its occurrence, it leads to states of stress that can be sustained by concrete as they are inside the failure envelope (see zones T-C-C, C-T-T and T-T-T in Fig. 2.15, where C stands for compression and T for tension). Therefore,

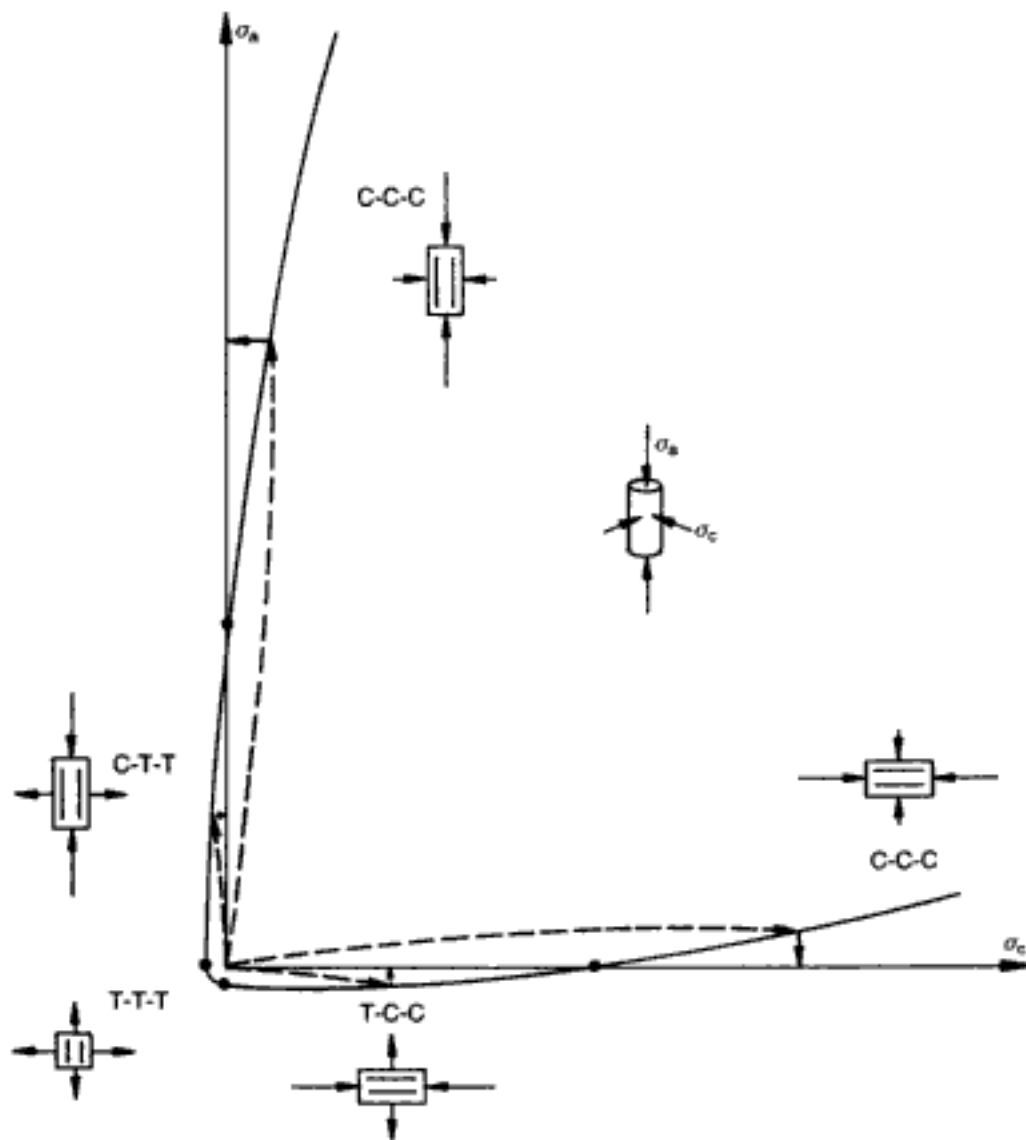


Fig. 2.15. Effect of stress combination or 'zone' on the failure of concrete⁵⁶ (Note: dashed (arrowed) lines indicate loading paths that eventually hit the failure envelope, at which point sudden unloading (towards the relevant axis σ_a , σ_c as shown by the arrows) leads to stress states that lie inside the failure envelope for cases T-C-C or C-T-T and outside it for case(s) C-C-C)

the process can be stabilized at both the material and structural level, provided that those tensile stresses can be redistributed to adjacent steel or concrete elements. For this type of failure, where at least one stress component is tensile, the fracture mechanism involves the presence of a relatively small number of fissures with the same orientation (orthogonal to the maximum principal tensile stress), which suggests that the material is insignificantly damaged in a direction parallel to these fissures. It may be assumed, therefore, that any change of the stress state will be gradual (from triaxial to biaxial, or from biaxial to uniaxial, or from uniaxial to a complete loss of load-carrying capacity). On the other hand, for fully-compressive states of stress (zones C-C-C in Fig. 2.15), cracking would cause an immediate loss of load-carrying capacity as indicated schematically in Fig. 2.14(a). Therefore, local failures in compression are best presented as localized failures of the material in the three directions (i.e. loss of stiffness in all directions). After all, at least one stress component has a high compressive value (certainly in excess of the uniaxial strength) and this implies that a relatively large number of fissures are present, suggesting that extensive damage is taking place in the material, which then loses all its load-carrying capacity. This is why a distinction will henceforth be made between 'tensile cracking', termed simply 'cracking', and 'compressive cracking' which is equivalent to, and is thus denoted as, 'local failure of the material'. However, it is important to recall the argument put forward in section 1.5 (and also mentioned above) that 'concrete in a structure never fails in compression', and, hence, the above discussion on the post-ultimate compressive-stress states ('local failure') may be regarded as irrelevant. Nevertheless, as stressed in section 1.6, the present FE model does not prevent fully-compressive stress states from developing at failure (this lack of C-C-C failure modes will be shown in Chapters 3 and 4 to be a *result* of analysis and not an *a priori* imposed condition): thus the need formally to include this possibility as one of the failure criteria.

In view of the preceding discussion, the main features of the fracture mechanism in, and subsequent properties of, concrete relevant to the FE model, may be summarized as follows.

- Under increasing stress, concrete behaviour is that of an isotropic continuum until the stress level reaches a peak value. Beyond this level, either 'local failure' or 'cracking' occurs. Should the former be operative, with the strength envelope reached in compression (zones C-C-C), concrete would suffer a complete loss of stiffness in all directions and hence would no longer be able to sustain any stresses. It is, however, the 'cracking' mechanism which one invariably finds in the course of structural analyses and hence its importance in subsequent work.

- A crack plane forms when concrete reaches the strength envelope in tension (zones C-C-T, C-T-T and T-T-T). Such a plane is orthogonal to the maximum principal tensile stress existing just prior to cracking. The presence of an open crack plane causes a complete loss of material stiffness in its orthogonal direction, and, therefore, direct tensile and, in principle, shear stresses can no longer be transferred across the crack plane (but see subsequent sections for the presence and role of the so-called shear-retention factor). When cracking occurs, a discontinuity is introduced into the hitherto continuous material, and this must be allowed for by suitable changes in the characteristics of the stiffness matrix (by means of either the smeared- or discrete-crack approach — see section 2.4.3.2).
- Cracking takes place predominantly in zones of high tensile stress and strain concentrations, thus relieving these (see Fig. 2.16). As a result, stress redistribution is also associated with cracking; in this way, the tensile stresses that existed before the formation of the crack have to be transformed into equivalent residual forces and redistributed to adjacent concrete and/or steel zones.
- While the cracking process tends to relieve the tensile stress and strain concentrations orthogonal to the crack, as a result of the ensuing stress redistribution, new zones of high tensile stress and strain concentrations are created near the crack tips, orthogonal to the crack-extension path. Depending on the amount of stress 'redistribution' within the structure, a given crack can be either stable or unstable. At a given load level, a stable crack extends only to a certain length whereas an unstable crack propagates until it induces structural failure.
- When the crack path intersects a reinforcing bar, loss of bond between steel and the surrounding concrete results over a certain length of bar on both sides of the crack, as shown schematically in Fig. 2.16(b). This question of bond between steel and concrete will be taken up again in section 2.4.4.
- Finally, it is important to note that the fracture mechanism outlined above applies merely to the initiation of a single crack. Cracking in RC structures under increasing load involves the interaction of many such cracks, each of which initiates and propagates. Such interaction may be quite complex, and many propagation mechanisms are possible, as, for instance: all cracks extend at the same time; a few cracks extend first, with other cracks developing later; single cracks propagate one by one. Any of these processes of crack propagation may occur in the course of a given applied (finite) load step, and the crack pattern at the end

of the convergence run should reflect as closely as possible the actual pattern of cracks that would have resulted in the real structure, bearing in mind that a finite load step in an FE analysis usually represents a quicker rate of loading than that in an actual test. In addition, the three types of crack propagation listed above are also relevant in the course of the various iterations themselves within a given load step, as will be seen in Chapters 3 and 4.

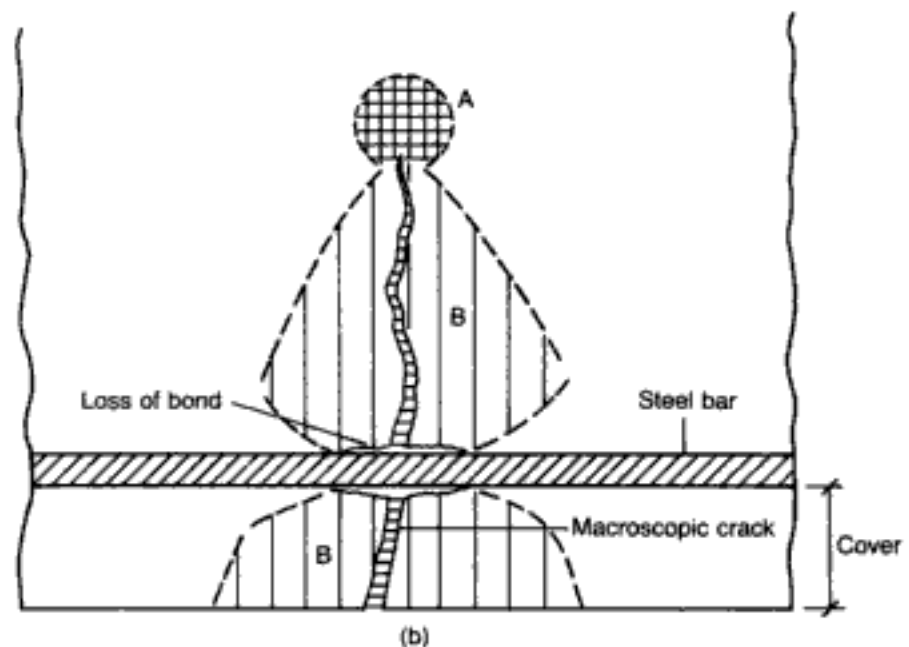
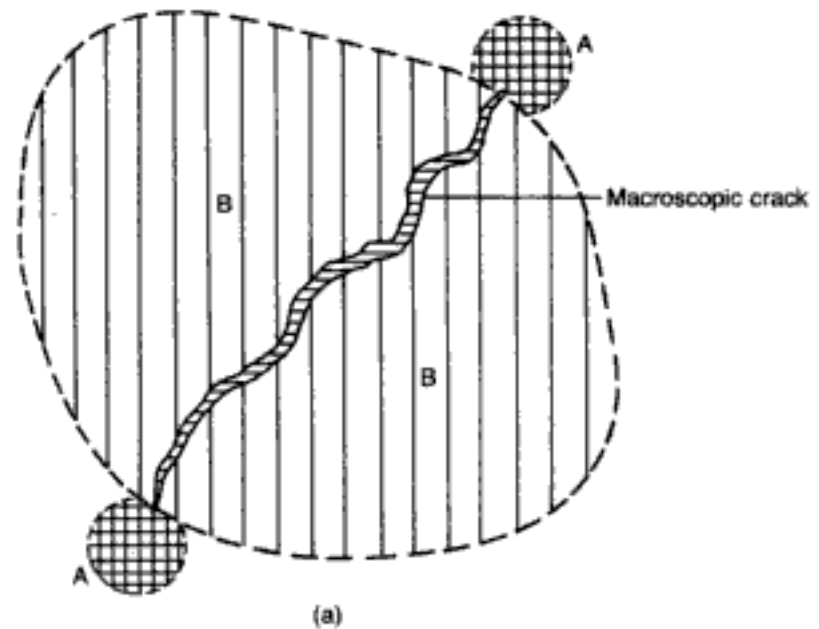


Fig. 2.16. Schematic representation of cracking in concrete, where *A* marks the zones of high tensile stress concentrations near the crack tips, while *B* represents zones where the tensile stresses orthogonal to the crack have been relieved.⁵⁴ (a) plain concrete; (b) reinforced concrete

2.4.3.2. *The smeared-crack approach*

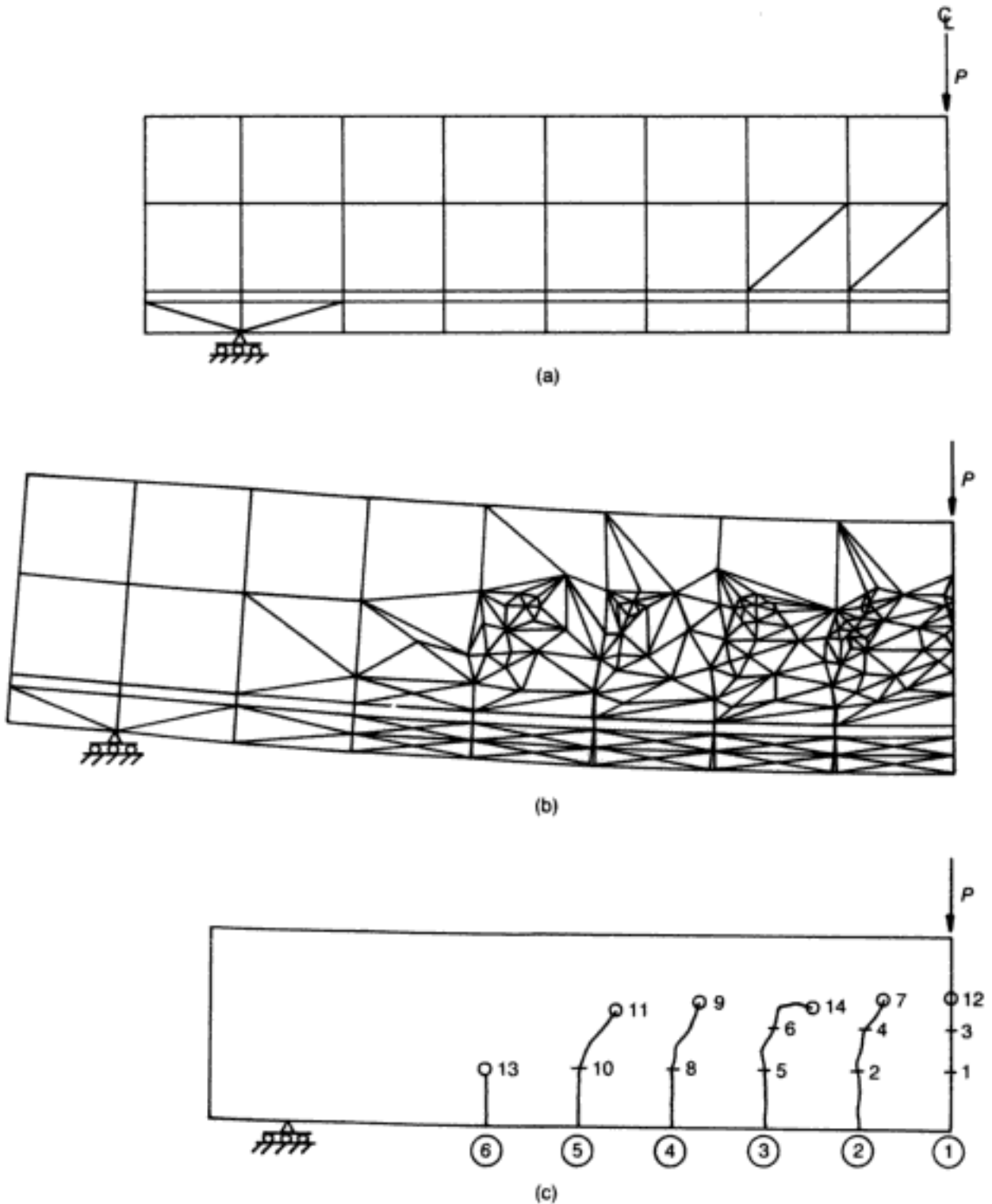
A characteristic feature of cracking is the inherent discontinuity that arises along its path, referred to in the preceding section. On the other hand, the FE model is essentially a continuum-mechanics technique. Such an apparent incompatibility between problem and modelling tool requires the development of special schemes which, while in keeping with the general notion of 'continuity' in the FE solution, exhibit drastic and sudden changes in the material at the location of cracks. Two basic schemes, that constitute the fundamental alternatives to crack modelling, are the discrete-crack approach and the smeared-crack approach.

The discrete-crack approach introduces an actual gap in the FE mesh at the location of a crack. It achieves this by doubling and separating the nodal coordinates lying along individual crack paths. This implies important changes in the numbering of nodes and element connectivities which, in turn, affect the global stiffness matrix. The first discrete-crack model appears to have been used by Ngo and Scordelis.⁷⁷ Early versions of the discrete approach to crack modelling were relatively crude since the crack-propagation path had to follow the boundaries of existing elements. Later on, a technique which automatically redefines the mesh as cracking propagates, apparently without bias in respect of the orientation of cracks, was proposed by Saouma and Ingraffea.⁷⁸ This appears to require intricate programming techniques and still to be significantly restricted in use since complicated mesh refinements become necessary to accommodate the propagation of only a few discrete cracks. Figure 2.17 shows a representative FE mesh necessitated by the presence of only six discrete cracks. This mesh generated near failure should be compared with the relative simplicity of the original mesh. Therefore, it is evident that, owing to practical limitations on the number of FEs, discrete-crack predictions are constrained by FE mesh sizes, in addition to the large effort required for the constant redefinition of the mesh topology, even for plane-stress cases (see Fig. 2.17); in this respect, it is important to note that the discrete-crack technique does not seem to have been applied to 3-D cases (or even to 2-D axisymmetric problems), for which practical difficulties can easily be appreciated. Two further possible complications may be envisaged as cracking progresses in the course of discrete modelling: one is the formation of 'elongated' FEs, i.e. those possessing large ratios between sides (as in the case of many of the elements making up the mesh in Fig. 2.17(b)), with consequently poor(er) numerical performance; the other possible difficulty concerns the subdivision of the mesh (in parts at least) to such a degree that the material data used for the analysis (and based on the average properties of a test specimen of finite size) become of doubtful validity.

It might be argued that the discrete-crack approach allows the

Fig. 2.17. Example of the application of the discrete-crack approach:⁷⁸ (a) initial FE mesh configuration; (b) FE mesh configuration near failure; (c) crack pattern near failure

natural description of individual cracks and, also, it would seem, of the phenomenological processes that are deemed to occur between these cracks. Therefore, the approach appears to be quite suitable, at least, to localized phenomena, such as aggregate interlock, concrete-steel bond and dowel action (see, for example, reference 79). However, meaningful constitutive relations for these local phenomena are very sparse and, in addition, it appears that such effects play a secondary role on the mechanisms of resistance



to applied load in concrete structures.^{51,52} What is important in a discrete-crack approach is the ability to model the high tensile stresses taking place at the crack tips, and it is in this respect that a major disadvantage of the scheme (or of the alternative approach, where a single crack within an element is dealt with by fracture mechanics — see reference 80) manifests itself. For, there is simply no reliable experimental data on the material behaviour in the region of the crack tips, where high stress concentrations govern the initiation and subsequent spread of cracking; and this problem is further compounded by the fact that, at such microscopic level, the true heterogeneous nature of concrete can no longer be ignored, thus posing formidable problems even to the powerful analytical tools afforded by present-day fracture-mechanics theory.

The above outline of the discrete-crack approach was undertaken in order to show why its alternative, the smeared-crack method, adopted in the present FE model, represents, in the current state of knowledge (as regards, primarily, material data, but also numerical capabilities), the more realistic — although, admittedly, less ambitious — technique for crack modelling. The method, whose first practical application seems to have been the predicted response of a nuclear prestressed vessel under inner pressure,⁸¹ and which has subsequently formed the basis for most FE analyses of structural concrete, makes use of the drastic material property changes caused by, and at the location of, cracking as a means of simulating discontinuity. Such changes are achieved by removing or reducing the stiffness properties in the direction orthogonal to the crack, without introducing any gap in the initial mesh, and leaving the latter unchanged throughout the analysis. Since material properties are evaluated only at specific points in an element, such as the integration points or the nodes, the alteration of material properties due to cracking consequently affects the contributing region from which these properties are evaluated, hence *smearing* the effect of cracking over the whole of that region. In fact, a 'single' crack represents an infinite number of parallel fissures throughout that part of the element related to an integration point or a node. As the present work is based entirely on the isoparametric formulation, the points around which the smearing of cracks takes place are always the integration points. Thus, for example, in the case of the under-integrated eight-node quadratic element shown in Fig. 2.10, a single crack affects one quarter of the element. This 'smearing' of material properties over a finite region of the element models the relief of tensile stresses orthogonal to a crack (see Fig. 2.16).

The essence of smeared modelling, therefore, is the setting up of cracked areas by modification of the stiffness properties and stresses (equilibrium conditions) at the relevant Gauss points, i.e. those points used for the numerical integration of stiffness matrices and for the calculation of residual forces. Thus, while discrete

models account for stiffness losses by doubling the nodes lying on individual cracks, smeared models simply replace uncracked **D**-matrices by cracked ones. (Equilibrium conditions are lost in both cases either as a result of mesh modifications (discrete models) or directly through stress corrections (smeared models); subsequently, such equilibrium is re-established by means of residual forces in both cases.) The fact that no mesh modifications are required throughout an analysis based on the smeared-crack approach not only constitutes a signal computational advantage in this technique, as mentioned already, but also allows the element size to be kept similar to that of the specimens from which the constitutive relations and fracture criteria were derived (the latter, an important practical consideration, will be touched upon later, when the effect of FE mesh size on numerical predictions is considered).

2.4.3.3. Incremental stress–strain relationships for cracked concrete

This section deals with the **D**-matrices for cracked concrete for both 2-D (plane stress, and axisymmetric problems) and 3-D analysis. While, before cracking, the **D**-matrix is isotropic, obeying the constitutive laws applicable throughout the ascending branch (at the material level — see, for example, Fig. 2.14), after cracking, the material becomes anisotropic and the previous constitutive relationships can no longer be used, as they were derived for concrete in the uncracked state. Since there are few reliable data on the deformational characteristics of cracked concrete, it will henceforth be assumed that the properties of a *cracked* **D**-matrix remain constant during further loading. (These properties are updated only if and when a second crack develops at the same Gauss point, and then, again, the new stiffness is maintained constant; should a third, and final, crack occur — as, possibly, in 3-D or axisymmetric problems — it would lead to the last updating of the **D**-matrix.) Such an assumption is both necessary (in the absence of relevant experimental information) and reasonable (since the main governing factor once cracking occurs is further cracking rather than any detailed/accurate description of deformation in between two consecutive cracks at a given location where, in any case, load is likely to be shed towards uncracked regions).

Two-dimensional problems (plane-stress case). Before a crack is introduced, the constitutive relations at each integration point may be expressed in the form

$$\begin{bmatrix} \Delta\sigma_x \\ \Delta\sigma_y \\ \Delta\tau_{xy} \end{bmatrix} = \frac{E}{1-\nu^2} \begin{bmatrix} 1 & \nu & 0 \\ \nu & 1 & 0 \\ 0 & 0 & (1-\nu)/2 \end{bmatrix} \begin{bmatrix} \Delta\epsilon_x \\ \Delta\epsilon_y \\ \Delta\gamma_{xy} \end{bmatrix} \quad (2.58)$$

which is readily obtainable by setting $\Delta\sigma_z$ (as well as the shearing quantities) to zero in (2.44). The above incremental stresses and strains refer to 2-D Cartesian global axes (x, y) , and the material 'constants' are understood to be tangent properties corresponding to the current stress state. Since, before cracking, the \mathbf{D} -matrix is isotropic, (2.58) holds in any set of directions, including principal axes. Following cracking, however, the stress state changes from biaxial to uniaxial as a crack forms orthogonally to the direction of maximum principal tensile stress; the constitutive matrix then becomes anisotropic, being now described with reference to local coordinates x' and y' (across and along the crack respectively)

$$\begin{bmatrix} \Delta\sigma'_x \\ \Delta\sigma'_y \\ \Delta\tau'_{xy} \end{bmatrix} = \begin{bmatrix} 0 & 0 & 0 \\ 0 & E & 0 \\ 0 & 0 & \beta G \end{bmatrix} \begin{bmatrix} \Delta\epsilon'_x \\ \Delta\epsilon'_y \\ \Delta\gamma'_{xy} \end{bmatrix} \quad (2.59)$$

A possible alternative for E in the above is the retention of $E/(1-\nu^2)$, for reasons that will be outlined subsequently in the discussion of the more general 3-D case (for $\nu = 0.2$, say, the difference between the two approaches gives a factor of only 1.04). As the matrix relation (2.59) is deemed to hold for all subsequent load steps (unless a second crack forms), such a description implies that the material has permanently lost its stiffness across the crack, not only in tension but also in compression. (The latter notion is an approximate but reasonable assumption in the case of *monotonic* loading, where any posterior crack closure — if it occurs — is localized and unlikely to affect significantly ultimate-load predictions.) It will be noticed that, although the stress-strain relationship along the crack corresponds to 'uniaxial' characteristics (but with values derived from properties along the crack for the biaxial conditions which existed just before cracking — in these biaxial conditions, it is evident that one of the principal stresses was tensile, otherwise, in theory at least, biaxial compression failure would lead to total loss of stiffness (i.e. in both directions) at that location), some (residual) shear stiffness exists between the faces of the crack. Its magnitude is only a fraction of the isotropic shear rigidity before fracture, and is determined by β , the so-called 'shear-retention factor' (SRF), which can take on any value between 0 and 1. The role of the SRF and the actual values to be assigned to it will be described subsequently.

The adoption of local coordinates following the directions orthogonal and parallel to the crack means that, before the relevant stiffness matrix (in the set of global axes) is formed, the anisotropic matrix $[\mathbf{D}]$ must be rotated in accordance with the standard formula involving the transformation matrix (see (B.5) in Appendix B). This requires the use of the angle $\bar{\theta}$ subtended between $\Delta\sigma'_x$ at the time of cracking and x (i.e. the angle defining the direction orthogonal to the crack).

Upon further loading of the structure, a second crack might form at the same Gauss-point location if the strength envelope is exceeded once again. In such circumstances, a comparison is first made between the angles subtended by both cracks with the x axis: if these are not near-coincident (if they are, second cracking is ignored), complete local material failure is deemed to have occurred as a result of the loss of load-carrying capacity in two non-parallel directions. All the coefficients of the constitutive matrix $[D]$ are then set to zero, although the βG term could still be retained for purposes of improving numerical stability (an option to be explored later, when 3-D problems are discussed).

Two-dimensional problems (axisymmetric case). An axisymmetric stress state leads essentially to a 2-D problem somewhat akin (but not identical) to the plane-strain situation, or the plane-stress case but with an additional hoop-stress component. With the assumption of perfect rotational symmetry implicit, this additional hoop stress is also a principal stress component and, as such, has no shear associated with it. The isotropic incremental relationship between stresses and strains in a global set of axes before cracking can, therefore, be derived directly from (2.44) by setting the two relevant shearing-stress components to zero

$$\begin{bmatrix} \Delta\sigma_r \\ \Delta\sigma_a \\ \Delta\sigma_h \\ \Delta\tau_{ra} \end{bmatrix} = \frac{E(1-\nu)}{(1+\nu)(1-2\nu)} \begin{bmatrix} 1 & \frac{\nu}{1-\nu} & \frac{\nu}{1-\nu} & 0 \\ \frac{\nu}{1-\nu} & 1 & \frac{\nu}{1-\nu} & 0 \\ \frac{\nu}{1-\nu} & \frac{\nu}{1-\nu} & 1 & 0 \\ 0 & 0 & 0 & \frac{1-2\nu}{2(1-\nu)} \end{bmatrix} \begin{bmatrix} \Delta\epsilon_r \\ \Delta\epsilon_a \\ \Delta\epsilon_h \\ \Delta\gamma_{ra} \end{bmatrix} \quad (2.60)$$

where the subscripts 'r' and 'a' stand for radial and axial directions (corresponding to the plane-stress axes used in expression (2.58)) while the 'h' subscript refers to the hoop direction. Figure 2.18 shows the global axes in axisymmetric analysis by reference to a typical 'slice' bounded by two radial planes. Once again, E and ν are tangent material properties corresponding to the current state of stress.

Following a similar approach to that for the plane-stress case, the state of stress changes from axisymmetric to biaxial after the first crack, and from biaxial to uniaxial after the formation of a second crack at the same integration point. However, two different types of cracking can now occur, namely circumferential cracks (Fig. 2.18(a)), and radial cracks (Fig. 2.18(b)). The first crack type affects the structure along a circumferential path inclined at a constant angle to the horizontal/vertical plane(s); such cracks

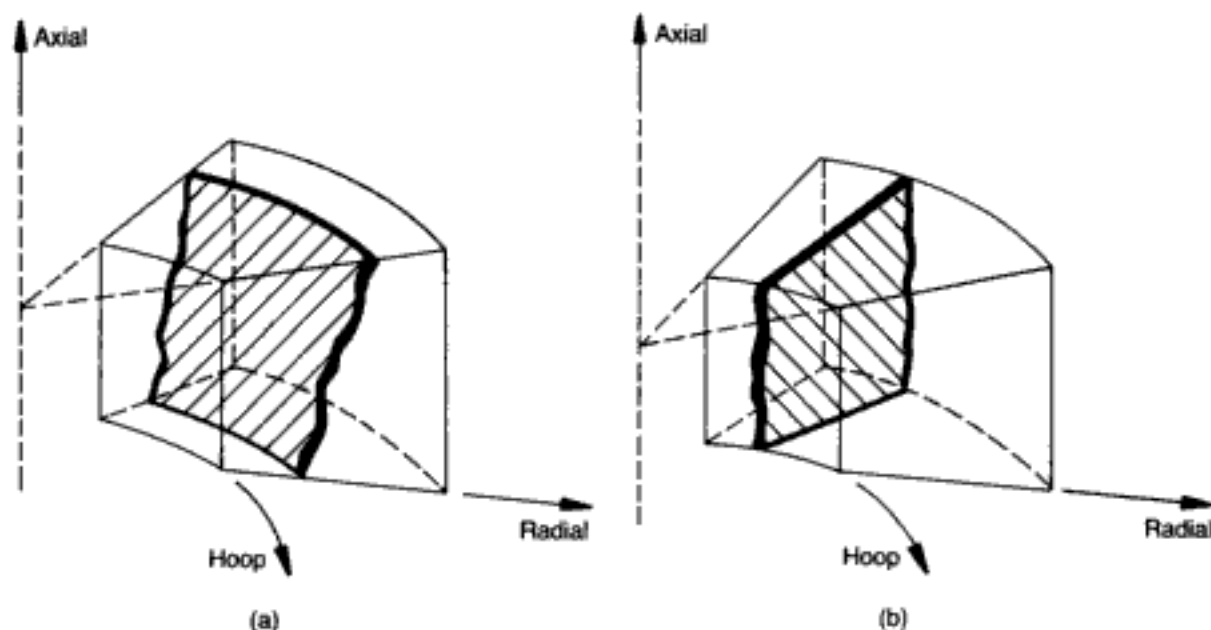


Fig. 2.18.
Axisymmetric
cracking: (a) circum-
ferential crack;
(b) radial crack

are similar to those that occur in plane-stress problems. Radial cracks are caused by an excessive tensile hoop stress and are, therefore, equivalent to an infinite number of fissures extending along directions connecting (radially) the outer circumference to the vertical axis of rotational symmetry; no angle is associated with them since all hoop differential displacements are zero; nor is there an SRF across radially cracked planes, as these are planes of symmetry that make any 'hoop' shear stresses inadmissible.

Four different combinations of radial and circumferential cracks at the same integration point are possible, each one involving a specific form of \mathbf{D} -matrix anisotropy for post-cracking treatment. Clearly, whenever *one circumferential crack* occurs, a rotational transformation (see (B.5) in Appendix B) is necessary in order to obtain the \mathbf{D} -matrix in global coordinates. The four possible crack combinations are listed below, together with their corresponding constitutive matrices. (The third and fourth rows of these always denote hoop and shear stresses respectively, while, when circumferential cracking is involved, rows one and two correspond to the directions across and along the crack respectively.)

Case 1. One circumferential crack (Fig. 2.19(a); coordinate transformation is needed):

$$\begin{bmatrix} 0 & 0 & 0 & 0 \\ 0 & E' & \nu E' & 0 \\ 0 & \nu E' & E' & 0 \\ 0 & 0 & 0 & \beta G \end{bmatrix} \quad (2.61)$$

where

$$E' = \frac{E}{1-\nu^2} \quad (2.62)$$

(or, alternatively, the non-zero coefficients E' and $\nu E'$ could retain their previous form, i.e. $E(1-\nu)/[(1+\nu)(1-2\nu)]$ and $\nu E(1-\nu)/[(1+\nu)(1-2\nu)]$ respectively, as will be explained subsequently — see the section on 3-D problems).

Case 2. One radial crack (Fig. 2.19(b); no coordinate transformation is needed):

$$\begin{bmatrix} E' & \nu E' & 0 & 0 \\ \nu E' & E' & 0 & 0 \\ 0 & 0 & 0 & 0 \\ 0 & 0 & 0 & G \end{bmatrix} \quad (2.63)$$

Case 3. One circumferential crack and one radial crack (Fig. 2.19(c); coordinate transformation is needed):

$$\begin{bmatrix} 0 & 0 & 0 & 0 \\ 0 & E & 0 & 0 \\ 0 & 0 & 0 & 0 \\ 0 & 0 & 0 & \beta G \end{bmatrix} \quad (2.64)$$

Case 4. Two circumferential cracks (Fig. 2.19(d); no coordinate transformation is needed):

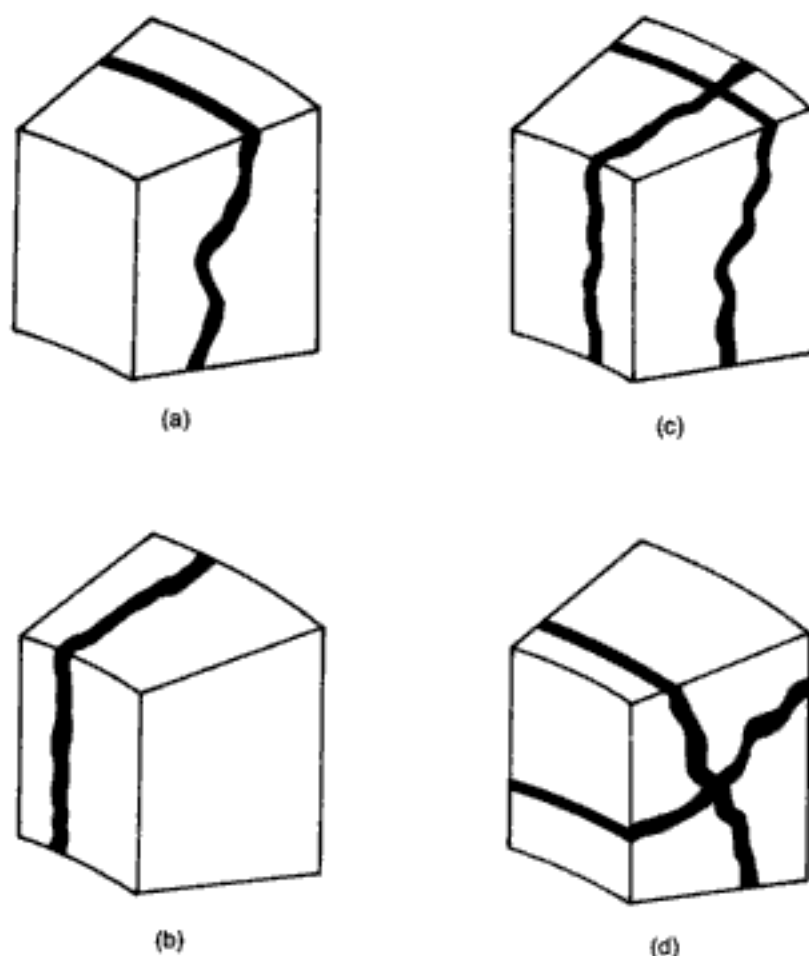


Fig. 2.19. Combinations of axisymmetric cracks:⁵⁴ (a) one circumferential crack; (b) one radial crack; (c) one circumferential and one radial cracks (d) two circumferential cracks

$$\begin{bmatrix} 0 & 0 & 0 & 0 \\ 0 & 0 & 0 & 0 \\ 0 & 0 & E & 0 \\ 0 & 0 & 0 & 0 \end{bmatrix} \quad (2.65)$$

where, once again, the retention of βG is optional (see 3-D case below).

Finally, the local-failure criterion is similar to that for the plane-stress case, except that a third crack is required to cause complete loss of stiffness at the given Gauss point. When this occurs, all coefficients of $[D]$ become zero (with the possible exception of βG).

Three-dimensional problems. The 3-D isotropic D -matrix relating increments of stresses and strains before cracking is given by (2.44). When the state of stress at a Gauss point reaches the triaxial envelope involving at least one principal tensile component for the first time, a crack plane is assumed to form in the direction orthogonal to the maximum principal tensile stress. As explained previously, such a tensile stress is set to zero and transformed into equivalent unbalanced forces (to be distributed throughout the surrounding zones), and the adopted incremental constitutive relationships in local axes (defined with respect to the cracked plane — see the system (x', y', z') in Fig. 2.20) are subsequently given the following matrix expression

$$\begin{bmatrix} \Delta\sigma'_x \\ \Delta\sigma'_y \\ \Delta\sigma'_z \\ \Delta\tau'_{xy} \\ \Delta\tau'_{xz} \\ \Delta\tau'_{yz} \end{bmatrix} = \begin{bmatrix} 2G + \mu & \mu & 0 & 0 & 0 & 0 \\ \mu & 2G + \mu & 0 & 0 & 0 & 0 \\ 0 & 0 & 0 & 0 & 0 & 0 \\ 0 & 0 & 0 & G & 0 & 0 \\ 0 & 0 & 0 & 0 & \beta G & 0 \\ 0 & 0 & 0 & 0 & 0 & \beta G \end{bmatrix} \begin{bmatrix} \Delta\epsilon'_x \\ \Delta\epsilon'_y \\ \Delta\epsilon'_z \\ \Delta\gamma'_{xy} \\ \Delta\gamma'_{xz} \\ \Delta\gamma'_{yz} \end{bmatrix} \quad (2.66)$$

where the third local axis (z') is orthogonal to the crack plane and the first and second Cartesian axes (x', y') lie on it (see Fig. 2.20). (It should be noted that, as in previous instances, the above stress and strain increments are due to *subsequent* load increments and, hence, even though they are computed by reference to the principal directions existing *at* cracking, the total stresses and strains in such directions are no longer principal.) The constitutive coefficients at the relevant Gauss point are set equal to the corresponding coefficients of the last uncracked D -matrix (under triaxial conditions) at that point, even though it could be envisaged, for zones of compression with one crack, that the use of biaxial stress-strain laws on planes parallel to the crack might be more rational (in a *smear*-crack model) until a second crack forms; however, this represents too refined an approach, especially in view of the lack of knowledge on the constitutive relations for

cracked concrete, as pointed out earlier. Besides, the presence of the βG terms (representing residual shear stiffness across the plane of the crack) implies that the conditions along the crack's plane are not quite plane-stress ones, but that the region still represents some sort of 'continuum'. Therefore, it is for these reasons that the coefficients $2G + \mu$ and μ may remain unchanged as (2.44) becomes (2.66). (The difference between (2.66) and (2.58) consists of the factors $(1 - \nu)^2 / (1 - 2\nu)$ (which converts $E / (1 - \nu^2)$ into $2G + \mu$) and $(1 - \nu) / (1 - 2\nu)$ (that converts $\nu E / (1 - \nu^2)$ into μ): taking, for example, $\nu = 0.2$, the first factor is only 1.07 while the second is considerably larger (1.33); nevertheless, the final structural predictions are insensitive to either approach once a crack forms since the accurate description of the stiffness of cracked regions once fracture has taken place is relatively unimportant.) Such reasoning also explains earlier remarks on 2-D problems, when attention was repeatedly drawn to the option of retaining the same form for the various material coefficients throughout the cracking sequence.

If the state of stress at a given Gauss point reaches the triaxial envelope in tension a second time, then a second crack plane is

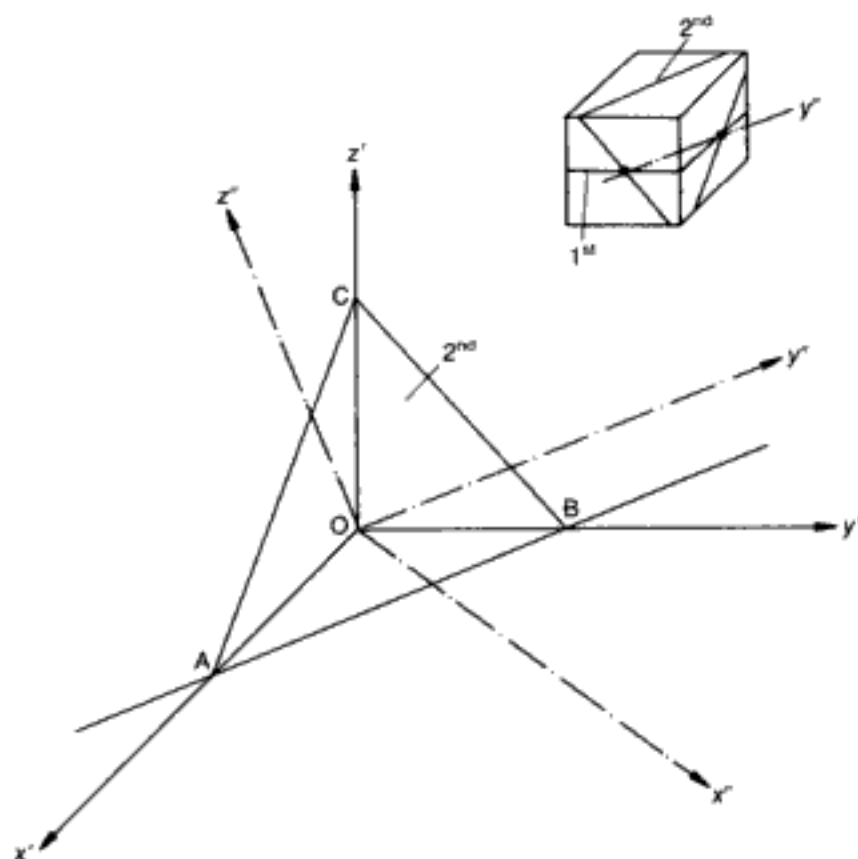


Fig. 2.20. Local axes for a Gauss point with one and/or two cracks (first crack parallel to plane OAB, second crack parallel to plane ABC; it should be noted that, following the second crack, y'' defines the direction of the only remaining direct stiffness)⁵⁶

assumed to form (unless the two planes of fracture are near-coincident). This new crack plane is now orthogonal to the current maximum tensile principal stress and, consequently, is not necessarily orthogonal to the first crack plane. The combination of the two fracture planes only leaves stiffness in the direction of the intersection of both planes (direction y'' or AB in Fig. 2.20). As for the one-crack case, some residual shear stiffness has to be kept in order to improve the conditioning of the cracked stiffness matrices. Explicitly, the incremental constitutive relationships adopted for this case are as follows

$$\begin{bmatrix} \Delta\sigma_x'' \\ \Delta\sigma_y'' \\ \Delta\sigma_z'' \\ \Delta\tau_{xy}'' \\ \Delta\tau_{xz}'' \\ \Delta\tau_{yz}'' \end{bmatrix} = \begin{bmatrix} 0 & 0 & 0 & 0 & 0 & 0 \\ 0 & 2G+\mu & 0 & 0 & 0 & 0 \\ 0 & 0 & 0 & 0 & 0 & 0 \\ 0 & 0 & 0 & \beta G & 0 & 0 \\ 0 & 0 & 0 & 0 & \beta G & 0 \\ 0 & 0 & 0 & 0 & 0 & \beta G \end{bmatrix} \begin{bmatrix} \Delta\epsilon_x'' \\ \Delta\epsilon_y'' \\ \Delta\epsilon_z'' \\ \Delta\gamma_{xy}'' \\ \Delta\gamma_{xz}'' \\ \Delta\gamma_{yz}'' \end{bmatrix} \quad (2.67)$$

where the new axes are now defined by the double primes in Fig. 2.20. In line with previous discussion, $2G+\mu$ is retained at present for the second diagonal term instead of simply E (for $\nu=0.2$, for example, these two terms differ only by a factor of 1.1).

If the state of stress reaches the failure envelope either in compression (i.e. all three principal stresses — present in the global axes because of the 'continuum' implied by the βG factors — being compressive) or for a third time in tension, two options may be considered. The first option is to impose a zero constitutive matrix, i.e. a complete loss of stiffness in all directions, and the second is to use a matrix with only residual values of βG for the three shear-stress components. The latter option arises again for the same reason as for one-crack and two-crack cases, its chief aim being the improvement of numerical stability. A comparison between these options will be presented in Chapter 4, where the corresponding **D**-matrices will be referenced as Z3 and G3, respectively.

As in 2-D modelling, the matrices in (2.66) and (2.67) are valid only in the local set of axes shown in Fig. 2.20 and, hence, they require a transformation to global coordinates (see Appendix B). Therefore, all the coefficients of the constitutive **D**-matrix for the stress-strain relationships for one-crack and two-crack Gauss points with respect to 3-D global axes (x, y, z) will, in general, be non-zero. On the other hand, both Z3 and G3 matrices corresponding to a third cracking (or, theoretically, full compressive failures at any stage) are clearly isotropic.

The above outline completes the description of cracking at a single Gauss point. The updating of the stiffness properties in a structure when several cracks occur simultaneously at various

locations upon incrementing the load will be considered in subsequent chapters as the need for adequate crack-propagation procedures and stiffness-updating strategies becomes evident.

2.4.3.4. The shear-retention factor: its role on the conditioning of stiffness matrices and actual physical evidence

In section 2.4.2.4, it was shown how the use of numerical integration leads to expression (2.46) for the element stiffness matrix. It was also pointed out there that the 3×3 block of coefficients of the \mathbf{k} -matrix relating to the degrees of freedom of any pair of nodes (block $[\mathbf{k}]^U$ in (2.47)) is the addition of the contributions of the n Gauss points of the finite element ($[\mathbf{k}]^U = \sum_{i=1}^n [\mathbf{k}]_i^U$). Although these blocks are not calculated in practice, such blocks could be obtained by means of expression (2.48).

Consider now the contribution of a Gauss point at which one crack has appeared. If, for convenience, it is assumed that the local set of axes (fixed to the crack plane as shown in Fig. 2.20) coincide with the global set of axes, substitution of the adopted \mathbf{D} -matrix (as given by (2.66)) into expression (2.48) leads to the following expression for block $[\mathbf{k}]_i^U$

$$[\mathbf{k}]_i^U = w_i J_i \begin{bmatrix} a_1 n_1 m_1 + G(n_2 m_2 + \beta n_3 m_3) & a_2 n_1 m_2 + G n_2 m_1 & \beta G n_3 m_1 \\ a_2 n_2 m_1 + G n_1 m_2 & a_1 n_2 m_2 + G(n_1 m_1 + \beta n_3 m_3) & \beta G n_3 m_2 \\ \beta G n_1 m_3 & \beta G n_2 m_3 & \beta G(n_1 m_1 + n_2 m_2) \end{bmatrix}_i \quad (2.68a)$$

where, for clarity, $n_1, n_2, n_3 \equiv b_{x1}, b_{y1}, b_{z1}$; $m_1, m_2, m_3 \equiv b_{x2}, b_{y2}, b_{z2}$; $a_1 \equiv 2G + \mu$; $a_2 \equiv \mu$.

If, next, a zero value for β is assumed, the contribution of the Gauss point to the $[\mathbf{k}]^U$ block of the stiffness matrix of the element reduces to the following

$$[\mathbf{k}]_i^U = w_i J_i \begin{bmatrix} a_1 n_1 m_1 + G n_2 m_2 & a_2 n_1 m_2 + G n_2 m_1 & 0 \\ a_2 n_2 m_1 + G n_1 m_2 & a_1 n_2 m_2 + G n_1 m_1 & 0 \\ 0 & 0 & 0 \end{bmatrix}_i \quad (2.68b)$$

This expression shows formally that, if $\beta = 0$ and the local axes coincide with global axes, a one-crack Gauss point makes no contribution to the coefficients that relate forces and displacements in the third global direction; this is a consistent consequence of the complete loss of stiffness in the direction orthogonal to the crack plane that the \mathbf{D} -matrix in (2.66) implies. It follows, therefore, from (2.68) that, in the absence of a shear-retention factor, and for an element with all the integration points cracked in parallel planes, the \mathbf{D} -matrix in (2.66) leads to either zero values

Table 2.1. Number of zero eigenvalues of brick-element stiffness matrix (plain concrete, aspect ratio $1 \times 1 \times 1$).⁸² It should be noted that six of the zero eigenmodes always relate to basic rigid-body motions

Number of parallel cracks	SRF	Quadratic 3-D element		
		Serendipity (20 nodes) $2 \times 2 \times 2$ $3 \times 3 \times 3$		Lagrangian (27 nodes) $3 \times 3 \times 3$
None	—	12	6	6
All Gauss points	0.1	20	10	10
All Gauss points	0	36	29	36

in the diagonal of the element stiffness matrix (if the cracks are parallel to one of the global planes) or to ill-conditioning (otherwise). In practical situations, it is common to have whole concrete FEs in tensile zones so that all their integration points may crack. Admittedly, such cracks will seldom be exactly parallel. However, small pivots must be expected. This explains why the use of a non-zero β is *numerically* essential for brittle modelling regardless of its physical meaning.⁸² The present argument is reinforced by some eigenvalue tests of the \mathbf{k} -matrix for a plain-concrete element, modelled by brick elements of the serendipity (HX20, used with both under-integration ($2 \times 2 \times 2$) and full integration ($3 \times 3 \times 3$)) and Lagrangian (HX27) types. The results are summarized in Table 2.1. (The results in Table 2.1 are, of course, independent of the adopted set of axes, as the eigenvalues of a \mathbf{K} -matrix are invariants, since any \mathbf{K} -matrix is a second-order tensor.) It is evident that the number of mechanisms increases as one goes from the uncracked to the cracked ($\beta=0.1$) case and, significantly, this increase is even more drastic when β is reduced from 0.1 to 0. (It may also be of interest to note that the ratio of the mechanisms for the cracked ($\beta=0.1$) and uncracked FEs is the same for all three FEs used and that, therefore, no conclusion about their relative performance in the present context of numerical stability can be reached.)

As mentioned in section 2.3.2, the mechanisms of the stiffness matrix are those modes of deformation of the DOF of the FE that do not require any strain energy to occur.⁶² The elastic strain energy U associated with a given set of nodal displacements \mathbf{d} is given by

$$U = \frac{1}{2} \mathbf{f}^T \mathbf{d} = \frac{1}{2} \mathbf{d}^T [\mathbf{k}] \mathbf{d} \quad (2.69)$$

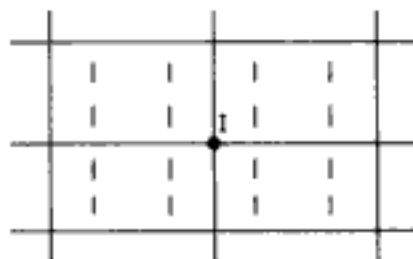
where \mathbf{f} is the corresponding set of nodal forces (i.e. $\mathbf{f} = [\mathbf{k}] \mathbf{d}$, as in (2.20)). Therefore, if \mathbf{d} is an eigenvector of the element stiffness matrix (i.e. $[\mathbf{k}] \mathbf{d} = a \mathbf{d}$) of zero eigenvalue, it follows from (2.69) that $U = 0$. Hence, the number of zero eigenvalues

is the number of mechanisms, and their corresponding eigenvectors are the mechanisms of the element stiffness matrix. Since a solid admits three translations and three rotations without straining (rigid-body motions), it is usually considered that the \mathbf{k} -matrix of a brick FE should have six mechanisms (six zero eigenvalues); and any mechanisms in excess of six are referred to as spurious mechanisms. As may be seen in Table 2.1, even uncracked under-integrated elements present some spurious mechanisms; nevertheless, they are often regarded as better elements than their fully-integrated counterparts.⁸³ However, as cracking sets in, the likelihood of (additional) spurious mechanisms increases, especially if the SRF is set to zero; and it is, therefore, to minimize this increase that the brittle nature of the material modelling requires the assignment of a non-zero value to β . (Thus, for example, Hand *et al.*⁸⁴ (who referred to spurious mechanisms simply as 'unstable cracked configurations') pointed out empirically that a zero SRF could not be used. In this respect, expressions (2.68) give a formal rational explanation for this, irrespective of the order of integration.)

With regard to the conditioning of the \mathbf{K} -matrix of the structure, the decay of its coefficients tends to be less important than that of the \mathbf{k} -matrix of the cracked elements, since the presence of adjacent uncracked elements and/or steel elements improves the numerical conditioning. Nevertheless, Fig. 2.21 shows an example in which the horizontal displacement of a node is rather loosely connected to the structure ($\beta \neq 0$) or fully unconnected ($\beta = 0$). As will be discussed in Chapter 4, situations similar to the above may give rise to early divergences as a result of the propagation of spurious mechanisms.

What is the value actually assigned to β ? Before answering this question, it should be pointed out that the SRF is a parameter clearly associated with the notion of 'aggregate interlock'. Now, contrary to the widely-held view that 'aggregate interlock' plays an important role in transferring shear across cracked areas, experimental evidence points to the opposite conclusion.⁵² The latter may be reinforced by FE modelling itself coupled with earlier — but, originally, misinterpreted — experimental data,⁵¹ and this will be presented in Chapter 3. Therefore, a large value of β (say between 0.5 and 1) is physically unrealistic; moreover, its effect would be to (spuriously) attract load on account of the large (fictitious)

Fig. 2.21.
Disconnection of the horizontal DOF of node 1 due to (near) parallel cracking of surrounding FEs⁵⁶



stiffness associated with it (the numerical implications of which will be discussed in Chapter 4). On the other hand, it has just been shown that zero or small values (say $\beta \sim 0.01$) of SRF lead to ill-conditioning of the stiffness matrices of the cracked elements. Results of numerical experimentation^{54,85} — to be adduced in Chapter 3 — suggest that, in general, analytical predictions are fairly insensitive to values of the SRF in the range of $0.1 \leq \beta \leq 0.5$. As a consequence, therefore, it appears that a suitable value for β is around 0.1, which is in keeping with the negligible effect of 'aggregate interlock', on the one hand, while meeting the constraints imposed by the requirements for numerical stability, on the other.

2.4.4. Description of the reinforcing steel

On the basis of deformational and yield characteristics of the steel reinforcement (section 1.4.3), the constitutive properties and failure criterion for the FEs representing the steel bars may readily be imposed. This is done by correcting the stress values (in accordance with the initial-stress technique — section 2.4.2.5) so as to satisfy the constitutive relationships, providing updated stiffness properties (E_t) corresponding to the current state of stress, and performing failure-criterion checks based on the ultimate strain value. As explained in Chapter 1, perfect plasticity is never imposed on the final branch of the stress-strain plot even in the case of mild steels which approximate such an extreme condition (in terms of average, but not actual, strains, bearing in mind the dynamic nature of steel yielding⁸⁶); instead, a small, but finite, value is given to E right up to the ultimate strain ϵ_u .

In what follows, a brief outline of the incremental relations for steel is given by reference to the more general 3-D case. Additionally, the interaction between steel and concrete is considered by reference to bond and tension stiffening, and, here, it will be shown how the present simplified treatment — in the context of smeared modelling — avoids the unjustifiably laboured efforts often adopted in respect of these phenomenological parameters.

2.4.4.1. Incremental relations for the three-node uniaxial element

For a curved-line element oriented with respect to the (x, y, z) set of Cartesian global coordinates, let s represent the length measured along its axis, so that $t = (dx/ds, dy/ds, dz/ds)$ is then the tangent vector. On the assumption that the displacements are kept small, the longitudinal displacement, u_s , can be obtained from the scalar product of the tangent vector and the vector of global displacements $u = (u_x, u_y, u_z)$

$$u_s = t \cdot u \quad (2.70)$$

Since only the axial stiffness of the reinforcement is deemed to be of significance, the single strain component of interest is

Hidden page

Finally, stress conditions give rise to residual nodal forces which are calculated as follows

$$\Delta \mathbf{f}_r = - \int ([\mathbf{b}]^T \Delta \sigma_r) (A_s) (ds/d\xi) d\xi \quad (2.76)$$

As for the brick and the 2-D elements, expressions (2.75) and (2.76) are calculated by means of Gaussian integration.

2.4.4.2. Concrete–steel interaction

This comprises two main aspects.

Bond. The question of bond modelling between steel and concrete is often given prominence in the course of development of an FE model for structural concrete. Symptomatic of this attitude are the early attempts to analyse concrete structures by FEs, in which spring linkages were introduced to mimic bond slip through linear⁷⁷ or nonlinear⁸⁷ laws. Although many subsequent investigations were based on the simplifying assumption of perfect bond (e.g. reference 67), much effort is still being expended in implementing bond-slip laws. In the past, such ‘laws’ have ranged from arbitrarily assigned ‘spring’ constants to ‘theoretical’ relationships, the latter sometimes incorporating a certain degree of experimental feedback from the scarce, limited, and often dubious data currently available.

The present model adopts the perfect-bond assumption, implicit in the coincidence, throughout the analysis, of the steel-element nodes with the nodes of the corresponding (adjacent) concrete-element(s) edges. (Since all elements are of the second order and a unique parabolic interpolation can be adjusted between the three nodes of a given edge, the coincidence between steel and concrete-element edges guarantees the same displacements (i.e. perfect bond) for concrete and steel at the same location.) Three arguments may be adduced for such an approach.

First, the notion of perfect bond is compatible with the thinking behind the smeared-crack model, in the sense that detailed description of localized effects is avoided. In this respect, it is important to stress that the earlier mention of bond loss between steel and concrete in the vicinity of a crack (see section 2.4.3.1 and Fig. 2.16(b)) does not contradict the perfect-bond assumption since the smeared-crack approach spreads the effect of cracking to such an extent that integration points in bar elements represent, generally, bar lengths which usually far exceed the localized regions where bond slip occurs, thus precluding a minute account of the steel–concrete interaction.

Secondly, reliable experimental information of wide applicability on bond-slip characteristics is, as suggested above, not available. In fact, experiments attempting to determine bond–stress against slip–displacement curves exhibit, typically, a large scatter of data as regards both individual investigations (see, for example, reference 88) and the overall picture that emerges from a

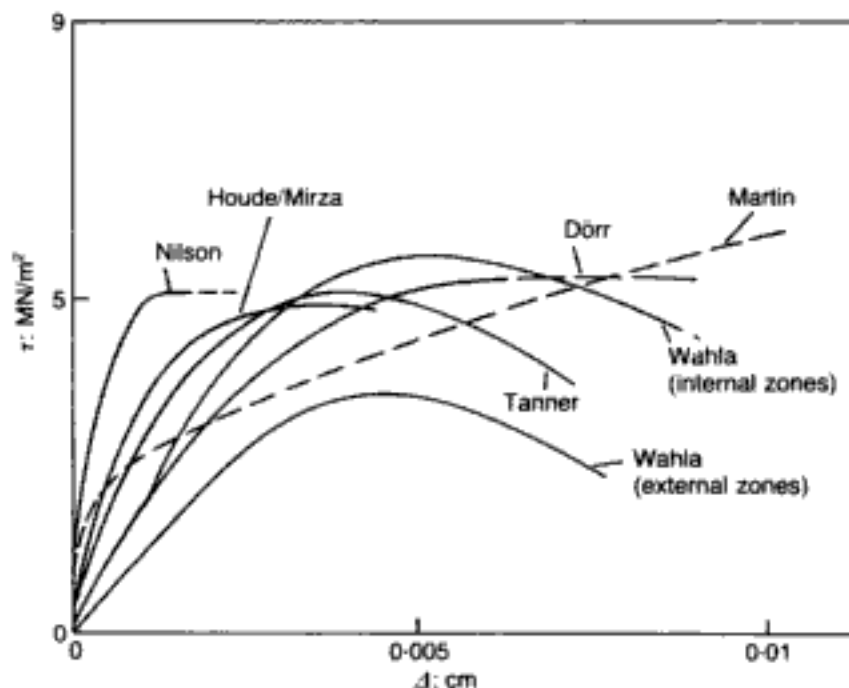


Fig. 2.22. Some of the proposed bond-stress versus slip-displacement curves^{56,89}

comparison of characteristics proposed by various authors (see Fig. 2.22, taken from González Vidosa's adaptation⁵⁶ of the relevant data in the ASCE Task Committee's state-of-the-art report on the FE analysis of RC structures⁸⁹). It is not surprising, therefore, that theoretical bond-slip curves used for nonlinear analysis often differ significantly from each other, as may be seen, for instance, by reference to the characteristics adopted by Nilson⁸⁷ and Labib and Edwards,⁹⁰ depicted in Figs 2.23(a) and 2.23(b) respectively. When such variability and the fact that slip transverse to the reinforcement is governed by different characteristics are considered, it is evident that any refinement implicit in the departure from the perfect-bond condition cannot be accepted with a sufficient degree of confidence.

Thirdly, and most importantly, there is the actual value of the bond stress itself. On the basis of Fig. 2.22 (and, of course, Fig. 2.23(a)), an order of magnitude for the maximum bond stress of around 5 N/mm^2 appears to be relevant. For the failure envelope in tension (depicted in Fig. 1.59) to reach such a value, the concrete strength f_c must exceed, approximately, the 80 N/mm^2 mark. It is evident, therefore, that the concrete in the vicinity of the concrete-steel interface will usually have cracked in tension before the maximum bond stress could be developed. Similar conclusions may be reached by reference to the characteristic of Fig. 2.23(b), which suggests that no slip occurs below a bond stress of $8\sqrt{f_c}$ (with f_c in lb/in^2) or, equivalently, $8\sqrt{(f_c)/12}$ (with f_c in N/mm^2).⁹¹ This implies that, for slip to take place, the bond stress must be around twice the tensile strength of concretes with an f_c of around $20\text{--}30 \text{ N/mm}^2$; and, once again, parity between maximum bond stress and tensile strength is attained only in the high-strength concrete range of $f_c \sim 80 \text{ N/mm}^2$ and above. Hence,

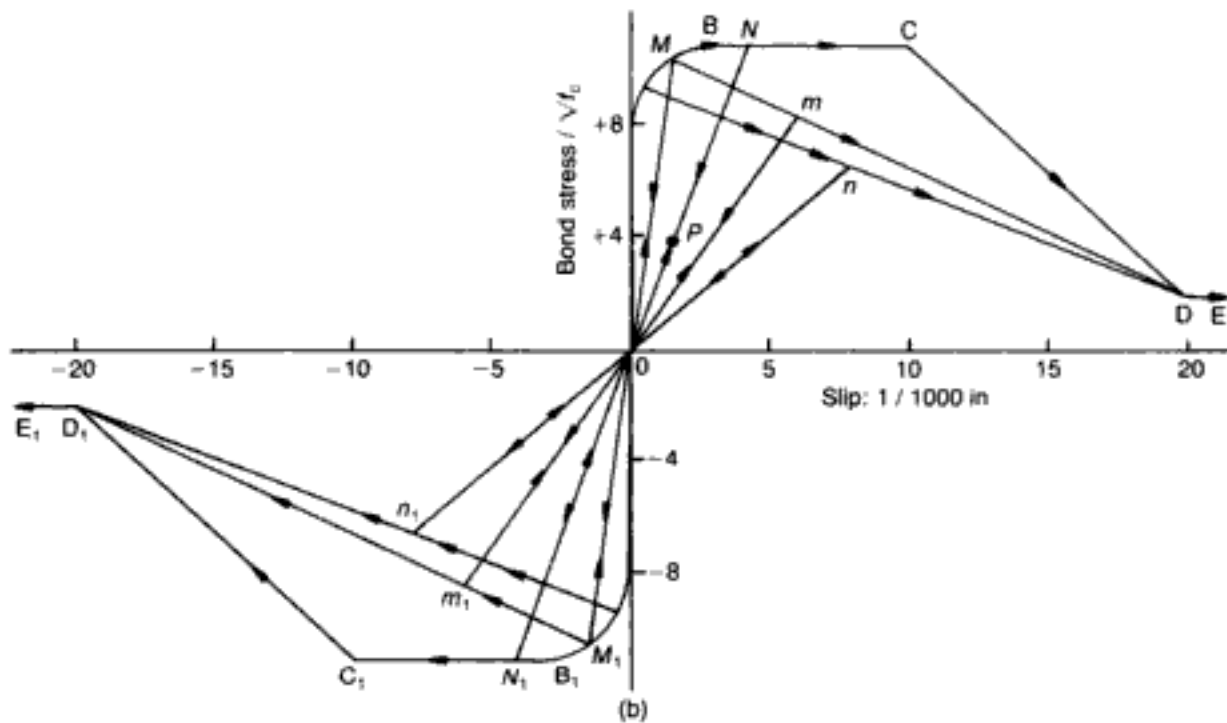
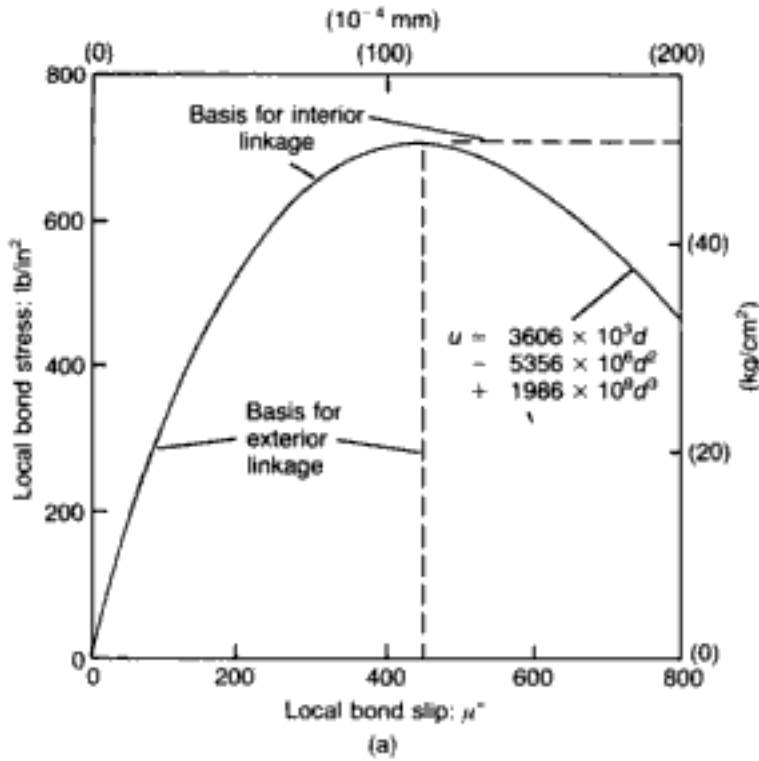


Fig. 2.23. Some bond-slip curves used in nonlinear FE analysis: (a) Nilson;⁸⁷ (b) Labib and Edwards⁹⁰

it may be concluded that, for most structural concretes, tension failure occurs in the reinforcement region before the development of maximum bond stresses there, so that the assumption of perfect bond in the analysis is justified on the basis that there is no need to model concrete once macrocracking has caused it to lose its stiffness. (In fact, since there is no guarantee that the bond-slip models in Figs 2.22 and 2.23 necessarily hold for $f_c > 80 \text{ N/mm}^2$, the present argument justifying perfect bond might

even be extended to encompass the upper range of high-strength concretes.)

Tension stiffening. In the present model, once cracking in the vicinity of, and orthogonal to, the reinforcement takes place, the stiffness of the concrete is set to zero, as for the case of plain concrete. Such a simplification ignores the so-called 'tension stiffening' effect, which may be illustrated by reference to a steel bar encased in concrete and subjected to tension, as depicted schematically in Fig. 2.24. The stiffness of such an arrangement exceeds that of the steel alone even after macrocracking, which

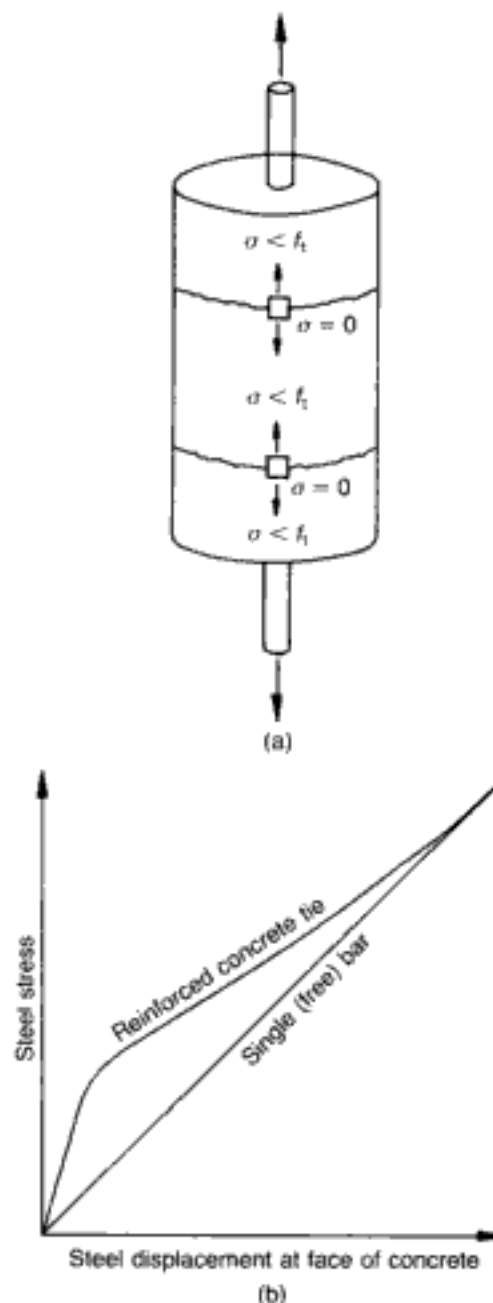


Fig. 2.24. RC tie subject to tension: (a) steel bar encased in concrete with the latter continuing to carry load away from the macrocracks; (b) 'tension stiffening' represented by the difference in stiffness of the two systems, namely the composite structure and the bare bar respectively

points to the fact that the concrete in between cracks (where the stresses σ are below f_t , the tensile strength) contributes to the overall stiffness of the system, as the tensile stresses are transferred from steel to concrete by bond action. Clearly, with progressive cracking and bond destruction, the stiffness of the RC tie tends towards that of the bare bar. Specific plots following the generic trend of the one shown in Fig. 2.24(b) may be found in a number of references, some of them based on analytical modelling (e.g. the short eccentric tensile member analysed in reference 87), others derived from actual experiments (e.g. the tension test described in reference 92).

The neglect of tension stiffening is most unlikely to influence ultimate-load predictions,^{56,71,93} especially for structures exhibiting ductile behaviour, for which the 'tie' effect has nearly been reduced to that of the steel acting alone (see Fig. 2.24(b)). Deflection predictions might be more sensitive to such a simplification, but the complexity that would result if concrete elements adjacent to steel bars were treated differently from 'plain concrete' elements elsewhere (with consequent problems of mesh (re)definition) would not justify the extra refinement. Therefore, while recognizing that local stress redistributions could be affected by the lack of allowance for tension stiffening, this simplification appears to be justified on the grounds of both ease of modelling and the requisite accuracy of predictions (as will be seen in subsequent chapters).

Finally, a small but pertinent point on the terminological confusion that is often encountered in the literature seems called for. Models for the tensile characteristics of plain concrete which do not recognize the brittle nature of the material but use descending branches of the type shown in Fig. 2.25 (which, if at all present

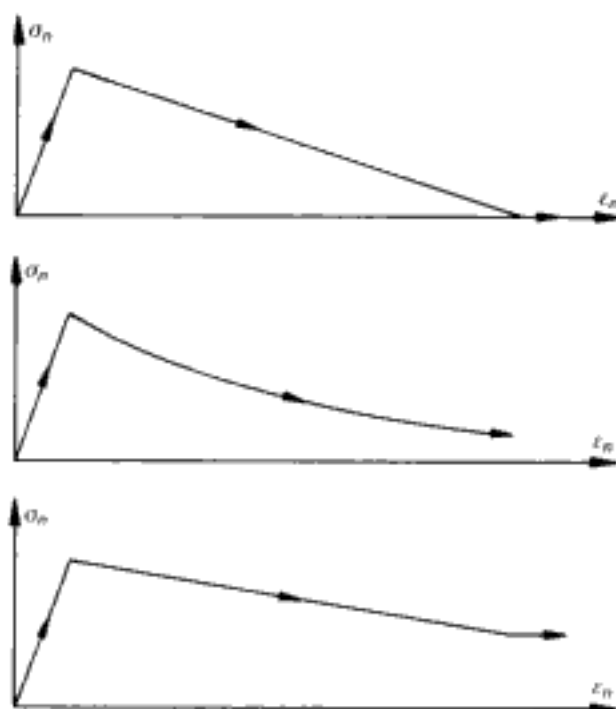


Fig. 2.25. Typical 'strain softening' models for the direction normal (orthogonal) to a crack plane⁵⁶

in actual material tests, are likely to be caused by the interaction between testing device and specimen, as pointed out in section 1.2) sometimes have these descending (i.e. 'strain softening') characteristics referred to as 'tension stiffening'. The reason for this appears to be that, historically, the concepts associated with 'tension stiffening' proper (as illustrated in Fig. 2.24) were also gradually — and, it would seem, largely imperceptibly — adopted for plain concrete. The possible confusion — or, at least, terminological interchangeability — of what is implied by 'tension stiffening' should be borne in mind so as to distinguish between two quite distinct phenomenological notions.

2.5. An overview of material and procedural factors influencing finite-element predictions

Following its appearance in the mid 1950s,⁹⁴ the FE method has become the most widely-used numerical technique in engineering analysis. A decade after its inception, this powerful computational tool began to be applied to the nonlinear analysis of concrete structures.^{77,81} However, despite the relatively rapid proliferation of works in this area by the early 1980s,⁸⁹ it was quickly recognized that the use of nonlinear FE packages for structural concrete was seldom adopted in design,⁹⁵ in spite of the gradual — but ever widening — acceptance of the limit-state philosophy in codes of practice; and, now, more than a decade later, the attitude of the practising engineer remains largely unchanged. The main reason for this appears to be the general lack of confidence in the overall reliability of the predictions of the various FE models proposed for concrete, as most of these are notoriously deficient with regard to evidence of their applicability, namely the assurance with which they may be used to analyse arbitrary structural forms rather than the specialized structure(s) for which they have been devised and/or against which their predictions were 'tuned' or simply tested. Such an outcome stems from three major factors. First, there is often scant attention given to the true response of concrete at the material level, either because of little regard to actual experimental data or on account of dubious interpretation of experimental results in an attempt to fit preconceived constitutive theories: it is to overcome this serious shortcoming that special care was taken in Chapter 1 to outline a realistic modelling of material behaviour, based purely on empirical data obtained through the testing of concrete under generalized, triaxial and — above all — *definable* stress conditions; and a signal advantage of the material model is the fact that both failure and constitutive laws require only a single parameter (f_c) for their full definition which, in addition to being readily obtainable, presents less scatter than any other material characteristic. Secondly, most of the numerical packages proposed to date tend to be lacking in a thorough study of their *objectivity*, namely of the effect on predictions of changes in the various parameters that made up the basic model; while some of these parameters have been discussed

already and others are to be considered in subsequent chapters, all of them will be enumerated in this section. Thirdly, many of the existing packages are also notoriously deficient with regard to their *generality*, i.e. their applicability to arbitrary structural forms rather than to the specialized structure(s) for which they have been devised and/or against which their predictions were tested: that the present FE model does possess such a feature will become apparent through a study of the wide range of problems described in Chapters 3 and 4.

In the evaluation of the objectivity of the model, those components or parameters of the analysis may be distinguished on which there is a broad agreement from others on which there is no obvious general consensus at this stage of development (see, for example, reference 56). In the first category, the following can be included: the two well-established techniques of crack-modelling, namely smeared and discrete cracking; the use of residual forces so as to follow the nonlinear constitutive relations while adhering to the equilibrium requirements of the structure; the strength envelopes for concrete under multiaxial stress conditions; and the nonlinear stress–strain relations *up to about failure*. Clearly, these well-established model components are of a basic or ‘primary’ nature on account of their cardinal significance to successful numerical analysis. By contrast, many of the components making up the second category of parameters, which are often still the object of widely differing views, sometimes tend to be regarded as being of secondary importance although some of them may, in fact, play a key role in certain situations. In any case, a rigorous study of a model’s objectivity requires that careful consideration should be given to these ‘secondary’ parameters, although their large number precludes an exhaustive investigation of each one of them. Such ‘secondary’ model components may conveniently be subdivided into material parameters (post-peak characteristics of the stress–strain relations, ‘aggregate interlock’, ‘tension stiffening’, ‘dowel action’, bond between steel and concrete), and parameters associated with procedural effects stemming directly from the numerical scheme adopted (iterative method, number of cracks allowed per iteration and/or cracking sequence followed, FEs chosen, numerical-integration rule used, mesh definition/size, loading path).

The presentation of the subject matter in hand, namely the ‘secondary’ parameters, will follow the above subdivision between ‘material’ and ‘procedural’ factors. Clearly, while some of these factors might sensibly be ascertained on the basis of existing evidence, conclusions regarding others can be reached with reasonable certainty only through a set of numerical experiments (as described in subsequent chapters).

Besides the key source of objectivity of the material model (i.e. the choice of f_c to define behaviour up to failure and failure

itself), 'strain softening' and 'aggregate interlock' appear to be the two parameters most likely to affect predictions. The complete lack of post-peak characteristics is in keeping with both a proper interpretation of available meaningful experimental evidence (as discussed at length in Chapter 1), and the fact that the peak stress in compression is never actually reached in a structure (as explained in sections 1.5 and 1.6, and also borne out by all the case studies gathered in this book). Thus, even if any hypothetical 'strain softening' relations in compression were to be included in the analysis, they would make no difference to the results, and, hence, the question of their objectivity need not arise at all. Descending branches in tension, on the other hand, which are also discarded in the present model (as opposed to many other packages), not only do not have a reliable experimental basis either, but may even lead to numerical difficulties (as suggested in Chapter 4). The lack of any strain-softening branches is, of course, a consequence of the brittle-material model followed. Another consequence is the notion that cracked concrete makes only a minor contribution to overall structural strength and, in this respect, the low value of SRF adopted accords with the view (espoused in section 2.4.3.4) that 'aggregate interlock' plays an insignificant role in the load-carrying capacity of a member. That the chosen β value(s) is (are) capable of reliable predictions while, at the same time, providing the necessary degree of numerical stability, will be justified in subsequent chapters (especially in Chapter 3); while, as mentioned previously, the related question of options Z3 and G3 for the fully-cracked material is explored in Chapter 4.

There are three factors that ought to be considered in the modelling of those regions of the structure where reinforcement is located, and of these the first concerns the so-called 'dowel action' of the bars themselves. Here, the sole stiffness component along the axis of the reinforcement is compatible with the view that the effect of any 'dowel action' is insignificant, as described elsewhere.⁵² The second factor is the question of the bond between steel bars and surrounding concrete, the justification for perfect (full) bond having been given already (section 2.4.4.2). Finally, there is the 'tension stiffening' factor, an effect that is not considered in the present model which, in accordance with the smeared-crack philosophy, assumes all the material in the region of the cracks to have lost its stiffness in the direction orthogonal to the cracks. The arguments for such a simplification have also been outlined in section 2.4.4.2, while recognizing the fact that this might have some bearing on the accuracy of computed deformations by underestimating the stiffness of the relevant parts of the structure.

It is difficult to discuss the six procedural factors listed previously, which might affect nonlinear FE predictions of concrete structures, without recourse to actual numerical examples and/or

tests. Therefore, only some general observations will be made at this stage, postponing most of the detailed recommendations until the necessary parametric studies on procedural effects have been carried out in Chapters 3 and 4 through a set of typical numerical experiments.

Past experience has shown that the use of arbitrary nonlinear algorithms in the FE analysis of concrete structures is, generally, not feasible, and that specific strategies must be evolved which allow for the special characteristics of the material model. Therefore, the optimum choice of nonlinear strategy would depend, for example, on whether brittle or strain-softening features were adopted, and this will be discussed at length in Chapter 4, although some background to the INRM-based algorithms used is to be touched upon in Chapter 3 which deals with 2-D problems. Closely related to the question of nonlinear strategy is the decision on what cracking sequence and/or number of simultaneous cracks is to be adopted. Numerical experiments dealing with such matters will be conducted in both Chapters 3 and 4, the latter also exploring the effect of crack formation on stiffness-updating strategy.

The general suitability of the various quadratic elements chosen is well established for linear problems. In the case of nonlinear analysis of concrete structures, the second-order elements of the serendipity family have also been widely used (in addition to the constant-strain triangle) by investigators in this field (see, for example, reference 56). However, the performance of the latter isoparametric-element types may be influenced by the integration rule adopted. As pointed out in section 2.3.2, major economies in computing time result from the use of under-integration, and predictions may even be improved over those of their more formal fully-integrated counterparts. It is for these reasons that the analyses of 2-D problems in Chapter 3 are carried out by means of under-integrated elements. The use of under-integration will be justified in Chapter 4, where the objectivity of predictions is to be looked at by reference to the numerical-integration rule employed for the serendipity elements; it will be shown there that the warnings against under-integration in nonlinear FE modelling of structural concrete that are sometimes raised by analysts need not cause undue concern. A brief comparison between serendipity and Lagrangian elements will also be included in the objectivity study of 3-D FEs (Chapter 4).

Mesh-configuration and FE size are potentially important factors in both linear and nonlinear problems, as they govern the degree of approximation to the continuum. For linear stress analysis, it is usually agreed that, as the mesh is refined, accuracy improves: such mesh refinement is especially recommended in zones where localized effects take place (e.g. load concentrations, sudden changes in geometry, etc.); and although, in principle, accuracy can increase only up to an optimum number of DOF, after which

a substantial decay in accuracy follows,⁹⁶ set by the practical limitations connected with unavoidable round-off errors in the course of solution of large equation sets, present-day computing power is usually sufficiently large to ensure that quite fine meshes can be used even for the more complex structural problems.

In the case of nonlinear problems in which failure is associated with cracking, the latter can induce deceptive effects in those local regions that are either subject to stress concentrations/singularities or contain previous cracks. For such instances, the finer the mesh, the sooner crack initiation occurs for a given value of applied load so that, in principle, FE analysis involving cracking based on a strength criterion would, in the limit of mesh refinement, converge — incorrectly of course — towards a zero-load prediction.^{97,54} Even for finite (but, 'sufficiently' small) mesh sizes, stress redistributions induced by early cracking in some regions can affect numerical stability locally, precipitating premature structural collapse as successive iterations spread these local disturbances throughout the structure. One possible way of averting such difficulties is to stiffen the mesh locally as, in fact, engineers and/or experimentalists actually do when designing suitable construction details at support or anchorage zones (an example of such a technique will be given in Chapter 3). A more general and elegant approach to avoiding mesh-size dependency, however, is simply to adopt a 'coarse' mesh, thus bypassing the possible predominance of localized effects over the overall behaviour of the structure which, after all, is of primary interest. This notion might be difficult to accept from an analyst's point of view but will readily be acceptable to an engineer. Moreover, it is in keeping with the thinking permeating this book, namely a realistic modelling of structural concrete on the basis of existing and reliable material data. Bearing in mind that the experimental conditions under which the constitutive relations (at the engineering level) were derived involved measurements taken from strain gauges that were approximately two to three times larger than the maximum aggregate size used in the concrete mix, it is clear that a lower-bound limit to the size of an FE is provided by such a gauge length. This also ensures that the assumptions of homogeneity and isotropy of the material might safely be invoked; otherwise, small FE sizes would require different constitutive relations for the aggregate particles and cement paste, involving also separate discretizations of these, as well as adhesion and/or bond characteristics between the two separate material constituents. Were such complex (microscopic) relationships even currently available, it is evident that the adoption of mesh sizes lower than the suggested 'two-to-three times the aggregate size' would quickly limit the range of structures which it would be feasible to model from a computing perspective. The preceding philosophy also has implications for the generally accepted notion of convergence to the correct solution

as the mesh is refined: in the present context, this is not considered to be meaningful, as the material characteristics stem from a cylinder or cube test which is sufficiently large to enable the *average* material properties of what is really a heterogeneous mix to be sensibly derived, interpreted, and eventually incorporated into (large-scale) structural analysis.

While the validity of the material data establishes the lower bound of FE dimensions, the upper bound that would be needed for adequate accuracy remains largely a somewhat subjective choice to be based mainly on the analyst's engineering judgement. As Bédard⁵⁴ suggests, the upper bound should be compatible with the maximum size that is considered representative of structural behaviour. He goes on to give two illustrative examples, namely a plain-concrete prism compressed concentrically by strip loading (requiring a minimum of two 'column' elements on either side of the (symmetrical) centreline so as to allow for a reasonable stress-gradient description), and an RC beam under two-point loading (demanding at least two to three 'layers' of elements above the reinforcement in order to detect the stress distribution throughout the compressive zone and depth). Bédard also points out the desirability of ensuring that the 'shape ratio' (i.e. the ratio of longest to shortest sides of an element) does not exceed about 3 (although 'shape ratios' above this value have also been used in some problems, without apparent difficulties), and argues that as regular a grid as possible throughout the structure should generally be aimed at on account of both accuracy and ease of automatic mesh generation.⁵⁴

Finally, among the procedural factors that need to be considered, there remains the effect of loading path on predictions. In discussing this parameter, it is useful to distinguish between load increments that precede first cracking and those that are applied subsequently. In principle, a single load increment should suffice up to the formation of the first crack(s) in the structure owing to the fairly 'mild' nonlinear nature of the (isotropic) constitutive relationships corresponding to the ascending stress-strain branches, and also because the failure envelope is not stress-path dependent (see section 1.3.3.2). Therefore, it is clear that the onset of cracking will not be affected by the loading path and that a relatively small number of iterations will suffice for convergence to the correct solution (corresponding to initial cracking) in a single load step. An estimate of the size of load step required could be provided by a preliminary linear computer run that will indicate the location of the 'critical' tensile stress and the magnitude of the applied load at which this would occur.

That recourse to incremental techniques ought to be made after cracking has begun is apparent on account of the 'strong' nature of the nonlinearities associated with sudden crack formations. The sudden appearance of many simultaneous cracks could produce

results that depend on the size of the load step used and, furthermore, could easily give rise to numerical instability. Ideally, extremely small load steps, which would ensure that each time load is incremented a single crack would form (or, in special cases, a small number of cracks at different locations where the failure envelope happens to have been reached simultaneously) would remove most of the uncertainties associated with possible load-path dependency. Such an option is clearly unrealistic, however, with regard to the computational effort required. Instead, relatively few load steps are applied and, in the course of each, several cracks usually take place; it is for this reason that care must be exercised in following a suitable crack-propagation strategy within each load step and, also, iteration.

In practice, it is found convenient to adopt a constant size of load step throughout the entire loading history. The load-increment size is usually taken to be 5% or 10% of the estimated ultimate load, which ensures that only 10 to 20 load steps are needed, while adequate accuracy is achieved for all practical purposes. The effect of varying the load-step size will briefly be considered in Chapter 3, in order to illustrate the degree of load-path dependency to be expected in nonlinear predictions of the present type.

2.6. A brief outline of the smeared-model package

This section contains a brief description of the main features of the nonlinear FE program. The outline is drawn from the much more detailed presentation of the 3-D model by González Vidosa,⁵⁶ but the basic logic is equally applicable to the 2-D version. As explained in section 2.3, the nonlinear features of the analysis have been implemented within a standard linear package (FINEL), the latter having been dealt with in section 2.3.1. In addition to the smeared analysis under static loading thus incorporated into the modular structure of FINEL, two post-processing programs were developed for plotting, and these constitute an important part of the nonlinear package as will become apparent when the deflected shapes and crack patterns of the various problems to be discussed in subsequent chapters are presented. The present section, however, is concerned with the iterative flow of modules of the smeared analysis, describing also the main modifications introduced in the linear stress modules so as to account for material nonlinearities, number of cracks allowed per iteration, and Newton–Raphson updating strategies.

The linear stress analysis of FINEL provides the backbone for the smeared analysis, as is evident from Fig. 2.26, which shows the flow of modules of the nonlinear strategy. A typical input file required to run an actual nonlinear example appears in Fig. 2.27: the problem in question represents a plain-concrete prism acted upon concentrically by strip loading across half its end faces. It may be seen that options can be input by using the Jn and Rn register facilities (e.g. LET J4 020202 specifies $2 \times 2 \times 2$ Gauss

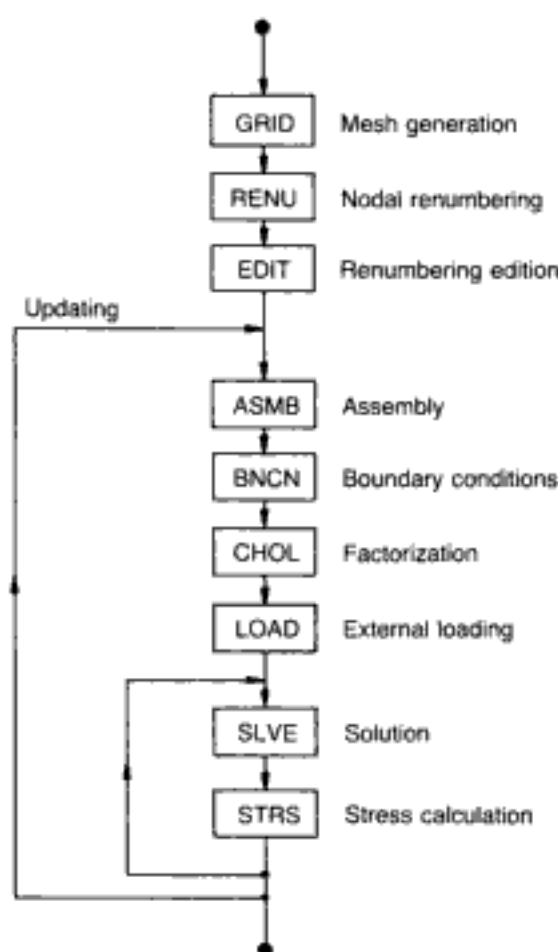
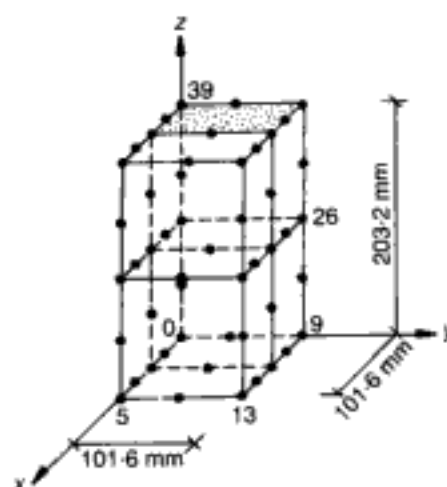


Fig. 2.26. Flow-chart of modules in the smeared analysis⁵⁶

points). By reference to Fig. 2.26, it is clear that, once an iteration is performed, the program returns either to the assembly module (updating iteration) or to the solution module (non-updating iteration) depending on the Newton–Raphson strategy adopted. Updating iterations require reformulation of \mathbf{D} -matrices (and hence also of \mathbf{k} -matrices) while non-updating iterations follow a constant-stiffness strategy. The iterative flow of modules is achieved by executive commands in the nonlinear input file (see Fig. 2.27). The input data required for the first iteration goes up to the first END STRS card, while the next three sets of cards are for a non-updating iteration, an updating iteration and a new load-step increment respectively.

Before the modifications of the linear modules through the editing of their executive subroutines are discussed, it should be pointed out that some additional storing facilities had to be implemented in order to save intermediate results which are required at different stages of the analysis. In this way, the following could be dealt with: data in respect of the analysis (such as the Newton–Raphson strategy, convergence variables, number of cracks allowed per iteration, number of new cracks, etc.); data relating to the FE and its Gauss points (i.e. nodal numbering, strains, stresses, cracking information, etc.); and storage of some long arrays (e.g. increments



(a)

```

ANALYSIS STRESS-SMEARED
*
* concrete prism under a strip load
*
LET J4      020202      : 2 x 2 x 2 Gauss points;
LET J5      000202      : SRF D-mtx, 2 cracks/iter, "single crack";
LET J6      035001      : 3 iter/up, 50 load steps, MIXNR:
LET R0      0.1         : 0.1 MPa; maximum residual stress (convergence);
LET R1      0.01        : maximum relative residual stress (convergence);
LET R2      100         : maximum residual force (divergence);
LET R3      0.005       : maximum residual force (convergence);
LET R4      0.1         : Shear retention factor;
*
* mesh generation
*
REGI COOR      0.      0.      0.      101.6  0.      0.
                0.     101.6    0.      101.6  101.6    0.
                0.      0.      203.2   101.6  0.      203.2
                0.     101.6    203.2   101.6  101.6   203.2

ELEM HX20
MATE STIF      20000.    0.2
MATE STRENGTH  26.9
REGI SHEX      1  2  3  4  5  6  7  8      2  1  2
*
* first iteration
*
COOR GENE
FIXE FACE      1  2  1      1  2  6      3
FIXE FACE      1  4  1      1  2  14     2
FIXE FACE      1  3  2      1  6  14     1
FIXE FACE      3  3  1      39 40 44     1
FIXE FACE      3  3  1      39 40 44     2
LOAD UDSL      -1.   3   3  3  1      39 40 44
END STRS
*
* non-updating iteration
*
RE-E SLVE
END STRS
*
* updating iteration
*
RE-E ASMB
END STRS
*
* new load-step
*
RE-E ASMB
LOAD UDSL      -1.   3   3  3  1      39 40 44
END STRS
*
*
END JOB

```

(b)

Fig. 2.27. Example of application of the nonlinear program to static ultimate-load analysis.⁵⁶ (a) FE discretization; (b) smeared-analysis input file

of applied nodal forces, increments of nodal displacements, total nodal displacements, total reactions, residual nodal forces, various statistics (especially cracking-information arrays) for each load step, etc.). Also, and as mentioned earlier, two programs were written for plotting purposes (it should be noted that any input file of these two is an output file of a previously executed program). These programs provide plots of deflected shape and crack pattern of a reference section, one plot per converged load step plus one plot of the last performed iteration. The first program reads and processes deflection and cracking information of converged load steps and, also, of the last performed iteration. It then drops some redundant information and provides an output file with the strictly necessary data for the plots. The second program queues this file to a plotter; as the latter program is the one that includes calls to plotting subroutines, it is plotter-dependent.

It is evident from Fig. 2.26 that the first three modules (the one for the mesh generation and the two renumbering modules) are equally suited to both linear and nonlinear analyses. Therefore, the actual modifications necessary to implement the smeared-analysis strategy are carried out only for the remaining six linear modules. A brief summary of the main features of such modifications is given below. It should be noted that, since the smeared modelling of cracking requires the **D**-matrices of the Gauss points, most of the changes relate to the assembly and the stress-computation modules (ASMB and STRS respectively). The assembly module ASMB performs the numerical integration of the tangent stiffness matrices of the elements and then it assembles the tangent stiffness matrix of the structure; it also includes several initialization subroutines. In fact, the first time the subroutine is called, i.e. at the first iteration of the analysis, it performs some initialization tasks, including printing of mesh connectivities and performing a dummy assembly to set up some assembly variables, such as the block size by which the program splits the stiffness matrix of the structure. Other tasks include the reading of any relevant data specified by the Jn and Rn registers in the input file (see Fig. 2.27), including options such as number of Gauss points, Newton–Raphson updating strategy, number of cracks allowed per iteration, etc. There is also initialization of the **D**-matrices of all concrete Gauss points to values in accordance with the material modelling described in Chapter 1 (section 1.4.1) (therefore, any Young's moduli and Poisson's ratios specified in the input file for concrete are ignored). The initialization stage is completed by the calculation of **B**-matrices and Jacobians for all concrete and steel Gauss points. It should be recalled that, since the analysis assumes small displacements and strains, both **B**-matrices and Jacobians keep their initial values (calculated in global coordinates by the relevant element subroutines) throughout the analysis.

The numerical integration of the tangent stiffness matrices of the elements is performed by either of two subroutines. One of these (which includes two optional integration schemes⁵⁶) recalculates stiffness matrices for all elements (concrete and steel), while the other recalculates stiffness matrices of only those concrete elements that contain newly-cracked Gauss points plus the stiffness matrices of all steel elements (since the latter elements require relatively little computational effort, their stiffness matrices are always recalculated). The choice between the two subroutine options relates to the chosen Newton–Raphson updating strategy and it may affect numerical stability, as will be discussed in Chapter 4. Finally, it should be noted that, although it would seem natural that the updating of **D**-matrices should be carried out in this module (ASMB), it is actually done in module STRS. That fact is due to the possibility of selective updating of **D**-matrices at the end of module STRS, since the selective-updating decision is taken just after the end of the current iteration (module STRS) so that any related information is readily accessed in that module.

The BNCN module sets up two vectors that relate to boundary conditions: the first vector contains the numbers of DOF being restrained, while the second contains the values of these restraints (non-zero if there are applied displacements). This information is specified by command `FIXE` in the input file (e.g. `FIXE FACE` in Fig. 2.27). The executive subroutine of the nonlinear module differs from the one of the standard `FINEL` only in that the former is constantly bypassed following the first iteration of the analysis.

The module `CHOL` factorizes the tangent stiffness matrix of the structure by means of Choleski's method ($[K] = [L][U]$). As for the boundary-conditions module, its executive subroutine is practically identical to the standard subroutine of `FINEL`. The difference lies in that the latter performs the factorization provided that the stiffness matrix is positive definite, even though the matrix may be ill-conditioned, whereas this is not the case in the nonlinear version. This difference was implemented in order to avoid an excessive number of iterations for the last non-converged load step (which, in spite of the introduced 'short-cut' usually still takes about one-third of the total number of iterations), and to ensure that any converged load step was attained without ill-conditioning of the tangent stiffness matrix.

It should be recalled that the increment of nodal forces is the addition of applied (external) forces and residual forces. The latter appear for equilibrium purposes as a result of stress corrections introduced at the previous iteration in order to follow a nonlinear stress–strain relationship. The external-loading module `LOAD`, however, calculates only those equivalent nodal forces due to applied loading, i.e. loading caused by either applied forces or non-zero imposed displacements ($-[K_{ur}] \Delta d_r$, as will be shown below). Residual forces are calculated in module `STRS` (previous

iteration), where stress corrections take place, and added to applied forces (if any) in module SLVE. Therefore, the executive subroutine of the module LOAD is executed only at the first iteration of each load step.

The module SLVE calculates increments of nodal displacements and increments of reactions, and updates their total values. Subscripts u and r denote unrestrained and restrained displacements (and forces associated with them) respectively. Upon rearrangement of coefficients, the set of equations of a given iteration can be partitioned as follows

$$\begin{bmatrix} [\mathbf{K}_{uu}] & [\mathbf{K}_{ur}] \\ [\mathbf{K}_{ru}] & [\mathbf{K}_{rr}] \end{bmatrix} \begin{bmatrix} \Delta d_u \\ \Delta d_r \end{bmatrix} = \begin{bmatrix} \Delta f_u \\ \Delta f_r \end{bmatrix} \quad (2.77)$$

where $[\mathbf{K}_{ij}]$ are partitions of the tangent stiffness matrix of the structure ($[\mathbf{K}_{uu}]$ is the deflated tangent stiffness matrix, i.e. the matrix relevant to the case when $\Delta d_r = \mathbf{0}$ and Δf_r is not required); Δd_u , Δd_r are increments of displacements; and Δf_u , Δf_r are increments of nodal forces (f_r being the reactions). From the above equation, Δd_u , Δf_r are found through

$$\Delta d_u = [\mathbf{K}_{uu}]^{-1}(\Delta f_u - [\mathbf{K}_{ur}]\Delta d_r) \quad (2.78a)$$

$$\Delta f_r = [\mathbf{K}_{ru}]\Delta d_u + [\mathbf{K}_{rr}]\Delta d_r \quad (2.78b)$$

While the standard executive subroutine SLVE includes the calculation of Δd_u by Choleski's method ($[\mathbf{K}_{uu}]$ is factorized and stored in the ZFILE in module CHOL), the nonlinear subroutine version also includes the computation of reactions f_r .

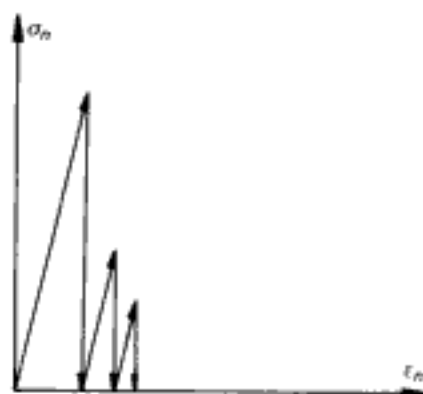
It is the stress module STRS which contains most of the smeared-analysis tasks and hence it differs fundamentally from its linear counterpart. Broadly, two different parts make up its executive subroutine. The first part is a block of stress computations: it calculates and corrects total stresses, sets up newly-cracked Gauss points, and calculates the residual forces due to stress corrections. The second part checks whether or not convergence is achieved for the current load step and then a decision is made on the type of updating for the next iteration.

The role of the first part of the STRS module is quite substantial. Increments of strains and stresses, stress corrections, and residual forces are calculated from increments of nodal displacements in two subroutines, one for concrete and the other for steel Gauss points. While the subroutine for concrete Gauss points will be described in detail later on, it should be noted at this stage that it checks whether or not the states of stress at these Gauss points are outside the failure envelope described in section 1.4.2. Those concrete Gauss points that exceed the envelope form the set of prospective crack locations; however, the present subroutine neither sets up any new crack(s) nor corrects any state(s) of stress outside the failure envelope. With regard to steel Gauss points, its

subroutine also checks whether or not any of them change from one branch to another of the trilinear stress–strain relationship (section 1.4.3). The next step depends on the crack-propagation criteria adopted (to be discussed at length in Chapters 3 and 4). If the ‘total crack’ criterion is specified in the input file, then all prospective cracks are set up (the actual crack implementation is carried out by a subroutine especially earmarked for this task), i.e. the number of new cracks is equal to the number of prospective cracks. On the other hand, if a ‘single crack’ criterion is specified, then only one (or a small number of) new crack(s) is allowed in the current iteration. In the latter instance, prospective cracks are sorted out according to the percentage by which their state of stress exceeds the failure envelope (i.e. τ_0/τ_{0u} — see section 1.4.2), so that only those which exceed failure conditions by the largest margin are actually set up in the current iteration. Clearly, while there are prospective cracks, convergence cannot be fulfilled and the external load is kept constant, as will be discussed below. It should be borne in mind that any stress corrections in the preceding subroutine components within module STRS give rise to residual forces that are stored for the next iteration.

The above two subroutines for concrete Gauss points, dealing with failure criteria and crack implementation respectively, require further description. The first of these subroutines, based on checks for possible macrocracking, begins by calculating increments of global strains from increments of nodal displacements, and then updates total strains. If a Gauss point is uncracked, i.e. not cracked in previous iterations, concrete is assumed to be isotropic and increments of stress can be directly calculated in global directions, since its **D**-matrix is invariant for any set of axes. On the other hand, if the Gauss point is already cracked, then the material is anisotropic and its **D**-matrix is only valid in local (cracked) directions, as discussed in section 2.4.3; hence, increments of strains are transformed to local directions in order to compute stress increments and total stresses in these local directions. The next step depends on the type of Newton–Raphson updating strategy for the current run. For example, if a given Gauss point is already cracked but its **D**-matrix has not been updated to allow for this crack occurrence (i.e. an isotropic **D**-matrix is kept), then its state of stress has to be corrected (namely by setting to zero the stress orthogonal to the crack plane); otherwise, the stress state of the cracked Gauss point would not be in accordance with the new situation implied by cracking. (That the use of iterative procedures which keep **D**-matrices either permanently or temporarily uncracked (i.e. modified or mixed INRM, respectively) attracts direct tensile stresses across crack planes in subsequent iterations which have to be set equal to zero is illustrated schematically in Fig. 2.28. (It should be noted that, even though the assumption of uncracked properties is implicit in the lack of the updating of

Fig. 2.28. Residual tensile stresses across a crack plane for a modified or mixed INRM (the latter with a fixed sequence of non-updating/updating of iterations, of which only the former are shown in the figure)⁵⁶



the **D**-matrix, the initial-stress approach is used in recognition of the fact that cracking has been signalled in the iterative procedure.) This gives rise to successive residual forces which, sometimes, may lead to non-convergent solutions (modified INRM) or to early divergent analyses as a result of propagation of spurious mechanisms (mixed INRM), as will be illustrated in Chapter 4 by reference to the case study of beam OA-1.) This task of stress correction across cracks is performed by a special subroutine when either constant-stiffness or mixed Newton–Raphson strategies are followed (i.e. Figs 2.5(b) and 2.5(c)). Once the state of stress in local directions has been corrected, stresses are transformed to global directions. It is then that a check is performed to ascertain whether or not the state of stress is outside the failure envelope: this requires the calculation of principal and octahedral stresses. Finally, any state of stress inside the envelope is corrected simply in accordance with the constitutive relations as outlined in section 1.4.1.

The subroutine for the implementation of cracking may be described by reference to the case when a first crack is set up at a concrete Gauss point. Second and third cracks (or, in principle, compressive failures) are set up in a similar way, consistent with the **D**-matrices defined in section 2.4.3. First, the variable that defines the cracking situation at that location is updated. Then, there follows the calculation of principal stresses and directions, and of the relative magnitudes of the principal stresses. This ordering of stress magnitudes is used so as to determine which column of the matrix defining the axes change relates to which principal stress. Plotting information is then calculated by a subroutine which determines the intersection angle of the crack plane with the plotting plane and also checks whether or not both planes form an angle smaller than 45° . (Such plotting information is directly relevant to 3-D modelling.⁵⁶) Finally, and consistent with the notion of cracking, the maximum tensile stress is set to zero, local stresses are transformed to global directions and residual forces are computed. It should be noted that the **D**-matrices are not updated here, for that operation depends on subsequent updating decisions.

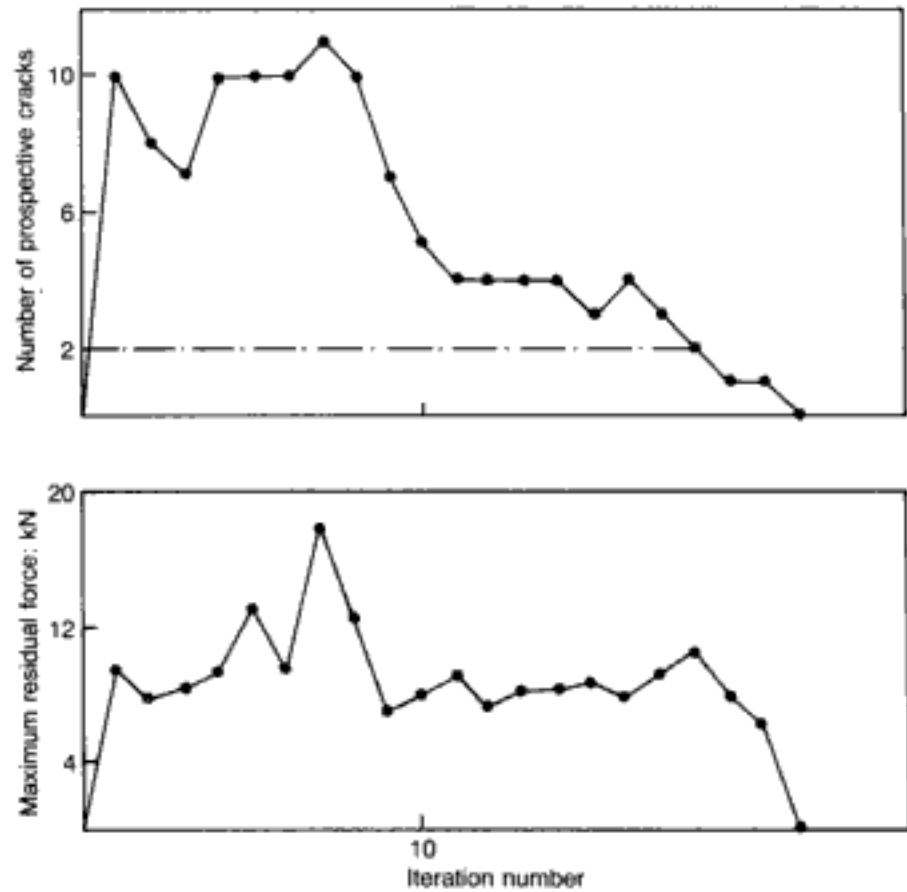


Fig. 2.29. Typical curves of number of prospective crack locations and residual forces for a converged load step (load step = 25 kN, 2 cracks allowed per iteration)⁵⁶

The second part of the STRS module is concerned with convergence and updating decisions. First, a check is made on whether or not the convergence criteria discussed in section 2.4.2.6 are fulfilled. This requires convergence of residual magnitudes (i.e. forces, deformations, stresses, strains), and it also requires 'yield' and 'cracking' convergence, i.e. that no steel Gauss point has changed from one linear branch to another and that there are no prospective cracks left. In practice, the cracking criterion is usually the most restrictive, for residual forces decrease very rapidly when there are no new cracks. In this respect, Fig. 2.29 shows the number of prospective cracks and residual forces for a typical converged load step (this is taken from reference 56 and corresponds to one of the case studies described in Chapter 4 (beam A-1)). If all convergence criteria are fulfilled, the next iteration follows a new load increment. It is then that a decision is made on the type of updating for the next iteration. In Chapter 4, three Newton–Raphson strategies are considered: the initial-stiffness method; the mixed Newton–Raphson method; and a selective-updating method that updates only newly-cracked concrete locations as well as steel locations where yielding takes place, i.e. it updates only **D**-matrices relating to 'strong' nonlinear changes, while it does not update matrices relating to 'mild' nonlinear changes (as will be shown in Chapter 4, this selective updating, which was

implemented initially to improve efficiency, was also found to improve numerical stability with respect to the mixed Newton–Raphson method). Finally, **D**-matrices are updated: this may be done either at all Gauss points or selectively, depending on the updating subroutine chosen.

The above overview of the smeared FE package encompasses the key features of material and structural modelling outlined in this and the previous chapter. The application of the nonlinear FE model to 2-D and 3-D problems forms the subject of Chapters 3 and 4 respectively.

3. Two-dimensional analysis

3.1. Introduction This chapter describes the structural response up to failure of a wide range of concrete structures that are amenable to 2-D representation. Although the more general 3-D version of the package must be employed when tackling arbitrary structural forms which do not conform to plane-stress or axisymmetric simplification, the 2-D program is extremely useful when the latter type of modelling is admissible on account of economy (computational effort, input/output), ready visualization, and relative ease with which parametric studies may be conducted. Much of the strategy of the FE model was developed in the course of the 2-D studies, but some further refinement took place when the model was extended so as to encompass 3-D structures. The various decisions on numerical strategy will be illustrated when the relevant 2-D and 3-D problems that served as the basis for such computational options are presented in Chapters 3 and 4 respectively.

In what follows, a summary of the background that led to the development of a systematic numerical procedure is outlined first. This objectivity-study background is then followed by the presentation of the various results which show the generality of the 2-D model. Here, first, plain concrete (PC) members are analysed. Then, the bulk of the 2-D analyses, which deal with reinforced concrete (RC) components, follow. In the majority of cases, experimental data for the numerical run being investigated is available, and this is used as the basis for estimating the accuracy of the relevant analytical prediction. Besides the ultimate-load value, two other important aspects of structural response — crack pattern and deformation — are also given consideration although these will not always be discussed here, partly because of the need to maintain reasonable conciseness of presentation but also because the experimental information in question reports only the collapse load. In the case of experimentally recorded displacements, it should be borne in mind that, as failure is approached, displacement transducers are often removed in order to avoid damage to them, so that no displacement information is available beyond a certain load; in such instances, the analytical predictions may well appear to overestimate the ductility of the structure. Conversely, at high load levels, time effects may sometimes cause deformations to increase even at constant load, and this may produce apparent deflection underestimates in analytical predictions.

The 2-D package provides crack and deformation patterns of the structure at each load step. These plots always show the mesh

of isoparametric concrete elements, the boundaries of which are defined by full lines onto which dashes may be superimposed to denote the presence of reinforcing steel. In plane-stress analysis, the first appearance of a crack at a Gauss point is indicated by a double dash oriented along the direction of cracking; in subsequent load steps the same crack is denoted by a single dash. Clearly, a second crack may form at the same Gauss point, intersecting the first crack at the appropriate angle. The same convention holds for circumferential cracks in axisymmetric analyses, while radial cracks are denoted by two concentric circles at the first appearance of a new crack and by a single circle for the same crack in subsequent load steps. Yielding of the steel is sometimes indicated by a heavy dot (first yield; $0.8 f_y < \sigma < f_y$) or by a heavy dot superimposed onto a cross (second yield; $\sigma \geq f_y$) (see Fig. 1.67).

The various deformed shapes and crack patterns are usually specified by the total load applied and the relevant load-step number. In addition, the displacement magnification factor may range from 1 to 100 (e.g. D.M. = 1 means no magnification). The appearance of very large and/or completely unrealistic deformed shapes (e.g. with boundaries of elements overlapping) gives a readily visualizable warning that the numerical results are meaningless. This usually occurs at the last performed iteration within the final load step, i.e. the one following the last converged load step, and is an indication of a mechanism associated with collapse. Sometimes, however, local failures may occur, with some nodes free to move in certain direction(s) owing to local mechanisms, even though the numerical solution may be stabilized at higher load levels (an interesting example of such a case is given in reference 54, and other instances will be shown in this chapter). In either case, therefore, the deformed-shape plots provide invaluable assistance in assessing the actual value of the MSL (as defined in section 2.4.2.6).

3.2. Guidelines for a systematic numerical procedure

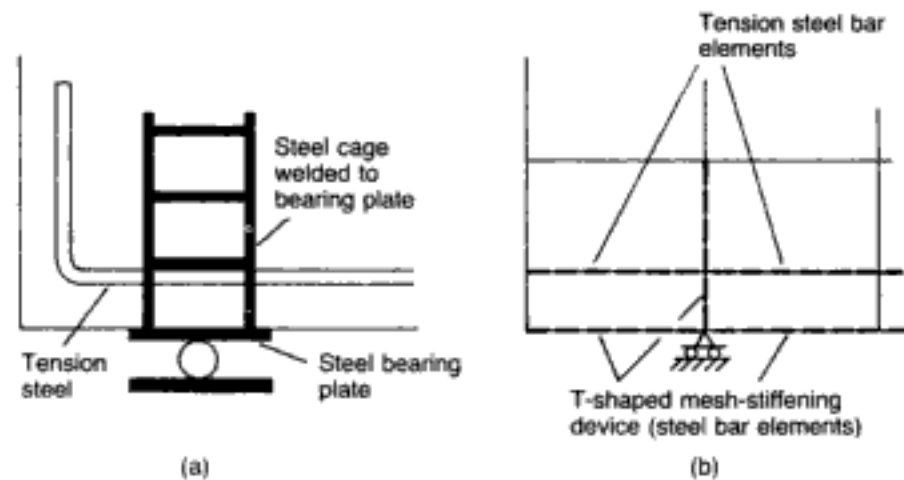
The main material and procedural factors that need to be addressed in the course of searching for a reliable FE model for structural concrete have already been touched upon in Chapter 2, while a more detailed study of the resulting objectivity is to be described in Chapter 4 by reference to the 3-D FE package. For present purposes, however, further background to the basis for some of the remarks made in Chapter 2 is to be given in this section, in the context of the 2-D package. The material and procedural factors that will be considered are: shear-retention factor β ; FE mesh configuration; loading path; and crack-propagation strategy. Most of the recommendations stem from the work of Bédard⁵⁴ who conducted a number of parametric studies on these four factors.

It was shown by Bédard that the analytical predictions for both PC and RC structures appear to be practically insensitive to β when

the latter is confined to the range of 0.1–0.5. He also showed that difficulties may arise as β tends to its extreme values, as illustrated by runs in which β was set to 0.01 and 0.9 respectively.^{54,85} On the other hand, Bédard also gave an example in which equally good results were obtained by varying β from 0.01 to 0.9; for this example, however, the extent of cracking was minimal even at the last sustained load step. Thus, as one would expect, β is likely to influence nonlinear predictions only in those structures where cracking is extensive and develops at early loading stages. As Bédard points out, this explains why in some previous nonlinear analyses carried out by other authors, structures that exhibited little cracking before failure yielded no significant difference throughout the full range of β values. The above evidence, therefore, justifies the recommendations of section 2.4.3, namely the use of $0.1 \leq \beta \leq 0.5$, with either of the two extreme values equally acceptable (in general), although the lower limit is more rational on theoretical grounds.

The FE mesh configuration is possibly the most subjective among the various factors considered here. Nevertheless, some guidelines along the reasoning outlined in section 2.5 can be put forward. As argued in Chapter 2, the minimum mesh size should not fall below two to three times the aggregate size used for the concrete mix, while the upper bound is set by what could be termed the maximum element size that might be considered representative of the overall behaviour of the structure (two examples of the latter were given in section 2.5). In zones of localized high stress concentrations, early cracking may locally upset numerical stability (and this might then spread elsewhere, precipitating premature structural collapse); a possible consequence could be a degree of mesh-size dependency in such regions. Now, in actual structures, applied load concentrations are usually catered for by adequately designed construction details (e.g. at support or anchorage zones); this type of 'good design practice' suggests a similar local stiffening of the FE mesh as, for example, in the case depicted in Fig. 3.1,

Fig. 3.1. Load-concentration zone at a support:⁵⁴ (a) local construction detailing; (b) corresponding FE mesh stiffening



which shows a typical support detail and its introduction into the FE discretization.⁵⁴ Such a 'mesh stiffening' device stabilizes concrete locally without affecting the overall stress pattern elsewhere, thus avoiding early numerical instabilities.

The influence of the loading path, i.e. load-step size, was investigated by Bédard⁵⁴ by reference to a PC prism, a PC cylinder, and an RC beam. For the last two structures the magnitude of the load step was found to be an insignificant factor on nonlinear predictions. Thus, load increments amounting to about 10% of the estimated MSL appear to be adequate for purposes of both accuracy and economy, as suggested in section 2.5. The PC prism did show some dependency for such load steps, the predictions stabilizing only below 5% of the MSL; however, such an effect is more related to the very rapid development of cracks within a load step, and hence to numerical problems associated with crack-propagation strategies which are discussed next.

The type of crack propagation is by far the most influential factor on analytical predictions. After all, there is a major distinction between actual behaviour/experiments and nonlinear incremental modelling. In the former, cracks initiate and propagate one by one or several at a time and, also, at different rates, namely in a stable manner at low load levels (the propagation stopping when the load is kept constant), or in a less stable manner as the load is increased until the rate of propagation becomes uncontrollable leading to structural failure (thus, cracking continues to propagate even under constant load). Incremental modelling, on the other hand, imposes load increases which are both discrete and sudden, so that crack propagation occurs and stops; if (numerical) stability cannot be attained, structural failure is assumed to have taken place and the computer run terminated.

As pointed out in section 2.5, infinitesimally small load steps would lead to either a single or a very small number of cracks forming within each such load step. For finite load steps, however, several cracks might form 'simultaneously', and the next question to arise is how best to preserve numerical stability through an adequate choice of crack-propagation strategy. At one extreme, there is the possibility of allowing only one crack to form at a time (at the most 'critical' location); after the numerical procedure has been stabilized, the next most critical possible crack location is checked, and so on until all possible prospective cracks have been investigated one by one before proceeding on to the next load step: such a procedure will be termed the 'single-crack approach' (SCA). At the other extreme, all prospective locations of material failure could be allowed to crack simultaneously within one cycle of iterations: this approach will be referred to as the 'total-crack approach' (TCA).

Clearly, the SCA should generally offer better prospects of achieving numerical stability since the controlled appearance of

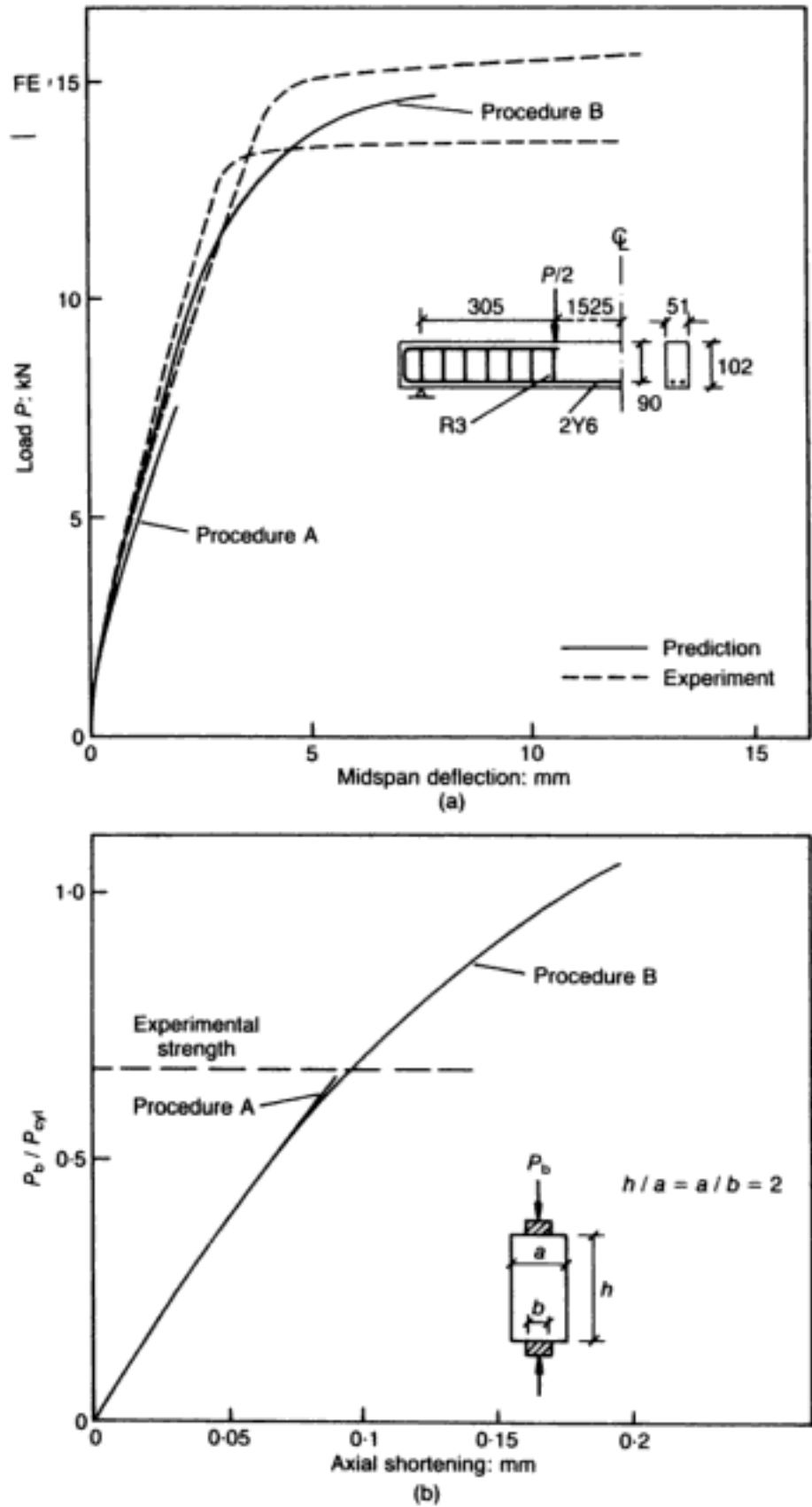


Fig. 3.2. Predicted total load-deflection relationships using procedures A (TCA) and B (SCA), and experimental evidence:⁵¹ (a) RC beam under two-point loading (all dimensions in mm); (b) PC prism under strip loading ($P_{cyl} = P_b$ for $a = b$)

cracks helps keep in check the associated large residual forces, and this is usually found to be the case in the analysis of 2-D RC structures. For PC structures, both schemes often yield comparable results in 2-D modelling, with the exception of the PC prism under strip loading; for the latter structure type, 2-D analyses produce consistently superior predictions when the TCA scheme is adopted. Thus, for example, Fig. 3.2, which depicts the load–deflection relationships for both a typical RC beam and a PC prism under strip loading, illustrates that, while numerical instabilities associated with the TCA cause premature failure of the RC structure, the SCA appears to be unsuitable for the prism under strip loading; for the latter structural system, it is the earlier failure predicted by the TCA which gives adequate answers.

The need to adopt the TCA strategy in the course of analysis of a large number of prisms subjected to strip loading led to a distinction being made between RC and PC components in early investigations.^{51,54,85,98,99} Accordingly, it was argued that the allowing of cracks to be formed simultaneously at all locations where the criterion for cracking is fulfilled during a particular iteration (TCA) was more suitable for PC structures, i.e. in situations where the dynamic aspect of the fracture processes is more pronounced. On the other hand, the allowance of one crack only at the location where the state of stress is most critical during a particular iteration (SCA) could be deemed to be more representative of RC structural behaviour, i.e. where the presence of steel slows down the rate of macrocracking. In subsequent work on the 3-D model, however, it was realized that prisms under strip loading could not realistically be analysed with a 2-D model (see Chapter 4) — after all, a prism able to expand laterally can hardly be said to conform to plane-stress conditions when acted upon by a strip load across one of its plan dimensions. Nevertheless, it turns out that the MSL overestimate implicit in 2-D analyses of this structural type is more or less exactly cancelled out by the early instability associated with the TCA when this is applied to such problems. For other PC structures amenable to 2-D analysis, both the SCA and the TCA usually yield comparable results.

The crack-propagation strategies for 2-D modelling may therefore be summarized as follows. The SCA is to be used for RC structures. (A more detailed study of this procedure, showing why, namely on account of its more (numerically) stable nature, it is generally beneficial in most structural forms — RC and PC — will be outlined in Chapter 4.) While either the SCA or the TCA can be used for PC structures, the latter is usually adopted for the PC components since it also enables prisms under strip loading to be studied by means of 2-D analyses even though a formal 3-D analysis is required for these; the reason for such an apparent paradox is that the application of the TCA to prisms under

strip loading analysed as a plane-stress problem causes early numerical instability which acts as an almost exact compensating factor for the overestimate implicit in the 2-D modelling of this 3-D structural problem.

3.3. Plain concrete structures

3.3.1. Various prisms and cylinders under concentrations of load

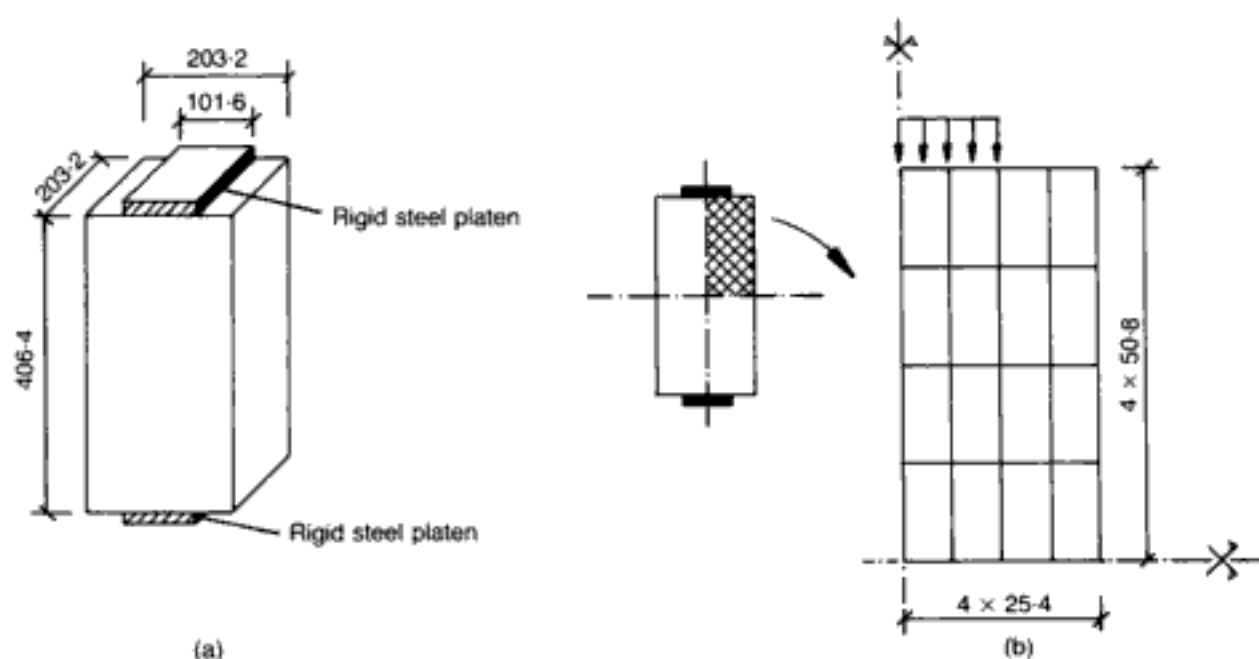
In this section, several specific PC prisms and cylinders are analysed in order to illustrate typical predictions of the 2-D model for such specimens. More general parametric results for these basic PC structural forms will follow subsequently.

3.3.1.1. Prism under concentric strip loading over one-half of each end face

The details of the specimen (with $f_c = 26.9 \text{ N/mm}^2$) — one of several prisms tested by Niyogi¹⁰⁰ — and its FE mesh subdivision appear in Fig. 3.3. Owing to symmetry, only one-quarter of the structure is analysed, with roller supports imposed along the two centrelines (i.e. movement is allowed along the axes of symmetry). The friction likely to be acting at the specimen—rigid platen interface is also mimicked in the analysis; thus, the latter assumes infinite friction to apply there, with the five nodes under the load consequently restrained against horizontal movement.^{54,85} The maximum aggregate size of 13 mm made possible the use of a 4×4 regular mesh.

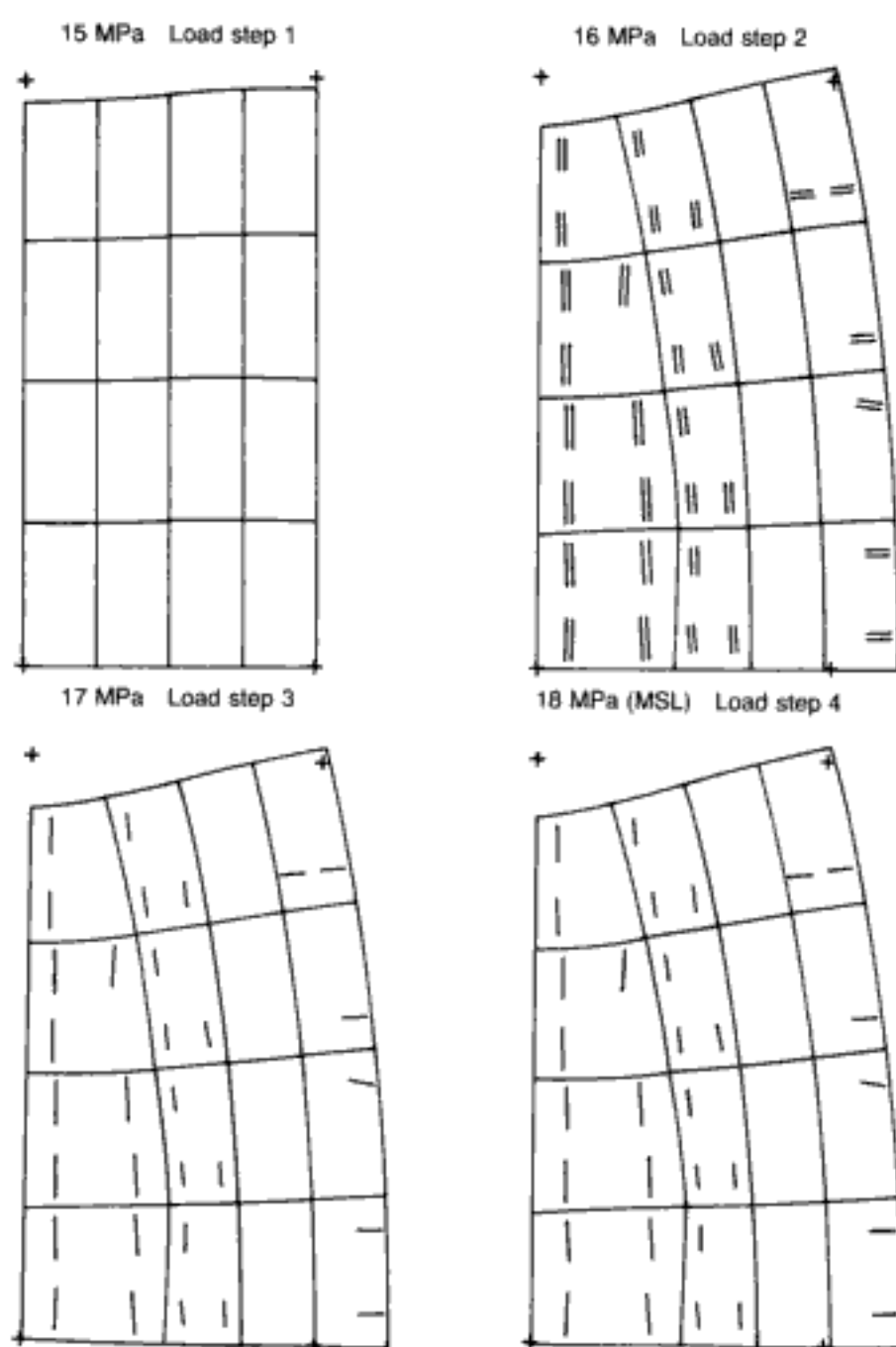
Fig. 3.3. PC prism under concentric strip loading over one-half of each end face:⁸⁵
(a) experimental data;
(b) FE mesh used in the analysis (All dimensions in mm)

The adoption of a load step of 1 N/mm^2 leads to a predicted collapse load of 18 N/mm^2 , which practically coincides with the $0.65f_c (= 17.4 \text{ N/mm}^2)$ value recorded experimentally. Larger load steps can cause earlier failure, the reason being the very explosive nature of cracking, which is both sudden and widespread. (However, it should be noted that, for PC specimens such as this



one, where no cracks occur until the ultimate load is approached, the usually uniform load steps from zero up to failure may be replaced by the more economical run which uses a single large load step up to first cracking (the latter being detected approximately by a preliminary linearly-elastic run), followed by smaller load increments therefrom.) The late and extensive nature of cracking may be seen by the analytical crack patterns shown in Fig. 3.4, obtained on the basis of an initial load step of 15 N/mm^2 and subsequent load steps of 1 N/mm^2 . It is interesting that all the cracks appear suddenly at around 16 N/mm^2 , no further cracking occurring in the next two load steps that lead up to collapse.

Fig. 3.4. PC prism under concentric strip loading over one-half of each end face:⁵⁴ crack patterns and deformed shapes (D.M. = 100) near collapse



3.3.1.2. Prism under concentric strip loading over one-quarter of each end face

This specimen is similar to the previous case study (see Fig. 3.3) except that the applied load covers only the central quarter of each end face. The relevant strength characteristics¹⁰⁰ are $f_c = 26.2 \text{ N/mm}^2$, bearing stress at first cracking $= 0.78f_c (= 20.5 \text{ N/mm}^2)$, ultimate bearing strength $= 0.82f_c (= 21.5 \text{ N/mm}^2)$. With the same adopted mesh as in Fig. 3.3(b), a preliminary elastic analysis gave 17.5 N/mm^2 as the (estimated) load for first cracking: this became the initial load step, with subsequent increments of 1 N/mm^2 .⁵⁴ The actual analytical load at first cracking was then found to be 20.5 N/mm^2 while the MSL value obtained was $0.86f_c (= 22.5 \text{ N/mm}^2)$, the latter comparing quite closely with the experimental value. Figure 3.5 depicts the cracking sequence prior to failure.

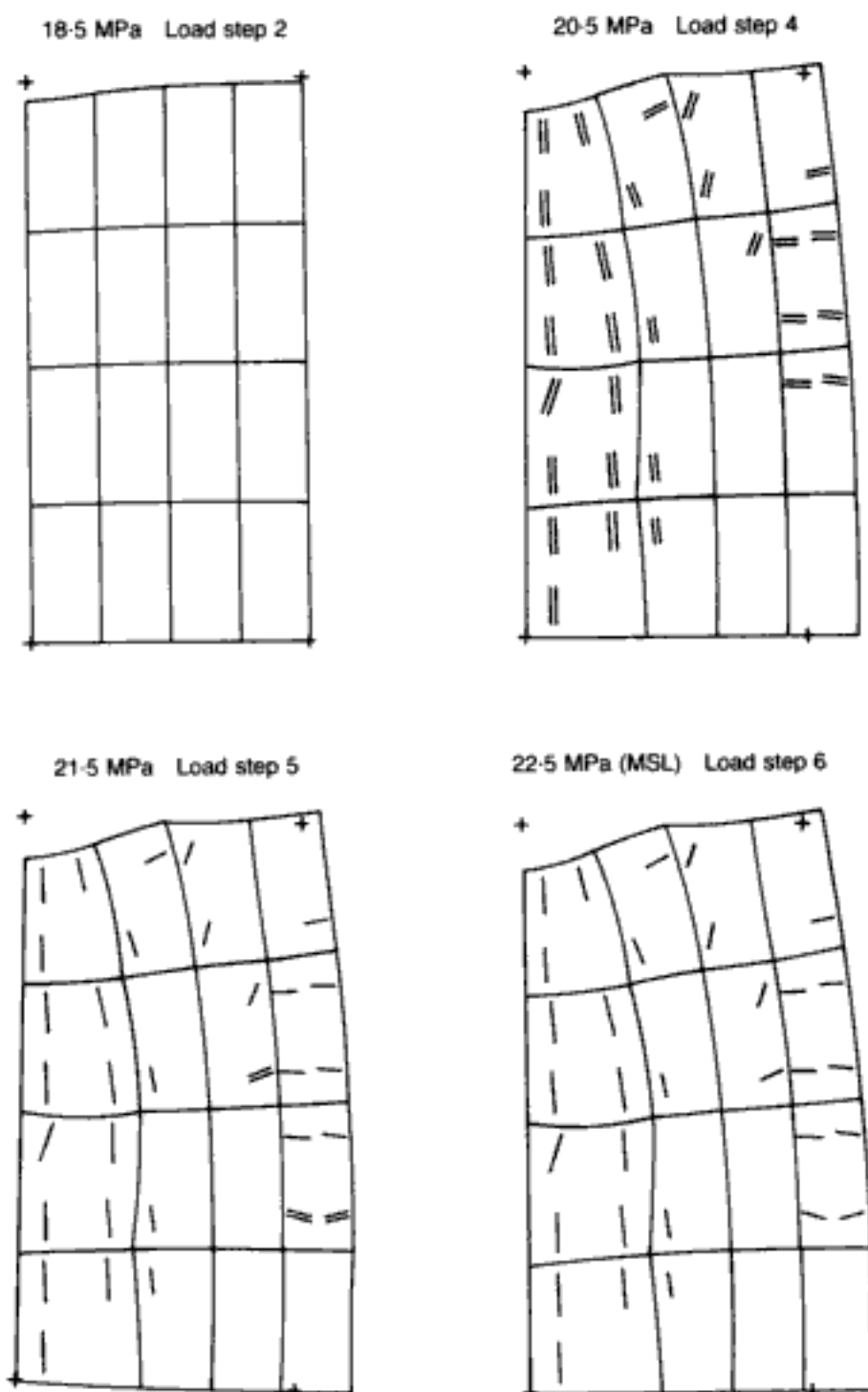
3.3.1.3. Prism under eccentric strip loading over one-quarter of each end face

Kotsovos and Cheong²³ tested a PC prism by applying two eccentric (but colinear) strip loads throughout one-quarter of the top and bottom faces, as shown in Fig. 3.6(a). A uniform 4×4 mesh was adopted in the analysis of one-half of the prism.⁹⁹ The material characteristic was $f_c = 48 \text{ N/mm}^2$, and the experimental failure stress was found to be $0.94f_c (= 45 \text{ N/mm}^2)$. By adopting a constant load step of 2 N/mm^2 throughout the whole loading history, the analysis predicted a maximum sustained load equivalent to $0.88f_c (= 42 \text{ N/mm}^2)$ which, again, compares well with experimental evidence. The strains and deflections of the numerical model and the tested prototype also correlate quite closely (see, for example, Fig. 3.6(b)), as do the intermediate and final cracking patterns. The latter appear in Fig. 3.7. There is no cracking during the first five load increments. At load step 6, horizontal cracking appears on the extreme left along the centreline and, in the next load step, vertical cracks also form next to the loaded area. The failure mechanism is one where the horizontal and vertical cracks spread until they join.

3.3.1.4. Cylinder under concentric patch loading over one-quarter of each end face

This PC cylinder provides the first example of axisymmetric — rather than plane-stress — analysis. As experimental reference, Bédard⁵⁴ still used one of the prisms tested by Niyogi¹⁰⁰ — see Fig. 3.3(a) for the member's dimensions — but the test specimen in question was now acted upon by centrally located square patch loads (i.e. the loaded area was $101.6 \text{ mm} \times 101.6 \text{ mm}$), rather than by strip loading (i.e. covering an area $101.6 \text{ mm} \times 203.2 \text{ mm}$). Justification for this is forthcoming from the well-established experimental fact that uniaxial compression tests carried

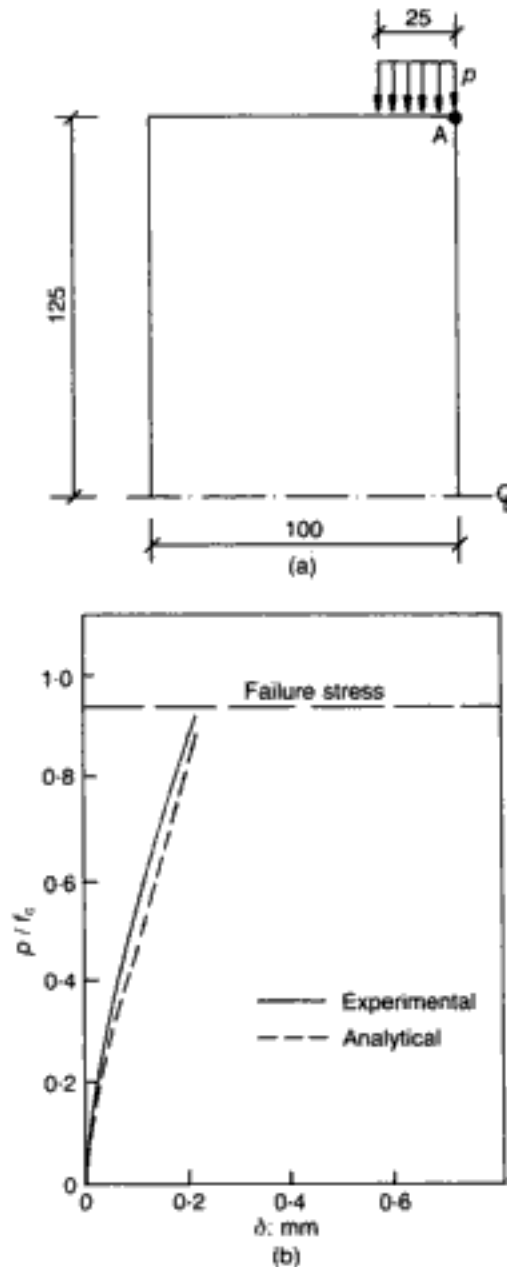
Fig. 3.5. PC prism under concentric strip loading over one-quarter of each end face:⁵⁴ crack patterns and deformed shapes (D.M. = 100) near collapse



out on specimens having a square or circular cross-section will fail at approximately the same ultimate load provided that the height and the height-to-diameter ratio are the same.¹⁰ In the present case, Niyogi's test data can be compared to results for cylinders on condition that the 'total area' over the 'loaded area' is kept the same for the same height specimens. Here, this ratio is 4.

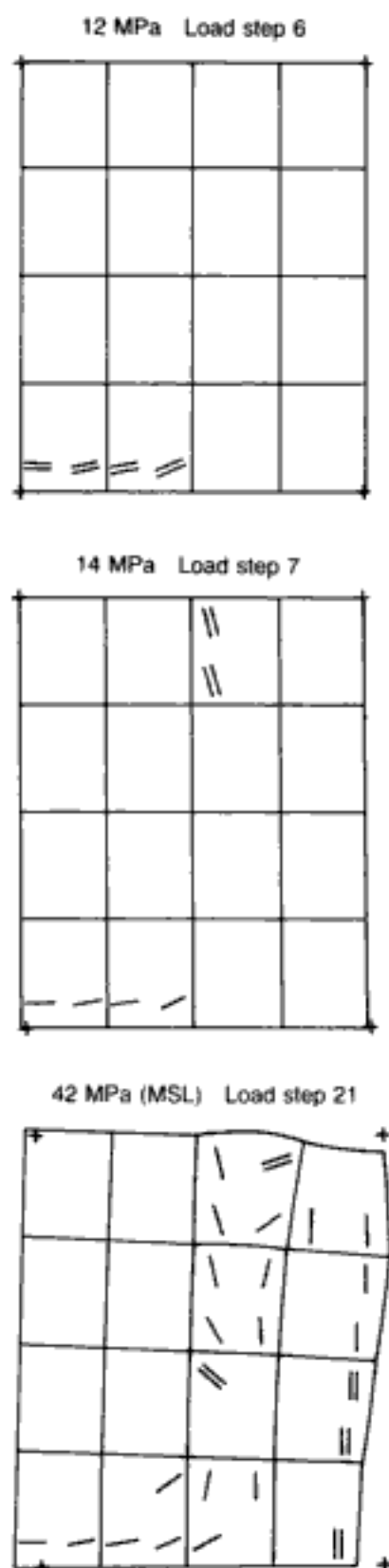
Viewed in elevation, the axisymmetric mesh for one-eighth of the cylinder under central circular patch load on one-quarter of each face is the same as that adopted for one-quarter of the prism

Fig. 3.6. PC prism under eccentric strip loading over one-quarter of each end face:⁹⁹ (a) experimental data (all dimensions in mm); (b) applied stress (p/f_c)—vertical deflection at point A (δ) relationships



under strip load on one-half of each face (see Fig. 3.3(b)). As in previous case studies, the assumption of infinite friction is made at the specimen—platen interface, thus preventing relative movement between these surfaces. An initial elastic estimate of first cracking yielded 19.5 N/mm^2 as the initial load step, after which load increments of 1 N/mm^2 were adopted.⁵⁴ In the nonlinear analysis, cracking first occurred at 26.5 N/mm^2 in the form of a circumferential crack just underneath the edge of the patch load, the cylinder failing at the subsequent load step with an additional radial crack at the edge of the specimen (see Fig. 3.8). Since the experimental results were $f_c = 28.8 \text{ N/mm}^2$, with an ultimate bearing stress of $1.06 f_c (= 30.5 \text{ N/mm}^2)$, the MSL of $27.5 \text{ N/mm}^2 (= 0.96 f_c)$ underestimates the test value by about 10% — an acceptable margin of error, especially in view

Fig. 3.7. PC prism under eccentric strip loading over one-quarter of each end face:⁹⁹ crack patterns and deformed shapes (D.M. = 20) at various load stages

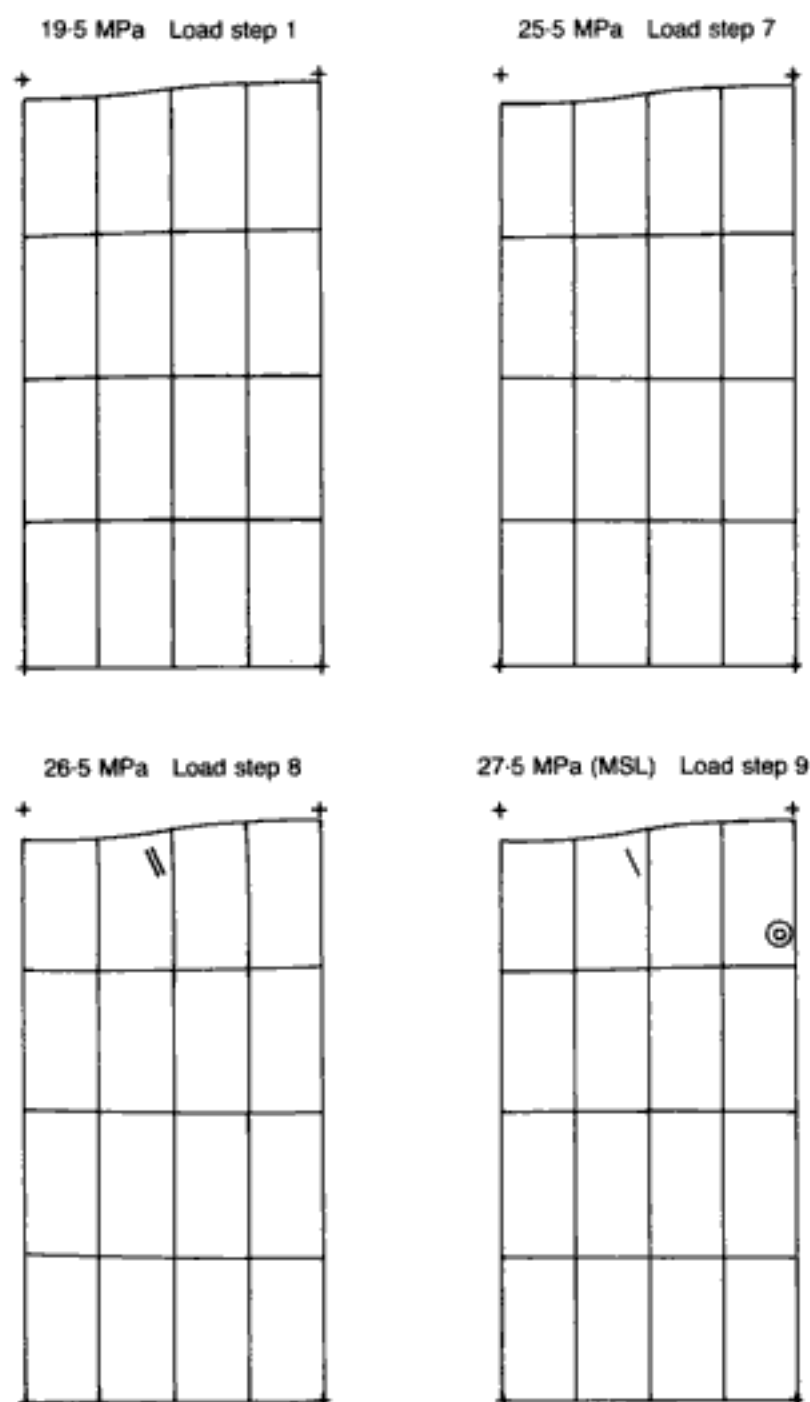


of the approximate nature of the comparison between analysis and experiment. However, it will be demonstrated in section 3.3.1.5 that, by varying the assumed boundary conditions, a better correlation is possible.

3.3.1.5. Cylinder under concentric patch loading over one-sixteenth of each end face

The relevant test data from the comparable prism tested by Niyogi¹⁰⁰ is $f_c = 33.9 \text{ N/mm}^2$, ultimate bearing stress = $2.38 f_c$ ($= 80.7 \text{ N/mm}^2$). With only the inner top element in the (now axisymmetric) mesh of Fig. 3.3(b) loaded, the analysis proceeded with an initial load step of 28 N/mm^2 and subsequent increments of 2 N/mm^2 .⁵⁴ The resulting MSL value was 60 N/mm^2 ($= 1.77 f_c$). Figure 3.9 shows that cracking initiates at 32 N/mm^2 through a radial crack underneath the patch load, with the formation

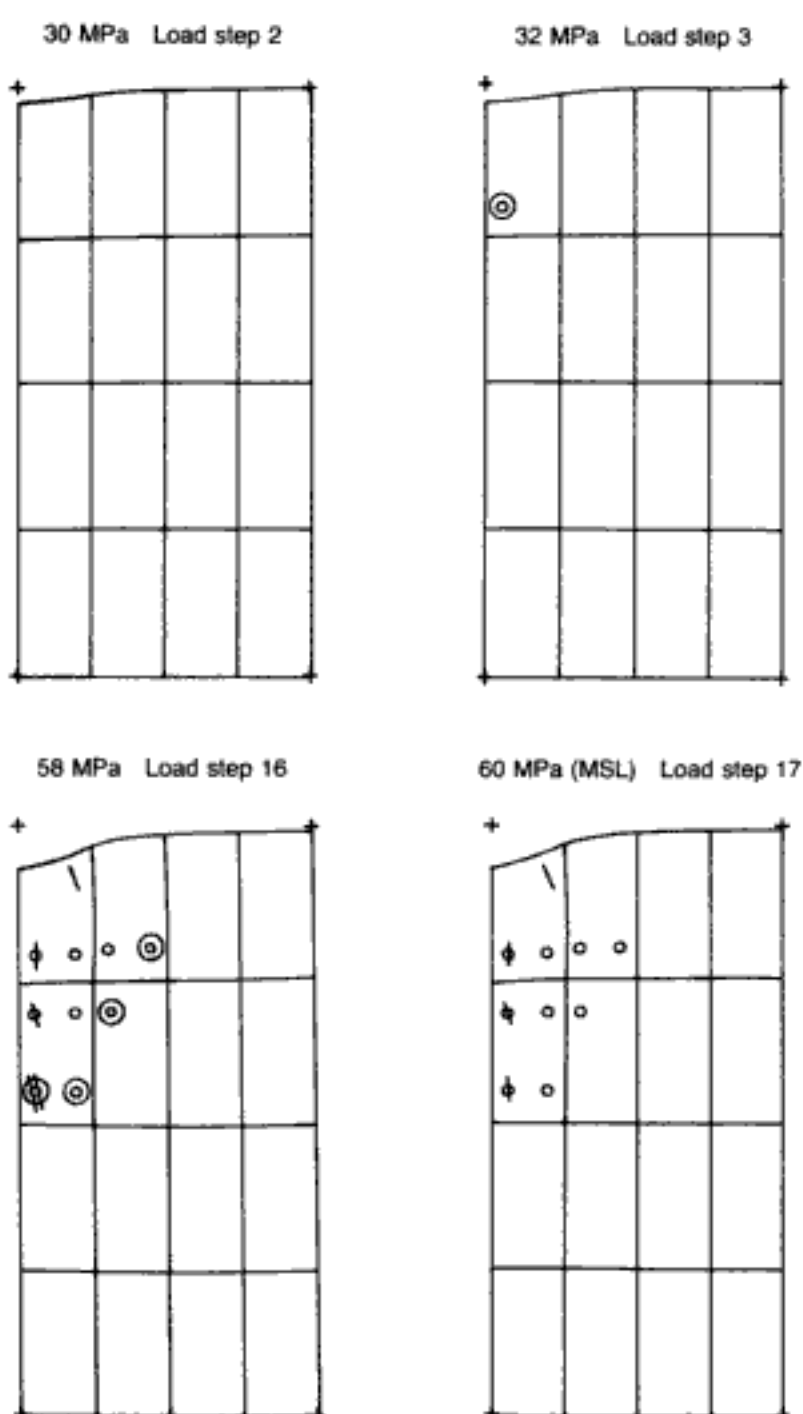
Fig. 3.8. PC cylinder under concentric patch loading over one-quarter of each end face:⁵⁴ crack patterns and deformed shapes ($D.M. = 100$) near collapse



of additional radial and circumferential cracks as collapse is approached: the final pattern indicates heavy cracking, but densely located around the initial crack.

The analytical underestimate of the experimental collapse pressure by 26% is too large to be explained solely in terms of the difference between cross-section and loaded-area shapes. If, however, allowance is made for the possibility that the patch-loaded specimens of Niyogi were compressed in such a way that the interaction between specimen and loading platen departed from the full-friction extreme, a dramatic improvement in the correlation

Fig. 3.9. PC cylinder under concentric patch loading over one-sixteenth of each end face:⁵⁴ crack patterns and deformed shapes ($D.M. = 100$) at first cracking and near collapse



between test and numerical collapse-pressure values is obtained. Thus, for example, the adoption of the other extreme of surface interaction, namely zero friction between specimen and loading platen (by allowing the nodes under the loaded area to displace freely in the horizontal direction), causes the analytical prediction for the MSL to become $2.24f_c$. Similarly, a re-analysis of the cylinder studied in section 3.4.1.4 with the 'no friction' condition yields an MSL of $1.04f_c$. The close correlation of these analytical predictions with the corresponding results of Niyogi ($2.38f_c$ and $1.06f_c$ respectively) could certainly be explained if frictionless conditions had actually been attained in Niyogi's tests; however, another important boundary-condition factor is the range of load types encompassed by the extremes of uniform pressure and uniform displacement, and this will be explored in subsequent sections and also in Chapter 4. What the present results do show is the potentially very significant influence that the boundary conditions at the loaded interface have on analytical/experimental results of PC components.

3.3.2. Parametric study of prisms and cylinders under concentrations of load

3.3.2.1. Scope

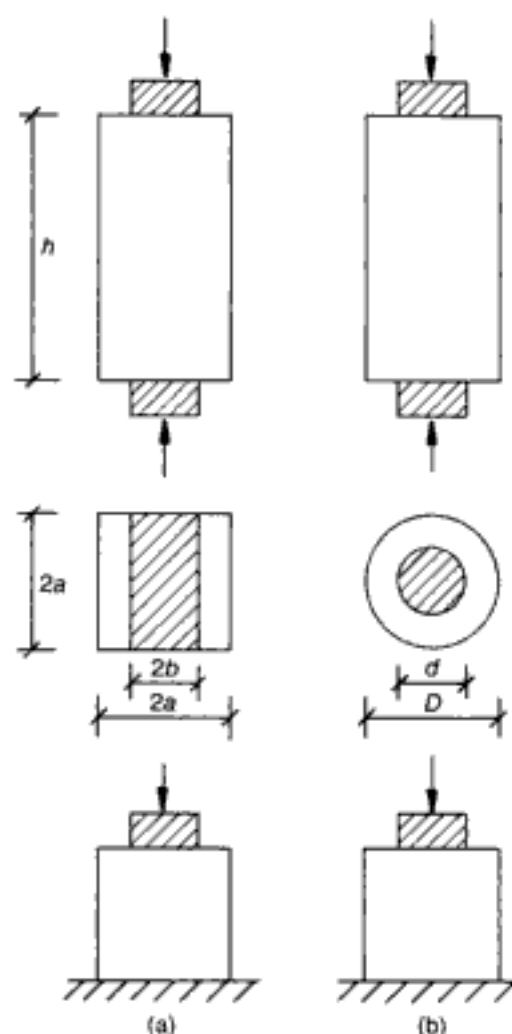
The structural forms to be investigated consist of prisms and cylinders loaded concentrically in the axial direction over a limited area on one or both ends. There is adequate experimental information on the behaviour of such structures, as they represent a simplified version of the problem of large concentrations of load that is frequently encountered in civil engineering design. Anchor plates in prestressed concrete structures, bridge bearings over piers, concrete hinges and bearing blocks are examples of 'bearing' problems.

The present work has been based on a study of the following cases:⁶⁰

- (a) prisms ($2a \times 2a \times h$) loaded axially at one end or both ends over a 'strip' concentric area ($2b \times 2a$) as shown in Fig. 3.10(a); the investigation has been based on a plane-stress analysis
- (b) cylinders ($D \times h$) loaded axisymmetrically at one end or both ends over a circular area with diameter d (see Fig. 3.10(b)); the behaviour has been investigated by means of an axisymmetric analysis.

In the present parametric studies, special care has been taken to mimic as closely as possible the actual experimental boundary conditions. Thus, the above structural forms have been subjected to a uniform boundary *displacement* — rather than load — since the behaviour predicted by the analysis is compared with that established experimentally by loading specimens through rigid platens.^{100,101} Such platens, in contrast to flexible platens, induce a state of uniform displacement in the loading direction.

Fig. 3.10. PC specimens under concentrations of load at one or both ends.⁶⁰
 (a) prisms;
 (b) cylinders



Furthermore, no displacement across the loaded surface has been allowed in the analysis, since the experimental data used for the comparison have been obtained from tests in which no attempt has been made to reduce the frictional restraint at the interface between the concrete specimens and the steel platens.

The ratio $\sigma_b = \text{applied load}/\text{loaded area}$ is termed 'bearing' stress and the maximum value of σ_b is generally known as 'bearing' strength (f_b). The loaded area A_1 normalized with respect to the total cross-sectional area A orthogonal to the loading direction is given by $r = A_1/A$. The inverse of r , $R = 1/r$, becomes $R = a/b$ and $R = (D/d)^2$ for the plane-stress and axisymmetric cases respectively.

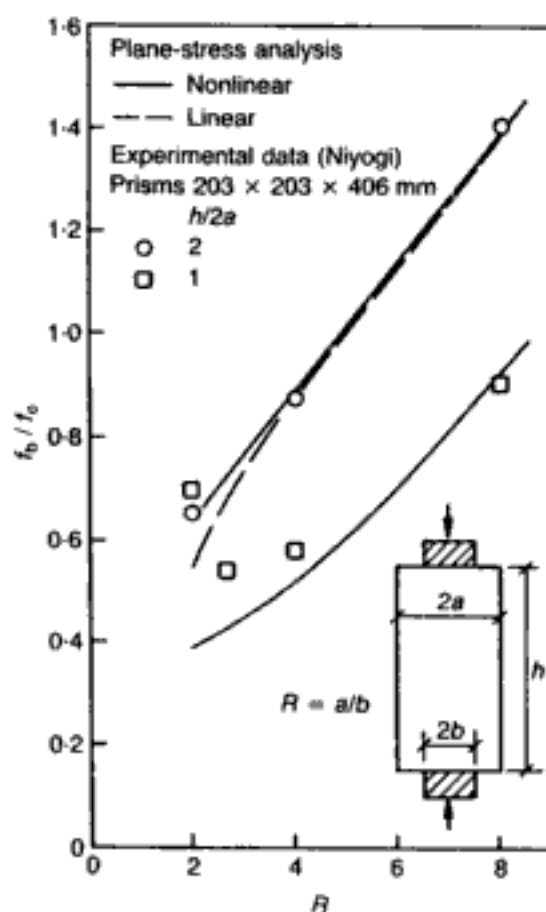
The variation of f_b with R has been established for both study cases by varying the parameters b and d . The effect of the height h of the structure and that of the concrete strength f_c (where, as usual, f_c is the uniaxial cylinder compressive strength) on the above variation has also been established. All the FE meshes used in the modelling of one-quarter of a prism and one-eighth of a cylinder consisted of a four-element subdivision heightwise, while the number of elements in the direction orthogonal to the loading

was 4, 5 or 6, depending on specimen type and its R value (see reference 60).

The presentation of the principal results is given in Figs 3.11–3.17 (plane-stress analysis) and 3.18–3.22 (axisymmetric analysis). Figures 3.11, 3.12, 3.15, 3.18 and 3.19 describe the variation of bearing strength with the loaded area for the various cases investigated. These figures also include experimental values obtained from the works of Niyogi¹⁰⁰ and Hawkins.¹⁰¹ The experimental values given in Figs 3.15 and 3.19 have been obtained from tests on cubes with a side length varying between 100 mm and 300 mm and the variation of these data reflects the effect of the specimen size, i.e. the smaller the size of the specimen the higher its strength.¹⁰² Both bearing strength and loaded area are expressed in a normalized form, since such a form of representation facilitates the comparison of results. The bearing strength is also expressed in a normalized form in Figs 3.16, 3.17 and 3.22 which show the effect of concrete strength and specimen height on bearing strength.

The variation of the displacement of the loaded surface with increasing bearing stress is shown in Figs 3.13 and 3.20, in which the bearing stress is also expressed in a normalized form, while Figs 3.14 and 3.21 give a representation of the deviation of the

Fig. 3.11. Variation of bearing strength with loaded area for prisms loaded at both ends⁶⁰



results obtained by linear analysis from those obtained by nonlinear analysis. Typical fracture modes of the structures may be illustrated by reference to the cracked patterns for the cylinder discussed in section 1.5.2 (see Fig. 1.83).

Fig. 3.12. Variation of bearing strength with $h/2b$ ratio for prisms loaded at both ends⁶⁰

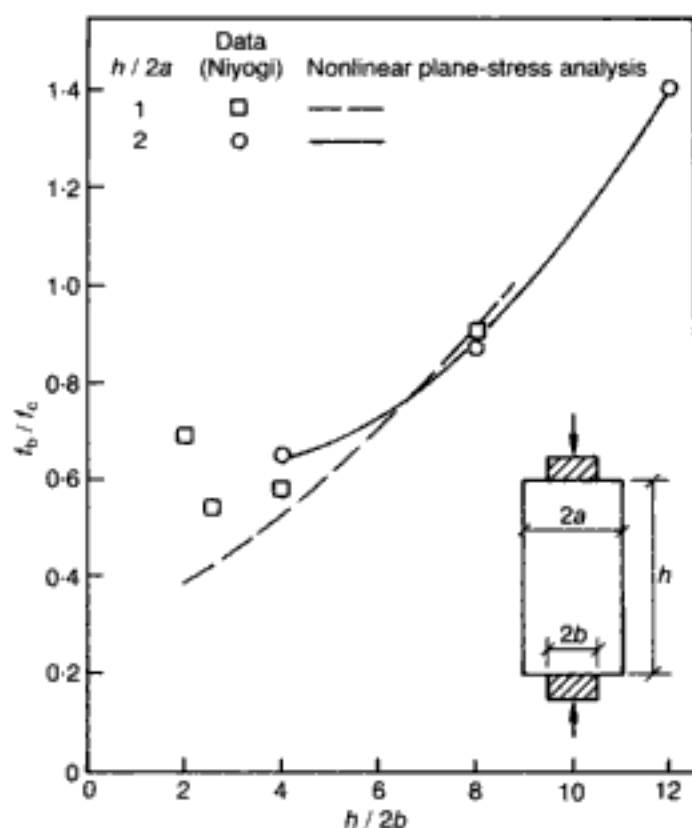
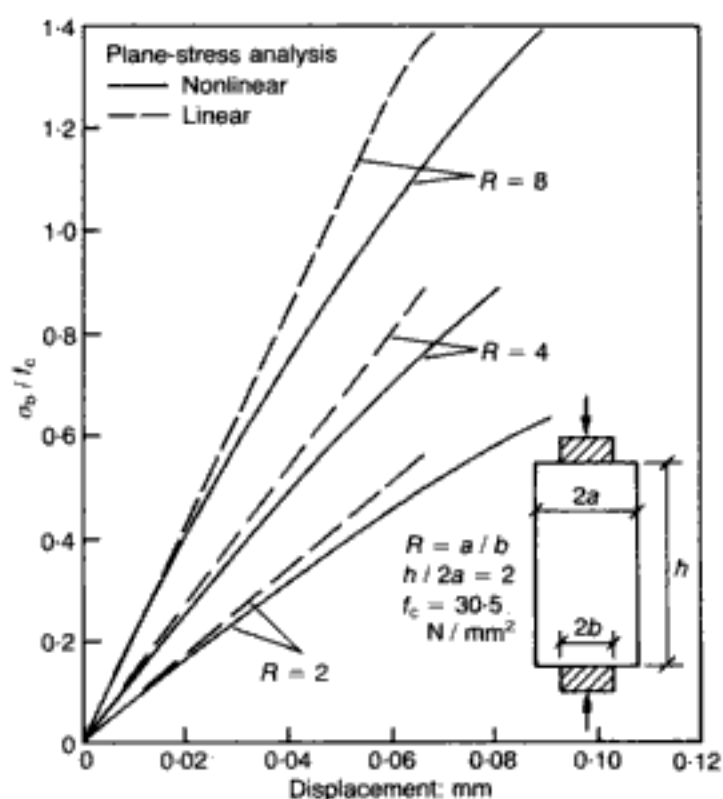


Fig. 3.13. Variation of displacement of loaded surface with increasing bearing stress for prisms loaded at both ends⁶⁰



Hidden page

Fig. 3.16. Effect of concrete quality on bearing strength predicted by plane-stress analysis⁶⁰

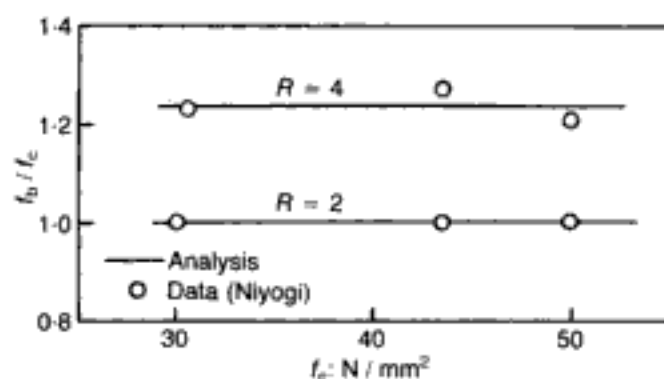


Fig. 3.17. Effect of prism height on bearing strength predicted by plane-stress analysis⁶⁰

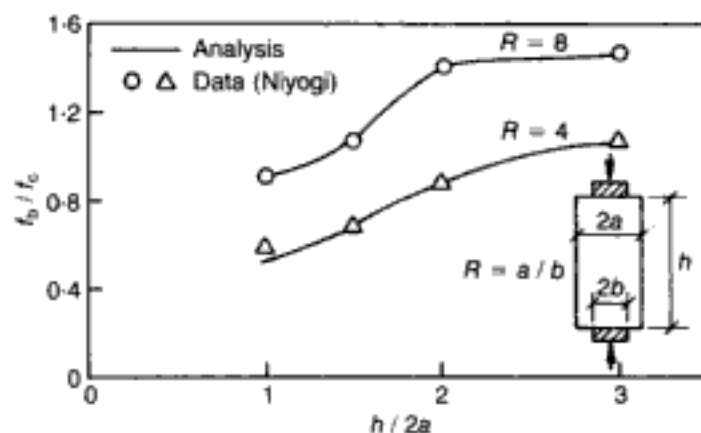


Fig. 3.18. Variation of bearing strength and crack-initiation stress level with loaded area for cylinders loaded at both ends⁶⁰

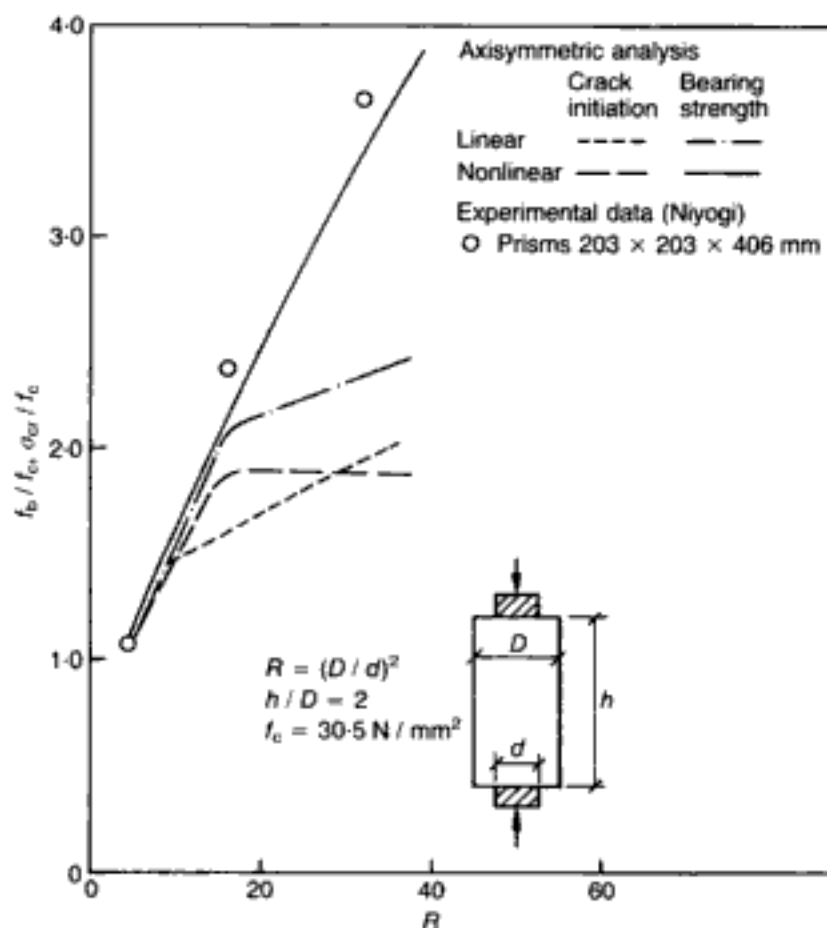
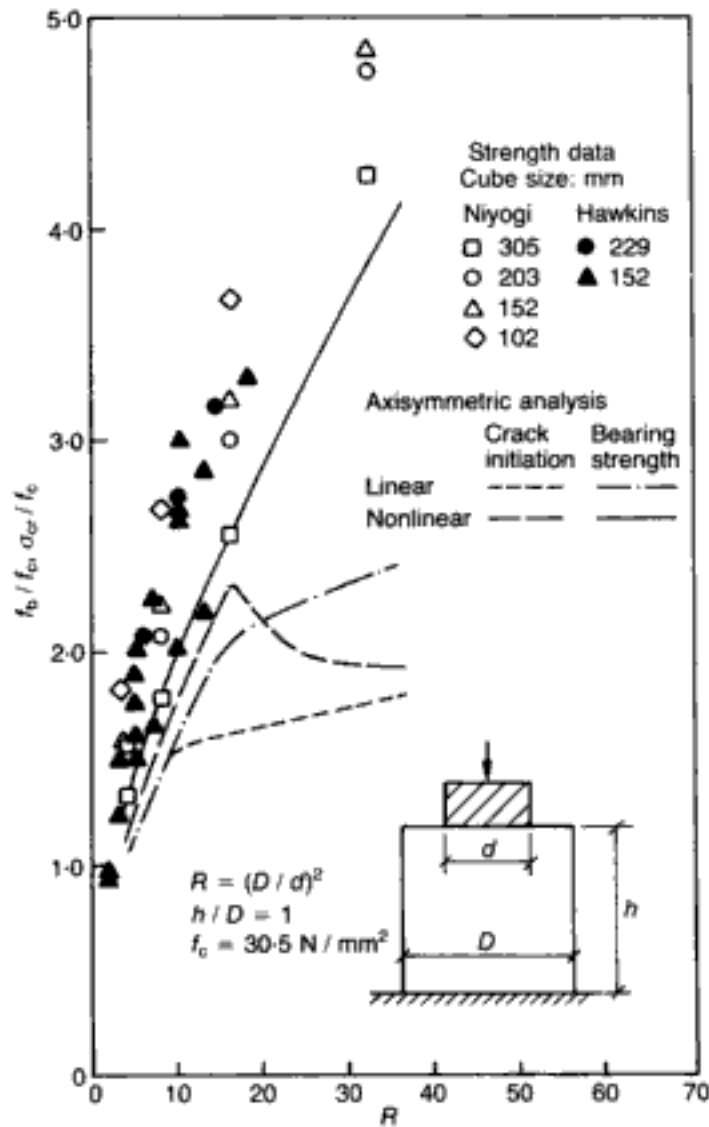


Fig. 3.19. Variation of bearing strength and crack-initiation stress level with loaded area for cylinders loaded at one end only⁶⁰



of triaxiality may be underestimated — especially near load concentrations — by the model. With these limitations in mind, it is to be expected that, although the present plane-stress parametric study should convey the appropriate trends and yield reasonably accurate predictions, the latter may sometimes show departures from the experimental results — corrections of such departures necessitating the 3-D model of Chapter 4.

Figure 3.11 indicates a very good correlation between the bearing-strength results predicted by the nonlinear analysis and those obtained from the tests on prisms (especially those with $h/2a = 2$) loaded over a concentric strip area $2b \times 2a$ at both ends. The triaxial state of stress which exists in the region of the loaded area as a result of the frictional restraint at the specimen-platen interface should have an effect on the strength of the specimens for values of the $h/2b$ ratio smaller than approximately 2.5 (see section 1.2.1.2), and this effect should be reflected in the experimental results; such behaviour is illustrated in Fig. 3.12 which

Fig. 3.20. Variation of displacement of loaded surface with increasing bearing stress for cylinders loaded at both ends⁶⁰

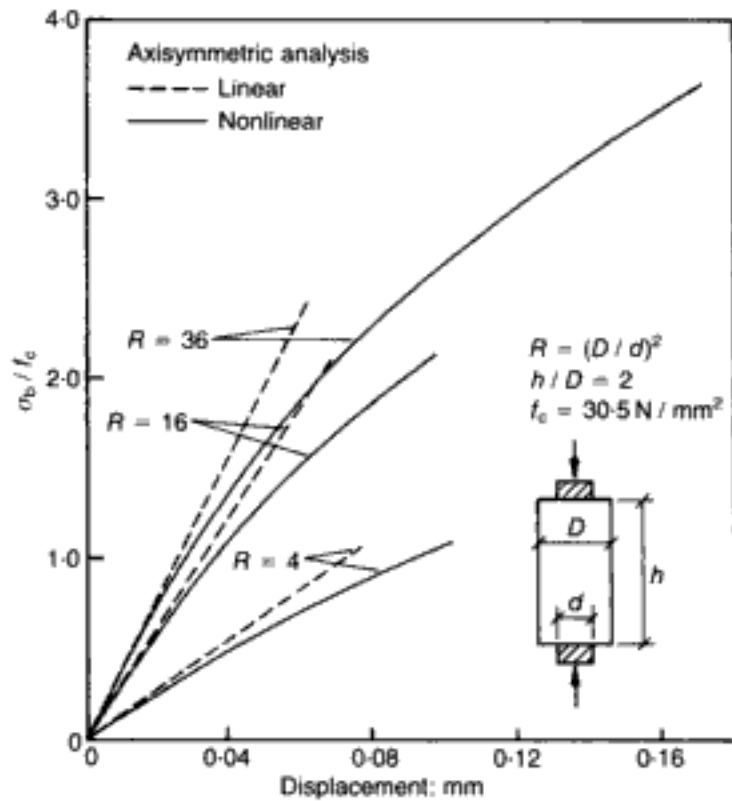
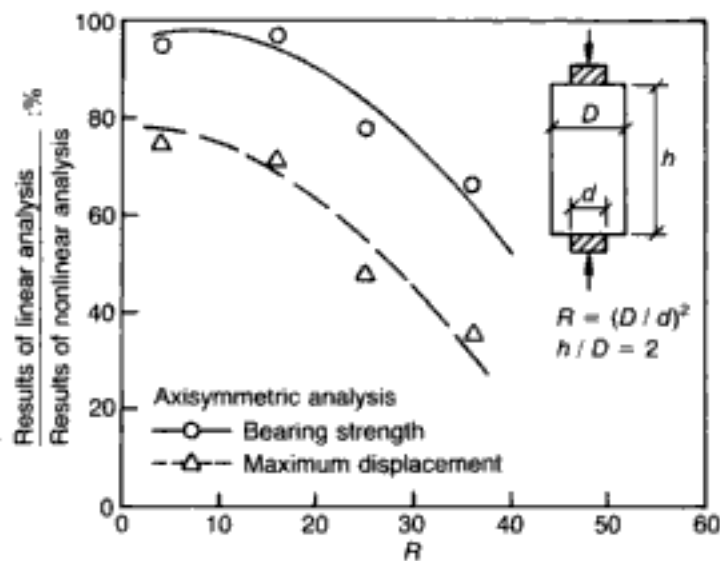


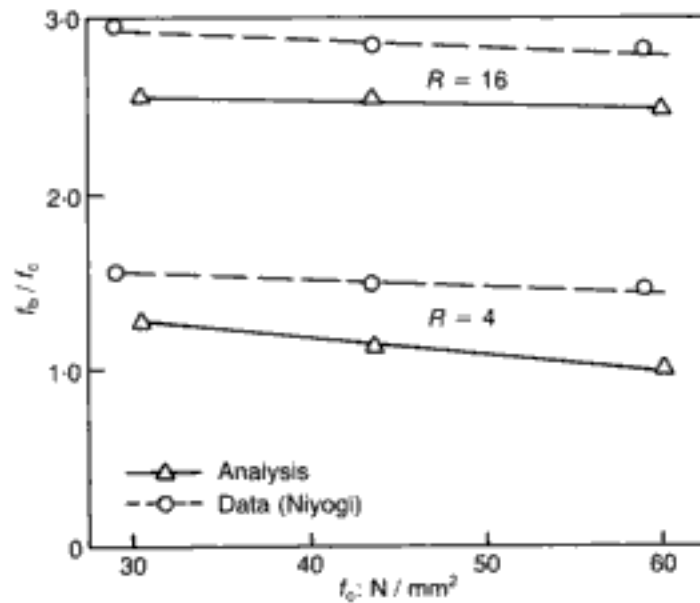
Fig. 3.21. Variation with loaded area of bearing strength and maximum displacement of loaded surface predicted by linear analysis expressed as percentages of the values predicted by nonlinear analysis⁶⁰



shows a deviation of the experimental values from the analytical results for $h/2b \leq 3$ (and which increases with decreasing $h/2b$) since the biaxiality of the 2-D analysis cannot fully allow for the triaxial effect.

It is interesting to note that the linear analysis also yields a realistic prediction of the bearing strength which improves as the loaded area is reduced (see Fig. 3.11). However, the displacement of the loaded surface predicted by this analysis is always smaller than that obtained from the nonlinear analysis (see Fig. 3.13). The variations of the maximum displacement and bearing strength with

Fig. 3.22. Effect of concrete quality on bearing strength predicted by axisymmetric analysis⁶⁰



the loaded area as predicted by the linear analysis for prisms with $h/2a = 2$ are shown in Fig. 3.14 expressed as percentages of the values predicted by the nonlinear analysis. The figure indicates that the maximum displacement predicted by the linear analysis is essentially independent of the loaded area and has a value slightly smaller than 80% of the value predicted by the nonlinear analysis. On the other hand, the bearing strength predicted by the linear analysis increases from a value of about 85% up to a value of about 100% of the value predicted by the nonlinear analysis as the loaded area decreases from a value corresponding to $R = 2$ to $R > 4$.

The effect of the frictional restraint at the specimen-platen interfaces on bearing strength is more pronounced on the experimental results obtained from tests on cubes ($h/2a = 1$) loaded at one end only over a concentric strip area $2b \times 2a$. This effect causes the deviation of the above results from those predicted by the analysis (both linear and nonlinear) which begins at about $R = 4$ (see Fig. 3.15). Once again, this is attributable to the fact that the analytical prediction of strength is based on the use of a biaxial strength envelope whereas the actual strength of the specimens is dictated by a predominantly triaxial compression state of stress.

In the assumption that the uniaxial cylinder compressive strength f_c can be used as a realistic descriptor of the concrete quality, Fig. 3.16 indicates that concrete quality has practically no effect on bearing strength. On the other hand, Fig. 3.17 indicates that bearing strength increases with the height of the specimen, which is in good agreement with the experimental trends. It may be noted, however, that the figure does not include values of h smaller than $2a$, since for such values the plane-stress condition is violated more severely than for taller specimens.

Axisymmetric analysis. Both Figs 3.18 and 3.19 indicate that the variation of bearing strength with loaded area predicted by the nonlinear analysis is in good agreement with the experimental values obtained from references 100 and 101. The figures also show the analytically predicted variations with loaded area of the stress level sufficient to cause crack initiation (σ_{cr}), and it is interesting to note that, while for values of R up to approximately 16 the above variations exhibit trends similar to those of the variations of the bearing strength, i.e. a steep increase of the stress level with decreasing loaded area (σ_{cr} and f_b being of comparable magnitudes), for higher values of R this trend changes dramatically and the 'cracking' stress level remains essentially constant (and well below f_b). In fact, for the case in which load is applied at one end only, σ_{cr} decreases abruptly when R exceeds a value of about 16 before it attains a near-constant value.

It seems from the above, therefore, that for values of R greater than about 16 the increase in bearing strength with decreasing loaded area is due to a dramatic increase in the load-carrying capacity of the *cracked* structure. This increase appears to result from the fact that, for such values of R , a much higher external load is required to cause cracking to extend outside the region beneath the loaded surface where cracking initiates in all cases. Collapse occurs soon after the cracks extend outside this region (see, typically, Fig. 1.83).

However, since the axisymmetric analysis imposes an axisymmetric mode of cracking, the reduction in the stiffness of the cylinder predicted by the analysis is larger than that which is actually experienced by the structure, where full cracking symmetry may not, in fact, be realized. This larger reduction in the stiffness may cause the small deviation of the predictions of bearing strength from the experimental values which begins at about $R = 16$ (see Fig. 3.19). For smaller values of R , the stress sustained by the structure in excess of that causing crack initiation is relatively small and, as a result, the reduction in stiffness due to the axisymmetric cracking has a smaller effect on the predicted bearing strength.

Figures 3.18 and 3.19 also indicate that the levels of bearing strength predicted by the linear analysis are lower than those predicted by the nonlinear analysis. Although initially the above predictions are relatively close, the difference between them increases with decreasing loaded area and progressively becomes considerable. Such behaviour is considered to reflect the inability of the linear material to delay the cracking processes by internal stress redistributions. The displacements of the loaded surface predicted by the linear analysis are also always smaller than those predicted by the nonlinear analysis (see Fig. 3.20). A clearer indication of the above behaviour is presented in Fig. 3.21 which shows the variations of the maximum displacement and bearing

strength, as predicted by the linear analysis, expressed as percentages of the values predicted by the nonlinear analysis.

In contrast to the plane-stress results, which indicate that concrete quality has no effect on bearing strength, the analytical results of Fig. 3.22 show that bearing strength decreases with increasing concrete strength f_c . The figure also includes experimental values¹⁰⁰ which exhibit a similar trend.

3.3.2.3. Conclusions

As explained in section 1.5, for all cases studied, collapse of the structure occurs without the compressive strength of concrete having been exceeded anywhere within the structure. Both plane-stress and axisymmetric analyses predict that cracking will occur in regions subjected to a state of stress with at least one of the principal stress components being tensile. For the cases investigated, the most critical state of stress is that which causes cracking to occur in the region shown in Fig. 1.83(b). With increasing load, this cracking propagates only into other regions subjected to similar states of stress, i.e. with at least one of the principal stress components being tensile, up to the formation of a crack pattern corresponding to the collapse stage (see Fig. 1.83(c)). For reasons outlined in Chapter 1, such a behaviour is found to hold for all PC and RC structures analysed in this and the next chapter.

It is well known that elastic theory may often provide good predictions within the working range of the material (see, for example, reference 9). The present study shows that, while analyses based on linear material properties may sometimes also produce acceptable predictions at higher load levels, they often yield considerable underestimates of the strength and deformational characteristics of PC structures.

3.3.3. Parametric study of the effect of boundary conditions on prisms and cylinders under concentrations of load

3.3.3.1. Scope

Problems of large concentrations of load in actual PC structures are tackled mainly on the basis of experimental studies conducted on small-scale concrete specimens such as cubes, prisms, cylinders, etc., loaded over a limited area on one end or both ends (for a number of such studies, see reference 103). The results obtained from such tests, however, are influenced by secondary effects caused by the boundary conditions imposed on the specimens by the various testing techniques used. For example, depending on the testing method, the boundary conditions in the direction orthogonal to the loaded surface may vary from a uniform state of stress to a uniform state of displacement. Furthermore, depending on the technique used to reduce friction at the specimen-platen interfaces, frictional forces may be developed such as to induce either a restraint to, or an extension of, the specimen across its loaded surface. Secondary effects of boundary

conditions are not readily definable experimentally and their effect on the behaviour of the specimen is difficult to establish. On the other hand, it is possible through numerical simulation¹⁰³ to specify given boundary conditions and to predict the specimen behaviour realistically, as will presently be shown.

Prisms and cylinders such as those defined in Fig. 3.10 are to be modelled through the 2-D meshes described in section 3.3.2, keeping the height-to-lateral dimension constant at a value $h/2a$, $h/D = 2$. These structural forms have been subjected to either a *uniform displacement* or a *uniform load* in the direction *orthogonal* to the loaded surface. Each of these boundary conditions has been combined with a displacement *along* the loaded surface that is either *fully restrained* or *completely free*. The above can be considered as providing the bounds to a wide range of conditions which may be represented schematically as shown in Fig. 1.2.

3.3.3.2. Results and discussion

Figures 3.23 and 3.24 show that both plane-stress and axisymmetric analyses predict an increase in bearing strength with decreasing loaded area (i.e. increasing R) for all cases investigated. Although values of R greater than 8 have not been investigated, it should

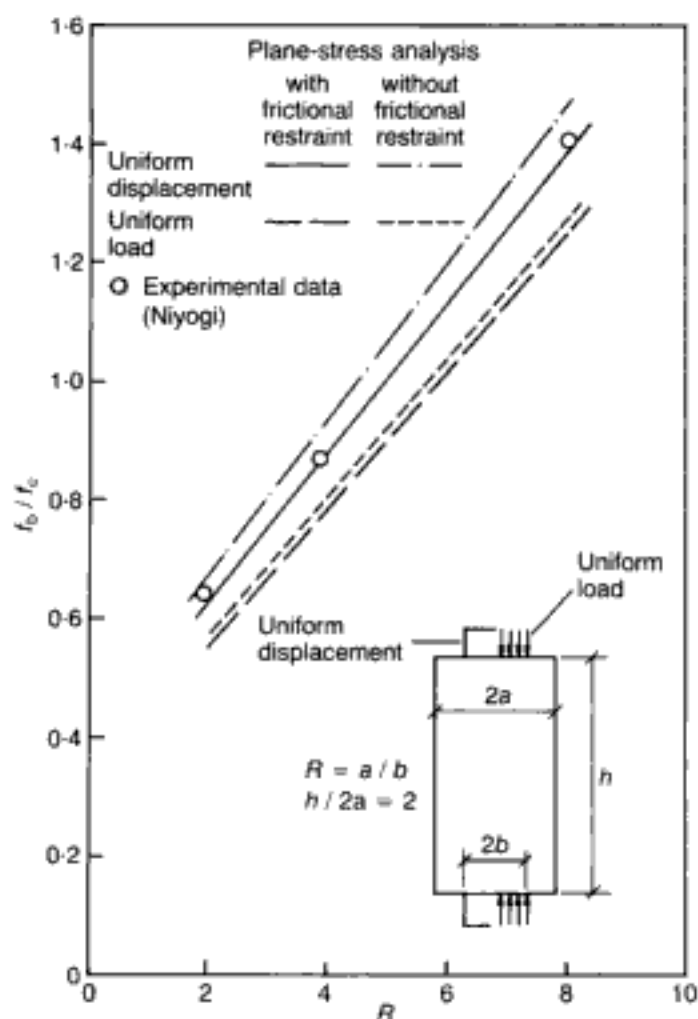


Fig. 3.23. Variation of bearing strength with size of loaded area as predicted by the plane-stress analysis for prisms under strip loading¹⁰³

be noted that the increase in bearing strength with R predicted by the plane-stress analysis should have an upper-bound limit imposed by the closed-form shape of the biaxial strength envelope of concrete (see section 1.4.2). On the other hand, the strength envelope of concrete under triaxial compressive stress states is open-ended in stress space (see section 1.4.2) and, therefore, the strength properties of the material should not impose any such limit on the predicted increase in bearing strength with R for the axisymmetric case.

The increase in bearing strength with R is considered to be attributable to an increase of the load-carrying capacity of the material in the region beneath the loaded surface caused by the multi-axial compressive state of stress which exists in this region. Such a state of stress is predominantly the result of the restraint imposed on the lateral expansion of the material in the above region by the surrounding concrete. The effectiveness of this restraint increases with R (since R is a measure of the volume of the surrounding concrete) and causes bearing strength also to increase.

However, the lateral expansion of the material in the region beneath the loaded surface is also restricted by the full restraint of displacement along the loaded surface imposed on some of the structural forms investigated. For a plane state of stress, this appears

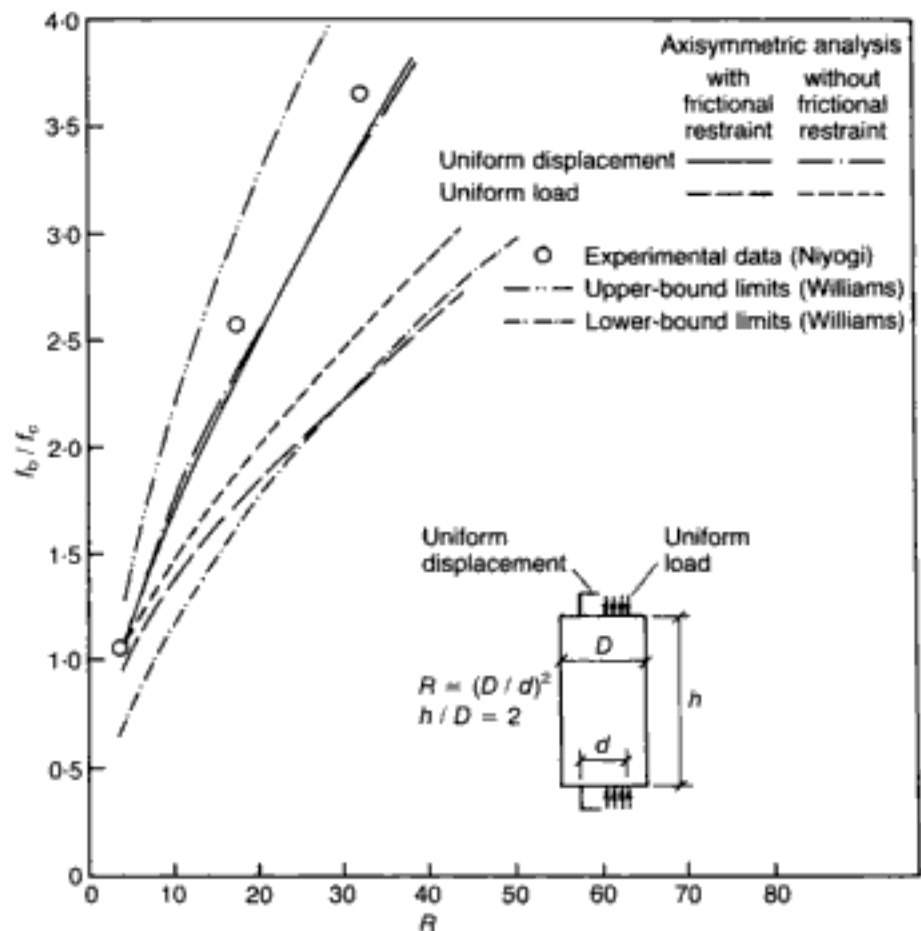


Fig. 3.24. Variation of bearing strength with size of loaded area as predicted by the axisymmetric analysis for concentrically loaded cylinders¹⁰³

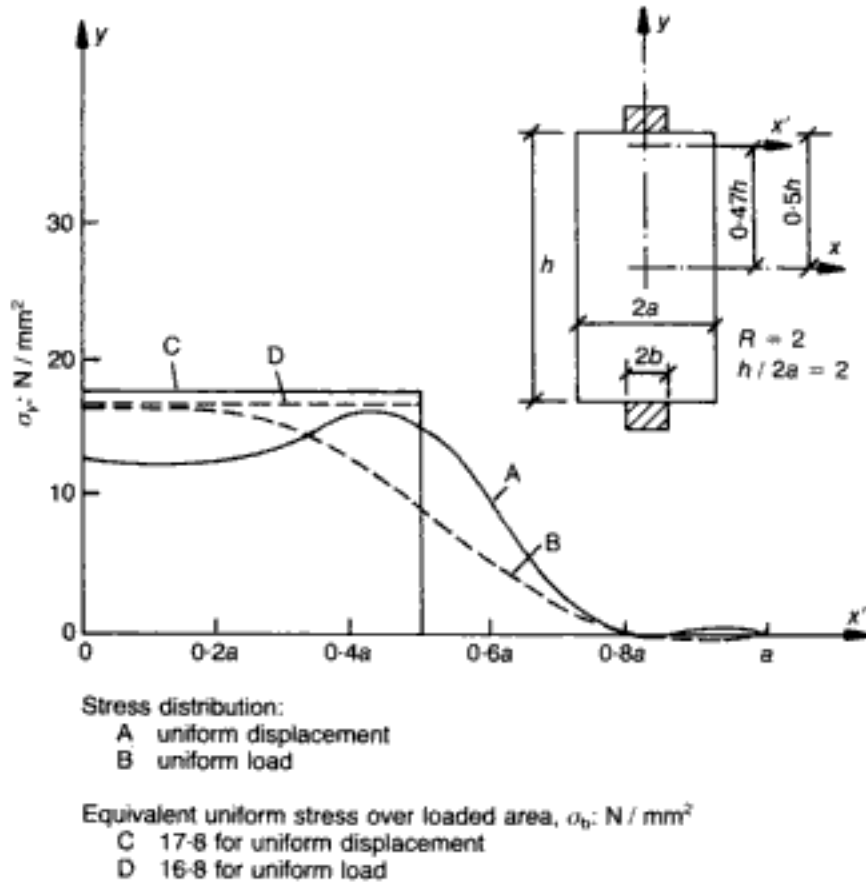


Fig. 3.25. Typical stress distribution in concrete for a cross-section parallel to the loaded surface (plane-stress analysis)¹⁰³

to reduce the effectiveness of the restraint imposed by the surrounding concrete, since Fig. 3.23 shows that the bearing strength predicted for the prisms with fully restrained displacement along the loaded surface is lower than that of the prisms with complete freedom of displacement. For an axisymmetric state of stress, the analysis predicts similar behaviour only for the cylinders subjected to a uniform load, as Fig. 3.24 indicates that the bearing strength predicted for the cylinders subjected to a uniform displacement is essentially independent of the restraint imposed on the displacement along the loaded surface.

It is interesting to note in Figs 3.23 and 3.24 that the effect on bearing strength of the lateral restraint conditions is substantially less than that of the *type* of applied load. In fact, the effect of the lateral restraint conditions on bearing strength is comparatively small. On the other hand, both plane-stress and axisymmetric analyses predict that the bearing strength of the structural forms subjected to a uniform displacement is substantially higher than that when they are subjected to a uniform load. Bearing strength is related directly to the distribution of the normal stress on cross-sections parallel to the loaded surface. Typical stress distributions predicted on a given cross-section for the cases of applied uniform displacement and load are shown in Fig. 3.25. This figure indicates that, although the distributions exhibit the same *maximum* stress values, they are equivalent to a uniform stress over the loaded

surface of 17.8 N/mm^2 for the applied uniform displacement case and 16.8 N/mm^2 for the applied uniform load. It appears, therefore, that a higher applied load in the form of a uniform displacement is required to cause a peak stress concentration equivalent to that caused by a uniform load. Since collapse of the structure has been found to be associated with a loss of load-carrying capacity of the material in the region of these stress concentrations, the structural forms subjected to uniform displacement exhibit a higher bearing strength.

Figures 3.23 and 3.24 also show that, for the structural forms where displacements along the loaded surface are fully restrained while a uniform displacement is applied in the orthogonal direction, the predicted bearing strength appears to correlate very closely with experimental values obtained from tests using rigid steel platens without any lubrication or other technique being employed to reduce friction at the specimen-platen interfaces.¹⁰⁰ The good correlation of predicted and experimental relationships between bearing strength and loaded area may be considered as an indication that the boundary conditions assumed for the analysis simulate closely the actual boundary conditions imposed on the specimens by the testing method used in the above experiments. Furthermore, Fig. 3.24 shows that the relationships predicted by the analysis lie within the upper and lower limits proposed by Williams¹⁰⁴ from an analysis of experimental data.

Although cracking which occurs in the region of the stress concentrations may cause stress redistributions, it has been found that the shapes of the stress distributions shown in Fig. 3.25 remain essentially unchanged with increasing load. Typical distributions of the normal stress on a given cross-section parallel to the loaded surface predicted by the plane-stress and the axisymmetric analyses for the structural forms investigated under various boundary conditions are shown in Figs 3.26 and 3.27. These figures indicate that, under a given displacement or load, the structural forms with free displacement along the loaded surface are subjected to higher compressive and tensile stress concentrations. Since the nonlinear behaviour of concrete becomes more pronounced with increasing stress (see section 1.4.1), these higher stress concentrations result in a reduction of the modulus of elasticity of the material in the region of the stress concentrations, which may account for the lower stiffness of the structural forms with free displacement along the loaded surface indicated by the relationships between bearing stress and the displacement of the loaded surface in the direction of loading shown in Figs 3.28 and 3.29.

Figure 3.30 shows typical representations of the cracking processes under (a) increasing load and (b) increasing displacement, predicted by the plane-stress analysis for the prisms subjected to the various boundary conditions investigated. In all cases, collapse of the prisms has been caused by cracking which initiates in the

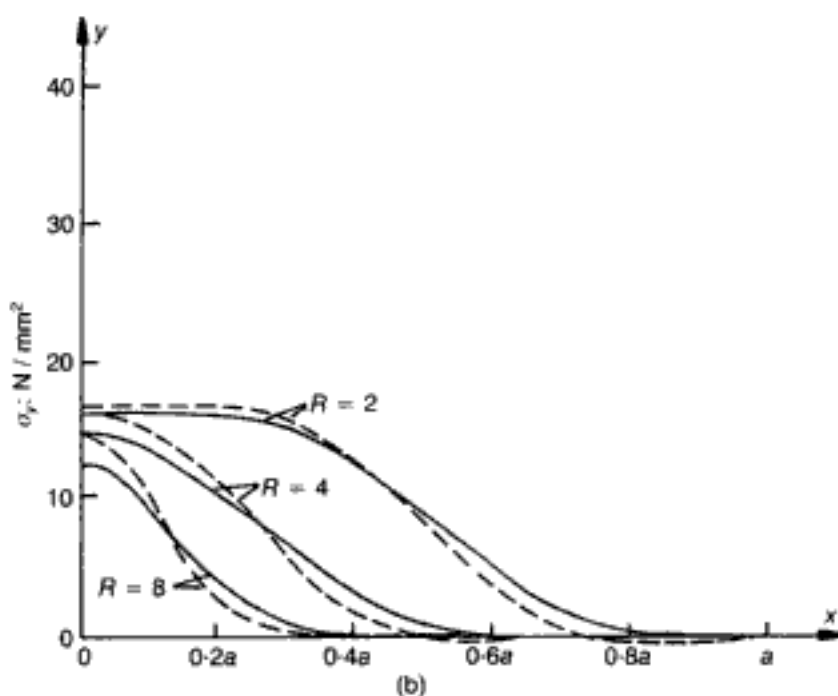
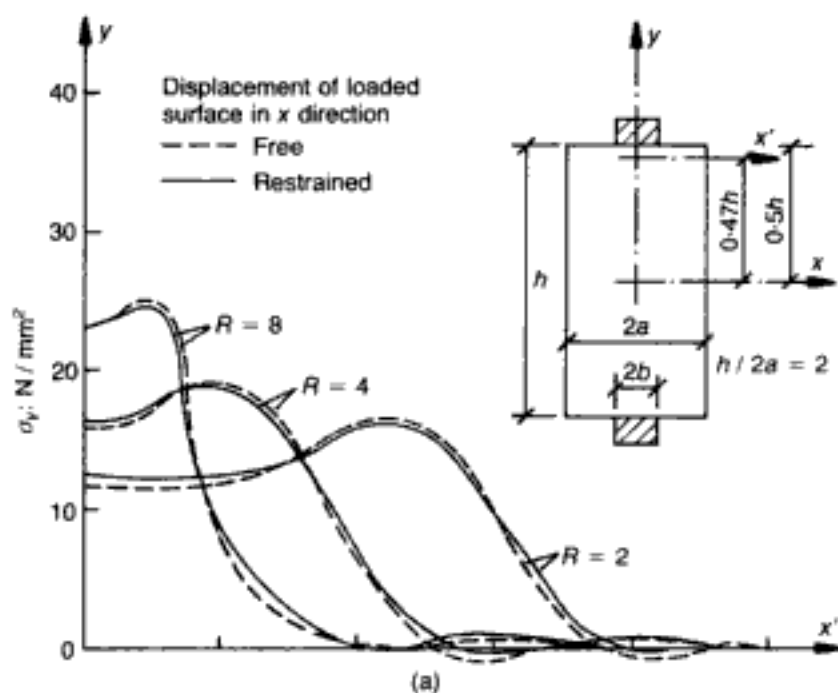
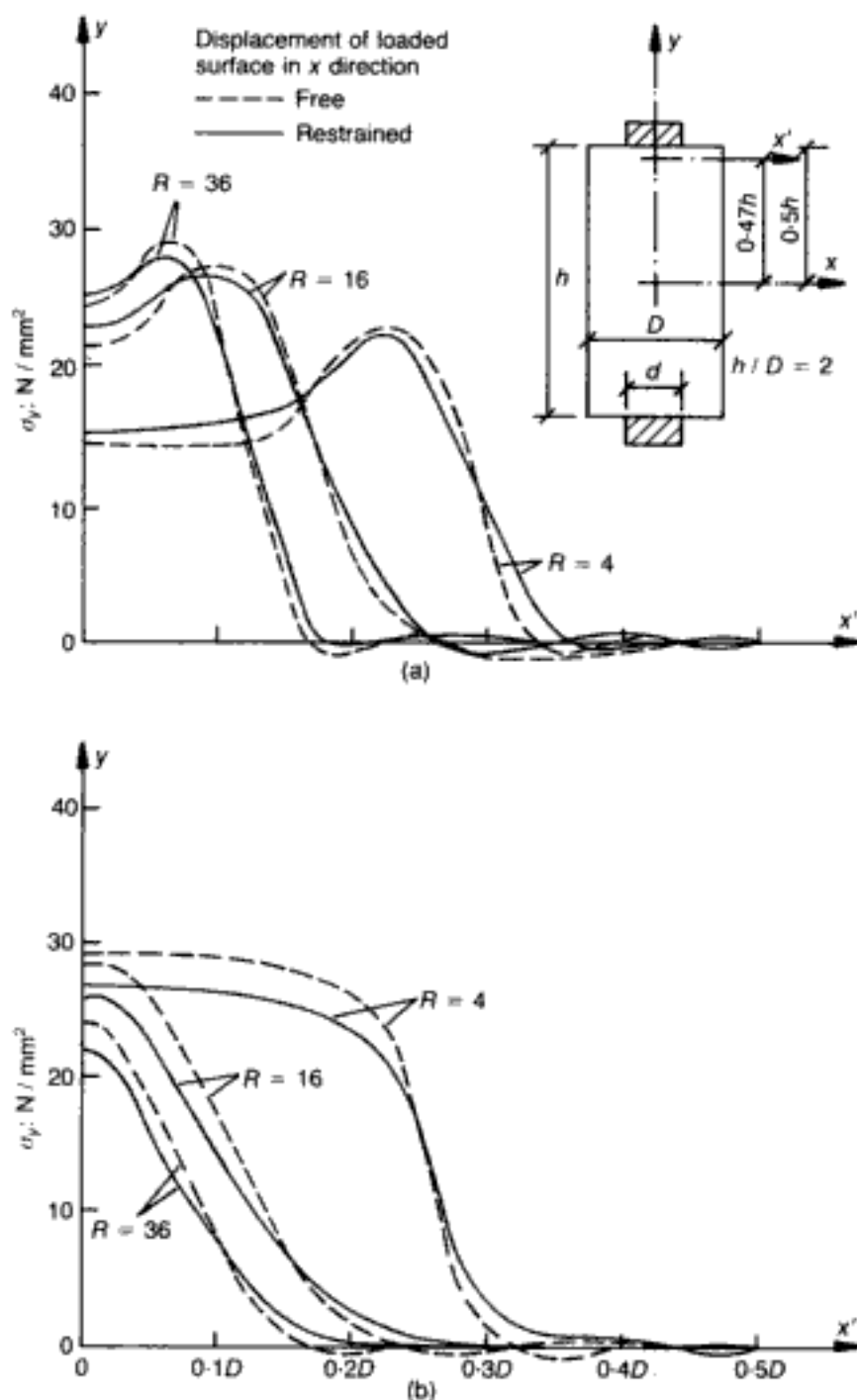


Fig. 3.26. Typical stress distributions in concrete for a cross-section parallel to the loaded surface as predicted by the plane-stress analysis for prisms with various sizes of loaded surface.¹⁰³ (a) for uniform displacement $v = 0.08 \text{ mm}$; (b) for uniform load $\sigma_b = 16.8 \text{ N/mm}^2$

region beneath the loaded surface where a high principal compressive stress is combined with a principal tensile stress. This is the region where the high compressive stress concentrations shown in Fig. 3.26 exist. Cracking spreads towards the central zone of the prisms in a direction inclined with respect to the loading direction as indicated in the figures. The degree of inclination has been found to depend on both R (i.e. the size of the loaded surface) and the lateral restraint of displacement along the loaded surface. It may also be noted from Fig. 3.30 that collapse of the prisms whose displacement along the loaded surface is fully restrained

Fig. 3.27. Typical stress distributions in concrete for a cross-section parallel to the loaded surface as predicted by the axisymmetric analysis for cylinders with various sizes of loaded surface:¹⁰³ (a) for uniform displacement $v = 0.08 \text{ mm}$; (b) for uniform load $\sigma_b = 28.8 \text{ N/mm}^2$



occurs at the stress level which causes crack initiation, whereas the prisms with free displacement across the loaded surface collapse at a slightly higher stress level.

Figure 3.31 depicts typical representations of the cracking processes predicted by the axisymmetric analysis. Under an axisymmetric stress state, cracking of the cylinders occurs both circumferentially and radially and, as for cracking under a plane-stress state, it initiates in the region beneath the loaded surface where a principal compressive stress is combined with a principal tensile stress. Figure 3.31 also shows that, in contrast to the behaviour under plane states of stress, axisymmetric cracking

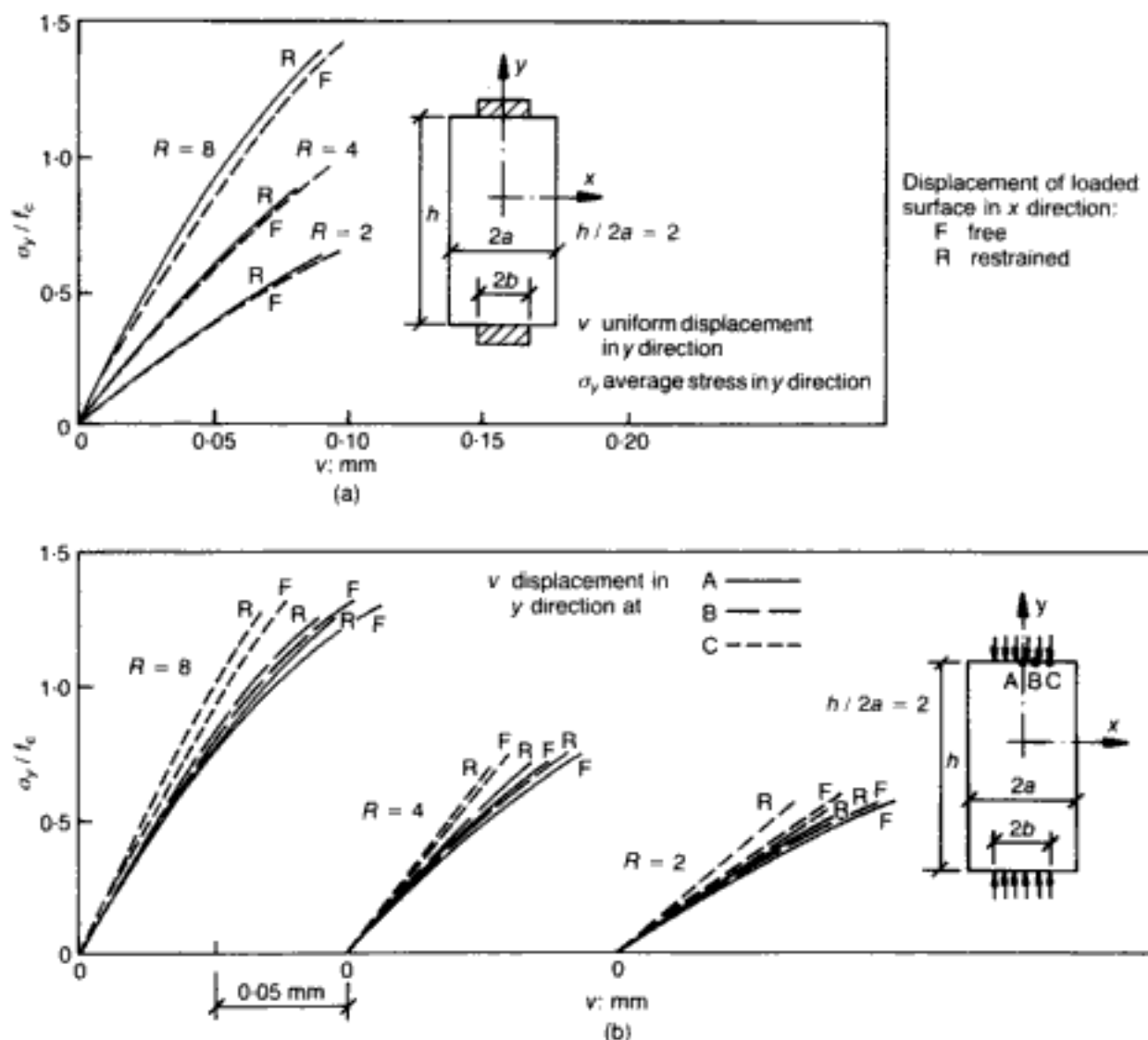


Fig. 3.28. Variation of displacement at the loaded surface with bearing stress as predicted by the plane-stress analysis:¹⁰³ (a) for uniform displacement; (b) for uniform load

initiates under bearing-stress levels much lower than those which cause collapse. However, as for the case of plane stress subject to uniform load (but not uniform displacement), the bearing stress sufficient to cause crack initiation within the cylinders with free displacement along the loaded surface is lower than that sufficient to cause crack initiation within the cylinders with fully restrained ends (this appears to hold for both uniform-load and uniform-displacement instances). The figure also indicates that, with increasing load or displacement, cracking propagates progressively outside the region beneath the loaded surface, and collapse occurs when the radial cracks reach the side surface of the cylinders and the member collapses through instability. (It should be noted that the last crack patterns correspond to the non-converged solution and, hence, represent a post-failure phenomenon.)

3.3.3.3. Conclusions

The following findings emerge from the preceding numerical parametric study.

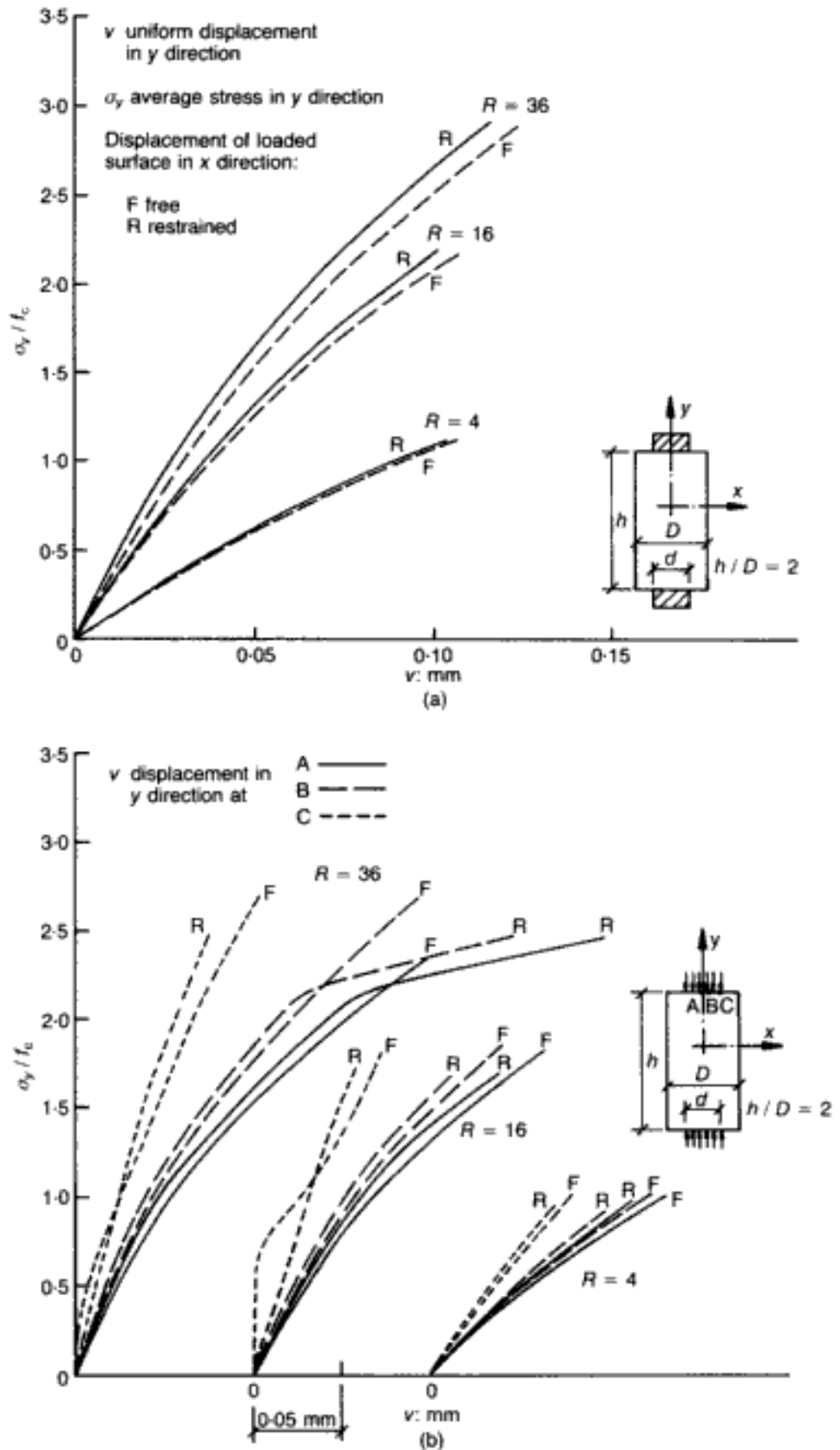


Fig. 3.29. Variation of displacement at the loaded surface with bearing stress as predicted by the axisymmetric analysis:¹⁰³ (a) for uniform displacement; (b) for uniform load

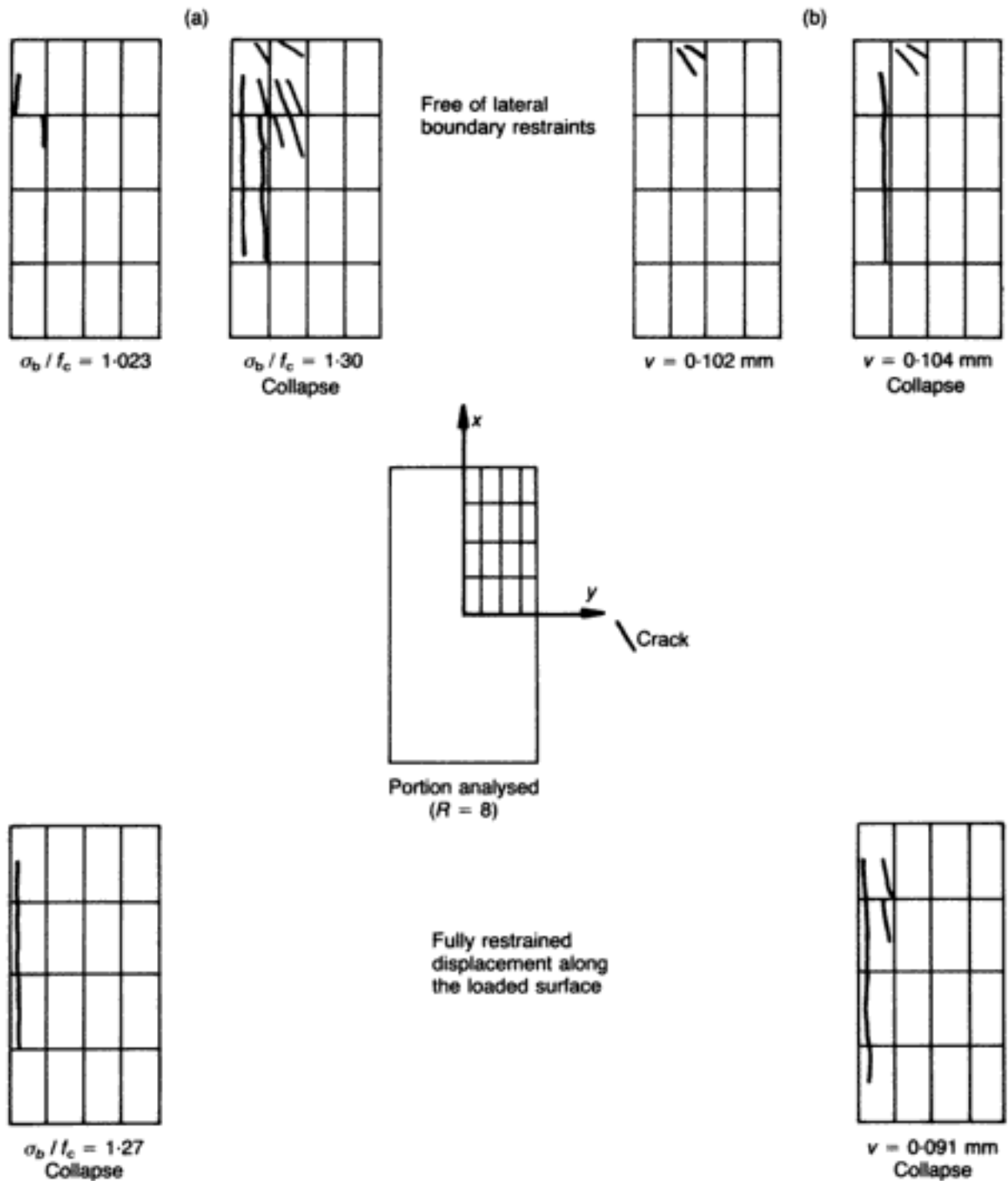
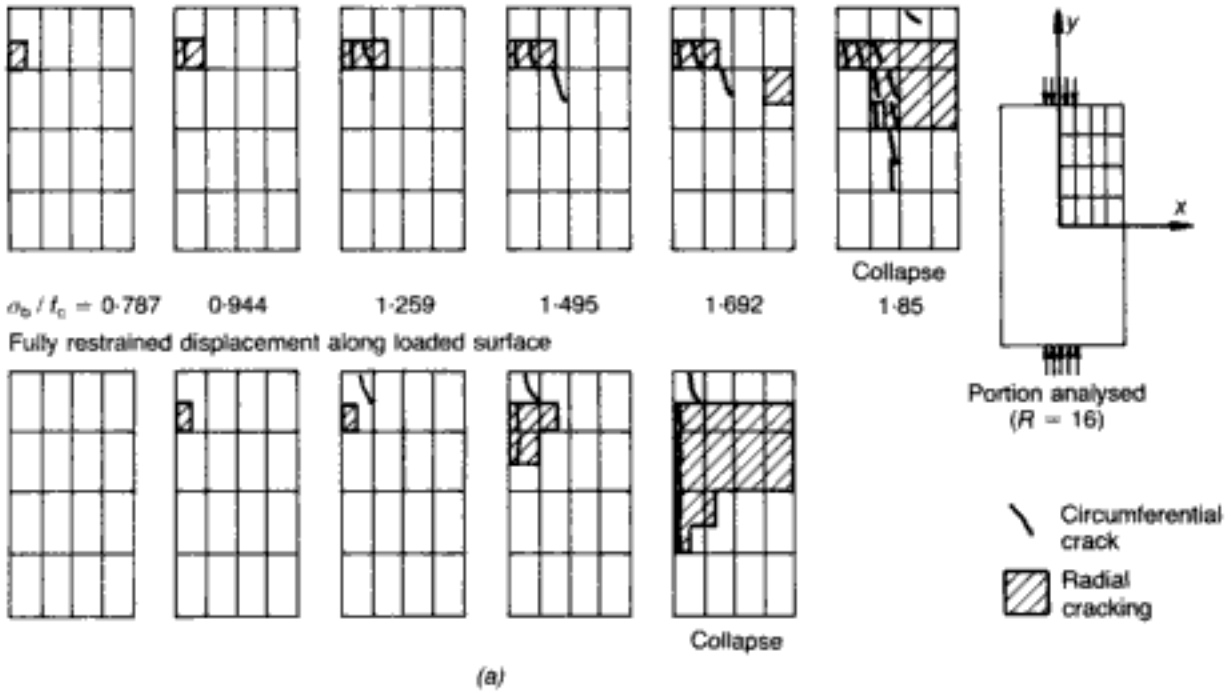


Fig. 3.30. Typical crack patterns for prisms under increasing load or displacement as predicted by the plane-stress analysis.¹⁰³
 (a) for uniform load;
 (b) for uniform displacement

- (a) Bearing strength increases with decreasing loaded area. Such behaviour appears to result from the increase of the load-carrying capacity of the material in the region beneath the loaded surface caused by the multiaxial compressive state of stress which is induced by the restraining effect on deformation of the concrete surrounding this region.
- (b) The predicted bearing strength is in close agreement with experimental values when the boundary conditions assumed by the analysis simulate closely those imposed by the testing techniques.
- (c) The structural forms with free displacement along the

Free of lateral boundary constraints



Free of lateral boundary constraints

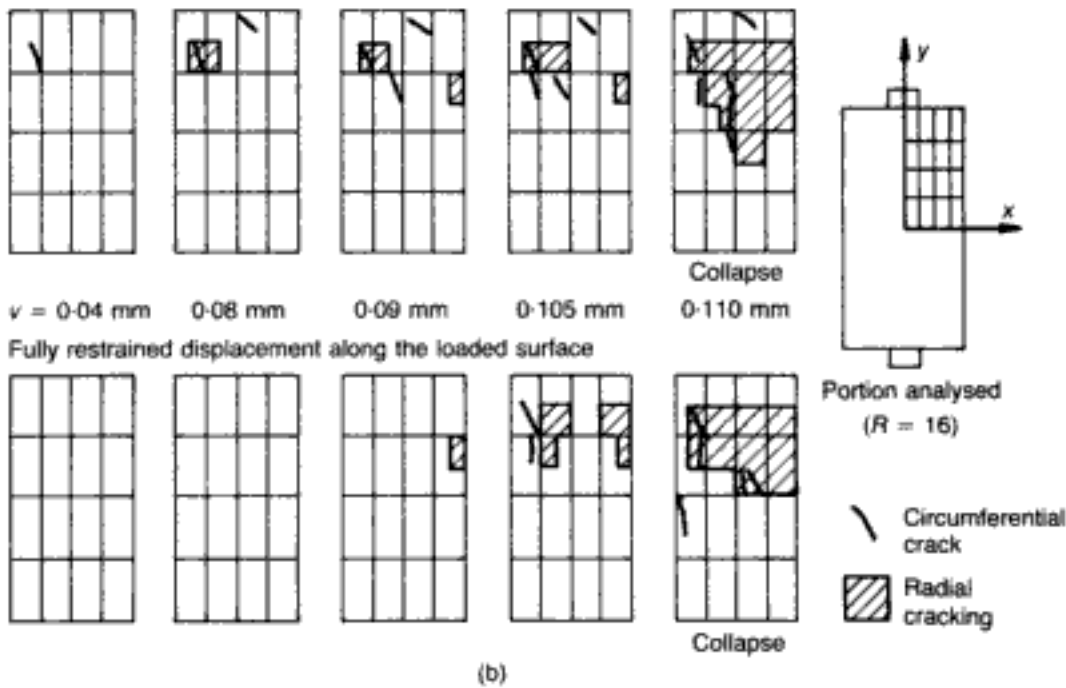


Fig. 3.31. Typical crack patterns for cylinders under increasing load or displacement as predicted by the axisymmetric analysis.¹⁶³ (a) for uniform load; (b) for uniform displacement

loaded surface exhibit a bearing strength higher than that of the fully restrained structural forms.

- (d) The bearing strength of the structural forms subjected to a uniform displacement is higher than that of the structural forms subjected to a uniform load.
- (e) The effect on bearing strength of the type of applied load (uniform displacement or uniform load) is substantially higher than that of the lateral restraint conditions.

- (f) The stiffness of the structural forms with fully restrained displacement across the loaded surface is higher than that of the structural forms with free displacement across the loaded surface.
- (g) Cracking initiates in the region beneath the loaded surface where high principal compressive stresses combine with at least one principal tensile stress. In the case of axisymmetrically compressed cylinders, collapse is caused by the above cracking extending to the side surfaces of the structure.
- (h) Under plane-stress states the levels of bearing stress at crack initiation and collapse almost coincide, whereas under axisymmetric stress states the cracking process occurs in steps with increasing load or displacement and crack initiation begins at a level much lower than that corresponding to bearing strength.

3.3.4. Hollow sphere under hydrostatic pressure

Haynes¹⁰⁵ reports the experimental details of a PC sphere (specimen 1) subjected to slow hydrostatic loading. This component was assembled from two hemispheres cast separately and jointed together with epoxy glue (see Fig. 3.32(a)). The material strength stood at $f_c = 35.8 \text{ N/mm}^2$.

The numerical modelling of the structure⁹⁸ was first conducted on the assumption that the sphere was geometrically perfect. This produced a 40% overestimate of the experimental implosion pressure (i.e. 42 N/mm^2 as against 29.9 N/mm^2). However, as argued by Bédard,⁵⁴ the actual structure was far from perfect, as evidenced by both the construction details and the measuring equipment which interfered and even altered the symmetry of the sphere. On the basis of publications related to the construction and testing of cylinders, a geometrically imperfect mesh was developed with a 15% variation in mean thickness and a 1.5% variation in mean radius (see Fig. 3.32(b), where the top half is a geometrically perfect mesh with 15 elements whereas imperfections are gradually introduced from top to bottom over the 15 elements in the bottom half: the dashed lines represent the perfect contour). Using the above imperfect mesh, the predicted implosion pressure was 36 N/mm^2 , i.e. only 20% higher than the experimental value — an adequate result in view of the estimated nature of imperfection magnitude and type. It is clear, therefore, that the ignoring of geometric imperfections in spheres of this type may lead to unrealistic predictions.

Bédard⁵⁴ showed that the analytical pressure–radial displacement curves for both perfect and imperfect spheres were practically coincident up to the lower MSL value (the characteristic for the imperfect sphere being only marginally less stiff). However, no test data could be found to establish the correlation of the deformational behaviour. Bédard also reported the absence of any

cracking even at MSL levels for both the perfect and imperfect shells.

3.4. Reinforced concrete structures

3.4.1. Beams

This section presents results for various RC beams (but excluding deep beams, which will form the subject of section 3.4.2). In general, the prediction of the behaviour of girders failing in flexure is readily achieved by both 2-D and 3-D models (see, for example, Fig. 3.2(a) — typical instances of under-reinforced beams will also be given in Chapter 4) and hence most of the examples to be presented will address the more difficult problem of beams failing in 'shear', as well as case studies which provide fundamental information at the phenomenological level. The choice of the various problems to be described has been determined by the following threefold aim. First, the provision of evidence of the predictive accuracy of the model by reference to those structures that — unlike members failing in flexure — are known to be less amenable to numerical predictions. Secondly, several basic tenets of present-day design philosophy are called into question, such as the notion of critical cross-section, the role of 'aggregate interlock', and the concept of 'shear' failure. Thirdly, some of

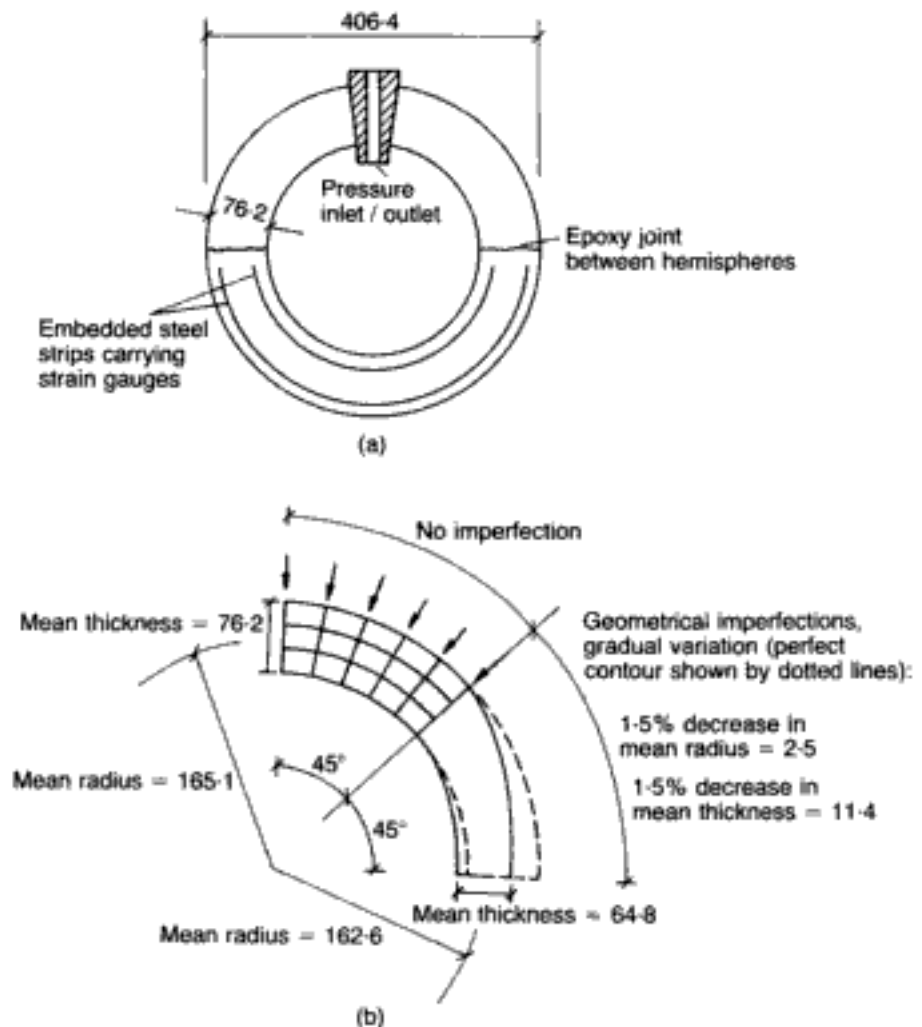


Fig. 3.32. PC sphere under external pressure.¹⁰⁵ (a) experimental data for sphere No. 1; (b) adopted FE mesh with and without geometric imperfections (All dimensions in mm)

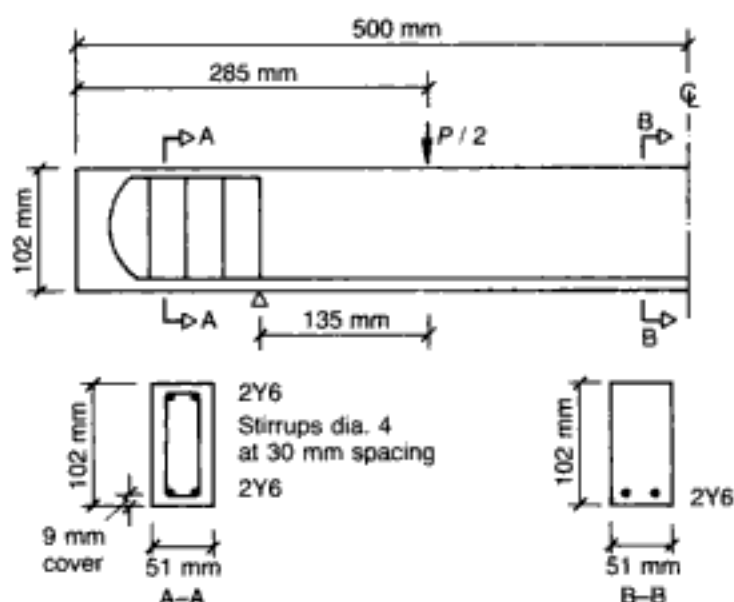


Fig. 3.33. Experimental data for the beam under two-point loading with vertical stirrups in the overhangs (only one-half of the beam is shown)⁹⁹

the examples consist of members exhibiting unorthodox design characteristics (mainly reinforcement detailing): while designed originally to test some of the current code concepts, their departure from ordinary design practice also provides a test for the predictive power of the FE model when this is applied to new structural forms, namely those components which are most likely to need numerical modelling in the absence of relevant guidelines.

3.4.1.1. Beams with untypical reinforcement details

As part of an ongoing research programme into shear behaviour of girders, two series of tests on beams with somewhat unorthodox reinforcing details were carried out in the Concrete Structures Laboratories at Imperial College. The results of two beams (one from each series) were subsequently used as a basis of comparison for the 2-D FE model.⁹⁹

Simply supported beam under two-point loading, with vertical stirrups in the overhangs. Figure 3.33 shows the beam from the first test series to be modelled numerically. The cylinder strength of the concrete was 35 N/mm^2 , while the yield stresses of the main bars (bent back and anchored — see Fig. 3.33) and stirrups were found to be 690 N/mm^2 and 545 N/mm^2 respectively. The total failure load P , applied through a spreader beam as a two-force system, was recorded as 36 kN. The original FE mesh adopted for one-half of the beam can be inferred from Fig. 3.34(a), which depicts the deformed shape and crack pattern at the ultimate load $P = 38 \text{ kN}$ obtained by using a load step of 2 kN. (As explained previously, dashed lines indicate the presence of steel reinforcement; it should be noted that the bottom concrete cover has been neglected as its effect is clearly negligible.) It is interesting that the numerical scheme continued to converge up to $P = 44 \text{ kN}$ but, beyond $P = 38 \text{ kN}$, warnings of matrix ill-conditioning showed

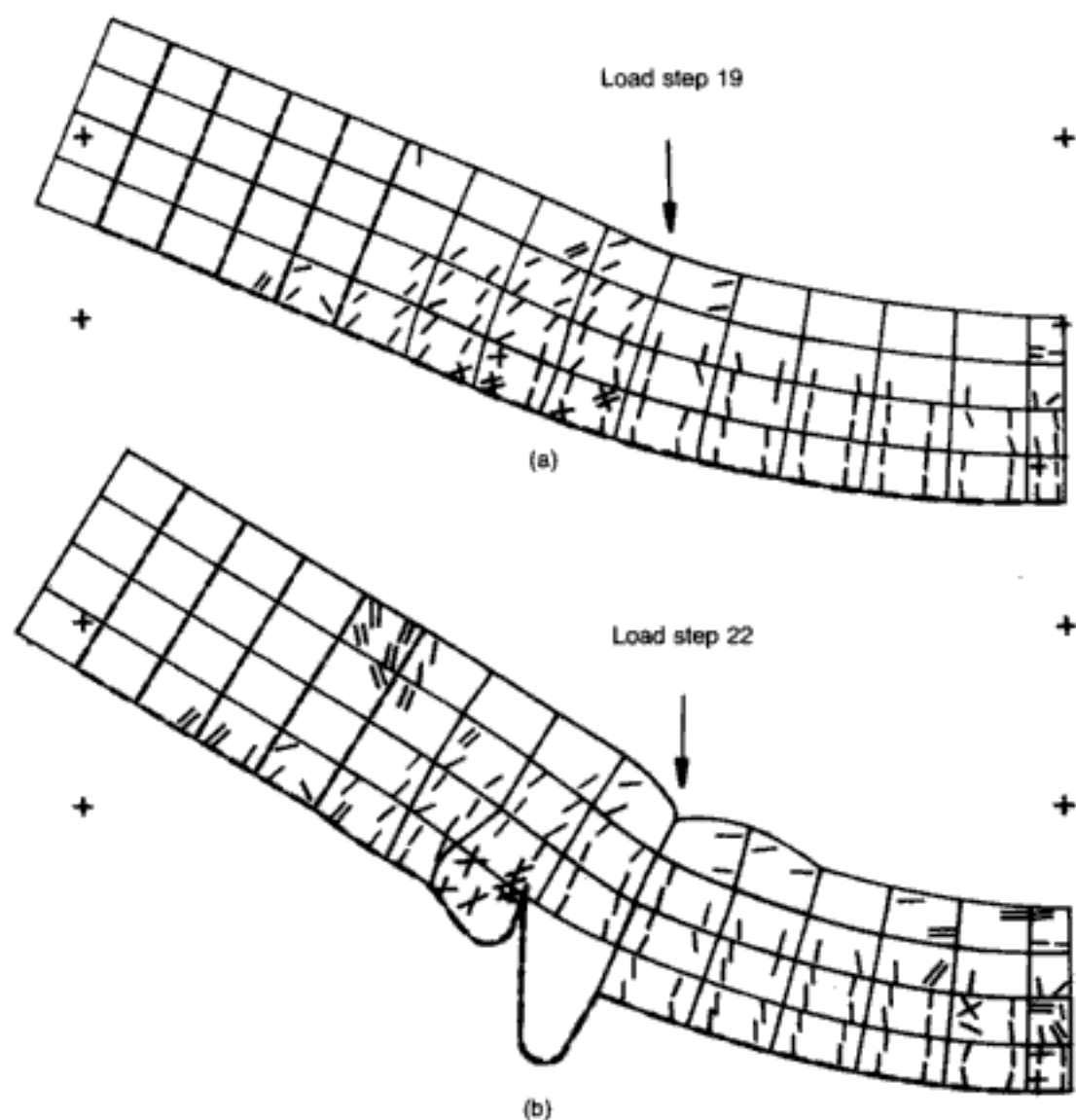


Fig. 3.34. Crack patterns and deformed shapes for the beam under two-point loading with vertical stirrups in the overhangs ($D.M. = 30$):⁹⁹ (a) load step 19 ($P = 38$ kN); (b) load step 22 ($P = 44$ kN > MSL)

the unreliability of these higher-load values. It is worth pointing out that some of these suspect loads above $P = 38$ kN gave rise to compressive stresses in excess of the strength envelope of concrete, a feature never observed in this or other case studies when there is no equation ill-conditioning. (Another similar instance will be described in section 3.4.6.) The graphical facilities of the package were also useful in detecting that the results for $P > 38$ kN, although they meet the usual convergence criteria, are, nevertheless, spurious. Beyond $P = 38$ kN, the deformations of the beam take on shapes which are physically meaningless: as an example, the last shape, obtained before analytical divergence was signalled in the program, appears in Fig. 3.34(b). In view of the above arguments, it can be concluded that $P = 38$ kN can be taken as the ultimate theoretical load for the beam, and this is in excellent agreement with the experimental value $P = 36$ kN. The cracking pattern of the tested beam is also accurately predicted by the model

(the total local failure of the concrete — indicated by intersecting cracks — at the bottom of the beam in the region of the shear span should be noted).

Simply supported beam under two-point loading, with compression and shear reinforcement at midspan. The details of one of the beams from the second series of tests referred to above appear in Fig. 3.35. The main steel bars and the stirrups possess the same characteristics as in the previous case study. The two longitudinal bars acting in the compression zone have identical cross-sectional and material properties as the stirrups. Again, the strength of the concrete was 35 N/mm^2 .

The concrete mesh for the previous case study was adopted. Once again, the bottom cover was neglected; clearly, this cannot be done in the compression zone, but the horizontal steel in this region was slightly displaced so that it coincided with the top face of the beam. As the experimental failure load was $P = 39 \text{ kN}$, a load step of 4 kN was chosen in order to test the accuracy of the model at larger load increments (in this case 10% of the expected failure load).

Figure 3.36(a) shows the response of half of the beam to the application of the first load step, with early flexural cracking in the midspan, as expected. Figure 3.36(b) corresponds to the ninth load step, at $P = 36 \text{ kN}$. With a further load increment the solution fails to converge, and hence the theoretical collapse load lies between 36 kN and 40 kN . By halving the load step, last convergence is attained at $P = 38 \text{ kN}$, so that one can conclude that the analytical and experimental values of P are practically identical. Figure 3.36(b) gives a reliable indication of the extent and type of cracking near the ultimate load.

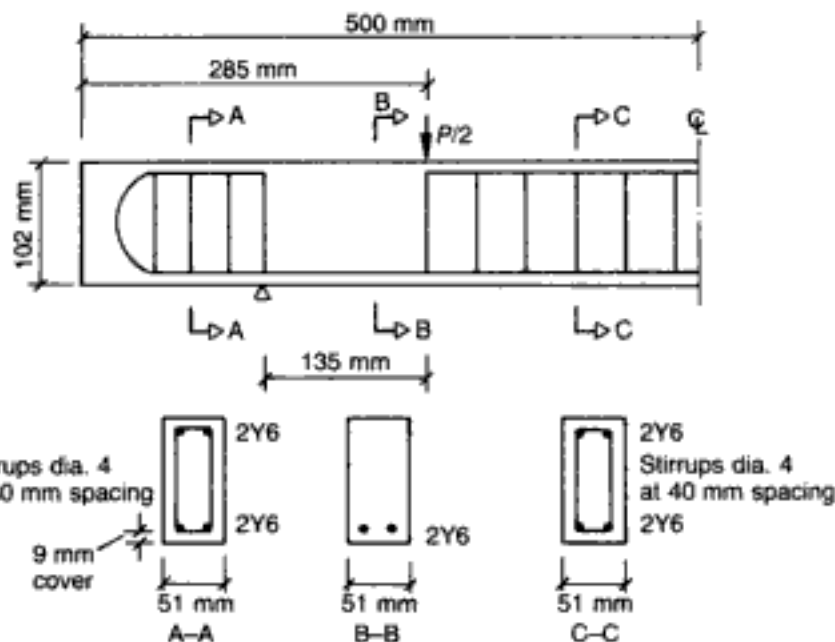


Fig. 3.35. Experimental data for the beam under two-point loading with compression and shear reinforcement at midspan (only one-half of the beam is shown)⁹⁹

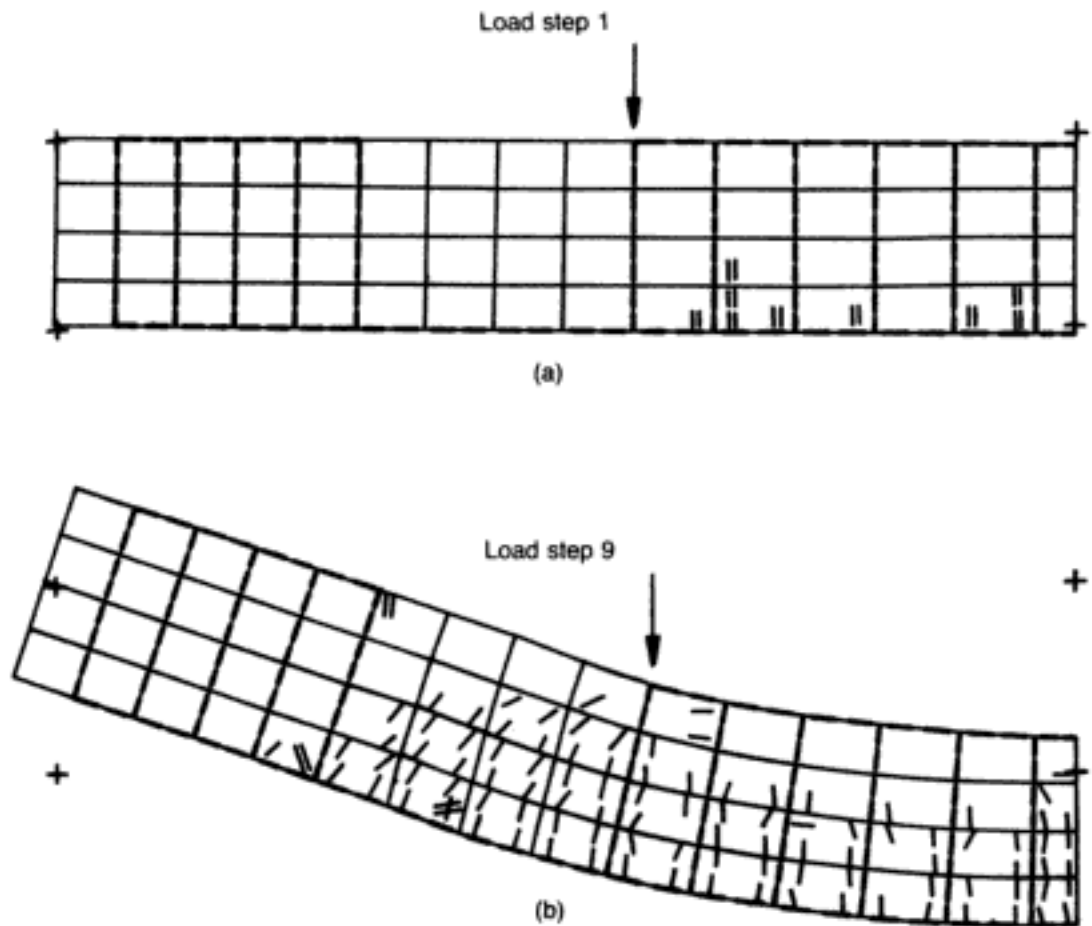


Fig. 3.36. Crack patterns and deformed shapes for the beam under two-point loading with compression and shear reinforcement at midspan ($D.M. = 30$).⁹⁹ (a) load step 1 ($P = 4 \text{ kN}$); (b) load step 9 ($P = 36 \text{ kN} = \text{MSL}$)

3.4.1.2. Phenomenological insight

The question of 'aggregate interlock'. A fundamental aspect of concrete behaviour which the model may help to clarify concerns the question of the effect of the so-called 'aggregate interlock' on beam behaviour. The adoption of a low value for the shear-retention factor in the present model implies that aggregate interlock does not seriously affect beam strength. This, however, contrasts strongly with the widely-held view that aggregate interlock is the most significant contributor to shear resistance (e.g. reference 106). Such a view is based largely on experimental information¹⁰⁷ which has indicated that RC beams with cracks preformed in the region below the neutral axis (with the intention of eliminating aggregate interlock) have a load-carrying capacity about 30% lower than that of ordinary (i.e. 'uncracked') beams. In an attempt to resolve this problem, the 2-D FE program was used to analyse two beams which were identical but for the fact that one was initially uncracked, while the other had preformed cracks below the neutral axis.⁵¹ The beams are simply supported and are subject to two symmetrically located point loads. Figure 3.37(a) shows the deformed shape of the initially uncracked beam under ultimate load conditions; also shown are the FE mesh adopted, the reinforcing steel (as usual, indicated by broken lines — any bottom concrete

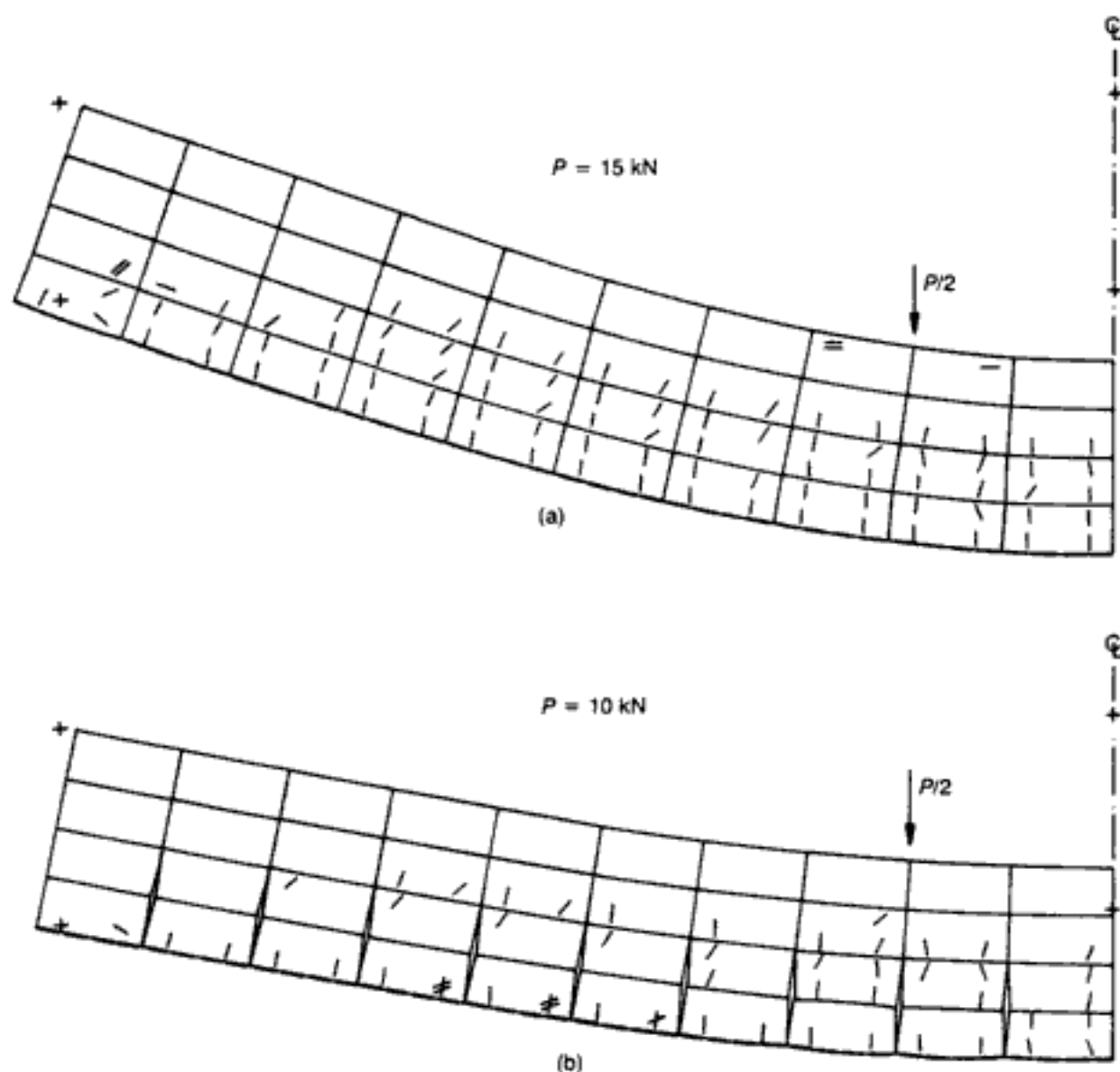


Fig. 3.37. Effect of aggregate interlock. Crack patterns and deformed shapes at collapse of simply supported beams under two-point loading (only one-half of the beam is shown):⁵¹ (a) initially uncracked beam; (b) beam with preformed cracks

cover has been neglected in the analysis), and the final pattern and orientation of the cracks. The ultimate-load conditions for the beam with the preformed cracks are predicted in Fig. 3.37(b) (the opening of the vertical cracks as one moves away from the supports should be noted). It is evident that the mere introduction of initial cracks has caused a drop of about 30% in the load-carrying capacity of a beam despite the fact that the model used practically ignores aggregate interlock. Since this drop in strength correlates closely with the experimental values of beams with preformed cracks mentioned earlier,¹⁰⁷ it can be concluded that aggregate interlock cannot have a significant effect on shear resistance.

The above finding can be supported by the following additional argument.¹⁰⁸ Once cracking occurs, the remaining stiffness in the post-cracking concrete is negligible, contrary to current codes' thinking. Although not referred to explicitly, the aggregate-interlock concept forms the backbone of code provisions for shear design. Yet, this concept is in direct conflict with the fundamental

failure mechanisms of concrete, since a crack propagates in the direction of the maximum principal compressive stress and opens in the orthogonal direction (see section 1.3.3). Therefore, if there were a significant shearing movement of the crack faces, which is essential for the mobilization of aggregate interlock, then this movement should cause branching in all localized regions where aggregate interlock is effected. Needless to say, the occurrence of such crack branching has not been reported to date.

Structural behaviour of typical RC beams. As repeatedly pointed out, one of the main conclusions of analytical investigations of concrete structures is that, in all cases studied, structural collapse occurred without concrete failing in compression anywhere within the structure, but that failure was initiated in the form of cracking in regions under a state of stress with at least one of the principal stress components being tensile. Such localized cracking could propagate into regions subjected to wholly compressive states of stress only after these states of stress were transformed so as to have one of their principal stress components tensile.

Figure 3.38 indicates fully the main stages of the progressive cracking process an RC beam undergoes under increasing load. Such a cracking process is typical for all RC structural forms investigated, in that crack formation and extension eventually transform the beam into a tied arch.⁵⁷ Collapse always occurred as a result of failure of the arch, which was preceded by near-horizontal splitting of the compressive zone of the beam.

Such a mode of failure is compatible with the failure mechanism proposed earlier, which states that splitting of the compressive zone can occur only as a result of the development of tensile stresses induced by volume dilation of the concrete in regions subjected to large compressive stresses. Such a failure mechanism implies that structural behaviour is independent of the strength characteristics of concrete in compression; hence, a failure criterion describing the conditions for failure under combined compression-tension should, in practice, be sufficient for purposes of analysis.

The above tied-arch response of an RC beam also lends support to the compressive-force path (CFP) concept, which postulates that the causes of beam failure are associated with the development of tensile stresses in the region of the path along which the compressive force is transmitted to the supports and not, as is widely considered, with the stress conditions in the region below the neutral axis.¹⁰⁹ The latter view is justified further by the earlier argument regarding the negligible role of aggregate interlock. Additional support for the need to view/analyse the member as a whole comes from a reappraisal of the notions of 'critical cross-section' and 'shear failure', advocated by present codes but in clear conflict with both experimental and analytical evidence, as will be shown next.

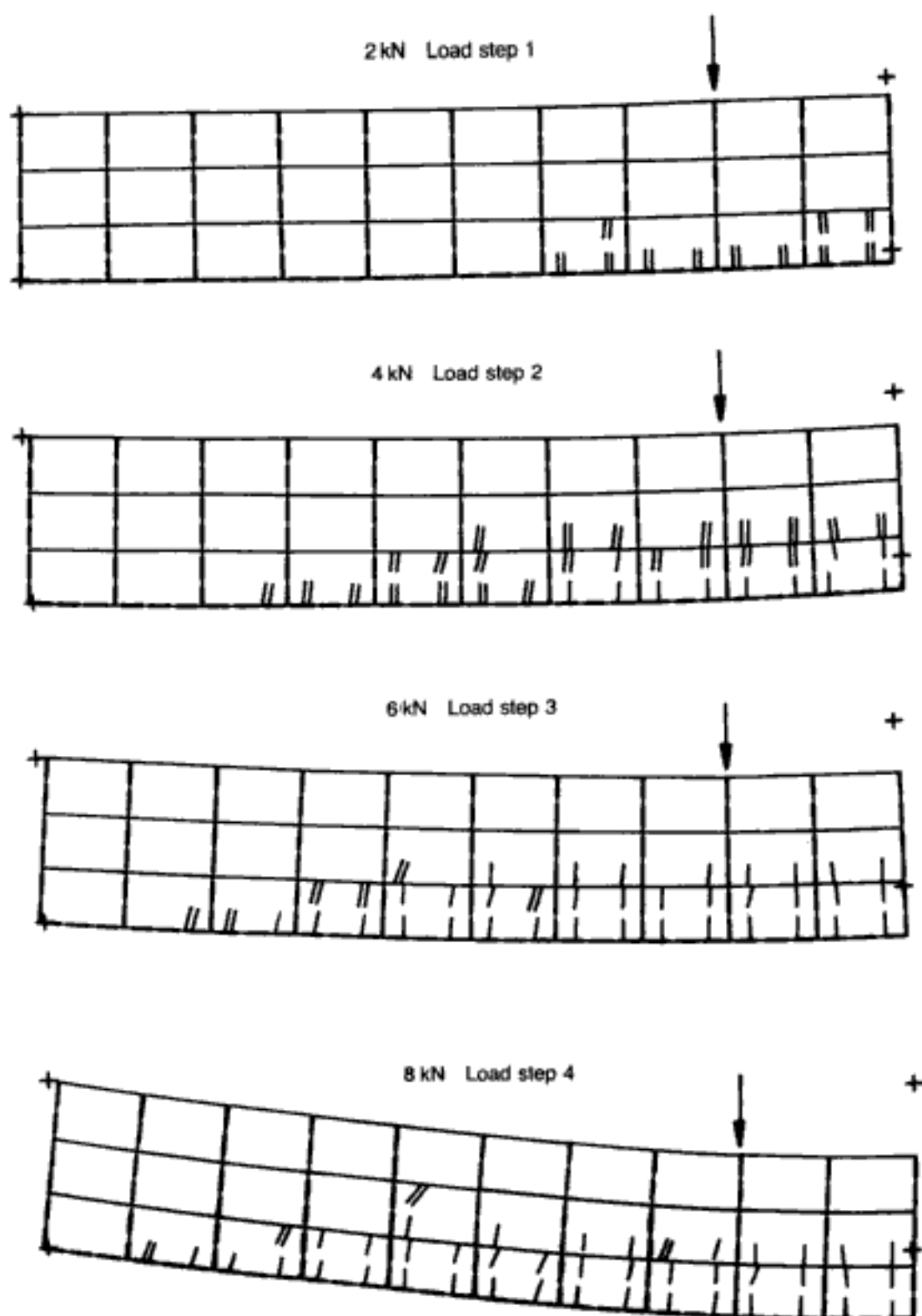


Fig. 3.38 (above and overleaf). Structural behaviour and cracking process of a typical RC beam under increasing two-point load throughout its full loading history⁵⁷

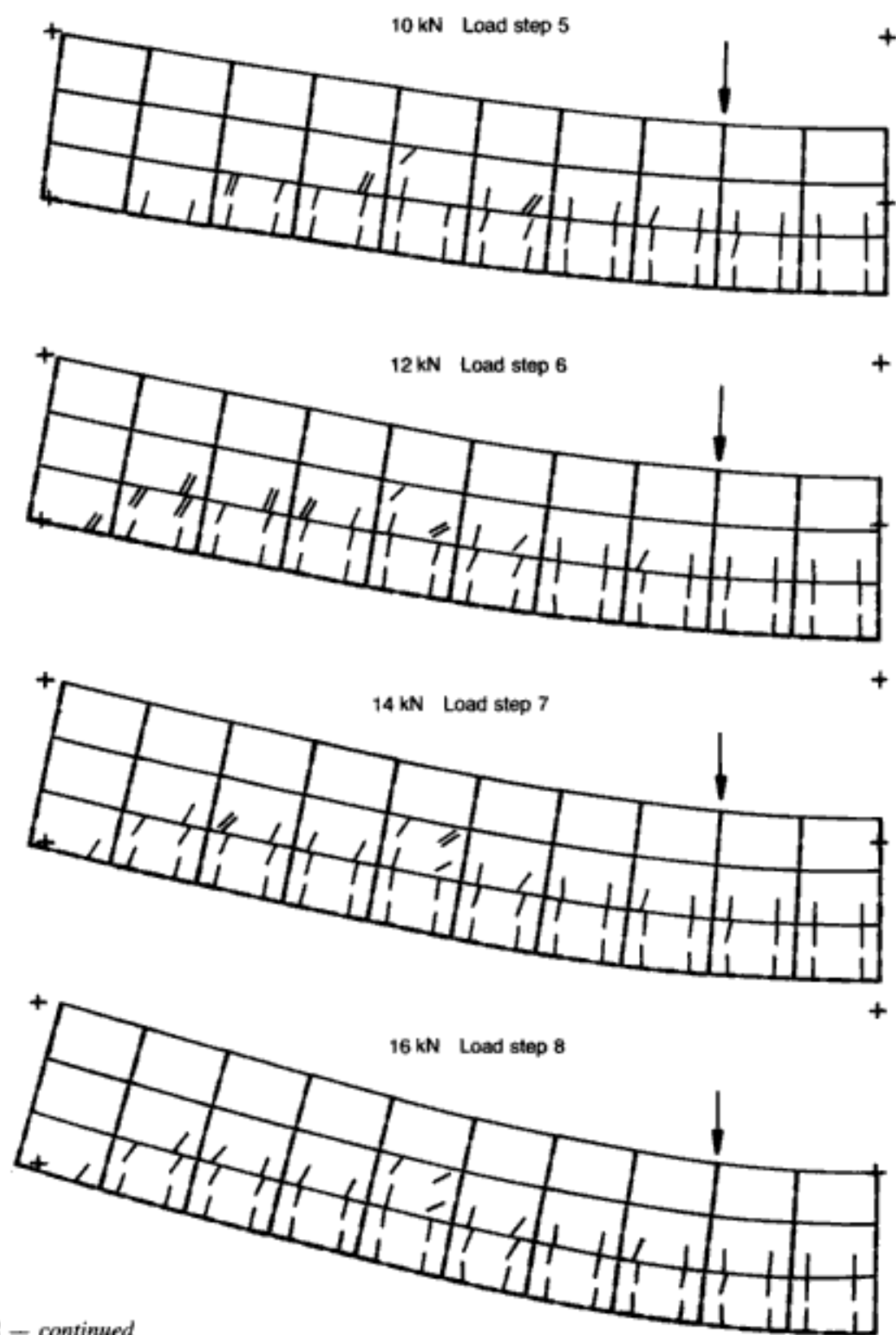


Fig. 3.38 — continued

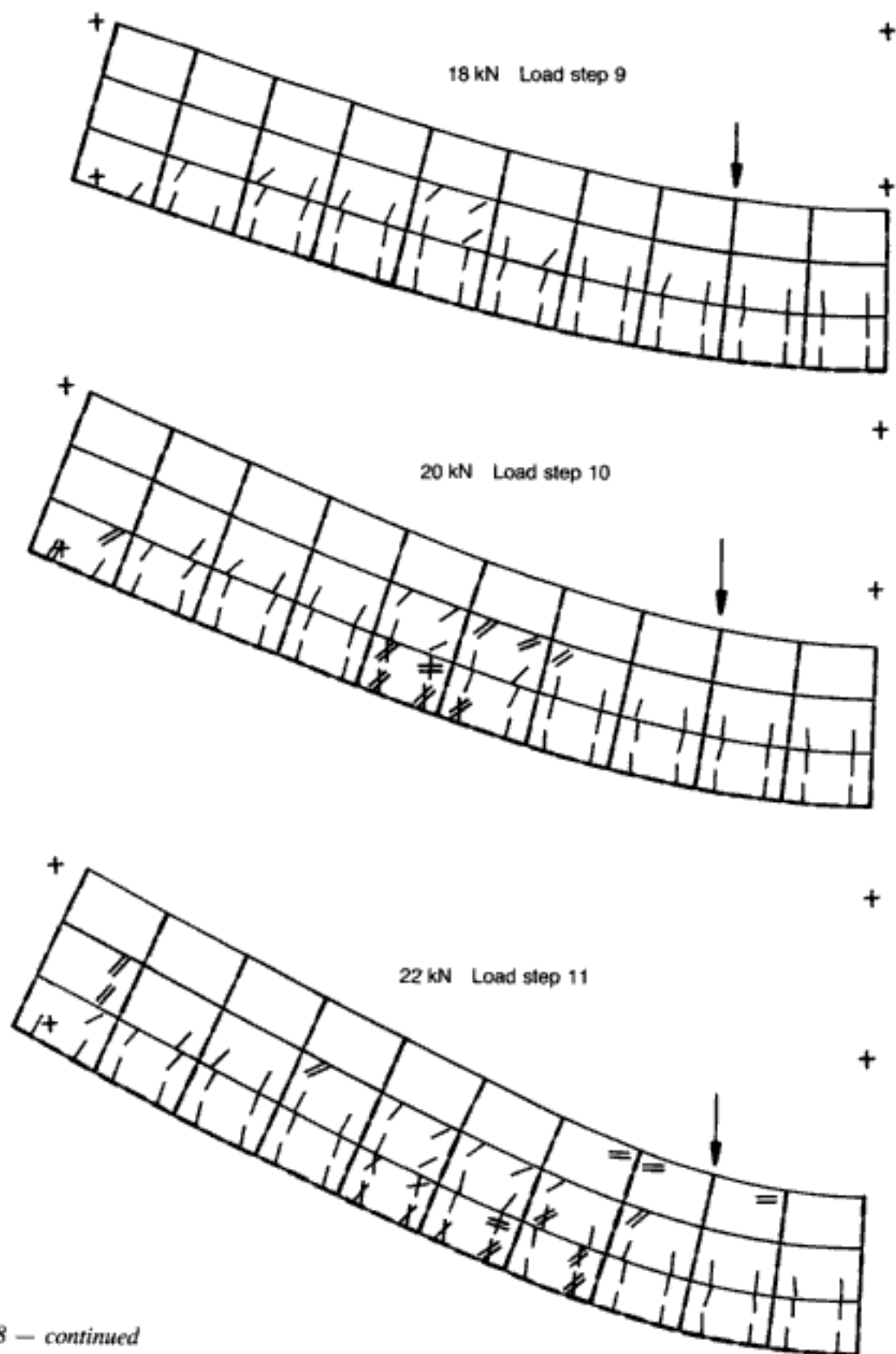
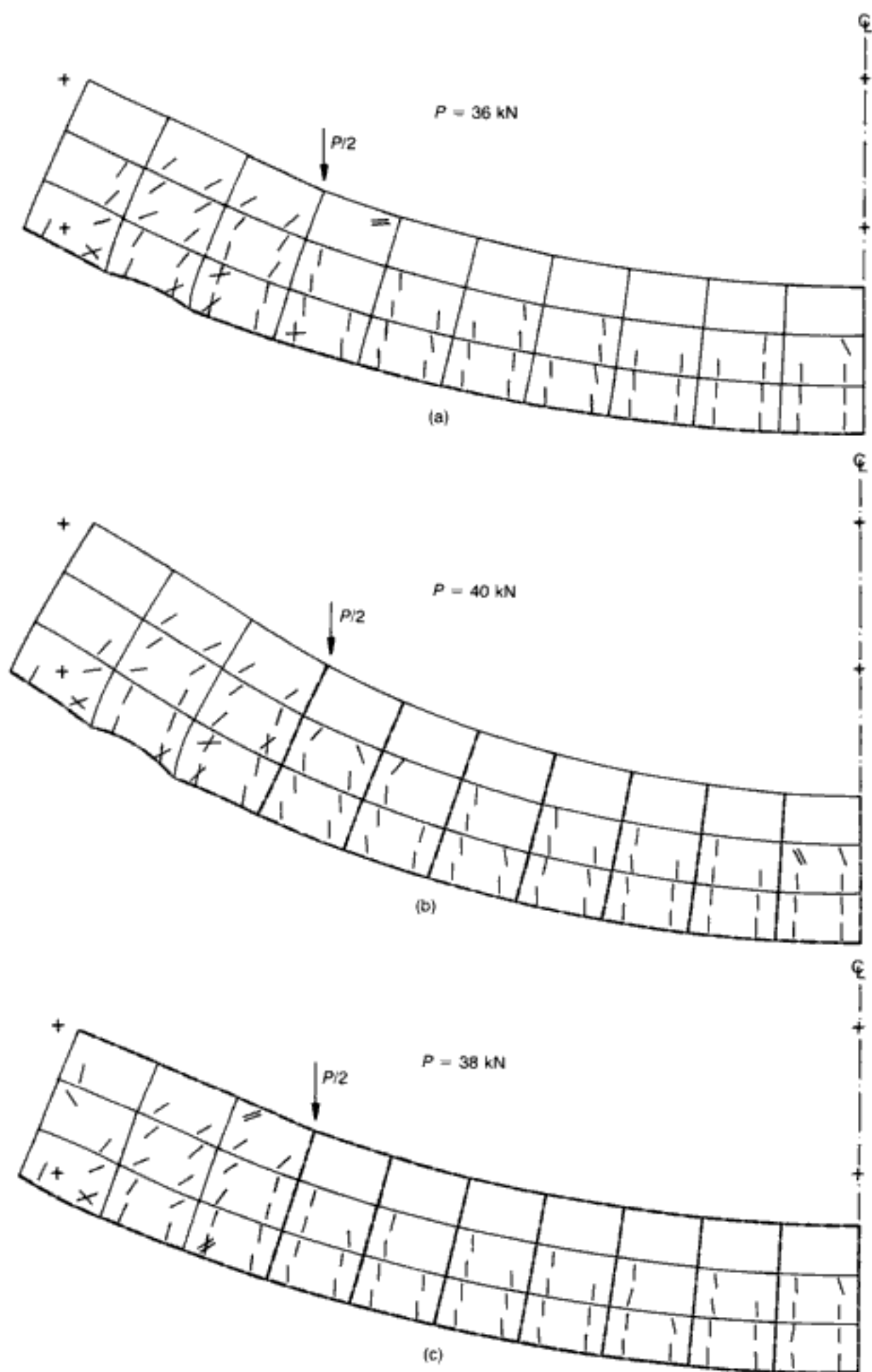


Fig. 3.38 — continued

A reappraisal of the concept of 'shear' capacity of 'critical' sections. The FE model has proved instrumental in providing considerable insight into the general question of 'shear' failure in RC beams. The postulate that this type of failure is usually associated with tensile stresses that develop in the region of the path along which the compressive force is transmitted to the supports, and not with the stress conditions below the neutral axis as is widely believed, was mentioned above. On the basis of this postulate, the absence of shear reinforcement in the case of beams subjected to two-point loads (and having a shear span-to-depth ratio of between approximately 1.0 and 2.5) should cause eventual collapse as a result of the failure of the compressive zone in the middle span and in the region adjacent to the load point. This mode of failure is accurately predicted by the program, as can be seen in Fig. 3.39(a), which depicts the collapse condition of a beam without shear reinforcement and with a shear span-to-depth ratio of 1.61 (the formation of the last crack just inside the middle span, as postulated, should be noted). The collapse should be preceded by the formation of severe inclined cracking in the shear span and this, too, is evident from Fig. 3.39(a). It is generally considered that such a 'shear' failure of a beam can be prevented only by the placing of shear reinforcement, such as links, within the shear span. However, since the actual collapse of the member has been shown to take place in the middle span, it can be argued that the addition of links within the middle, rather than the shear, span can also prevent 'shear' failure and allow the beam to develop its full flexural capacity. That this is indeed the case is illustrated in Fig. 3.39(b), which shows the collapse of a beam identical to that of Fig. 3.39(a) except that shear links have now been added to the middle span. It can be seen that 'shear' failure has thus been prevented, the member attaining its flexural capacity with a resulting increase in ultimate load of some 10%. A third case study is presented in Fig. 3.39(c). Here, compression reinforcement has been added to the beam of Fig. 3.39(b). The result is a drop in load-carrying capacity, and it can be concluded that the placing of compressive reinforcement without links within the shear span leads to failure of the shear span and thus renders ineffective the links within the middle span. The explanation for this is that the additional steel, far from increasing the strength of the beam, causes

Fig. 3.39 (facing). Modes of 'shear' failure. Simply supported beams with various reinforcing arrangements under two-point loading (only one-half of the beam is shown, with P = total load at failure).⁵¹ (a) main (tension) reinforcement only; (b) additional shear reinforcement within the middle span; (c) additional shear reinforcement within the middle span and compression reinforcement



a change in the CFP, which now becomes sharper with consequent increase in the tensile force¹¹⁰ that initiates cracking. In this respect, it is important to realize that the notion of a 'critical' cross-section is not always adequate in the case of concrete members: a clear illustration of this is provided by Fig. 3.39(c), which shows that the addition of compressive reinforcement has actually weakened the member as a whole. It should be stressed that all the above three examples summarized in Fig. 3.39 represent the modelling⁵¹ of a series of beams tested previously,¹¹¹ and are in excellent agreement with their experimental counterparts.

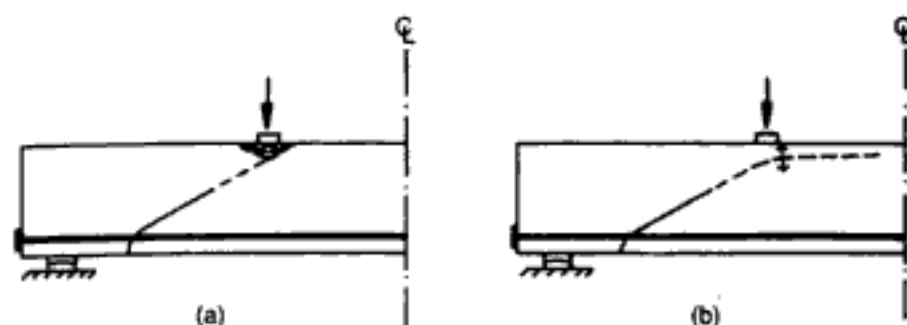
Further analytical evidence of the inadequacy of current code concepts as regards shear is available for beams with shear span-to-depth ratios (a_v/d) between 1.0 and 2.5,¹¹² and, also, greater than 2.5.¹¹³ This is presented below.

Behaviour of beams with $1.0 < a_v/d < 2.5$. Shear design procedures are generally considered to be unsatisfactory in spite of the considerable efforts that are continuously made to revise them. Perhaps the reason for this is that very few attempts have been made to date to reappraise the theoretical concepts that form the basis of these procedures. These concepts stem mainly from the widely held view that RC beams without stirrups fail in shear when the shear capacity of a critical section is exceeded. Thus, the objective of all current design procedures is to assess realistically the amount of shear reinforcement required to carry that portion of the shear force that cannot be sustained by concrete alone.

However, it will be shown by FE analysis (and this has been verified by experiment¹¹¹) that, for beams under two-point loading with shear span-to-depth ratio values up to between approximately 2.0 and 2.5, the causes of shear failure cannot be explained in terms of the concept of shear capacity of critical sections. This is because, on the basis of this concept, beams with the same geometry and tension reinforcement, but without stirrups within the shear span, should have the same load-carrying capacity irrespective of the presence of stirrups outside this span; and yet, it will be seen that the load sustained by beams with stirrups within the middle, and not the shear, span is significantly larger than that of beams without any stirrups. Furthermore, it will become evident that the load sustained by the former beams is essentially equal to that of beams with stirrups within the shear span.

For values of the shear span-to-depth ratio a_v/d between approximately 1.0 and 2.5, RC beams without shear reinforcement subjected to two-point loading are generally considered to suffer a crushing mode of failure when the applied load increases to the level at which the diagonal crack that forms within the shear span at an earlier load stage penetrates into the compressive region towards the loading point (see Fig. 3.40(a)).¹⁰⁶ However, such

Fig. 3.40. RC beams with values of a_v/d between 1.0 and 2.5 under two-point loading.¹¹² (a) generally accepted mode of failure; (b) presently proposed mode of failure



a crushing mode of failure in the region of the loading point is unlikely since the multiaxial compressive state of stress that exists there will cause a local increase of concrete strength.¹¹⁰ Instead, it is proposed that the diagonal crack will branch almost horizontally toward the compressive zone of the middle span of the beam in order to bypass this high-strength region. The path of crack branching should be that of a compressive-stress trajectory which, as indicated by the change in the direction of the CFP, is characterized (for local equilibrium purposes) by the presence of a resultant tensile force at right angles to the compressive path near the tip of the diagonal crack (see Fig. 3.40(b)). Failure, therefore, will occur within the middle span under compression-tension stress conditions.

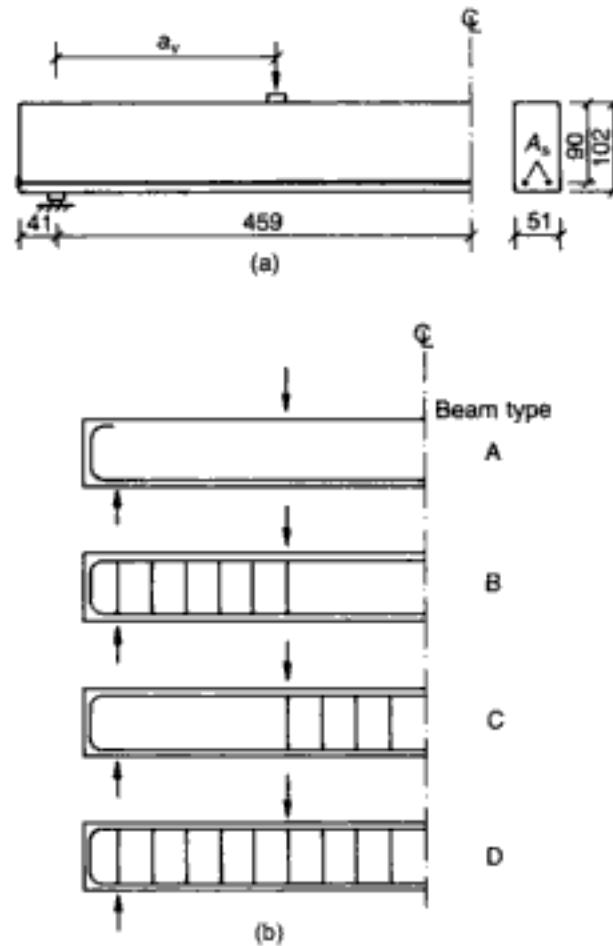
The implication of the proposed failure mechanism is that the presence of shear reinforcement within the shear span, although it may delay occurrence of diagonal cracking, will not necessarily lead to a substantial increase in load-carrying capacity and ductility of the beam. In contrast, shear reinforcement placed in the middle span of the beam may be more efficient since it will delay, or may even prevent, the propagation of the diagonal crack into the middle span.

To this end, the work to be described is concerned with an attempt to verify the validity of the proposal by FE analysis. The work is based on a comparative study of strength and deformational characteristics, as well as the fracture processes, of various RC beams with the same geometry and loading conditions (two-point loading) but with shear reinforcement placed within the shear span or within the middle span or throughout the whole length of the beam. Although attention is focused on the behaviour of beams with a_v/d smaller than 2.5, the behaviour of beams with larger a_v/d has also been investigated for comparison purposes. Accordingly, the values of a_v/d selected were 2.27 and 3.4; however, only the results for $a_v/d = 2.27$ will be discussed here, as the latter value falls within the range of a_v/d being considered (for the results of $a_v/d = 3.4$, see reference 112).

The geometric characteristics and reinforcement of the beams were selected to be similar to those of beams whose behaviour was also investigated experimentally. The beams were of 918 mm

Fig. 3.41. RC beams with values of a_v/d between 1.0 and 2.5 under two-point loading:¹¹²

(a) geometric characteristics (all dimensions in mm);
(b) arrangement of shear reinforcement



span and 102 mm height by 51 mm width cross-section with an effective depth d of 90 mm (see Fig. 3.41(a)). The cross-sectional areas A_s of the tensile reinforcement used were 84.83 mm^2 (under-reinforced beams) and 135 mm^2 (over-reinforced beams). The uniaxial cylinder compressive strength f_c of the concrete and the yield stress f_y of the tension steel were 38 N/mm^2 and 502 N/mm^2 respectively.

For each a_v/d and A_s , four types of RC beam containing different arrangements of shear reinforcement were investigated (Fig. 3.41(b)):

- Type A — without shear reinforcement
- Type B — shear reinforcement within the shear span only
- Type C — shear reinforcement within the middle span only
- Type D — shear reinforcement throughout the span

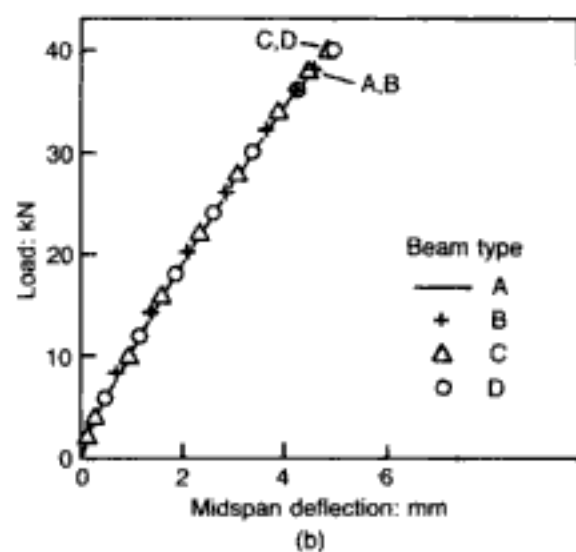
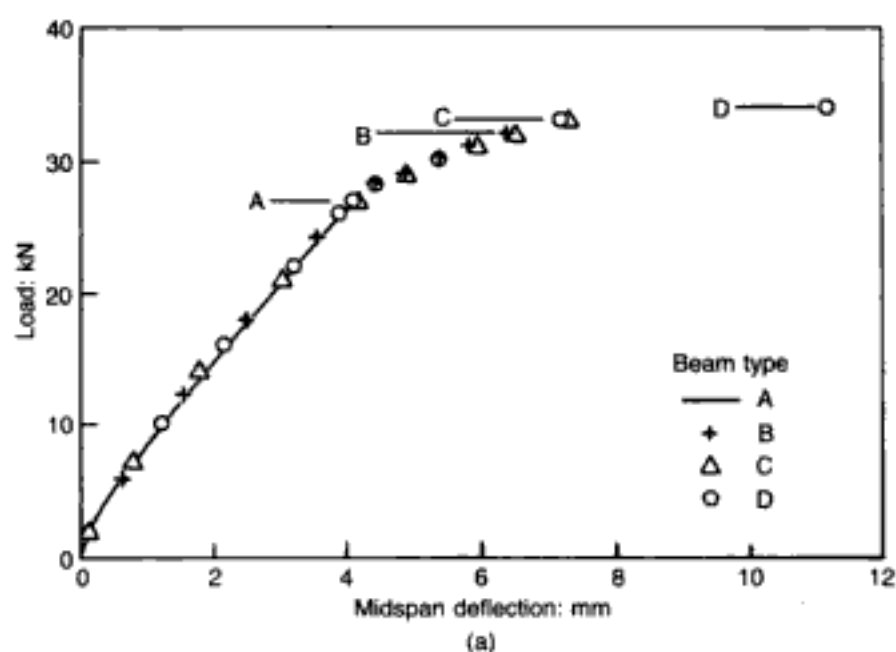
In all cases, the shear reinforcement had cross-sectional area $A_v = 16.09 \text{ mm}^2$, spacing $s = 51 \text{ mm}$, and yield stress $f_{yv} = 417 \text{ N/mm}^2$.

The FE mesh adopted for one-half of the span consisted of 30 elements (10×3) above the reinforcement and 10 elements for the cover. The main results of the analytical investigation are summarized in Table 3.1 and Figs 3.42 and 3.43. Table 3.1 gives

Table 3.1 Maximum load-carrying capacity in kN predicted by FE analysis and ACI 318-77 for RC beams with $a_v/d = 2.27$ under two-point loading¹¹²

Beam type	$A_s = 84.83 \text{ mm}^2$		$A_s = 135.0 \text{ mm}^2$	
	FEA	ACI	FEA	ACI
A	27	10.2	38	10.9
B	32	31.8	38	40
C	33	10.2	40	10.9
D	34	31.8	40	40

Fig. 3.42. Predicted load-deflection relationships for the RC beams with $a_v/d = 2.27$ under two-point loading:¹¹² (a) under-reinforced beams ($A_s = 84.83 \text{ mm}^2$); (b) over-reinforced beams ($A_s = 135.0 \text{ mm}^2$)



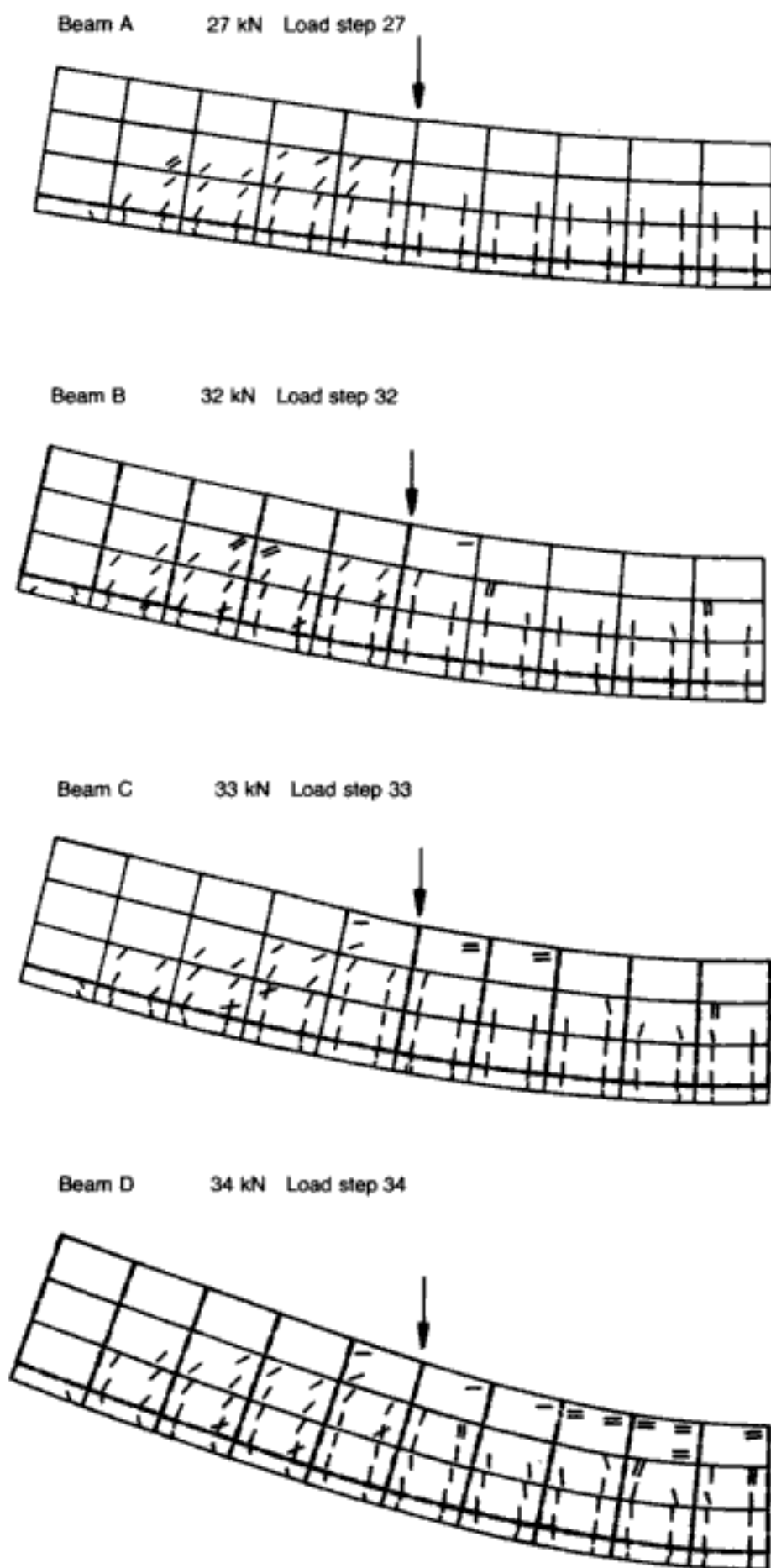


Fig. 3.43. Typical macrocrack pattern and deflected shape at the MSL for the under-reinforced beams ($A_s = 84.83 \text{ mm}^2$) with $a_v/d = 2.27$ under two-point loading¹¹²

the predicted maximum load that can be sustained by the beam in question together with values calculated on the basis of the ACI Standard (ACI 318-77),¹¹⁴ while the predicted load-deflection relationships are shown in Fig. 3.42. Finally, Fig. 3.43 indicates typical patterns of macrocracking and deflected shape corresponding to the maximum load sustained by the various beams. It should be noted that predicted values of both the maximum load and maximum deflection should be considered as lower-bound values since any triaxial compressive stress conditions that may develop when the ultimate-strength capacity is approached (see section 1.5.2) cannot fully be allowed for by the plane-stress analysis employed. However, since such triaxial stress conditions are set up only once the collapse load is practically attained, they should affect only the plastic or near-plastic deformational behaviour rather than the strength characteristics of a beam,¹¹² and this is borne out by the plane-stress analysis predictions depicted in the earlier Fig. 3.2(a). Nevertheless, the predicted deflections in Fig. 3.42 are still useful, even if such a usefulness might be of a comparative nature.

Table 3.1 indicates that, for beams with $a_v/d = 2.27$, the maximum load-carrying capacity of the type C beams (shear reinforcement within the middle span) is higher than that of the type B beams (shear reinforcement within the shear span), irrespective of the amount of tension reinforcement. Such behaviour supports the proposal that collapse of these beams is caused by failure of the compressive zone of the middle span under compression-tension stress conditions and not by failure of the region of the loading point under a wholly compressive state of stress. The use of shear reinforcement, therefore, for preventing failure of the middle span rather than delaying the occurrence of the diagonal crack within the shear span leads to a higher load-carrying capacity of the beams. It is also interesting to note in Table 3.1 that the placing of shear reinforcement throughout the span generally improved the load-carrying capacity of the beams in spite of the fact that the plane-stress analysis employed did not allow for any increase in the compressive strength of concrete in the compressive zone of the middle span arising from the transverse restraint induced by shear reinforcement.

Also included in Table 3.1 are the values of the maximum load-carrying capacity calculated by using the procedures recommended by ACI 318-77.¹¹⁴ For beams with shear reinforcement within the shear span (beams B and D), these values were calculated on the basis of the flexural capacity. On the other hand, the maximum load-carrying capacities of the beams without shear reinforcement within the shear span (beams A and C) were assessed on the basis of the shear capacity. It is interesting to note that, while the table indicates a close correlation between the calculated values and those predicted by the analysis for beams B and D, the values

calculated on the basis of the shear capacity are significantly smaller than the analytical predictions. This deviation is attributed to the inadequacy of the concepts that form the basis of the shear design procedures.

Figure 3.42(a) shows the load-deflection relationships predicted for the various beam types with $A_s = 84.83 \text{ mm}^2$ (under-reinforced concrete beams). The figure indicates that type A beams (i.e. the beams without shear reinforcement) exhibited a brittle load-deflection relationship considered to be indicative of 'shear' failure. Shear reinforcement either delayed or prevented such failure and resulted not only in an increase in load-carrying capacity but also in ductile behaviour. What is significant is the superior ductility of beam C over beam B.

In contrast with the above behaviour, all beams with $A_s = 135 \text{ mm}^2$ (over-reinforced concrete beams) exhibited a brittle load-deflection relationship irrespective of the presence of shear reinforcement (Fig. 3.42(b)). Beam C still deflected more than beam B, although the difference was only slight. However, as discussed previously, the maximum deflection predicted for the beams with shear reinforcement throughout the span should be considered as a lower-bound limit since the plane-stress analysis employed does not allow fully for the confining effect of the shear reinforcement.

The macrocracking patterns predicted for the under-reinforced beams with $a_v/d = 2.27$ under their maximum sustained load (Fig. 3.43) indicate that type A beam (beam without shear reinforcement) failed at the next load increment since it could not sustain the extension of diagonal cracking through the compressive zone. Placing shear reinforcement within the shear span (type B beam) resulted in an increase of the load essential to cause such an extension of diagonal cracking.

For type C beams (shear reinforcement within the middle span only), diagonal cracking extended inside the compressive zone towards the loading point at an earlier load stage equivalent to that which caused collapse of the type A beam. However, biaxial compressive stress conditions in the region of the loading point combined with the presence of shear reinforcement prevented extension of the crack within the compressive zone of the middle span. Furthermore, when the extension occurred (Fig. 3.43), the presence of shear reinforcement prevented immediate failure. This occurred at the next load stage.

The presence of shear reinforcement throughout the beam (beam D) both delayed the extension of diagonal cracking within the shear span towards the loading point and helped the compressive zone of the middle span to sustain a substantially larger amount of cracking (Fig. 3.43).

The typical cracking process for all the beams investigated may be exemplified by the gradual stages of macrocracking and

deformed shapes for the type C under-reinforced beam with $a_v/d = 2.27$.¹¹² These are essentially similar to those of the beam depicted in Fig. 3.38 but with some additional cracks in the shear span of the type C beam resulting from the absence of links there.

To summarize, the 2-D FE analysis of the under-reinforced and over-reinforced concrete beams with a_v/d smaller than 2.5 subjected to two-point load has indicated that placing shear reinforcement within the middle span rather than the shear span results in a significant improvement of both load-carrying capacity and ductility of the beams. Such behaviour supports the view that, unlike beams with a_v/d greater than 2.5 (these will be considered next), failure of the members is due to branching of the diagonal crack within the shear span toward the compressive zone of the middle span and not to crushing of the compressive region around the loading point.

Behaviour of beams with $a_v/d > 2.5$. As shown above, for the range $1.0 < a_v/d < 2.5$, the causes of shear failure are associated with the stress conditions in the region of the path along which the compressive force is transmitted to the supports and not with the stress conditions in the region of the beam below the neutral axis, as is widely believed. It will be shown next, through additional numerical modelling, that the former view can also provide a realistic explanation of the causes of shear failure of beams with shear span-to-depth ratios greater than a value of between approximately 2.0 and 2.5, and that, therefore, it may form a suitable basis for the review of current shear design procedures. The various arrangements of stirrups to be studied are based on the schematic description of failure summarized in Fig. 3.44 (this will be discussed subsequently).

The geometric characteristics and reinforcement of the beams investigated were selected to be similar to those of beams whose behaviour has been investigated experimentally. The beams were under-reinforced with 1000 mm span and 102 mm by 51 mm cross-section, and with an effective depth d of 93 mm (Fig. 3.45(a)).

The cross-sectional areas of the tension reinforcement were

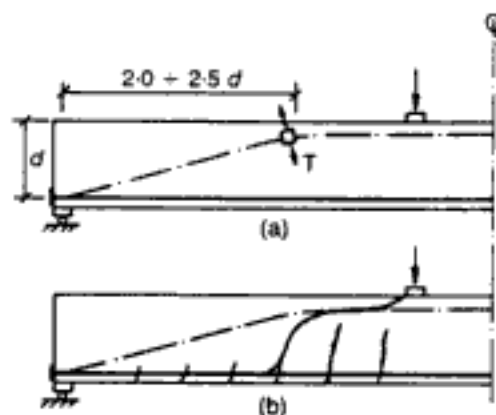


Fig. 3.44. RC beams with values of a_v/d greater than 2.5 under two-point loading:¹¹³ (a) path of compressive force; (b) mode of failure

56.55 mm² and 84.83 mm². The uniaxial cylinder compressive strength f_c of the concrete and the yield stress f_y of the tension steel were 35 N/mm² and 690 N/mm² respectively.

The beams were subjected to two-point loading with values of the shear span a_v equal to 300 mm and 400 mm, corresponding to values of a_v/d approximately equal to 3.30 and 4.30 respectively. For each a_v/d and A_s , four types of RC beam containing different arrangements of stirrups were investigated (Fig. 3.45(b)):

- Type A — without stirrups
- Type B — stirrups throughout the span
- Type C — stirrups within the region of the shear span between the cross-section at the support and that at a distance of 200 mm from the support
- Type D — stirrups throughout the span except in the region(s) reinforced with stirrups in type C beams.

In all cases the stirrups had cross-sectional area $A_v = 16.09$ mm², spacing $s = 51$ mm, and yield stress $f_{yv} = 417$ N/mm².

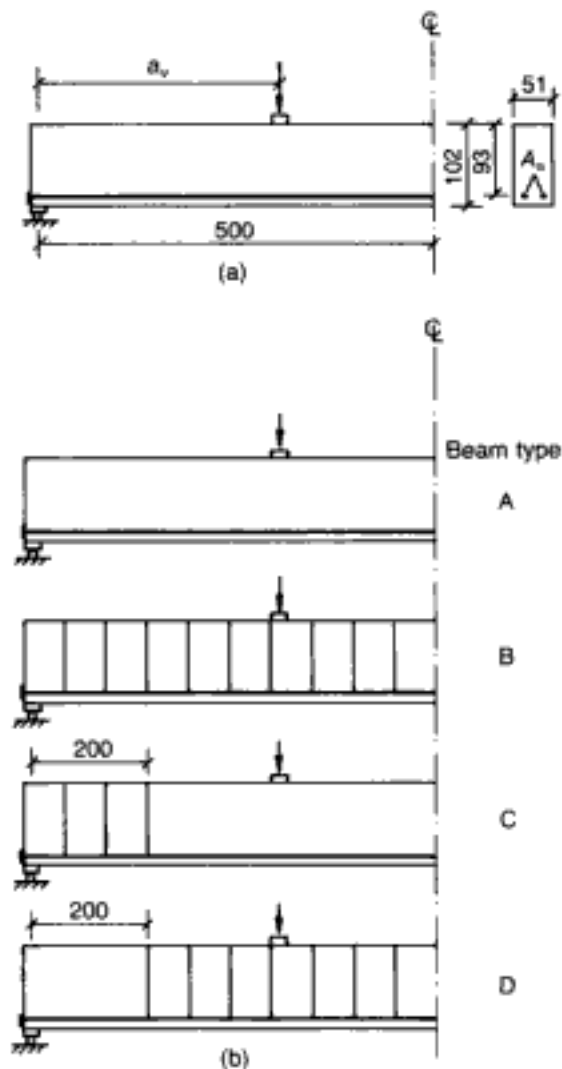


Fig. 3.45. RC beams with values of a_v/d greater than 2.5 under two-point loading:¹¹³
 (a) geometric characteristics;
 (b) arrangement of shear reinforcement
 (All dimensions in mm)

Once again, a plane-stress analysis was deemed adequate (especially for strength predictions) despite the inherent biaxial (instead of triaxial) conditions, as explained previously. The FE mesh for the earlier study (i.e. $a_v/d < 2.5$) was also adopted, except that the cover was now neglected. The main results are summarized in Table 3.2 and Figs 3.46, 3.47 and the previously given Fig. 3.38. Table 3.2 gives the predicted maximum loads that can be sustained by the beams together with values calculated on the basis of the recommendations of the British Code of Practice CP 110.⁵³ These latter values correspond to the flexural capacity of the beams. The predicted load–deflection relationships are shown in Fig. 3.46, in which, for comparison purposes, the loads have been normalized with respect to the predicted maximum load P_A sustained by the appropriate beam A. As usual, the predicted values for both load and deflection correspond to the level at which the solution converged for the last time. At the next load increment the solution failed to converge, and hence the theoretical collapse load lies between the value given in the table and that corresponding to the next load increment. The predicted values in Table 3.2 and Fig. 3.46, therefore, represent lower-bound values for failure. Finally, Fig. 3.47 indicates typical patterns of macrocracking and deflected shapes corresponding to the maximum load sustained by the beams, while Fig. 3.38 illustrates the typical cracking process (by reference to beams B) right up to failure.

On the basis of the concept of shear capacity of a critical section, beams A, C and D must have similar load-carrying capacity since they have no stirrups either throughout or in a large part of their shear span where the shear force is constant; and yet, Table 3.2 indicates that, while beams A and C indeed have the same load-carrying capacity in most cases, beam D has a load-carrying

Table 3.2. Maximum load-carrying capacity in kN predicted by FE analysis and CP 110 (flexural capacity) for RC beams with $a_v/d = 3.3$ and 4.3 under two-point loading.¹¹³ (Note: P_A is ultimate load P_u (MSL) for type A beams predicted by FE analysis)

Beam type	$A_v = 56.55 \text{ mm}^2$				$A_v = 84.83 \text{ mm}^2$			
	a_v/d							
	3.3		4.3		3.3		4.3	
	P_u	P_u/P_A	P_u	P_u/P_A	P_u	P_u/P_A	P_u	P_u/P_A
A	18	1.0	14	1.0	20	1.0	16	1.0
B	22	1.22	14	1.0	24	1.20	20	1.25
C	18	1.0	14	1.0	22	1.10	18	1.13
D	22	1.22	14	1.0	24	1.20	20	1.25
CP 110	20.8	1.11	15	1.07	25.6	1.28	19.2	1.20

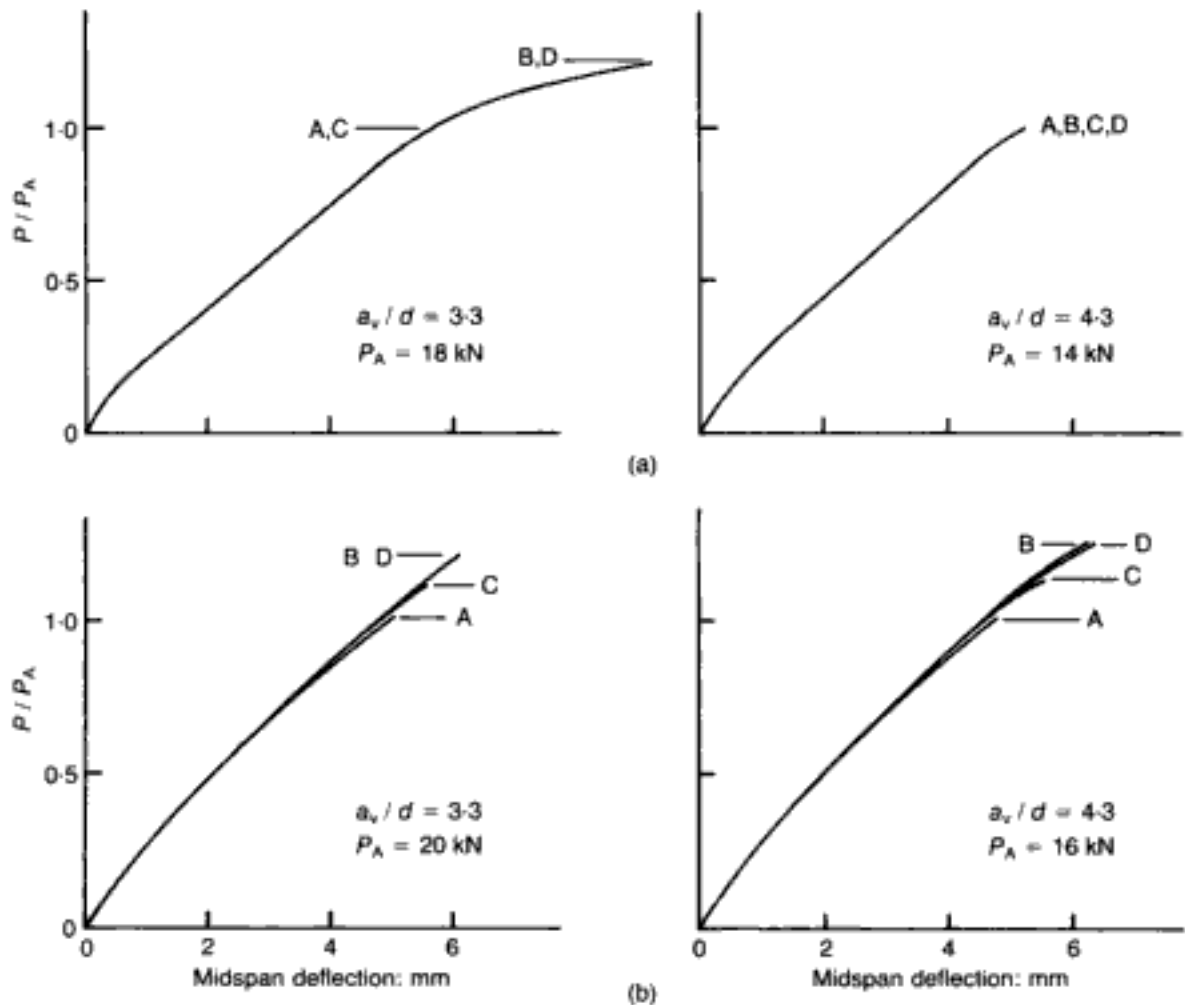


Fig. 3.46. Predicted load-deflection relationships for the RC beams with $a_v/d > 2.5$ under two-point loading.¹¹³ (a) $A_s = 56.55 \text{ mm}^2$; (b) $A_s = 84.83 \text{ mm}^2$

capacity significantly greater than that of beam A. Furthermore, the load-carrying capacity of beam D is essentially equal to that of beam B, which is reinforced with stirrups throughout the shear span in compliance with the code (CP 110) design provisions. Clearly, the above results cannot be explained by the concept of shear capacity of critical sections. A more convincing explanation can be postulated on the basis of the concept of the compressive-force path, in which a beam without stirrups fails owing to the development of tensile stresses within the compressive zone. It has been suggested that a possible cause for the development of such stresses is the shape of the path along which the compressive force is transmitted to the supports.¹¹⁰ This may be illustrated as follows.

A beam subjected to two-point loading with a_v/d greater than a value of about 2.5 is characterized by a path of compressive force consisting of two near-linear portions connected by a smooth curve in the region of the compressive zone at a distance between approximately $2.0d$ and $2.5d$ from the support (Fig. 3.44(a)). This change in the direction of the compressive force generates, for equilibrium purposes, a resultant tensile stress intersecting the obtuse angle of the near-linear portions. When the capacity of the

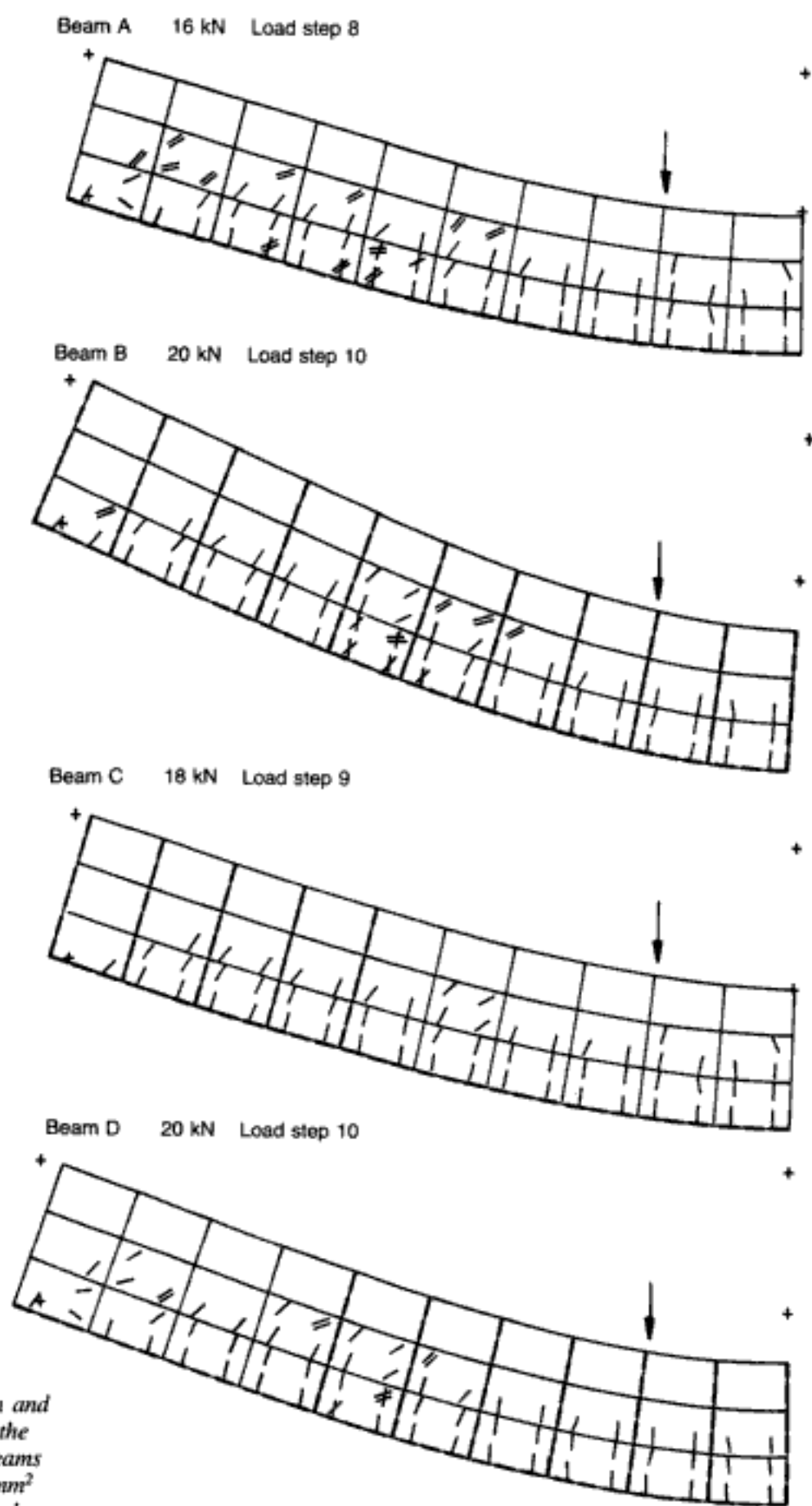


Fig. 3.47. Typical macrocrack pattern and deflected shape at the MSL for the RC beams with $A_s = 84.83 \text{ mm}^2$ and $a_v/d = 4.3$ under two-point loading¹¹³

region to sustain the combined compression-tension stress field is exceeded, then the flexural crack closest to this region propagates near-horizontally towards the point load and causes collapse (Fig. 3.44(b)).

Thus, the placing of stirrups within the shear span beyond a distance of approximately $2.0d$ from the support prevents the occurrence of the near-horizontal crack and hence increases the load-carrying capacity of the beam. On the other hand, the placing of stirrups within the region of the shear span extending to approximately $2.0d$ from the support is ineffective and hence does not improve the load-carrying capacity of the beam. Therefore, it appears from the above that, unlike the concept of the shear capacity of critical sections, the concept of the compressive-force path provides a rational explanation of the strength results summarized in Table 3.2.

Furthermore, the previously described results imply that the presence of stirrups does not transform the beam into a truss (with or without a constant angle of the inclined compressive strut) as widely considered. Rather, it appears to cause a stress redistribution within the compressive zone by causing a transfer of the tensile stresses which cannot be sustained by concrete alone to the steel.

It is significant that, of the beams tested, only types B and D attained in all cases their flexural capacity as predicted by the code (CP 110) design provisions (see Table 3.2). Beams A and C failed before their flexural capacity was attained, except for the beams with $A_s = 56.55 \text{ mm}^2$ and $a_v/d = 4.30$ which also failed in flexure on account of their low percentage of tension reinforcement.

It is interesting to note in Fig. 3.46 that the predicted load-deflection relationships for the beams indicate brittle behaviour in most cases. However, since the beams were under-reinforced, such brittle behaviour should characterize only beams A and C which failed before their flexural capacity was attained. In contrast to the behaviour of beams A and C, beams B and D should exhibit ductile behaviour since they failed in flexure. As explained earlier, the underlying causes of ductile behaviour are associated with triaxial stress conditions which develop in the compression zone of the beam when its flexural capacity is attained. The method of analysis employed in the present work, however, does not allow for fully-triaxial stress conditions since it is based on the assumption of plane stress. Hence, the method is not always appropriate in predicting ductile behaviour for beams failing in flexure. Nevertheless, even though recourse must be made to the 3-D FE model of Chapter 4 for predicting the load-deflection plots once the peak load for some of the beams is approached, the characteristics of Fig. 3.46 are still useful for comparison purposes (i.e. the behaviour of the beams relative to one another), which constitute the aim of this study.

Figure 3.47 shows the crack patterns and the deflected shapes

of the beams with $A_s = 84.83 \text{ mm}^2$ and $a_v/d = 4.30$ under the maximum sustained load. Both macrocracking patterns and deflected shapes, however, are typical for all cases investigated. The figure indicates that beam A suffered extensive inclined cracking which must eventually have led to failure since the beam failed before its flexural capacity was attained. A characteristic feature of the failure mode of this beam is the complete loss of load-carrying capacity (indicated by the intersecting cracks) of the concrete in the region of the tensile zone adjacent to the tension reinforcement. Such loss of load-carrying capacity renders the resistance of the shear force through beam action impossible and questions the hypothesis of Kani¹¹⁵ that shear failure occurs when the flexural capacity of a concrete cantilever between two consecutive cracks is exceeded.¹¹³ The figure also indicates that the presence of stirrups within the region of the shear span extending to a distance of 200 mm from the support (beam C) reduced the amount of inclined cracking but was insufficient to cause an increase of the load-carrying capacity. (It is clear from Table 3.2 that the MSLs for beams A and C are identical for the two cases with $A_s = 56.55 \text{ mm}^2$ while, for the other two cases ($A_s = 84.55 \text{ mm}^2$), the discrepancy between A and C is within the order of magnitude of the load step, namely the accuracy inherent in the analysis.)

In contrast with the above behaviour, placing stirrups throughout the beam span (beam B) both reduced the amount of inclined cracking within the shear span and allowed the beam to attain its flexural capacity. It is interesting to note, however, that although in beam D the absence of stirrups in the region of the shear span extending to a distance of 200 mm from the support caused the formation of practically as many inclined cracks as they formed in beam A, the presence of stirrups in the remaining span was sufficient to allow the beam to attain its flexural capacity, as discussed previously.

Figure 3.38 indicates the process of macrocracking of beam B with $A_s = 84.83 \text{ mm}^2$ and $a_v/d = 4.30$ under increasing load. The figure also indicates the deflected shape of the beam at various loading stages up to failure. (Both the process of cracking and the deflected shapes are typical of all the beams investigated.) The figure shows that macrocracking initiates in the middle span of the beam and progressively spreads towards the supports with increasing load. Concurrently, the macrocracks extend towards the compressive zone and, as expected, those within the shear span exhibit a slight inclination towards the point load. Under a load of 14 kN the macrocrack pattern is characterized by a deep macrocrack which occurs at a distance between approximately 200 mm and 250 mm from the support. Once this deep macrocrack forms, the macrocrack pattern remains unchanged for load increments up to 18 kN. Further loading causes complete loss of

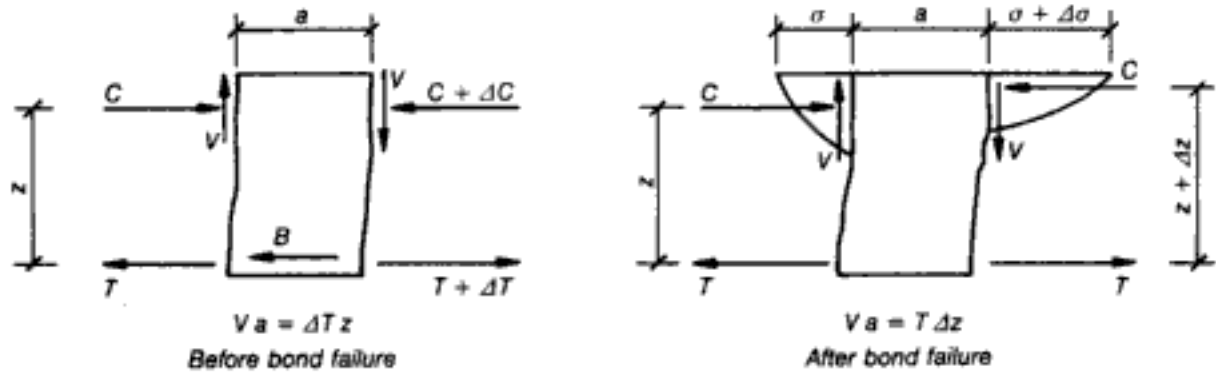


Fig. 3.48. Schematic representation of the effect of bond failure on the stress condition in the compressive zone¹¹³

load-carrying capacity of the concrete in the region of the deepest macrocrack adjacent to the tension reinforcement (i.e. two intersecting cracks) and, as discussed below, this local failure is perhaps the underlying cause of the collapse of the beam when the load increases beyond the MSL of 20 kN.

Figure 3.38 also shows the macrocrack pattern under a load of 22 kN which was not sustained by the beam, as divergence in the analytical solution took place at load step 11. The figure indicates that failure occurred due to extension of the macrocracking into the compressive zone and near-horizontal splitting of this zone in the region of the point load.

It is interesting to note that, in most cases, failure of the beams was preceded by complete loss of load-carrying capacity of the concrete in localized regions adjacent to the tension reinforcement. The effect of such localized failure — which may be considered equivalent to bond failure — on the internal actions within the compressive zone is depicted in Fig. 3.48. This figure indicates the change in the equilibrium conditions of a beam element between two consecutive cracked sections after bond failure, assuming that arch action is negligible before bond failure occurs. From the figure, it can be seen that the loss of the bond force results in an extension of the right-hand side flexural crack sufficient to cause an increase Δz of the lever arm z , such that $C\Delta z = Va$. However, the extension of the flexural crack reduces the depth of the neutral axis and thus increases the intensity of the compressive stress block at the right-hand side of the element. Concrete in this region will be the first to reach the stage where volume dilation occurs, and such volume dilation will induce tensile stresses in the surrounding concrete which has not yet reached the volume dilation stage in compression. Thus, the compressive zone is subjected to compression-tension stress conditions in localized regions and the beam will fail when the concrete strength in these regions is attained. As outlined in Chapter 1, such failure is characterized by cracking in the direction of the maximum principal compressive stress and this may explain the presence of longitudinal (i.e. horizontal) cracking in the compressive zone characterizing the failure mode of the beam in Fig. 3.38. It appears, therefore, that

this failure mechanism is an alternative mechanism to that discussed previously by reference to Fig. 3.44 for the development of tensile stress in the compressive zone where the CFP changes direction.

In summarizing the results of this study, from which it may be seen that the FE analysis has extended the findings of beams with $a_v/d < 2.5$ to those with $a_v/d > 2.5$ also, it is evident that, in general, the predicted behaviour is incompatible with the concept of 'shear' capacity of 'critical' sections. The obtained results support the view that shear failure is associated with the development of tensile stresses within the compressive zone and, in particular, the region of the compressive zone between the sections including: (a) the loading point, and (b) a point lying at a distance of about twice the beam depth from the support; this implies that the stirrups sustain tensile stresses developing within the compressive zone rather than transform the beam into a truss as widely considered. An alternative possible mechanism for the development of such tensile stresses appears to be associated with the destruction of bond between steel and concrete when the bond stresses are critical.

3.4.1.3. Beams with and without stirrups under central point load

The well-known series of beam tests of Bresler and Scordelis¹¹⁶ has provided the basis for many an attempt to reproduce the experimental results numerically. In general, such an aim has proved notoriously difficult, especially when attempting to attain good predictions for all beams without altering the various material and procedural factors of a given package. Leaving aside the often-blatant disregard for the actual behaviour of concrete at the material level exhibited by various FE models for structural concrete proposed to date, it appears that the complexity of the beams in question warrants a fully 3-D analysis in which formal triaxial conditions are catered for. While such an approach will be adopted in Chapter 4, the results of modelling the beams by means of the plane-stress package⁸⁵ will be reported, despite that latter's unavoidable shortcomings for such challenging members.

Beams without stirrups. The experimental data (including the observed crack pattern at collapse for a similar, but related, beam) for this member, denoted as beam OA-1,¹¹⁶ is shown in Figs 3.49(a) and 3.49(b), while the adopted mesh is depicted in Fig. 3.49(c) (the local mesh-stiffening device introduced over the support(s) should be noted; this was adopted so as to avert possible early numerical problems near concentrations of load, as discussed in section 3.2). The failure load of the test is reported as 334 kN, with a central deflection of 6.6 mm. With the adoption of an initial load step of 30 kN and subsequent (uniform) load steps of 20 kN, the numerical prediction becomes 410 kN (the deflections at 330 kN

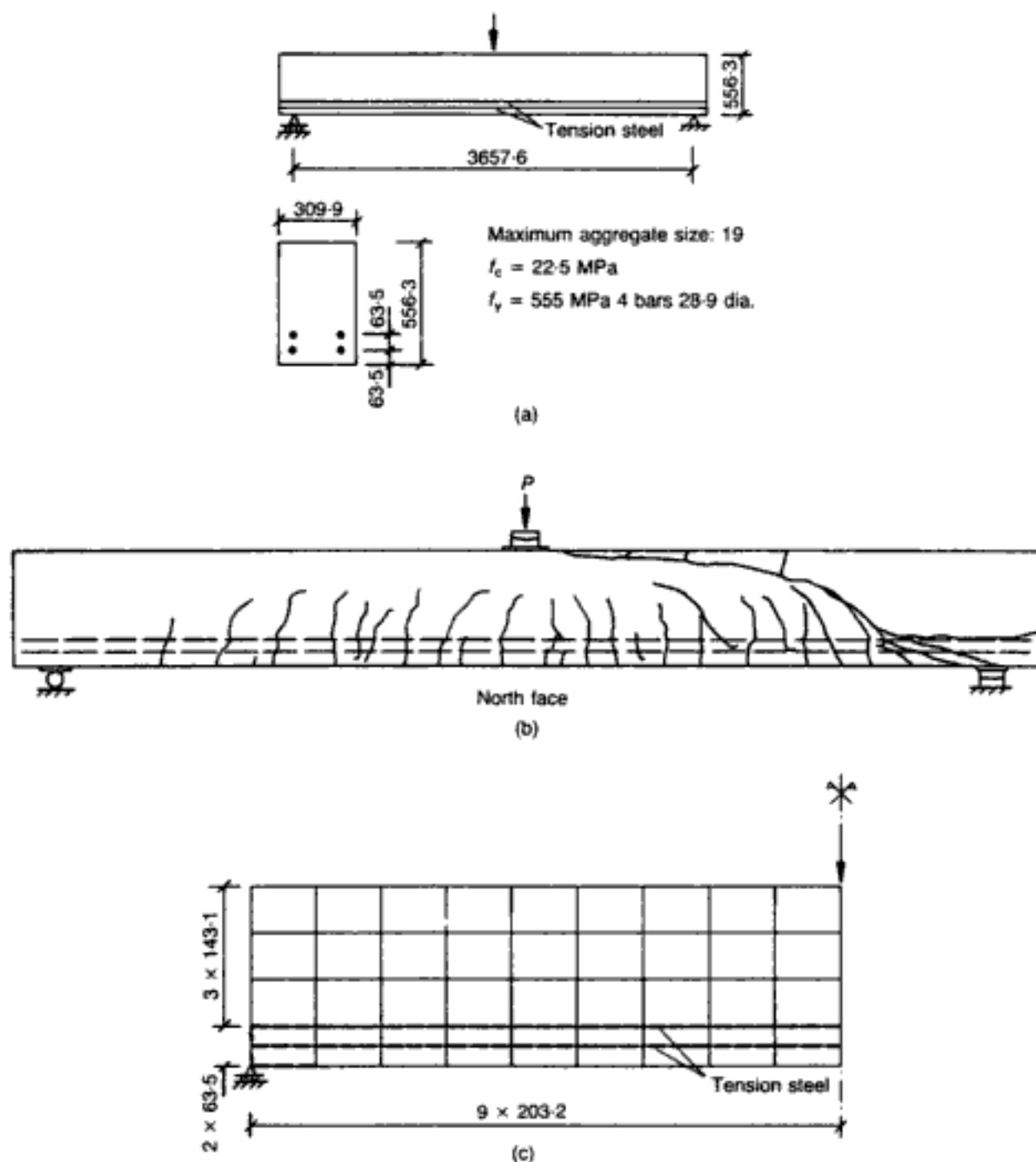
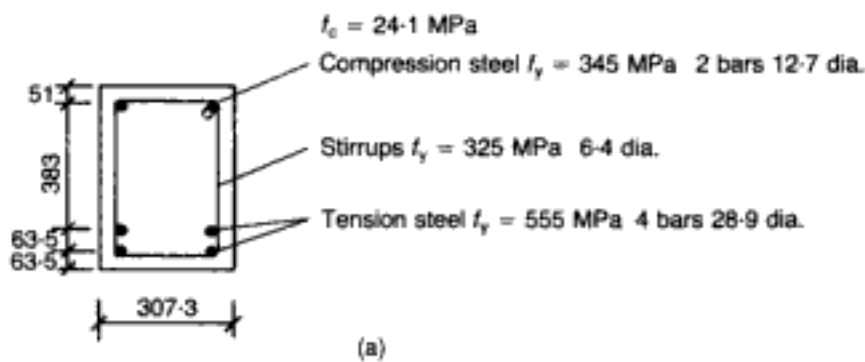
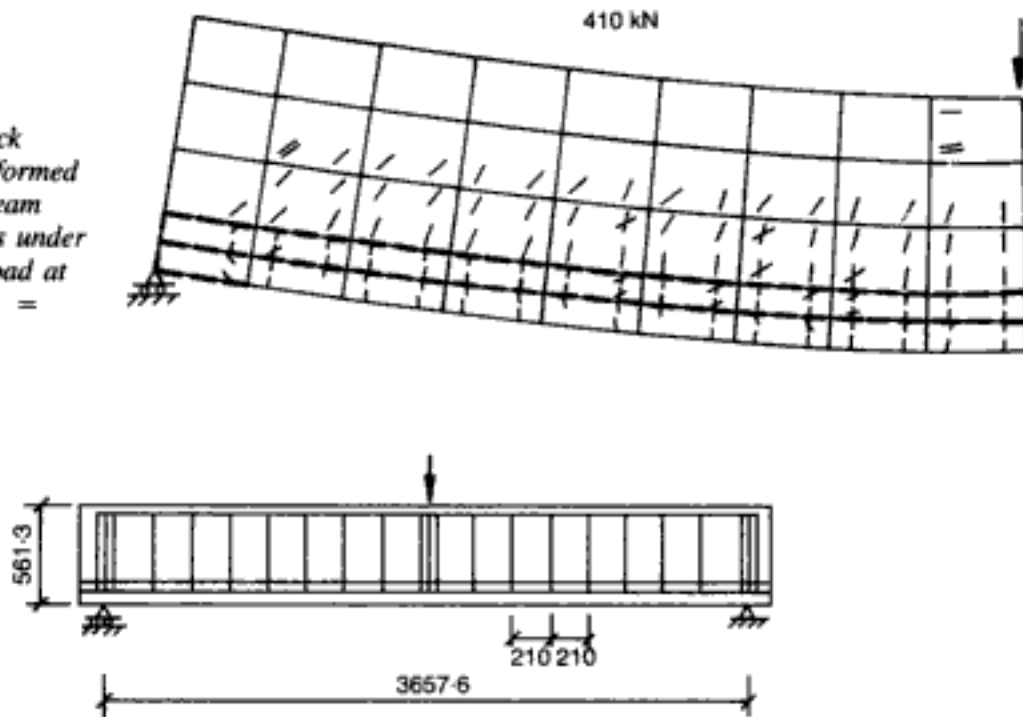


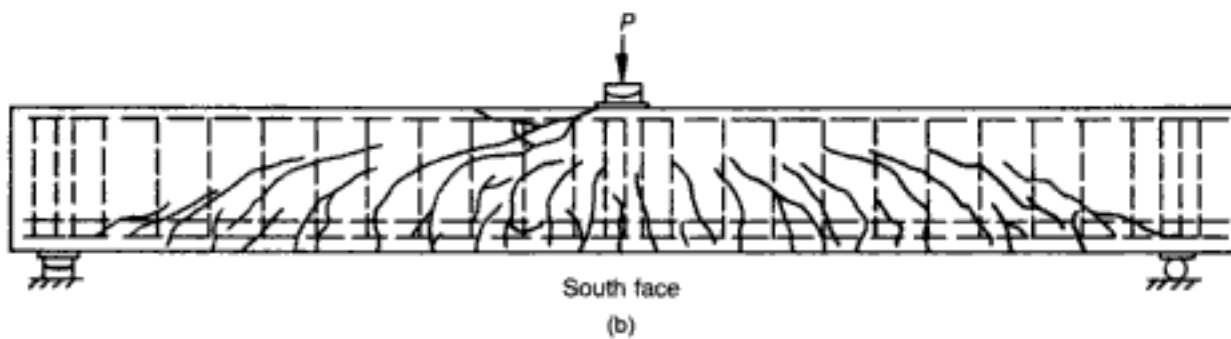
Fig. 3.49. RC beam without stirrups under central point load.⁸⁵ (a) member characteristics; (b) observed crack pattern at ultimate load for a similar (and related) member (OA-2);¹¹⁶ (c) FE mesh used in the analysis (All dimensions in mm)

and 410 kN were 6.68 mm and 8.78 mm respectively). Such an overestimate, however, was obtained by setting $\beta = 0.5$.^{54,85} That the value of β has a somewhat larger effect than usual in this difficult problem can be seen by quoting the value of ultimate load obtained with $\beta = 0.1$, the more theoretically acceptable value (see section 3.2): the collapse load is then 370 kN,⁵⁴ a much better prediction (the deflections at 330 kN and 370 kN were 7.13 mm and 8.81 mm respectively). However, even $\beta = 0.5$ yielded realistic estimates of cracking (Fig. 3.50 — cf. Fig. 3.49(b)) and stiffness (the latter will be discussed in Chapter 4, where this problem will be re-analysed with the 3-D model).

Fig. 3.50. Crack pattern and deformed shape of RC beam without stirrups under central point load at the MSL (D.M. = 25)⁸⁵



(a)



(b)

Fig. 3.51. RC beam with stirrups under central point load:⁸⁵ (a) member characteristics (all dimensions in mm); (b) observed crack pattern at ultimate load

Beam with stirrups. This example is derived from beam A-1 reported in reference 116. Essentially, beam A-1 differs from beam OA-1 through the presence of stirrups and compression reinforcement, as may be seen in Fig. 3.51(a) (the local stiffening provided in the experimental set-up in the regions of load concentration should be noted). Collapse of this member is reported to have occurred at a load of 467 kN. The adoption of the mesh

Fig. 3.52. Predicted and experimental load–deflection curves for the RC beam with stirrups under central point load⁸⁵

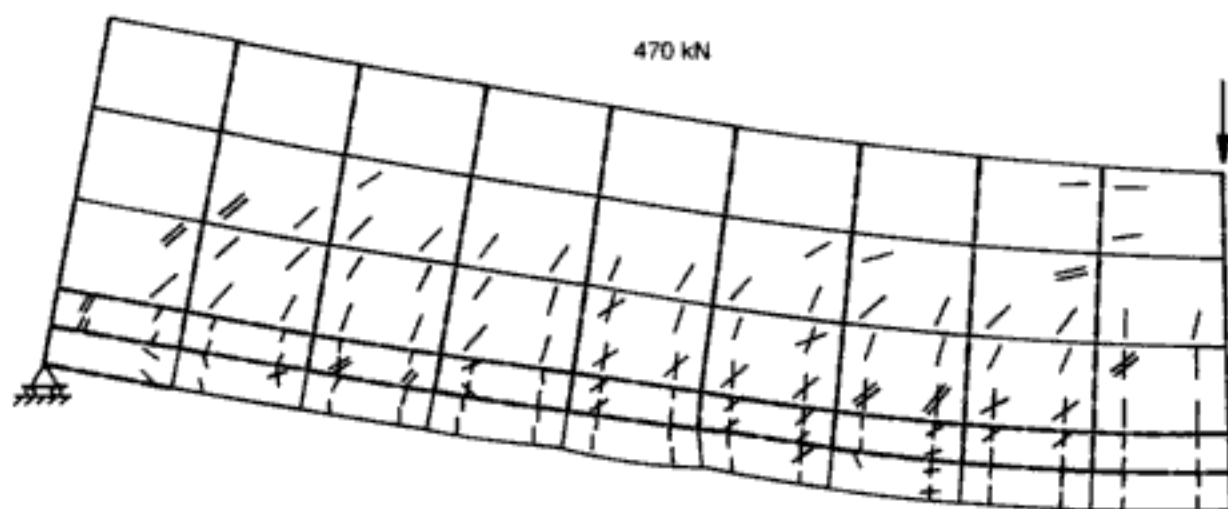
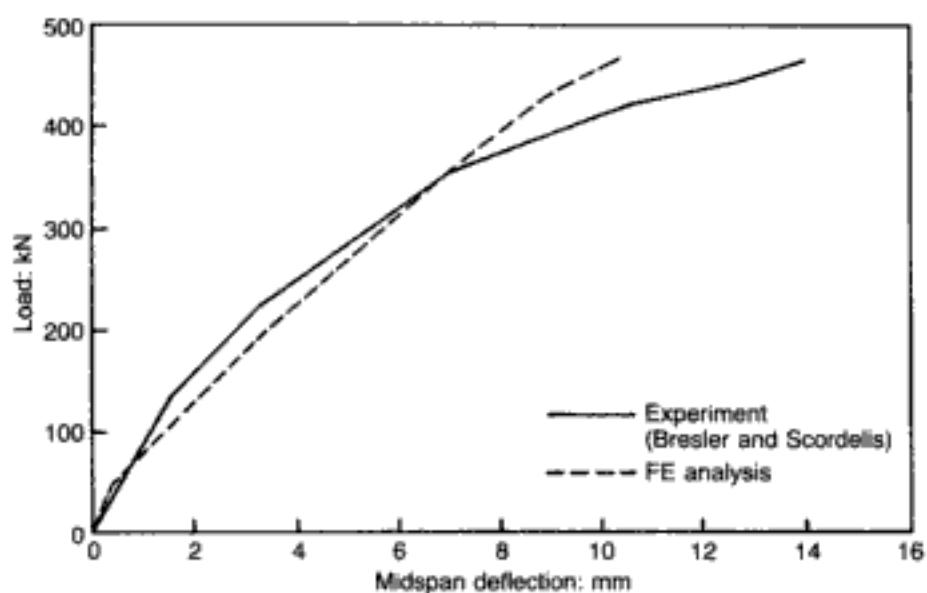


Fig. 3.53. Crack pattern and deformed shape of RC beam with stirrups under central point load at the MSL ($D.M. = 25$)⁸⁵

and load steps used for beam OA-1 leads to a numerical prediction of 470 kN, a surprisingly good result in view of the expected limitations of the 2-D model when applied to this problem. As pointed out in reference 85, investigations by other authors which reported realistic predictions for the case of the beam without shear reinforcement could not generate such 'good' predictions in the case of the beam with shear reinforcement as well. In addition to the failure load, predictions of the load–deflection curve (Fig. 3.52) and the crack pattern (Fig. 3.53 — cf. Fig. 3.51(b)) may be seen to correlate closely with the experimental results. (Although the analytical central deflection at the MSL underestimates the experimental value by 27%, the load–deflection curves are quite close to one another over most of their range.) As for the previous example (beam OA-1), the present case study (beam A-1) will be reassessed in Chapter 4.

3.4.2. Deep beams

Although deep beams are prone to out-of-plane effects and should preferably be analysed in three dimensions, plane-stress analysis

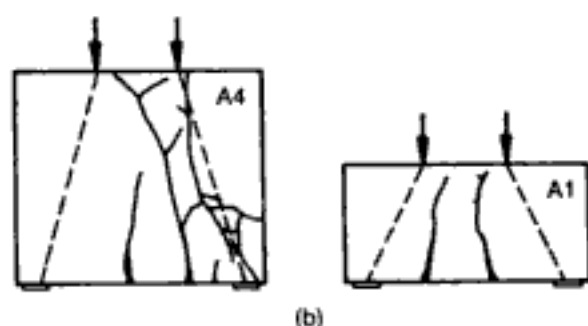
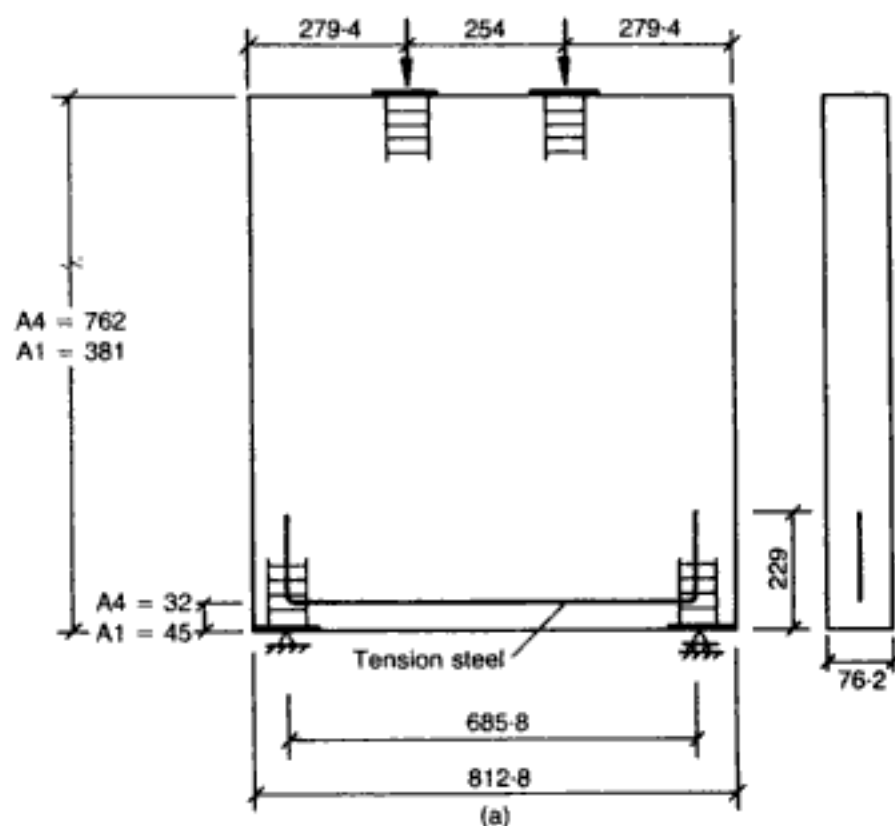


Fig. 3.54. Deep beams A4 and A1:⁵⁴ (a) experimental data (all dimensions in mm); (b) observed crack patterns at ultimate loads

of such members still yields acceptable answers for practical design guidelines. The latter is illustrated through four examples.

3.4.2.1. Deep beams under two-point loading

The following two examples model the behaviour of members drawn from the series of deep-beam tests reported in reference 117. The two members selected for analysis have similar geometric and loading characteristics except for the overall depths which are 762 mm (beam A4) and 381 mm (beam A1) respectively. The experimental data for both beams (including the observed crack patterns at collapse) are given in Fig. 3.54, the tension steel consisting of a single 9.5 dia. bar characterized by $f_y = 317 \text{ N/mm}^2$. The f_c values are 27.3 N/mm^2 (A4) and 24.2 N/mm^2 (A1) respectively.

Bédard⁵⁴ analysed the two members by adopting the following mesh configurations for one-half of the beam: 3 (spanwise) \times 4 (depthwise) for A4 (neglecting cover since this represents only

Hidden page

Hidden page

Hidden page

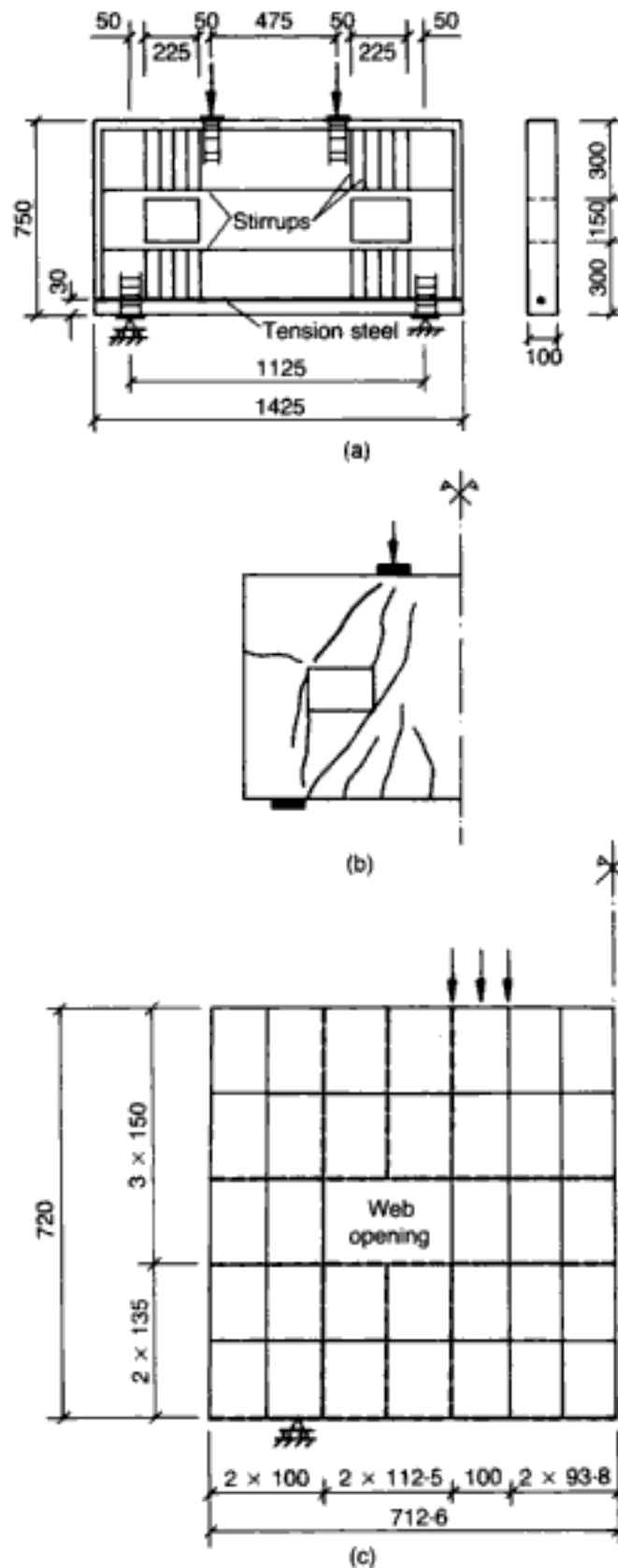


Fig. 3.57. Deep beam with web openings NW7 0.3/4:⁵⁸ (a) member characteristics; (b) observed crack pattern at ultimate load; (c) FE mesh (All dimensions in mm)

concentrations at the corners of the large opening can also be noticed; diagonal cracks usually form at much higher load levels in deep beams without openings. These stress concentrations lead subsequently to steel yielding (starting with the lower left-hand

Hidden page

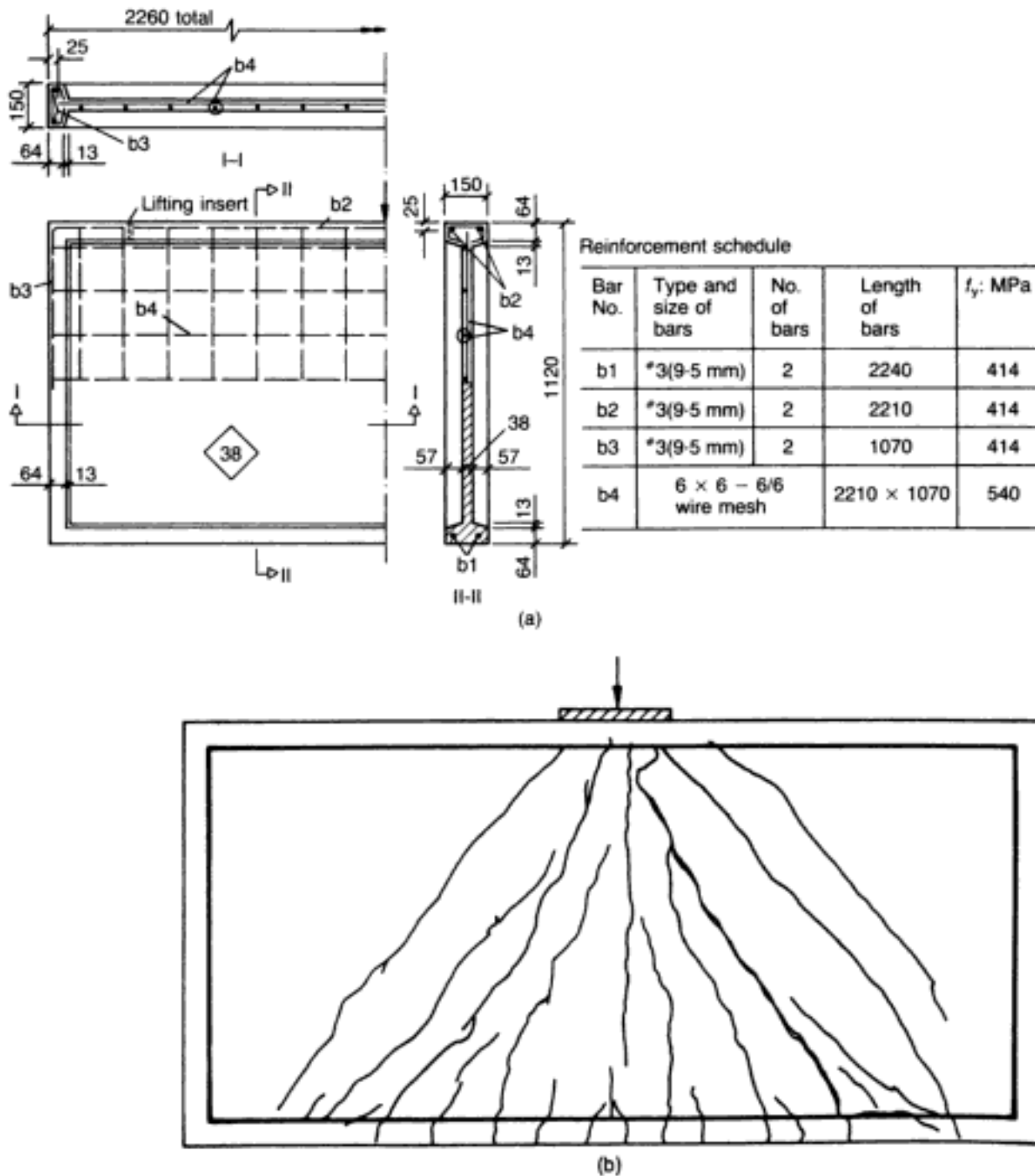


Fig. 3.60. Deep beam with complex reinforcement P111:¹²⁰
 (a) member characteristics (all dimensions in mm);
 (b) observed crack pattern at ultimate load

3.4.2.3. Deep beam with complex reinforcement subjected to a concentrated load at midspan

Figure 3.60 shows a deep beam, under a central point load, the reinforcement detailing of which is quite involved, consisting of four different types of steel bar. The material data — $f_c = 38 \text{ N/mm}^2$ while the f_y values for the various steels are listed in Fig. 3.60(a) — have been taken from reference 120, where the experimental failure load of the beam-panel considered here (specimen P111) is given as 267 kN. The observed crack pattern at collapse appears in Fig. 3.60(b).

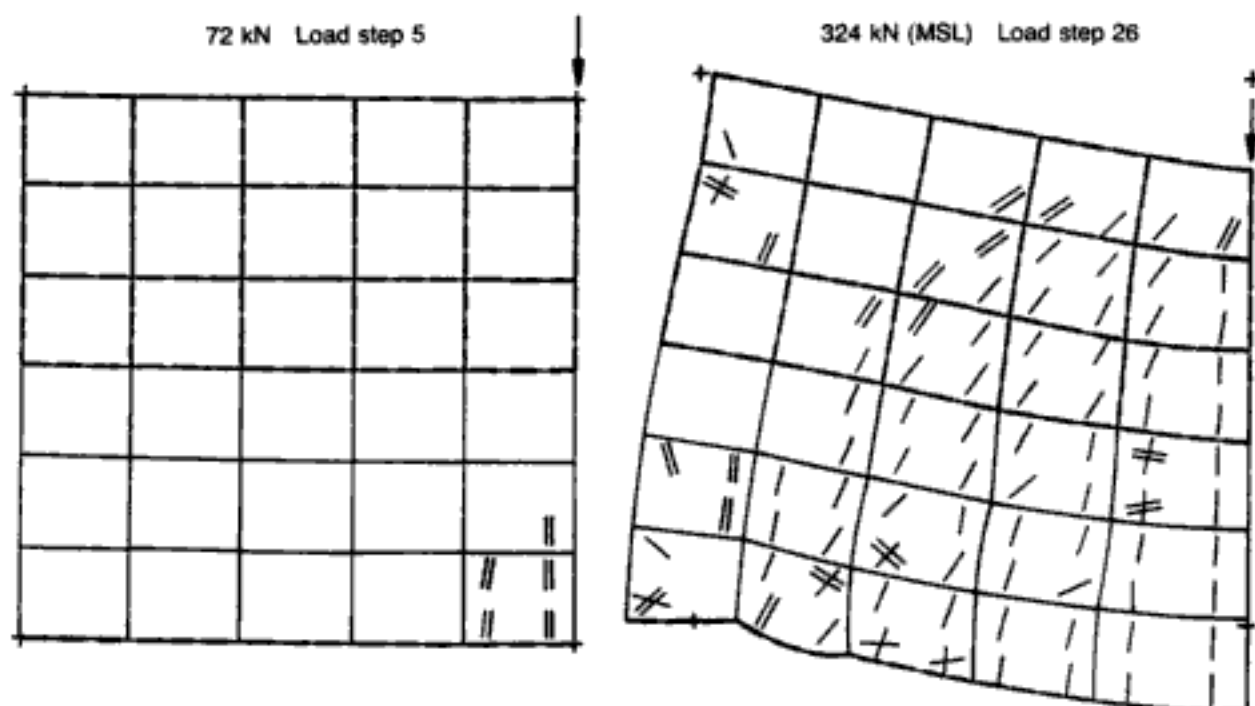


Fig. 3.61. Crack patterns and deformed shapes at load levels corresponding to crack initiation and MSL for deep beam with complex reinforcement P111 (D.M. = 20)⁹⁹

A simple and fairly coarse FE mesh was adopted in the modelling of one-half of the beam, as may be seen in Fig. 3.61.⁹⁹ This entailed changes to the actual configuration so as to eliminate the concrete ribs and cover (both top and bottom) and, more drastically, a more concentrated 'smearing' of the upper reinforcement by replacing the five horizontal and eight vertical bars by four and six line elements respectively. Such changes were introduced in order to illustrate that, even with these simplifications, the model provides an estimate which is adequate for engineering purposes, as the analytical value of failure load obtained was 324 kN (an overestimate of 21%). (An additional approximation in the analysis stems from the use of an f_c value based on tests on cylinders with a height-to-diameter ratio of 2,¹²⁰ rather than 2.5, which, as will be discussed in section 4.5.2.3, can result in overestimates in f_c of some 10%. This, in turn, would clearly account for a sizeable portion of the present MSL overestimate.) This figure is numerically reliable since it was attained for both a coarse and a fine load steps (36 kN and 12 kN respectively). As observed experimentally,¹²⁰ the first cracks to appear were vertical flexural cracks in the web, under the point load: this occurred at 72 kN (for both load steps), and can be seen in Fig. 3.61. The pattern of cracks at the ultimate load of 324 kN is also in very good agreement with experimental observations,¹²⁰ with cracks emanating from the loaded area to the bottom of the beam: see the MSL pattern, which refers to the result for the smaller load step. Furthermore, such a crack pattern is, once again, consistent with the 'tied frame' model for deep beams mentioned in section 3.4.2.1.

3.4.3. *Structural walls*

Reinforced-concrete structural walls are widely considered to provide an efficient bracing system and to offer great potential for both lateral-load resistance and drift control; hence their widespread use, not only for high-rise but also for low-rise buildings in areas of high or moderate seismicity. These members are usually referred to as 'shear' walls (a term which will also be adopted henceforth interchangeably with the more correct description of a 'structural' wall) but, while the lateral loading seems to justify this popular description, it will be shown in the course of the present studies that the ultimate behaviour of the wall cannot be associated with a predominantly 'shear' mechanism, as generally implied. Yet, such walls are designed as cantilever beams with concrete, above the neutral axis, and longitudinal reinforcement resisting the combined action of gravity loads and bending moment, whereas the region of the wall below the neutral axis provides shear resistance to the action of the horizontal forces, and horizontal reinforcement sustains the portion of the shear force in excess of that which can be sustained by concrete alone. The horizontal reinforcement is assessed by using one of a number of methods invariably based on the 'truss analogy' concept which stipulates that, once inclined cracking occurs, the beam behaves as a truss with concrete between the inclined cracks forming compression struts and the horizontal reinforcement constituting the tension ties.

More recently, however, it has been found that the above design method is not always safe since the wall shear capacity, as predicted on the basis of the 'truss analogy' concept, often overestimates considerably that established by experiment^{4,121,122} (see also Fig. 3 in the Introduction). This suggests that the 'truss analogy' does not provide a realistic description of the mechanism of shear resistance. Instead, and as was the case with the simply supported beams described previously, a more rational and accurate model for shear resistance is associated with the strength of concrete in the region of the path along which the compressive force is transmitted to the supports, with the portion of the member below the neutral axis making an insignificant, if any, contribution. Thus, while typical detailing of tested shear walls may be as depicted in Fig. 3.62(a), a better alternative is to modify such reinforcement details by strengthening the compressive zone (through an increase in the amount of compression reinforcement) while 'weakening' the region below the neutral axis (by reducing the horizontal reinforcement) as shown in Fig. 3.62(b).¹²² (Henceforth, vertical and horizontal steel characteristics will be denoted by subscripts v and h respectively, as indicated, for example, in Fig. 3.62(a).) Whatever the design adopted, it is evident that reliable FE modelling of shear walls is of the utmost importance, whether to anticipate the possibility of failure below the design level in the case of walls complying with current practice, or to predict reliably

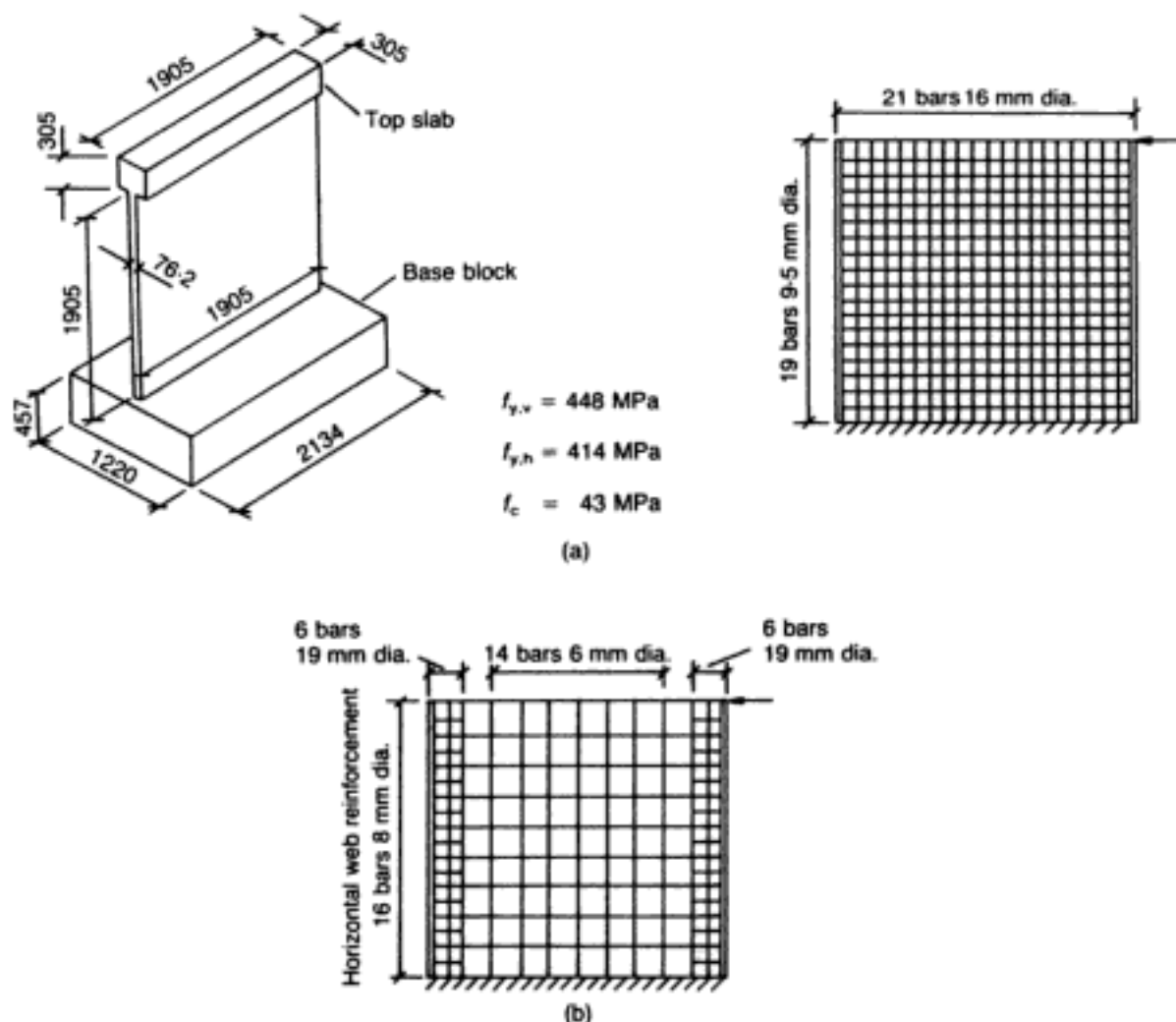


Fig. 3.62. Structural walls: (a) design details of a typical wall investigated in reference 121 (all dimensions in mm); (b) reinforcement details of wall with strengthened compressive zone¹²²

the improved performance of members in which the compressive zone has been strengthened. Figure 3.63 shows typical meshes adopted in the course of one such modelling exercise.¹²³

3.4.3.1. Modelling of test data

The accuracy of the 2-D FE model for analysing shear walls has been validated by reference to a wide range of experimental information gathered from various studies conducted up to 1986,^{4,121,124-126} as well as more recent tests, some of which questioned the validity of current design procedures based on the 'truss analogy' concept.^{127,128} The walls for the first of these sets of test data represent the critical storey element of a structural wall system with rectangular, barbell or flanged cross-section, subjected to various combinations of vertical and horizontal loading. The height-to-width ratio h/l of these elements varied from 0.5 to 2.4, whereas their thickness-to-width ratio b/l varied from 0.04 to 0.08. Vertical and horizontal reinforcement was distributed over the whole width of the wall. The ultimate strength of the reinforcement varied from 570 N/mm² to 765 N/mm², while the uniaxial compressive strength of concrete encompassed the range of

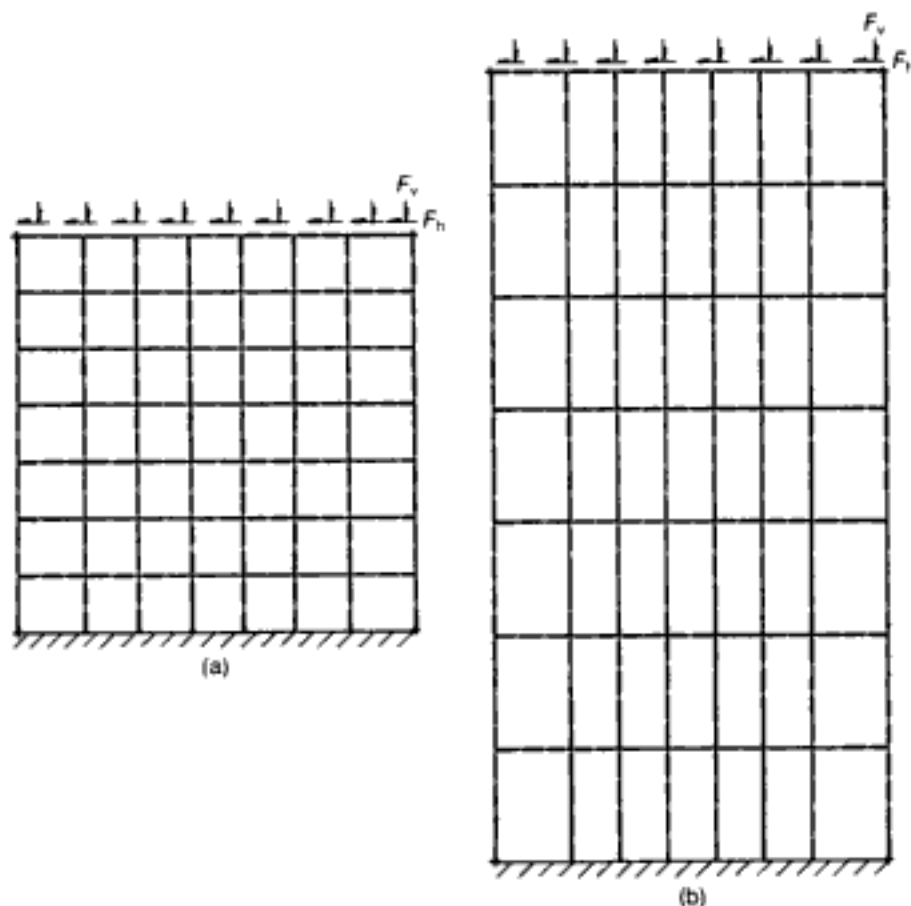


Fig. 3.63. FE meshes adopted for the analysis of two wall types.¹²³
 (a) type I; (b) type II

28–50 N/mm². The design details of a typical wall are given in Fig. 3.62(a), while the FE mesh adopted for the analysis is a 7 × 7 grid of the type depicted in Fig. 3.63(a), except that the element size is uniform throughout.^{122,129}

In this simplified 7 × 7 grid, the equivalent steel areas of the vertical reinforcement and the confinement of the concealed wall columns were placed at the two extreme vertical columns of the concrete elements, while the steel area corresponding to vertical and horizontal web reinforcement was arranged at the boundaries of the intermediate concrete elements. For simplification purposes, concrete cover of the extreme steel bars was ignored. The presence of either a top beam or slab was allowed for by simply including the appropriate stiffness of this element at the top layer of reinforcing steel. By clamping the element nodes along the lower boundary of the wall, a realistic description of foundation fixity was provided. The model was loaded with uniformly distributed edge pressure and traction along the upper boundary of the wall. Constant pressure simulated the applied constant vertical load, while edge traction simulated the incremental applied horizontal load. Between 15 and 20 load steps were applied in each run before the wall reached its ultimate horizontal-load stage. As can be seen by reference to Fig. 3.64, the program yielded excellent strength predictions for the 11 cases covering a wide range of structural wall systems: the typical accuracy of the analysis rarely exceeded

Hidden page

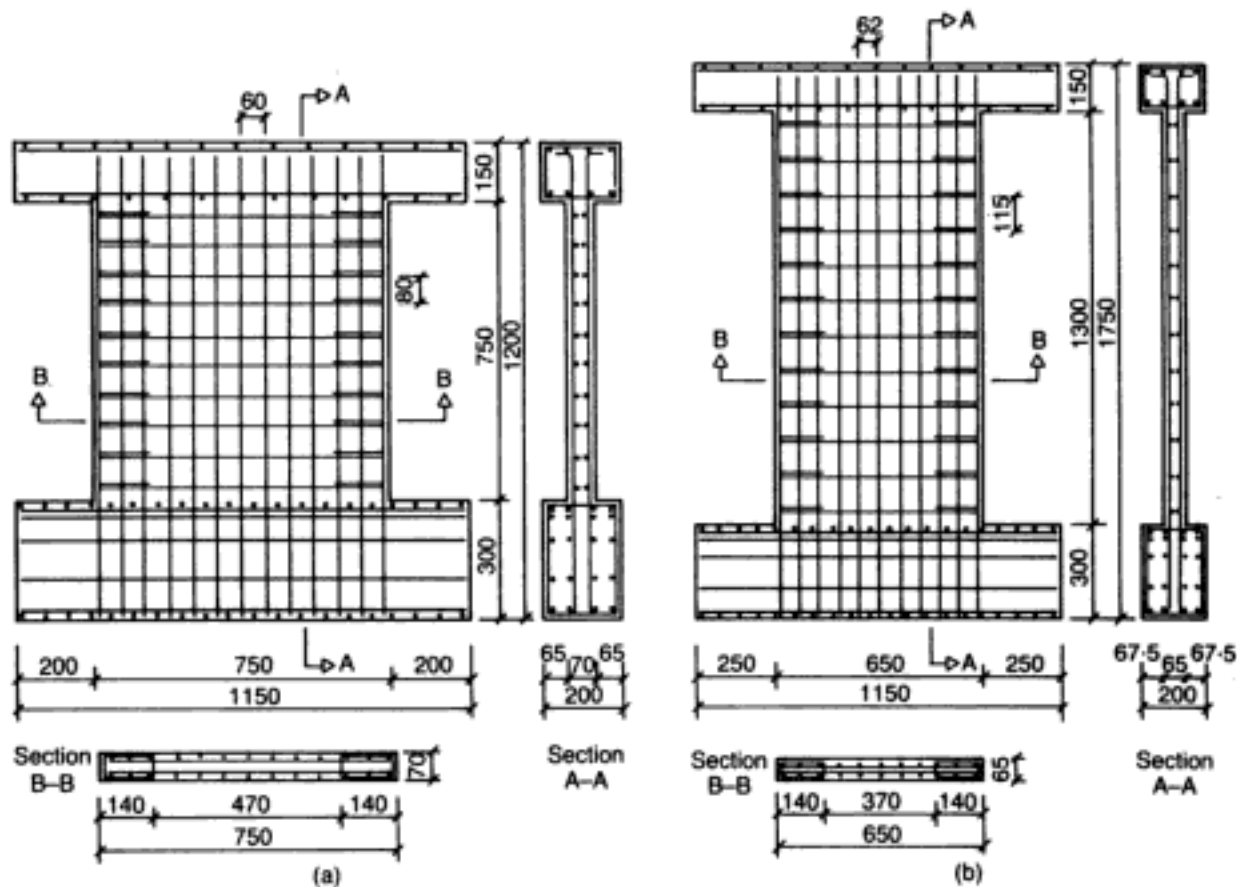


Fig. 3.65. Geometry and reinforcement details for thirteen walls consisting of two specimen types:¹²⁸
 (a) type I; (b) type II
 (All dimensions in mm)

Additional horizontal reinforcement in the form of stirrups confined the wall edges, mild-steel bars of 4 mm diameter being used for this purpose. The yield (f_y) and ultimate (f_u) strength characteristics of the 8 mm, 6.25 mm and 4 mm bars used were as follows: $f_y = 470, 520, 420 \text{ N/mm}^2$ and $f_u = 565, 610, 490 \text{ N/mm}^2$ respectively.

The remaining material and loading data for the various walls form part of the information contained in Table 3.3. This indicates the cube strength f_{cu} at the day of testing (the cylinder strength f_c was taken to be 85% of this value). Also listed are the percentages of reinforcement used for each of the specimens. Vertical reinforcement was designed in compliance with the recommendations of the ACI Building Code¹¹⁴ for a given combination of axial force and bending moment at the base of the wall. Except for walls SW17 and SW26, horizontal reinforcement was also designed in compliance with the recommendations of the ACI Building Code to safeguard against shear failure. In an attempt to test the validity of current shear design provisions, the horizontal reinforcement for walls SW17 and SW26 was significantly less than that specified by the code; in all other respects, the wall reinforcement was similar to that of the other type I and II walls respectively. Three levels of constant vertical force F_v (simulating dead and live gravity loads of a structural system) were adopted in the testing programme; they correspond to 0.0, 0.1

Hidden page

Hidden page

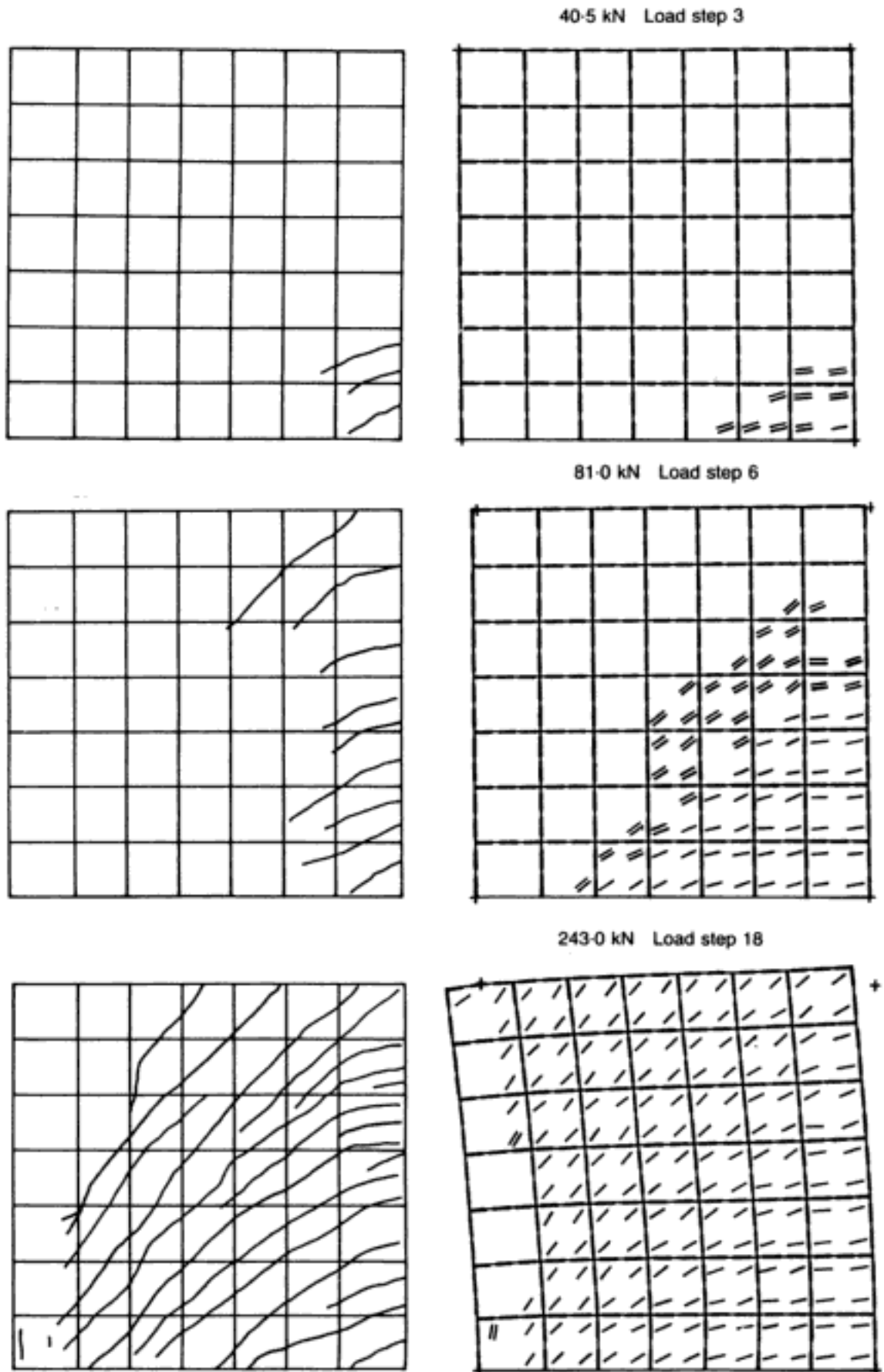


Fig. 3.68. Comparison of experimentally obtained and analytically predicted crack patterns (at approximately corresponding load levels) for type I specimen SW11 ($D.M. = 20$)¹²³

Hidden page

previously, such triaxial stress conditions lead to strength values which are higher than those predicted on the basis of plane-stress assumptions and, therefore, the present analytical predictions should be considered to represent lower-bound values of the failure load.

A comparison of typical load–deflection curves predicted by the analysis with the corresponding curves obtained experimentally (see Figs 3.66 and 3.67) indicates that the plane-stress analysis cannot yield a very accurate prediction of the ductile deformation of the wall at the ultimate limit state. Such behaviour is compatible with experimental information⁵⁷ which indicates that the ductile behaviour of under-reinforced concrete sections is associated with triaxial stress conditions, rather than uniaxial stress-strain characteristics as is widely considered. As discussed above, the plane-stress analysis adopted in the present work cannot describe triaxial stress conditions. The improvement in analytical deflections achieved by using the 3-D FE model will be discussed in Chapter 4. It is also interesting to note that the experimental load–deflection curves indicate a structural response which is ‘softer’ than that predicted by the analysis. The causes of such behaviour should be attributed to time-dependent effects which are associated with the dynamic aspects of the cracking process of concrete and are not allowed for in the present analysis. These dynamic effects are accentuated for load levels beyond that causing yielding of the tensile reinforcement, and their effect on the experimental load–displacement curves becomes even more pronounced owing to the method adopted for the tests. The testing method involved the application of successive load increments up to failure, each of them maintained constant for a time sufficient to allow crack detection and marking, and resulted in load–displacement curves with displacement ‘plateaux’ whose size increases with the load increment. Figures 3.66 and 3.67 indicate that eliminating these ‘plateaux’ from the curves results in a much closer correlation between predictions and experiments.

Figures 3.68 and 3.69 show a close agreement between the crack patterns predicted by the analysis and those established experimentally for two typical (type I and type II) walls. From these figures, it can be seen that macrocracking initiates at the lower tensile edge of the wall and spreads progressively towards the lower compressive zone with increasing load. The process is typical for all the walls investigated. It is interesting to note the near-vertical cracking of the lower compressive edge of the wall at the last analytical load step. Such cracking, which is in compliance with the experimentally observed mode of failure,¹²⁸ eventually transformed the adjacent wholly-compressive state of stress into a state of stress with at least one stress component tensile, and resulted in an immediate loss of load-carrying capacity. Finally, it is significant that specimens SW17 and SW26 also reached their shear capacity and failed in a ductile manner in spite of the fact

that they contained much less horizontal web reinforcement than that specified by the ACI Code in order to safeguard against shear failure; this and other findings prompted the parametric study described in the following section.

3.4.3.2. Parametric study

Several interesting conclusions emerged from the experimental programme on the 13 structural walls¹²⁸ discussed in the preceding section. These may be summarized as follows, bearing in mind, of course, their tentative nature in view of the perforce limited scope of the test programme which allowed only a partial investigation of the main parameters.

1. For all cases investigated, it was found that, while axial compression reduces both vertical and horizontal displacement, it also causes an increase in horizontal load-carrying capacity and secant stiffness characteristics; this observed increase becomes more pronounced with increasing height-to-width ratio.
2. In contrast to what is widely believed, the horizontal web reinforcement does not appear to have a significant effect on shear capacity. Furthermore, since the reduction of the web horizontal reinforcement to almost half the value specified by building codes does not affect the failure load, this effect cannot be accounted for by the 'truss analogy' concept.
3. The strength and deformational response of the walls were found to be independent of the uniaxial concrete strength characteristics within a range of 30–55 N/mm² (but see the later section where the effect of concrete strength is studied analytically (by reference to the ultimate shear strength of a wall), a parameter not specifically investigated in the experiments).
4. Failure of the walls occurred as a result of nearly vertical splitting of the compressive zone in the region of the tip of the inclined (type I) or the deepest flexural (type II) crack, followed by splitting of the whole compressive zone. The failure region was more extensive with decreasing height-to-width ratio and increasing axial load.
5. Shear resistance appears to be associated with the development of triaxial compressive stress conditions within the compressive zone near the base of the wall where the flexural moment attains its maximum value.

Based on the good correlation between experiments and analysis outlined in the previous section, a parametric analytical study of shear walls was conducted¹²⁹ in order to both confirm and extend (or, if necessary, modify on the basis of a larger number of case studies) the above experimental findings, thus providing design

information essential for the improvement of current code provisions for ultimate limit-state design. The results of this parametric study, conducted on RC walls of rectangular cross-section representing the critical storey element of a structural wall system subjected to actions F_v (constant) and F_h (increasing to failure), are described below. (The 7×7 mesh (Fig. 3.63) is adopted throughout.)

The variables for the study were chosen by a review of current design procedures, which led to the conclusion that uncertainties exist with regard to the validity of the analytical expressions recommended for both shear strength and strength under the combined action of axial force and bending moments.¹²⁷ The main variables of the analytical investigation were

1. height-to-width ratio h/l
2. normalized vertical force $v = F_v/(bf_c)$
3. amount and distribution of flexural reinforcement as well as the confinement reinforcement of the wall's edge members
4. amount of vertical (ρ_v) and horizontal (ρ_h) reinforcement (given either as a ratio, ρ , or as a percentage, $\rho(\%)$) of the total wall cross-sectional area or of the wall web. (Henceforth ρ_v will be used to denote any vertical reinforcement, whether web or edge (both now encompassing, somewhat more loosely, 'flexural' reinforcement); however, unless specific mention is made of edge reinforcement, ρ_v usually implies vertical web steel (which, in the case of uniformly distributed reinforcement, can also extend to the edge regions).)
5. concrete strength f_c .

Although structural walls without horizontal reinforcement are the exception rather than the rule in current structural practice, basic features of their behaviour should be established before the effect of additional parameters is considered. Hence, the 2-D FE package was employed first to investigate the effect of uniformly distributed vertical reinforcement on such walls with various height-to-width ratios. The analysis of these walls was also intended to yield evidence that would clarify uncertainties related to the validity of current code provisions with regard to the flexural capacity and the contribution of concrete strength to the overall shear capacity of the member.

The next step comprised the investigation of the behaviour of walls with height-to-width ratios of two, one, and one-half (designated henceforth as types A, B, and C respectively) aimed at establishing the effect on the horizontal load-carrying capacity of the amount of horizontal reinforcement, the level of constant vertical load, the reinforcement details, and the concrete strength. Over 100 numerical tests were performed in order to study the

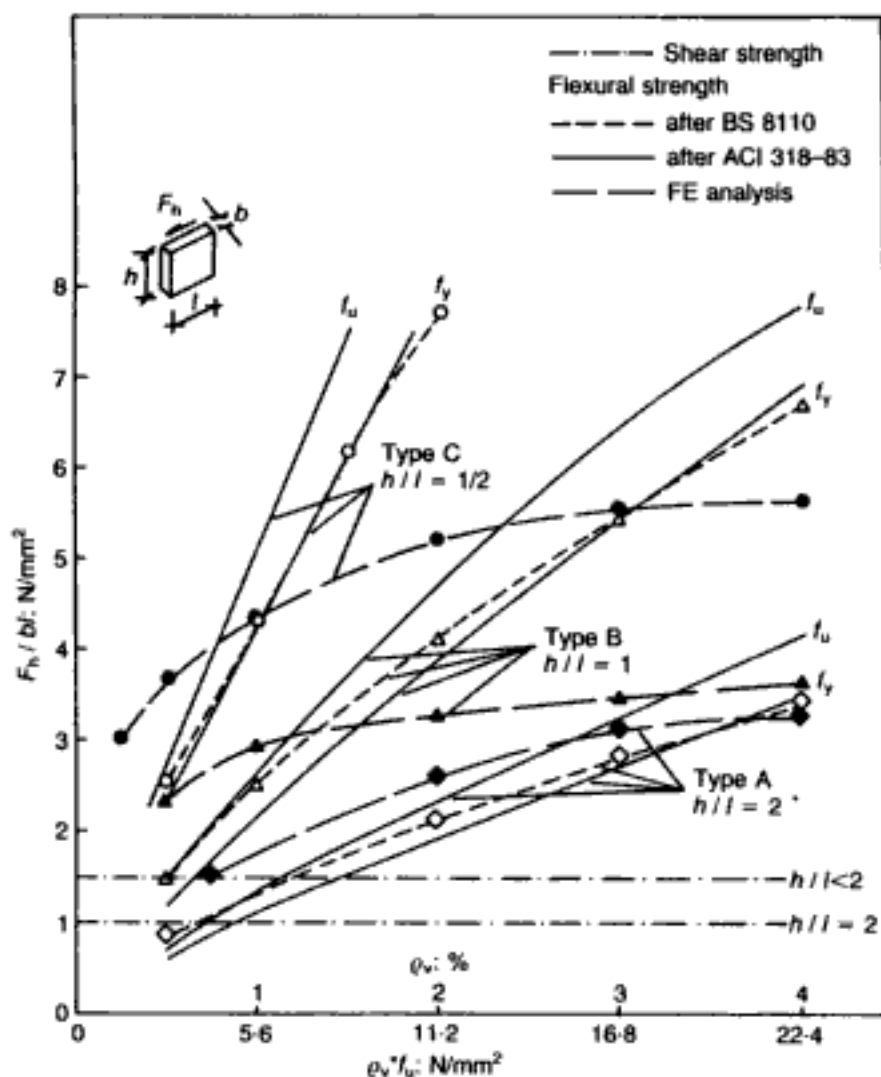


Fig. 3.70. Variation of horizontal-load capacity of walls, without horizontal reinforcement, with amount of uniformly distributed vertical reinforcement¹²⁹

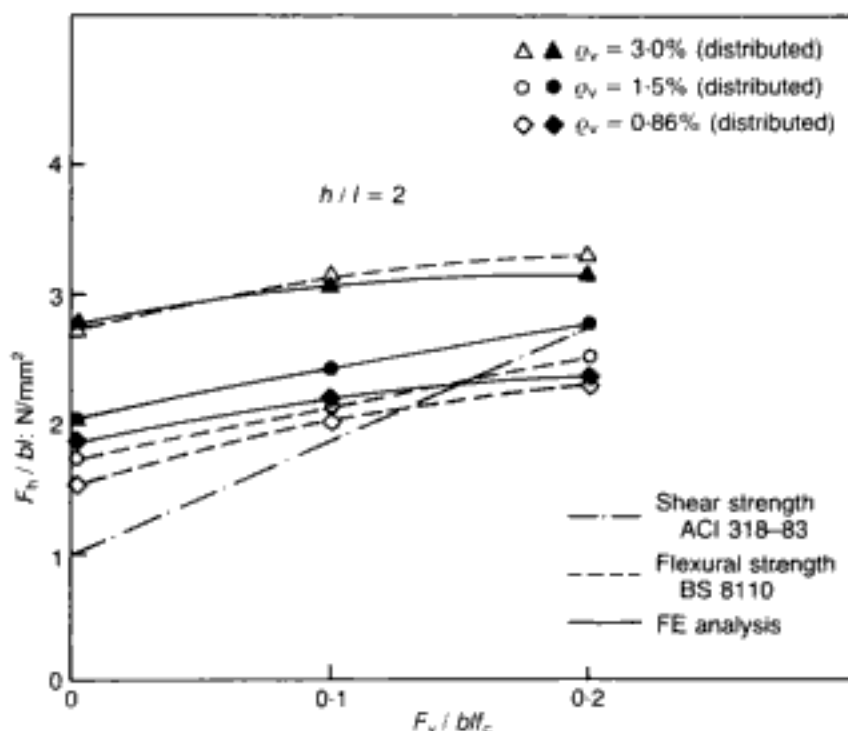
influence of these parameters. When flexural reinforcement within the concealed columns was considered (i.e. 'concentrated' or 'edge' vertical reinforcement), it was placed in the region of the wall edges within a distance of 15% of the wall width from either extremity of the cross-section.

The material characteristics were similar to those chosen for the experimental programme summarized in Table 3.3, so as to check the validity of the behaviour predicted by the analysis. The f_u values of the vertical and horizontal reinforcement were 560 N/mm² and 517 N/mm² respectively, whereas the f_c was 35 N/mm², unless stated otherwise.

The main results of the investigation are summarized in Figs 3.70–3.82, with the ultimate horizontal-load capacity expressed in terms of the maximum sustained shear stresses applied to the top of the wall (i.e. $F_h/(bl)$, where F_h represents the horizontal load at collapse). Figure 3.70 shows the influence of the amount of uniformly distributed vertical reinforcement on the ultimate horizontal-load capacity of rectangular walls without horizontal reinforcement. (Zero vertical or horizontal reinforcement in the

Hidden page

Fig. 3.73. Variation of horizontal-load capacity with normalized vertical force for type A walls¹²⁹



indicated in Figs 3.72 and 3.74, whereas Figs 3.75–3.77 show the effect of normalized axial load on the strength of type A walls employing various amounts of horizontal and vertical reinforcement. A typical interaction diagram of a type B wall is shown in Fig. 3.78, which also includes design details of the wall. The effect of concrete strength on the horizontal load-carrying capacity of a typical type B wall is presented in Fig. 3.79.

Figures 3.80 and 3.81 show the variation of ultimate capacity of type C walls with the amount of horizontal reinforcement and normalized axial load respectively. Finally, Fig. 3.82 indicates the deflected shape and various stages of the macrocracking process typical for all types of wall investigated under increasing horizontal load. The load stages correspond to the following: (1) crack initiation; (2) significant inclined cracking; (3) one load step before the ultimate load level; and (4) maximum load-carrying capacity.

Since the evaluation of the adequacy of code predictions for modes of failure and ultimate horizontal-load capacity of the walls was one of the main objectives of this study, most of the figures include the corresponding flexural and shear predictions obtained from the BS 8110⁵⁵ and the ACI 318-83¹³⁰ respectively. (Again, code estimates for both flexural and shear strengths are expressed in terms of the relevant stresses $F_h/(bl)$.) The findings of the parametric study may be summarized as follows.

Effect of vertical reinforcement. Figure 3.70 indicates that, when the amount of flexural reinforcement ρ_v is less than 4%, type A walls fail under a horizontal load higher than that corresponding to flexural strength as predicted by the codes (bearing in mind that code predictions are based on f_y and not f_u). According to code

Fig. 3.74. Variation of horizontal-load capacity with amount of horizontal reinforcement (for varying amounts of vertical reinforcement) for type B walls:¹²⁹
 (a) $\rho_v = 3\%$; (b) $\rho_v = 1.5\%$ and 1%

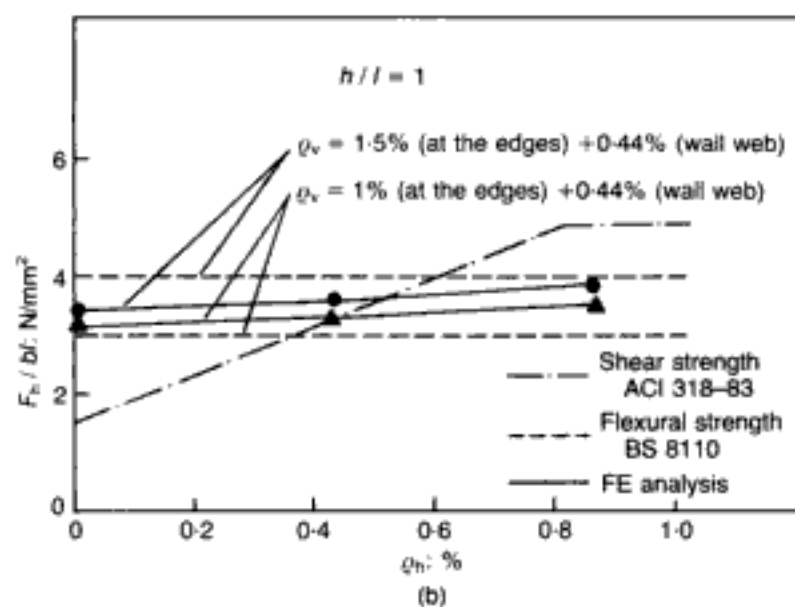
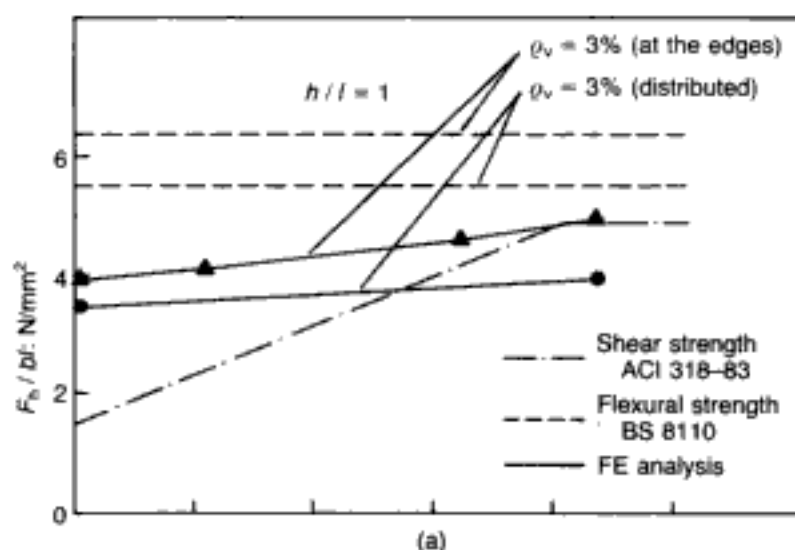


Fig. 3.75. Variation of horizontal-load capacity of type B walls with amount of horizontal reinforcement for various levels of normalized axial load ($\rho_v = 3\%$ at edges)¹²⁹

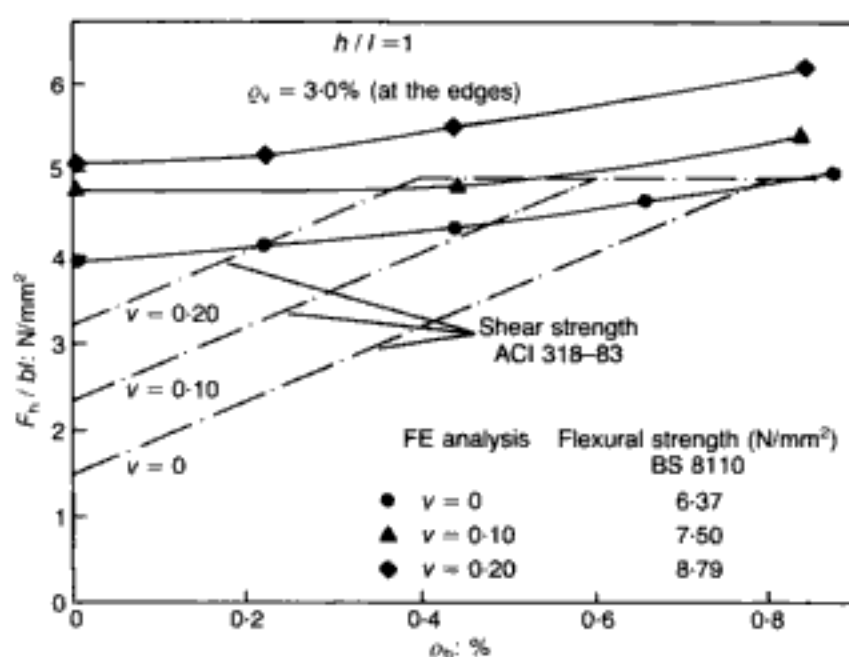


Fig. 3.76. Variation of horizontal-load capacity of type B walls with amount of horizontal reinforcement for various levels of normalized axial load ($\rho_v = 1.5\%$ at edges + 0.44% in wall web)¹²⁹

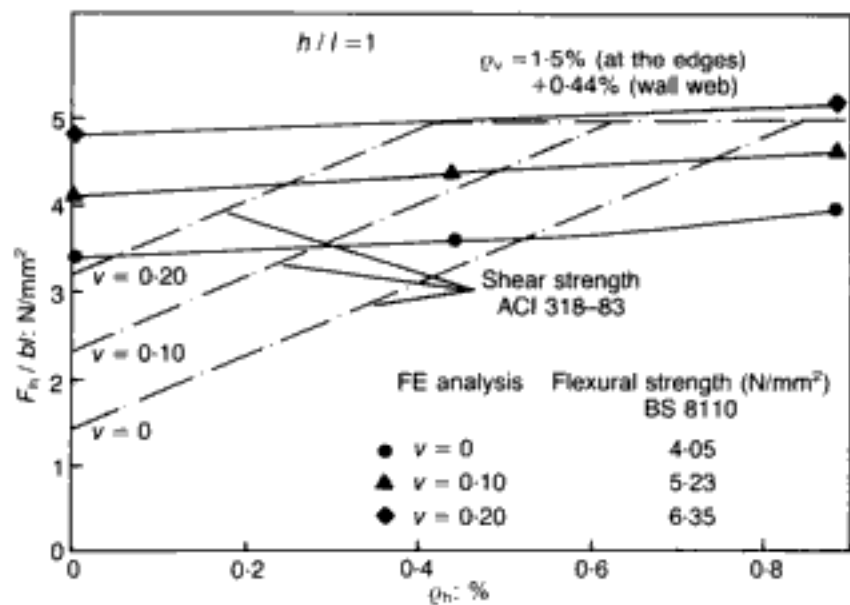
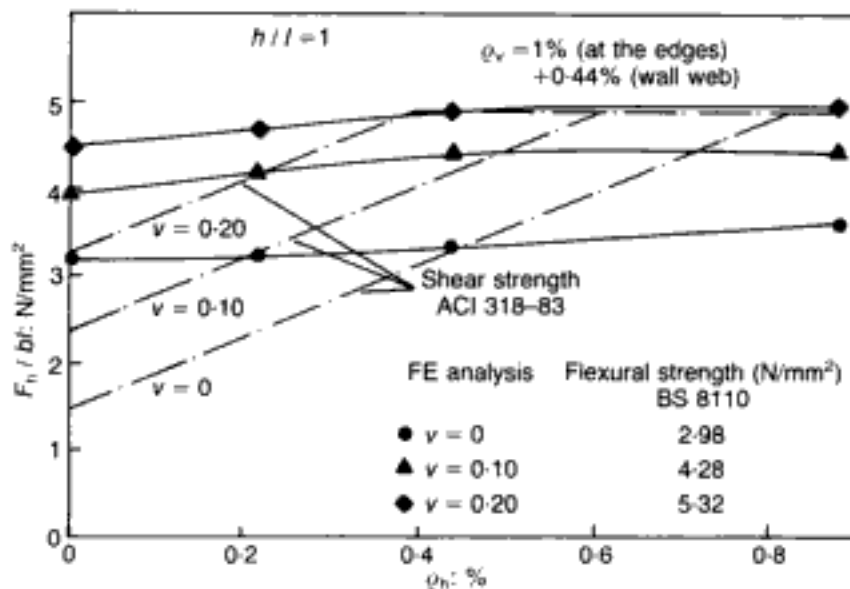


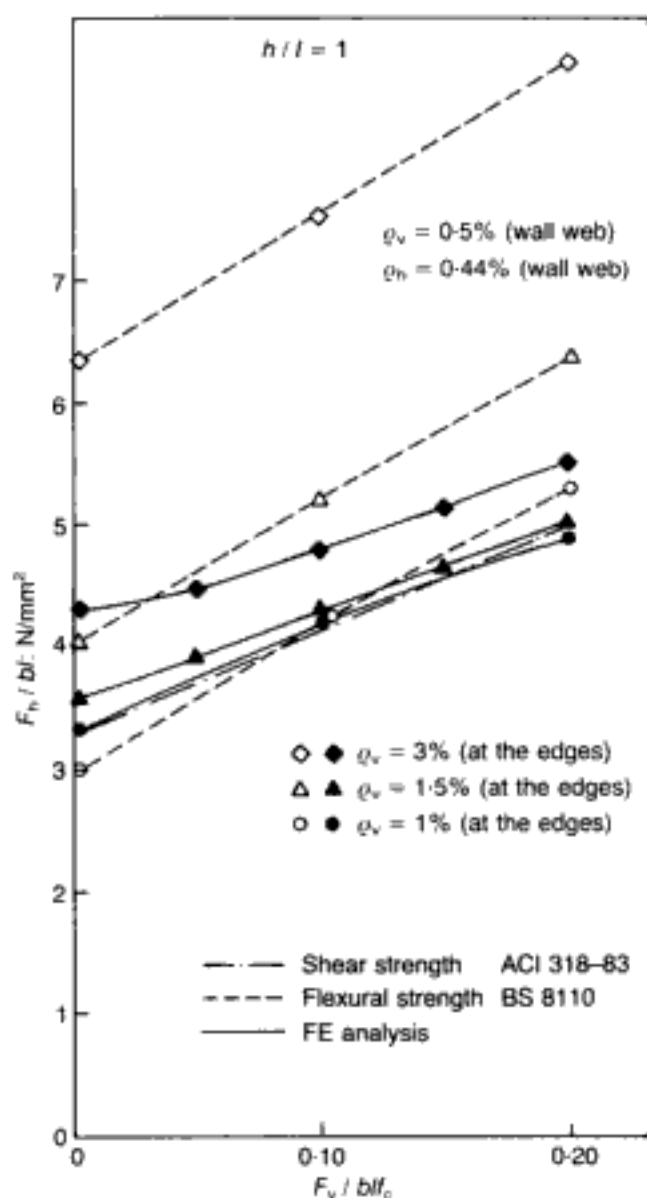
Fig. 3.77. Variation of horizontal-load capacity of type B walls with amount of horizontal reinforcement for various levels of normalized axial load ($\rho_v = 1\%$ at edges + 0.44% in wall web)¹²⁹



design procedures, such walls should have failed in shear when $\rho_v > 0.5\%$. Hence, in practice, some horizontal reinforcement, often in excess of the nominal 0.25% , should be provided for type A walls if a failure in flexure is desirable. And yet, the FE analysis results shown in Fig. 3.70 indicate that, despite the lack of horizontal web reinforcement, type A walls sustained loads higher than those corresponding to shear capacity and those corresponding to flexural capacity.

For walls with height-to-width ratios less than or equal to one (types B and C), the analytically predicted wall capacity is lower than the flexural capacity when the amount of vertical reinforcement is higher than 1% . However, even for these cases the horizontal load-carrying capacity predicted by current shear design provisions is significantly less than the strength predicted by the analysis.

Fig. 3.78. Variation of horizontal-load capacity with normalized vertical force for type B walls¹²⁹



Such results appear to indicate that present code provisions for shear design underestimate the contribution of the uniformly distributed vertical reinforcement to shear capacity, with this contribution becoming more effective with a decreasing height-to-width ratio as shown by the deviation of the results predicted by the analysis from those predicted by the codes. Such behaviour is in compliance with the experimental findings of the Portland Cement Association (PCA).¹²⁴

It is also interesting to note in Fig. 3.70 that, for the case where the analytical predictions are smaller than the code values, the values predicted by the analysis deviate from the code predictions of ultimate flexural capacity, the deviation increasing with ρ_v . The equation for ultimate flexural capacity recommended by the background material of the ACI building code¹³¹ for earthquake-resistant wall design assumes that a large proportion of the vertical reinforcement yields before the concrete strain at the extreme

Fig. 3.79. Variation of wall shear strength V_u with concrete strength f_c by reference to a type B wall:¹²⁹ (a) V_u expressed in terms of stresses; (b) V_u normalized with respect to either f_c or $\sqrt{f_c}$

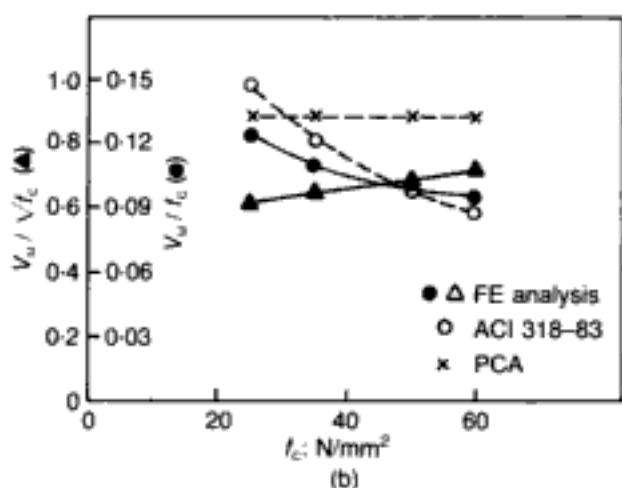
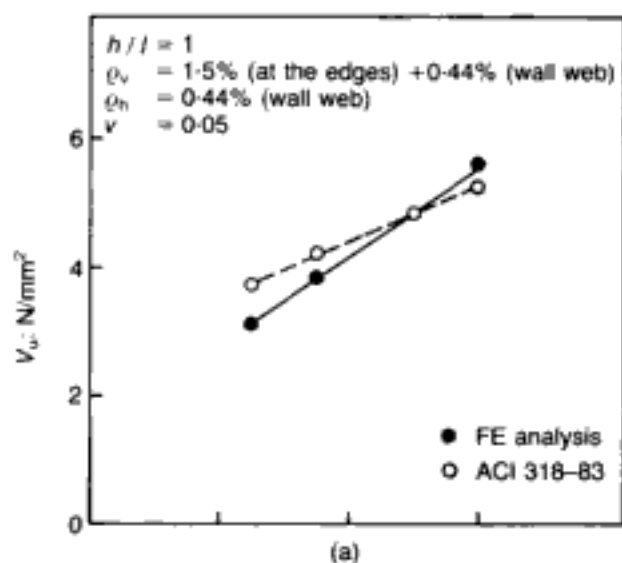
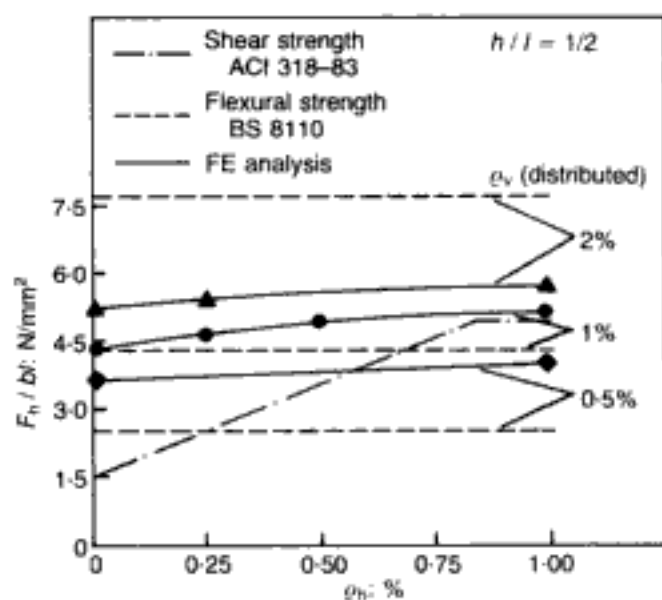


Fig. 3.80. Variation of horizontal-load capacity with amount of horizontal reinforcement for type C walls¹²⁹



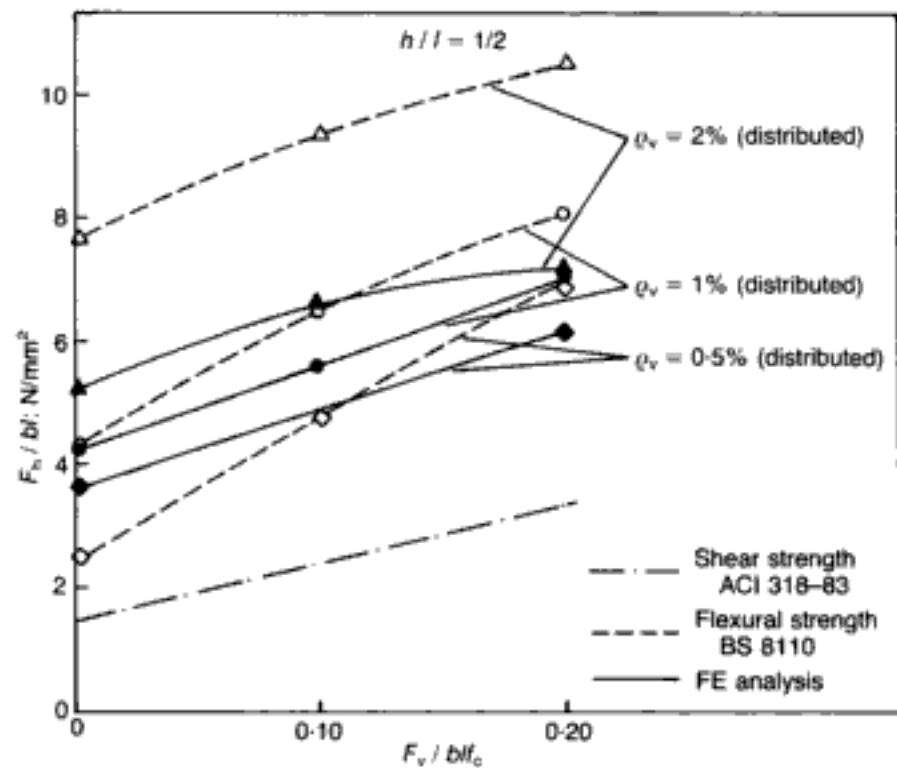


Fig. 3.81. Variation of horizontal-load capacity with normalized vertical force for type C walls¹²⁹

compressive fibre attains its critical value (i.e. under-reinforced cross-section). The validity of this assumption is questionable, however, and this assumption is probably the main cause of the deviation of the code predictions (based on the use of either the yield (f_y) or ultimate (f_u) steel stresses) from the analytical results.

Figure 3.71 illustrates the role of both the height-to-width ratio and the amount of vertical reinforcement on the load-carrying capacity of a wall with a given cross-section. The figure shows that, as found elsewhere for beams,¹³² for a constant cross-section and a certain amount of vertical reinforcement, the increase of height-to-width ratio results in an increase of the ratio of the shear capacity to flexural capacity.

It is clear from the preceding discussion that the effect of height-to-width ratio and the amount of vertical reinforcement are not adequately accounted for in current codes. Expressions describing the concrete shear-stress contribution to wall resistance not only prove conservative but also appear not to provide an indication of the type of failure a wall is prone to exhibit at the ultimate limit state. Furthermore, the mode of wall failure is dependent primarily on the height-to-width ratio; the amount of vertical reinforcement affects considerably the load level at which a particular mode of failure occurs, rather than the mode of failure itself.

Effect of horizontal reinforcement and detailing. Figures 3.72, 3.74 and 3.80 indicate that the walls failing under a horizontal load higher than that corresponding to flexural capacity, as predicted by code provisions, still exhibit a slight increase in

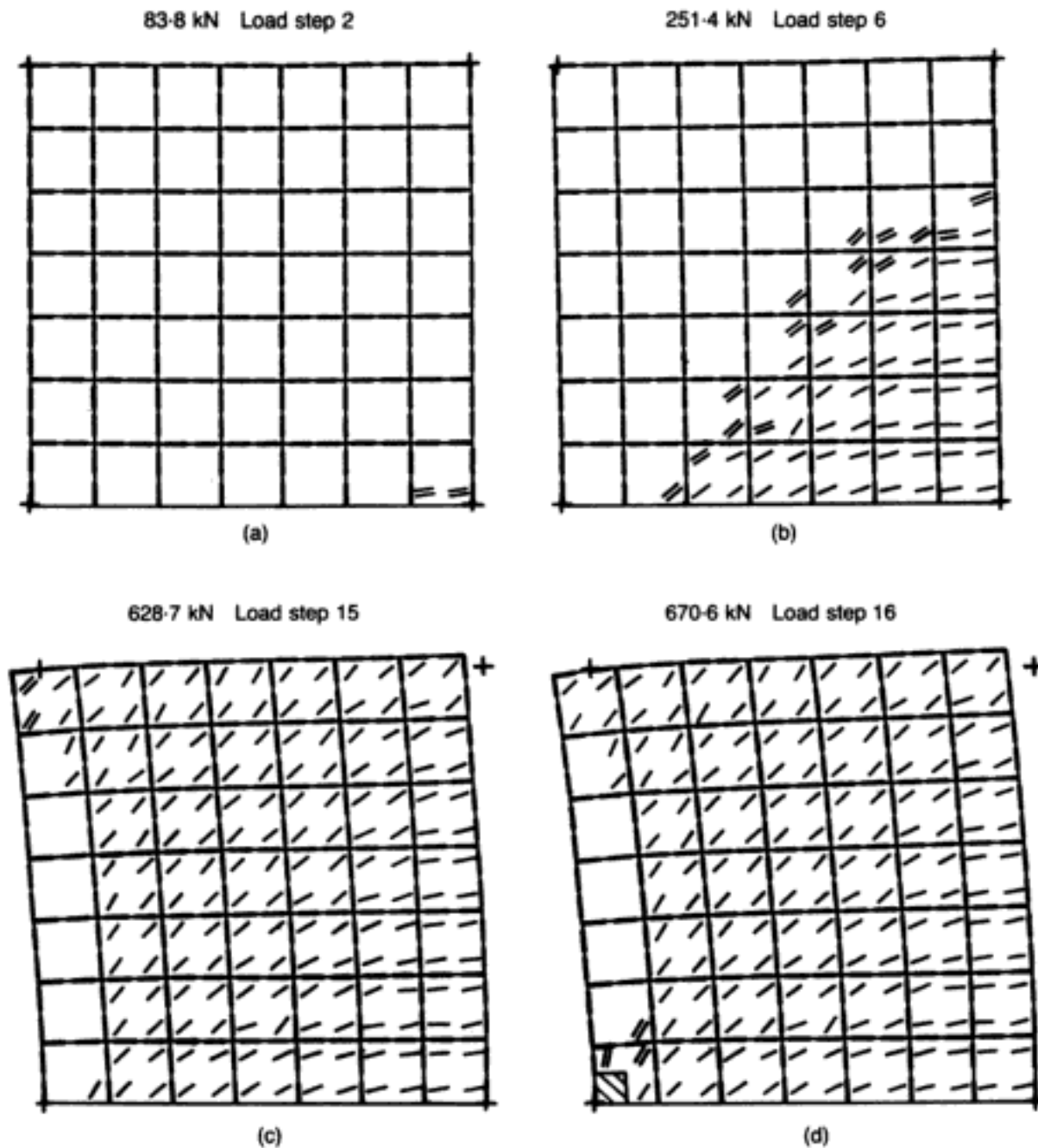


Fig. 3.82. Crack patterns and deformed shapes of a typical wall at various load steps corresponding to some of the main stages of its structural response:¹²⁹ (a) crack initiation; (b) formation of significantly inclined cracking; (c) one load step prior to the MSL; (d) MSL

strength with increasing amounts of horizontal reinforcement. On the other hand, for walls failing under a horizontal load below flexural capacity, 'shear' failure is critical, and here code provisions predict a linear increase of shear capacity with increasing percentage of horizontal reinforcement from a lower level representing the contribution of concrete to shear resistance to an upper level corresponding to 'crushing' of the concrete 'struts' of the 'truss' model.^{133,134} (Beyond this level, they predict that shear capacity remains constant.) The analysis indicated, however,

Hidden page

Hidden page

Hidden page

Causes and mechanism of failure. It is evident from the preceding parametric study that code provisions for shear walls may often lead to inaccurate and even non-conservative designs. This is not only true for 'shear' failure clauses but can even extend to the guidelines for flexural failure when high axial load and/or horizontal reinforcement are present in the design.¹²⁷ Clearly, an understanding of the underlying causes of the actual failure mechanism is essential if the true behaviour of structural walls is to be anticipated. In order to confirm and complement the failure mechanism and associated cracking processes discussed previously by reference to experimental results obtained at Imperial College,^{127,128} a representative case stemming from the analytical parametric study will now be presented. Figure 3.82(a) shows the initiation of typical flexural cracking of walls at low load levels, while the early inclined cracking and the extensive flexural and inclined cracking of the wall are depicted in Figs 3.82(b) and 3.82(c) respectively. The figure shows that macrocracking initiates at the lower tensile zone of the wall and spreads progressively towards the lower compressive zone with increasing load. This process is typical for all the walls investigated. At one load step before failure, the depth of the compressive zone has been reduced to only a small portion of the wall width (see Fig. 3.82(c)). Despite the small depth of this compressive zone, its high shear resistance arises as a result of volume dilation which is restrained either by concrete in the adjacent regions, for the case of plain concrete, or mainly by confining reinforcement, such as that used in the edges of the walls tested. Failure under such compressive stress conditions is characterized by cracking in the direction of the maximum principal compressive stress, and this explains the near-vertical splitting of the compressive zone at the base of the wall where the flexural moment attains its maximum value. This is seen in the next load step (Fig. 3.82(d)) and is confirmed by tests.¹²⁸

The analytically obtained local stresses in the vicinity of the lower compressive zone show that a biaxial compressive stress state, indicated by the shaded region in Fig. 3.82(d), occurs within the compressive zone, with the maximum principal compressive stress at the last load step reaching a value nearly 1.2 times the uniaxial cylinder compressive strength. Despite the occurrence of such large compressive stresses at the wall base, the analysis indicated that the compression-tension stress conditions developing in the adjacent locations are more critical and lead to longitudinal cracking within these locations, shown by two closely spaced parallel lines in Fig. 3.82(d), which results finally in an immediate loss of load-carrying capacity.

Such behaviour indicates a common underlying cause of failure described fully by the concept of the compressive-force path which, as explained in earlier sections, postulates that the strength of a structural member is associated with the triaxial concrete strength

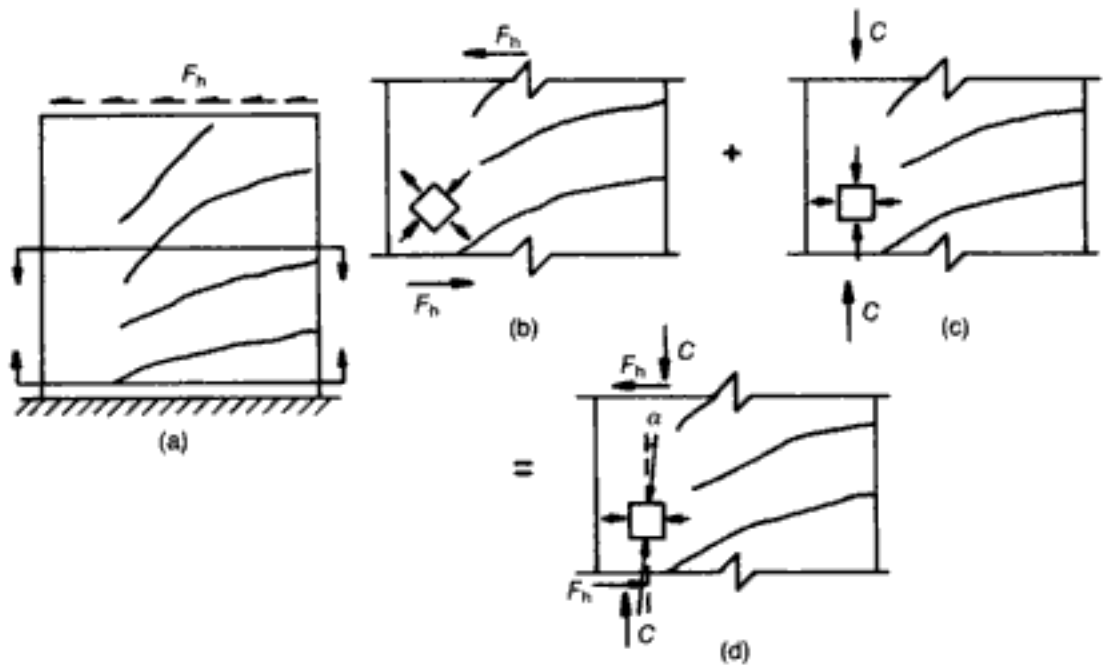


Fig. 3.83. Schematic representation of the failure mechanism in a structural wall.¹²⁸ (a) typical wall at incipient failure; (b) effect of shear force F_h leading to tensile stresses; (c) effect of large compressive force C giving rise to volumetric expansion and hence multiaxial stresses; (d) combined effect of (b) and (c) producing a state of multiaxial compression countering the local tensile stresses due to shear, and leading to an inclined compressive-force resultant sufficiently large to equilibrate the horizontal shear force

and the development of tensile stresses in the region of the path along which the compressive force is transmitted to the supports. The validity of this view is supported by the analytical evidence presented and discussed previously. It was the concentration of the vertical reinforcement at the wall edges together with the placement of additional confinement reinforcement that resulted in a significant increase of load-carrying capacity despite the considerable reduction of vertical and horizontal web reinforcement to near-nominal levels. The preceding reinforcement details enhance the multiaxial compressive stress conditions in the lower compressive edge, thus increasing locally the strength and deformability of concrete. The presence of axial loading also resulted in an increase of the load-carrying capacity owing to the increased depth of the compressive zone at the ultimate level.

Therefore, the compressive zone is the most significant contributor to wall resistance, with the region below the neutral axis devoid of the importance usually assigned to it. Furthermore, the wall does not have to behave like a truss, as assumed in much of current design thinking, in order to explain how shear forces are sustained after inclined cracking has occurred. In fact, Fig. 3.83 illustrates schematically the mechanism providing shear resistance to the lower part of the compressive zone of the wall

Hidden page

Hidden page

Although the detailed results and ensuing conclusions are to be based on the above two series of tests, two further series of slabs were analysed later and their main results will also be listed briefly at the end of this section. While the third series complements the analytical findings based on the experiments reported in reference 138, the final test series used is derived from subsequent research.¹⁴⁰ In all four test series the boundaries of the slabs were simply supported, and the mandatory flexural reinforcement consisted of both radial and circumferential reinforcement. The cylinder strength was estimated at 80% of the tabulated cube strength except for test series 2 where the concrete-strength data were available directly in terms of f_c .

3.4.4.1. Presentation of results

The main results of the present investigation, concerning test series 1 and 2, are here summarized, together with information essential for their interpretation, in a form suitable for subsequent discussion. All the data are contained in Table 3.5 and Figs 3.84–3.94.

Table 3.5 gives the relevant information concerning the geometry and material properties of the RC slabs analysed, together with both experimental and predicted ultimate loads. Figure 3.84 shows predicted load–deflection curves for the four circular slabs of test series 1 (the experimental curves were not reported), while Fig. 3.85 depicts both experimental and predicted curves for the five square slabs of test series 2. Figure 3.86 represents typical stages of the deformed shape and crack pattern of a slab that exhibits ductile behaviour and, for the same slab at its maximum sustained

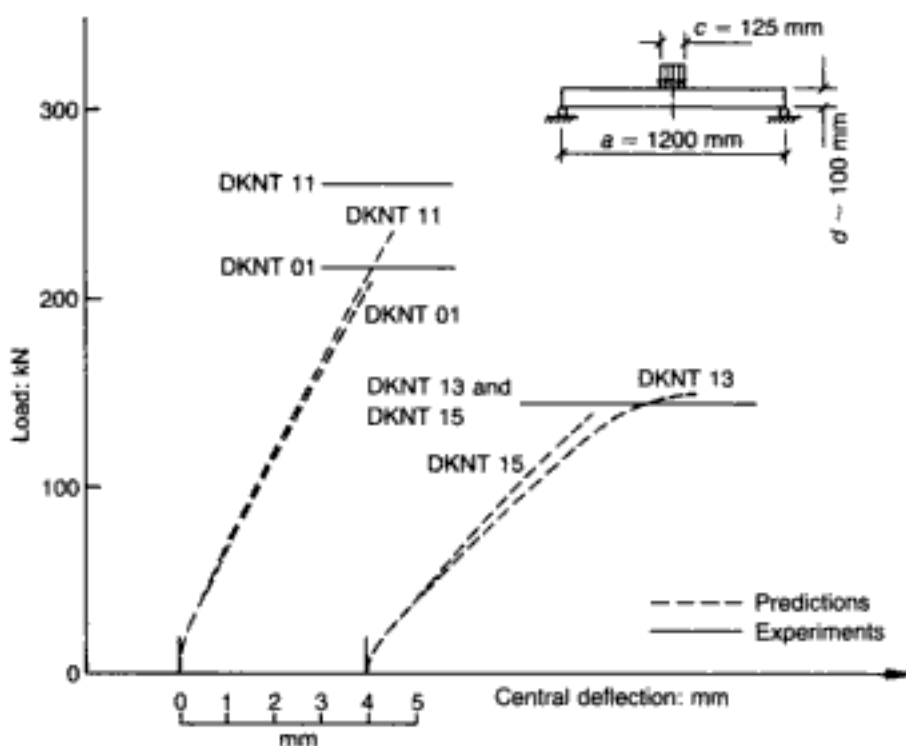


Fig. 3.84. Predicted load–deflection curves for the four circular slabs of test series 1 and comparison between predicted and experimental ultimate loads¹³⁷

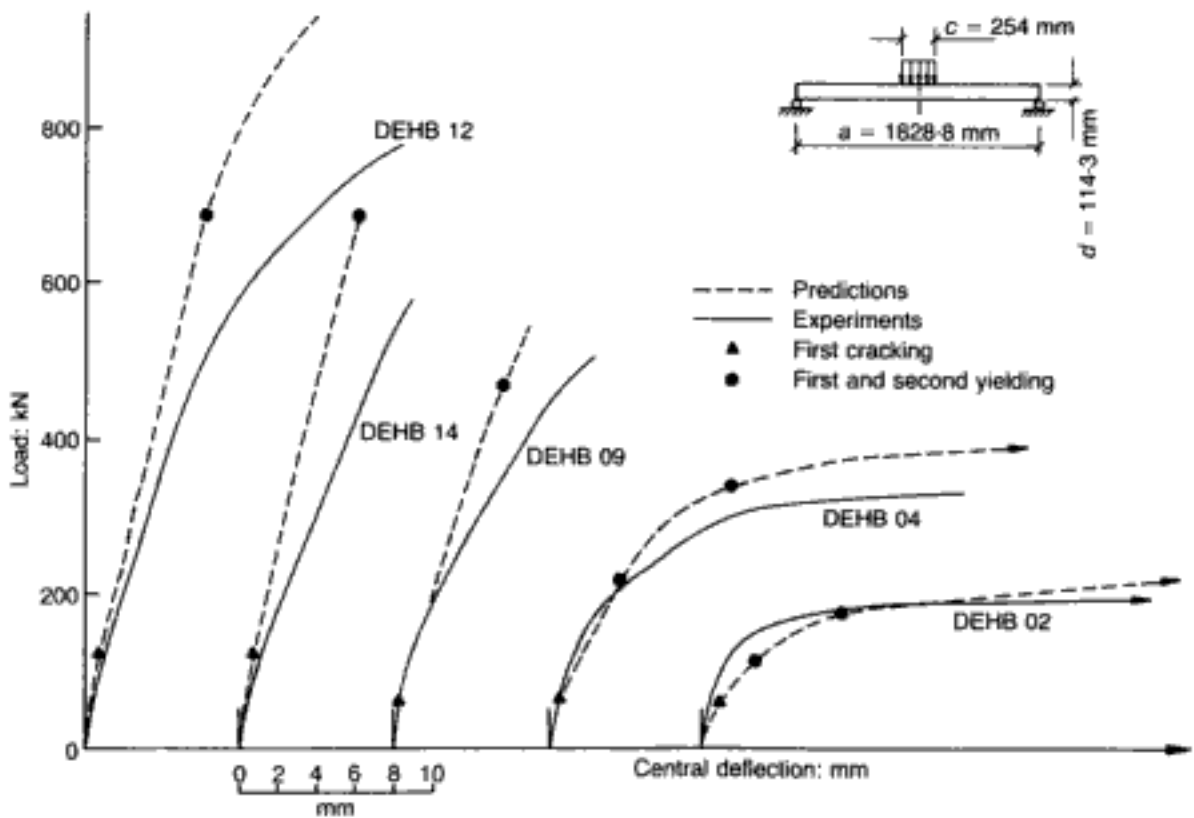


Fig. 3.85. Comparison between predicted and experimental load-deflection curves for the five square slabs of test series 2¹³⁷

load, Fig. 3.87 shows the predicted distribution of strains and stresses sustained by concrete (ϵ_c , σ_c) within the compressive zone (at the Gauss points closest to the surface of the slab), as well as the distribution of strains in the flexural reinforcement (ϵ_s). (Owing to axisymmetry, only one-half of the slab is shown, with the origin at the centreline. It should be noted that the punching load is applied by imposing vertical displacement restraints throughout the loaded area and then subjecting the structure to the edge reaction force; such a modelling is consistent with the notion that the punching pressure is usually due to a column, the axial stiffness of which can be taken to be rigid with respect to the transverse stiffness of the slab.)

Figure 3.88 exhibits typical strains sustained by concrete within the compressive zone. This information does not belong to either series of tests being studied but has been taken from other work,¹⁴¹ since it provided additional data on the strain distribution for the problem presently considered.

The results for a slab exhibiting brittle behaviour appear in Figs 3.89 and 3.90. This information is presented in the same format as for the case corresponding to ductile behaviour (i.e. Figs 3.86 and 3.87). Figure 3.91 refers to two similar slabs (one with, the other without, stirrups). It shows the variation, with increasing load, of the strains of concrete within the compressive zone at a distance $0.1d$ from the column face (d is the effective depth), as well as the effect of the presence of stirrups upon these strains.

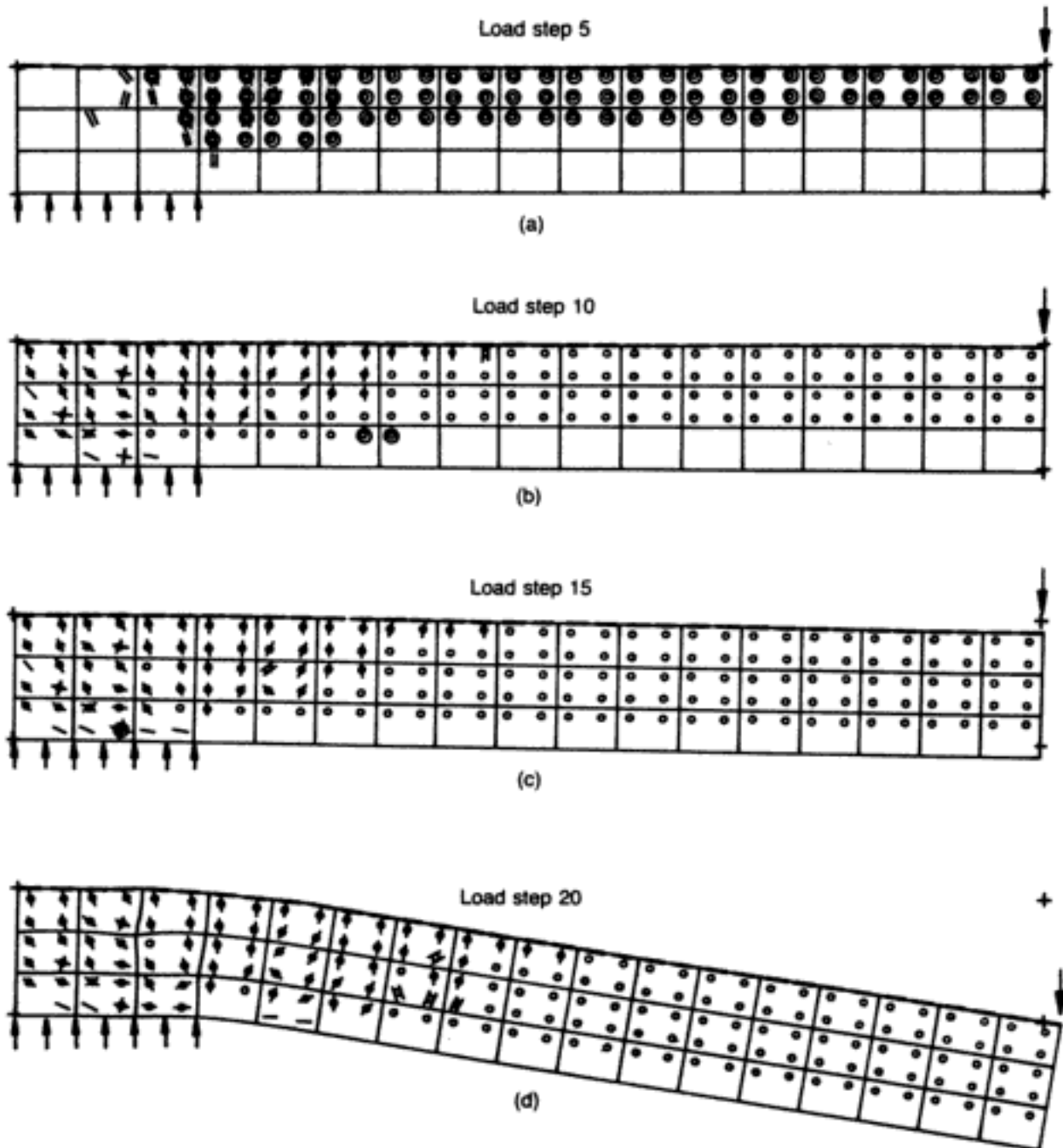


Fig. 3.86. Crack patterns and deformed shapes for four typical load stages for slab DEHB 02 (ductile type of failure):¹³⁷ (a) load step 5 (first cracking); (b) load step 10; (c) load step 15; (d) load step 20 (MSL)

(As before, these values refer to the Gauss points closest to the surface of the slab.)

Figures 3.92 and 3.93 correspond to a slab with transverse reinforcement. Once again, the information follows the format of the earlier case studies (i.e. Figs 3.86, 3.89 and 3.87, 3.90 respectively).

Finally, Fig. 3.94 shows the magnitude and direction of the principal stresses sustained by concrete within the compressive zone in the vicinity of the column face for a slab exhibiting brittle behaviour. The figure also includes an assessment of the equilibrium between the external load and the internal forces in the compressive zone at the column face.

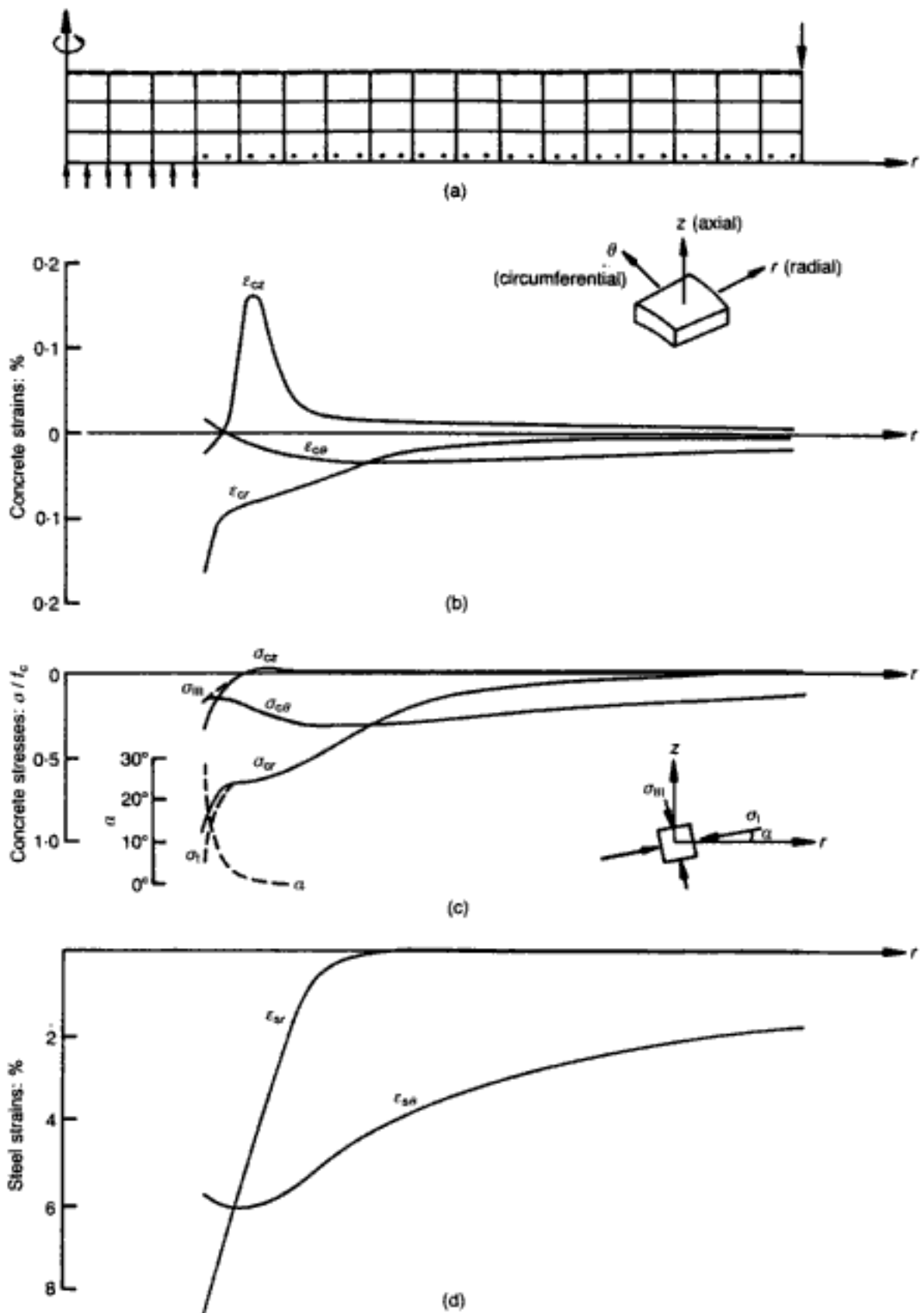


Fig. 3.87. Some of the predicted strain and stress distributions for slab DEHB 02 at MSL:¹³⁷ (a) half the cross-section of the slab showing FE mesh and Gauss points (indicated by dots) at which the strains and stresses sustained by concrete in the 'compressive zone' are computed; (b) concrete strains in the 'compressive zone'; (c) concrete stresses in the 'compressive zone'; (d) steel strains

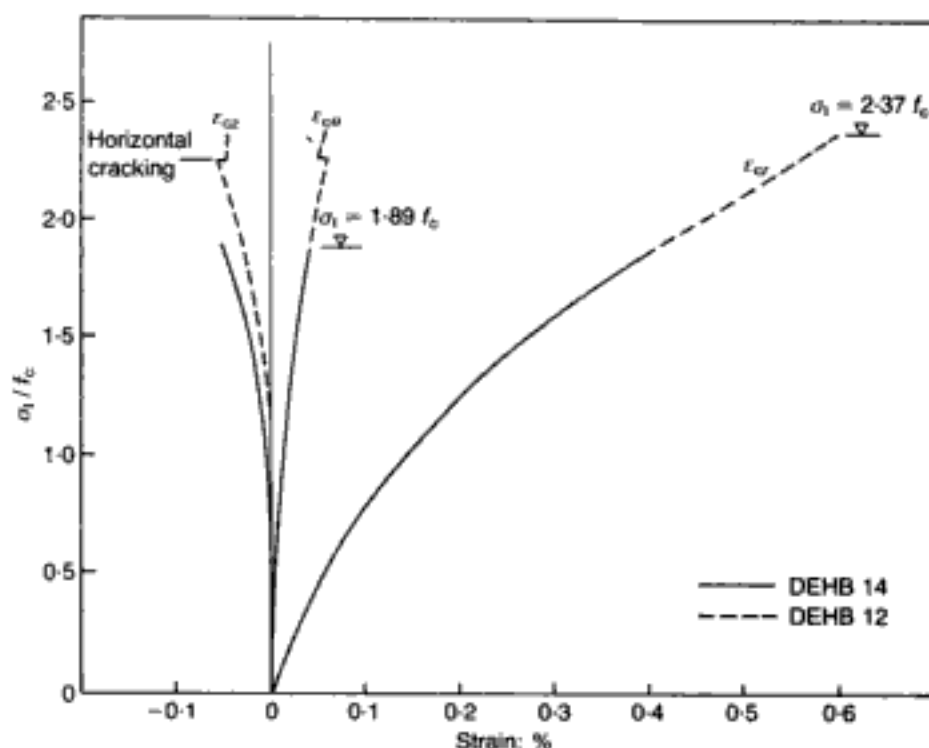


Fig. 3.91. Variations of concrete strains in the compressive zone with load for slabs DEHB 14 and DEHB 12 (at a distance $0.1d$ from the column face)¹³⁷

respectively, of the stress-strain relationship given in Fig. 1.67.

Typical stages of both the deformed shape and the crack pattern of slab DEHB 02 are indicated in Fig. 3.86. Cracking begins approximately at 25% of the ultimate-load level in the form of both radial and circumferential cracks. Radial cracks spread throughout the top face of the slab and increase in depth with increasing load up to five-sixths of the slab depth (at ultimate conditions) so that the tension zone is divided into radial segments. In contrast to radial cracks, circumferential cracks spread to only about half the span (at the tension face), and increase in depth with increasing load, but at a lower rate than was the case with radial cracks.

As Fig. 3.87 indicates, it appears that circumferential strains and stresses are higher than the corresponding radial values, except within the area extending to a distance of approximately $2d$ from the column face. A similar trend for the distribution of strains has been reported elsewhere,^{141,142} as indicated in Fig. 3.88. It is interesting to note in Fig. 3.87(c) that the maximum principal compressive stress σ_1 sustained by concrete exceeds that of the uniaxial cylinder compressive strength; the causes for such behaviour are discussed later. Also interesting is the fact that the direct tensile strains in the z (axial) direction exhibited by concrete within the compressive zone remain low throughout the load history, except for those occurring within a distance of $0.5d$ to $1.0d$ from the column face when horizontal cracking takes place at the last three load steps (see Fig. 3.86(d), which shows the last load step, and also Fig. 3.87(b)). It is important to point out that

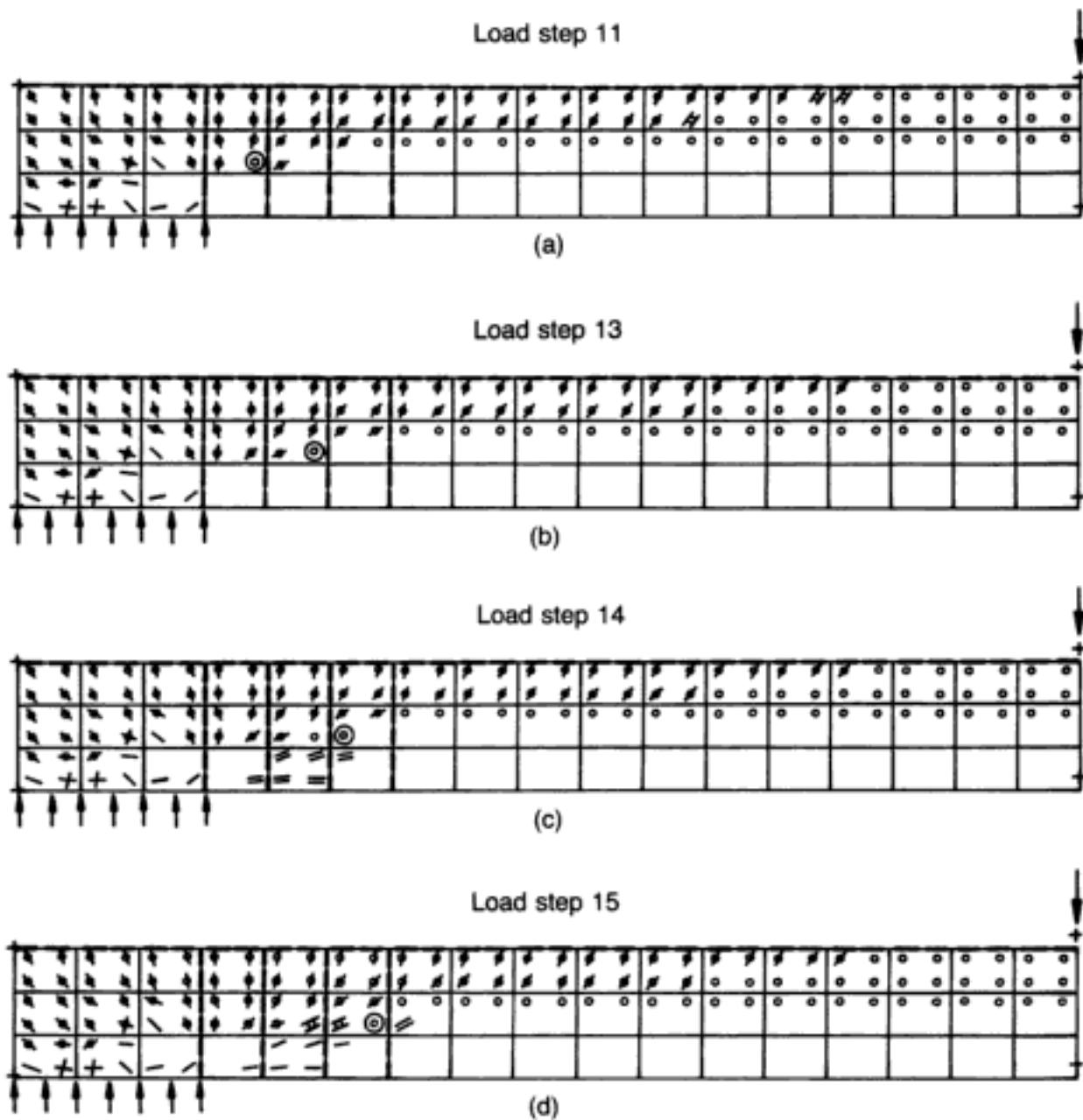


Fig. 3.92. Crack patterns and deformed shapes for some of the last load stages for slab DEHB 12 (brittle type of failure but for the case of stirrups):¹³⁷ (a) load step 11; (b) load step 13; (c) load step 14; (d) load step 15 (MSL)

a triaxial compressive state of stress exists in the vicinity of the column face; however, as the axial stress σ_{cc} diminishes rapidly away from this location, the stress state becomes one of nearly biaxial compression at a distance of about $0.5d$ from the column face (see Fig. 3.87(b)).

Finally, the predicted steel strains reach values as high as 6% and 8% in the circumferential and radial directions respectively. In this regard it is significant to note that, for the second series of tests,¹³⁹ it was found that the recording equipment was incapable of measuring the strains of steel when these became larger than 2%.

Brittle-type behaviour. Figure 3.85 shows the load–deflection curves of slabs DEHB 09 and DEHB 14, which are typical of the brittle-type behaviour of slabs highly reinforced and without

Hidden page

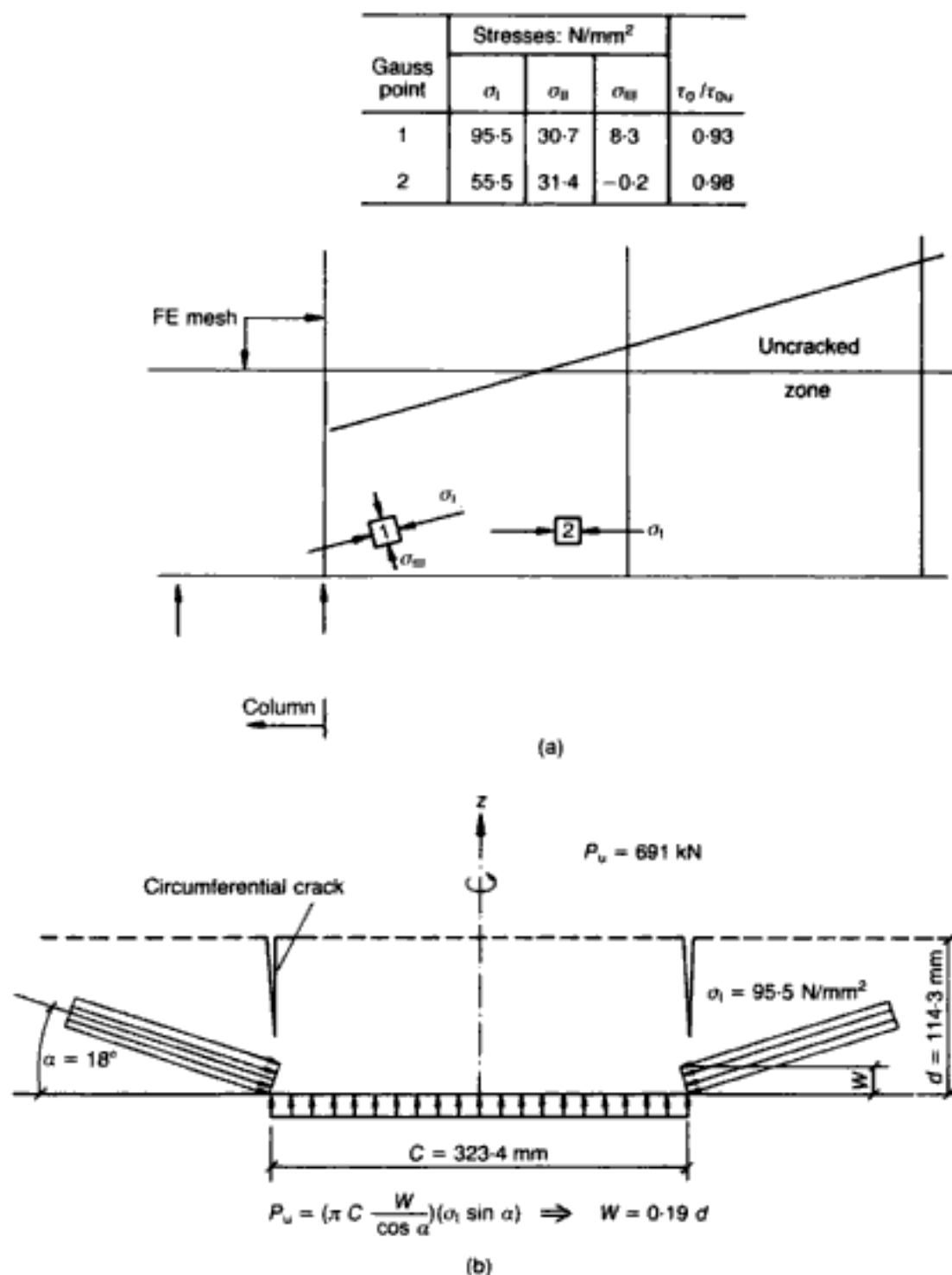


Fig. 3.94. Triaxial effects in the vicinity of the column for slab DEHB 14 at MSL.¹³⁷ (a) local stress states in the 'compressive zone'; (b) approximate assessment of equilibrium assuming average values for stresses and angles at Gauss point 1

stirrups. In agreement with experimental evidence,¹⁴² it appears that failure of this type of slab occurs as a result of punching before the flexural reinforcement reaches its ultimate strength and, therefore, before the ultimate flexural strength is fully developed. This mechanism of punching is discussed later.

The typical stages of the deformed shape and the crack pattern for slab DEHB 14 are shown in Fig. 3.89. As for ductile cases, cracking occurs in the form of radial and circumferential cracks. As before, radial cracks spread throughout the top face and divide the tension zone into radial segments. However, for the case of

brittle behaviour, radial cracking occurs at a lower rate and the crack depth is smaller than that for the slab exhibiting ductile response. In contrast to radial cracks, circumferential cracks increase in depth up to two-thirds of the slab depth in the periphery of the column; beyond that region, their depth is small and the cracks do not extend to the region of the supports. These observations agree with the fact that the depth of the neutral axis increases with the amount of tension reinforcement for the same load level; therefore, the depth of cracks for highly reinforced slabs must be smaller than for those lightly reinforced (compare Figs 3.86 and 3.89).

Figure 3.90 indicates that, as for the ductile case described earlier, circumferential strains and stresses within the compressive zone are larger than the corresponding radial values, except within the area extending, in this case, only up to a distance of approximately $0.75d$ from the column face. As shown in Fig. 3.91, it appears that a high radial strain of up to 0.4% develops within the compressive zone by the column face. It is interesting to note that a high triaxial compressive state of stress occurs in the vicinity of the column face, where the maximum principal compressive stress σ_1 reaches a value nearly twice that of the uniaxial cylinder compressive strength f_c and the minimum principal stress σ_{III} a compressive value of approximately $0.15f_c$. However, this triaxial stress state is reduced to a nearly biaxial compressive stress state from a distance of about $0.5d$ from the column face (see Fig. 3.90(c)). It is also interesting that no horizontal (i.e. circumferential) cracking occurs within the compressive zone up to the maximum sustained load (Fig. 3.89(d)). The occurrence of such horizontal cracking is considered to cause the brittle collapse of the structure by removing the previously mentioned triaxial stress conditions. (The latter hold right up to collapse: hence, the horizontal cracks in the compression zone appear suddenly just beyond the MSL — namely at the next load step, at which the analysis diverges — so that they cannot be seen in Fig. 3.89(d).)

The predicted strains of the flexural steel remain below the yield value (Fig. 3.90(d)). This, of course, is in agreement with experimental data for highly reinforced slabs.¹⁴²

Effect of stirrups on brittle-type behaviour. Slab DEHB 12 has been selected as a typical case for a slab over-reinforced longitudinally and with stirrups. It should be noted that this element is similar to slab DEHB 14, which was considered in the previous section, the difference being the addition of transverse reinforcement (see Table 3.5).

As Fig. 3.85 indicates, the load–deflection curves of slabs DEHB 12 and DEHB 14 are similar up to the ultimate load of the latter. It is interesting to note that, in spite of an increase of 36% in the (analytical) ultimate load, the tension reinforcement

Hidden page

σ_{III} (although, clearly, the actual conditions are, in general, more complex, i.e. the maximum and intermediate principal stresses are not equal). First, when this failure envelope is reached just below f_c (point A), the loss of tensile stresses leads to a state of stress that is just inside the failure envelope (point A'). Secondly, the redistribution of stresses involved is rather small and, hence, can be accommodated easily without large overstressing of adjacent regions (i.e. AA' is small).

On the other hand, it is a well-known feature of over-reinforced slabs that failure occurs before the ultimate strength of the reinforcement is reached or even without the occurrence of any yielding of the steel reinforcement. As mentioned earlier, for this type of brittle behaviour, a highly triaxial compressive stress state occurs within the compressive zone in the vicinity of the column face during the last load stages (see point 1 in Fig. 3.94(a)). As Fig. 3.94(b) shows, the vertical component of the quasi-radial principal stress σ_1 over the compressive zone is capable of equilibrating the external load. It should be noted that, assuming average values, the depth required for equilibrium is $0.19d$, while the actual length associated with Gauss point 1 is $0.167d$; this ignores contributions of the remaining half of the uncracked zone, where the stresses are much lower.

In spite of such a state of stress by the column face, the analysis shows that it is the nearly biaxial compressive stress conditions that occur at adjacent locations that are more critical (see the table in Fig. 3.94(a), where the deviatoric stress at point 2 has almost reached its critical value despite the fact that σ_1 there is much smaller than at point 1) and lead to horizontal cracking within these locations, which results in an immediate loss in load-carrying capacity. So sudden is this loss that these cracks do not appear in Fig. 3.89(d), as they are associated with a load increment just beyond the last stable load step (i.e. 11). The reason why the loss of confinement of the triaxial compressive state caused by the horizontal cracking in this area is so catastrophic is that, unlike the case of ductile behaviour, the maximum principal stress is almost twice f_c (this is to be compared with a value below f_c for the ductile case). Such a high triaxial stress state, therefore, can no longer be sustained nor redistributed. Once again, it is helpful to refer to the failure envelope in Fig. 1.69(b) which gives an approximate qualitative picture of the loss of tension, i.e. point B moves to point B', and thus immediate collapse of the slab ensues.

For the case of slabs over-reinforced and with stirrups, it appears that transverse reinforcement is capable of delaying the occurrence of the horizontal cracking which, as mentioned previously, leads to collapse of slabs over-reinforced and without stirrups. In this respect, Fig. 3.92(c) indicates that for slab DEHB 12 such cracking

starts at a load level 27% higher than that of slab DEHB 14. Once such horizontal cracking occurs, it also appears that the stirrups are capable of controlling the spread of tensile axial strains toward adjacent locations, as can be seen from Fig. 3.93(b) by comparing the ϵ_{cc} values near the column at load steps 11 and 15. However, it is found that the development of these horizontal cracks causes yielding of the stirrups so that tensile axial strains eventually reach the column face area, leading to the loss of confinement of the high triaxial compressive stress conditions in that region. As explained previously for brittle cases without stirrups, high triaxial stress conditions can no longer be sustained, and a sudden collapse of the slab occurs. (The maximum principal stress appears to be even higher than for the brittle (without stirrups) case — σ_1 is more than twice f_c — so that, once again, a stable state of stress redistribution cannot be attained.) The presence of stirrups, however, does lead to partial yielding of the main reinforcement, but this is localized (at the support; see Fig. 3.93(d)) and is restricted to initial (first) yielding only (see Fig. 3.85). Therefore, such yielding is not sufficient to increase the ductility of the member to a noticeable (overall) structural level, and there is no significant deflection warning at failure. On the other hand, unlike the case devoid of stirrups where horizontal cracking in the compression zone near the support led to immediate failure, the slab with transverse reinforcement exhibits a somewhat more gradual crack development (see the last two load steps in Fig. 3.92). Whether such localized cracking becomes visible before failure depends on the degree of plastification of the main reinforcement and, for the particular case studied, this was limited to primary yielding, as mentioned previously.

3.4.4.4. Conclusions

Within the scope of the present analytical study, several conclusions appear to be justified. First, in view of the good correlation between the nonlinear FE analysis model and the experimental data, it would seem that the 2-D package can be used with confidence in studying, both quantitatively and qualitatively, problems of punching in RC slabs even when certain geometrical simplifications are introduced. (More reliable predictions in the case of rectangular slabs and the modelling of eccentric loading can be carried out by the 3-D version of the numerical model — see Chapter 4.) Such analytical accuracy is especially pertinent in a problem for which a recent research survey¹⁴³ reports serious errors in codes of practice. In particular, the ACI and British methods (and, sometimes, the Australian Standard) tend to give unsafe predictions. (In reference 143 — where, incidentally, the problem is still described as one of punching 'shear' — it was found that, 'on average, the ACI prediction is 1.57 times the measured strength and the

Hidden page

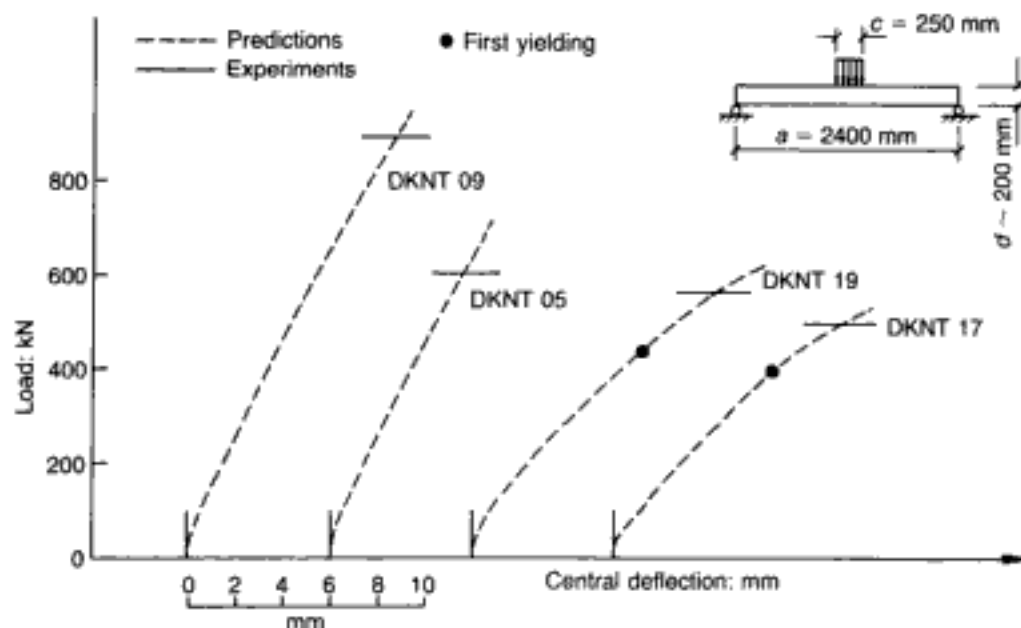


Fig. 3.95. Predicted load-deflection curves for the four circular slabs of test series 3 and comparison between predicted and experimental ultimate loads¹⁴⁴

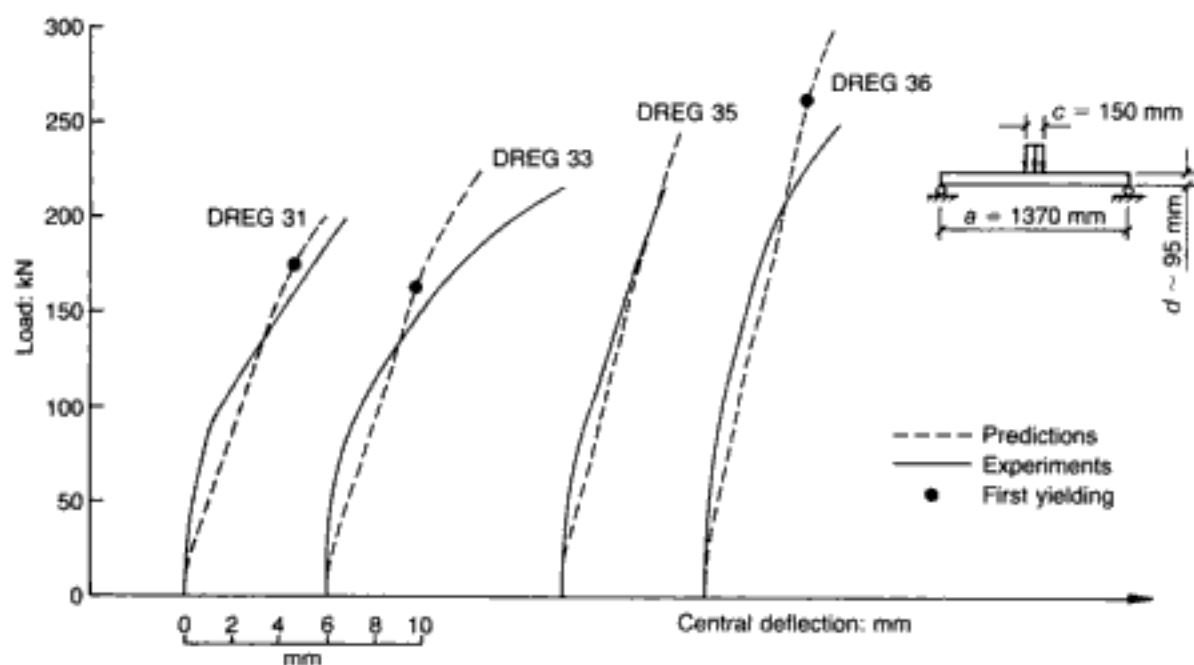


Fig. 3.96. Comparison between predicted and experimental load-deflection curves for the four circular slabs of test series 4¹⁴⁴

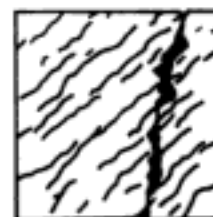
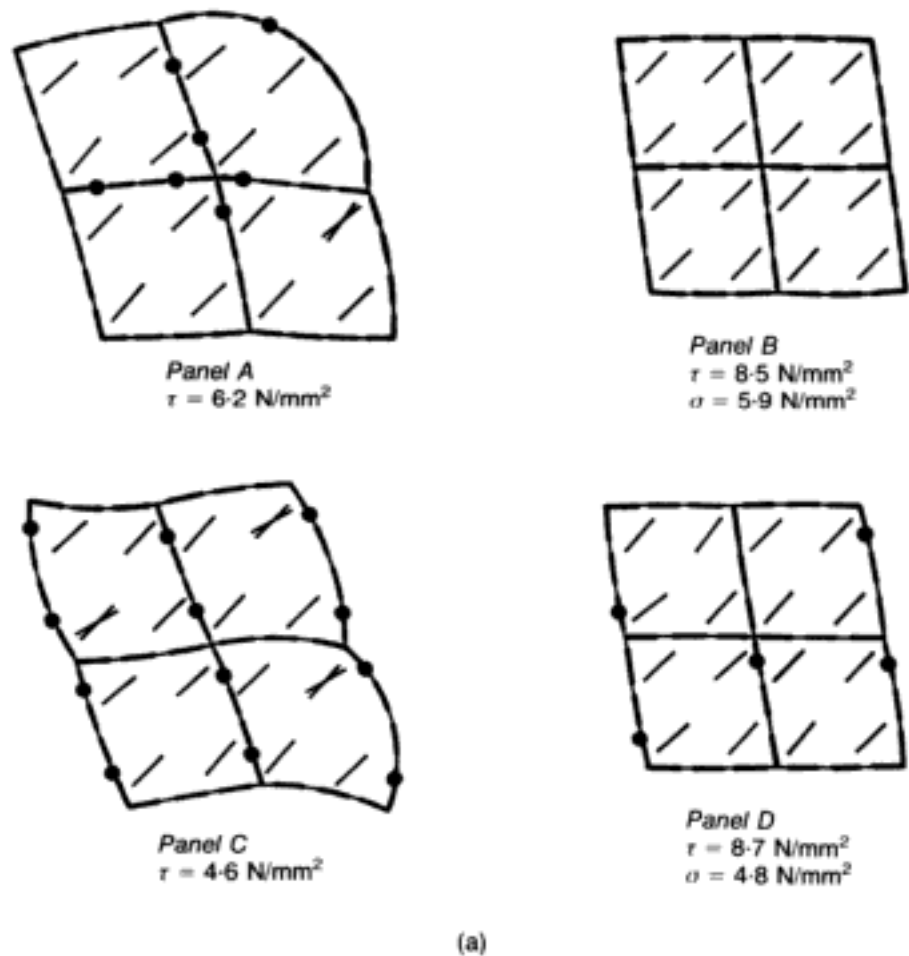
corresponding value for the British Standard is 1.41 times', while the Australian Standard procedure 'at times gravely overestimates' the strength of certain flat plates.)

The above results are representative of a wider pool of 2-D problems of punching in slabs. Further cases of circular slabs are summarized in Table 3.6, and Figs 3.95 and 3.96 (for further details, see reference 144). Test series 3 consists of four additional slabs taken from the experiments reported in reference 138. These

Hidden page

Hidden page

increased simultaneously.) The experimental programme is summarized in Fig. 3.97(b). The FE mesh adopted to represent the panels⁹⁸ is simply a 100 mm \times 100 mm square grid of four concrete elements and twelve steel bar elements, as shown on the deformed shape representation of the four panels at the ultimate-load level in Fig. 3.98(a). (Only a representative portion of the whole specimen was analysed since there are no size effects, the stress states being uniform throughout the specimen at any load stage; a full-size panel modelling confirmed this, enabling subsequent runs to be carried out more economically by means of the 2 \times 2 mesh.) For typical intermediate load stages, reference may be made to panel A, as illustrated in Fig. 3.99.⁵⁴ Cracking occurs early on (at 1.8 N/mm²) throughout the whole panel, but



Panel D

(b)

Fig. 3.98. Typical failure modes of shear panels: (a) predicted for all four panels (D.M. = 45);⁹⁸ (b) observed for panel D^{98,147}

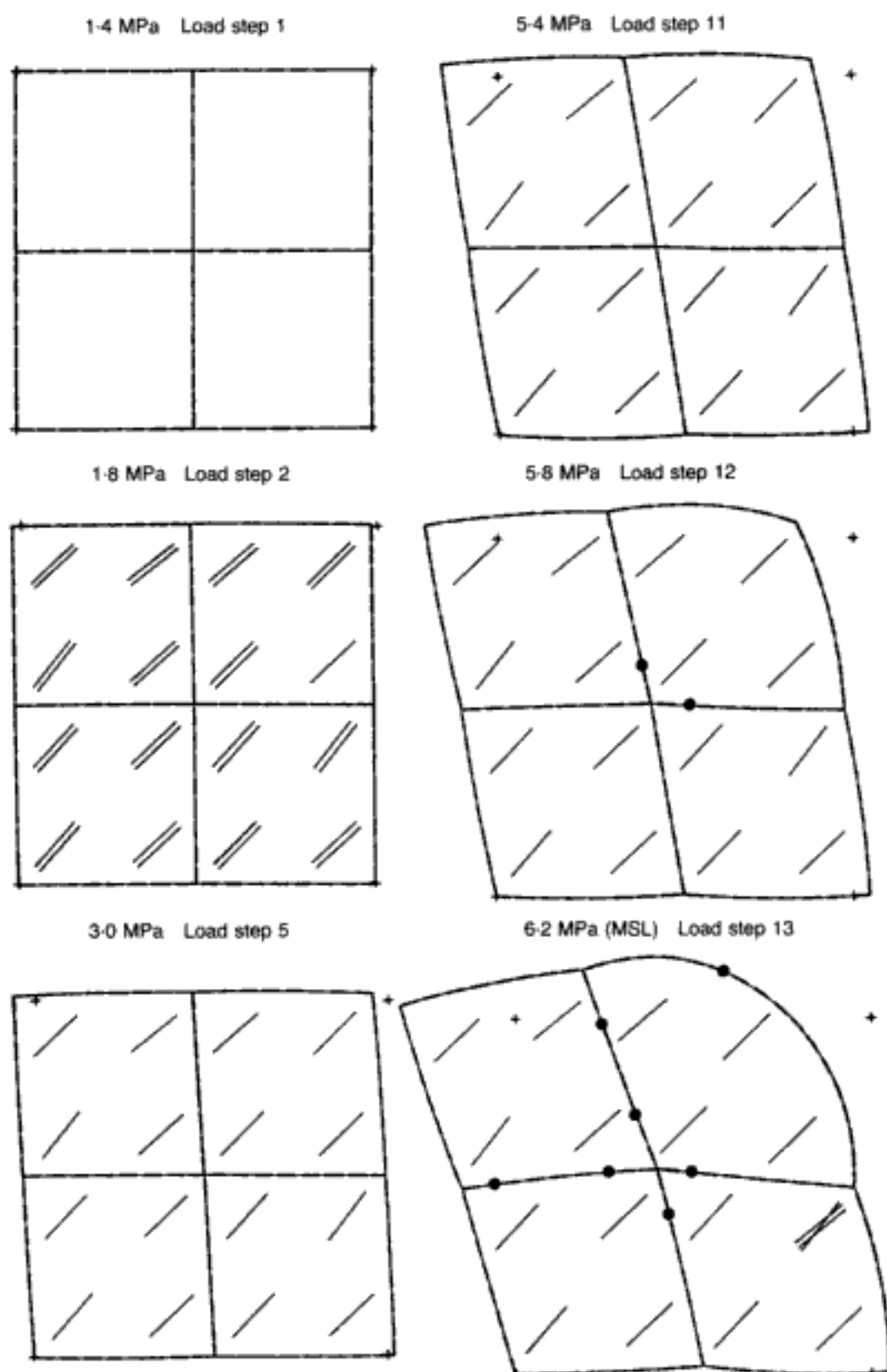


Fig. 3.99. Crack patterns and deformed shapes ($D.M. = 45$) for panel A at various load stages⁹⁸

the member fails at 6.2 N/mm^2 as the steel gradually yields (shown by the black dots).

The experimental crack pattern for panel D in Fig. 3.98(b) can readily be compared with the predicted one in Fig. 3.98(a) to show essentially the same uniform pattern of diagonal cracks over the

entire surface. It is interesting to note that equal biaxial compression has no influence on the layout of uniformly distributed diagonal cracks since, in compliance with the failure mechanism of concrete described in Chapter 1, any cracking that may be caused by equal biaxial compression should occur on the plane of this stress state. The correlation of deformational behaviour is reported in terms of strains and stresses in Fig. 3.100 where good agreement between experiment and predictions can be seen. The predicted ultimate levels are within 15% of the experimental values for panels A, B and C, whereas the FE analysis overestimates the experiment by 47% in the case of panel D, the worst prediction of the ultimate level ever obtained in the course of analytical modelling by means of the present 2-D package. In this respect, it is interesting to mention that the shear panels are cases of 'actual' predictions, since Collins¹⁴⁷ proposed to research groups from all over the world to submit analytical predictions before the test results were published. As a result, 24 different research groups from eleven countries submitted predictions which ranged as shown in Table 3.7. It should be noted that the average of all predictions for panel D was also significantly above the experimental value by roughly the same amount as the present overestimate, thus raising the question of the accuracy of the test data itself.

This is confirmed by a closer look at the analytical results, which reveals that the steel had already started to yield before biaxial

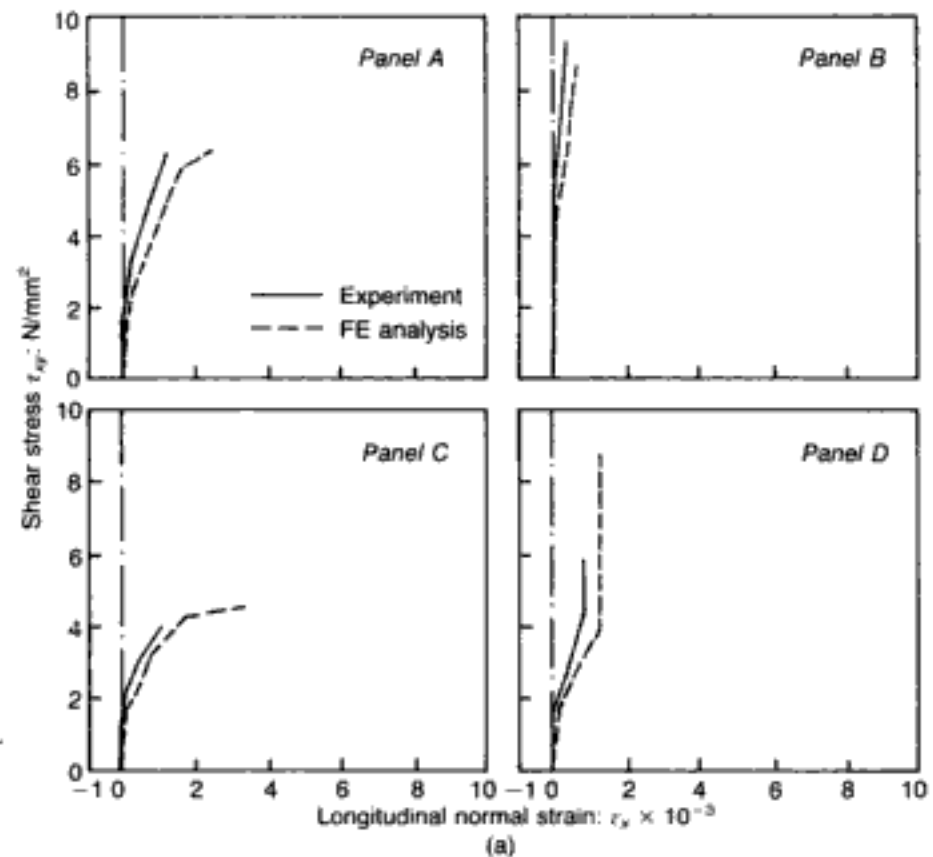


Fig. 3.100 (right and facing). Predicted and experimental stress-strain curves for shear panels:⁹⁸ (a) strain ϵ_x ; (b) strain ϵ_y ; (c) strain γ_{xy}

Hidden page

Table 3.7. Summary of ultimate shear-stress predictions for four shear panels analysed by various research groups before release of experimental results^{54,98,147} (all values in N/mm^2)

Panel	All research groups combined			Present 2-D FE model	Experimental values
	Range	Average	Standard deviation		
A	4.4–8.8	7.1	1.2	6.2	6.3
B	3.9–15.2	9.0	2.9	8.5	9.1
C	2.1–5.7	4.2	0.8	4.6	4.0
D	3.7–16.5	8.3	3.2	8.7	5.9

compression was applied on the specimen (i.e. for applied pure shear $< 3.86 N/mm^2$). If that was actually the case, instability could have developed in the specimen, leading to early experimental failure due to effects beyond the scope of the analytical modelling. In fact, the mode of failure of the specimen, which is characterized by a very pronounced vertical crack near the right-hand side of the specimen (see Fig. 3.98(b)), supports the above explanation.

3.4.6. Corbels

The structural behaviour of corbels, partly elucidated through photoelastic studies in Germany in the mid 1960s for the case of unreinforced elements at low working loads,¹⁴⁸ poses a particularly challenging task if their rational design is to consider, in addition to the implicit geometrical complexity, ultimate-load conditions and the presence of reinforcement detailing. Therefore, the nonlinear FE package appears to be of special relevance to such structural-concrete members. Its performance for such a purpose may be illustrated by reference to the numerical modelling by Bédard⁵⁴ of one of the many specimens that form part of the tests reported in reference 149.

The element in question is specimen 13, an RC corbel subjected to vertical loading, for which $f_c = 31.6 N/mm^2$ and $f_y = 351.6 N/mm^2$, with the other relevant experimental data given in Fig. 3.101. Figure 3.102 shows the FE mesh adopted in the analysis, which consisted of an initial load of 36 kN, followed by 24 kN load steps. The deformed-shape and crack-pattern plots for some of the more relevant load steps appear in Fig. 3.103. It is evident that the large distortions exhibited at load step 19 raise doubts about the actual physical existence of the maximum load 468 kN at which convergence is still attained. Such a view is confirmed by the apparent occurrence of compressive failures at some of the Gauss points at load step 19, so that it can be concluded that the physically meaningful MSL value is associated with the earlier load step (i.e. 444 kN). (Although Bédard⁵⁴ is not explicit on the question of matrix ill-conditioning warnings, these are almost certain to have taken place at the final 'converged' load step, as

Hidden page

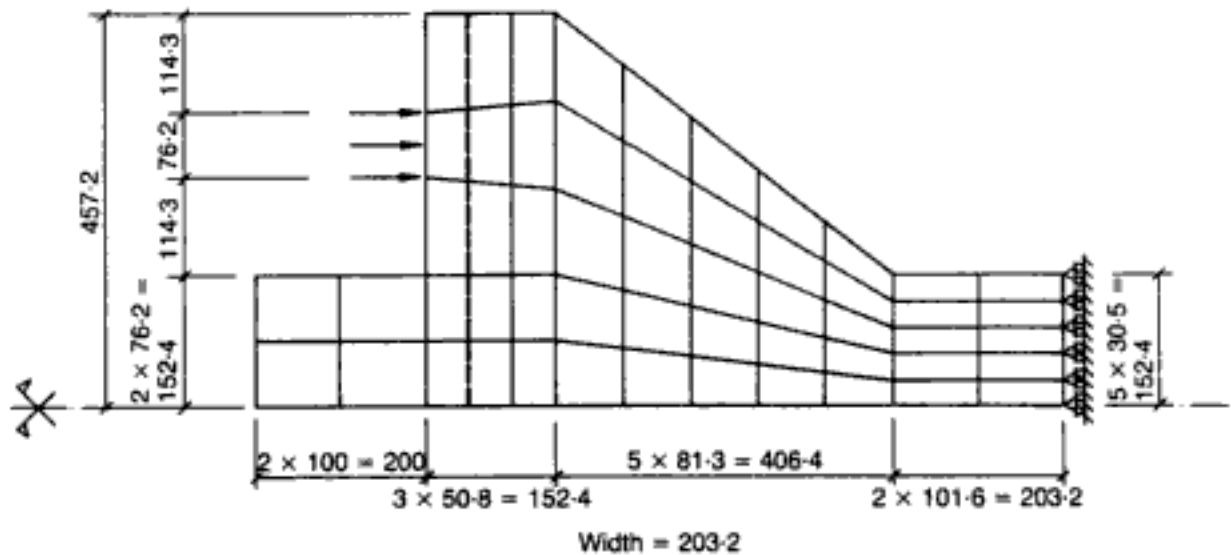


Fig. 3.102. FE mesh adopted for corbel 13 (all dimensions in mm)⁵⁴

It is customary to classify the modes of failure in corbels into four 'principal' and two 'secondary' types.^{148,149} One of the former, referred to as 'flexural tension' is associated with extensive yielding of the main reinforcement, and the type of failure is characterized by a very wide flexural crack at the junction of the column and the corbel. On the evidence of Fig. 3.103, it is clear that corbel 13 failed in such a mode, which is in keeping with the experimental results,¹⁴⁹ as may be seen from Fig. 3.101(b).

3.4.7. Shells

Although the study of shell structures is beyond the scope of the present work, some examples of the possible application of the nonlinear FE model to these structural forms will be given to show that reasonable estimates of their response can be obtained despite the fact that the specialist nature of most of these structures requires, in principle at least, some modifications to the FE package which, in its current version, is aimed at reproducing the behaviour, up to ultimate conditions, of plain and/or reinforced concrete structural forms for which material nonlinearity is of paramount significance. Thus, for example, sandwich cylinders require more attention to be given to the steel-concrete behaviour in composite construction, where steel plays a more important role while concrete may be subjected to passive — rather than active — restraint conditions. (The constitutive relations of Chapter 1, relevant to concrete under active confinement, need to be modified when concrete is subjected to passive confinement as in composite construction such as, for example, steel-encased concrete columns. This topic has been the subject of recent studies at Imperial College — references 150–152.) Similarly, thin — as opposed to very thick — shells may exhibit strong nonlinearities of the geometric type beyond their working-load conditions, with large displacements and even instability influencing collapse. While current work is under way to address these phenomena, it may be interesting to list here two examples of shell analysis which, in spite of their approximate

nature and obvious shortcomings, appear to yield sensible predictions of the overall behaviour at failure.

3.4.7.1. Sandwich cylinder under external pressure

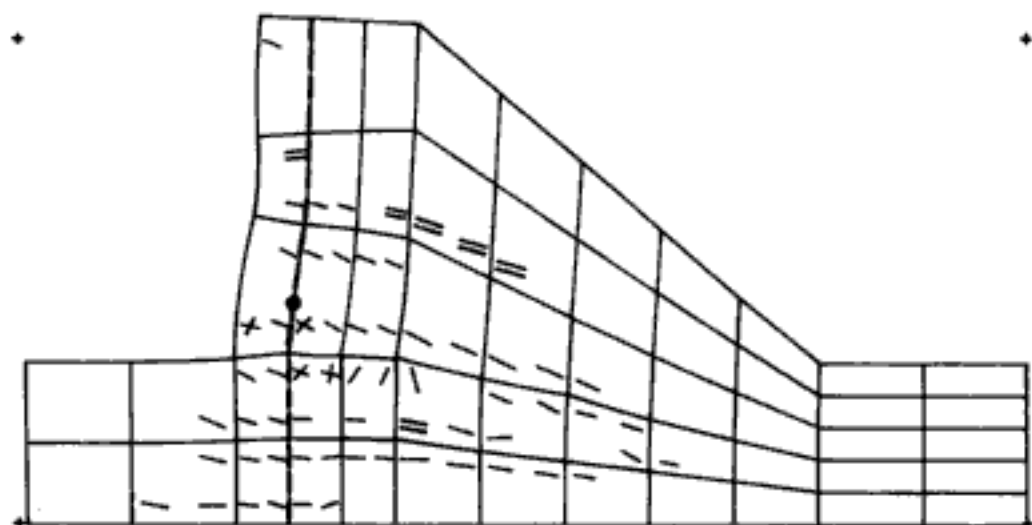
The following example is based on cylinder 5.3, a typical specimen from the series of tests, reported in reference 153, on sandwich cylinders purporting to model structures for sub-sea oil production operating at pressures of up to 21 N/mm^2 (equivalent to depths of 2 km below the sea surface). These specimens consisted of two concentric steel skins, with the annular space between them filled with microconcrete. Screws projecting from each skin into the annulus acted as shear connectors with the concrete filler. The composite structures were subjected to uniform external pressure.

Figure 3.104(a) contains the experimental data related to the geometry of cylinder 5.3 (the material data are $f_c = 0.8f_{cu} = 50.4 \text{ N/mm}^2$ and $f_y = 223 \text{ N/mm}^2$), while the FE mesh adopted in the axisymmetric analysis⁵⁴ is shown in Fig. 3.104(b). The numerical procedure was begun with an initial load step of 3 N/mm^2 for the external pressure, with subsequent constant increments of 2 N/mm^2 . The type of construction under investigation hardly suffers any cracking before failure, a fact which may be seen by reference to the deformed-shape plots at various pressure levels depicted in Fig. 3.105; as expected, it is the steel which plays a predominant role. The theoretical pressure at the MSL of 25 N/mm^2 overestimates the experimental value (20.7 N/mm^2) by 21% (cf. the prediction of 13.8 N/mm^2 stemming from the theoretical analysis described in reference 153 — an underestimate of 33%). This is a satisfactory correlation when it is noted that, in addition to the approximations implicit in the analysis of sandwich cylinders by the present package intimated earlier, the constitutive relations used have been derived for normal concrete whereas the filler employed in the experiments consisted of microconcrete (maximum aggregate size = 3 mm). Now, although the adopted constitutive relationships for normal concrete may also be used as an approximation for microconcrete provided that f_c is the same, it should be recalled¹⁰ that, for mixes having the same uniaxial compressive strength, the failure envelope of a mortar differs little from the failure envelope of a normal concrete but the microconcrete deformations are usually larger than for ordinary concrete.

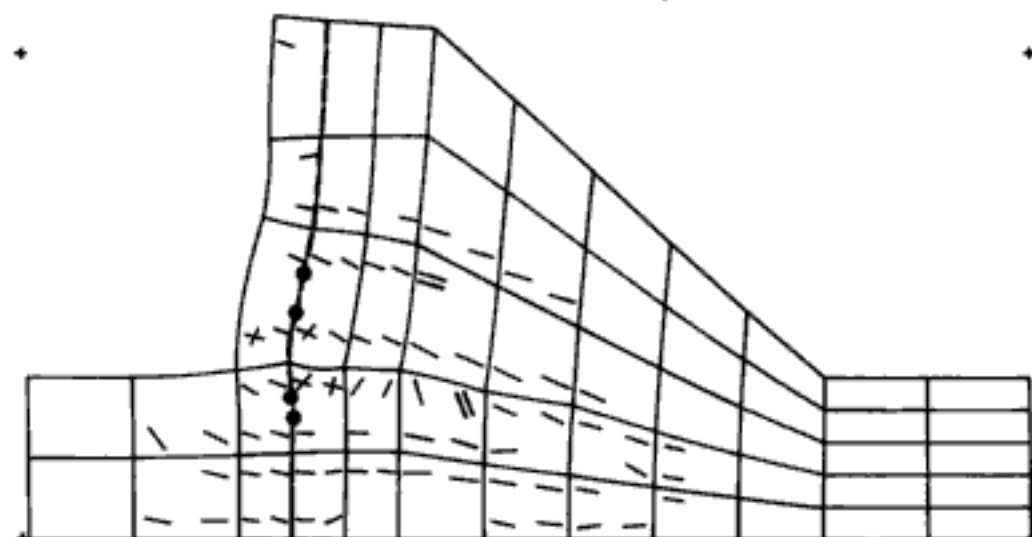
While only the experimental failure pressure was reported, the analysis predicted an approximately bilinear pressure—radial displacement (at the base of the inner steel skin) relation defined by the change in slope at (12 N/mm^2 , 0.15 mm) and the ultimate conditions at (25 N/mm^2 , 0.63 mm).⁵⁴ In an attempt to assess the influence of imperfections, Bédard⁵⁴ also analysed the same cylinder by decreasing (from top to bottom) the mean radius (by 1%) and the mean thickness (by 10%). The MSL value for the

Hidden page

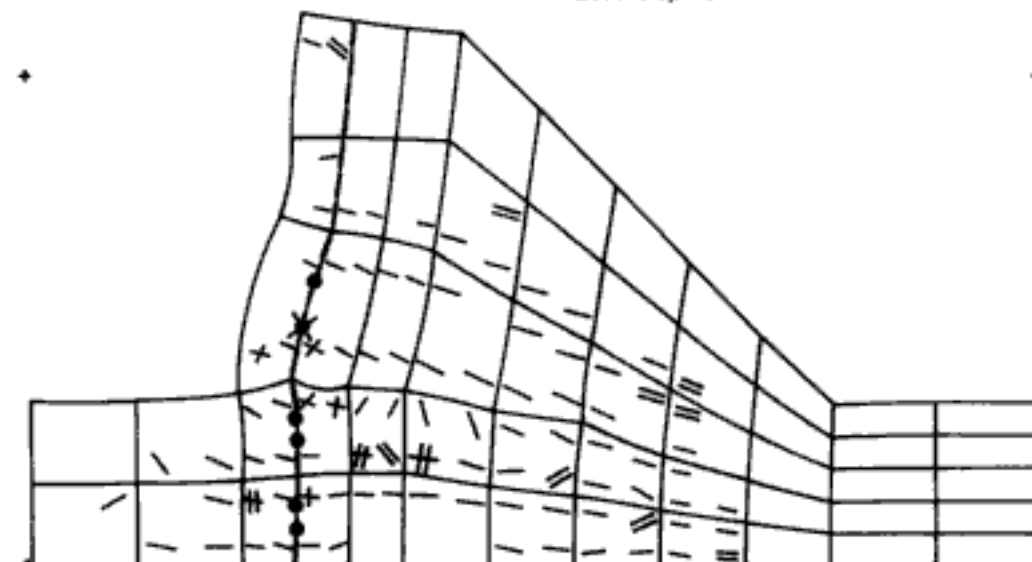
348 kN Load step 14



396 kN Load step 16



444 kN Load step 18



Hidden page

Hidden page

Hidden page

ultimate pressure was unchanged, which suggests that the sandwich construction is relatively insensitive to such imperfections, as was intended in its original design.¹⁵³ The pressure–radial displacement plots for both perfect and imperfect cylinders were near-coincident, the latter being only marginally less stiff (as was the case with the hollow sphere described in section 3.3.4).

3.4.7.2. Dome under central point loading

The strength of concrete domes used as roofs is usually well in excess of the maximum loads (mainly self-weight and possibly snow) they are likely to carry. As such, their design is still based largely on elastic theory.¹⁵⁴ On the other hand, ultimate-strength philosophy is relevant when concrete domes used, for instance, as covers for cylindrical structures are subjected to possible overloads such as the impact of a falling object in an offshore environment. Circular domes of this type have been the subject of an experimental study at Imperial College under the direction of Professor S.H. Perry, and one such shell (a control specimen, i.e. loaded statically as a reference datum for the impact tests), acted upon by a concentrated load at its apex, was analysed by means of the 2-D axisymmetric model.¹⁵⁵

The shell shape, FE mesh and crack pattern at failure (MSL) are shown in Fig. 3.106. Bearing in mind that no geometric nonlinearity was allowed for and that a certain degree of uncertainty in the actual boundary conditions existed, the analytical collapse load of 494 kN compares well with the experimental value of 425 kN (Perry, private communication). However, this example is not intended to serve as a formal case of analysis but, rather, as an instance that, even without the introduction of some of the features required in a proper nonlinear analysis of a thin shell, the present version of the FE model is still capable of predicting the structural behaviour of concrete shells, such as their predominantly membrane action which gives rise to their strength and stiffness. In this respect, the almost total cracking throughout the structure in Fig. 3.106 should be noted, as the very thin — but, nevertheless, effective — line of compressive thrust is practically reduced to zero width.

3.4.8. Membrane action in flexural members

Although membrane action in structures subjected to forces transverse to their own plane is generally associated with curved elements (shells or arches), such in-plane action may sometimes also occur in what are usually considered to be primarily flexural elements. This can be achieved by introducing horizontal restraints, i.e. in the plane of the element, which often results in considerable enhancement of its load-carrying capacity.

Compressive membrane action leading to strength gain in laterally restrained beams and slabs has been the subject of intensive research at Queen's University, Belfast, under the direction of

Hidden page

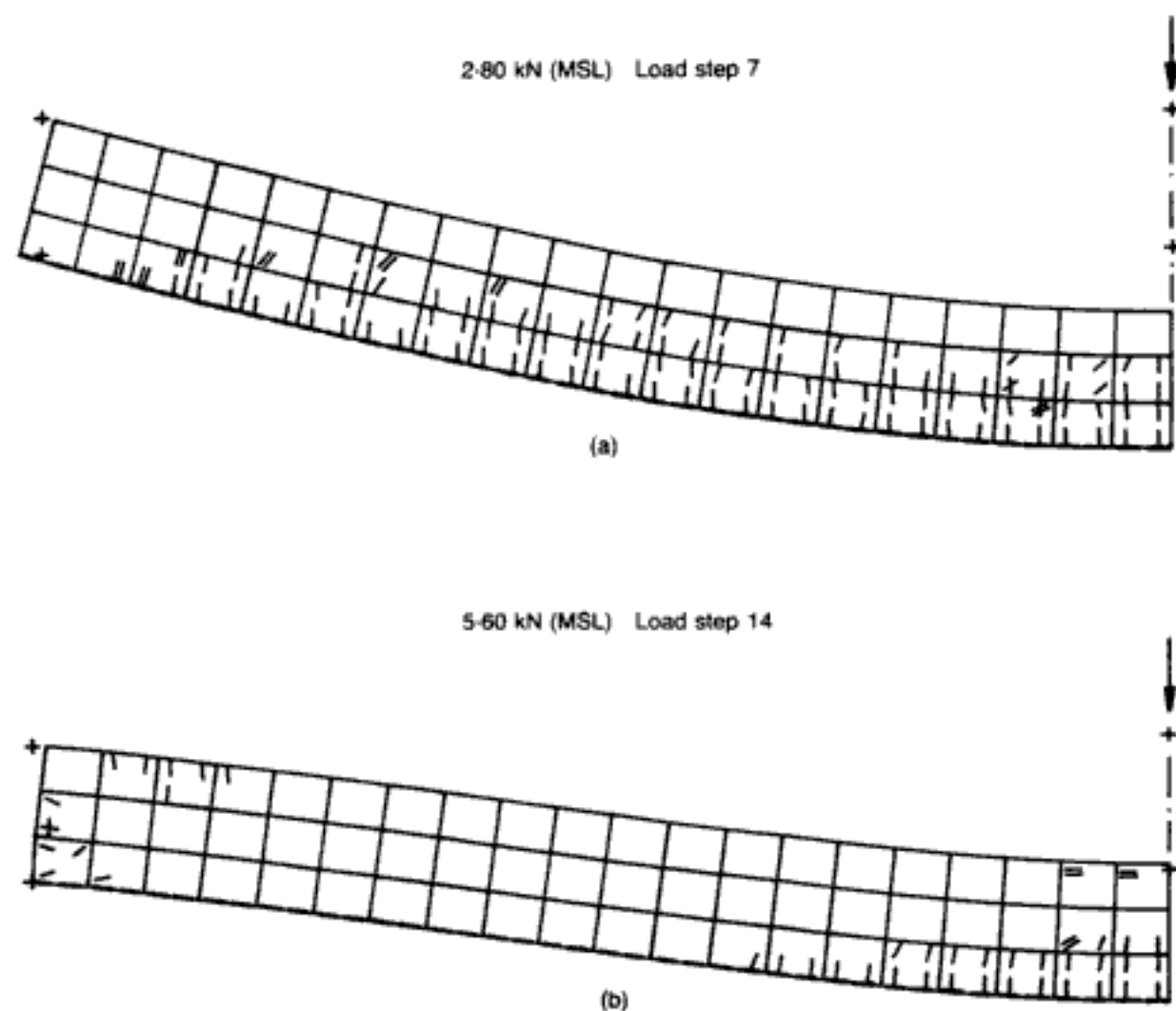


Fig. 3.107. Crack patterns and deformed shapes at failure for a typical simply supported beam under point load at midspan:¹⁵⁵ (a) ends allowed to displace horizontally; (b) ends fully restrained against horizontal movement

(especially of unusual members, reinforcement, or connections) but, more generally, towards an improvement over current design philosophies. In this respect, it is important to realize that the notion of a 'critical' cross-section is not always adequate (or, indeed, safe) in the case of limit-state design of concrete elements. Admittedly, it would be impractical to attempt to estimate the strength of a complete concrete structure, consisting perhaps of many members, by means of the present nonlinear computer program. Instead, what is advocated is a preliminary (elastic) analysis which would help to identify the more critical elements: the latter could then be the object of a more detailed design in terms of actual strength and the ways in which this could be improved.

The use of the package for design purposes enables fairly comprehensive parametric studies to be undertaken on problems of specific interest, leading to practical formulae which are both simple and rational. In the past, the lack of a reliable analytical model for concrete structures meant that parametric studies were usually of a predominantly experimental nature, thus limiting their scope because of the relatively small number of tests which could be carried out with the time and resources which are typically

available. Any accompanying theoretical work tended to be restricted to the particular problem under investigation and, *ipso facto*, its scope could not lie outside the experimental programme. The present FE package enables a radical reversal of approach to be undertaken. Full parametric studies can be carried out numerically in a relatively short time and certainly much more cheaply than their experimental counterparts. (In this regard, the relative economy of the 2-D model, when compared with its more formal 3-D counterpart, makes the former a more likely tool for parametric studies of the type presently carried out on PC prisms and cylinders, and RC shear walls.) Then, on the basis of these theoretical results, rational design formulae could be deduced. Finally, the whole investigation should be wound up by the conducting of a small number of select experiments as a check on the theoretical findings, especially those which might appear to contradict current views.

Finally, the FE scheme has the potential to elucidate certain *phenomenological aspects* such as, for example, the question of aggregate interlock, the load-carrying mechanism along compressive paths in a structure (which, in turn, helps explain the different modes of 'shear' failure), etc. In this respect, the most important phenomenological feature to emerge from the present chapter is perhaps the fact that, in all the structural configurations analysed so far, failure has invariably been initiated by the appearance of tension in localized regions of the structure, such local tensile failures leading to overall collapse before the ultimate strength of concrete in compression is exceeded anywhere within the structure. This validates the notion that the key feature of concrete, namely the sudden volumetric expansion prior to failure, always leads to triaxial conditions in a structure, and confirms the simple failure mechanism at the material level put forward in Chapter 1. Such mechanisms of failure are often difficult to detect experimentally since the observed crack pattern after a test is really an indication of *post-failure* phenomena showing the *effects* rather than the *causes*; on the other hand, the FE model can detect such causes numerically in the course of the last load steps.

4. Three-dimensional analysis

4.1. Introduction The formal 3-D FE model is used in the present chapter in order to analyse those structural forms where 2-D analysis is not possible either on account of arbitrary geometry (such as, for example, T-beams) or because the complexity of the seemingly 2-D structure warrants a fully-triaxial (i.e. 3-D) approach (e.g. prism under strip loading). In addition, some essentially plane-stress problems (e.g. prestressed concrete (PSC) beams) are also analysed by means of the 3-D package as they were studied after the latter became available, these problems being used as further tests for the performance of the 3-D FE model. (A comparison between the relative predictive capabilities of the 2-D and 3-D models in the case of problems amenable to either package will be made in section 4.4 by reference to shear walls.) The range of problems considered in Chapter 3 is extended herewith not only with regard to geometrical complexity (e.g. T-beams, rectangular slabs) but also in terms of other structural parameters such as, for instance, prestressing, concrete strength, and brickwork.

As in the preceding chapter, besides the all-important structural strength (i.e. the most relevant characteristic from the viewpoint of limit-state design philosophy), consideration is also usually given to the predicted crack patterns and deformed shapes. With regard to the plotting convention for the latter two aspects of structural response, it should be mentioned that, in all cases, the plots are superimposed onto the mesh lying on the plane parallel to the reference plane xz , as will be illustrated by subsequent examples. The symbols used for the various cracks at the relevant Gauss points are to be interpreted as follows: oriented dashes represent the intersection of a crack plane with the plotting plane xz whenever the angle subtended between these two planes exceeds 45° . However, if both planes form an angle smaller than 45° , then the crack plane is simply indicated by a circle (hence, two cracks both forming an angle of less than 45° to xz at one location cannot be distinguished one from the other). Three cracks at the same Gauss point are indicated by an asterisk symbol. The following are in keeping with the earlier convention for the 2-D package: the presence of steel bars is marked by dashed lines superimposed onto the relevant edge(s) of the appropriate concrete element(s); displacement shapes at the various load levels are suitably magnified, and the appearance of very large and/or distorted shapes helps to identify quickly the onset of a mechanism (whether real or numerical in nature); finally, load step '777' plots relate to the last performed iteration in an analysis (at the load step that follows

the maximum sustained load), while, if at all specified, D.M. = N indicates that displacements have been magnified N times.

Before embarking on the objectivity and generality studies of the model and its subsequent application to specific problems, some broad remarks will be made in the next section regarding the numerical strategies for nonlinear FE analysis of structural concrete in general and the present 3-D model in particular. These observations are not intended as dogmatic statements purporting to put forward rules of general validity; rather, they are meant to elucidate the possible causes for the occurrence of certain numerical instabilities and to provide sensible guidelines for their avoidance based on both physical reasoning and computational experience.

4.2. Some observations on numerical instabilities in the smeared-crack approach

This section considers various possible problems that may be encountered in the course of structural-concrete analyses by means of the brittle material model. Ways of dealing with such problems are suggested as outlined in references 82 and 156, and are illustrated by two examples (with the main results summarized in Figs 4.1 to 4.5) which, in the past, have proved difficult to predict in a reliable manner. Finally, the fundamental difference between the proposed FE model and most other models proposed to date is discussed briefly by reference to both procedural and material strategies.¹⁰⁸

A key aspect of computational strategy for problems of the present type is the order of integration adopted in the course of evaluating the stiffness matrices, a point already raised in section 2.3.2. The use of second-order Gaussian numerical integration (reduced integration/under-integration) for the parabolic elements of the serendipity family is regarded as a well-established procedure for linear stress analysis.⁶¹ Furthermore, such under-integrated elements have been found to improve the predictions of shear stresses and strains that can be obtained by means of the third-order Gaussian schemes (full integration).⁸³ The reason for this remains unclear although, for the under-integrated element, optimal Gauss-point locations⁶¹ and equivalence with mixed models¹⁵⁷ have been suggested. However, the use of under-integration in 2-D nonlinear analysis of concrete structures has been questioned, since it is argued that its adoption can lead either to a premature divergence of the iterative procedure¹⁵⁸ or to the propagation of spurious mechanisms due to strain-softening localizations.¹⁵⁹ Such views appear to be in contrast with other work in which the four-point (2×2) integration scheme for the eight-node serendipity element was found to perform adequately (see, for example, Chapter 3, *passim*), and the whole question of numerical stability is further complicated by recent reports that even a full-integration (nine-point, or 3×3) approach for such elements may lead to the occurrence of 'hourglass' modes.¹⁶⁰

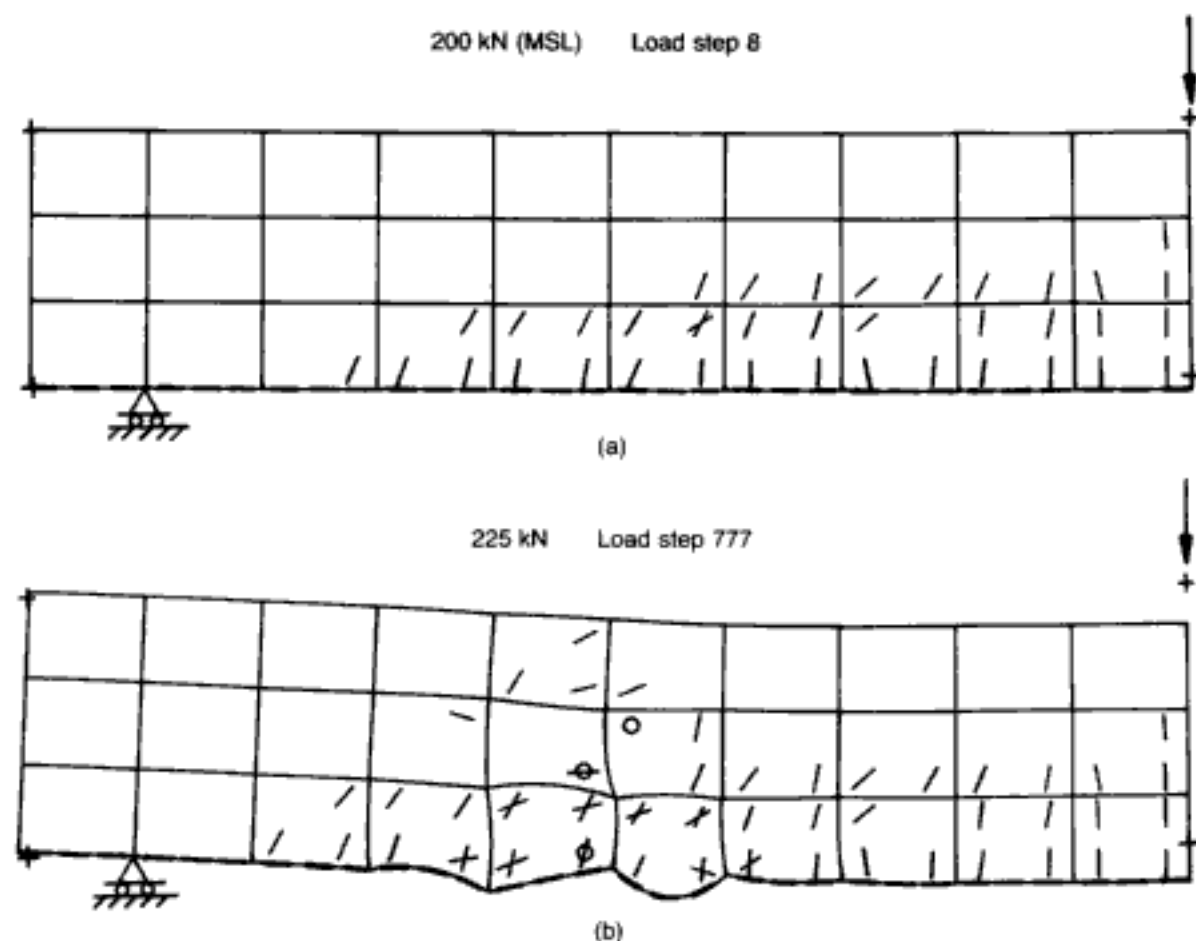


Fig. 4.1. Crack patterns and deformed shapes ($D.M. = 5$) for the RC beam OA-1 (under central point loading) obtained with the use of a mixed Newton-Raphson method (one complete updating every three iterations) and under-integration ($2 \times 2 \times 2$):⁸² (a) last converged load step; (b) last performed iteration

In the course of the development of the current 3-D smeared-crack model,⁵⁶ the propagation of spurious mechanisms has also arisen. This is not surprising since, by its very nature, the 3-D model is more likely to exhibit numerical instability than its 2-D counterpart. It is, therefore, within this 3-D context that the present section attempts to provide an insight into the underlying material and procedural factors that may cause the above numerical instabilities and gives some recommendations that have proved to reduce the risk of their appearance in a smeared-crack model.

In section 2.4.3.4, it was shown why, despite evidence which points to the fact that the SRF in cracked structural concrete tends to be negligible, the brittle nature of the material model requires the assignment of a non-zero value to this parameter. It is for this reason that the argument was made for setting always $\beta = 0.1$ since, on the one hand, such a value is consistent with the notion of a small SRF, while, on the other hand, it appears to be sufficient to provide the necessary numerical stability. In terms of numerical stability, therefore, it might seem somewhat paradoxical that those

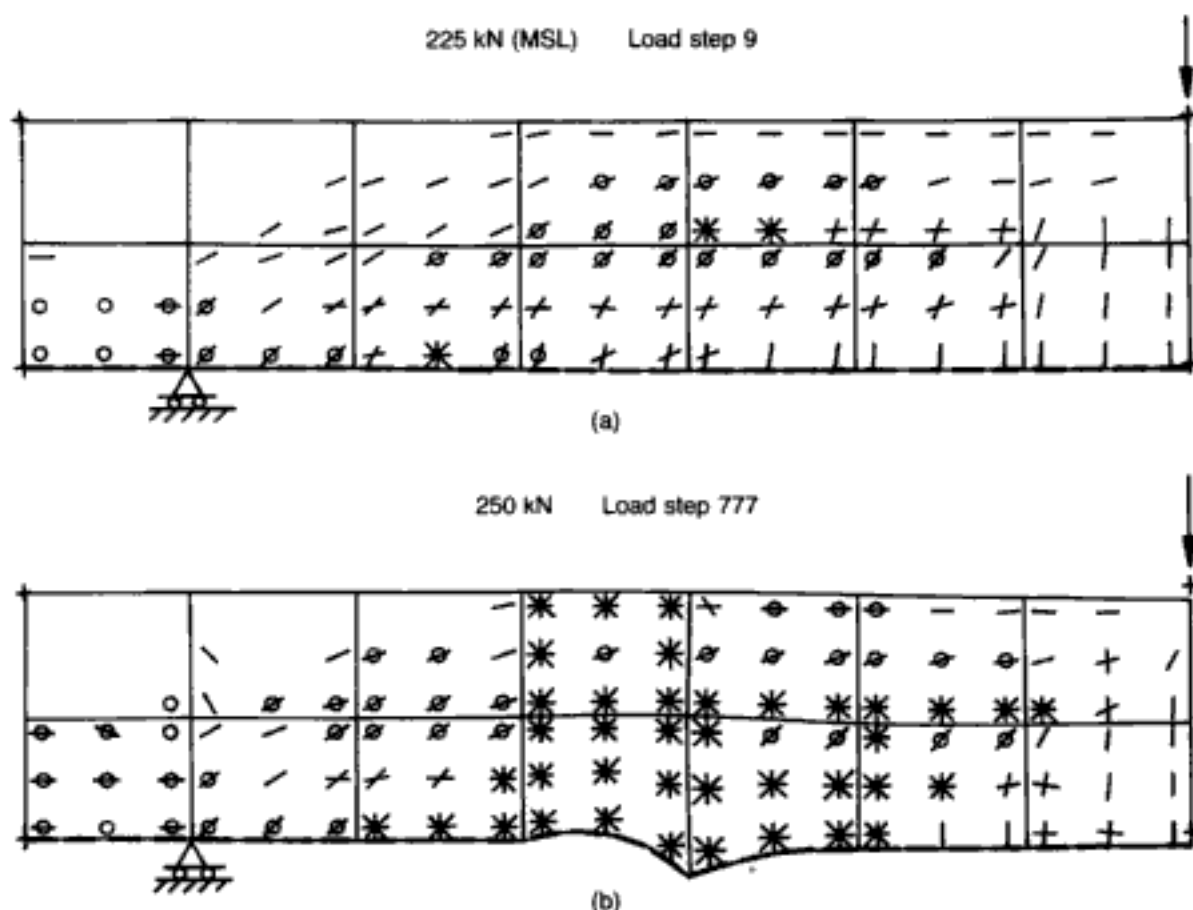


Fig. 4.2. Crack patterns and deformed shapes for the RC beam OA-1 (under central point loading) obtained with the use of a mixed Newton-Raphson method (updating only new crack locations) and over-integration ($3 \times 3 \times 3$);⁸² (a) last converged load step; (b) last performed iteration

workers who adopt a material model exhibiting tensile post-cracking softening relations,^{158,159} also tend to adopt values for β that are usually higher than 0.1. Irrespective of whether or not such tensile-softening and shear-retention properties are physically realistic, the presence of the former parameter in a secant — rather than a tangent — stiffness formulation means that the resultant secant matrix retains significant rigidity in the direction orthogonal to the cracks and, consequently, the numerical conditioning of the stiffness matrix should apparently be improved even if the SRF were to be neglected; the fact that, additionally, values of β in excess of 0.1 are usually adopted would seem to suggest that the numerical stability of such schemes is further improved. However, strain softening or a combination of uncracked (i.e. ascending) and strain-softening locations may give rise to localized instabilities and non-unique solutions, and cause premature divergence of the numerical procedure.^{74,159} At present, such instabilities are attributed to strain-softening modelling (and not to the iterative technique used); moreover, under-integration in these schemes is considered to be a further source of possible numerical difficulties,

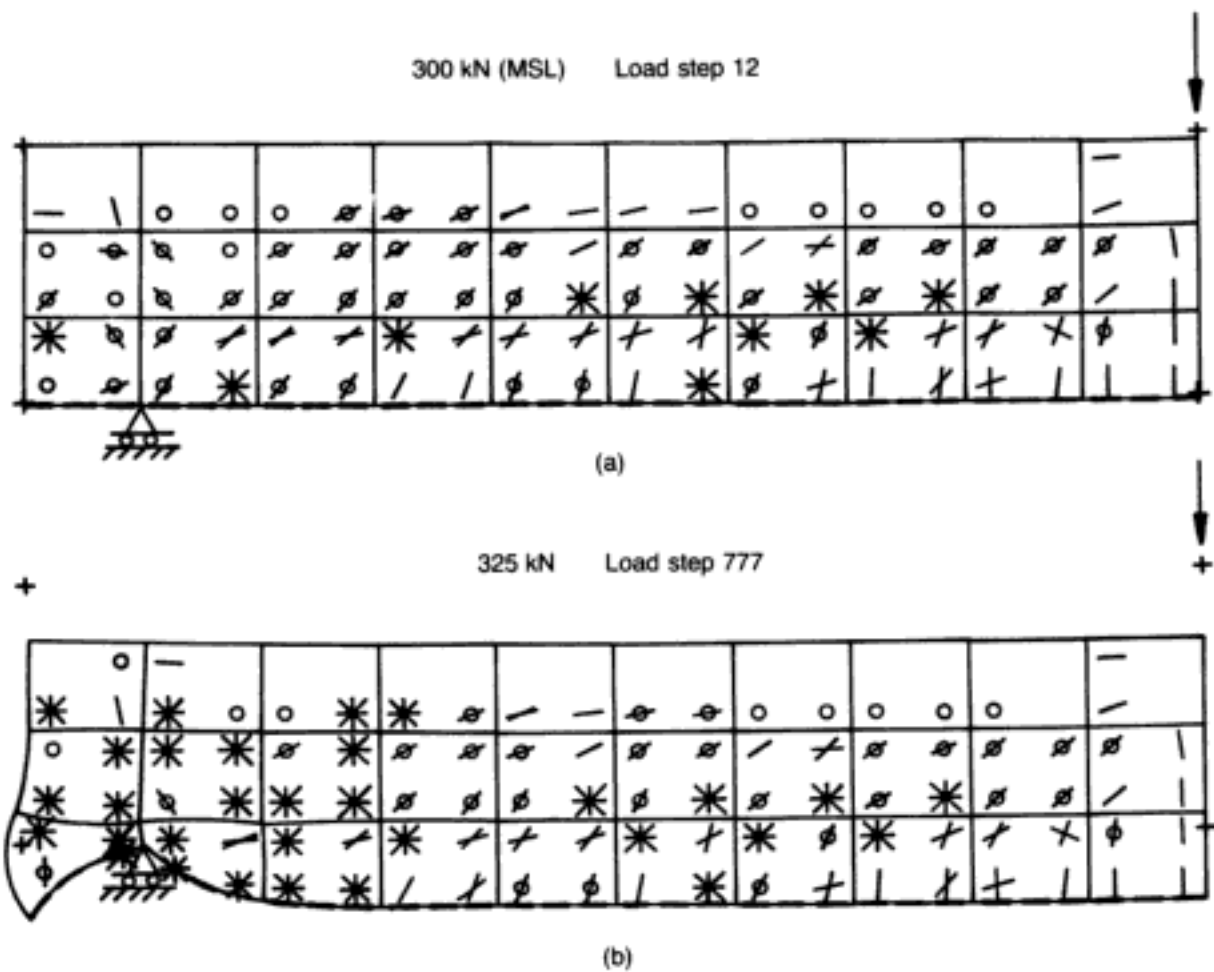


Fig. 4.3. Crack patterns and deformed shapes for the RC beam OA-1 (under central point loading) obtained with the use of a mixed Newton-Raphson method (updating only new crack locations) and under-integration ($2 \times 2 \times 2$):⁵² (a) last converged load step; (b) last performed iteration

leading to spurious responses associated with 'truncated hourglass modes'.¹⁵⁹

Now, if the material modelling includes post-cracking strain softening, stress release and redistribution take place gradually as cracks open. Thus, numerical procedures associated with such material modelling tend to be more stable than those involving the brittle material model, with which the sudden and complete release of tensile stresses as a result of cracking can by itself lead to the divergence of the numerical algorithm. In this respect, account must also be taken of the fact that the residual forces caused by a single 'brittle' crack may be of the order of magnitude of the external load step being applied. Hence, if all prospective cracks are allowed to occur at once (the 'total-crack approach' (TCA)), numerical divergence is very likely to be affected. However, a strategy by which cracks are allowed to occur one by one or in small numbers (the 'single-crack approach' (SCA)), while other prospective new cracks stand by until the numerical process is stabilized, causes a gradual release of residual forces and, therefore, improves the stability of the numerical procedure. In Chapter 3,

Hidden page

Hidden page

Hidden page

Hidden page

Hidden page

The use in smeared-crack modelling of the SCA, which allows the implementation of critical cracks to occur first, is also compatible with the physical nature of crack propagation within a structure, where the stress redistributions subsequent to crack initiation affect the stress conditions in neighbouring zones. In principle, and, as already pointed out in sections 2.5 and 3.2, if the load steps were to be infinitesimally small, sequential single cracking would generally result unless different locations were to attain the same level of (maximum) stress simultaneously. In view of the above arguments, it would seem that the allowance of all potential cracks to occur at once does not model adequately (or, at least, 'rationally') the actual nature of structural fracture. (Incidentally, it should be noted that the SCA appears to be essential for automatic discrete-crack models.¹⁶²) Furthermore, most tests of RC structures are far from following a really monotonic loading path up to failure. In fact, tests show that instant unloading occurs as soon as any cracking appears. (This is clearly observed on the recording equipment, as instant unloading of the hydraulic loading system takes place each time cracks develop within the structure; once cracking stabilizes, the load level before cracking is restored gradually and then more load is applied.) Unfortunately, experimental studies report only *stabilized* load-deflection curves. It would seem that most researchers accept the notion of strain softening and adopt it in their models, reasoning that it helps greatly with the control of cracking for a constant (analytical, but not experimental) load level and that it leads to more stable analyses; that this may not always be so will be explained below (but, in any case, analytical expedience certainly does not help justify the supposedly real existence of strain softening). The comparing of the present SCA to a form of strain softening (see Phillips in reference 108) is misleading, since the adoption of the SCA stems from the use (on obvious grounds of computational economy) of finite load-step increments. In the limit, if the load step were to become sufficiently small for one crack only to form within that particular load increment, the SCA and TCA would be entirely equivalent, with the puzzling situation in which the postulated 'form of softening' would become load-step dependent.

Finally, and despite claims to the contrary (Phillips in reference 108), the SCA does not lack objectivity since it always allows a crack to occur at the most critical stress-combination location independently of load-step size (allowance of more than one crack is simply an economic option in the case of a large number of Gauss points). Furthermore, as mentioned previously, the load level in actual tests is increased until unloading occurs as a result of crack propagation, i.e. until failure (cracking) conditions are met at the most highly stressed part of the structure; therefore, the SCA appears to be quite realistic even from a phenomenological point of view.

It has been suggested that all three runs pertaining to beam OA-1

(Figs 4.1 to 4.3) reveal spurious mechanisms, thus affecting every instance of prediction of the failure load (de Borst in reference 156). However, this is true only as regards the under-integrated element combined with the use of the Newton–Raphson method (Fig. 4.1). Thus, Fig. 4.1(b) shows a clear instance of early divergence due to the propagation of an ‘hourglass’ mechanism in the bottom zone of the mesh. As is well known, this type of local mechanism does not require any strain energy to propagate, but gives rise to huge displacements and, consequently, to huge strains and stresses that may exceed several times the order of magnitude of the stresses of the failure envelope. This is why the divergence criterion (in practice, very rarely attained) based on a maximum residual force exceeding 100 times the total load (i.e. 22500 kN in this run!) was reached. It is important to point out that the facility for plotting the last performed iteration (load step ‘777’) is especially useful for such a case, since the plot and the stresses of the last converged load step indicated that the beam was far from having reached the ultimate condition. On the other hand, the crack patterns corresponding to Figs 4.2 and 4.3 indicate quite clearly that structural failure is imminent so that the local mechanisms exhibited by Figs 4.2(b) and 4.3(b) correspond to post-peak behaviour and consequent ill-conditioning of the stiffness matrix under constant external load.

In order to query the present findings that reduced integration tends to give better results than full integration, arguments have been invoked with regard to the issue of mesh discretization (a finer discretization being used for the calculation with reduced integration — three elements over the height instead of two) and the belief that a small portion of the post-failure regime must be simulated before a statement on structural failure can be made (de Borst in reference 156). As to the first of these arguments, it needs only to be pointed out that different Gaussian integration orders imply different FEs since they lead to different stiffness matrices and hence, strictly speaking, to different discretizations. One way of comparing performances is, of course, the use of two meshes with the same number of degrees of freedom: this, in fact, was done for the example of the prism, the fully-integrated mesh being finer in terms of the number of Gauss points. On the other hand, with regard to the nonlinear analysis of concrete structures, the Gauss point carries the elementary unit of material information and, hence, one could argue that two FE meshes should also be compared in terms of their Gauss-point discretization: in the case of the analysis of the over-reinforced beam, this criterion was adopted by using meshes that are comparable (depthwise) in terms of Gauss points (and computational effort). The second argument, namely the notion that divergence of the iterative procedure does not automatically imply structural failure, is, by itself, a fair point, but one which should not be invoked independently of the

divergence criteria used. In this respect, it is important to recall (see section 2.4.2.6) that the present model's convergence checks are quite demanding: these include the requirements for small residual forces, small residual stresses at cracked Gauss points, and no violation of the failure envelope at any Gauss point irrespective of the angle between prior and subsequent cracks at any such point. The latter requirement is often violated by many a model based — usually in an attempt to compensate poor structural characteristics (e.g. stiffness) stemming from unrealistic material modelling — either on fixing the direction of second cracking perpendicular to the first (whether the cracks themselves are fixed or allowed to rotate) or on the use of 'threshold' angles between first and second cracks — see, for example, de Borst and Nauta¹⁵⁸ as well as their copious list of references. Here, it is worth pointing out that the restriction of threshold angles leads, in practice, to less restrictive convergence criteria as it amounts to the ignoring of spurious cracking deemed to be excessive as a result of overly predictions of stresses when the fully-integrated serendipity element is used. That such an approach is rather unreliable and arbitrary is evident when consideration is given to the wide range of threshold angles and shear-retention factors that must be called upon in order to obtain reasonable predictions from problem to problem (see, for example, references 158 and 160).

It is interesting to address the question of numerical instability encountered by those authors who adopt a strain-softening model, and who attribute such instabilities — at least partly — to the 'hourglass' mechanism that seems to arise as a consequence of under-integration.^{159,160} and even full integration.¹⁶⁰ A possible reason for such instability with inadequate load predictions may lie with the notion that stiffness — whether real or artificial — attracts loading. Now, in strain-softening models, first cracking is followed by a descending stress-strain branch, but the numerical procedures tend to rely on the secant approach, and this results in a considerable overestimate of the stiffness in the region of the crack. Therefore, once the peak tensile strength has been attained, the descending branch implies either unloading and subsequent reloading (in which case the secant stiffness does overestimate the stiffness in the region of the crack, hence resulting in an artificial attraction of loading) or, if the path does not deviate from the descending portion, the stiffness contribution is negative, a factor unlikely to improve matrix conditioning. Such effects (or, rather, their combinations) are very similar to the mixed Newton-Raphson procedure where the lack of immediate updating of the stiffness of newly-cracked zones may lead to early numerical instabilities, as shown in Fig. 4.1. A further source of local stiffness comes from the adoption of relatively high values of SRF. Such stiffening effects attract loading that may cause further cracking which would not occur in a physically brittle material where, once cracking

occurs, there is a complete local unloading. (It must be said, however, that the modelling of brittle material behaviour is not free from spurious cracking since even the small value of SRF used (and which is needed for stability, as explained in section 2.4.3.4) may lead to artificial stiffening of a crack zone; it is partly in coping with such spurious effects that some of the strategies outlined in the present section have been found useful.) Potential instabilities are further compounded when negative SRF values (shear softening) are adopted (e.g. reference 160). Again, the same reasoning to that just used in pointing to the possible effect of strain softening in the $\sigma-\epsilon$ relation applies to the $\tau-\gamma$ descending branch, so that combinations of (high) positive and negative SRF values is a potential source of numerical instability. On the other hand, as the softening diagrams for β , as the strain across the crack increases, tend to a zero value,^{73,160} their implementation can cause numerical difficulties when $\beta \leq 0.1$ for the reason adduced in section 2.4.3.4.⁵⁶

In view of the above reasoning, the predominant tendency of most analysts to devote the bulk of their efforts to modelling the post-cracking behaviour at the material level, despite the fact that the stiffness of cracked concrete zones is significantly lower than that of uncracked concrete regions, must be queried. Hence, while in reality the load attracted by cracked concrete is insignificant, the post-cracking characteristics imposed on the various models result in an artificial attraction of load to regions essentially devoid of stiffness, with consequent numerical instabilities that often lead to spurious results; and this is the reason why many analysts maintain that 'the numerical modelling of post-cracking behaviour can have a crucial effect on the analysis' (e.g. Phillips in reference 108). On the other hand, the present approach is based on the argument that, instead of creating numerical instability through post-cracking 'features' that are of no structural relevance, crack description should concentrate on eliminating — or at least minimizing — numerical problems. It should be stressed that such an approach does not 'ignore' post-cracking behaviour (see Phillips in reference 108); instead, this is described in a simple manner: i.e. allowance is made for the occurrence of first and second cracking (without restrictions on crack orientation), which causes partial loss of load-carrying capacity and, eventually, third cracking which is equivalent to a complete loss of load-carrying capacity. However, post-cracking features used by others, which artificially exaggerate the actual stiffness of cracked concrete, are ignored; therefore, the present approach takes account of both physical reality (low stiffness of cracked concrete) and numerical practicality (minimizing the risk of numerical instability). Clearly, although free from the physical aberrations and numerical complications implicit in strain-softening models, the brittle material model cannot by itself avoid numerical instability in all cases (even when coupled

with the apparently favourable effect of under-integration — see Fig. 4.1): in addition, a judicious choice of iterative technique is vital, as shown in this and the following section.

4.3. Performance of the three-dimensional finite-element model

In this section, the performance of the 3-D package is summarized on the basis of what constitutes possibly the most thorough study^{56,161,163–165} of the objectivity and generality of any concrete FE model to date (whether two-dimensional or three-dimensional). With the material input limited to the two parameters f_c and $\beta = 0.1$, a 'constant' (or, rather, consistent) FE model requires a similarly suitable choice of those procedural components of the package which are essential for an effective implementation of the material model and whose effects can be determined with reasonable certainty only through a set of numerical experiments. Thus, on the basis of an objectivity study of three structural forms (with the investigation encompassing the optimum iterative method, the number of cracks allowed per iteration, the FE type (especially in respect of the under-integration or full integration of the usual quadratic elements), the degradation of the **D**-matrices upon cracking, etc.), the best numerical strategies were established which then, too, became 'constant' parameters for general use. Once this was achieved, the generality of the model was tested on a further set of five structural components of wide-ranging type and complexity.

4.3.1. Objectivity study

Studies of the objectivity of nonlinear FE models for concrete are relatively scarce. Clearly, a complete study of all the factors affecting nonlinear predictions of concrete structures cannot be achieved owing to time and resource limitations. It is for this reason that a preliminary consideration of the problem^{56,161} isolated those parameters for which there is universal agreement or which, on the basis of previous parametric studies, may be determined with a fair degree of certainty. Then, a selective choice of those parameters which, from among the remaining factors, appeared to be more relevant, was made as the basis of the objectivity study.

It could be said that the three fundamental advances achieved in the FE analysis of concrete structures relate to the introduction of the smeared technique, the use of the residual-forces method, and the adoption of multiaxial concrete properties. In addition, a large number of other factors exist, relating either to the definition of material properties/parameters (e.g. post-peak characteristics of the stress-strain relations, aggregate interlock, tension stiffening, dowel action, bond between steel and concrete — henceforth 'material' factors) or to the procedural effects stemming directly from the FE analysis itself (e.g. iterative method, number of cracks allowed per iteration, FE chosen, mesh definition, numerical-integration rule — henceforth 'objectivity' factors). With regard to the material factors, most of which have already been discussed, it is important to recall that, in the proposed model,

both the constitutive laws for concrete and its failure criteria require only a simple parameter for their definition, namely the uniaxial cylinder compressive strength f_c . Undoubtedly, f_c presents less scatter in comparison with other parameters relating to concrete properties, such as the uniaxial tensile strength, initial Young's modulus, fracture energy, etc. Therefore, the adopted law for concrete appears to be the first important source of objectivity of the present model, since the value of f_c is generally reported and is usually reliably obtained, while other properties are rarely measured and, when they are, their accuracy may be open to question. The second and last material parameter required in the present model is the SRF. Even though it was pointed out earlier that predictions are not greatly affected by values of β between 0.1 and 0.5, and the fact that the use of $\beta = 0.5$ may sometimes play a compensating role for the stiffness underestimate stemming from the neglect of the tension-stiffening effect (thus improving certain displacement predictions⁵⁴), the adoption of $\beta = 0.1$ has been argued both from a physical point of view and on grounds of numerical stability. The only material factor that remains to be considered, therefore, refers to the question of whether the constitutive **D**-matrices of regions where the failure envelope has been reached a third time ought to consist of null coefficients (version Z3) or should retain the βG diagonal terms corresponding to the degraded shear stiffness (version G3). Both options must, therefore, be investigated in the present objectivity study.

The objectivity factors related to the numerical analysis which are relevant to the FE modelling of concrete structures, and whose influence is still open to discussion (for a comprehensive bibliography, see reference 56) are: procedures to simulate the rate of macrocracking; iterative technique; propagation of spurious mechanisms; FE mesh; FE type (especially in respect of the Gaussian-integration order). The options for some of these factors in the present numerical investigation are discussed below.

As outlined in section 2.3.2 (see also Fig. 2.9), the FEs used in the 3-D model are the 20-node serendipity element (HX20) and the 27-node Lagrangian element (HX27) for concrete modelling; and a three-node parabolic element (LM03), with axial stiffness only, for reinforcement bars. These elements are probably the most extensively used 3-D FEs, with proven performance in linear problems, and they can be found in any FE textbook. All of them are isoparametric with parabolic shape functions and, hence, they can adjust to non-straight boundaries. While the numerical integration of the Lagrangian element is always carried out by means of the $3 \times 3 \times 3$ rule, two Gaussian-integration rules are considered for elements HX20 ($2 \times 2 \times 2$ or $3 \times 3 \times 3$ Gauss points) and for element LM03 (2 or 3 Gauss points, depending on the order of integration adopted for the associated brick elements). Although the Lagrangian element requires a larger

computational effort than the 20-node FE, its use is adopted for comparison purposes. In addition, as the 27-node element includes a complete second-order polynomial, it may improve 20-node predictions in problems with a large number of degrees of freedom (DOF) by reducing round-off errors.⁹⁶ Moreover, the Lagrangian element allows a more flexible distribution of steel bars because of its mid-face and centre nodes. (In the case of the serendipity element, of course, the steel elements must coincide with the edges of the solid elements.) On the other hand, on account of its large number of DOF, the Lagrangian element is more likely to lead to singularities if under-integrated than is its serendipity counterpart (reference 61; see also section 2.3.2); accordingly, the $3 \times 3 \times 3$ rule was adopted whenever the former element was used. Finally, it should be noted that other non-Gaussian integration schemes^{166,167} — e.g. 15 integration points for element HX20 — can reduce the computational effort for elements HX20B and HX27. However, they were not considered owing to their irregular pattern, which would have made difficult the post-processing of cracking plots and stress results.

The adoption of a (incremental) pure Newton–Raphson technique (i.e. the updating of $[\mathbf{K}]$ at every iteration) is precluded in analyses of the present type if the computational effort is to be kept within sensible limits. On the other hand, the (incremental) modified or initial-stiffness Newton–Raphson method (INITK), which does not update $[\mathbf{K}]$ in the course of iterations, and the (incremental) mixed Newton–Raphson method (MIXNR), where $[\mathbf{K}]$ is updated every few (herein, every three) iterations, although cheaper, may create serious convergence problems. As discussed in section 4.2, such difficulties stem from the build-up of very large residual forces that may lead to non-convergent solutions (usually INITK) or to early divergent analyses owing to propagation of spurious mechanisms (especially MIXNR). It was also shown in section 4.2 that the strategy which combines both computational economy and numerical stability may be achieved by updating all \mathbf{D} -matrices at the first iteration of each load step and then only updating the \mathbf{D} -matrices pertaining to the two sources of high localized (i.e. ‘strong’) nonlinearities (cracking of concrete and yielding of steel) as soon as these nonlinearities occur; this strategy of selective updating will henceforth be referred to as the NR-plus method.

Since the cracking in the brittle model tends to produce large residual forces, the number of cracks allowed to form in a given iteration must be controlled in order to avoid numerical instabilities. Two extreme strategies were discussed previously: the ‘total-crack approach’ (TCA), which allowed all prospective cracks to occur at once; and the ‘single-crack approach’ (SCA), with allowance of the formation of only one crack at a time (the most critical one) before any others were considered. In the present FE model, the

more stable and reliable SCA is adopted (but, in order to study the objectivity of the model, some runs using the TCA in the plain-concrete examples were also considered). Here, it should be stressed that the term SCA is used in a somewhat more general sense, thus denoting those cases where cracks are allowed to occur 'in small (pre-determined) numbers' (as the allowance of only one crack would be very restrictive in certain problem types — especially in 3-D): more specifically, (up to) two new cracks per iteration for element HX20A ($2 \times 2 \times 2$ Gauss points), this number being increased (up) to three for elements HX20B and HX27 ($3 \times 3 \times 3$ Gauss points).

The influence of the above objectivity factors (and of the types of **D**-matrices for totally-cracked Gauss points) on the predictions of the present model was studied by reference to the following three structural-concrete elements, which are described below: a PC prism under strip load; an RC beam failing in flexure; and an RC beam failing in shear. The correlation with experimental data was based on the three main aspects of structural behaviour, namely the ultimate-load level, the crack pattern at this level, and the load–deflection curve.

4.3.1.1. Case study 1: PC prism under strip loading

This case study (CS1), based on one of the PC prisms tested by Niyogi¹⁰⁰ through the application of concentric strip loads over one-half of each end face ($f_c = 26.9 \text{ N/mm}^2$, ultimate bearing stress = 17.4 N/mm^2), was analysed in sections 3.2 and 3.3.1.1 by means of the 2-D package and subsequently re-analysed in section 4.2 through the 3-D formulation which was shown to be mandatory for a problem of this type. One of the 3-D FE meshes now used is shown in Fig. 4.5. (Owing to the existence of three planes of symmetry, only one-eighth of the prism is analysed.) The details of seven computer runs and the predictions of ultimate loads are summarized by the corresponding top rows in Table 4.1. The factors being investigated in the present case study are, mainly, the crack-propagation procedure, the adopted FE mesh and the type of FE. The iterative procedure (NR-plus method) is kept constant throughout, and the load step adopted corresponds to 1 N/mm^2 .

Figure 4.5 shows a comparison of the deflected shapes and the crack patterns for runs 1, 2 and 3 at several load stages up to failure. It should be noted that these runs relate to the same mesh (as in Fig. 4.4), but correspond to elements HX20A, HX20B and HX27 respectively; i.e. the first three runs in Table 4.1 aim at studying the effect of element type. As in the experiments, the crack patterns show that vertical cracks develop in the inner zone of the prism (under the strip load), such cracking being due to transverse tensile stresses, and results in the outwards expansion of the prism that leads to failure due to instability ('buckling') of the inner portion;

Table 4.1. Summary of objectivity study:¹⁶¹ numerical runs and comparison between analytical (MSL) and experimental (EXP) ultimate-load results

Case study*	Run	FE type	FE mesh (x, y, z)	TCA or SCA	NR strategy	Z3 or G3	MSL/EXP
(1)	1	HX20A	2 × 1 × 2	SCA	NR-plus	G3	1.10
	2	HX20B	2 × 1 × 2	SCA	NR-plus	G3	0.87
	3	HX27	2 × 1 × 2	SCA	NR-plus	G3	1.10
	4	HX20A	2 × 1 × 1	SCA	NR-plus	G3	1.16
	5	HX20A	4 × 1 × 4	SCA	NR-plus	G3	1.16
	6	HX20A	2 × 1 × 2	TCA	NR-plus	G3	1.10
	7	HX20A	2 × 1 × 2	SCA	NR-plus	Z3	1.10
(2)	1	HX20A	3 × 1 × 1	SCA	NR-plus	G3	0.88
	2	HX20B	3 × 1 × 1	SCA	NR-plus	G3	1.03
	3	HX27	3 × 1 × 1	SCA	NR-plus	G3	1.03
	4	HX20A	6 × 1 × 2	SCA	NR-plus	G3	1.03
	5	HX20B	6 × 1 × 2	SCA	NR-plus	G3	0.96
	6	HX27	6 × 1 × 2	SCA	NR-plus	G3	0.96
(3)	1	HX20A	10 × 1 × 3	SCA	INITK	G3	0.15
	2	HX20A	10 × 1 × 3	SCA	MIXNR	G3	0.60
	3	HX20A	10 × 1 × 3	SCA	NR-plus	G3	0.90
	4	HX20A	10 × 1 × 3	SCA	NR-plus	Z3	0.82
	5	HX20A	10 × 1 × 3	SCA	NR-plus (†)	Z3	0.82
	6	HX20B	7 × 1 × 2	SCA	NR-plus	Z3	0.67
	7	HX20B	7 × 1 × 2	SCA	NR-plus (†)	Z3	0.82

* (1) PC prism.

(2) RC beam failing in flexure.

(3) RC beam failing in shear.

(†) Runs ignoring residual forces for second and third cracking.

this is accompanied by some horizontal cracks which appear near the surface of the member as a result of the curvature that the above expansion, combined with the vertical settlement of the inner zone, induces on the outer part of the prism. With regard to the effect of element type, and as can be seen by reference to Fig. 4.5, the predictions of element HX20B for first cracking (11 N/mm²) and ultimate load (15 N/mm²) are less than for the other two FEs (i.e. 12 N/mm² and 19 N/mm² for such levels); this is likely to be due to a stiffer performance of element HX20B, which results in earlier cracking. Although the approximation to the experimental ultimate load is similar for the three elements (109%, 86% and 109% respectively), the results show that the analysis with element HX20B is less stable than the analysis with element HX20A. As already discussed in section 4.2, this contradicts the results of de Borst and Nauta¹⁵⁸ who, by means of a strain-softening model, reported that the use of under-integrated elements leads to early divergences with respect to their fully-integrated counterparts.

Runs 4, 1 and 5 correspond to three different meshes with 2, 4 and 16 HX20A FEs (96, 153 and 465 DOF respectively). The cracking plots for the maximum sustained loads (20 N/mm²,

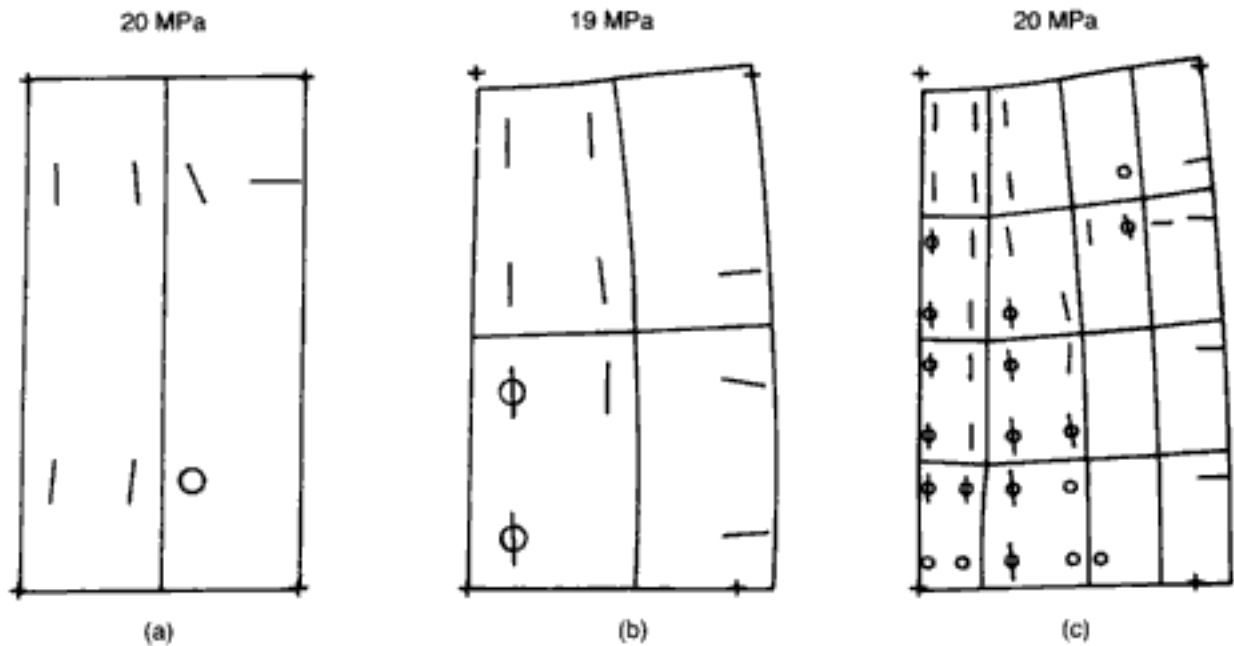


Fig. 4.6. PC prism under strip loading (CSI). Comparison of crack patterns and deformed shapes at maximum sustained loads:¹⁶¹ (a) two elements HX20A (run 4) (*D.M.* = 1); (b) four elements HX20A (run 1) (*D.M.* = 30); (c) 16 elements HX20A (run 5) (*D.M.* = 30)

19 N/mm² and 20 N/mm²) are shown in Fig. 4.6. Clearly, the mesh with two HX20A elements is a poor discretization of the prism, and this is reflected in the poor cracking pattern in Fig. 4.6(a). (Nevertheless, the prediction of ultimate load is as good as for the case with 16 elements.) With regard to the predictions for 4 and 16 elements, the increase in strength (although small) contradicts other work by Bažant and Cedolin,¹⁶⁸ which states that the refining of the mesh leads to increasingly lower predictions of strength for brittle concrete models. It is worth noting that the aspect ratio (width : height : depth) of individual FEs does not remain constant (1 : 4 : 2 for 2 elements, 1 : 2 : 2 for 4 elements, and 1 : 2 : 4 for 16 elements), and this can explain the small differences in ultimate-load predictions. It is also worth noting that the minimum size associated with the Gauss points is 25.4 mm, 25.4 mm and 12.7 mm respectively, so that further mesh refinements were not considered (following earlier discussion on minimum mesh size — section 2.5) since the maximum aggregate size used in the experiments was 13 mm.

The influence of the adopted crack-propagation procedure (SCA and TCA as defined previously) can be discussed by reference to runs 1 and 6 (element HX20A). For run 1, only up to two new cracks per iteration were allowed (i.e. 2/32 ~ 6% of the total number of Gauss points in the mesh), whereas all prospective cracks were allowed to form at any iteration for run 6. The same failure load and quite similar crack patterns are predicted in both cases. This is in contrast with previous predictions based on the 2-D model where the more stable approach (SCA) led to a poor prediction, a fact explained *on physical grounds* by the need to model the prism three-dimensionally. As discussed in section 3.2, the analysis of the same prism by means of the plane-stress model yielded a large

overestimate of the strength using the SCA (26 N/mm^2), while a good prediction was obtained when using the TCA. The current improvement of the objectivity of the analytical predictions can be explained by the expansion of the prism in the two transverse directions through 3-D modelling. A 2-D analysis can model only the main transversal expansion (shown in Fig. 4.5), while any expansion and secondary tensile stresses in the third direction (orthogonal to the plane in Fig. 4.5) are ignored as a result of plane-stress modelling. In this respect, Figs 4.5 and 4.6 show some circle symbols which, as explained earlier, stand for cracks forming an angle smaller than 45° with the plotting plane. Clearly, the plane-stress model could not detect this cracking, although, as explained in section 3.2, the TCA tends to cause early divergences due to explosive redistribution of residual forces, which happens to act as a compensating factor for what should, in effect, have been an overestimate. Clearly, when a 3-D analysis is adopted, the objectivity of the modelling is improved since the SCA always yields reliable estimates, as can be seen in Table 4.1 (runs 1–5, 7). The superior objectivity encountered in 3-D modelling may also be seen by the smaller discrepancy between the TCA and the SCA when compared with their 2-D counterparts. (In this particular case, both crack-propagation procedures yielded the same load predictions — and other such examples may be quoted⁵⁶ — but the more controlled release of residual forces by the SCA makes it generally more dependable from a numerical standpoint.)

With respect to the use of zero or residual βG values for the **D**-matrix of Gauss points with three cracks (Z3 and G3 **D**-matrices), the comparison of runs 1 and 7 is inconclusive, since no such third cracking takes place in the converged load steps. Finally, it is worth noting that all the predicted ultimate loads compare quite well with the experimental failure load (17.4 N/mm^2), and this is in spite of the difficulty of the analysis of this prism: the failure load is only 65% of its cylinder strength and corresponds to a minimum of the bearing strength-to-cylinder strength ratio (f_b/f_c) for strip loading (see Fig. 3.23). Although the experimental load–deflection curve is not reported by Niyogi¹⁰⁰ and, hence, no comparison with their analytical counterparts can be made, the numerical predictions for runs 1 and 3 are depicted in Fig. 4.7, showing the consistency of results stemming from Lagrangian and under-integrated serendipity elements.

4.3.1.2. Case study 2: RC beam under two-point loading failing in flexure

The second type of structural element used for the study of the objectivity of the model's predictions is an RC beam (beam B1) subjected to two point loads which failed in a ductile, flexural manner.²² Figure 4.8 shows the dimensions of the beam and the reinforcement detailing, while the experimental load–deflection

Fig. 4.7. PC prism under strip loading (CS1). Analytical load–vertical deflection (at the centroid of the loaded faces) curves for runs 1 and 3⁵⁶

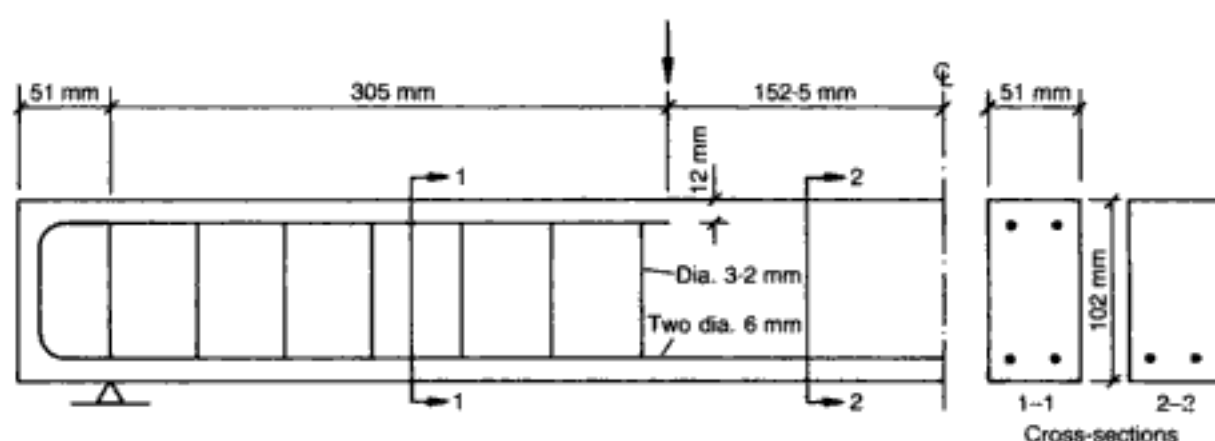
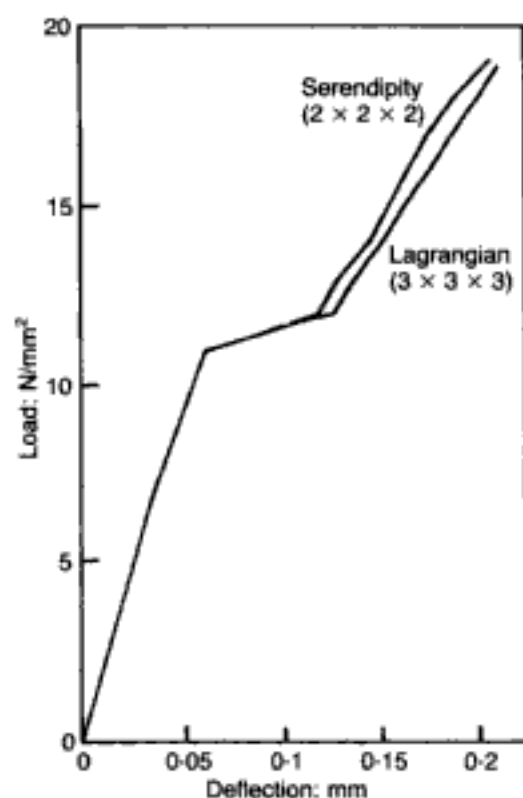


Fig. 4.8. RC beam under two-point loading (CS2). Dimensions and detailing of reinforcement^{22,56}

curves are depicted in Fig. 1.78. The ratio of shear span to effective depth (a_v/d) is equal to 3.33 and the percentage of tension steel is 1.2%. Transverse reinforcement was provided within the shear span so as to prevent a shear failure. In this respect, the experimental failure load (13.6 kN) is very close to the flexural failure load predicted by means of some current codes (e.g. BS 8110,⁵⁵ ACI 318–83,¹³⁰ CEB–FIP 78¹⁶⁹) when the experimental values $f_c = 37.8 \text{ N/mm}^2$, $f_y = 417 \text{ N/mm}^2$ are adopted (although, as explained in section 1.5.2, the experimental measurements of strains contradict the usual hypothesis of concrete behaviour governed by uniaxial σ – ϵ characteristics).

Figure 4.9 shows one of the two meshes used for the analysis of the beam, only one-quarter of which is analysed on account of symmetry. It should be noted that the cover of the tension steel

Hidden page

(SCA), the iterative technique (NR-plus method) and a constant load step of 1 kN are the same for all runs. It should be noted that runs 1, 2 and 3 relate to the same number of FEs. Runs 4, 5 and 6 are based on the element types used in runs 1, 2 and 3 respectively, but with double the mesh refinement (12 brick elements).

It may be interesting to note that, while the example of the prism under strip loading was used extensively for checking the subroutines of the computer program relating to cracking, this example was used for checking subroutines relating to the steel FE. After some trial runs, it was observed that yielding of steel (whether first or second) is a process that converges very slowly unless the (tangent) Young's modulus of the yielding locations is updated (e.g. if $f_y = 417 \text{ N/mm}^2$, as in the present example, $E_t \sim 200\,000 \text{ N/mm}^2$, $34\,000 \text{ N/mm}^2$ and 500 N/mm^2 for the 1st, 2nd and 3rd linear branches). Since the updating of the 3-node steel elements requires little computational effort (when compared with the concrete brick FEs), it was decided to update the properties of all the steel elements should any local yielding occur. During the early runs of this example, it was noticed that cracking was also a relevant source of slow convergence unless the cracked **D**-matrices were introduced into the set of equations instead of keeping the uncracked **D**-matrices. Furthermore, updating of all brick elements was found to be inefficient, since new cracks concentrated in one or two elements. Therefore, it was considered that updating of the **D**-matrices of the newly-cracked Gauss points — and recalculation of the **k**-matrices containing such Gauss points — simultaneously improved convergence and saved the high computing cost of updating the **D**- and **k**-matrices of the remaining brick elements. In this respect, it is worth noting that recalculation of the **k**-matrices of the 12 brick elements in a mesh such as that in Fig. 4.9 requires approximately the following number of multiplications: 544 000, 1 844 000 and 3 335 000 for elements HX20A, HX20B and HX27 respectively. The above computational economy explains why the method NR-plus was derived, even though similar predictions as with the mixed Newton–Raphson were obtained for both this beam and the prism under strip loading: i.e. there were no numerical-stability arguments requiring the use of the NR-plus strategy at this stage. As indicated in Table 4.1, the SCA was adopted in all runs. The number of new cracks allowed per iteration was equal to 2 for element HX20A, and 3 for elements HX20B and HX27.

Figure 4.10 shows a comparison between experimental and predicted (runs 4 and 5) load–deflection curves. The predictions of displacements are fairly good ($\sim 20\%$ larger than the experimental values at around 10 kN) up to the load level at which the steel yields in the analyses, and then become increasingly larger

Hidden page

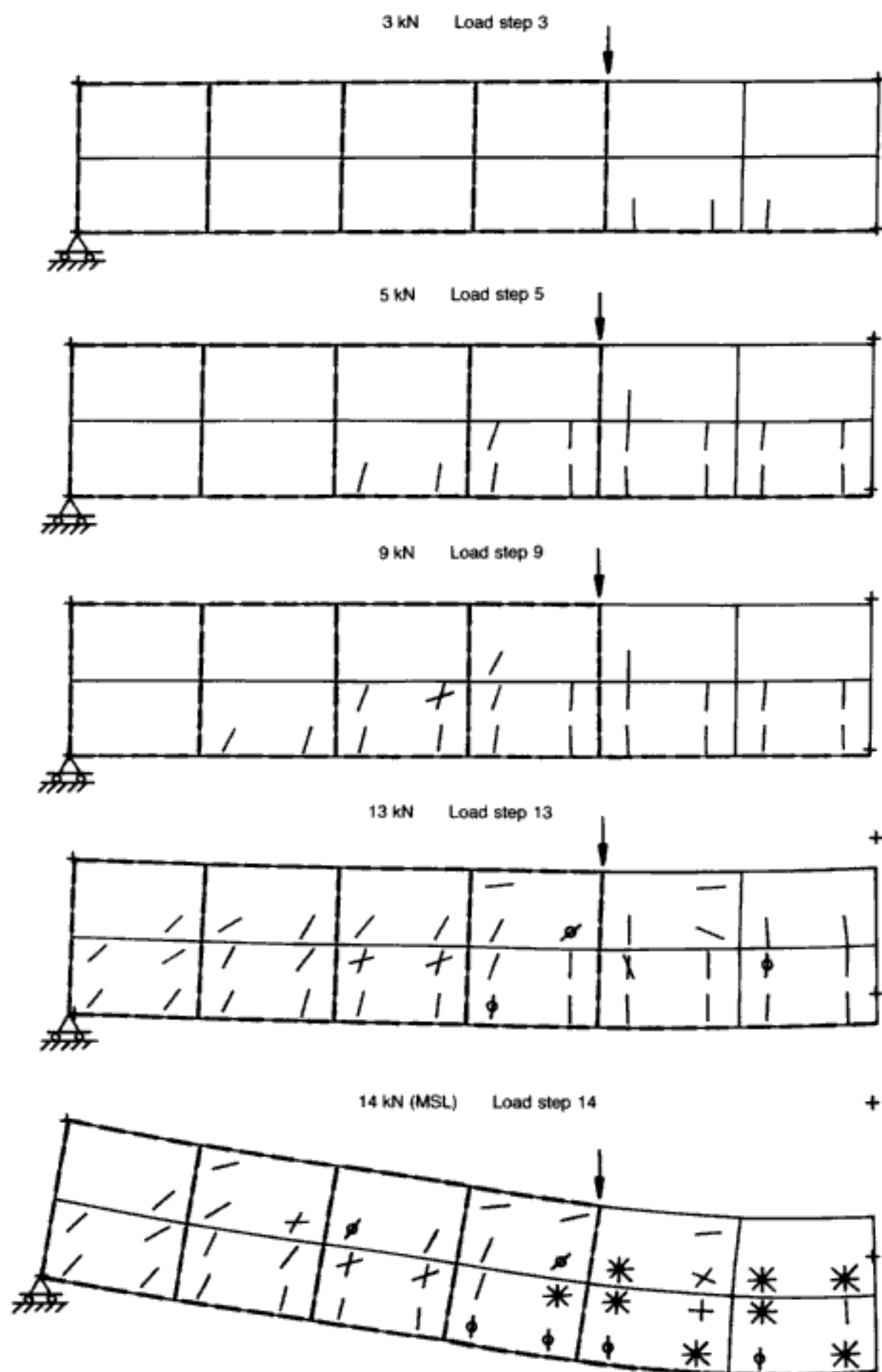
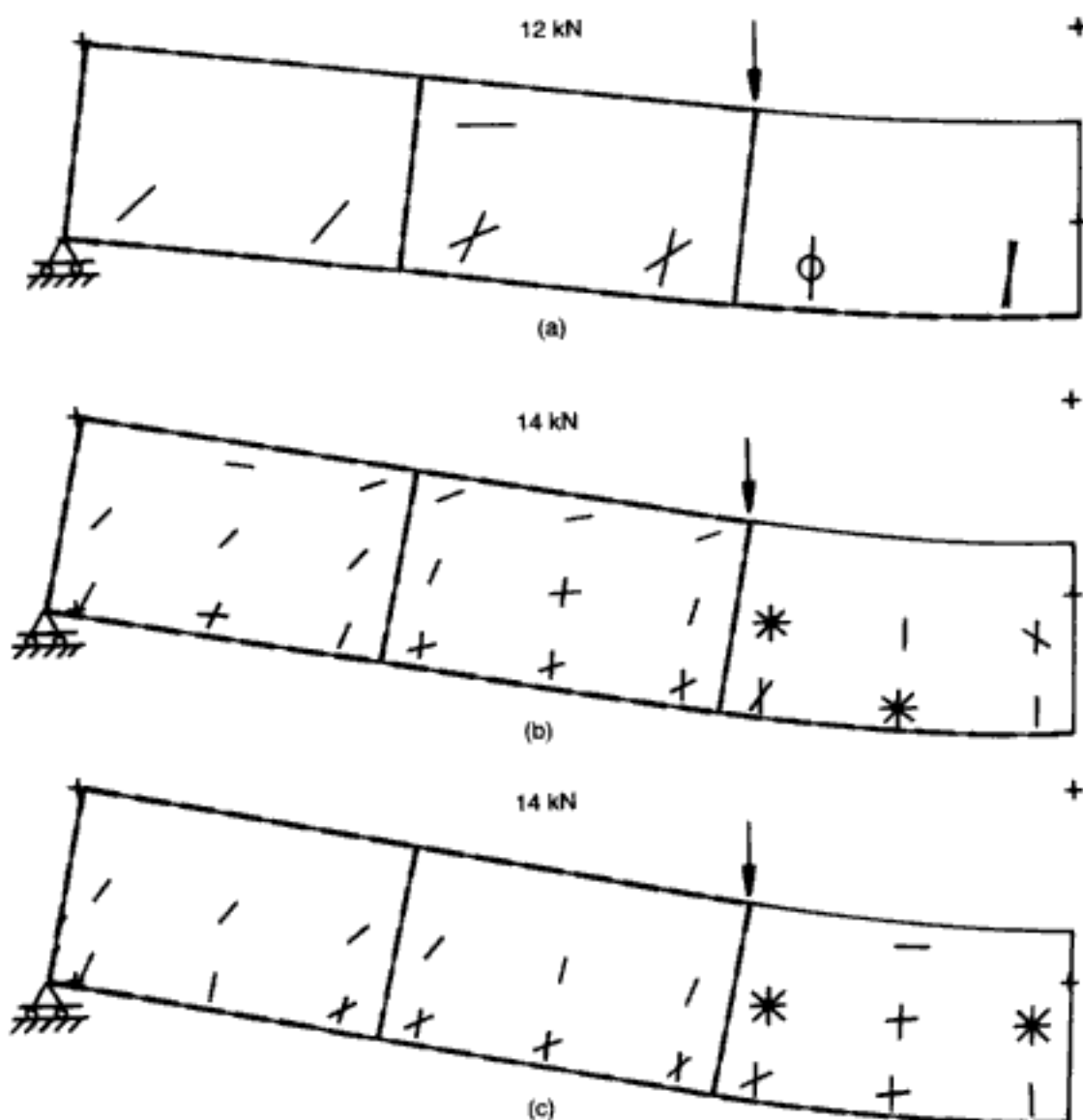


Fig. 4.11 (facing). RC beam under two-point loading (CS2). Crack patterns and deformed shapes at various load stages for run 4 (12 HX20A elements)¹⁶⁵

Fig. 4.12. RC beam under two-point loading (CS2). Crack patterns and deformed shapes at maximum sustained loads for a three-element mesh.¹⁶¹ (a) element HX20A (run 1); (b) element HX20B (run 2); (c) element HX27 (run 3)

within the compressive zone splits at 13 kN, but does not fail in compression, and this is another typical example of why strain-softening modelling in compression may be regarded as irrelevant for practical analyses.

The relative performance of the three FE types and the effect of the mesh size may be seen by reference to Figs 4.12 and 4.13. The main point to stress is the excessive cracking within the compressive path that is predicted by means of element HX20B (Figs 4.12(b) and 4.13(b)). As for the case of the prism under strip loading, this indicates that this element is overly stiff. Finally, it should be noted that the predicted failure loads are quite reasonable in all cases, since even for run 1 — where the mesh is very rough (especially in respect of the 'equivalent' distribution of vertical reinforcement) — the predicted failure load is 88% of the experimental value, while for runs 2 and 3 the prediction is excellent, even though the coarse mesh is retained. Therefore, the predictions appear to exhibit little sensitivity to the adopted FE mesh.



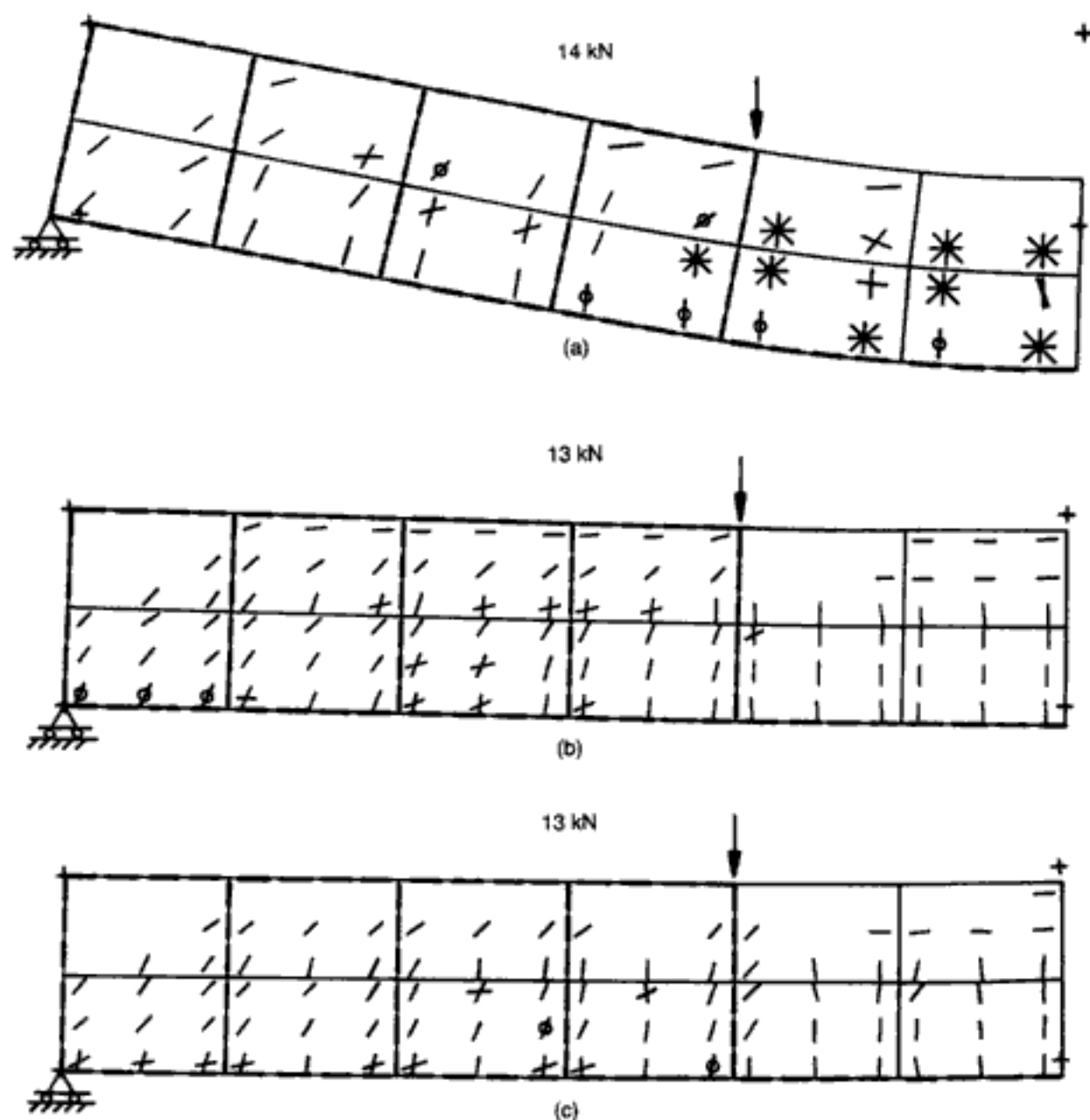


Fig. 4.13. RC beam under two-point loading (CS2). Crack patterns and deformed shapes at maximum sustained loads for a 12-element mesh.¹⁶¹ (a) element HX20A (run 4); (b) element HX20B (run 5); (c) element HX27 (run 6)

4.3.1.3. Case study 3: RC beam without stirrups under central point loading failing in shear

The last type of structural element in the present study of the objectivity of the model is the over-reinforced RC beam without stirrups reported by Bresler and Scordelis¹¹⁶ as beam OA-1. The dimensions of the beam and detailing of the tension reinforcement (anchored at both edges in order to prevent a bond failure) are shown in Fig. 3.49. The ratio of shear span to effective depth (a_v/d) is equal to 2.97 and the percentage of tension steel is 1.8%. High-strength steel ($f_y = 555 \text{ N/mm}^2$, $f_u = 958 \text{ N/mm}^2$) was used for the tension reinforcement so as to prevent a ductile failure. As pointed out in section 3.4.1.3, the beam failed in shear at 334 kN (6.6 mm of midspan deflection) without yielding of

the tension bars. Had it been attained, the flexural failure load would have been 508 kN.¹¹⁶ The shear-failure load predicted by current codes is 130 kN for CEB-FIP 78,¹⁶⁹ 236 kN for ACI 318-83¹³⁰ and 285 for BS 8110⁵⁵ (assuming a partial safety factor for concrete equal to 1). The shear failure was preceded by diagonal cracking from about 80% of the failure load (267 kN). Bresler and Scordelis do not report the crack pattern for beam OA-1 (12 ft), but report the crack pattern for beam OA-2 (15 ft, Fig. 3.49(b)) as typical for beams OA-1, OA-2 and OA-3. It is worth noting that beams OA-1 and A-1 (without and with stirrups, respectively — see section 4.3.2.2 for beam A-1) and/or beams OA-2 and A-2 have been the object of a number of FE studies^{73,78,85,159,170,171} which indicate the difficulties encountered in their nonlinear FE analysis.

Figure 4.14 shows the FE mesh used for the analysis of beam OA-1 by means of the serendipity element (only one-fourth of the beam is shown (and used in the analysis) on account of symmetry). As usual in analyses of this type, all the reinforcement was concentrated at a distance from the top face equal to the effective depth (the actual detailing used in the experiment consisted of two layers as indicated in Fig. 3.49(a)), the resulting cover being neglected, i.e. 95 mm out of the 556 mm of total depth were ignored. This deviation from the experiment is relevant in terms of the deformational response (though unlikely to affect greatly the ultimate-load prediction in view of the negligible contribution of cracked areas to the transfer of shear forces), but it was introduced so as not to run very large examples during the initial development of the present model because of limitation of computer resources. Nevertheless, as this section deals with the objectivity of the model, the accurate modelling of experimental data is not the principal aim, and hence the ensuing comparison between predictions for different numerical runs is not invalidated.

The details of seven computer runs and the resulting predictions of ultimate loads by reference to the corresponding experimental load are summarized at the bottom of Table 4.1. The effects of the iterative technique and of the order of numerical integration for element HX20 are now the main factors being studied. In all runs, the SCA (2 cracks per iteration for element HX20A and 3 cracks for element HX20B) and a constant load step of 25 kN were adopted.

Run 1 corresponds to the use of the INITK procedure, in which the stiffness matrix of the structure is never updated. The first cracks occurred at a load level of 75 kN (22% of the experimental failure load), and subsequent iterations — following the initial (uncracked) stiffness approach — did not yield a convergent solution, since the stresses orthogonal to the cracks were always larger than the maximum allowable residual-stress criterion (0.1 N/mm^2 — see section 2.4.2.6). Therefore, this run had to

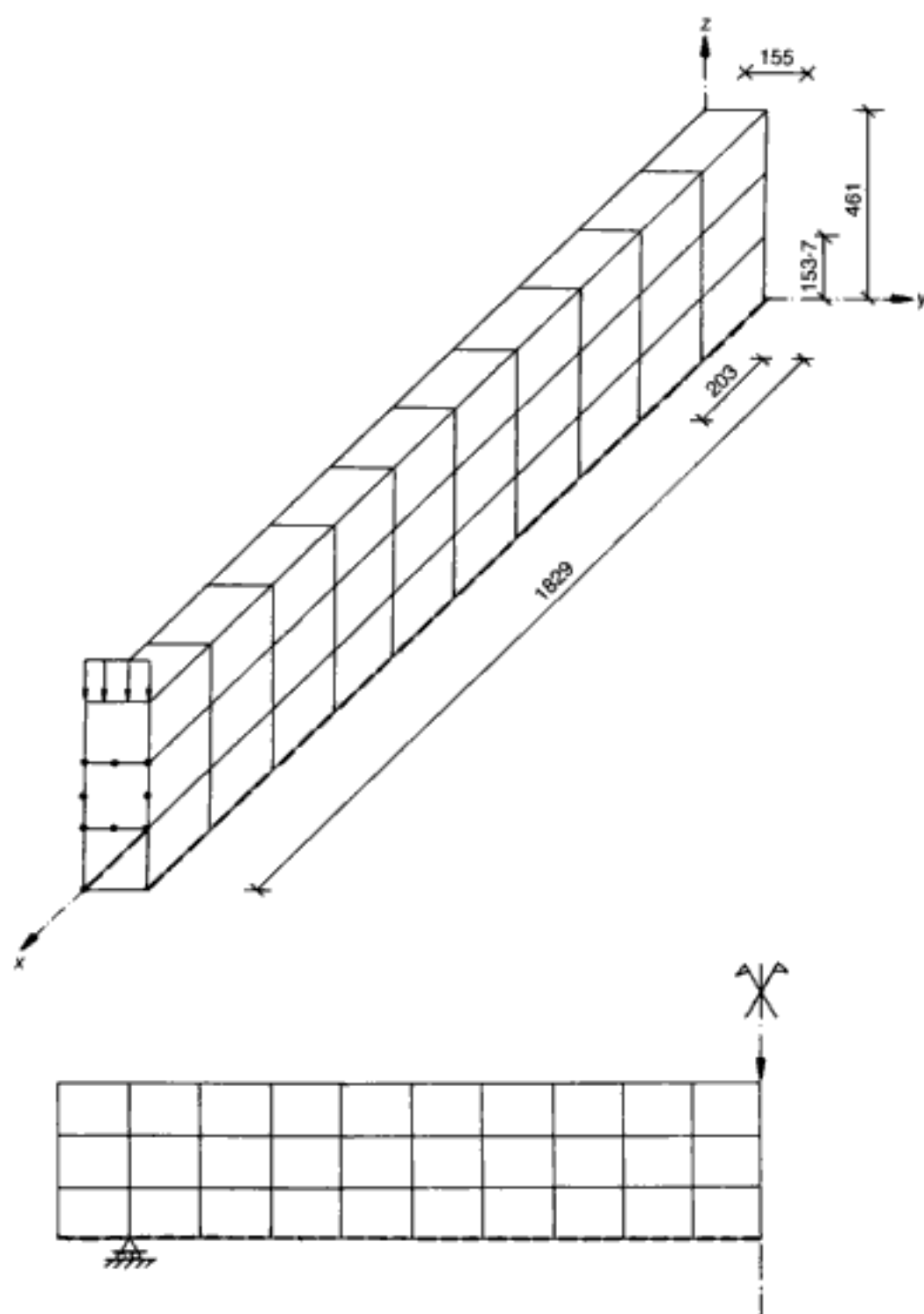


Fig. 4.14. RC beam without stirrups under central point loading (CS3). FE mesh for one-quarter of the structure, consisting of 30 brick elements (all dimensions in mm)¹⁶¹

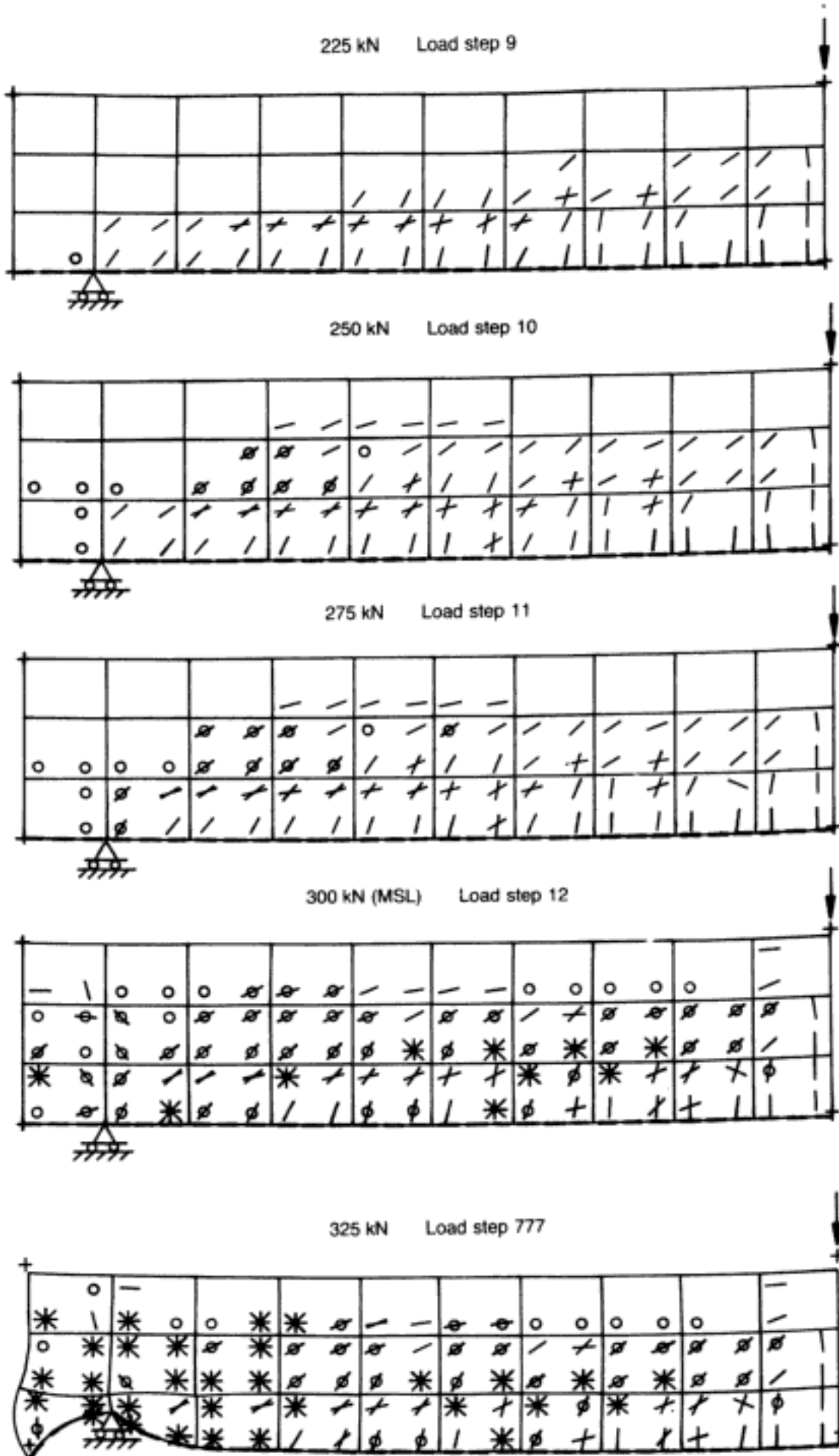
be aborted manually after several hundreds of iterations corresponding to an execution time similar to the rest of the runs in Table 4.1.

The numerical problems associated with run 2 were discussed in section 4.2, so as to illustrate the difficulties that might result from the MIXNR strategy (all the **D**-matrices of the mesh were updated every three iterations). The maximum sustained load and the load corresponding to the last performed iteration were 200 kN and 225 kN respectively (see Fig. 4.1), the crack pattern for the

latter load step showing an instance of early divergence due to the propagation of an 'hourglass' mechanism (spurious mechanism) in the bottom zone of the mesh. As mentioned in section 4.2, it is significant that Crisfield¹⁵⁹ reported a numerical instability in a 2-D analysis of beam OA-2 (using under-integration) due to post-cracking strain-softening concrete modelling at a load level of 44% of the experimental failure load; although the present analysis does not incorporate post-cracking strain softening, it appears that the use of the mixed Newton–Raphson method has a similar effect.

Figure 4.15 shows the deflected shapes and crack patterns at various load stages for run 3, which corresponds to the use of the NR-plus method. In contrast to run 2 (MIXNR method), the 'hourglass' mechanism in Fig. 4.1(b) (at 225 kN) does not occur, and the analysis proceeds up to a divergence load of 325 kN. (The corresponding MSL of 300 kN constitutes the best prediction of failure load from among seven runs.) It is important to recall that the NR-plus method immediately updates the **D**-matrices of newly-cracked Gauss points and, therefore, the actual stress–strain relation is strictly followed (with the stress across the crack suddenly dropping to zero upon cracking), while the use of the MIXNR method causes a 'search-for-convergence path' stress–strain relation that is similar to a strain-softening branch.⁵⁶ (Imagine Fig. 2.14(b) as the first of a sequential set of non-updated iterations, with the locus of their (decreasing) peak stress values resembling a falling branch.) The predicted crack-propagation process is as follows (Fig. 4.15). The first cracks take place for a load of 75 kN (22% of the experimental failure load), and subsequent cracking gradually propagates in depth and towards the support up to 225 kN (67%). A number of second cracks occur in the same zone where the above spurious mechanism propagated (see Fig. 4.15 for 200 kN). These cracks occur as a result of the presence of the SRF in the cracked **D**-matrices which, while required for numerical stability, stiffens (in shear) such Gauss points. In this respect, it can be argued that, should shear transfer across cracked areas be relevant in physical terms (e.g. owing to the often-postulated aggregate interlock), its modelling by means of a constant SRF would cause branching of the cracks, since even a small β ($= 0.1$) causes second cracks in the analysis; such additional cracking, however, is not observed in practice (see section 3.4.1.2). At a total applied load of 250 kN (75%), cracking affects suddenly the region where the compressive-force path changes direction (compare the predicted crack patterns for 225 kN and 250 kN in Fig. 4.15). It is worth noting that the latter cracking is similar in position and direction to the diagonal crack observed in the test (Fig. 3.49(b)). In the analysis, this cracking stabilizes in this and in the following load steps, and subsequently (300 kN) propagates towards the point load. Divergence of the iterative procedure takes place at 325 kN of total applied load as a result

Hidden page



of multiple cracking in the region of the support (see load step '777').

It should be noted that several Gauss points exhibit third cracks for run 3 at load step 12 (300 kN), which was attained on the basis of the use of the G3 option. On the other hand, the numerical procedure did not sustain this load level when a zero **D**-matrix (Z3 option) for such Gauss points was incorporated in run 4, for which the maximum sustained load became 275 kN.

Run 5 was carried out in order to assess the influence of second cracking on the prediction of the ultimate load, which is often said to be beneficial and/or relevant in numerical predictions. In this respect, it is worth noting that Ottosen¹⁷⁰ reported that the modelling of second cracks produced earlier divergence, and a more accurate prediction in the analysis of beam OA-2 (Ottosen's procedure predicted a significant gain in strength above the true load when second cracks were ignored). Therefore, run 5 does this partially by ignoring the residual forces caused by the second (and third) crack at a given Gauss point. As indicated in Table 4.1, the MSL remains the same (i.e. runs 4 and 5) for the present model with under-integration (see below for the case of full integration). However, the crack patterns of the last load stages for run 5 (Fig. 4.16) exhibit somewhat less multiple cracking, which for the present structural element may be regarded as 'spurious' cracking caused by artificial stiffening in shear caused by β . Nevertheless, the ignoring of any type of crack in certain cases appears to be a way of compensating for the limitations of the method of analysis; it is strongly recommended, therefore, that it should be avoided.

Finally, runs 6 and 7 correspond to the use of the NR-plus method and element HX20B ($3 \times 3 \times 3$ Gauss points). The FE mesh now differs from the mesh used earlier (runs 1 to 5) in that the number of FEs is smaller (14 elements instead of 30 — see Fig. 4.17) but relates to an increased discretization in the number of Gauss points (three layers, instead of two, giving still a total of 6 Gauss points in depth and 18 Gauss points between the support and the point load); hence the computational effort is similar for the two meshes. As Fig. 4.18 indicates, the deformational response of run 6 is slightly stiffer than that corresponding to the use of the under-integrated element (run 3), but all 3-D runs underestimate the true stiffness as cover is neglected. (In this respect, a 2-D analysis⁵⁴ that allowed for the total depth of the actual beam improved the stiffness prediction (while overestimating considerably the strength), as may be seen in Fig. 4.18. The 2-D analysis used $\beta = 0.5$ but even the run with $\beta = 0.1$ gave good stiffness correlation although this was slightly less accurate than the plot for $\beta = 0.5$;⁵⁴ the fact that $\beta = 0.5$ improves stiffness correlations over $\beta = 0.1$ is probably due to the higher SRF acting as a compensating factor for the neglect of tension stiffening in

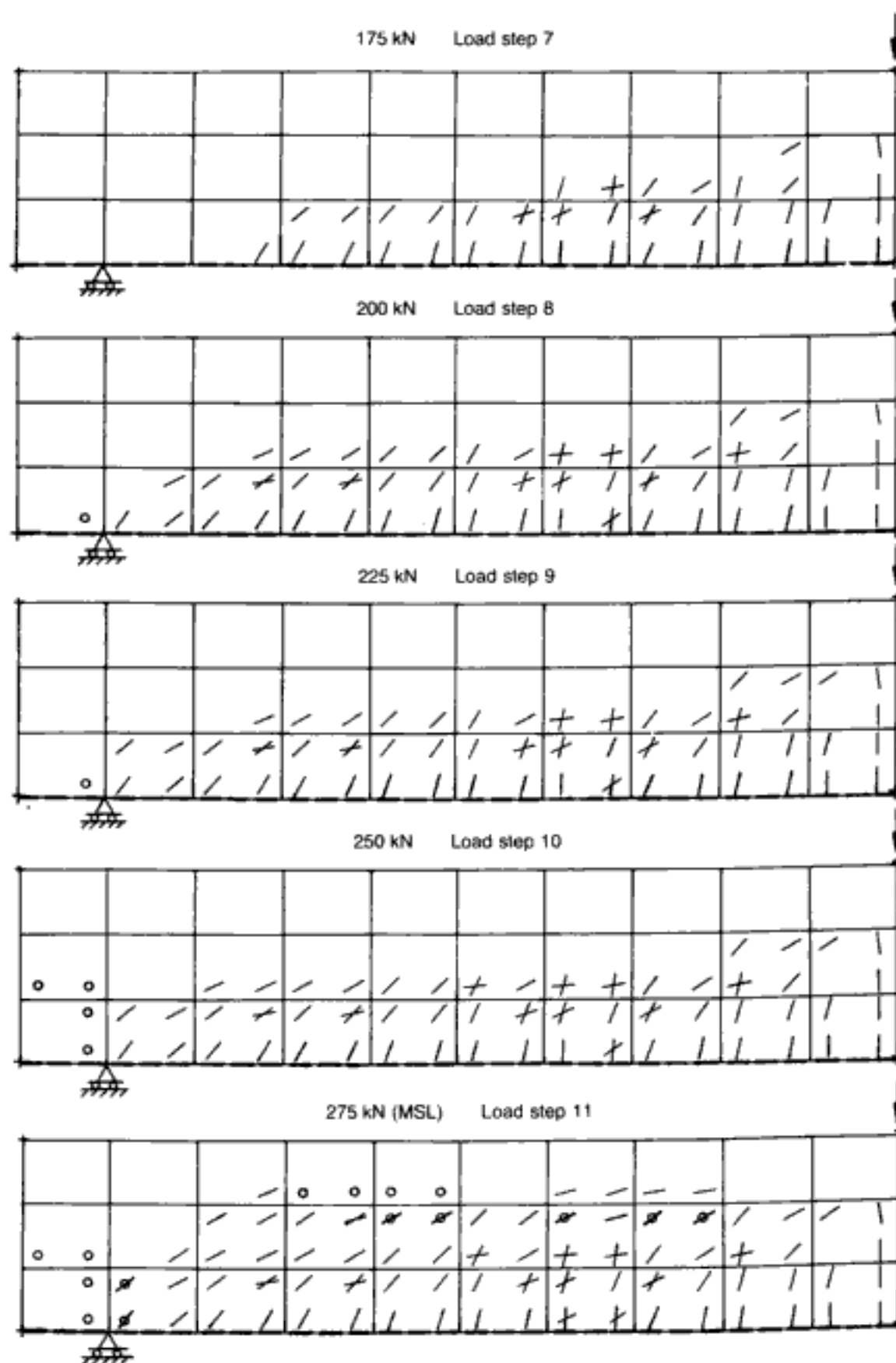


Fig. 4.16. RC beam without stirrups under central point loading (CS3). Crack patterns and deformed shapes at various load stages for under-integration combined with the ignoring of residual forces for second and third cracking (run 5)⁵⁶

Hidden page

Hidden page

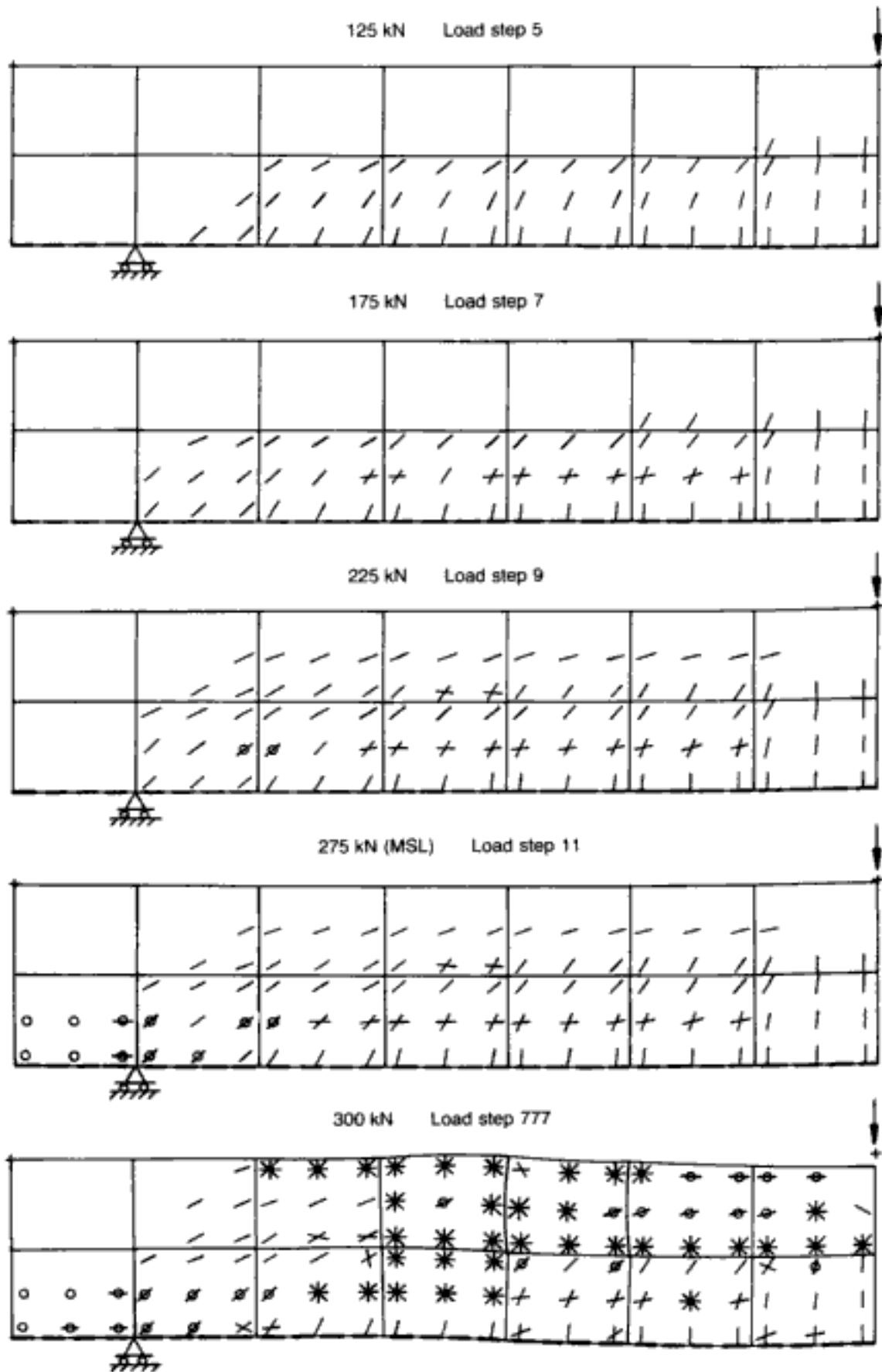


Fig. 4.19. RC beam without stirrups under central point loading (CS3). Crack patterns and deformed shapes at various load stages for full integration combined with the ignoring of residual forces for second and third cracking (run 7)¹⁶¹

Hidden page

Hidden page

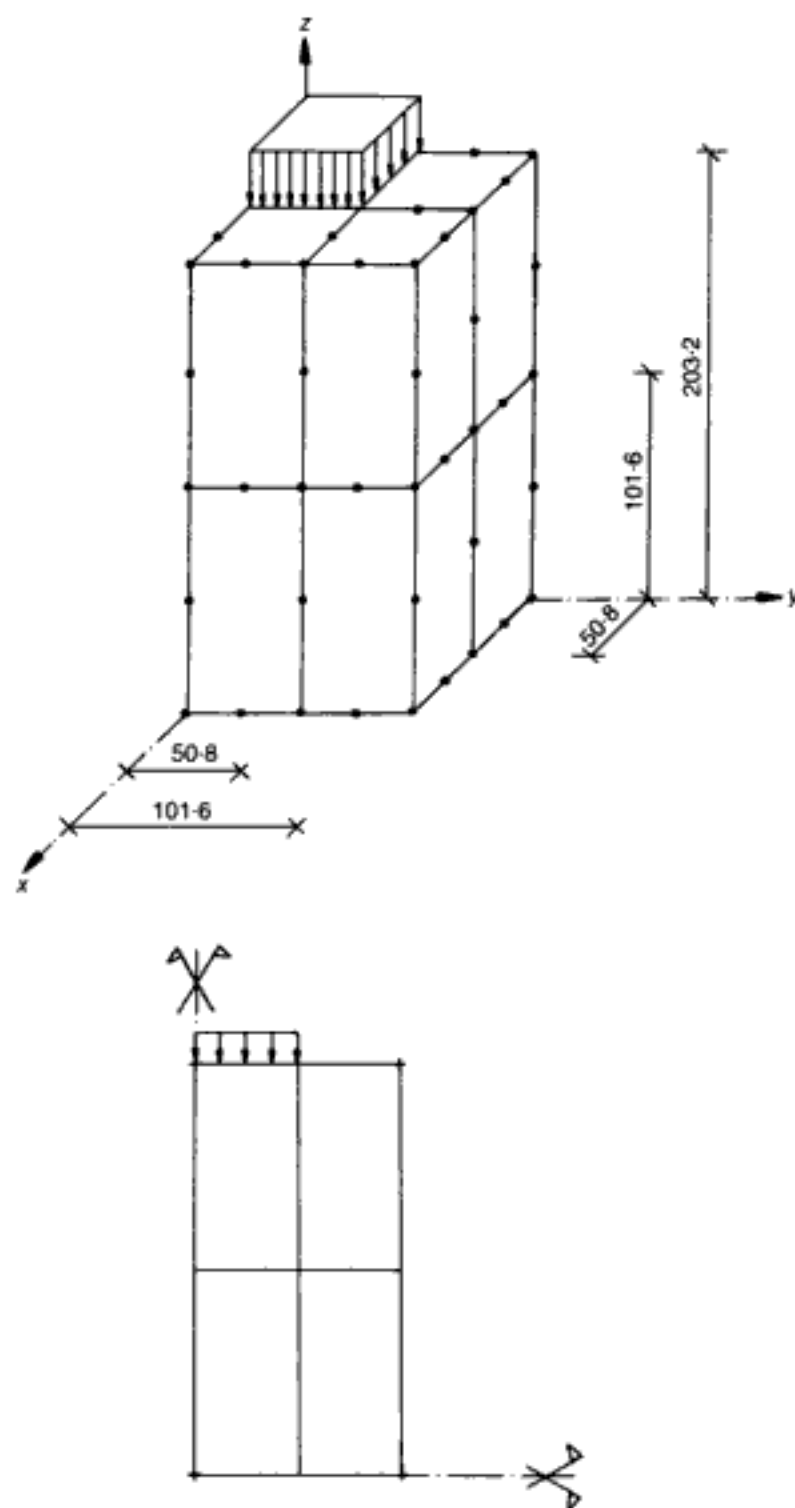


Fig. 4.20. PC prism under patch loading (CS4). FE mesh for one-eighth of the structure, consisting of eight brick elements (all dimensions in mm)¹⁶⁴

conditions, as shown in section 3.3.3. This is why two types of loading condition had to be considered in the present study. The first loading type is a uniformly distributed load, and this relates to a flexible bearing plate. The second type of loading is a constant applied displacement imposed at all nodal points of the loading area, which relates to a rigid bearing plate. For the latter case, the solution procedure is as follows (notation as in section 2.6): calculate nodal loads due to applied displacement ($-\mathbf{[K_{ur}]} \Delta d_r$), solve for unknown displacements ($\Delta d_u = \mathbf{[K_{uu}]^{-1}} \cdot (-\mathbf{[K_{ur}]} \Delta d_r)$),

Hidden page

TCA option instead of the SCA one, the predicted f_b result being unchanged (i.e. $MSL/EXP = 0.66$). This confirms the apparent lack of sensitivity of the 3-D model in PC analysis to the crack-propagation procedure noted earlier. Also, González Vidosa reported no difference between the G3 and Z3 options, noting that this is mainly due to the above-mentioned coincidence of first cracking and failure loads. Finally, it should be pointed out that, since the experimental load-deflection curve was not reported, no comparison can be made between analysis and test data of this type.

4.3.2.2. *Cast study 5: RC beam with stirrups under central point loading failing in shear*

This structural element is the over-reinforced RC beam with stirrups reported as beam A-1 by Bresler and Scordelis.¹¹⁶ It is similar to beam OA-1 (CS3), the difference being the addition of shear and compression reinforcement. The experimental details of beam A-1 (12 ft) and the experimental crack pattern of beam A-2 (15 ft) — the latter being reported as typical for both A-1 and A-2 — are as shown in Fig. 3.51. The failure of the beam was brittle and took place at 467 kN without yielding of the tension bars (the flexural failure load would have been 563 kN).¹¹⁶ Diagonal cracking began at the same load level as for the beam without stirrups (267 kN), but did not lead to collapse. Failure eventually occurred as a result of splitting of the compressive zone in the vicinity of the point load (see Fig. 3.51(b)). It is worth noting that beam A-1, too, is notorious in the difficulties as regards both code provisions (the approximate gain in strength with respect to beam OA-1 predicted by most current codes is only about 60% of the actual (experimental) gain) and analytical (existing 2-D) analyses (see below).

Figure 4.22 shows the FE mesh used for the analysis of beam A-1. Such a mesh is identical to that used for beam OA-1 (see section 4.3.1.3), but it now incorporates more steel elements in order to assess the effect of the additional transverse and compression reinforcement on the analytical prediction. As for beam OA-1, the cover of the tension reinforcement has been neglected, the relevance of which will be discussed later. Since the spacing of the stirrups is almost equal to that in the actual beam (203 mm instead of 210 mm), the adjustment required to keep the area per unit length the same was minimal. The compression steel was placed at the top face, and this also appears to be a relatively minor deviation from the test.

The MSL in the analysis is 450 kN, which compares well with the experimental failure load (467 kN). Figure 4.23 shows the crack patterns at various load levels up to failure. These patterns indicate that the fracture processes of the beam with stirrups (A-1) are quite similar to those of the beam without stirrups up to a total applied load equal to 225 kN (see Fig. 4.15 for beam OA-1). On the other

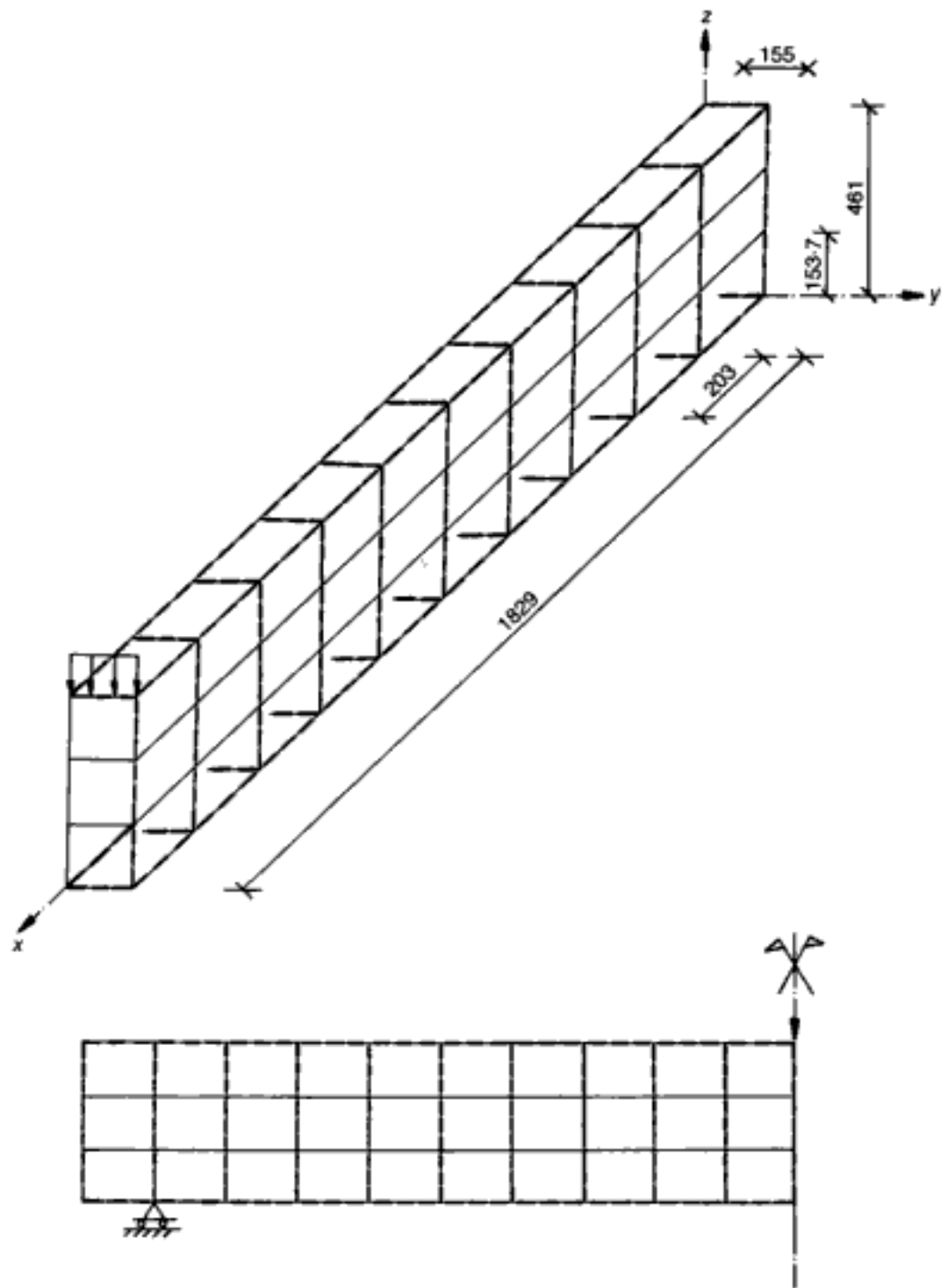


Fig. 4.22. RC beam with stirrups under central point loading (CS5). FE mesh for one-quarter of the structure, consisting of 30 brick elements (all dimensions in mm)¹⁶⁴

hand, the diagonal cracking that takes place suddenly in the analysis of beam OA-1 at 250 kN is delayed by the presence of stirrups, and it occurs gradually as the load increases (see Fig. 4.23 for 300 kN, 375 kN and 450 kN). The splitting of the compressive zone initiates at 350 kN, but does not lead to immediate collapse of the beam since the stirrups confine the compressive zone. As can be observed by reference to the crack pattern of the last performed iteration (load step '777' (475 kN) in Fig. 4.23), failure

Hidden page

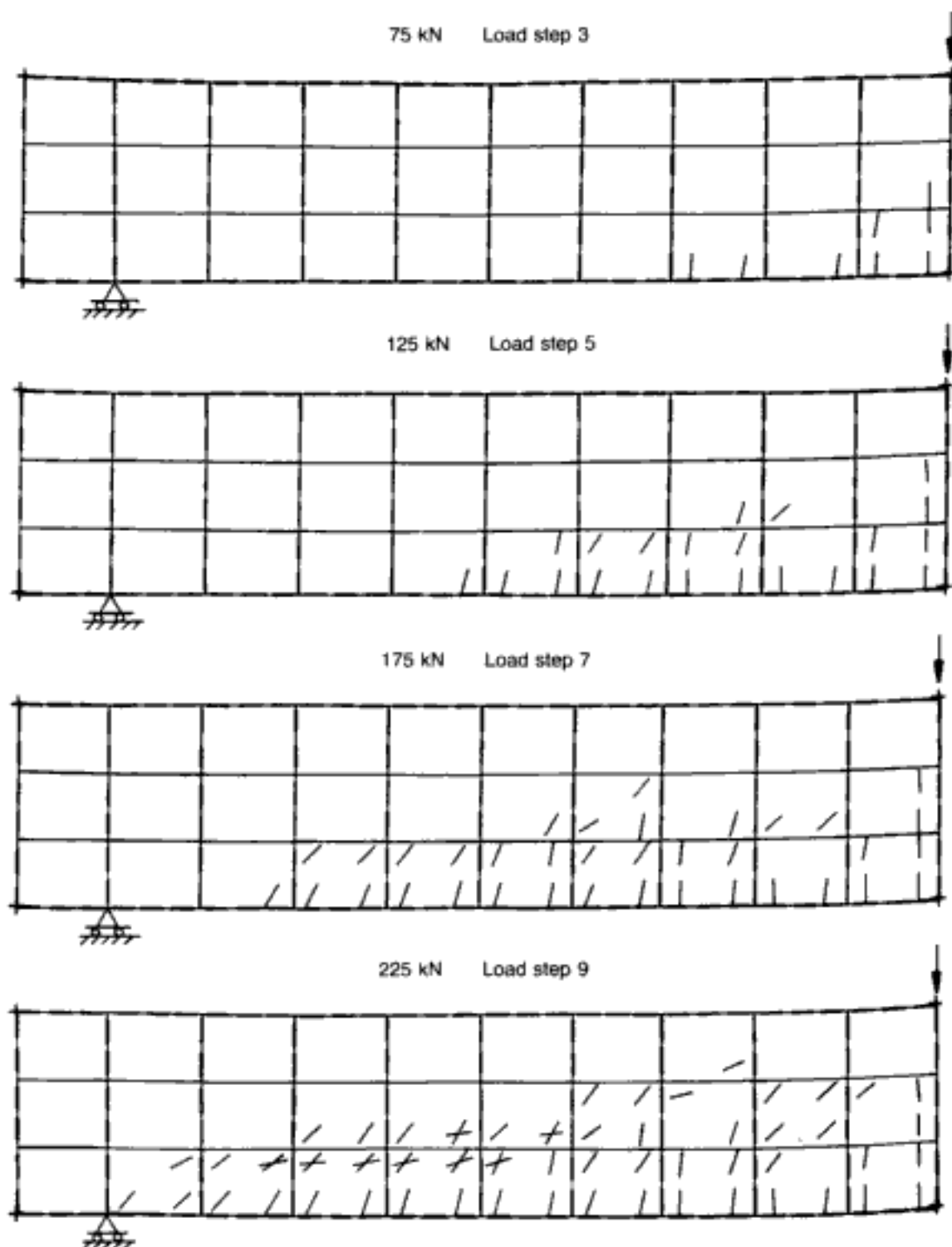


Fig. 4.23 (above and facing). RC beam with stirrups under central point loading (CS5). Crack patterns and deformed shapes at various load stages¹⁶⁴

loads at 200 and 1000 mm from the centreline. The beam is just under-reinforced, since the percentage of tension steel (consisting of 2 dia. 20 high-yield deformed bars) referred to the effective depth (set at 240 mm) is 2.75% whereas the corresponding balanced percentage is 3.2%. The web reinforcement comprises 2 dia. 1.6 vertical legs (as in section a-a in Fig. 4.25) spaced at 75 mm from the support up to the first point load, and at 25 mm from the latter up to a distance of 100 mm past the second point

Hidden page

The main feature of the beam is that it attained its full flexural capacity (just over 80 kNm) despite the high shear forces acting along the member and the low amount of web reinforcement. In this respect, Fig. 4.26 shows the bending-moment and shear-force diagrams corresponding to the experimental failure load (240.1 kN) and the ultimate shear force at the cross-section just to the left of the second point load that can be sustained according to the current American and British codes for structural concrete (about 13% and 19% of the experimental value respectively). As mentioned above, this beam was designed in compliance with the

Table 4.2. Comparison between experimental and analytical failure loads reported by several authors for beam data drawn from reference 116, including numerical case studies of beams OA-1 and A-1 modelled by the present 3-D package^{161,164}

Reference	OA-1 (1)	A-1 (2)	(2)/(1)	OA-2 (3)	A-2 (4)	(4)/(3)
Bresler and Scordelis ¹¹⁶ (experiments)	334	487	1.40	355	489	1.38
Cedolin and Dei Poli ⁷³ (2-D)	400	500	1.25	—	—	—
Ottosen ¹⁷⁰ (2-D)	—	—	—	358	405	1.13
Bédard and Kotsovos ⁸⁵ (2-D)	410	470	1.15	—	—	—
Balakrishnam and Murray ¹⁷¹ (2-D)	343	427	1.24	400	445	1.11
Present FE model ^{161,164} (3-D)	300	450	1.50	—	—	—

Fig. 4.24. RC beam with stirrups under central point loading (CS5). Comparison between experimental and analytical load-deflection curves¹⁶⁴

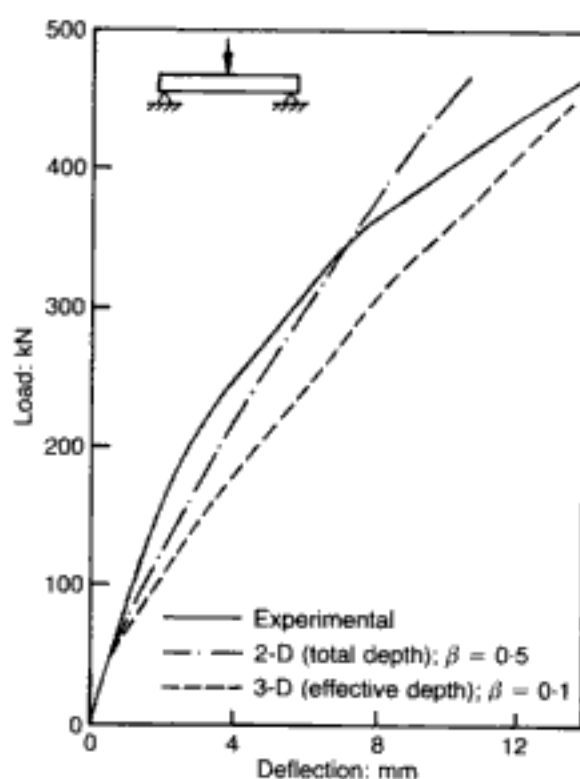


Fig. 4.25. RC T-beam under four-point loading (CS6). Experimental data: dimensions and detailing of reinforcement (all dimensions in mm)^{3,56}

concept of the CFP, its design details being significantly different than those specified by current code provisions.

Figure 4.27 shows the FE mesh used for the analysis of the T-beam (only one-quarter of which is considered due to the relevant symmetries). Such a mesh comprises 50 under-integrated 20-node elements for the concrete and 102 3-node elements for the reinforcement. A few relatively minor changes in the actual

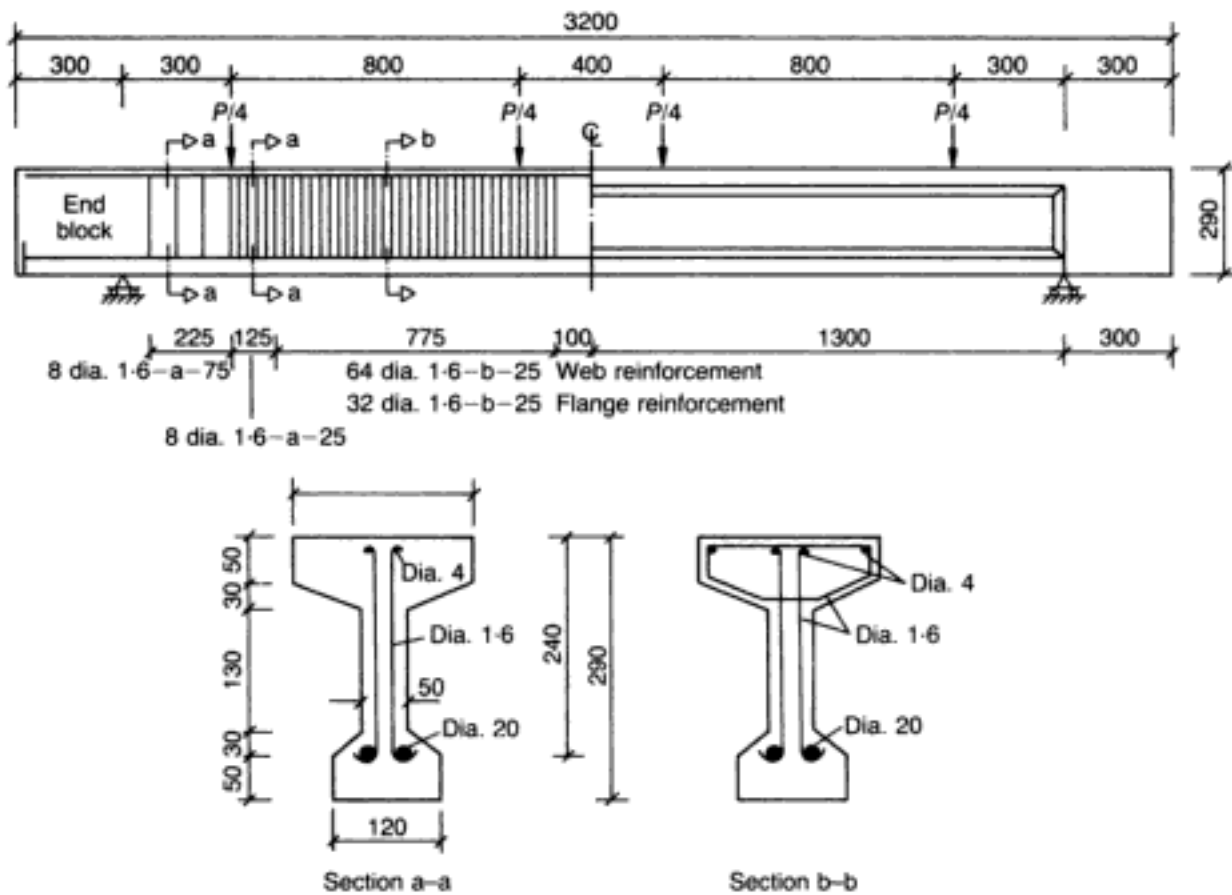
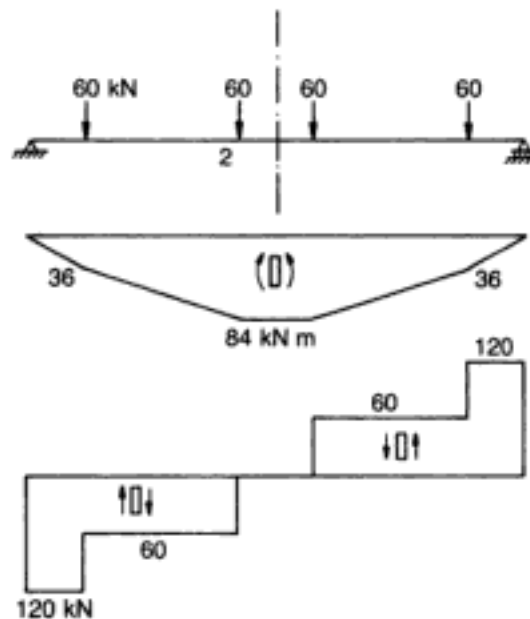


Fig. 4.26. RC T-beam under four-point loading (CS6). Bending-moment and shear-force diagrams for the failure load⁵⁶ (the maximum shear force that can be sustained according to ACI 318-83 and BS 8110 at cross-section 2 equal 8.1 kN and 11.4 kN, respectively — assuming partial safety factors equal to 1)



Hidden page

dimensions of the span and position of the loads were introduced, so as to use a regular mesh. Thus, the distance to midspan is 1280 mm instead of 1300 mm, the distance from the support to the first point load is 320 mm instead of 300 mm, and the length in pure flexure is 160 mm instead of 200 mm. As regards the tension reinforcement, it was 'smeared' to neighbouring brick edges in order to avoid two additional rows of brick elements (i.e. 20 HX20A extra elements); nevertheless, the total steel area and the effective depth are equal to those of the actual beam. More important deviations from the test were introduced in the modelling of the transverse reinforcement and the geometry of the cross-section near the support, the relevance of which will be discussed below and further investigated in section 4.5. First, the area of the transverse bars was adjusted so as to keep the same area per unit length as in the test; here, it must be noted that the spacing in the analysis is substantially higher (160 mm) than that in the test (75 mm and 25 mm). Secondly, no transverse reinforcement was provided in the analysis at locations past the central point loads as one moves away from the supports. Thirdly, the end block of the beam was ignored in the modelling.

The MSL in the analysis is 172.8 kN which is 72% of the experimental failure load (the load at which divergence takes place is 184.3 kN (77%)). Figure 4.28 shows the analytical crack patterns at various load levels up to failure (a comparison between experimental and analytical load-deflection curves will be given in section 4.5). The first flexural cracks appear within the flexural span at 23.0 kN and, subsequently, diagonal cracks oriented from the support to the point loads develop throughout the web of the beam (see Fig. 4.28 for 57.6 kN), in agreement with the experimentally observed crack pattern.³ Apart from a few additional cracks within the bottom part of the flange, the fracture process is almost stabilized up to a load level equal to 161.3 kN. At the MSL (172.8 kN), the stress of the tension reinforcement within the flexural span is just around the value of the experimental yield stress of the material ($f_y = 500 \text{ N/mm}^2$ for the dia. 20 bars). The divergence of the analysis occurs at 184.3 kN, and is triggered by the occurrence of vertical cracks within the compressive zone of the flexural span (see circle symbols at the top right-hand side of the patterns for 172.8 kN and 184.3 kN in Fig. 4.28, indicating fracture planes quasi-parallel to the longitudinal elevation view); these vertical cracks (additional to the (also critical) horizontal cracks indicated by the dashes) caused the symmetrical splitting of the cross-section of the beam, the T-section breaking up into two L-shaped halves. In this respect, it should be noted that the FE discretization does not incorporate the actual web and flange reinforcement (which delays the critical horizontal and vertical cracks respectively) past the central point

Hidden page

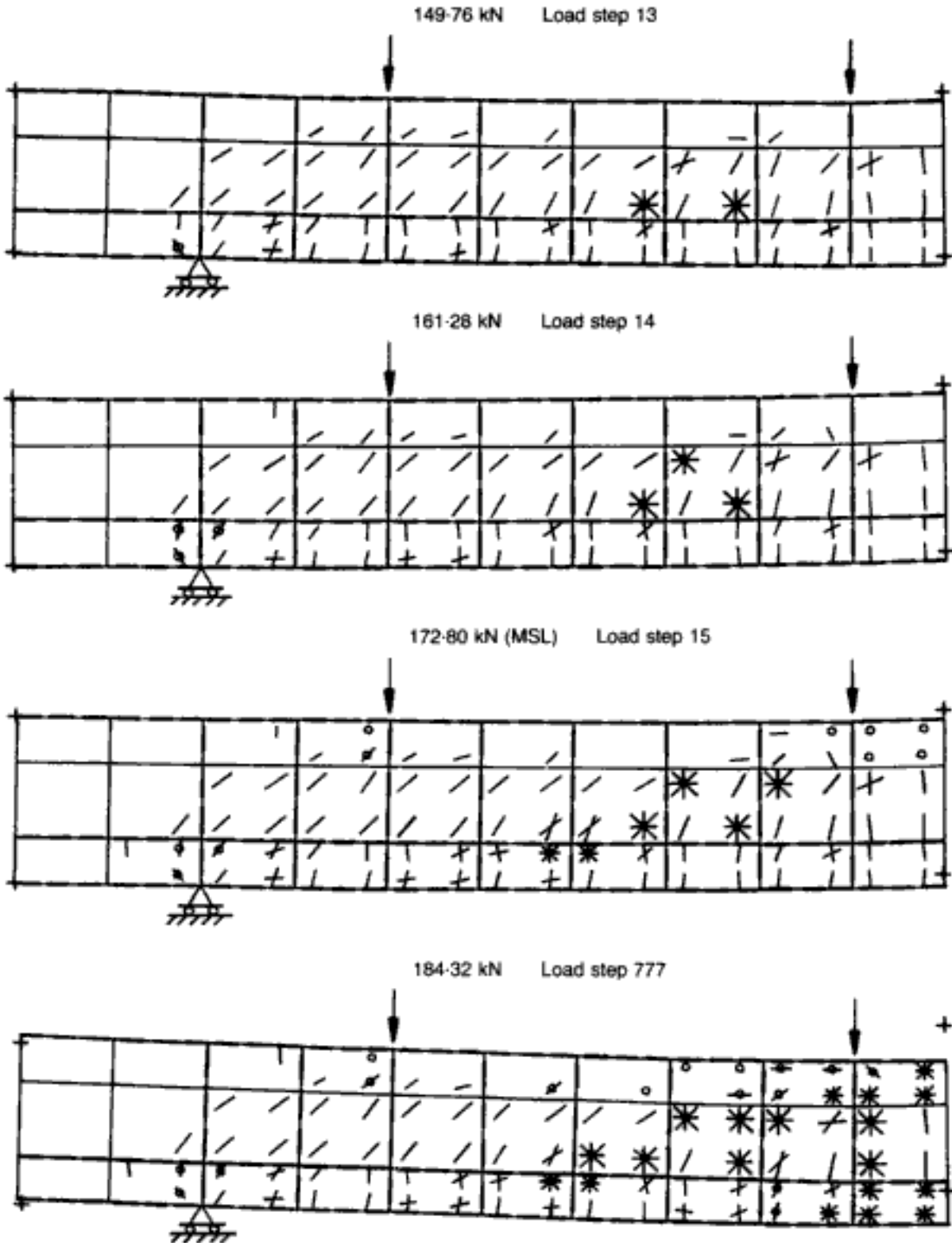


Fig. 4.28 — continued I-) section. In fact, the actual test specimen consisted of a solid rectangular cross-section throughout the length of the overhangs, which added to the overall member strength by impeding significant early cracking around the support; such cracking, however, may be seen in Fig. 4.28 for the simplified FE model used, where several multiple cracks cluster right next to the concentrated reaction. Clearly, such findings warrant a further analysis that

includes both the additional transverse reinforcement referred to above and the change in cross-section beyond the support, and such an analysis is reported in detail in section 4.5. For present purposes, it is helpful to summarize its main findings.

The fact that the somewhat disappointing modelling of the experimental strength of the member ($MSL/EXP = 178.3 \text{ kN}/240.1 \text{ kN} = 0.72$) is not due to any shortcoming inherent in the FE model, but stems merely from some fairly drastic simplifications in the reinforcement and geometry of the beam, may be seen by the prediction obtained once a more accurate distribution of the former and an improvement of the latter (through the addition of end blocks) are imposed: the MSL is then increased to 195.84 kN, i.e. $MSL/EXP = 0.82$. (Should reference be made to the load at divergence, the analytical prediction becomes 86% of the experimental load.) It is significant that such a marked improvement was obtained for a far coarser mesh than that used above, namely only half the number of elements were used in this improved prediction (i.e. 25 HX20A elements — see section 4.5), while more attention was paid to the actual detailing of the beam.

4.3.2.4. Case study 7: RC structural wall failing in flexure

The RC shear wall of rectangular cross-section subject to horizontal load, referred to as specimen SW11 in reference 128, where its characteristics and testing details are reported, provides another complex structural member against which the generality of the present 3-D FE scheme can be tested. The dimensions of the wall are a height and width of 750 mm, and a thickness of 70 mm. The vertical reinforcement consists of 2×13 dia. 8 bars distributed uniformly (60 mm spacing), and the horizontal web reinforcement comprises 2×10 dia. 6.25 bars (80 mm spacing). Stirrups comprising a 1 dia. 6.25 bar were placed within both lateral edges of the wall in order to provide confinement along the compressive path (the stirrups within the tensile zone were provided for symmetry so as to cater for possible load reversals in practice). The experimental details and crack pattern at failure have already been depicted in Figs 3.65(a) and 3.68 respectively. (For concrete and steel material properties, see also section 3.4.3.1 and Table 3.3.) Failure of the wall occurred at 260 kN of horizontal applied load, which corresponds to a shear force and a bending moment at the built-in support equal to 260 kN and 214.5 kNm respectively. (The lever arm of 750 mm is to be increased by 75 mm, i.e. the half depth of the top horizontal beam/flange through which the load was transmitted to the wall.) The flexural capacity of the horizontal section is 184 kNm and, hence, the flexural failure load would be 223 kN. Therefore, the actual failure may be regarded as an enhanced flexural failure.

Figure 4.29 shows the FE discretization adopted for the present

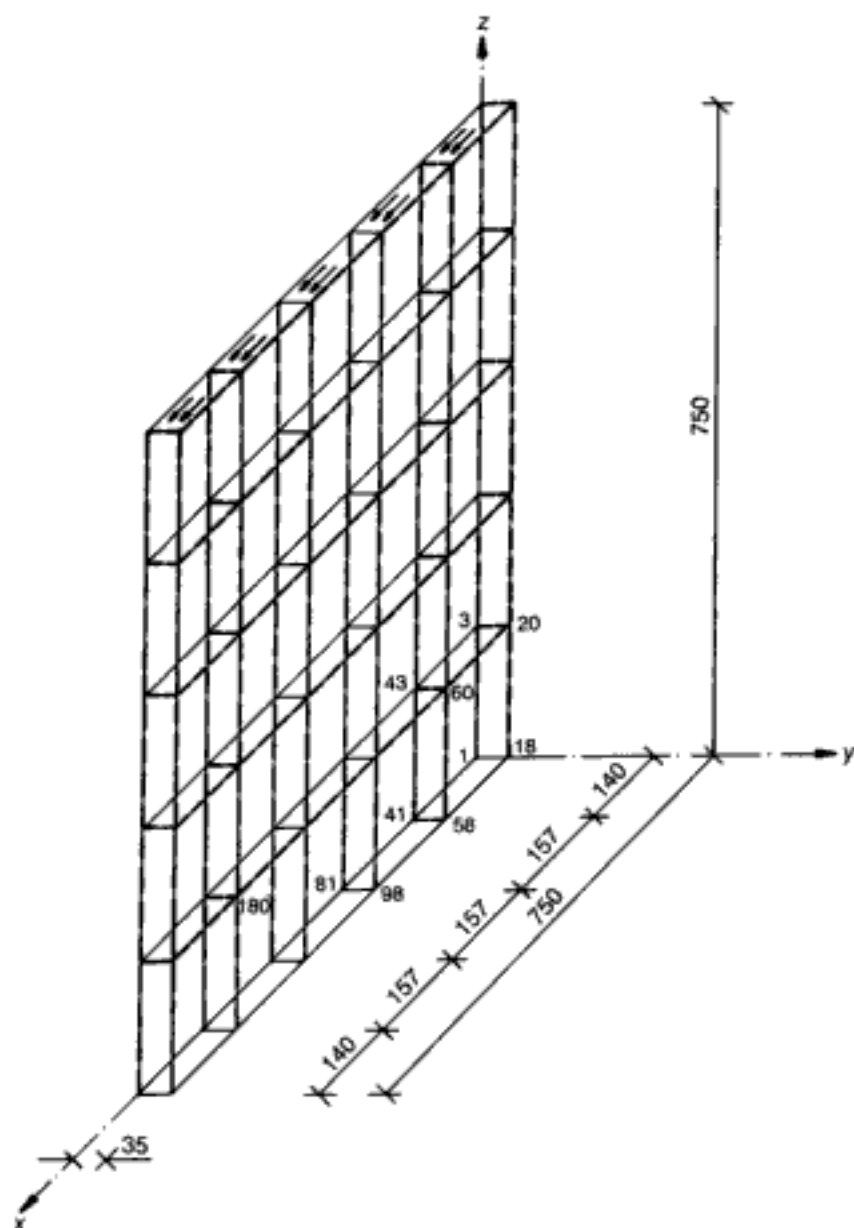
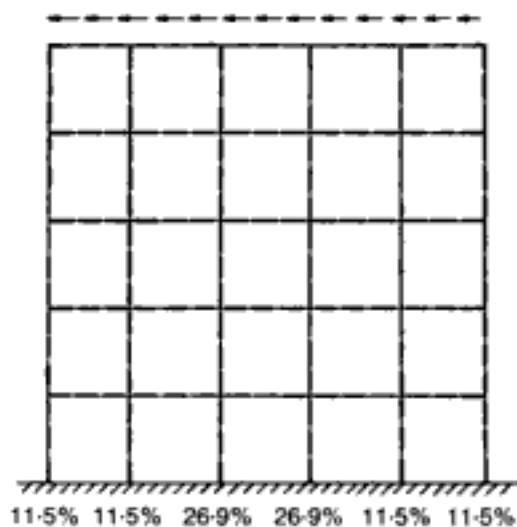


Fig. 4.29. RC structural wall failing in flexure (CS7). FE mesh for one-half of the structure, consisting of 25 brick elements (the percentages refer to the amount of vertical steel at the relevant location) (all dimensions in mm)¹⁶⁵



analysis. The mesh has 25 HX20A elements (228 nodes and 684 DOF) for the concrete, and 105 bar elements for the steel reinforcement as indicated by the dashed portions. (Only half of the wall is analysed owing to symmetry.) It should be noted that the total area of vertical reinforcement, and the area of vertical reinforcement held by the stirrups, are equal to those of the test. However, the distribution deviates from the uniform one in the test as the actual steel areas encompassed by each FE have been lumped onto its edges (the relevance of this will be discussed below). Also, while the confining effect of stirrups was allowed for by means of steel elements running across the thickness of the wall's edges, the quantity of steel along the horizontal reinforcement was kept constant throughout the width of the wall instead of increasing it in the edge zone by the amount corresponding to the stirrups' area (this may be seen from the table in references 56 and 165 containing the detailed breakdowns of steel areas for the mesh of Fig. 4.29). With regard to the web (horizontal) reinforcement, the area was adjusted so as to keep the same area per unit vertical length (the spacing in the test was 80 mm compared to 150 mm in the analysis). Another deviation from the test conditions relates to the boundary loading. In the test, the load was applied on one of the lateral faces of the top beam/flange referred to earlier, whereas the present analysis applies the load by means of surface tractions distributed uniformly on the five top FEs of Fig. 4.29. Nevertheless, the latter deviation from the test loading appears to play a secondary role, although its true relevance could be assessed by incorporating the beam to the wall in future FE discretizations.

The MSL in the analysis is 200 kN, which is 77% of the experimental failure load (the load at which divergence takes place is 220 kN (84.6%)). The analytical results may be discussed with reference to Fig. 4.30, which shows the analytical crack patterns and deformed shapes up to failure. The first flexural cracks appear in the tensile zone of the built-in edge at the total applied load of 60 kN (see Fig. 4.30). Subsequently, additional flexural cracks occur within the tensile zone of the wall and, then, cracking propagates extensively throughout the diagonal of the wall. The splitting of the compressive zone — accompanied by the yielding of the tension steel — at the built-in support initiates at 180 kN and leads to the collapse of the wall, which in the present analysis takes place for a total applied load equal to 220 kN. Such a failure mechanism compares very well with the experimental mode of failure, as can be seen by reference to the experimental crack pattern and corner splitting in Fig. 3.68. However, the analytical failure load underestimates the experimental value by 23% (15.4% should the load at divergence be considered). In this respect, it appears that the adopted FE discretization may not model adequately the confinement introduced by the stirrups in the compressive zone

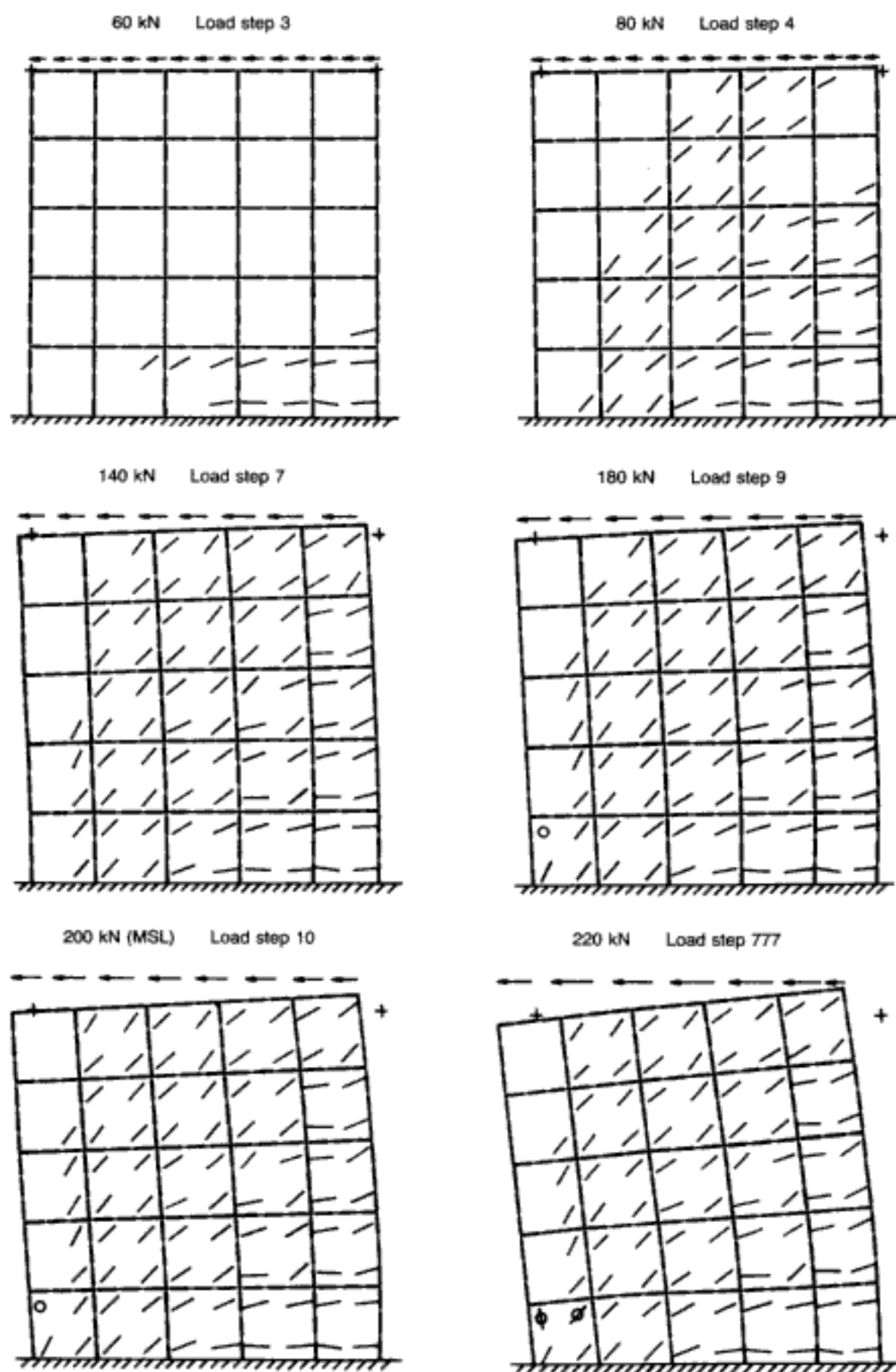


Fig. 4.30. RC structural wall failing in flexure (CS7). Crack patterns and deformed shapes ($D.M. = 20$) at various load stages¹⁶⁵

at the corner, since the spacing is about twice that of the test, and some of the steel from the stirrups has been ignored, as pointed out earlier. Another possible cause for the underestimate is the adopted distribution of vertical reinforcement (see Fig. 4.29), which deviates from the uniform distribution of the test. Although such a deviation is irrelevant in terms of the theoretical flexural capacity of the horizontal cross-section (187 kNm instead of 184 kNm), the amount of vertical reinforcement within the compressive zone increases the strength of the compressive path and, therefore, plays a beneficial role in the strength of the structural walls (references 122, 127 — see also section 3.4.3.2).

As for the previous case study (CS6), no attempt has been made to improve the accuracy of the prediction by refining the initially chosen mesh although, clearly, a somewhat finer mesh would have enabled a better modelling of the reinforcement in the compressive zone which, as suggested above, is relevant because of the importance of the amount of both main reinforcement and confining stirrups there. It is significant that the 2-D version of the present model that employs a somewhat finer mesh (7×7 instead of 5×5 elements), and hence permits a more accurate description of the reinforcement detailing, predicts an improved failure load which underestimates the experimental one by less than 10% (see section 3.4.3.1 and Table 3.3). However, similar predictive accuracy may be achieved by the adoption of the same, relatively coarse 3-D mesh (25 elements), but now with a better reinforcement representation (instead of spreading reinforcement evenly, allowance was made for the presence of the two concealed columns in the wall, which resulted in a denser steel distribution at the edges, where the compressive force is critical). This leads to a ratio $MSL/EXP = 232.05 \text{ kN}/260 \text{ kN} = 0.89$ (a smaller load step (13.65 kN as against the previous 20 kN) was also adopted in this rerun, so that the load at divergence was 245.7 kN). The analytical load–displacement curve which, for the original modelling, represented the only instance of a stiffer response than that for its experimental counterpart,⁵⁶ is then also improved (provided time-dependent effects in the test (arising as a result of extensive diagonal cracking of the wall and the yielding of the tension reinforcement¹²⁸) are also allowed for; this will be shown in section 4.4 by reference to the load–deflection curves for several wall specimens, and where a more detailed description of the improved run for wall SW11 may be found). Once again, it is the sensible modelling of the main geometric and — especially in this instance — reinforcing characteristics that is important rather than mesh refinement, if accurate predictions are to be attained.

4.3.2.5. Case study 8: RC slab exhibiting punching failure

The last structural element studied here is an RC square slab, denoted as B-14 in the paper by Elstner and Hognestad,¹³⁹ and

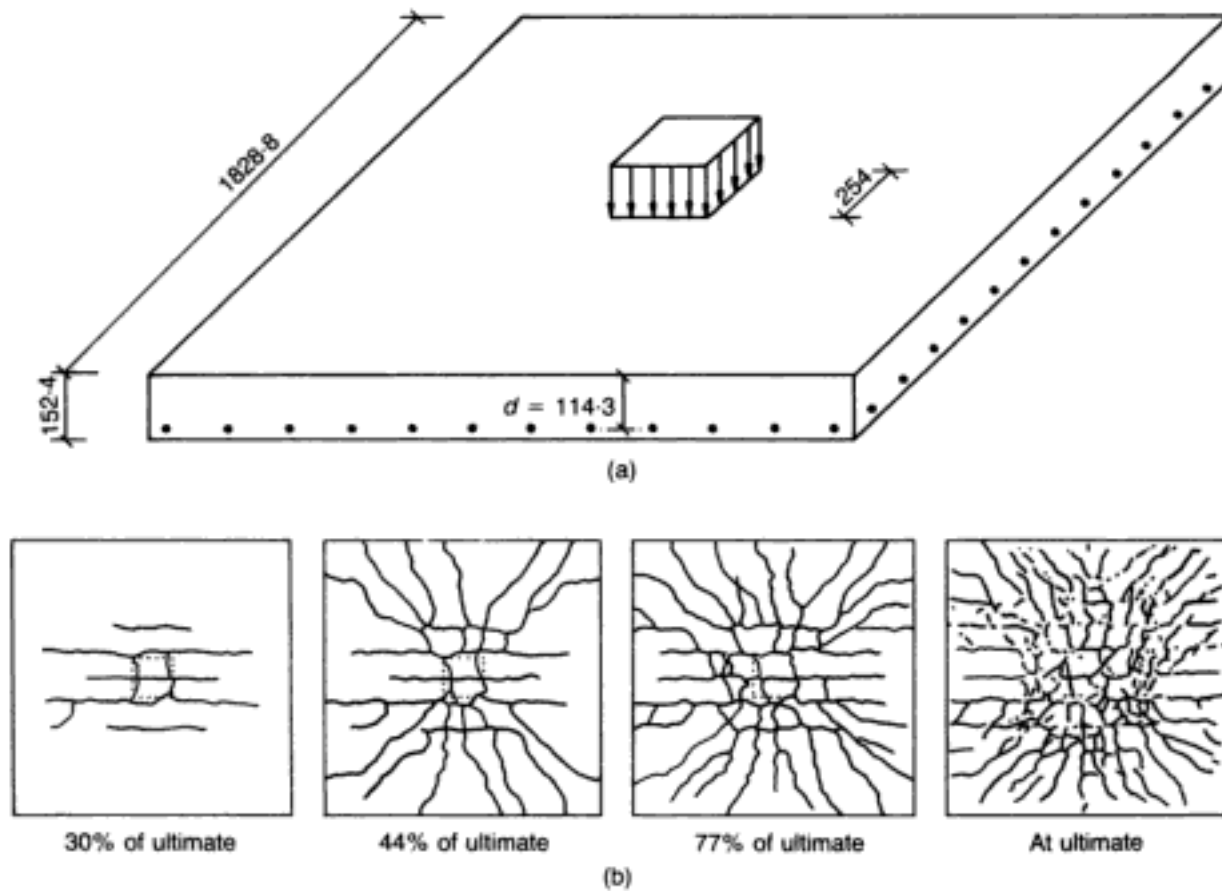


Fig. 4.31. RC slab exhibiting punching failure (CS8). Experimental data:^{56,139} (a) dimensions and detailing of reinforcement (all dimensions in mm); (b) crack patterns on the tensile face at various load stages

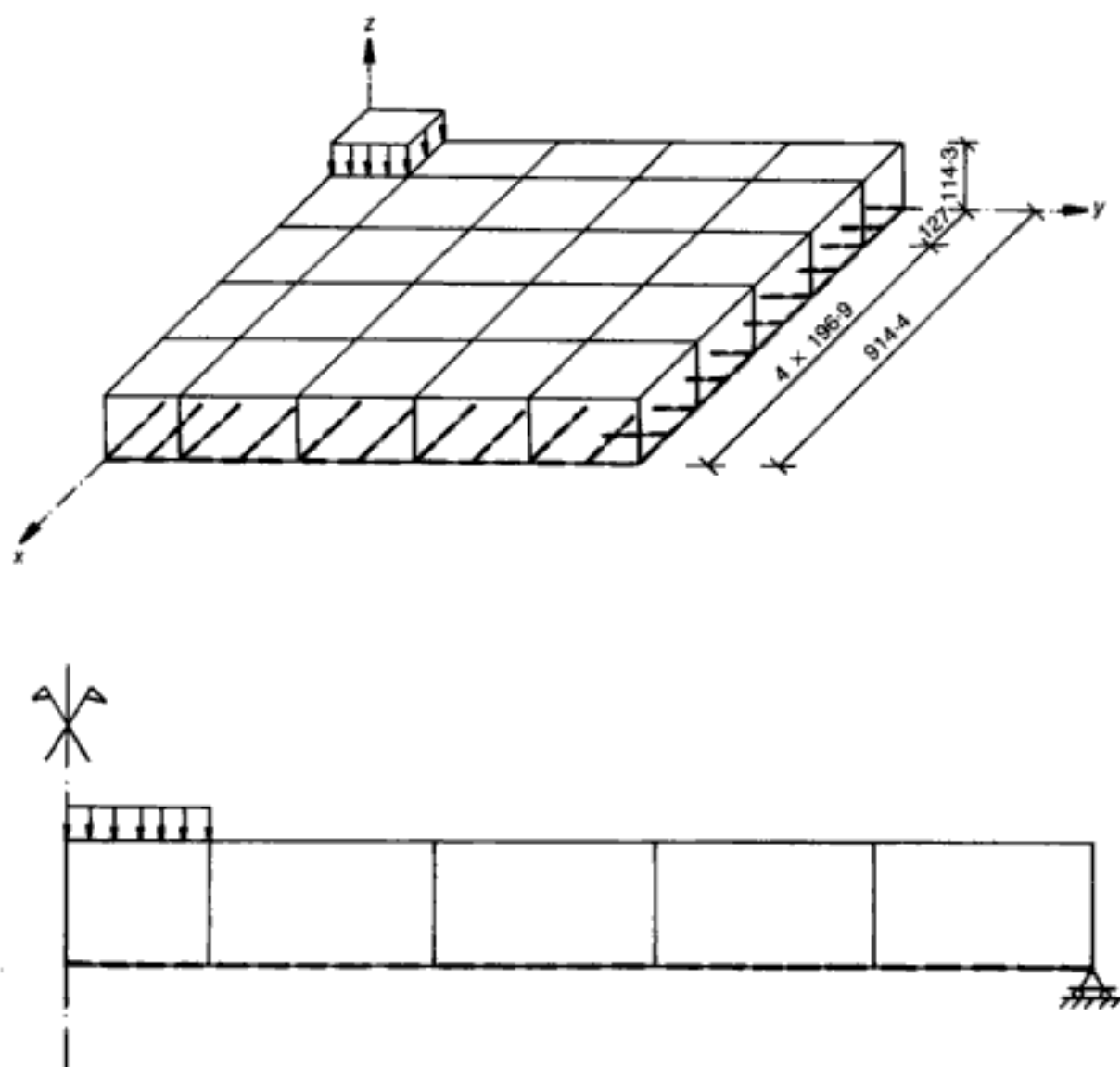
reported fully in this reference in respect of the relevant experimental details. Some of these have been summarized in Fig. 4.31, complementing the data given earlier in Chapter 3, where this structural component (referred to as slab DEHB 14) was analysed approximately by means of the axisymmetric option of the 2-D package. The percentage of tension steel was very high (3%) and the slab lacked any shear reinforcement (see Table 3.5). The RC plate was simply supported at all edges and corners, and subjected to a concentrated square load at midspan. Failure occurred as a result of punching at a load of 578 kN (130 kips) before any yielding of the tension bars (see section 3.4.4 and Table 3.5). It is worth noting that, according to the yield-line theory, the flexural failure load is 912 kN (i.e. 57.8% higher than the actual failure load).

The details of the adopted FE mesh are shown in Fig. 4.32. The mesh comprises 25 Lagrangian FEs (363 nodes and 1089 DOF) for the concrete, and 110 bar elements for the tension steel. Although only one-fourth of the slab is analysed on account of symmetry, it is clear that additional savings would be achieved by implementing 'edge' (i.e. triangular-based) brick elements, so as to also make use of the symmetry with respect to the diagonals and hence to analyse one-eighth of the whole slab. With regard to the choice of the Lagrangian FE mesh, it should be noted that, before its choice, three other serendipity meshes were considered

Fig. 4.32. RC slab exhibiting punching failure (CS8). FE mesh for one-quarter of the structure, consisting of 25 Lagrangian elements (all dimensions in mm)¹⁶⁴

for consistency with the other analyses in the present study (all incorporating under-integrated serendipity meshes); these were based on $5 \times 5 \times 1$ HX20A elements (228 nodes, 684 DOF), $5 \times 5 \times 2$ HX20A elements (360 nodes, 1080 DOF), and $9 \times 9 \times 2$ HX20A elements (1040 nodes, 3120 DOF). However, the Lagrangian mesh was preferred for the following reasons. The first alternative mesh (25 HX20A elements) had only two Gauss points across the thickness of the slab, and did not allow a good distribution of the tension steel in plan. Therefore, this discretization was considered too rough. The second alternative mesh (50 HX20A) elements) had four Gauss points across the thickness, but it still involved a poor modelling of the steel in plan. Finally, the third alternative mesh (162 HX20A elements) was discarded on account of the steep rise in computer resources inherent in the scheme.

As in the previous case studies, only one computer run incorporating the NR-plus iterative method and the single-crack procedure was carried out. The maximum number of new cracks



Hidden page

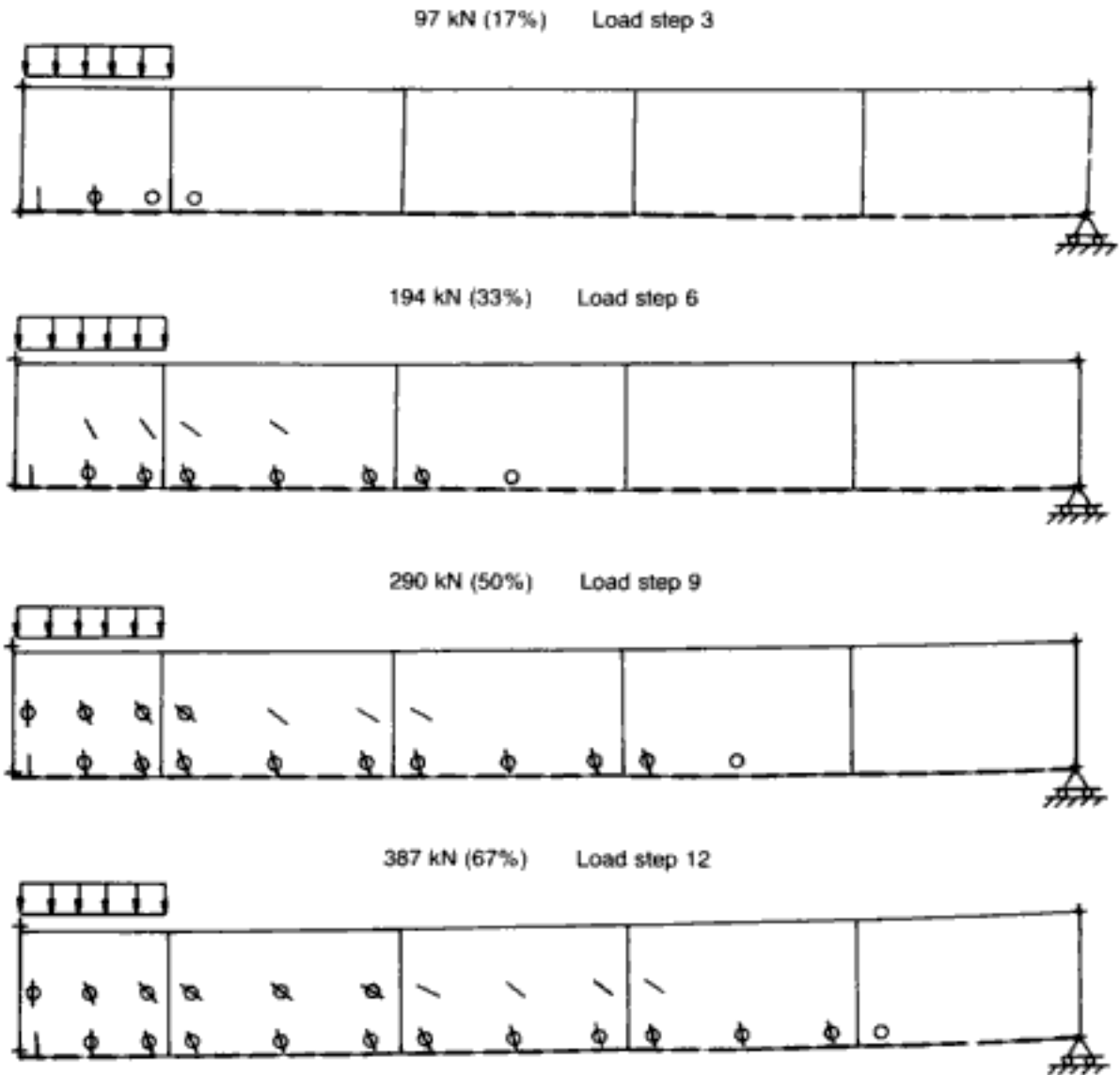


Fig. 4.33 (above and facing). RC slab exhibiting punching failure (CS8). Crack patterns and deformed shapes at various load stages (Note: the percentages refer to the ratio of analytical to experimental failure loads to facilitate comparison with Fig. 4.31(b))^{56,164}

slab behaviour; thus, it seems that the use of the under-integrated serendipity elements would have been preferable, but for the additional computational resource required, as mentioned earlier. Finally, the crack pattern of the last performed iteration (load step '777') shows that divergence takes place as a result of a local mechanism in the zone of the concentrated load, which occurs before yielding of the reinforcement. (For a more detailed explanation of the punching-failure mechanism in slabs, see section 3.4.4.3.)

4.3.2.6. Summary of results

The eight case studies that were analysed here numerically — representing, to the Authors' knowledge, the most complete generality study to date of any 2-D or 3-D FE model for concrete structures — cover a sufficiently wide range of structural-configuration types (including both plain concrete and reinforced concrete elements, as well as ductile and brittle types of failure)

Hidden page

divergence) of the experimental value), bearing in mind the simplification still present in the improved analysis. The two case studies where the deviation of the initial predictions was more substantial represent instances where the description of the reinforcement and/or the geometry in the 3-D FE model requires meshes which, without being finer than the originally adopted ones, incorporate a more sensible modelling of these two parameters

Fig. 4.34. RC slab exhibiting punching failure (CS8). Comparison between experimental and analytical load-deflection curves (Note: the 2-D analysis curve has been taken from Fig. 3.85, in which implied axisymmetry is based on approximating the 3-D problem to that of an 'equivalent' circular shape inscribed within the square plan; clearly, such a simplification results in poor deflection estimates)¹⁶⁴

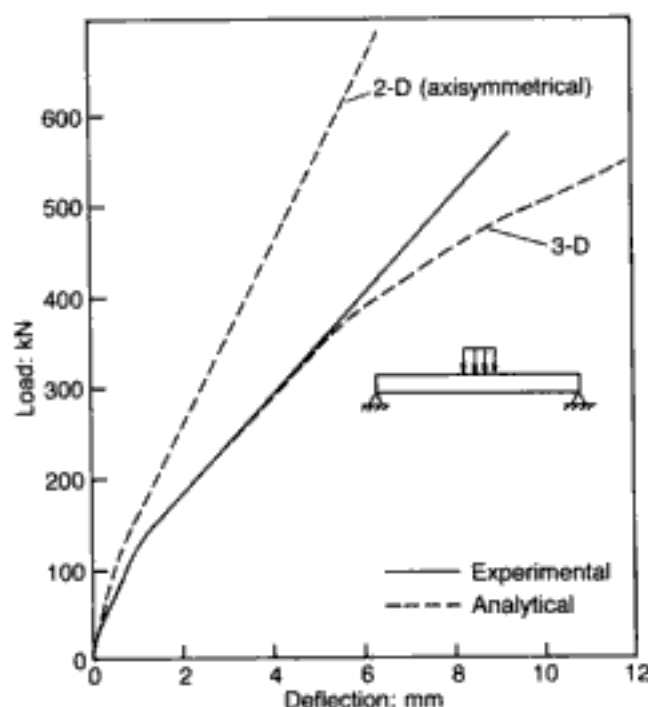


Table 4.3. Comparison between predicted and experimental failure loads and types of failure for eight structural elements modelled in 3-D objectivity and generality studies¹⁶⁵

Structural element	Failure load: analysis/experiment (MSL/EXP)	Types of failure: analysis/experiment
CS1:PC prism under strip loading	1.10	Brittle/Brittle
CS2:RC beam failing in flexure	1.03	Ductile/Ductile
CS3:RC beam OA-1 failing in shear	0.90	Brittle/Brittle
CS4:PC prism under patch loading	1.03	Brittle/Brittle
CS5:RC beam A-1 failing in shear	0.96	Brittle/Brittle
CS6:RC T-beam failing in flexure	0.82	Brittle/Limited ductility
CS7:RC structural wall failing in flexure	0.89	Ductile/Ductile
CS8:RC slab failing in punching	0.95	Brittle/Brittle

Hidden page

4.4. A comparative study of two-dimensional and three-dimensional analyses by reference to structural walls

With the 2-D and 3-D FE models now fully described and tested, a comparison of these two packages for those cases amenable to both options seems appropriate. Some indication of the relative merits of each scheme has already emerged on the basis of beams OA-1 and A-1, as well as the shear wall SW11, all members analysed both two-dimensionally and three-dimensionally. Nevertheless, a more systematic — if not parametric — investigation appears called for in order to elucidate the relative merits of 2-D and 3-D FE versions of the brittle model for structural concrete; in particular, while the plane-stress formulation is an obviously attractive procedure on account of both simplicity and economy, it is nevertheless important to assess the accuracy of such an approach and any inherent shortcomings which only the 3-D mathematical simulation can remove. The present study attempts to achieve this in the, admittedly, limited context of structural walls.

In section 3.4.3, a comprehensive modelling of walls was undertaken by means of the 2-D package. The investigation encompassed the analytical simulation of test data from a number of sources (including the series of tests conducted at Imperial College) as well as a fairly full parametric study of the various factors affecting structural-wall behaviour. It was shown that the adoption of a 7×7 FE mesh and a horizontal load-step size of the order of 5–10% of the estimated strength led to good predictions of load-carrying capacity. For example, despite the fact that data containing other authors' tests are seldom available in full detail in the relevant references, it is clear from Fig. 3.64 that the errors incurred in adopting the 2-D model are within the order of 10%, even though some of the analyses were based on considerable simplifications to the actual features of the original structure. (The larger errors occur in the predictions of barbell specimens of references 124 and 125; although the worst error for the latter may be deemed to be acceptable for practical purposes, higher accuracy is achievable through the more exact 3-D modelling.)

The overall trend of the deformational properties of structural walls may also be estimated by 2-D modelling although the high accuracy of the ultimate-load predictions is not usually achieved (for a typical example, see reference 172). One reason for the stiffer response of the numerical modelling is due to time-dependent effects (in the course of the loading history) which are rarely reported, so that no allowance can be made for them in the attempt to reproduce analytically the tests of others.

Structural-wall tests carried out at Imperial College ensured a more precise knowledge of the various input parameters. The experimental and predicted values of ultimate load for twelve such walls (encompassing a range of geometries and material properties and subjected to combined loading conditions) were given in Table 3.3. The very good accuracy of the 2-D option is evident. The

Hidden page

Hidden page

Hidden page

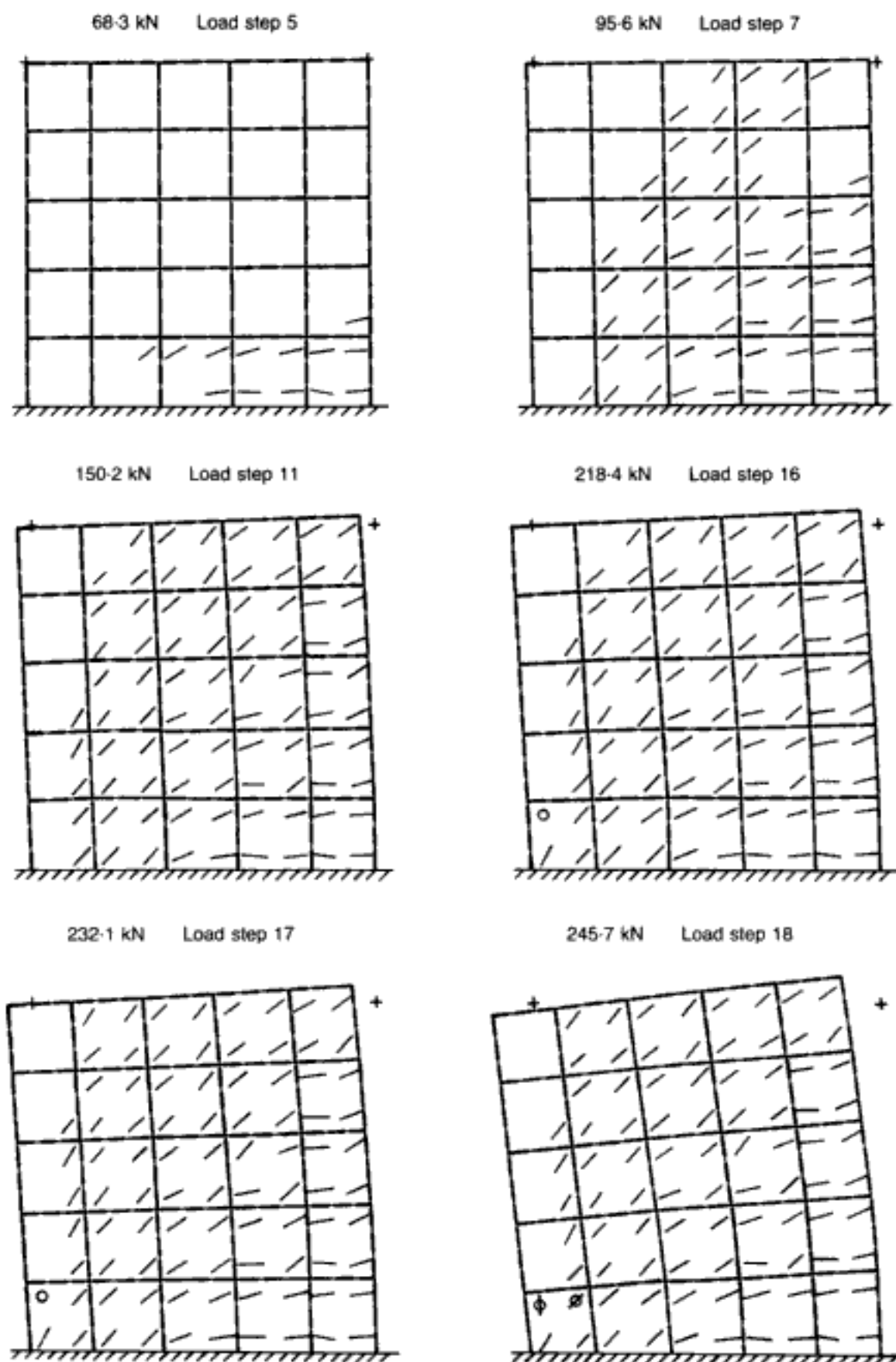


Fig. 4.35. Structural wall SW11. 3-D analysis:¹⁷² crack patterns and deformed shapes ($D.M. = 10$) at various load stages right up to failure

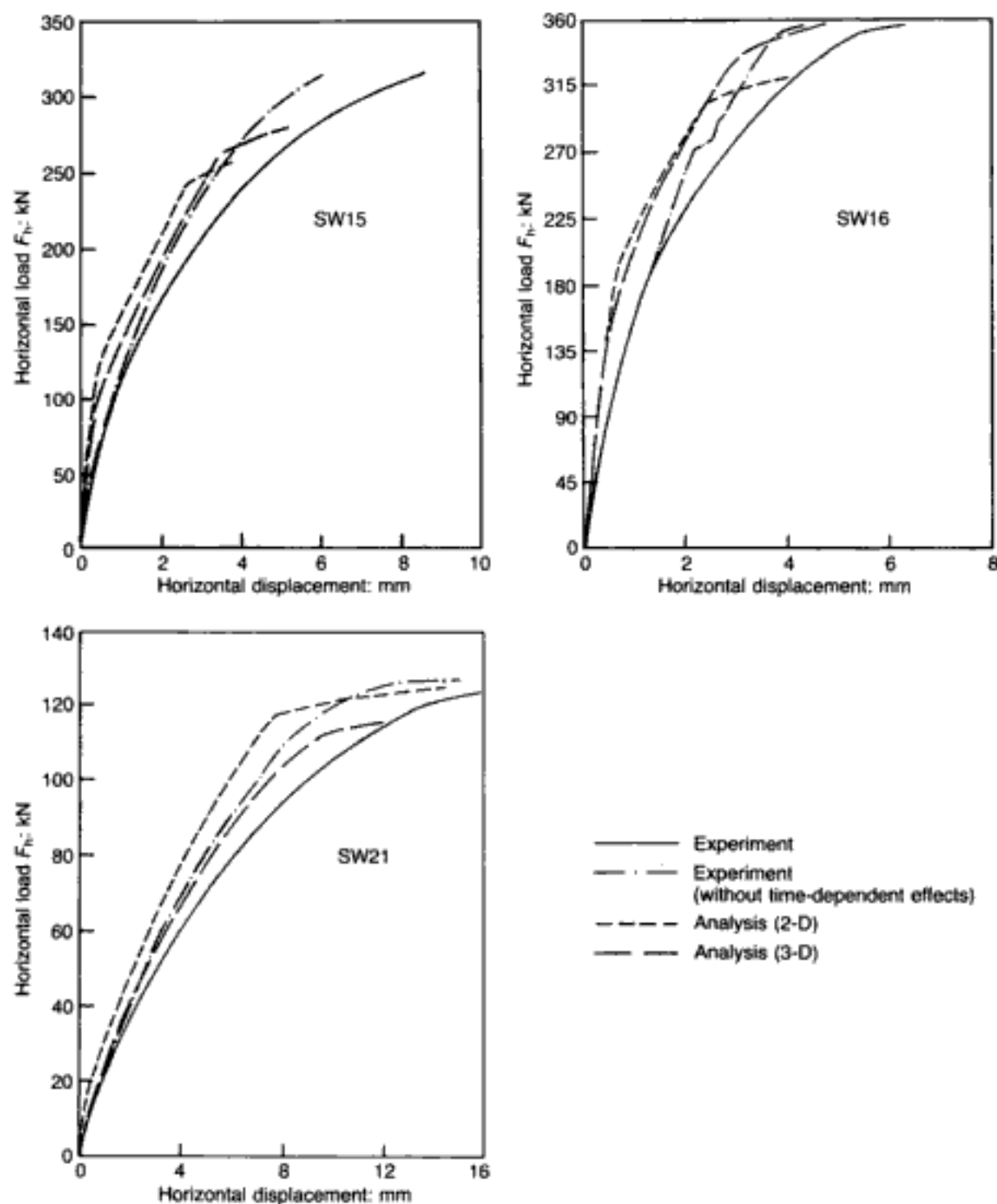


Fig. 4.36. Predicted (2-D and 3-D analyses) and experimental horizontal load-top horizontal displacement curves for wall specimens SW15, SW16 and SW21¹⁷²

is very similar to that of the 2-D model. Such an improvement is particularly evident for low axial loads irrespective of the height-to-width ratio of the wall (see, typically, the plots for SW15 and SW21 in Fig. 4.36); conversely, for high levels of pre-compression, there is little difference between 2-D and 3-D displacement predictions (see the plot for SW16 in Fig. 4.36).

To summarize, the superior performance of the 3-D model over its 2-D counterpart is evident in that a coarser mesh for the former yields results for strength and crack characteristics comparable with those of a finer plane-stress grid, as well as leading to

improvements — often considerable — in deformation characteristics. However, it is not difficult to envisage circumstances in which the 2-D option might be preferred as a satisfactory — and a more economical — alternative.

4.5. Modelling of normal-strength and high-strength reinforced concrete members, with special reference to T-beams

Not only is there a general scarcity of reported experimental data for high-strength concrete (HSC) components but, to the Authors' knowledge, no attempt to apply FE modelling (whether two- or three-dimensional) to this higher range of concrete strengths seems to exist in the literature. Since the material model described in Chapter 1 is applicable equally to both normal-strength and high-strength mixes, the present section extends the use of the FE package to HSC members. Emphasis is placed on the modelling of T-beams (encompassing, for comparative — material, structural and numerical — purposes, both ranges of concrete strength)¹⁷³ since experimental results for this structural form are available from laboratory tests performed at Imperial College;^{174,175} in addition, a high-strength rectangular member is also considered, this specimen representing one of the fairly rare instances of reported test data pertaining to HSC members and, as such, being clearly useful in assessing whether or not the generality of the FE package also extends to such concrete mixes.

Since the complicated geometry and reinforcement details of the T-beams studied cannot be reduced to 2-D treatment, 3-D analysis is, clearly, mandatory. Moreover, the triaxial conditions in general, and the relative degrees of triaxiality for the various concrete strengths in particular, in the members investigated, can be catered for better by the 3-D FE option. Accordingly, the elements for concrete and steel to be adopted throughout the present investigation are HX20A and LM03 (also under-integrated) respectively. Finally, with regard to the magnification factor for the deformed-shape plots at various load levels, D.M. = 5 is usually adopted except for some of the load step '777' plots (and, sometimes, that of its preceding load step (MSL)), for which deflections become quite large so that, for purposes of clarity, they are not magnified.

4.5.1. Economic modelling of RC T-beams

The analysis of the various HSC structural components is to be preceded by the modelling of a particular, normal-strength concrete (NSC) T-beam, which is studied by adopting a number of mesh discretizations in order to accomplish an economical solution without impairing the accuracy of the numerical predictions. This was done in order to establish the important features associated with T-beam modelling (thus improving the initial prediction of the member analysed in section 4.3.2.3 as CS6) and, also, to enable such members to be run in a medium-range computer (Masscomp MC5400), with its inherent limitations of memory and speed. The latter concern for economy is justified since, in addition to HSC

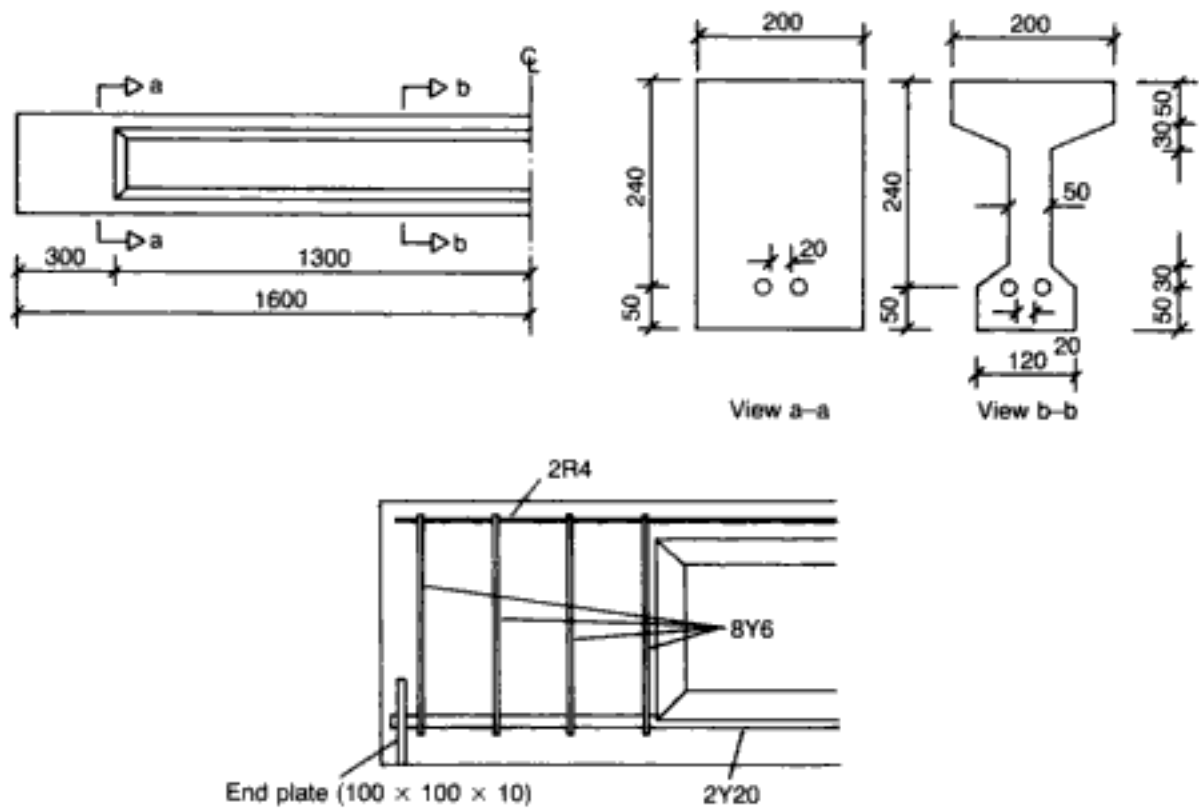


Fig. 4.37. Beam C. Main dimensions, and detailing information additional to that of Figs 2(a) and 4.25 (all dimensions in mm)^{3,173}

and NSC girders, prestressed concrete members of similar cross-section but much larger in size were within the scope of ongoing research at Imperial College (these will be discussed in section 4.6). For this reason, simplifications in both geometry and reinforcement seemed desirable, even though the present FE model is fully capable of handling the true geometry of any large member. The ensuing coarser mesh will be shown to lead to economic modelling without compromising the accuracy of numerical predictions (these constituting an improvement over the initial strength estimate for CS6 in section 4.3.2.3).

4.5.1.1. Modelling using 50 brick elements

The under-reinforced T-beam with stirrups under four-point loading (beam C), which forms the basis for the present economic modelling study, has already been described in section 4.3.2.3, and Figs 2(a) (Introduction) and 4.25. (It will be seen that in Fig. 2(a), web reinforcement type 1 refers to the 2 dia. 1.6 vertical legs while type 2 includes an additional 1 dia. 1.6 bar as flange stirrup, both these details being shown more clearly in Fig. 4.25.) Further detailing is now given in Fig. 4.37, showing a detailed description of the end block — an important component of the beam and of an accurate FE model, as will be illustrated subsequently. To eliminate the possibility of anchorage failure, the two main 20 mm diameter high-yield deformed bars were extended to about 280 mm beyond the support and welded onto steel end plates;

Hidden page

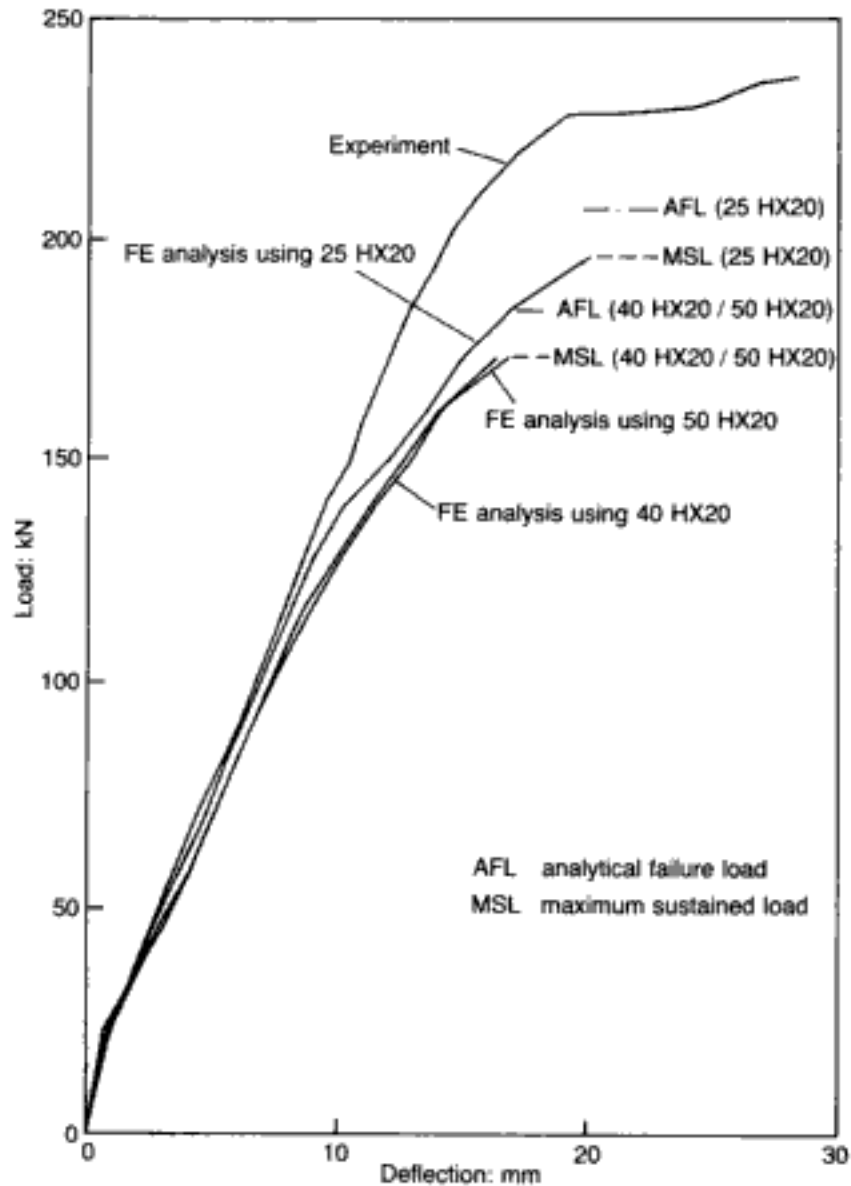


Fig. 4.38. Beam C. Comparison between experimental and analytical load-deflection curves, with the latter encompassing varying numbers of under-integrated brick elements HX20⁷³

is almost stabilized up to a load level equal to 161.28 kN. At the MSL (172.80 kN), the tension reinforcement in the flexural span yielded. As for the 50-brick mesh, the divergence in the analysis was triggered by the occurrence of vertical cracks within the compressive zone of the flexural span. The load-deflection curve for this analysis is practically identical to that of the earlier run (see Fig. 4.38). Thus, by comparing the MSLs, the crack patterns and the load-deflection curves for the 50-brick and 40-brick analyses, it can be concluded that a slight modification in the geometry (essentially, a reduction in the area) of a structural form below the neutral axis need not make an appreciable difference in the numerical predictions, which is in keeping with the notion espoused by the Authors that cracked concrete in regions subjected to predominantly tensile-stress conditions (such as zones below the neutral axis) makes only a minor contribution to the overall load-carrying capacity of a concrete structure. Since, in the present

Hidden page

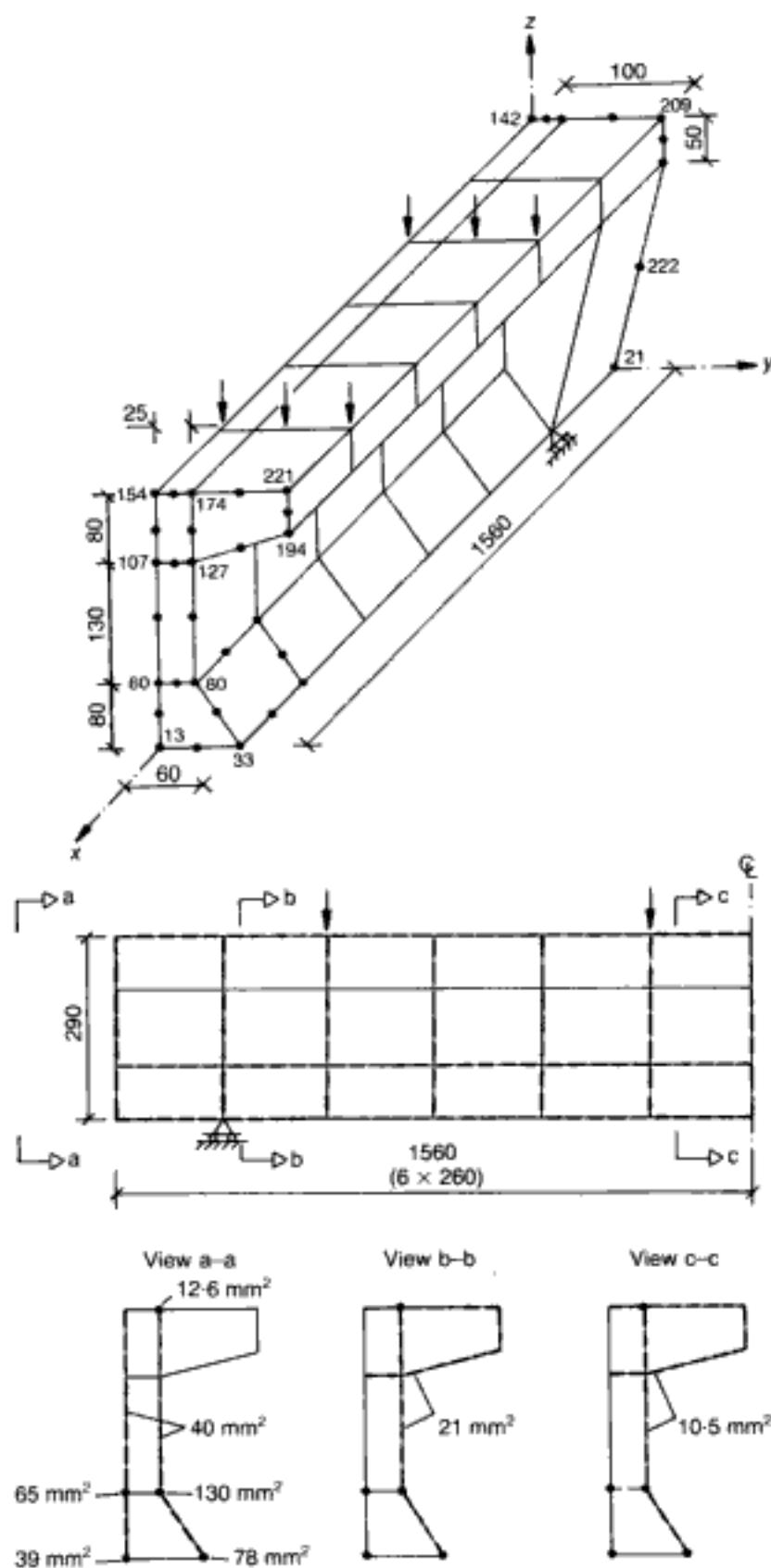
Hidden page

Hidden page

Hidden page

the web between point loads was severely cracked as well. Nevertheless, the beam continued to sustain load up to 195.84 kN, when the vertical crack in the top flange of the beam (half-way between the two point loads) became visible. The relevant load—

Fig. 4.41. Beam C.
FE mesh for one-quarter of the structure, consisting of 25 HX20A brick elements (all dimensions in mm)¹⁷³



deflection curve, shown in Fig. 4.38, gave a considerably better prediction than those of the previous two runs; in fact, it compares reasonably well with the experimental limited-ductility curve, especially when the numerically indeterminate prediction between the MSL and the load at divergence (the latter is denoted as AFL in Fig. 4.38) is taken into consideration.

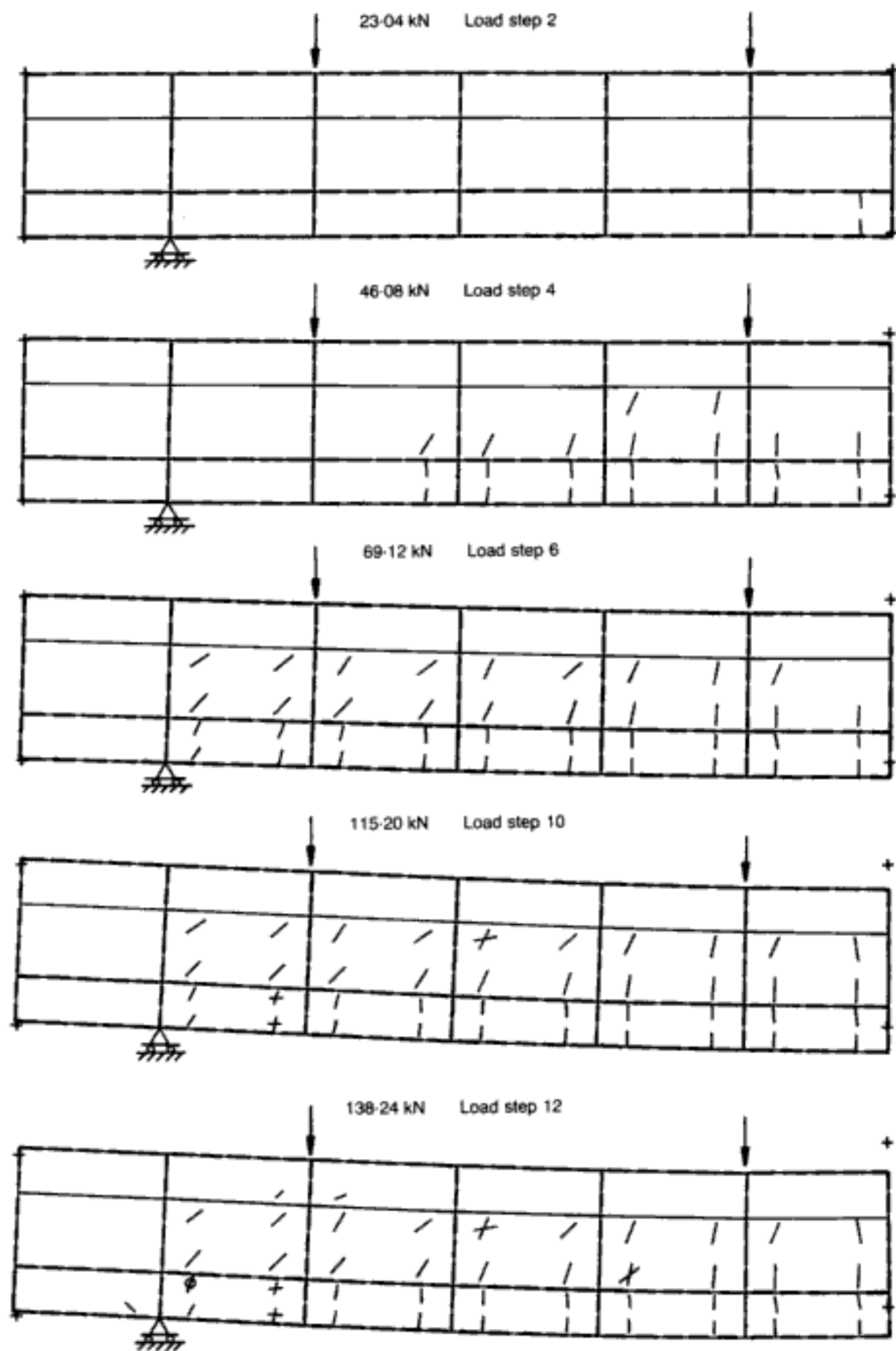
The presence of the necessary transverse reinforcement in the region beyond the second point load seems to delay the formation of early vertical cracking in the flange and thus enables the attainment of a larger load-carrying capacity, consistent with the experimental evidence. Another possible reason for the improved prediction might be the adoption of larger elements in the longitudinal direction, moving the Gauss points away from the loading locations; thus the Gauss points become less stressed, avoiding the triggering of early failure. Finally, it is significant that an additional run using a 24-brick FE mesh, which does not contain the element representing the end block in the 25-brick mesh but is otherwise identical with the latter, predicted the MSL to be equal to 184.32 kN. This load, being 6% less than the prediction of the present section, points to the effectiveness of incorporating the end block — an integral part of the specimen tested in the laboratory (and of good design practice) — in the numerical analysis; such a structural measure delays early cracking in the support zone through which the compressive force passes. A further improvement in the overall prediction could probably be achieved by adopting a spacing of the web and flange reinforcement which is closer to the actual details of the experimental beam.

4.5.2. Modelling of high-strength RC members

So far, all structural members analysed in this and the preceding chapter consisted of NSC mixes. In fact, a shear wall failing in flexure, made from concrete with a cylinder compressive characteristic of $f_c = 44.2 \text{ N/mm}^2$, represents the upper bound of material strength for which the material model has been tested in a structural sense, even though the constitutive laws and failure criteria proposed in Chapter 1 are valid for mixes with f_c values up to at least 100 N/mm^2 . With concrete strengths beyond the range $40\text{--}45 \text{ N/mm}^2$ constituting what are broadly considered to be HSC mixes, three beams made of concrete well above this range of material strength will now be analysed in order to establish the accuracy of the FE model outside the NSC design mixes.

4.5.2.1. Case study 1: high-strength RC T-beam subjected to four-point loading failing in flexure

The beam HSB1 tested at Imperial College^{174,175} and made from a concrete with $f_c = 69.5 \text{ N/mm}^2$ ($f_{cu} = 84.4 \text{ N/mm}^2$) is analysed in this section. This beam is very much akin to the member used in the previous economic-modelling study (beam C). Thus, the dimensions for beam C listed in Fig. 4.37 apply, as do the



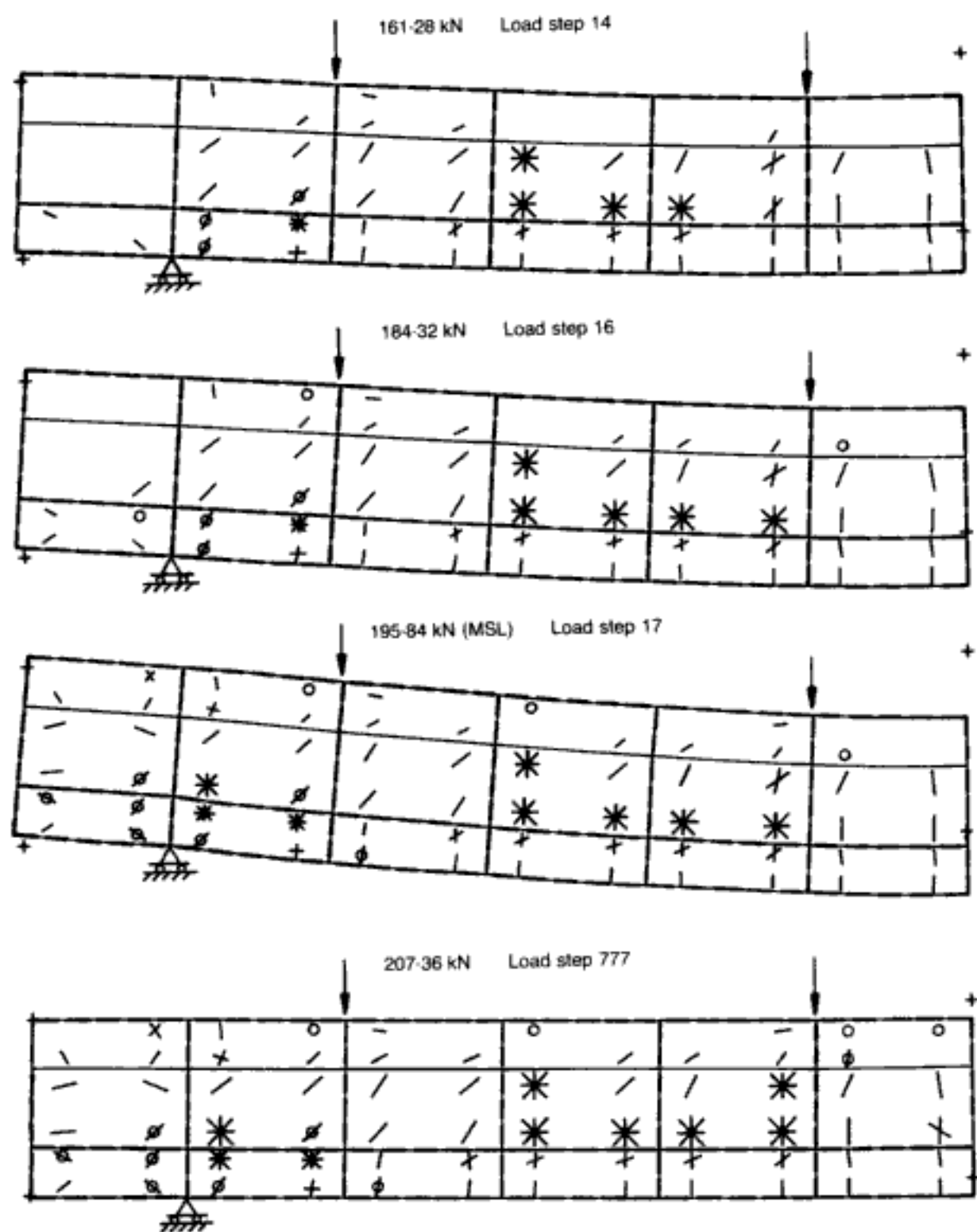
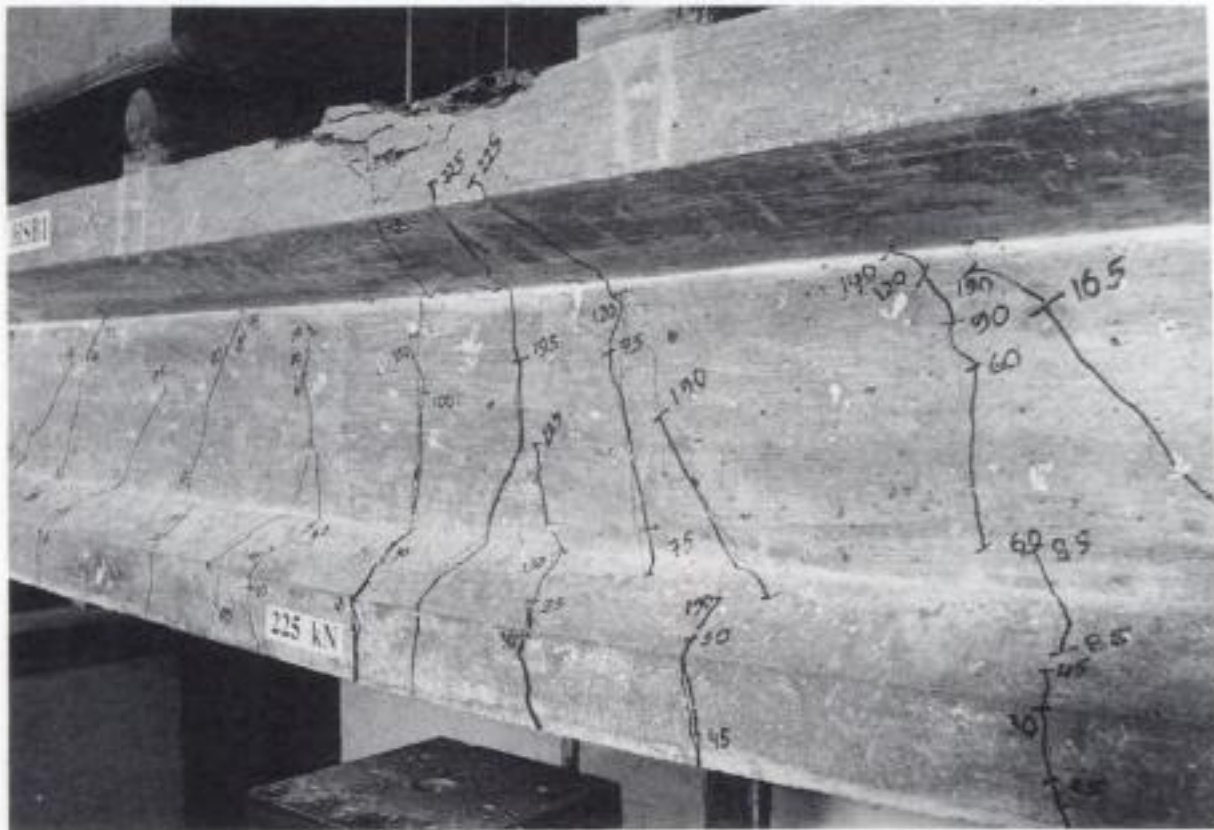


Fig. 4.42 (facing and above). Beam C (25 brick elements). Crack patterns and deformed shapes at various load stages¹⁷³

sizes of longitudinal-reinforcement bars and the reinforcement details for the end zones (except for the two additional compression-steel bars, as may be seen by reference to Fig. 4.43(a)).¹⁷³⁻¹⁷⁵ Although the properties (i.e. strength and bar size) of the transverse reinforcement of HSB1 were slightly different from those of beam C, its arrangement was similar to that of the latter member. Figures 4.43(b) and 4.43(c) show, respectively, the actual details of the

Hidden page



(c)

Fig. 4.43 — continued

the four 4 mm dia. mild-steel longitudinal bars at the top of the beam was to form part of a proper reinforcement cage rather than to contribute to the flexural capacity.¹⁷⁵⁾

The MSL in the analysis was 230.4 kN, which was about 1.5% above the experimental failure load (227 kN, of which 2 kN were due to the weight of the steel spreader beams). However, a closer investigation of the loading configurations adopted in both analysis and experiment reveals that the FE modelling actually underpredicted the ultimate load-carrying capacity of the experimentally tested beam. For the type of loading shown in Fig. 4.43(b), and considering each point load to be equal to P , the moment at midspan, at which the experimental failure takes place, is equal to $1400 P$. On the other hand, for the analytical loading pattern portrayed in Fig. 4.44, the moment at failure can be calculated to be equivalent to $1300 P$. Thus the analytical failure load should have been 7.7% higher than the experimental failure load, in order to attain the same flexural moment at failure. As such, the analytical prediction may be considered to be 6.2% lower than the actual experimental failure load. It is, however, important to note that, since HSB1 was designed in accordance to the CFP concept, its transverse-reinforcement details were significantly different from current code requirements. It contained a very low amount of web reinforcement. As a result, the failure load of HSB1, according to the British and American codes should have been 46.74 kN and 41.24 kN respectively¹⁷⁵⁾ and the member should

Hidden page

Hidden page

Hidden page

Hidden page

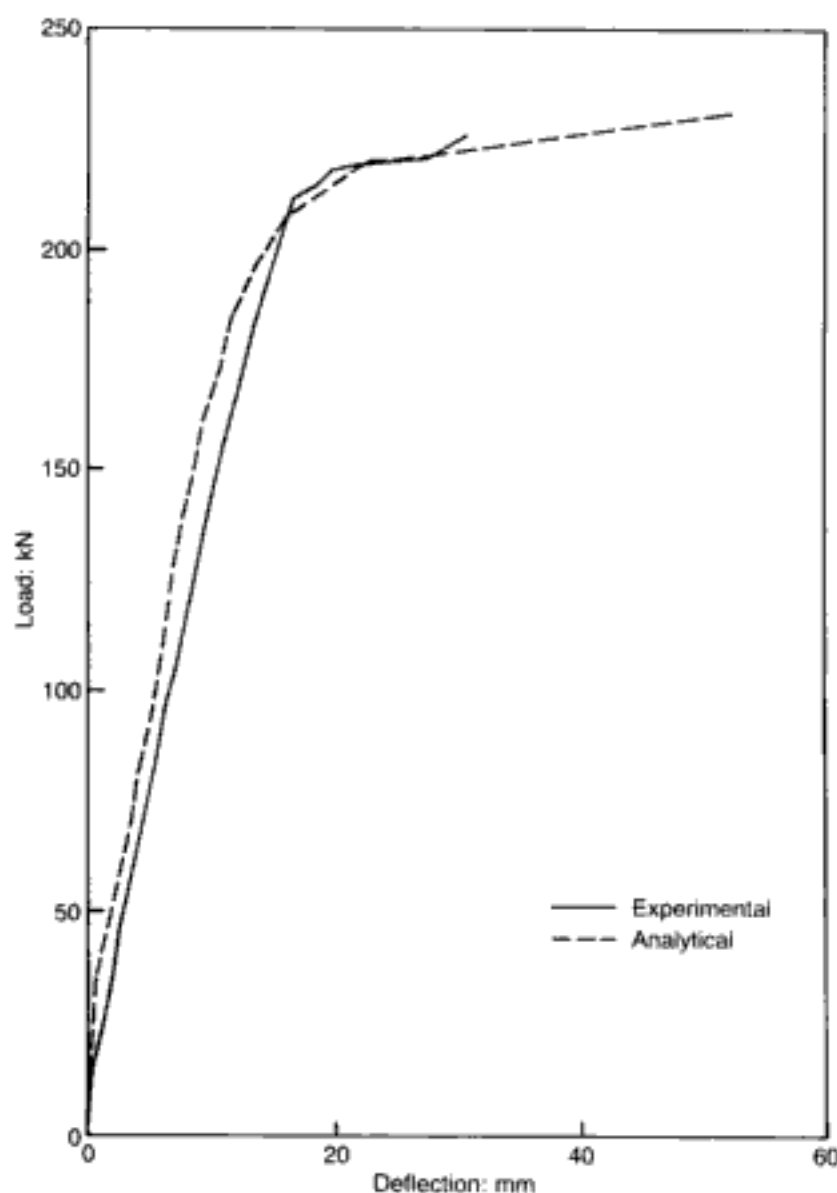


Fig. 4.46. Beam HSB1. Comparison between experimental and analytical load-deflection curves¹⁷³

levels up to failure and a comparison of the load-deflection curve with its experimental counterpart. As depicted in Fig. 4.49, the first flexural cracks occurred in the midspan and under the point load at 43.2 kN. Soon the web in the shear span was full of inclined cracks. The whole process stabilized at 115.2 kN, when a few cracks reached the bottom part of the top flange. The beam model ultimately sustained a load of 187.2 kN (i.e. 94% of the actual collapse load (200 kN)). At this MSL, vertical cracks formed in the upper half of the top flange (for a possible reason for this deep penetration into the compression flange, see reference 175) and this is in full agreement with the experimental evidence (see Fig. 4.47(b)), while the bottom steel in the flexural span actually reached yield in the previous load step. Figure 4.50 shows clearly the ductile behaviour of the beam, both experimentally and analytically, the two curves exhibiting good agreement, especially in respect of the

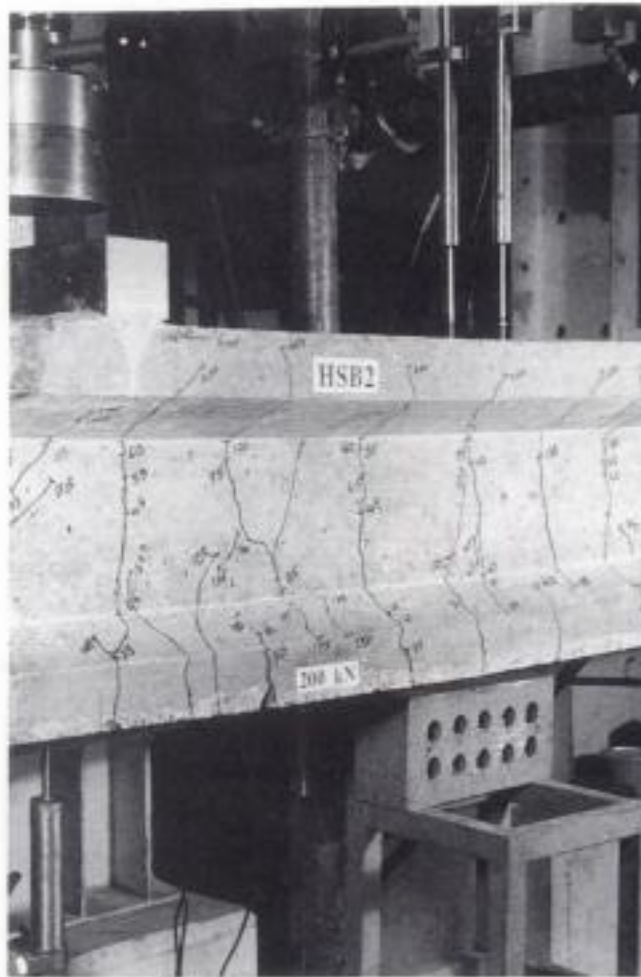
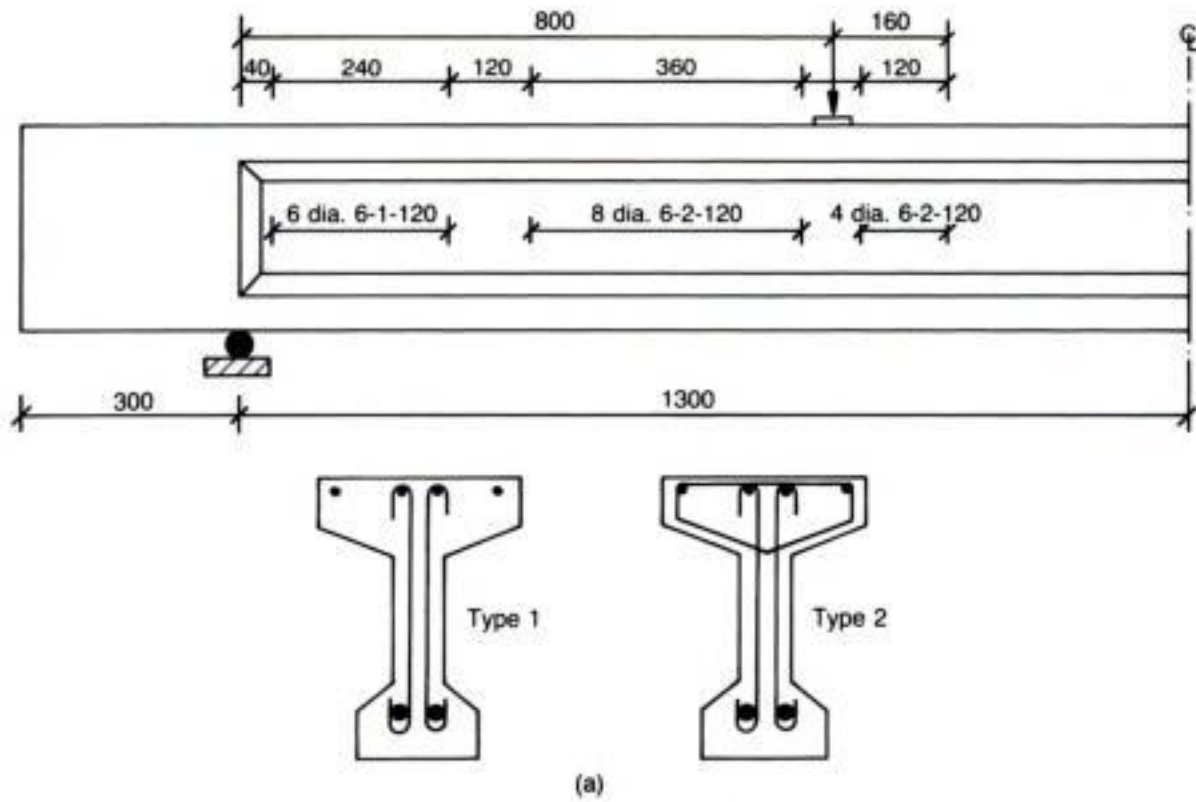


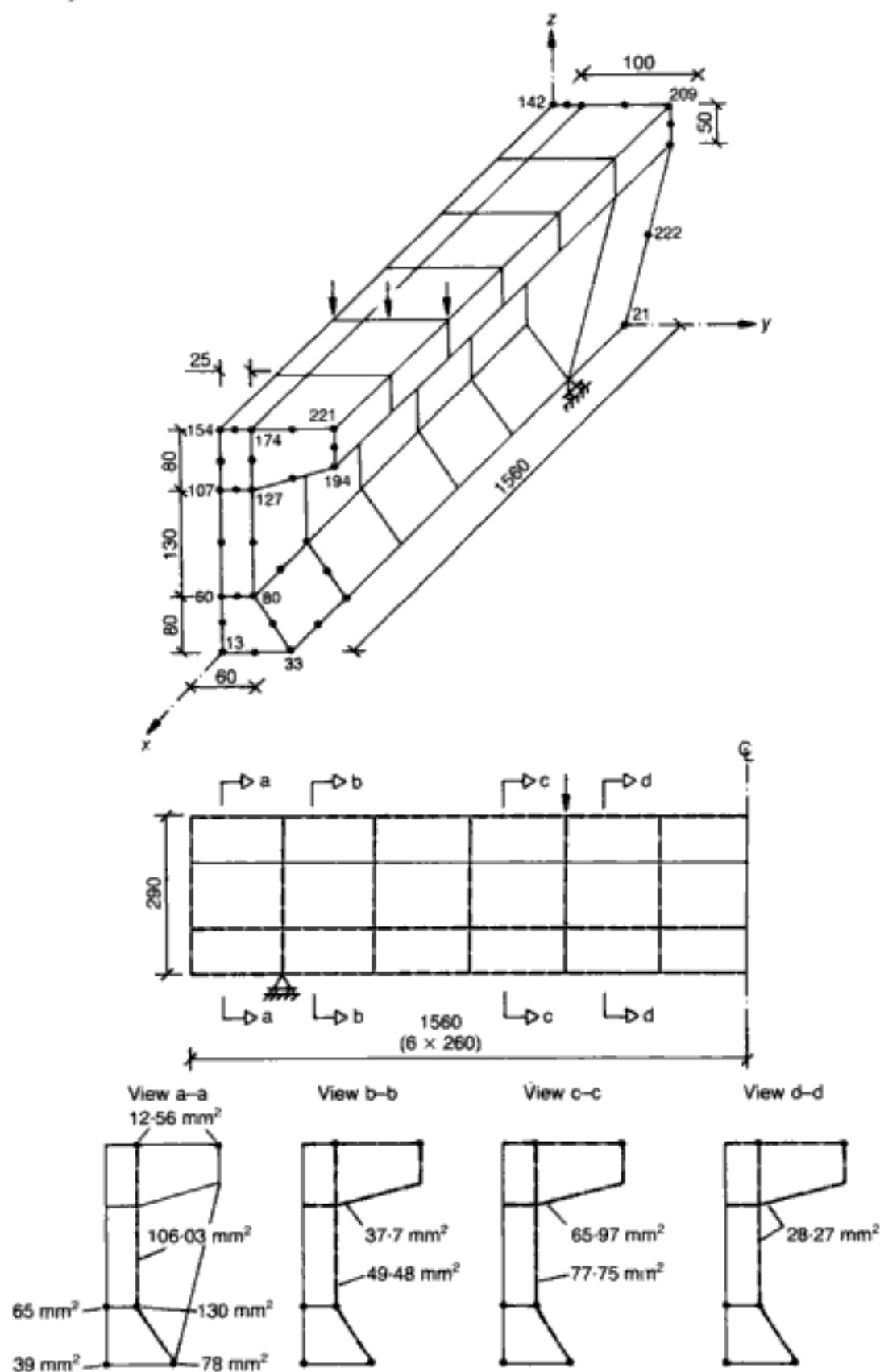
Fig. 4.47. Beam HSB2. Experimental data:¹⁷³⁻¹⁷⁵
 (a) dimensions and detailing of transverse reinforcement (all dimensions in mm);
 (b) crack pattern in the region where failure occurred

(b)

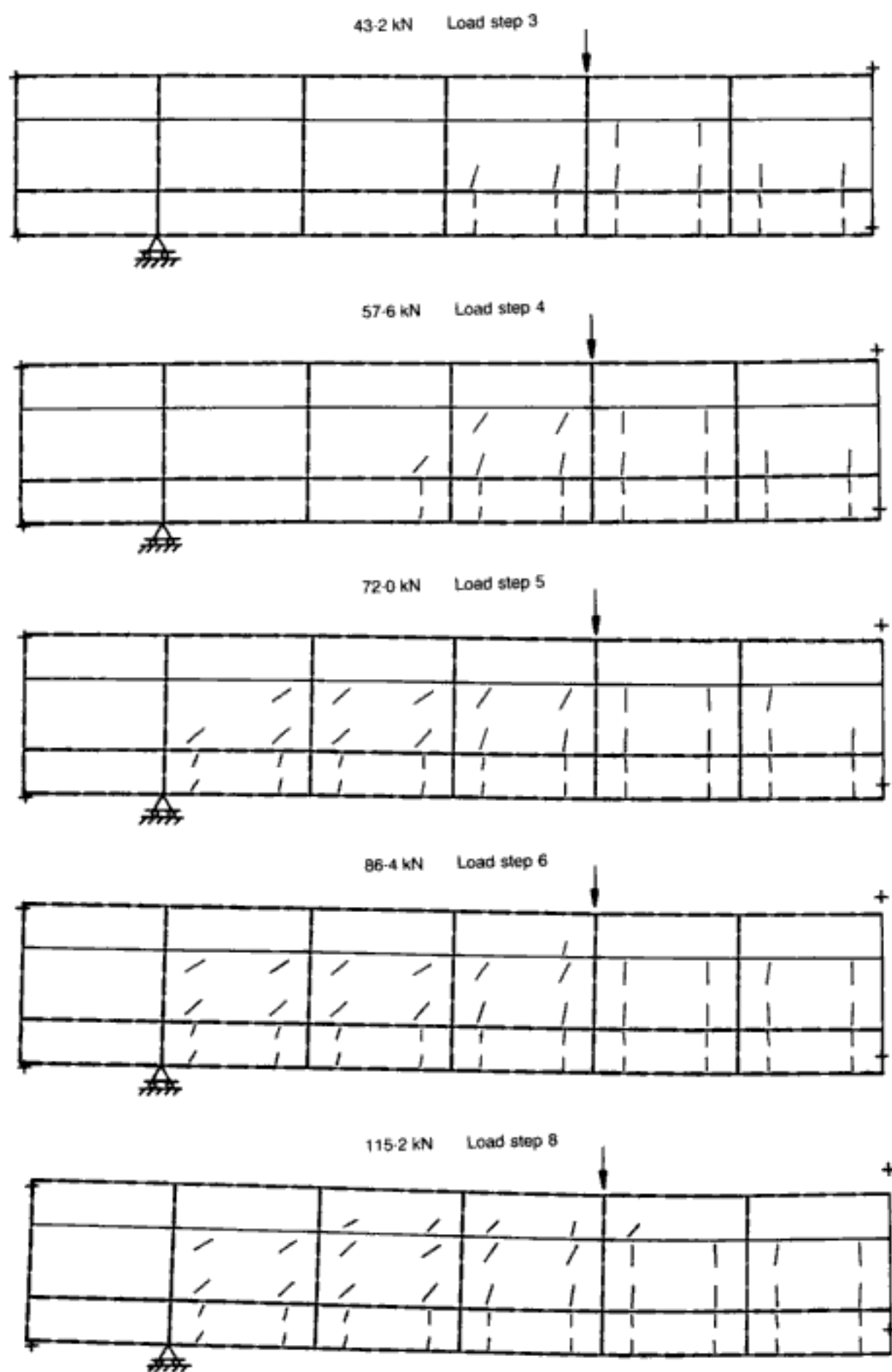
Fig. 4.48. Beam HSB2. FE mesh for one-quarter of the structure consisting of 25 HX20A brick elements (all dimensions in mm)¹⁷³

stiffness of the ascending branch and the ductility of the near-horizontal branch.

It may be interesting to report that a third T-beam (HSB3) was also tested and analysed.¹⁷⁵ This specimen was akin to HSB2 (with a third, additional, type of transverse reinforcement), except



Hidden page



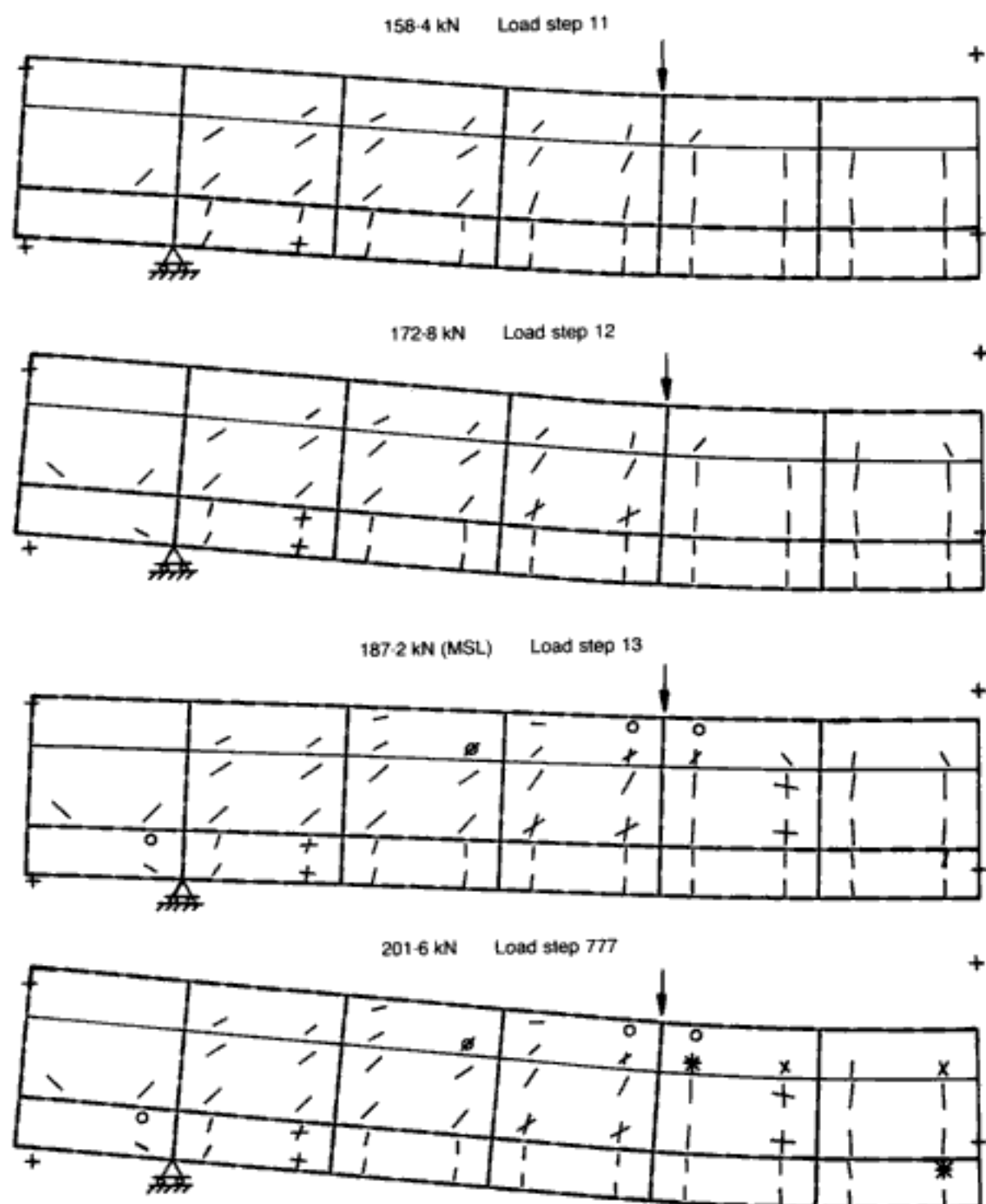


Fig. 4.49 (facing and above). Beam HSB2. Crack patterns and deformed shapes at various load stages¹⁷³

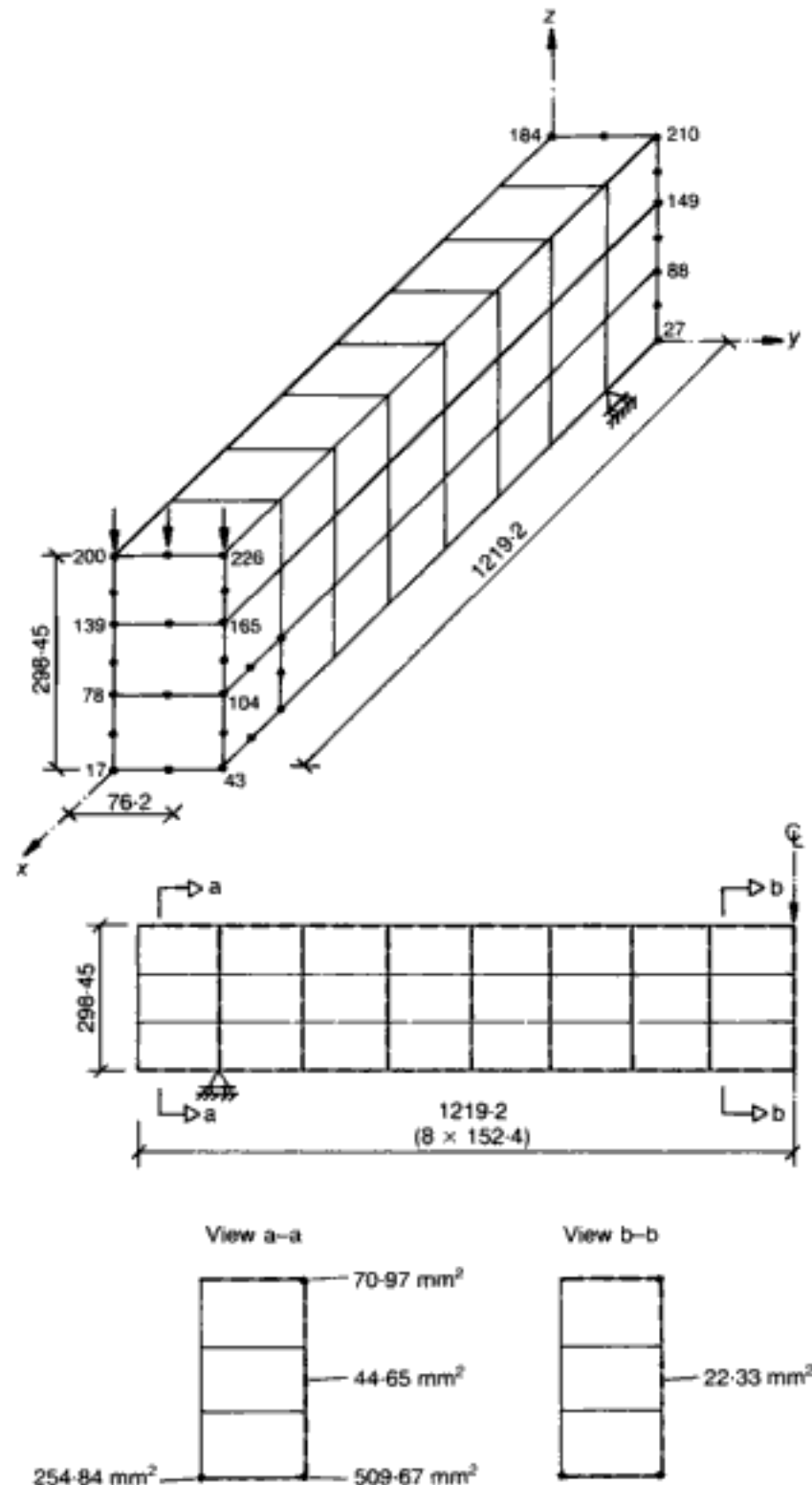
equal to the effective depth of the beam and the concrete cover was neglected altogether; in this respect, the adopted mesh is compatible with the minor contribution of the cracked areas to the transfer of shear forces and, thus, it appears that neglecting the cover can only affect the deformational response of the beam, while the ultimate-load prediction is insensitive to such a simplification as argued in earlier sections. The compression reinforcement was 'smeared' to the top edge of the beam; again,

Hidden page

Hidden page

relies greatly on the material properties. In this respect, it has already been pointed out that, in the absence of actual values of standard cylinder compressive strength, the value of f_c was estimated from 76.2 mm \times 152.4 mm cylinder strengths. But such an estimated f_c reported by the investigators¹⁷⁶ is applicable to the American standard cylinder having size 6 in \times 12 in. On the other hand, the input for f_c used in the FE model is based on the British

Fig. 4.52. Beam B150-11-3. FE mesh for one-quarter of the structure consisting of 24 HX20A brick elements (all dimensions in mm)¹⁷³



Hidden page

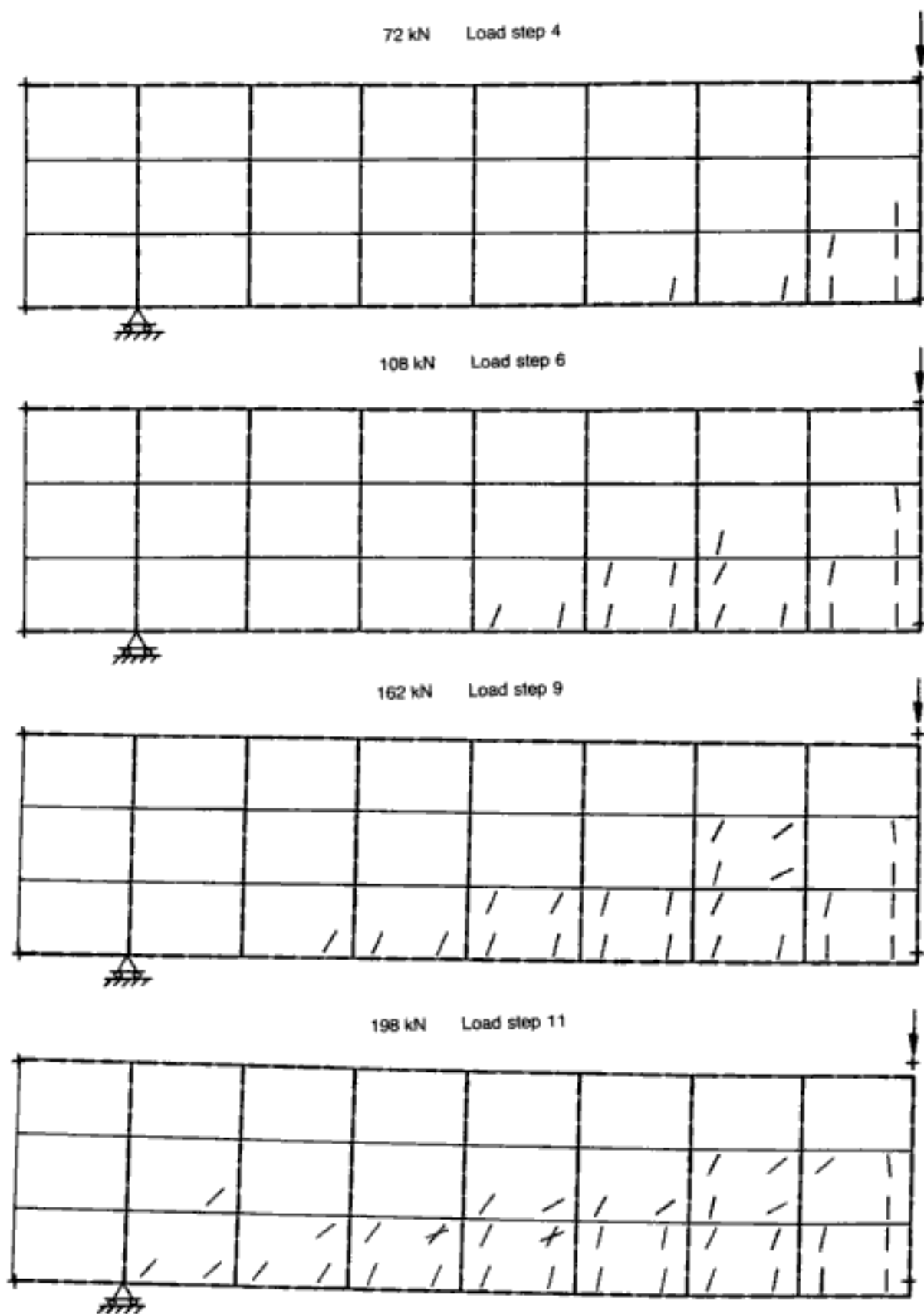
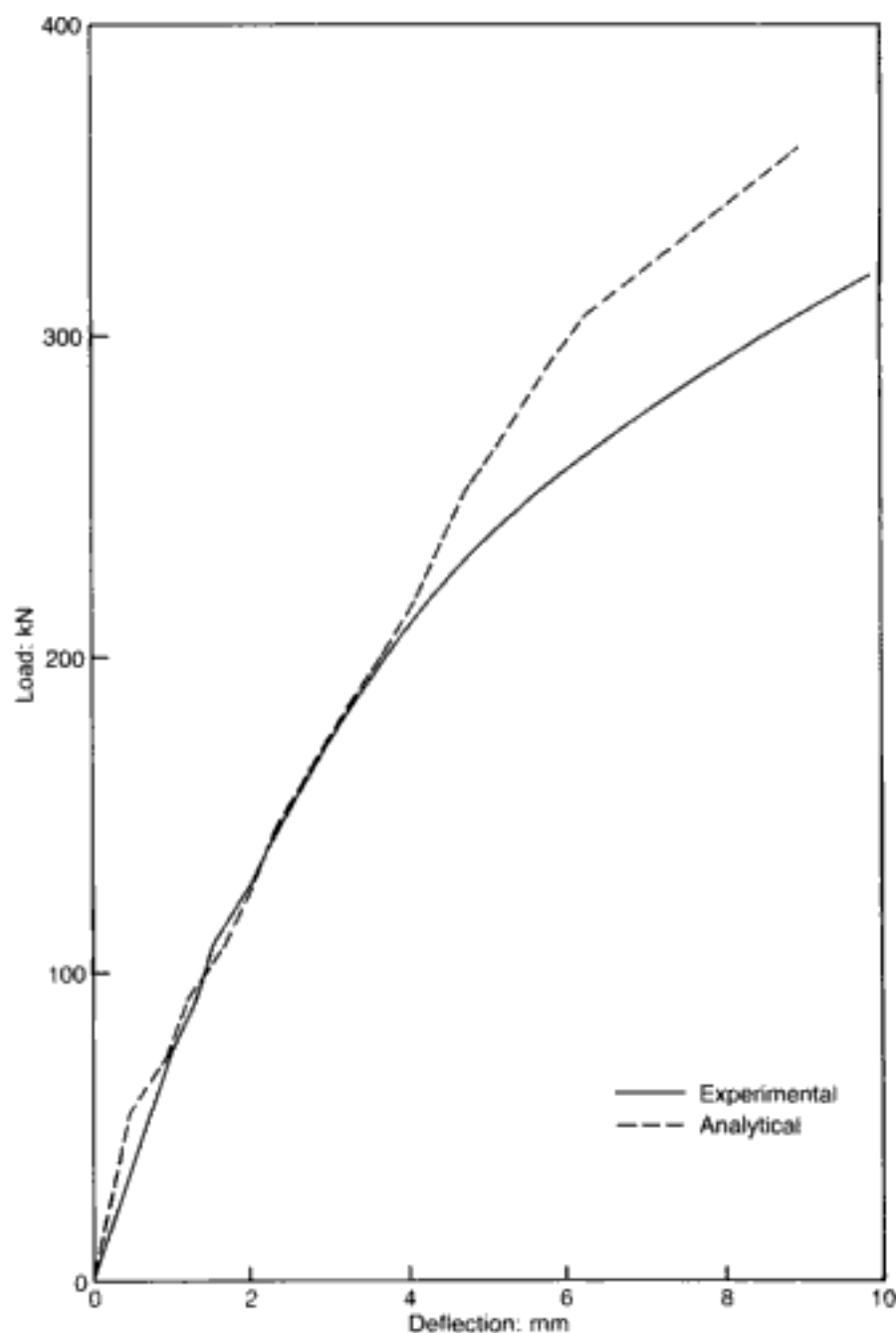


Fig. 4.53. Beam B150-11-3. Crack patterns and deformed shapes at various load stages¹⁷³

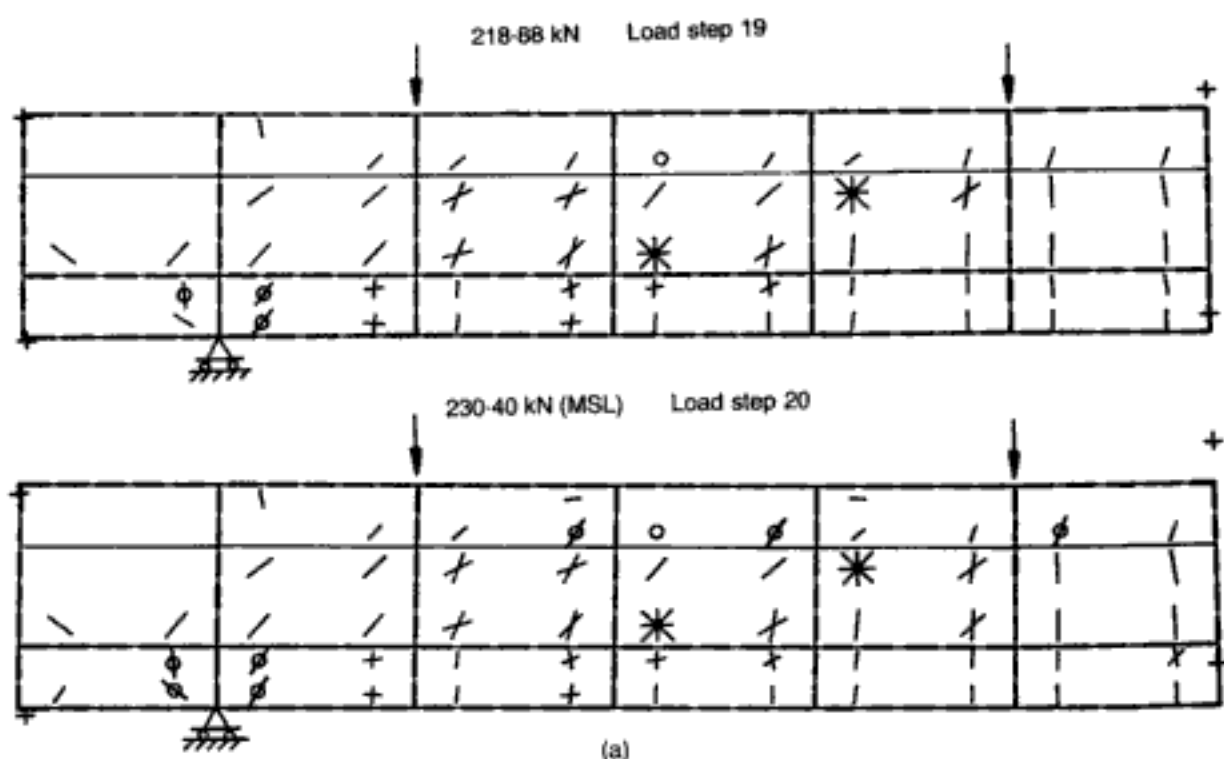
Hidden page

Fig. 4.54
(right). Beam
B150-11-3.
Comparison between
experimental and
analytical load-
deflection curves¹⁷³

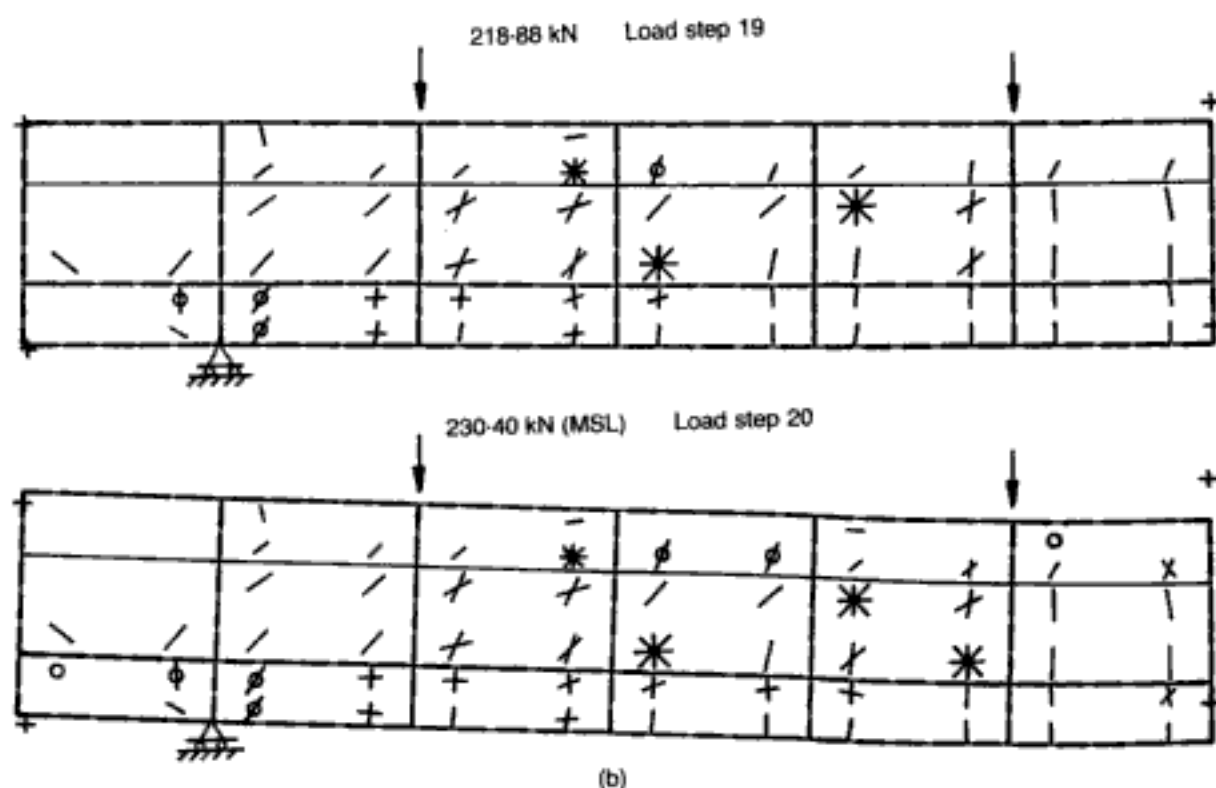
Fig. 4.55 (far right).
An analytical study of
flange-reinforcement
effectiveness in HSC
beams. Crack
patterns and deformed
shapes at the last two
converged load
steps:¹⁷⁵ (a) beam
HSB1 (with flange
reinforcement);
(b) beam HSB4
(without flange
reinforcement)



The ultimate load-carrying capacities of HSB4 and HSB5 were found to be equal to the load-carrying capacities of HSB1 and HSB2 respectively, signifying the apparently negligible role of flange reinforcement in the overall failure load of a member, as expected. On the other hand, and in contrast to NSC behaviour, the load-deflection curves of the beams without flange reinforcement were identical to their counterparts with flange reinforcement (the deflections at the ultimate failure load in beams without flange reinforcement being trivially smaller than their counterparts). The initial stages of the cracking processes of HSB4 and HSB5 were also found to be very much akin to those of HSB1 and HSB2, respectively.



(a)



(b)

In Fig. 4.55, the analytical crack patterns of the last two converged load steps of the nonlinear analyses of HSB1 and HSB4 have been shown (previous load steps are identical). It can be seen from the figure that, at a load of 218.88 kN, the top flange of HSB4 was subjected to more extensive cracking. The occurrence of a near-horizontal additional crack at the top-most Gauss point

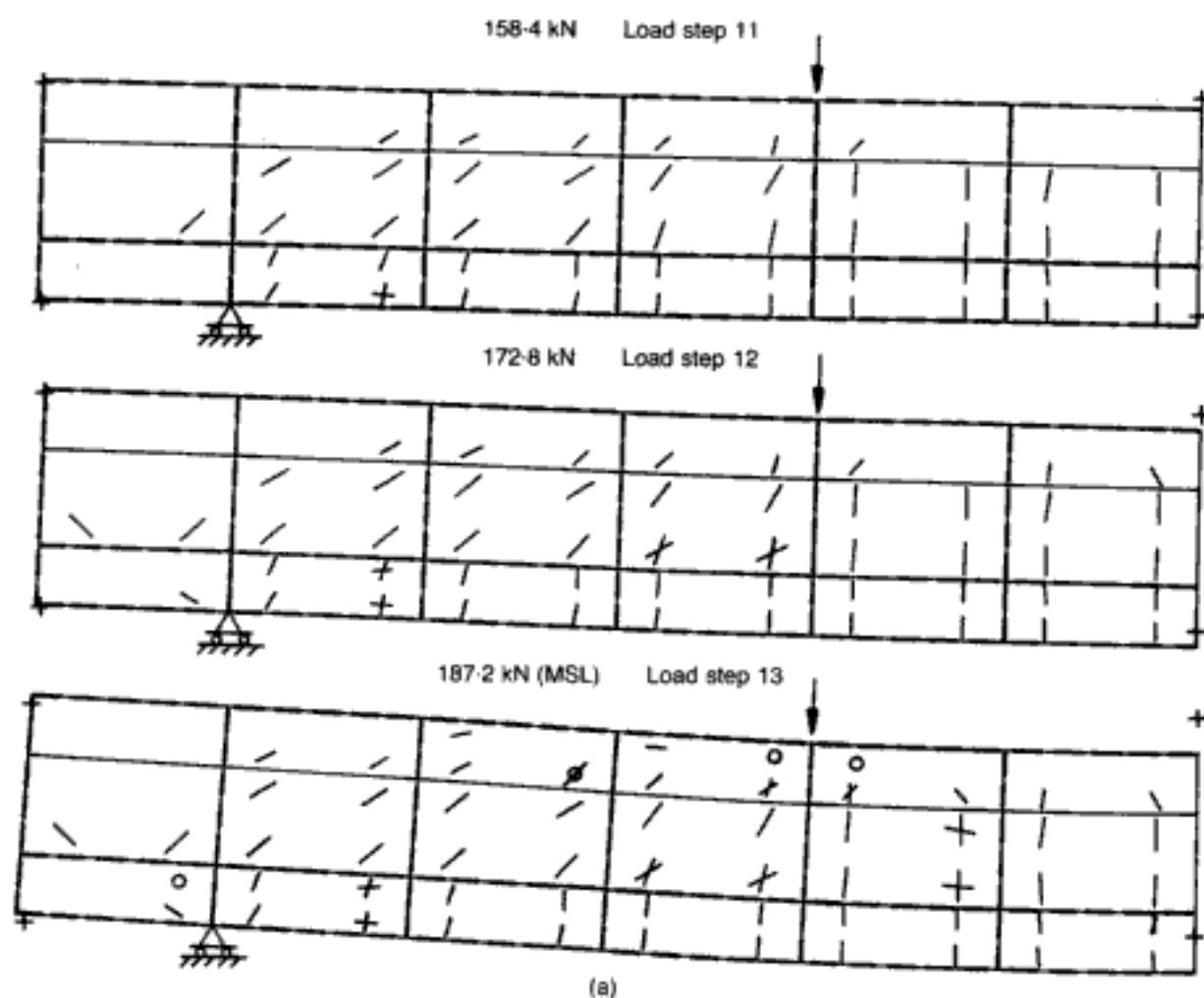


Fig. 4.56 (above and facing). An analytical study of flange-reinforcement effectiveness in HSC beams. Crack patterns and deformed shapes at the last three converged load steps.¹⁷⁵ (a) beam HSB2 (with flange reinforcement); (b) beam HSB5 (without flange reinforcement)

in the element nearest to the loading point close to the support and the complete loss of stiffness (marked by an asterisk) at another Gauss point in the same element, demonstrates clearly that, in the absence of flange reinforcement, cracks can penetrate deep into the flange. At the MSL of 230.40 kN, the web and top flange of HSB4 showed more pronounced cracking (as well as some additional deformation) than was the case for HSB1.

Similarly, the crack patterns of the last three load steps as obtained from the FE runs of HSB2 and HSB5 are shown in Fig. 4.56 (again, previous load steps yield identical crack patterns). At a load of 158.4 kN, one of the Gauss points near the support of HSB5 was slightly more cracked (marked by a cross) than HSB2. In the following load step, the top flange of HSB5 showed signs of additional cracks (identified by a circle with dash); the crack pattern of HSB2 at the same load step does not hint to similar cracks. At the MSL step, the top flange and web of HSB5 were more severely cracked as well. It appears from the final stages of the analytical crack pattern that the absence of flange reinforcement resulted in the widening of web cracks.

It is evident from the above numerical exercise that the triaxial

Hidden page

Hidden page

member (the limited ductility of the quasi-ductile beam made from normal-strength concrete could not be predicted so precisely by the FE discretization adopted). Furthermore, the role of flange reinforcement in achieving ductility in a NSC beam having been demonstrated experimentally,³ the present purely numerical studies have shown that the role of similar reinforcement towards the ductile behaviour of HSC beams is of less importance. Therefore, while the over-simplified modelling of flange reinforcement in HSB1 did not show much adverse effect on the prediction, it did affect the prediction of beam C at loads near failure, where flange reinforcement plays an active part. On the basis of such findings — admittedly, derived from the present limited analytical data — it would appear that a tentative conclusion might be that less attention need be given to the FE discretization of the reinforcement in the case of high-strength members. For, unlike their normal-strength counterparts, such components are known to exhibit less triaxial effects near failure and, hence, are less dependent on the actual confinement provided by the reinforcing steel. Such varying degree of 'triaxiality' between NSC and HSC structures, therefore, appears to make the latter type more amenable to simple modelling of complex reinforcement detailing.

4.6. Prestressed concrete beams

It is usual to view the design of prestressed concrete (PSC) members as somewhat of a speciality, with the implicit suggestion that their behaviour follows a structural philosophy that is, if not completely distinct from, then at least not quite coincident with, the approach and characteristics that are associated with RC design. (This thinking starts quite early on in the course of training of structural designers: in most undergraduate and postgraduate courses the analysis and design of RC and PSC structures are generally taught as separate subjects.) Yet, it is easy to argue that a PSC member may be viewed as an RC structure but with an additional, eccentric thrust force acting on it before the usual external loads are applied. (With the increasing use of higher-strength steels in RC members, even the usual gap between mild steel (RC) and high-strength steel (PSC) is now less clear-cut.) The adoption of this unifying approach for structural concrete in its broadest sense enables the ready extension of the FE model — so far applied to the analysis of PC and RC members made from a wide range of concrete strengths — to be accomplished so as to encompass PSC elements also.

4.6.1. Modelling of PSC members and scope of the investigation programme

The effect of prestressing in a PSC member is to induce initial stresses in the concrete and reinforcing steel. When the present model is used for the analysis of PSC structures, stresses in the concrete can be simulated by applying the total effective prestressing force on the structural member right at the first load step so that, in the subsequent load steps of the nonlinear analysis, only the increments of the non-prestressing applied forces are

Hidden page

Hidden page

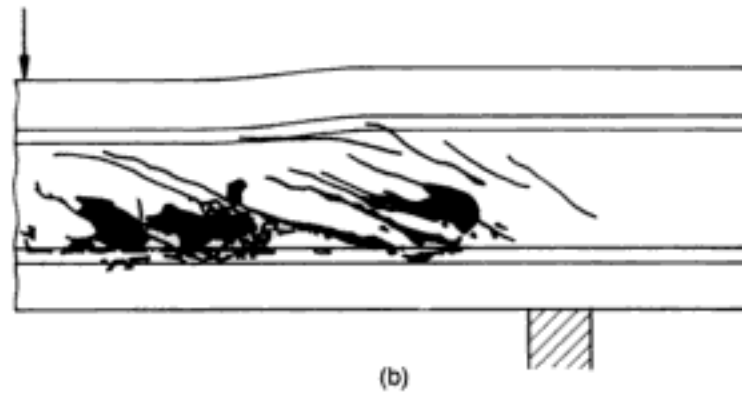
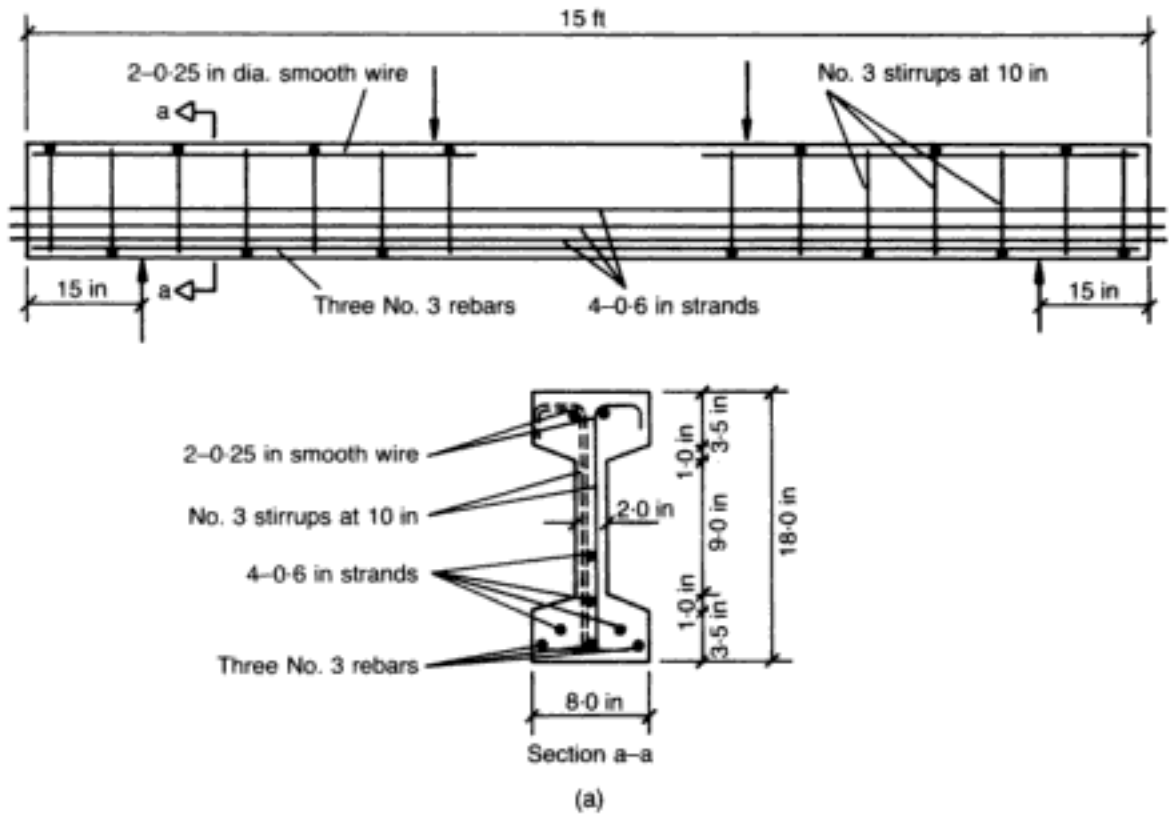


Fig. 4.58. Beam CW12. Experimental data:^{178,179}
 (a) dimensions and detailing of pre-stressing and reinforcing steel;
 (b) crack pattern after failure

side of the cross-section to the other (see Fig. 4.58(a)). However, for practical purposes it can be averaged and hence considered as symmetric; as a result, only one-fourth of the beam has been discretized on the basis of the assumed symmetry. Figure 4.59 also indicates the area of reinforcement of the various steel elements of the mesh. The prestressing and non-prestressing steel elements were treated separately. The former were 'smeared' to the adjoining brick-element edges in such a manner that the point of application of the resultant prestressing force remained unchanged. For purposes of estimating the (relative) length of the shear span, the distance of the centroid of the prestressing steel from the compression face has been considered as the effective depth (in the absence of explicit values in references 179 and 180). The effective prestressing stress, σ_p , was equal to 758.38 N/mm^2 .

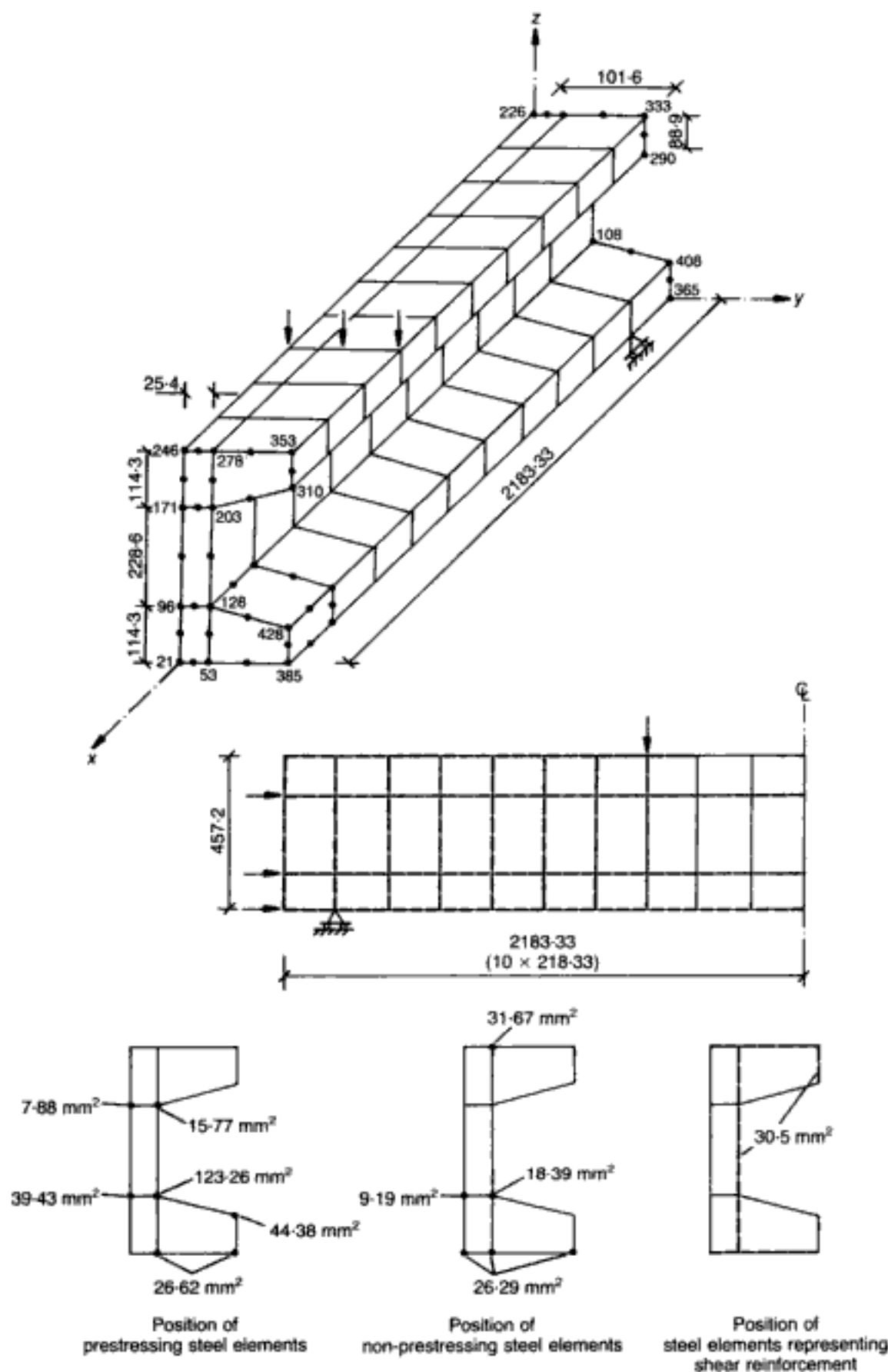


Fig. 4.59. Beam CW12. FE mesh for one-quarter of the structure consisting of 50 HX20A brick elements (all dimensions in mm)¹⁷⁸

After subtracting the value of σ_p from the stress-strain curve of the tendon, the $f_{y,model}$ and $f_{u,model}$ for the FE input were found to be equal to 990.29 N/mm^2 and 1090.57 N/mm^2 respectively. The non-prestressing steel area was also 'smeared' to its adjacent nodes in a similar manner. The compression reinforcement was placed at the top edge of the beam and was discontinued throughout most of the flexural span. The main modification introduced in the modelling of the shear reinforcement was that the original one-legged alternately-placed stirrups were replaced by equivalent two-legged stirrups to introduce symmetry across the longitudinal direction; however, the total area of steel per unit length (both in the web and flanges) was kept the same as in the actual beam.

The prestressing force was applied at the end of the beam as a constant force acting on the outside nodes of the prestressing steel elements. The amount of prestressing force at different nodes was varied depending on the area of the prestressing steel, so as to have everywhere the resultant prestressing force of the right magnitude and position. The vertical point loads were placed considering a_v/d to be equal to 3.75.

The maximum sustained load in the analysis was 323.38 kN, which is 15% higher than the experimental failure load of 281.11 kN. The analytical results may be discussed with reference to Figs 4.60 and 4.61, which show the analytical crack patterns up to failure and a comparison of the analytical and experimental load-deflection curves respectively. It should be noted that the experimental load-deflection curve, as obtained from reference 179, ends at a load of 267.76 kN, although the actual reported failure load mentioned previously was higher. At the first load step, in which the effective prestressing force was applied to the beam all at once, cracks appeared at the end block of the beam parallel to the direction of the prestressing force. The beam remained free from any flexural or shear cracks up to a load of 182.78 kN when, suddenly, web-shear cracks emerged along the whole length of the shear span. These cracks, which were formed at all Gauss points of the web elements (making an angle of about 22.5° with the longitudinal direction of the beam), resembled quite well the cracks that formed during the experiment, at the diagonal-cracking load of 170.8 kN. At a total applied load of 210.90 kN, the first flexural cracks appeared in the middle of the flexural span and also just below the point loads (see Fig. 4.60). One of the shear cracks extended towards the support at this stage. With the increase in load, flexural cracks were also formed in the shear span. At 309.32 kN, cracks near the loading points in the shear span started to propagate into the flange (hitherto uncracked) towards the actual point loads. At the MSL, additional cracks were formed in the top flange, defining more completely the compressive force trajectory; in addition, a vertical crack (indicated by a circle) in the top flange near the point load was visible. The analytical

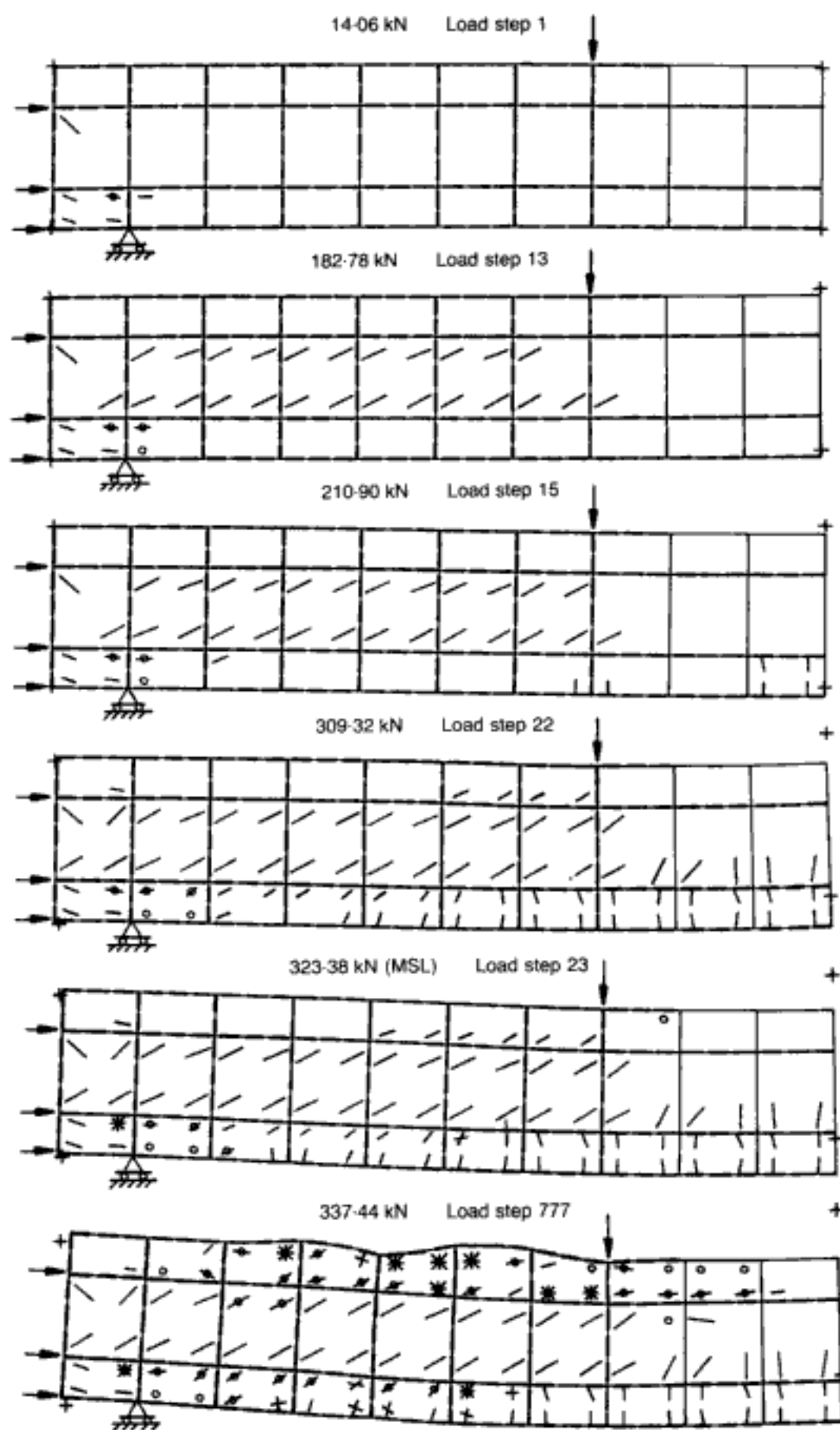


Fig. 4.60. Beam CW12. Crack patterns and deformed shapes ($D.M. = 5$) at various load stages¹⁷⁸

crack pattern at failure mimics accurately its experimental counterpart (see Fig. 4.58(b)).

As can be seen from Fig. 4.61, the analytical load—deflection curve practically coincides with its experimental counterpart up to the experimental failure load, and then continues to follow a tangential path up to the maximum sustained load. This increased load sustainment in the analysis can be explained with reference to the modelling of the stirrups. In order to keep the computational effort within sensible resources, symmetrical stirrups had to be introduced. In doing so, even though the total amount of reinforcement was carefully kept equal to the quantity used in the test, an additional confinement of the concrete was introduced in the analysis. It is important to recall that even a small amount of confining pressure (of the order of $0.1f_c$) is sufficient to increase the load-carrying capacity of concrete by more than 50% (see section 1.5.1). It is, therefore, reasonable to assume that, owing

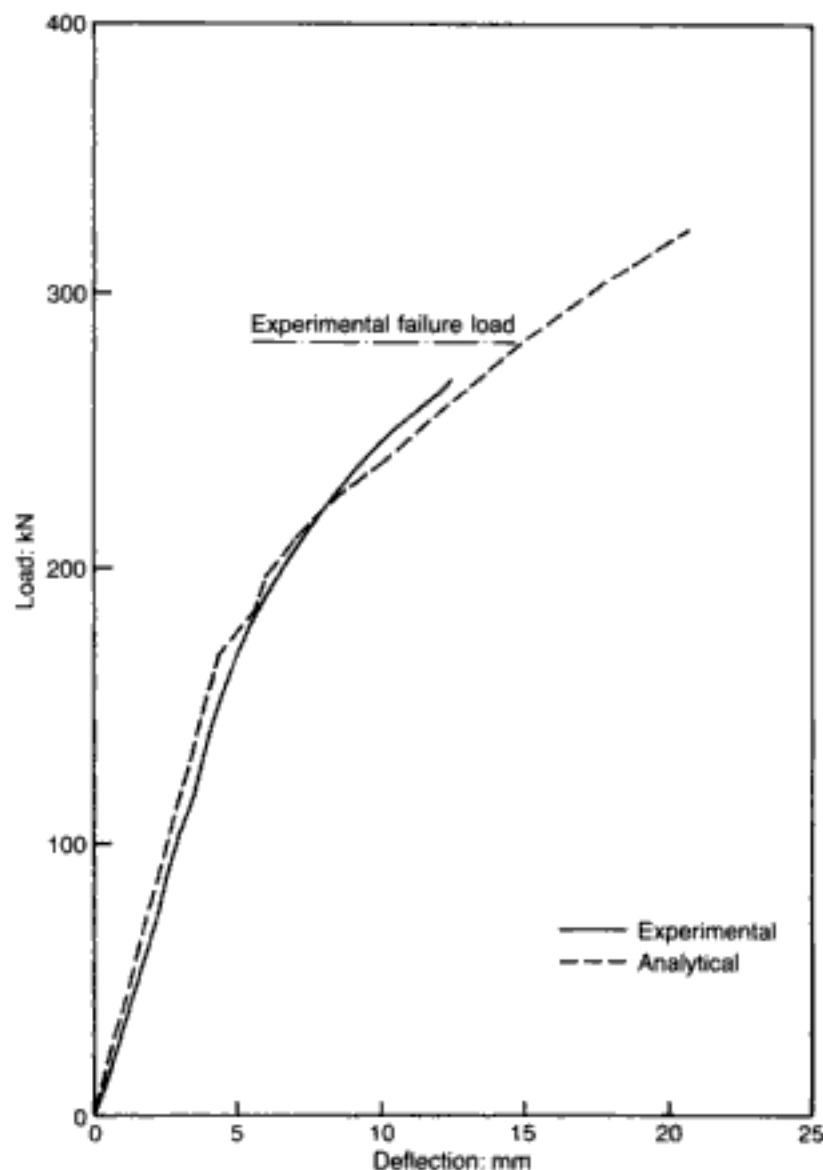


Fig. 4.61. Beam CW12. Comparison between experimental and analytical load—deflection curves¹⁷⁸

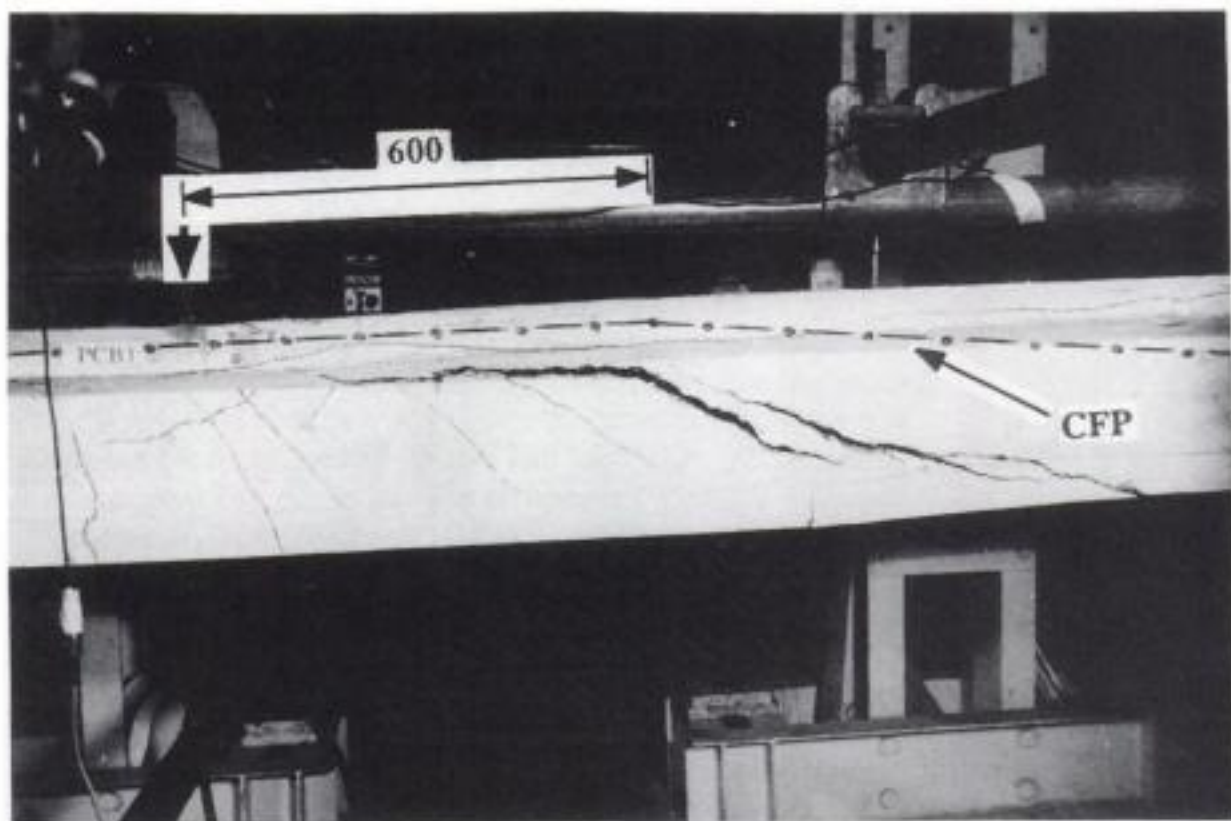
Hidden page

Hidden page

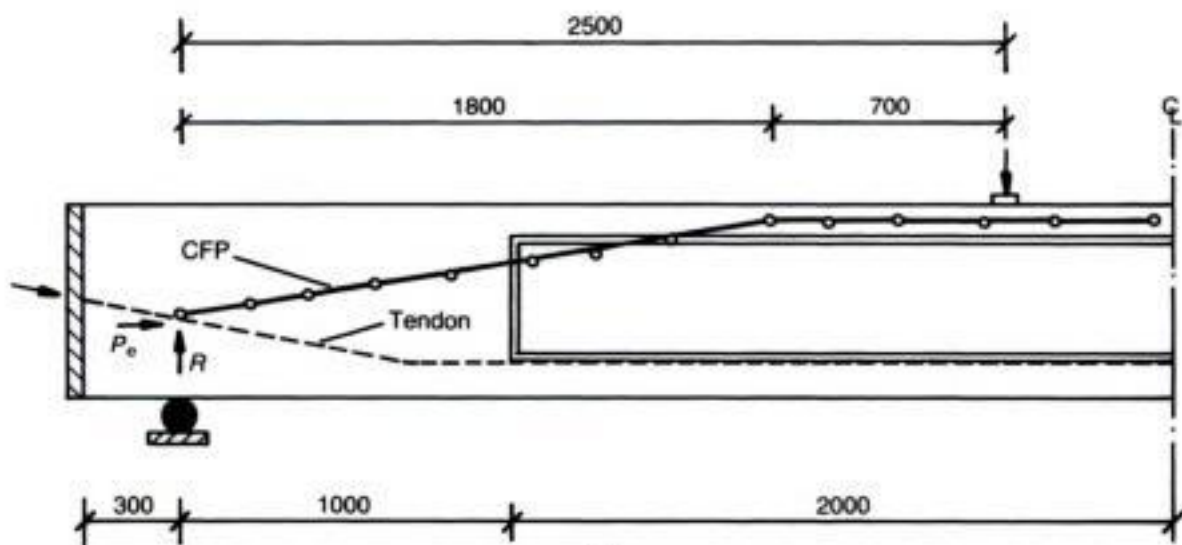
longitudinal cracking of the member. To prevent splitting and bursting, the end zones of the beams were provided with additional reinforcement in the form of stirrup and longitudinal bars (see Fig. 4.62(c)). Additional 8 mm diameter high tensile steel bars were welded longitudinally to the end plate to ensure that the latter component becomes an integral part of the beam when cast. As stirrups, 1.5 mm diameter wire was used.

Beam PCB1, analysed in this section, is a 6660 mm long girder, that is simply supported with a span of 6000 mm. The beam was subjected to a two-point loading with a shear span of 2500 mm. It is important to note here that, while the 5660 mm long beams PCB3, PCB6 and PCB7 had the straight tendon profile depicted in Fig. 4.62, PCB1 possessed a slightly inclined tendon profile along a distance of 1000 mm from the end. The depth of the tendons at the prestressing and support levels were 150 mm and 178.84 mm (as measured from the top of the beam) respectively. Beam PCB1 was tested¹⁸² in an effort to visualize the path through which the compressive force is transmitted in a PSC beam. The tendon profile of PCB1, along with the major crack pattern and the predicted compressive-force path, can be seen in Fig. 4.63. It is worth mentioning at this stage that the numerical modelling of the PSC T-beams, reported here, coupled with the experimental findings of these and other PSC beams, led to the verification of a physical model proposed for the realistic design of PSC members. While the experimental results and details of the physical model have been reported elsewhere,^{181,182} it is imperative to mention here that, according to this model, provision of design transverse reinforcement only at locations where the CFP changes its direction (i.e. an area where the resultant of the prestressing force and the reaction meet the centroid of the uncracked compression zone) is sufficient to lead the PSC structural member to a flexural form of failure, provided possible bond failure is prevented by placing additional 'hoop-like' reinforcement in the compression flange.

In order to test the basic ideas, the beam was neither designed to BS 8110, nor were the recommendations of the CFP concept implemented; such an approach ensured that the member would fail in shear, and thus the web of the beam was furnished with nominal reinforcement. Such nominal reinforcement was about 40% of the web reinforcement which is prescribed by BS 8110. On the other hand, such nominal web reinforcement could cater for only 60% of the transverse reinforcement (in accordance to the CFP design) which would have been needed, at locations where the CFP changes its direction, in order to sustain the tensile force that develops at those places. In this way, while both the BS 8110 and the CFP design requirements refer to flexural failure, in the actual test a shear type of failure was sought. However, in order to guarantee that the planned shear failure takes place as a result of the (additional) tensile stresses at the location where the CFP



(a)



(b)

Fig. 4.63. Beam PCB1.^{174,182} (a) crack pattern at failure and observed CFP; (b) tendon profile and predicted CFP (All dimensions in mm)

changes direction, and not as a result of bond failure, the flange of the beam was provided with an adequate amount of links, as can be calculated from CFP provisions. (For a detailed calculation regarding the assessment of web and flange reinforcement, as advocated by BS 8110 and CFP methods for flexural failure of PCB1 to have occurred, see reference 174.)

Beam PCB1 had two types of transverse reinforcement. Type 1 consisted of 1.5 mm dia. two-legged links extending from the top face of the beam to the level of the tension reinforcement, placed throughout that length of the beam having a T-section, at 100 mm

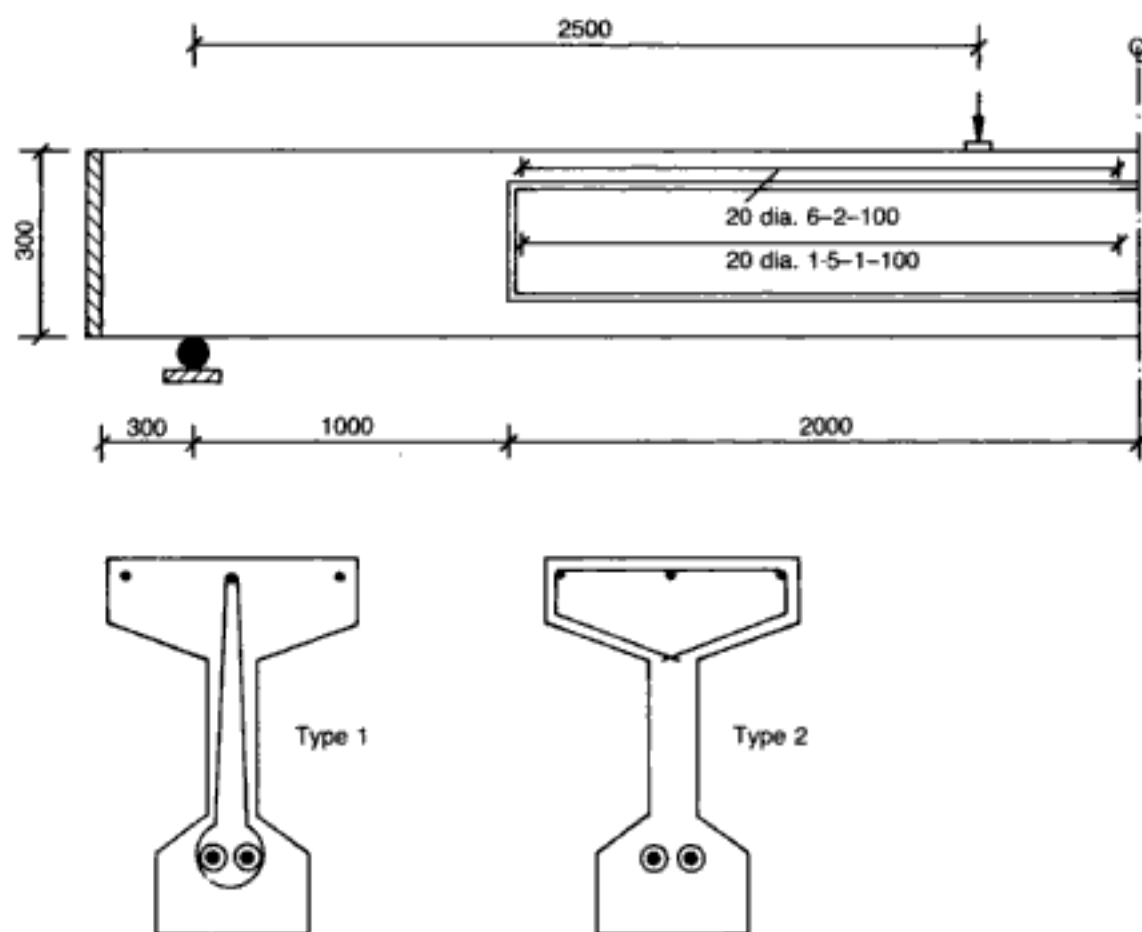


Fig. 4.64. Beam PCB1. Transverse reinforcement details (all dimensions in mm)^{178,182}

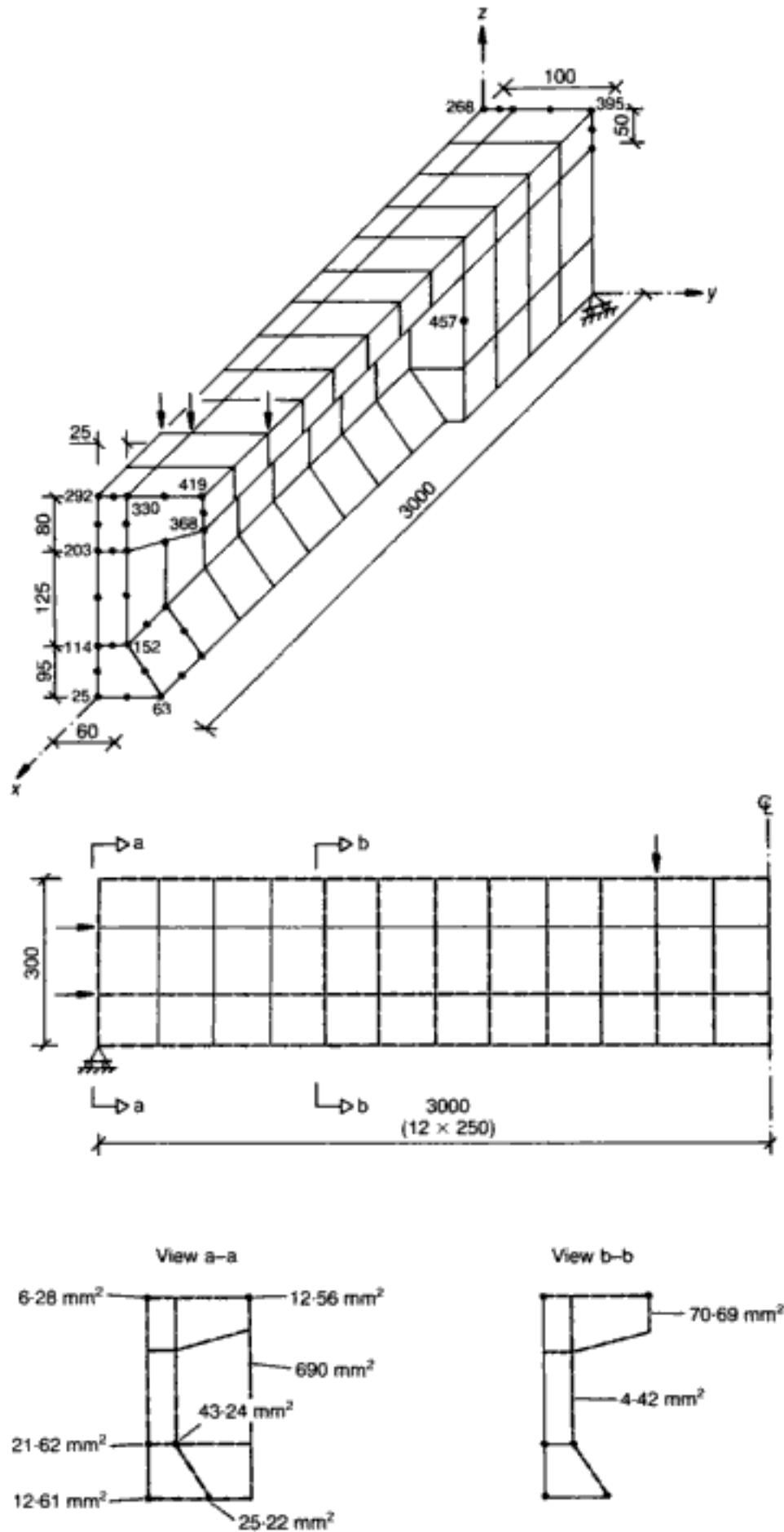
spacing. Type 2 reinforcement comprised 6 mm dia. links placed around the top flange of the beam (again, throughout the T-section portion) at a spacing of 100 mm. Details of the transverse reinforcement are shown in Fig. 4.64. The strength characteristics of the tendons and reinforcing bars used in the PSC T-beams analysed are listed in Table 4.5. The f_c value for PCB1 was 46.4 N/mm^2 .

The FE discretization adopted for the current analysis is given in Fig. 4.65. The mesh has 56 HX20 under-integrated brick elements for concrete and 182 LM03 bar elements for the steel (considering only one-fourth of the beam). (It should be noted that, in Fig. 4.65, there appear to be only 161 steel elements: this is because an additional 21 reinforcing bars at the end of the beam coincide with the location of other steel elements.) A few minor

Table 4.5. Characteristics for reinforcing bars used in case studies 2–5 (PCB1, PCB3, PCB6, PCB7)¹⁷⁸

Type of reinforcement	f_y : N/mm ²	f_u : N/mm ²
12.9 mm dia. stabilized strand	1684.5	1908.5
6 mm dia. high-yield steel	570	665
4 mm dia. mild steel	460	540
1.5 mm dia. mild steel	460	510

Fig. 4.65. Beam PCB1. FE mesh for one-quarter of the structure consisting of 56 HX20A brick elements (all dimensions in mm)¹⁷⁸



simplifications were adopted during the discretization process. The bottom flange of the T-section of the beam was replaced by a trapezoidal section, thus saving 12 brick elements. Such a step can be justified on the basis of the earlier investigations in section 4.5, which showed quite conclusively that, in the modelling of RC T-beams made from a wide range of concrete strengths, such a deviation from the actual shape of the bottom flange in the FE discretization has no impact on the overall prediction of the analysis. The rectangular section forming the end part of the beam, however, was properly discretized. On the other hand, the part of the beam beyond the support was omitted in the FE analysis, since the length of the member was quite large and hence the number of FEs was high. (In case studies 3, 4 and 5, the smaller spans allow overhangs to be included in the FE analysis without impairing the economy of the runs.) The total amount of steel used in the end plate was lumped onto the edges at the support. More significant changes were made in the modelling of the prestressing tendon. Although the actual tendon profile was inclined slightly towards the end of the beam (see Fig. 4.63), it was considered as a straight tendon; like the remainder of the tendon, it too was 'smeared' to the neighbouring brick-element edges. The effective prestressing force, however, was distributed at the nodes in such a manner that its resultant acted at the true tendon level at the support: this force being 49% of the ultimate strength of the strands, the yield and ultimate strength of the tendon were inputted as 754.73 N/mm^2 and 978.63 N/mm^2 respectively (thus omitting that part of the stress-strain curve involved in the prestressing process). The area of the transverse reinforcement was adjusted so as to keep the same area per unit length as in the actual beam. The loading configuration adopted in the analysis was the same as in the experiment.

The analytical findings can be seen by reference to Figs 4.66 and 4.67, which give, respectively, crack patterns at various load levels up to failure and a comparison of the load-deflection curve with its experimental counterpart. As depicted in Fig. 4.66, the first set of flexural cracks were formed in the pure flexural span at an applied load of 28 kN. (Unlike beam CW12, analysed in case study 1, where end-zone cracking took place, the presence of the steel end plate ensured that no such cracking due to prestressing occurred in PCB1). In the next two load steps of 4 kN each, the number of flexural cracks increased and a few inclined cracks were formed. When the applied load reached 40 kN, that part of the web which consisted of a T-section was subjected to a large amount of diagonal cracking. All the flexural cracks reached the intersection of the top flange and the web at this stage. At a load of 44 kN, new cracks were formed in the bottom flange, and both the web and the bottom flange incurred some additional cracking upon application of the next load step (48 kN). At the MSL level of 52 kN, which was about 92% of the experimental failure load of

Hidden page

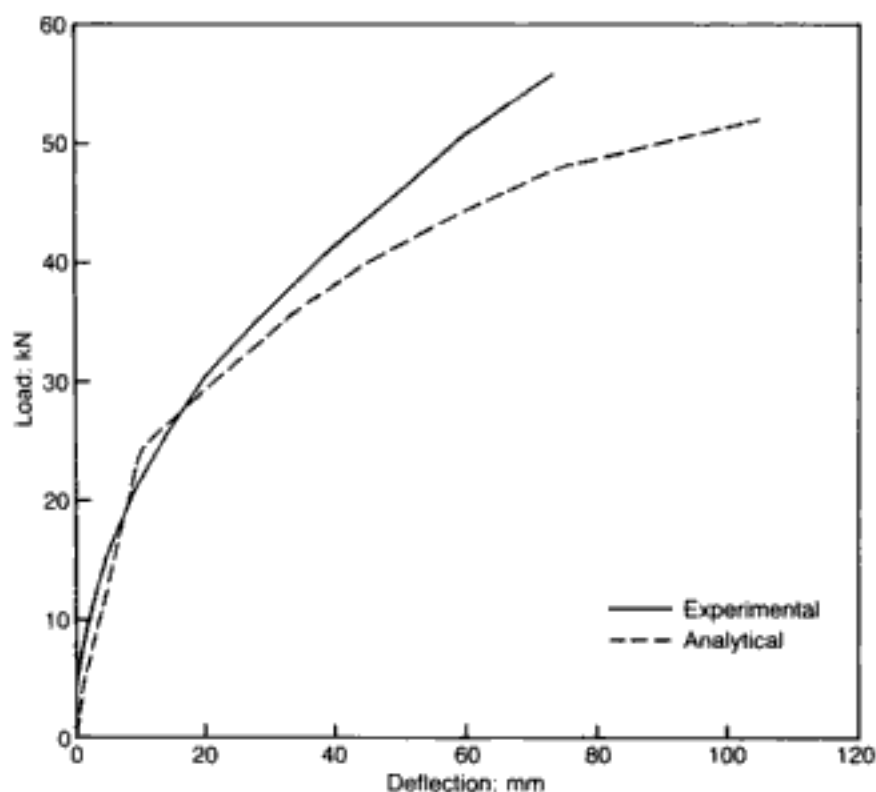


Fig. 4.67. Beam PCB1. Comparison between experimental and analytical load-deflection curves¹⁷⁸

57 kN, cracks entered into the top flange near the loading points. The crack patterns at MSL and at the load step '777' are similar. If the symbols comprising either crosses or circle with oriented dash (i.e. doubly-cracked zones), are connected by a hypothetical line, the pattern of cracking at failure can be visualized; and, in turn, from it the location of the change in CFP trajectory may be estimated. This location where the CFP changes direction is marked by the Gauss point having a circle and a dash. It may be seen that the numerical prediction of the crack pattern matches quite closely the experimental failure pattern of Fig. 4.63. The analytically obtained load-deflection curve, although slightly less stiff in the latter stages of loading than the experimental curve, also simulates fairly well the deformational response of the beam.

4.6.4. Case study 3: PSC T-beam subjected to six-point loading failing in shear

Details of the transverse reinforcement of PCB3 along with those of PCB6 and PCB7 are shown in Fig. 4.68. All these three beams were subjected to six-point loading. The transverse reinforcement of PCB3, prestressed to an effective prestressing force of about 50.7%, was designed for flexural failure in compliance with the provisions of BS 8110 (for the relevant design calculations, see reference 174). The f_c value for PCB3 was 46.3 N/mm². Figure 4.69 shows the crack pattern at failure.

The FE discretization adopted for the present analysis is shown in Fig. 4.70, with the mesh having 54 HX20 under-integrated brick elements to represent concrete and 164 LM03 bar elements for the steel (considering only one-fourth of the beam). (In the mesh of Fig. 4.70, only 146 steel links can be seen but this is because

Hidden page

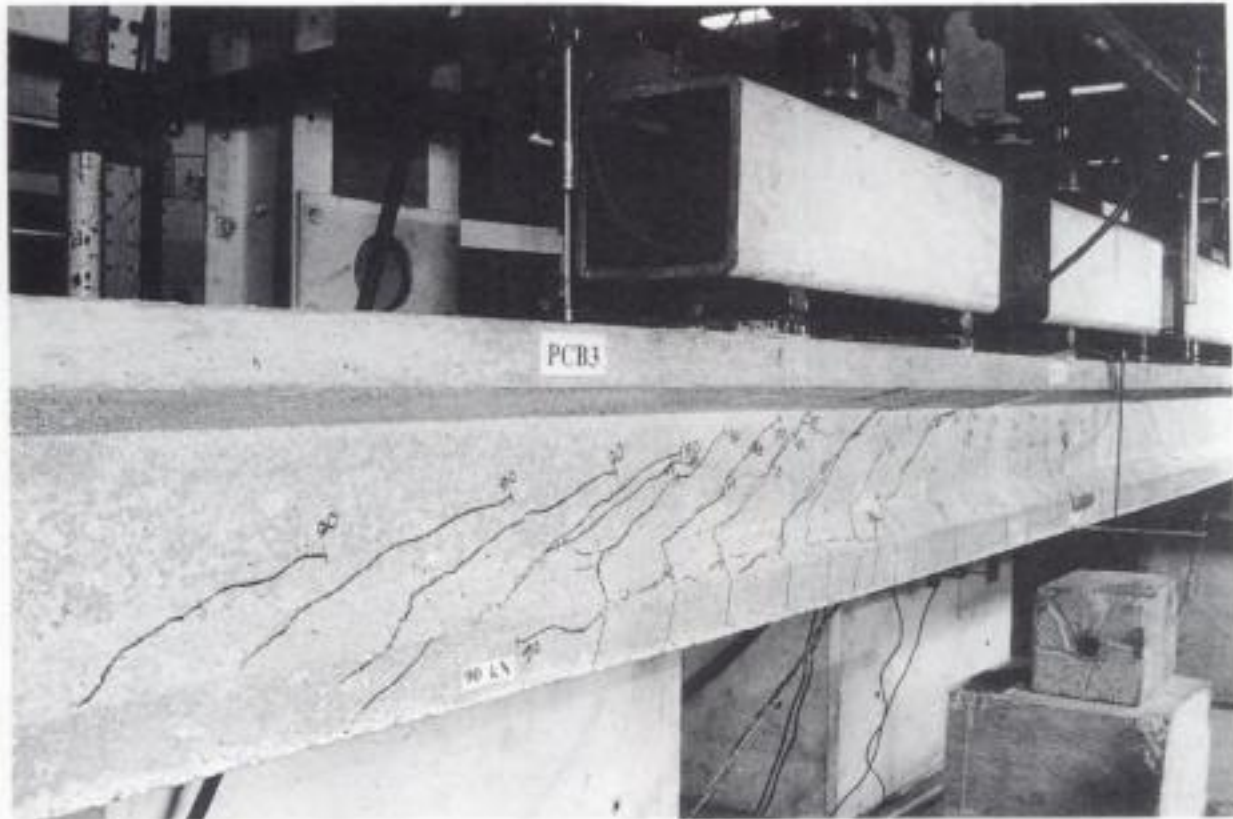


Fig. 4.69. Beam PCB3. Crack pattern at failure¹⁸²

of the overlapping of 18 reinforcing bars at the end of the beam with other steel elements.) A few minor changes for both the actual dimensions of the span and the position of the loads were introduced in order to use a regular mesh. The half-length of the beam (from the support to the centreline) in the model was 2513.5 mm instead of the actual dimension of 2500 mm. The overall length of the rectangular block was also reduced; its length overhanging the support was 228.5 mm instead of 300 mm, and the rectangular block from the support up to the beginning of the T-section was 457 mm long instead of the 500 mm used in the experiment. The loading point nearest to the support in the model was located at a distance of 1371 mm instead of 1357 mm; nevertheless, the distance between the point loads both in the analysis and in the experiment was 457 mm. These changes, however, seem to be of only very minor consequence, as the shear forces and bending moments at all the critical sections remain virtually unaffected by such modifications. It can be seen from Fig. 4.70 that the bottom flange has been modelled by adopting a trapezoidal shape in order to economize in the FE modelling: again, and as shown previously, this simplification has very little or no impact on the overall prediction of the model, as concrete below the neutral axis plays a much less vital role than widely believed. Figure 4.70 also indicates the area of reinforcement of various steel elements of the adopted mesh. All the steel elements were 'smeared' to the adjoining brick-element peripheries. Although the longitudinal top steel was placed at the top edge of the flange, the prestressing steel was smeared in such a manner that both the amount and its centroid

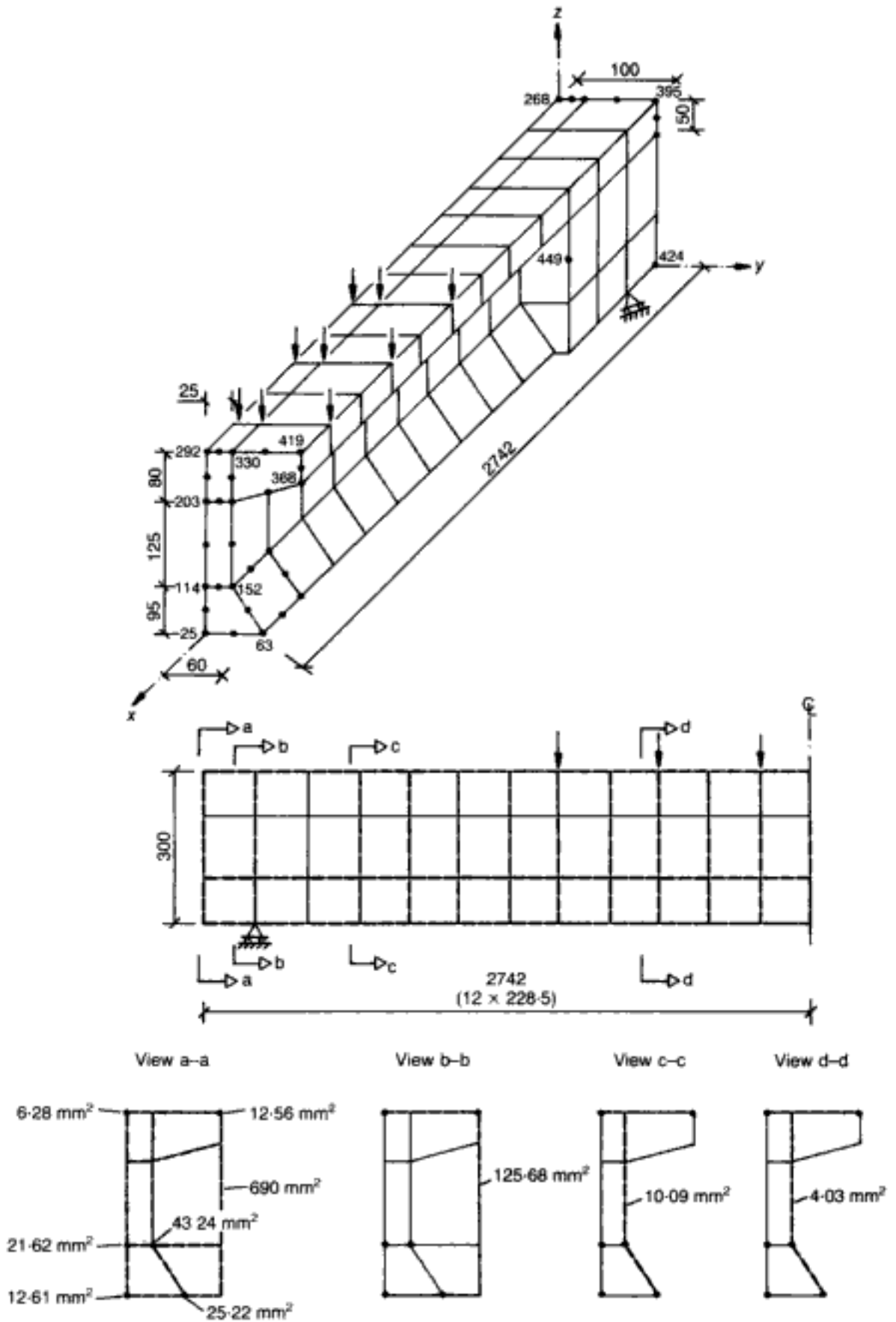


Fig. 4.70. Beam PCB3. FE mesh for one-quarter of the structure consisting of 54 HX20A brick elements (all dimensions in mm)¹⁷⁸

remained unchanged at the various nodes (hence the resultant prestressing force, both in magnitude and position, remained true to the actual value). The equivalent area of web and flange steel was calculated and smeared to the abutting brick-element edges in an effort to keep its amount per unit length unchanged. The vertical load was applied to the beam at a rate of about 6.67% of the failure load.

Figure 4.71 shows the analytical crack pattern at different load levels up to failure. The MSL in this analysis was 84.17 kN, which is about 92% of the load (including the dead load of the spreader beams) sustained by the beam in the experiment (91.5 kN). The first set of flexural cracks were seen in the midspan and under the innermost loading points at an applied load of 48.10 kN. At a load of 54.11 kN, the number of flexural cracks increased and they entered into the web. Initiation of shear cracks in the web could also be detected at this stage. When the load rose to 60.12 kN, the flexural cracks, formed near the midspan, reached the interface of top flange and web. At the next load step (11), the web of the beam was full of shear cracks. Upon the application of the next two load steps, the shear cracks of the web propagated downwards into the bottom flange and, in addition, the web under the inner loading points became more severely cracked. At the MSL of 84.17 kN, the severity of shear cracking was more pronounced and, one of the cracks, in the midspan of the beam, made its way into the compression flange; the overall crack pattern at this stage resembles quite closely the experimental one (Fig. 4.69). Examination of the cracking pattern for load step '777' reveals that, at the point of numerical divergence, quite a few diagonal cracks actually penetrated into the top flange. At the midspan of the beam, vertical and near-horizontal cracks also occurred. It seems that absence of flange reinforcement, in the form of hoops, helped the penetration of the cracks deep into the compression flange, and this, aided by inadequate transverse reinforcement at the CFP-change locations, prompted the beam to sustain a brittle (quasi-ductile) failure. The analytical and experimental load–deflection curves are compared in Fig. 4.72, the former tracing its test counterpart faithfully up to the very last step, where its peak falls just below the experimental value. It is apparent from the above exercise that the experimental findings of the PSC beam PCB3 have been adequately simulated by the FE modelling.

4.6.5. Case study 4: PSC T-beam subjected to six- point loading failing in flexure

The design reinforcement of PCB6, prestressed to an effective prestressing force of about 60%, was provided in compliance with the CFP concept, with the relevant calculations for flexural failure available elsewhere.¹⁷⁴ This member's actual dimensions and transverse-reinforcement details are depicted in Figs 4.62 and 4.68(b) respectively, while its crack pattern at failure appears in

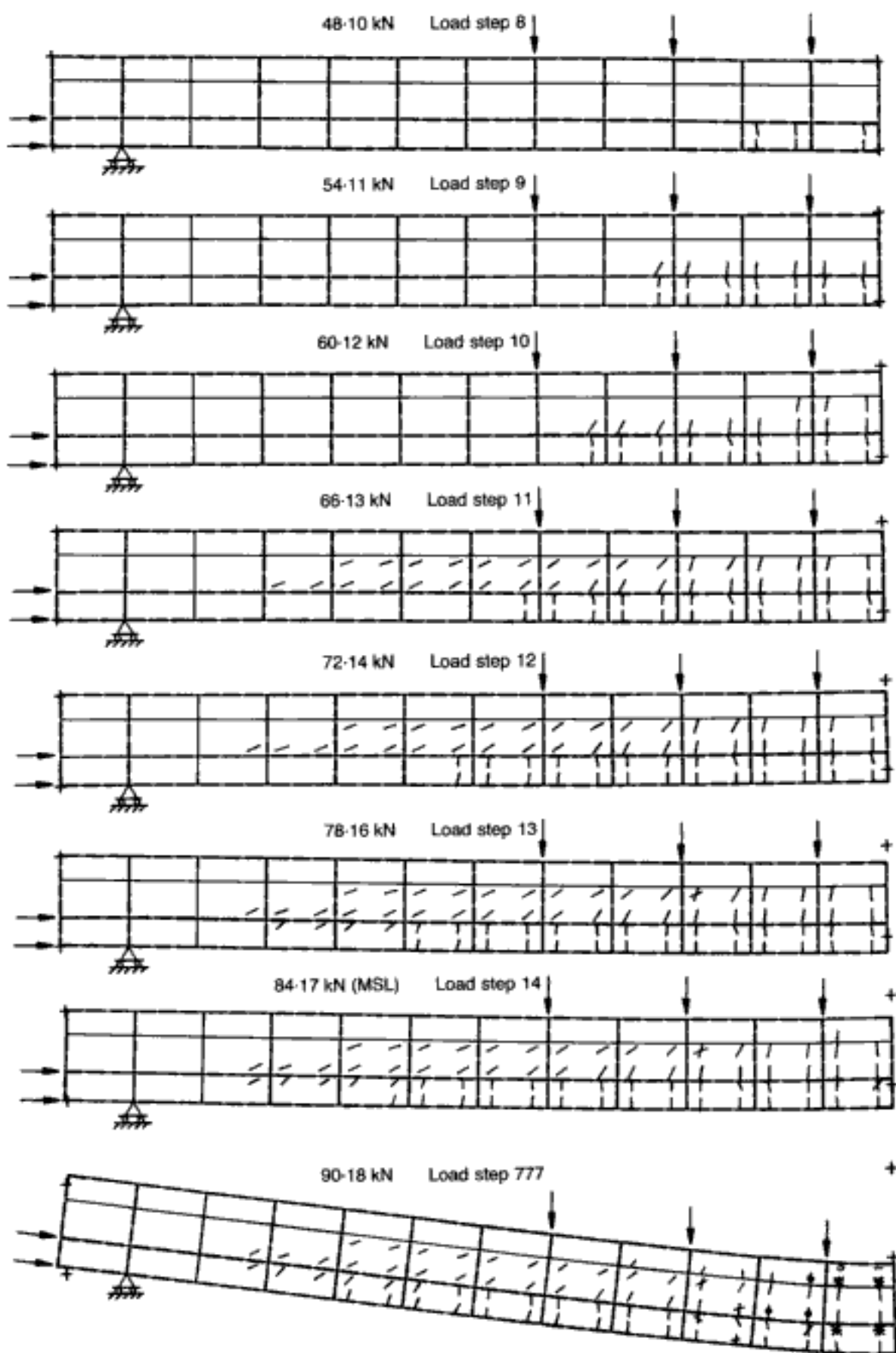


Fig. 4.71. Beam PCB3. Crack patterns and deformed shapes (D.M. = 1) at various load stages¹⁷⁸

Fig. 4.72. Beam PCB3. Comparison between experimental and analytical load-deflection curves¹⁷⁸

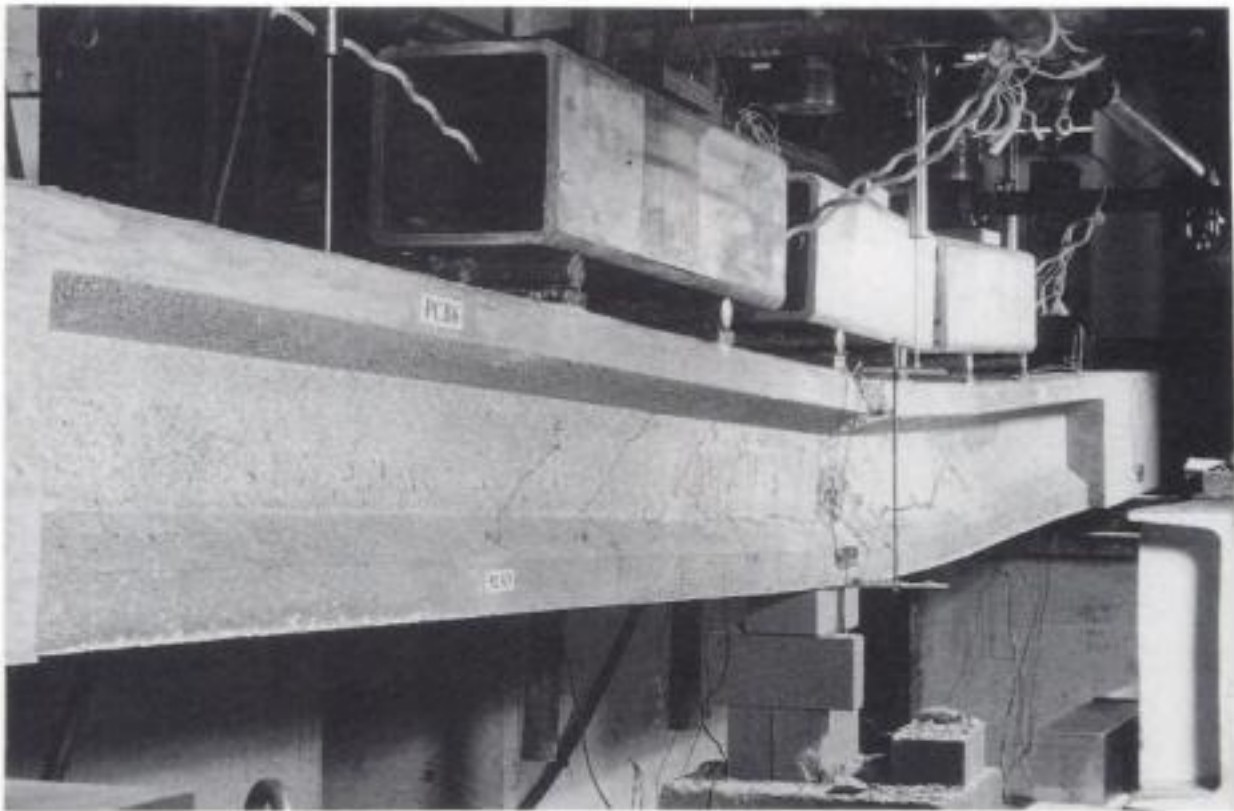
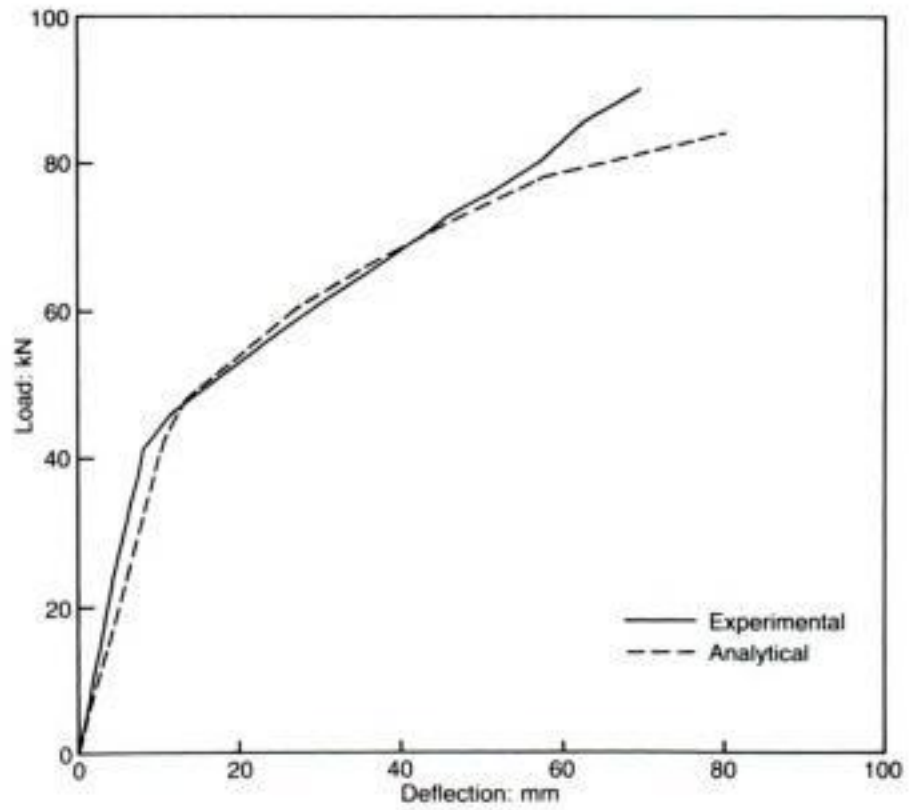


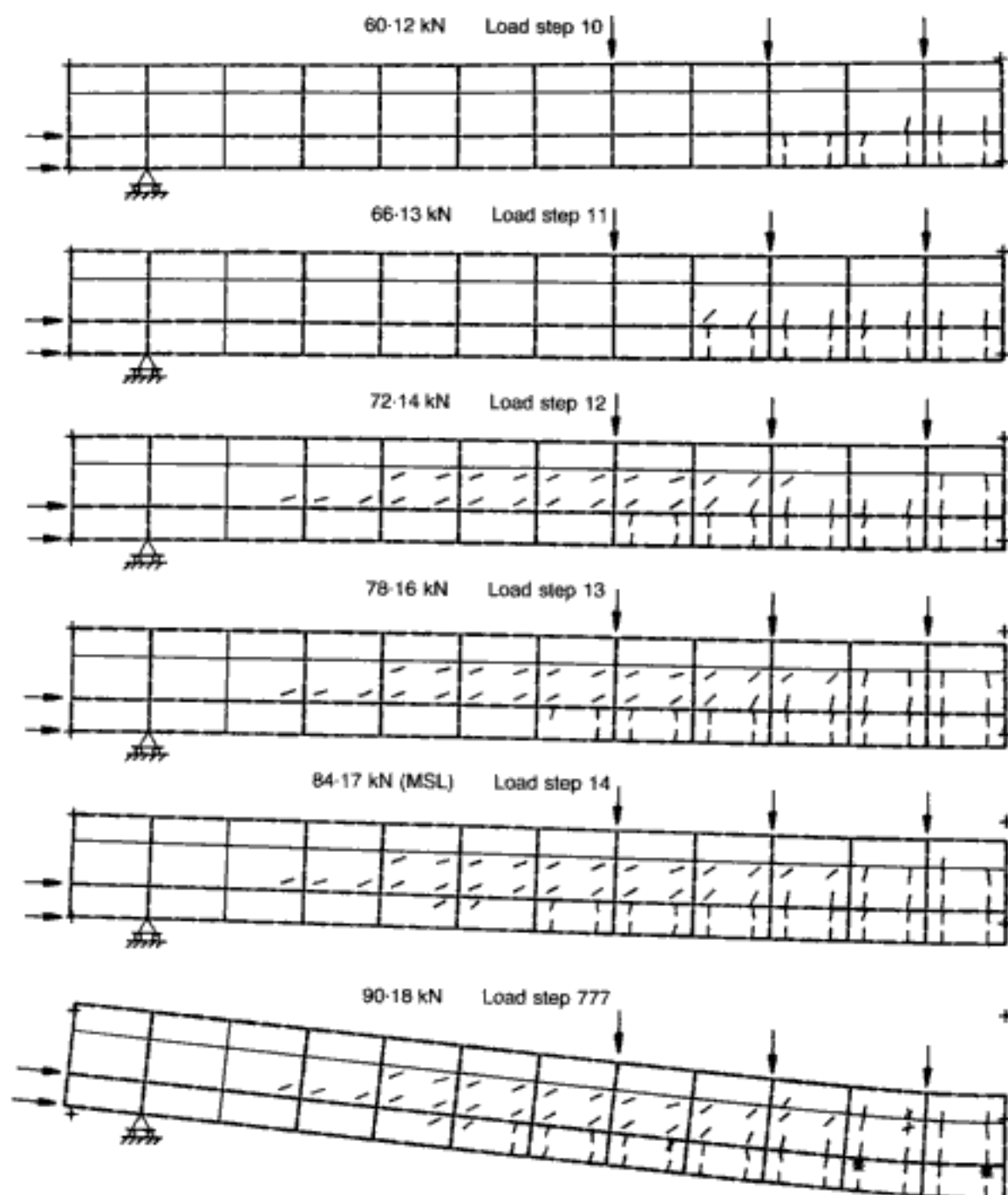
Fig. 4.73. Beam PCB6. Crack pattern at failure¹⁸¹

Fig. 4.73. (The failure load of 94 kN includes the weight (1.5 kN) of the spreader beams.) The f_c value for PCB6 was 45.7 N/mm².

The FE discretization adopted for the analysis of PCB6, consisting of 54 brick elements and 169 bar elements, is identical to that of PCB3 except for the location and area of transverse steel for the web and flange reinforcement in that part of beam PCB6 encompassing section types c-c in Fig. 4.74 (refer also to Fig. 4.68(b)). Once again, the FE mesh depicted in Fig. 4.74 has 18 reinforcing bars at the end of the beam that coincide in space with other steel elements.

The analytical crack patterns at different load levels up to failure appear in Fig. 4.75. The MSL predicted by the analysis was 84.17 kN, which was about 90% of the total load sustained by the beam in the experiment (94 kN). At 60.12 kN, the first set of flexural cracks appeared within the flexural span and below the inner point loads. In the subsequent load step, the number of flexural cracks increased. At a load of 72.14 kN, diagonal cracks oriented from the supports to the point loads developed throughout the web of the beam, while the central flexural cracks propagated upwards and reached the intersection of the web and the flange. In the following load step, the number of both flexural and shear cracks grew. On reaching the MSL level, the extension within the top flange of one of the flexural cracks of the flexural span could be seen, and the stress in the prestressing steel at the midspan of the beam passed the yield limit of the tendon. Inspection of the crack pattern at load step '777' reveals that, at failure, some of the flexural cracks in the midspan were greatly widened, as the material at the Gauss points corresponding to the relevant concrete elements collapsed (i.e. third cracking) in the FE analysis. The experimental crack pattern at failure (Fig. 4.73) is very similar to that for beam PCB3 (Fig. 4.69) except that the extent of cracking in the latter member was more widespread as one neared the support (see reference 174); it is significant that this trend is also detectable in the FE analyses (compare Figs 4.71 and 4.75). In Fig. 4.76, the applied load is plotted against the midspan deflection, the close agreement between experiment and analysis being apparent. The nature of both the experimental and the analytical curves points to a flexural failure of the beam, the actual ductility being adequately monitored in the analysis. Therefore, it is clear from the above analytical exercise that, on the one hand, the load-carrying capacity, the cracking process and the deformational response of the PSC beam PCB6 have been closely simulated by the adopted FE model, and, on the other hand, provision of localized transverse reinforcement (15 dia. 1.5 - 1 - 34 in Fig. 4.68(b)) at locations where the CFP changes its direction and additional 'hoop-like' reinforcement (36 dia. 1.5 - 2 - 20 in Fig. 4.68(b)) to prevent collapse of the compressive zone owing to bond failure of the tension reinforcement ensure the attainment of a ductile type of failure in a PSC member (in contrast to beam

Hidden page



PCB3 which, though designed for flexural failure in accordance to BS 8110, failed in shear).

4.6.6. Case study 5: an analytical investigation of a PSC T-beam made from high-strength concrete subjected to six-point loading failing in flexure

Now that the generality of the FE model has been established for both RC and PSC members made from a wide range of concrete strengths, the performance of PSC beams made from high-strength concrete can be studied from a purely numerical viewpoint. One such beam, designed to the CFP method (designated as PCB7) is presented and investigated analytically in this section. The dimensions and reinforcement details of the beam have already been given in Figs 4.62 and 4.68(c) respectively. This beam has been subjected to a similar amount of prestressing force as PCB6

Hidden page

Hidden page

Hidden page

performance of HSC beams with beams made from normal-strength mixes.

From the limited information obtained from the above FE modelling, it can tentatively be concluded that the model for designing PSC members in compliance with the CFP concept can be used in the design of PSC members made from HSC mixes as well.

4.6.7. Summary

The following main conclusions on PSC member analysis and design seem appropriate.

- (a) The FE model can mimic satisfactorily the experimental load-carrying capacity, deformational response, crack patterns and mode of failure of PSC members. It appears that the effect of prestressing in a PSC member can be represented within the nonlinear FE analysis by inputting the effective prestressing force as a constant load at the first load step, and by removing the part of the stress-strain curve of the steel tendon that was effectively utilized in the prestressing operation. (This simple approach, which bypasses the formal inclusion of initial stresses and strains works quite well for practical purposes.)
- (b) It has been demonstrated that detailed modelling of the compressive zone of a PSC member is more important than that of the portion of the member below the neutral axis. Thus, for example, while the imposed additional confinement in the compressive flange of case study 1 increased the load-carrying capacity of the compressive zone of beam CW12 and ultimately caused the attainment of an analytical failure load higher than its experimental counterpart, the

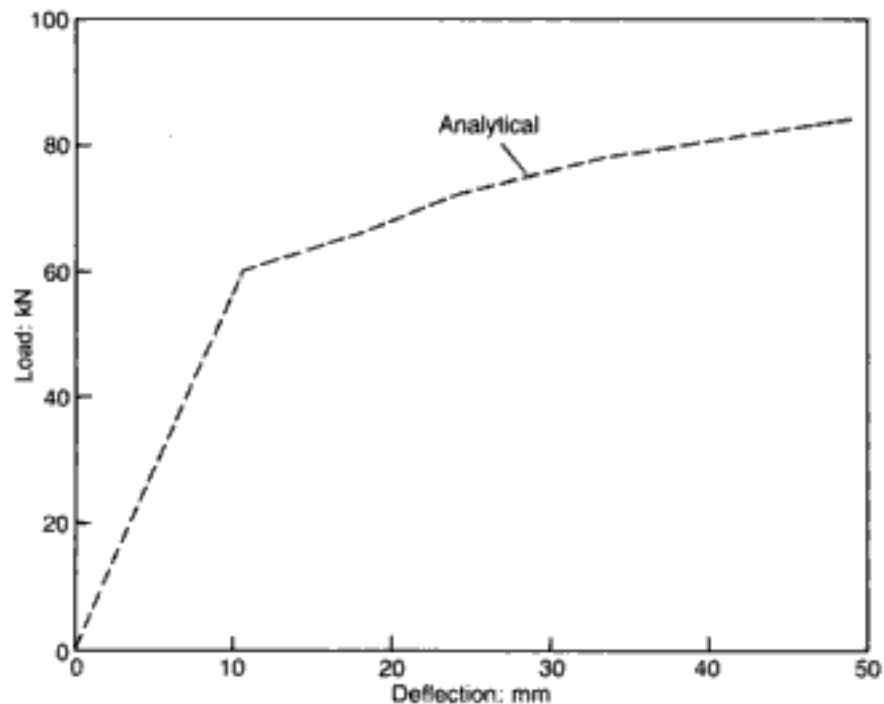


Fig. 4.79. Beam PCB7. Analytical load-deflection curve¹⁷⁸

slight reduction in the concrete areas of the tensile zone for case studies 2–5 apparently did not have any significant effect.

- (c) The numerical results obtained from case studies 2–4 have validated the experimental observations that provision of transverse reinforcement complying with the CFP concept results in a safer design solution than that based on current code tenets. The numerical experiment conducted on a HSC beam designed to the above concept has also shown the suitability of this approach in the design of PSC members made from HSC mixes.

4.7. The phenomenon of 'size effects' in structural concrete

4.7.1. Background

It is widely believed that the behaviour of structural concrete, as predicted by computer-based methods of analysis (such as, for example, the FEM), is significantly affected by the size of the structure or member that is being analysed. This size effect on the predicted behaviour is generally attributed to inadequacies in the modelling of the material properties, which form an essential part of any analysis approach. In an attempt to minimize such effects, therefore, current research work is focused largely towards improving material modelling.^{97,183,184} Thus, it is argued that the puzzling phenomenon of 'size effects', whereby the actual dimensions of certain concrete members seem to affect their behavioural characteristics, could be removed by incorporating factors at the material level that somehow allow for these size effects which are observed at the structural level.

It should be noted, however, that most of the research work on size effects carried out to date has been confined to cases where structural concrete is subjected to plane-stress conditions. Such conditions can easily be imposed in analysis but, in real structures, it is difficult, if not impossible, to prevent the occurrence of out-of-plane actions. Admittedly, in a controlled experiment such actions can be minimized and, when comparing analytical predictions with experimental values, it is implicitly *assumed* that out-of-plane actions are small enough to have a negligible effect on the experimentally established structural behaviour.

Throughout this and previous chapters, however, it has been consistently argued that the ignoring of small stresses often leads to misinterpretations with regard to the causes of the observed structural behaviour of concrete, since the presence of such stresses usually has a significant effect on concrete (material) strength. In fact, it will be recalled that the presence of even a small confining pressure causes a disproportionately large increase of concrete strength in the orthogonal direction, whereas a small tensile stress of a similar magnitude can reduce the strength to zero. It would appear, therefore, that, before any attempt is made to modify current material models so as to allow for size effects, it is essential to clarify the effect of the small unintended out-of-plane actions — inherent in any experiment — on structural concrete behaviour.

Hidden page

Hidden page

Hidden page

terms of volume) vary in the order (approximately) 1:25:130, and thus, their choice is fully justified for an investigation of the size effects on the predicted behaviour of structural concrete. It will be recalled from earlier sections that, while the failure of beam B1 was ductile, beams B150-11-3 and A-1 failed in a brittle manner.

Table 4.7 lists both the reported experimental ultimate-load values and their analytical counterparts for the three beams comprising this case study. It can be seen that the correlation between test results and the theoretical prediction is very close in all cases investigated. As the beams differ in size quite considerably, the close correlation between analytical and experimental values of the load-carrying capacity can be interpreted only as a demonstration of the negligible effect that the size of the beams has on the predicted structural-concrete behaviour.

4.7.2.3. Case study 3: RC beams without stirrups

Table 4.8 contains the details of the simply supported beams without stirrups adopted in the present pilot investigation. The data have been taken from that part of the work of Leonhardt and Walther¹⁸⁷ in which two different sets of geometrically strictly similar specimens formed the basis of an experimental investigation of the problem of size effects in structural concrete. The table also lists the reported experimental ultimate-load values as well as their analytical counterparts obtained by means of the present FE model. It can be seen that, unlike the preceding two case studies, the correlation between test results and theoretical predictions is now satisfactory only for the case of the smaller beam D1; for all other beams, the predictions overestimate consistently the load-carrying capacity by a margin which gradually increases with size and finally appears to stabilize at a maximum value of approximately 40% for series D, and 50% for series C.

As mentioned earlier, such a size effect on the predicted behaviour is usually attributed to inadequacies in the modelling

Table 4.8. RC beams without stirrups: data and comparison between experimental and predicted ultimate loads (P_u).¹⁸⁵ (Note: b is width; d is effective depth; a_v is shear span; L is span; ρ is tension-steel ratio)

Beam reference	Dimensions: mm				Material properties: N/mm ²		ρ	ω	P_u : kN		
	b	d	a_v	L	f_c	f_y			Test	Analysis	Analysis/Test
D1	50	70	210	520	38.0	460	0.0162	0.1961	14.8	15.3	1.03
D2	100	140	420	1040	38.2	435	0.0162	0.1845	44.4	49.0	1.10
D3	150	210	630	1560	39.5	421	0.0162	0.1727	89.2	125.0	1.40
D4	200	280	840	2080	36.1	448	0.0162	0.2010	148.0	204.0	1.38
C1	100	150	450	1000	40.0	433	0.0134	0.1451	44.0	48.0	1.09
C2	150	300	900	2000	40.0	433	0.0134	0.1451	132.5	156.0	1.18
C3	200	450	1350	3000	40.0	433	0.0134	0.1451	202.0	324.0	1.60
C4	225	600	1800	4000	40.0	433	0.0134	0.1451	310.0	450.0	1.45

of the material properties in structural-concrete analysis. However, this view cannot provide a realistic explanation of the fact that the current FE analysis yields size-independent predictions for case studies 1 and 2 and size-dependent predictions for case study 3; in fact, it is interesting to recall that the size ratio (expressed as a volume ratio) of beams B1 and A-1, in case study 2, for which the predicted ultimate loads are size-independent, is approximately 1:130 which is similar to that of beams D1 and C3 (~ 1:150), for which the prediction is evidently size-dependent.

In view of the above, it is considered that the cause of the size-dependent predictions in case study 3 relates to the development (during testing) of unintended out-of-plane eccentricities of the applied load which become more significant as the size of the specimen increases. Such unintended eccentricities create torsional effects which give rise to transverse tensile stresses within the specimens, leading to failure under a load which is lower than that expected to cause failure under in-plane loading conditions.

4.7.2.4. A possible explanation

The above three case studies, investigated by means of the FE package, yielded results which are compatible with the postulate that size effects in structural concrete under intended in-plane loading are likely to be due to unintended out-of-plane eccentricities of the applied load, induced by the testing method adopted. The validity of this postulate is supported by the present results which demonstrate that current material modelling can lead to predictions of structural-concrete response that are essentially size-effect independent provided that the effect of unintended actions is negligible. These results may be summarized as follows.

- (a) Slabs under concentric patch loading (for which it is self-evident that small unintended eccentricities have an insignificant effect on structural behaviour) exhibit size-effect independent behaviour.
- (b) Similarly, the predicted load-carrying capacity of RC beams with stirrups, under intended in-plane loading, has also been found to be size-effect independent; apparently, the presence of stirrups has been sufficient to withstand the additional tensile stresses caused by the torsional action induced by small unintended out-of-plane eccentricities.
- (c) In contrast with the above beam behaviour, the absence of stirrups leads to predictions which consistently overestimate experimental values by a margin that, depending on size, can be as large as an order of 50%. Further confirmation that this deviation of the predicted from the experimental values is due to unintended out-of-plane eccentricities, is currently the subject of an international collaborative programme of experimental research involving the National Technical University of

Athens, Imperial College, and the Structures Laboratory of the University of Tucumán (the latter under the direction of Professor R. Danesi).

4.7.3. A numerical experiment

4.7.3.1. Objective

Besides the eccentricities arising from small deviations from idealized (i.e. perfectly concentric) loading conditions, which were considered in the previous section, eccentric effects can also be due to material heterogeneity. In what follows, therefore, it is postulated that one of the causes of size effects is load-induced non-symmetrical cracking which is inherent in concrete owing to its heterogeneous nature. The validity of this postulate is to be tested by purely analytical means through the application of the FE package, in which the model used to describe cracking is capable of inducing non-symmetrical cracking in symmetrical structural members subjected to symmetrical loading.¹⁸⁶ It will be seen that the results demonstrate that the package can also provide a close fit to experimental values and, moreover, that the presence of stirrups (designed so as to prevent shear failure) is sufficient to diminish the effect of non-symmetrical cracking and, hence, eliminate size effects.

Earlier on, the unavoidable simplifications made to real boundary — and, in particular — loading conditions was put forward as a possible reason for the existence of 'size effects' as these were seen to reflect the ensuing simplified stress conditions that develop within a concrete structure and which, therefore, overlooked the influence that small 'secondary' tensile stresses may have on its load-carrying capacity. An example where such influences may be encountered is the case of RC beams, without stirrups, failing in combined flexure and shear. Thus, it was shown in section 4.7.2 that, while RC beams with stirrups are essentially free from size effects, the lack of stirrups leads to predictions of load-carrying capacity which are heavily dependent on the size of the beam, with the causes for such predictions having been attributed to unintended out-of-plane actions (rather than to the intended in-plane loading to which the beams are assumed to be subjected) in the course of experimental testing. Out-of-plane actions, however, may develop as a result not only of small externally induced unintended eccentricities of the applied (assumed in-plane) loading but also of flexural and inclined cracking which is non-symmetrical with respect to the vertical longitudinal plane at the mid-breadth of the beam: such non-symmetrical cracking is practically unavoidable in a heterogeneous material such as concrete. In the absence of stirrups, the small tensile stresses which develop within the structure under such unintended out-of-plane actions are likely to lead to premature loss of load-carrying capacity, and, in what follows, it is postulated that *this* is the underlying cause of size effects.

To demonstrate the connection between size effects and out-of-plane actions caused by non-symmetrical fracture processes in

structural concrete, the 3-D FE package is used to predict the behaviour of a number of geometrically strictly similar RC beams of various sizes, made of the same materials, with and without stirrups, which have been divided into two groups: group A, in which the beams have been modelled so as to undergo non-symmetrical cracking under increasing loading, and group B, in which the beams in group A have been modelled so as to undergo symmetrical cracking under the same loading conditions. The ensuing conclusions, therefore, are based on a comparative study of the numerically predicted behaviour of the beams in groups A and B, with the aim to establish the connection between non-symmetrical cracking and beam size, as well as to investigate the influence of the stirrups on size effects.

The occurrence of non-symmetrical cracking is mimicked in the following manner. As usual, when the ultimate-strength level for concrete is reached, a macrocrack is allowed to form *only* at the location where the stress conditions are the most critical. In fact, owing to the 'double-precision accuracy' used in the package, it is unlikely that the many decimal digits associated with the stress values at nominally symmetric locations will exactly coincide; thus, the stress conditions may even be found to be more critical in only one of two symmetrical locations within the structure. The adoption of such a procedure to describe the fracture process, therefore, may lead to numerically induced non-symmetrical macrocracking even for the case of symmetrical structural forms subjected to symmetrical loading. As it will be seen later, this feature of the package plays a key role in the present investigation of size effects.

Concrete has been modelled by the usually adopted option based on the 20-noded brick isoparametric elements with the $2 \times 2 \times 2$ (but, in one instance, the $3 \times 3 \times 3$) integration rule. The convention for indicating cracks at the relevant Gauss points is as described in section 4.1 except for the following additional information (stemming from the more carefully monitored fracture process): two closely spaced circles/dashes distinguish a crack which has just occurred at the current load stage from cracks which have formed during previous load increments, the latter being indicated in the usual way, namely single circles/dashes. (Since the primary concern in the present investigation is with the collapse load and fracturing sequence, the deformation shapes have not been shown in any of the present figures, i.e. D.M. = 0 throughout.)

4.7.3.2. *Structural forms investigated*

Tables 4.9 to 4.12 contain the details of the simply supported beams, with and without stirrups, adopted in the present investigation. The beams have been selected such as to be similar in geometry and main reinforcement to those from that part of the work of Leonhardt and Walther¹⁸⁷ in which two different sets of geometrically strictly similar specimens — one set of beams

Table 4.9. Group A of RC beams without stirrups: data and comparison between experimental and predicted ultimate loads (P_u).¹⁸⁶ (Note: b is width; d is effective depth; a_v is shear span; L is span; ρ is tension-steel ratio)

Beam reference	Dimensions: mm				Material properties: N/mm ²		ρ	P_u : kN		
	b	d	a_v	L	f_c	f_y		Test	Analysis	Analysis/ Test
D1	50	70	210	520	38.0	460	0.0162	14.8	15.3	1.03
D2	100	140	420	1040	38.2	435	0.0162	44.4	36.0	0.81
D3	150	210	630	1560	39.5	421	0.0162	89.2	90.0	1.01
D4	200	280	840	2080	36.1	448	0.0162	148.0	144.0	0.97
C1	100	150	450	1000	40.0	433	0.0134	44.0	48.0	1.09
C2	150	300	900	2000	40.0	433	0.0134	132.5	156.0	1.18
C3	200	450	1350	3000	40.0	433	0.0134	202.0	270.0	1.34
C4	225	600	1800	4000	40.0	433	0.0134	310.0	330.0	1.06

Table 4.10. Group A of RC beams with stirrups: data and comparison of predicted ultimate loads (P_u) with their group B counterparts.¹⁸⁶ (Note: b is width; d is effective depth; a_v is shear span; L is span; f_{yv} is stirrup yield strength; ρ , ρ_v are tension-steel ratio, stirrup-steel ratio respectively)

Beam reference	Dimensions: mm				Material properties: N/mm ²			ρ	ρ_v	P_u : kN	
	b	d	a_v	L	f_c	f_y	f_{yv}			Analysis	Group A Group B*
D1s	50	70	210	520	38.0	460	439	0.0162	0.0025	15.3	1.0
D2s	100	140	420	1040	38.2	435	439	0.0162	0.0025	57.6	1.0
D3s	150	210	630	1560	39.5	421	439	0.0162	0.0025	126.0	1.0
D4s	200	280	840	2080	36.1	448	439	0.0162	0.0025	234.0	1.0
C1s	100	150	450	1000	40.0	433	424	0.0134	0.0017	63.0	1.08
C2s	150	300	900	2000	40.0	433	424	0.0134	0.0017	168.0	0.93
C3s	200	450	1350	3000	40.0	433	424	0.0134	0.0017	384.0	1.07
C4s	225	600	1800	4000	40.0	433	424	0.0134	0.0017	540.0	1.07

*Predicted values for group B beams from Table 4.12.

Table 4.11. Group B of RC beams without stirrups: data and comparison of predicted ultimate loads (P_u) with their group A counterparts.¹⁸⁶ (Note: b is width; d is effective depth; a_v is shear span; L is span; ρ is tension-steel ratio)

Beam reference	Dimensions: mm				Material properties: N/mm ²		ρ	P_u : kN	
	b	d	a_v	L	f_c	f_y		Analysis	Group A* Group B
D11	50	70	210	520	38.0	460	0.0162	15.3	1.0
D22	100	140	420	1040	38.2	435	0.0162	49.0	0.73
D33	150	210	630	1560	39.5	421	0.0162	125.0	0.72
D44	200	280	840	2080	36.1	448	0.0162	204.0	0.71
C11	100	150	450	1000	40.0	433	0.0134	48.0	1.0
C22	150	300	900	2000	40.0	433	0.0134	156.0	1.0
C33	200	450	1350	3000	40.0	433	0.0134	324.0	0.83
C44	225	600	1800	4000	40.0	433	0.0134	450.0	0.73

*Predicted values for group A beams from Table 4.9.

Table 4.12. Group B of RC beams with stirrups: data and predicted ultimate loads (P_u).¹⁸⁶ (Note: b is width; d is effective depth; a_v is shear span; L is span; f_{yv} is stirrup yield strength; ρ , ρ_v are tension-steel ratio, stirrup-steel ratio respectively)

Beam reference	Dimensions: mm				Material properties: N/mm^2			ρ	ρ_v	P_u : kN
	b	d	a_v	L	f_c	f_y	f_{yv}			
D11s	50	70	210	520	38.0	460	439	0.0162	0.0025	15.3
D22s	100	140	420	1040	38.2	435	439	0.0162	0.0025	57.6
D33s	150	210	630	1560	39.5	421	439	0.0162	0.0025	126.0
D44s	200	280	840	2080	36.1	448	439	0.0162	0.0025	234.0
C11s	100	150	450	1000	40.0	433	424	0.0134	0.0017	58.5
C22s	150	300	900	2000	40.0	433	424	0.0134	0.0017	180.0
C33s	200	450	1350	3000	40.0	433	424	0.0134	0.0017	360.0
C44s	225	600	1800	4000	40.0	433	424	0.0134	0.0017	504.0

D and one set of beams C — formed the basis of an experimental investigation of the problem of size effects in structural concrete.

The FE meshes adopted for the analysis of the beams are shown schematically in Fig. 4.80. The figure indicates that, for the case of the smallest of beams D, the $9 \times 3 \times 1$ FE mesh with a $2 \times 2 \times 2$ integration rule adopted for all other beams has been reduced to a $5 \times 1 \times 1$ FE mesh with a $3 \times 3 \times 3$ integration rule. Such a change in mesh has been dictated by the small size of the beam, in order to comply with the condition that a Gauss point must describe the average stress/strain conditions of a space with a minimum dimension larger than about three times the size of the maximum aggregate of the concrete mix (section 2.5), while, as a consequence of the rough discretization along the vertical direction, the $3 \times 3 \times 3$ integration rule then becomes essential in order to be able to establish a reasonably accurate stress variation throughout the member depth. All beams have been analysed both without and with stirrups; in the latter case, the stirrups have been placed throughout the shear span. The beams with stirrups are designated by adding the ending s to the description of the beams without stirrups. Each beam has been analysed twice: first, by considering that the FE meshes of Fig. 4.80 represent half the specimens (symmetry with respect to the cross-section at midspan of the beams); and then, by considering that the same meshes represent one-quarter of the beams (two-fold symmetry with respect to the xz plane and the cross-section at the midspan of the beams). In the former case, the beams have been specified as group A beams consisting of beams D and C, without and with stirrups, designated as D1, ..., D4, C1, ..., C4, D1s, ..., C4s, while in the latter case, as group B beams also consisting of beams D and C, without and with stirrups, designated as D11, ..., D44, C11, ..., C44, D11s, ..., C44s. (It should be noted that the width of the mesh in group B beams was half that of the mesh of group A beams.)

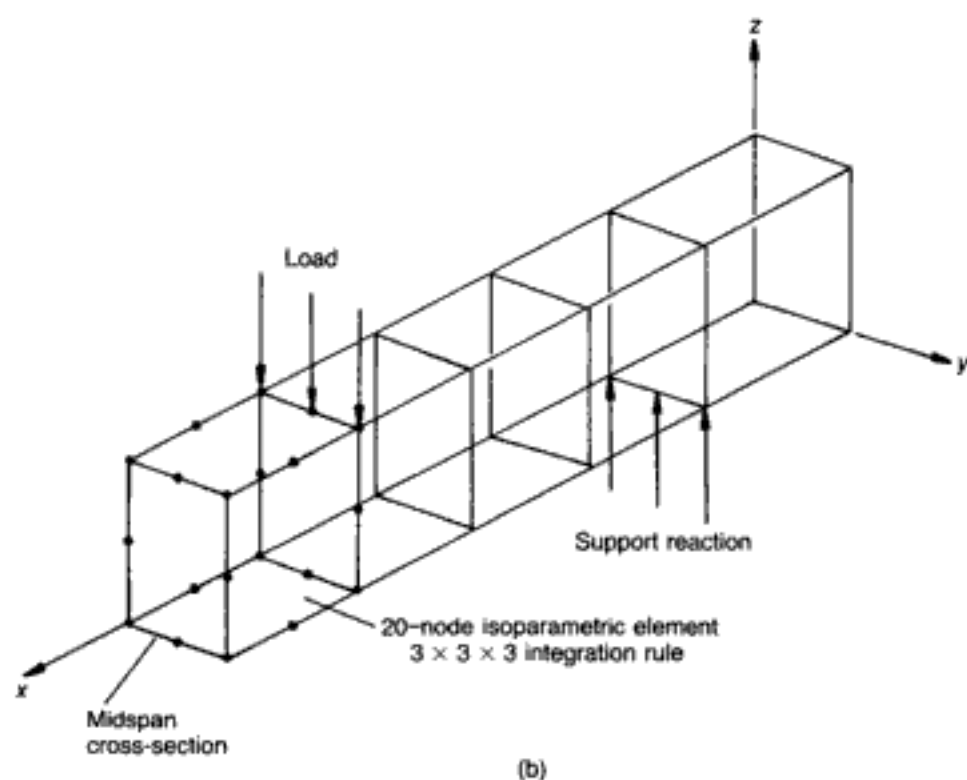
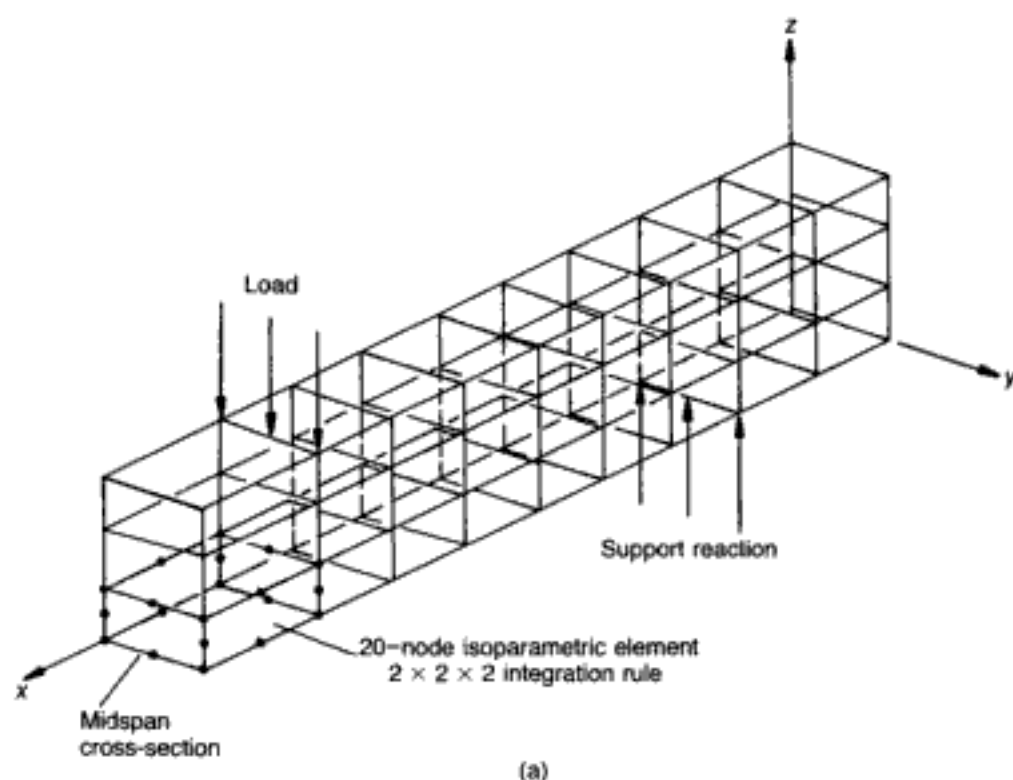


Fig. 4.80. FE meshes adopted for the analysis of beam series C and D:¹⁸⁶ (a) all beams except the smallest of beams D; (b) smallest of beams D

The basic difference in the analysis of the two groups of beams is that, for group B, symmetry, including symmetrical cracking, is imposed by the prescribed boundary conditions, i.e. by preventing the displacements of the two planes of symmetry at right angles to these planes, whereas for group A, the prevention of only the longitudinal displacements of the cross-section at midspan is insufficient to prevent non-symmetrical cracking. Thus,

Hidden page

Hidden page

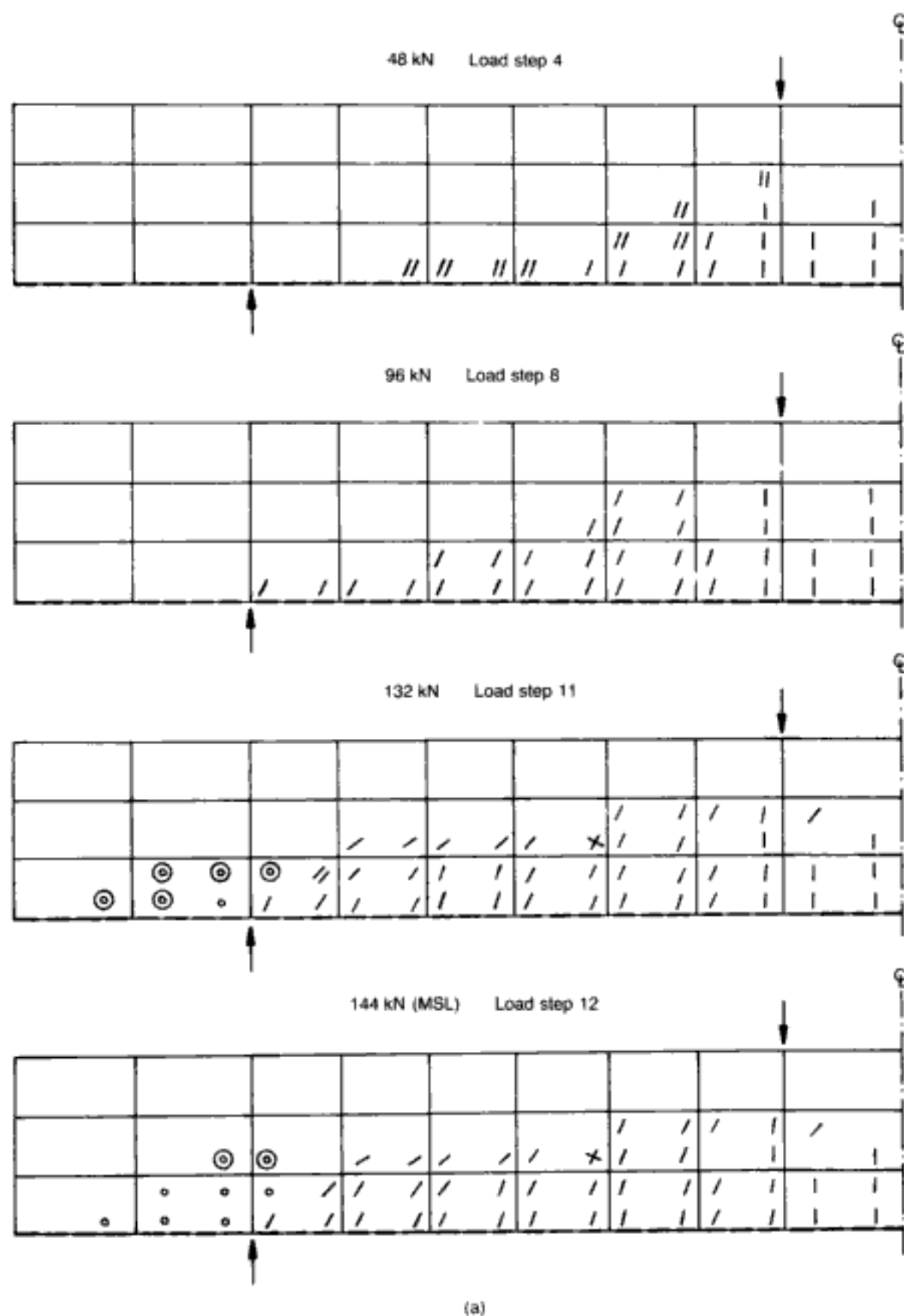


Fig. 4.85 (above and facing). Typical crack patterns for group A beams (non-symmetrical cracking) at various load stages.¹⁸⁶ (a) without stirrups (beam D4); (b) with stirrups (beam D4s)

Hidden page

Hidden page

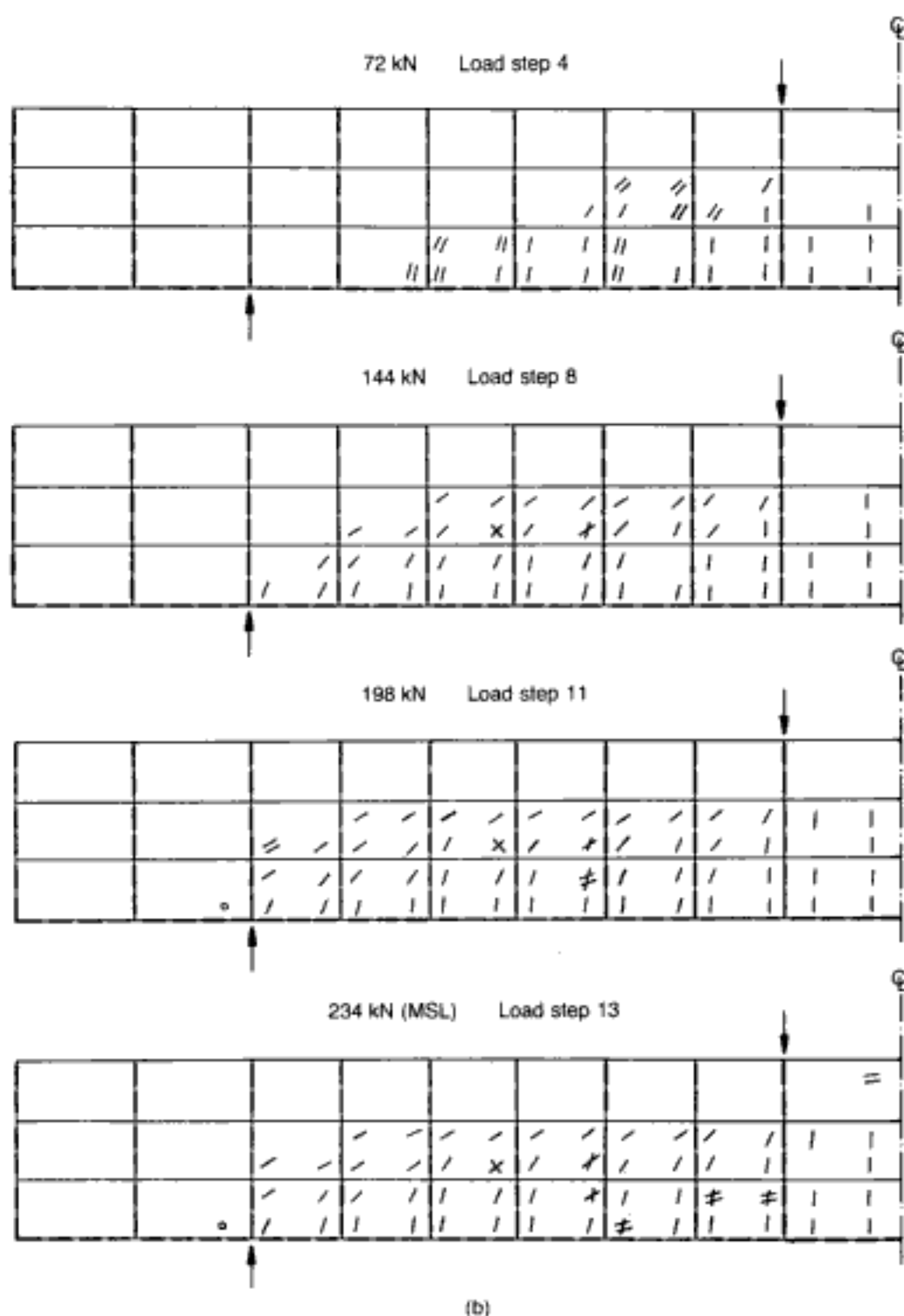


Fig. 4.86 (facing and above). Typical crack patterns for group B beams (symmetrical cracking) at various load stages.¹⁸⁶ (a) without stirrups (beam D44); (b) with stirrups (beam D44s)

The predicted values in Tables 4.9 to 4.12 demonstrate clearly that the load-carrying capacity of group A beams, without stirrups, decreases, as a percentage of that of their group B counterparts, with increasing beam size. The graphical representation of these results, depicted in Fig. 4.81, shows that the above reduction in load-carrying capacity exhibits a trend qualitatively similar to those of size effects as the latter are defined in practical structural design.

Within this context, size effects are associated with shear capacity and they are expressed in an empirical form such as, for example

$$s.e. = (400/d)^{1/4} \quad (4.4)$$

$$s.e. = 1.6 - d \quad (4.5)$$

which are the expressions recommended by BS 8110⁵⁵ and CEB-FIP 78¹⁶⁹ respectively, where *s.e.* is not smaller than 1 and *d* (with the appropriate units) is the depth of the critical cross-section. The graphical representation of these expressions, normalized with respect to their values for beam D1 (*d* = 70 mm), is also included in Fig. 4.81, which indicates that the correlation between the code and the analysis predictions is satisfactory, considering both the approximate nature of the code expressions and the random triggering of early failure through double-precision numerics. (It should be noted that the measured values of shear capacity are characterized by a large variability; in fact, the scatter of these experimental values is often larger than twice the mean value of the values.¹⁸⁸)

The correlation between the load-carrying capacity predicted here for the beams without stirrups and that established by experiment¹⁸⁷ is depicted in Fig. 4.82. The figure indicates that, for the case of the beams undergoing non-symmetrical cracking, the correlation is very close except for the case of beam C with *d* = 450 mm. Such a close correlation between the analytical and the experimental values is in support of the postulate that one of the main causes of size effects is load-induced non-symmetrical cracking, resulting from the heterogeneous nature of concrete, which appears to be adequately described by the FE package used in the present work. Another significant cause of the size effects has been postulated to be the small unintended eccentricities of the in-plane intended loading due to secondary testing-procedure effects which are inherent in any experimental set-up (section 4.7.2). The deviation of the predicted from the experimental value of the load-carrying capacity for beam C with *d* = 450 mm may reflect the latter (additional) effects which are not modelled in the present study.

Non-symmetrical cracking gives rise to transverse tensile stresses which weaken the path along which the compressive forces are transmitted to the supports, thus leading to a reduced load-carrying capacity in comparison with that of the beams suffering symmetrical cracking. However, the presence of stirrups (designed so as to delay shear failure and, hence, allow flexural failure to occur first) is sufficient to sustain the above tensile stresses: this is indicated in Fig. 4.83, which shows that the predicted values for the load-carrying capacity of the beams with stirrups, undergoing non-symmetrical cracking, correlate closely with those of the beams suffering symmetrical cracking. Such behaviour is consistent with

the fact that RC beams with stirrups are independent of size effects (and, significantly, are insensitive to secondary effects (such as small out-of-plane actions and/or heterogeneity) which the 'secondary' reinforcement can absorb); in fact, the load-carrying capacity of group A beams with stirrups, as a percentage of that of their group B counterparts is virtually constant (approximately equal to 1.0), and hence independent of the size of the beam (see Fig. 4.84).

The crack patterns predicted for a typical set of beams (beams D4, D4s, D44, and D44s) at various load steps up to the maximum sustained load are shown in Figs 4.85 and 4.86. Comparing the crack patterns exhibited by the beams without stirrups, it is interesting to note that non-symmetrical cracking occurs initially (load step 4) deeper in the region of the point load and, with increasing load, short inclined cracks spread faster towards the support than for the case of symmetrical cracking, the latter being characterized by a near-constant crack depth throughout the region covered by such cracking. Eventually, collapse of the beams is caused by in-plane (i.e. near-vertical) cracking which, for the case of non-symmetrical cracking, occurs in the region of the support (load step 12 in Fig. 4.85(a)), while for the case of symmetrical cracking, it occurs in the region of the point load at a higher load level (load step 17 in Fig. 4.86(a)).

Although the presence of stirrups does not change the above features characterizing the two different types of crack pattern, it prevents failure due to in-plane cracking and allows the beams to develop their full flexural capacity. Collapse eventually occurs as a result of the formation of horizontal cracks within the compressive zone as indicated in Figs 4.85(b) and 4.86(b).

4.7.3.4. *Summary and tentative conclusions*

The first part of the investigation (section 4.7.2) showed a consistent 'size effect' in the case of structural-concrete girders without stirrups and this correlated with the corresponding overestimate of FE predictions for which economic computational modelling constrained the structure to respond — and eventually crack — symmetrically with respect to the vertical plane that bisects the member along its longitudinal direction. In this, the second part of the study, the results obtained confirm, complement and extend the earlier findings by means of numerical mimicking of 'weaknesses' in the structure which, once the above symmetry constraint is removed, bring about early cracking, thus reducing the stress level associated with assumed symmetric behaviour. Therefore, the RC beams, studied by means of the FE model, yielded data which are compatible with the postulate that one of the main causes of size effects in structural concrete is non-symmetrical cracking which is inherent in concrete owing to its

Hidden page

number of tests at the material level for two types of brick unit were carried out at Imperial College.¹⁸⁹⁾

Two basic problems are to be studied in this section. The first relates to the change in compressive strength of a brick unit as its shape is varied. The second problem investigates how the number of mortar joints in a masonry wall affects its load-bearing capacity. In view of the preliminary nature of both studies, the findings and ensuing recommendations are to be regarded as tentative, pointing to, rather than dispensing with, further investigations in these areas.

4.8.1. Shape factors for brick units

4.8.1.1. Background

The background to the present attempt to provide a rational prediction of the way in which the strength of a brick unit, as obtained by means of a standard test, is affected by its shape can be summarized as follows. Consider a single brick compressed between platens to failure. If it were possible to ensure perfectly frictionless interaction at the specimen/platen interfaces, the unit would be subject to a simple state of uniaxial compression, and the failure stress attained would give a true indication of the strength of the material. In the actual test involving ordinary platens, however, frictional stresses are unavoidably set up at the loaded surfaces preventing the specimen from expanding at these loaded ends, as explained in Chapter 1. This gives rise to a complex three-dimensional state of stress around the ends of the unit. Clearly, if the ratio of height to lateral dimensions of the specimen is sufficiently large, such triaxial effects are of a local nature and hence the strength of the test piece will be practically the same as the true uniaxial strength of the material; on the other hand, if the test piece is short, its recorded strength will represent generally an enhancement over the true material strength as a result of the additional restraint of the platens.

Now, the published draft Eurocode No. 6¹⁹³ proposes an expression for predicting the characteristic compressive strength of masonry in which one of the terms is the normalized strength f_b of a brick unit of dimensions height \times width = 200 mm \times 200 mm. This normalized strength is, therefore, an 'index' value and relates the strength of the unit to the strength of a 200 mm cube unit which is made of the same material. This is, of course, an arbitrary size since the normalized strength of differently shaped units can be referenced to any size of unit; the choice of the size of unit could vary and, indeed, a 100 mm cube is now being discussed as the reference size. In order to allow for the fact that units of other dimensions will often be used to establish the strength of the unit (f'_b , say), EC6 proposes multiplying the obtained brick-unit strength (f'_b) in such tests by a simple geometric shape factor, say δ , so as to yield the normalized strength, i.e.

$$f_b = \delta \times f'_b \quad (4.6)$$

where δ is a multiplying factor to allow for the dimensions of the masonry. (In addition to δ , a 'wet to dry' conversion factor is applicable when the strength test has been performed on wet bricks.) The shape factor δ is given in Table B of the Preface to EC6. The values, as published, range from 0.54 through to 1.5 with a shape factor of 1 for a unit with height and width of 200 mm.

The purpose of the present investigation^{189,190} was to determine values for δ for a broadly similar range of shapes to those published in EC6 and for two common brick materials. A clay brick and a calcium silicate brick were used, both being solid, without frog or perforation. A more fundamental approach was deemed to be necessary, in the sense that true material data were to be ascertained first, by carrying out coupon-type tests, and, then, introducing this material data into the nonlinear FE model of the various brick shapes used, with the loaded surfaces of the unit completely restrained against horizontal movement (i.e. full friction).

4.8.1.2. Material testing

As discussed in Chapter 1, it is extremely difficult to achieve a situation in which a prism or cylinder of material compressed between steel platens is free from frictional (i.e. shearing) stresses at its loaded ends. On the other hand, it was shown in section 1.2 that, once the ratio of height-to-diameter/least lateral dimension of the test piece used is between 2 and 2.5, such end effects become of secondary importance and may be neglected. In the present investigation, cylinders or prisms of height-to-thickness ratio of 2:1 were cut for the two brick types tested. The specimens conformed to one of two sizes; they were either 25 mm \times 25 mm \times 50 mm or 40 mm \times 40 mm \times 80 mm. Some of the test specimens were cut perpendicular and some were cut parallel to the bedface (in order to estimate the degree, if any, of anisotropy). Both end surfaces of the specimen 'coupons' were machined plain and parallel to each other, being normal to the major axis of the specimen. In the testing machine, the axis of the specimen was located as near as possible to the centre of the platen. The machine had a spherical seat which provides free alignment. From the ensuing approximate standard test, the uniaxial strength of the material, f_c , as well as the axial and transverse strains (and hence Young's moduli and Poisson's ratios) at various load levels were found.

The results of the tests for both brick types (clay brick (CB) — 33 'coupons', calcium silicate brick (CSB) — 22 'coupons') have been reported in detail elsewhere.¹⁸⁹ Their nonlinear behaviour is very similar to that exhibited by concrete, and the similarity also extends to the failure mechanism of the test specimens, which is initiated by the appearance of macrocracks along the height of the specimen just before failure (when the transverse strain, and hence Poisson's ratio, suddenly begin to increase, taking on, quite rapidly, very large values). It is,

Hidden page

values, the more consistent set of results obtained here enables the mean of five test results to be adopted with confidence. The reason for the smaller scatter is thought to be the use of a spherical seat which allows the platen to rotate so as to maintain full contact with the brick surfaces, thus ensuring that the whole unit is loaded in a reasonably uniform manner: this is in contrast with the usual test arrangement, in which the position of the platen is a rigid one, hence resulting in a less uniform distribution of applied load.

4.8.1.3. Structural FE modelling

In attempting to model the effect of platen restraint on the strength of brick units, the 'coupon' material data were fed into the 3-D FE model for concrete since even the clay-brick material was shown to exhibit behaviour similar to that which brick units made of actual concrete would follow. Although full use of the symmetry of the brick units permits the analysis of only one-eighth of the structure, it was deemed to be conceptually easier to model the full width (T) of the brick while making use of the other two planes of symmetry, thus including one-half of the height ($H/2$) and one-half of the length ($L/2$): in this way, one-quarter of the brick was always analysed.

An initial parametric study was undertaken so as to ascertain the degree of mesh refinement needed. The (quarter) brick was subdivided into 6 elements (2 along the width, 3 along the height), 2 elements (both along the width), and 1 element respectively, and it was found that all the analytical predictions practically coincided. Therefore, the 6-element mesh was discarded in order to avoid unnecessarily lengthy computations; this was also in keeping with the notion that the volume associated with the Gaussian points within the element is best kept comparable with that of the cylinder/prism 'coupons' used in the tests (and, in this respect, the 6-element mesh was too fine), so that the material input to the numerical model is consistent with that actually obtained in the course of testing. The other two mesh sizes are more adequate in this respect, and their application to the quarter of the brick being analysed may be seen by reference to Fig. 4.87, with the corresponding node numbering also shown. The results of a comparative parametric study for the two meshes showed that (1) a load step of the order 10% of the ultimate load is sufficiently accurate, and (2) there is practically no difference between the 2-element and 1-element meshes. Therefore, it may be concluded that a single-element representation of one-quarter of the brick unit is quite sufficient on account of the very good performance of the 3-D isoparametric element. As shown repeatedly in previous sections, the adoption of under-integration offers both computational economy and precision and the eight Gauss points also provide a sensible number of stations for picking up stress variations within the (one-quarter brick) structure. Thus, in all subsequent

Hidden page

Table 4.13. Shape factors for brick units: results of the numerical parametric study in terms of average applied stress at failure (in N/mm^2)^{1/89,190}

L: mm	T: mm	H: mm	CB unit failure stress when $f_c = 50 N/mm^2$	CB unit failure stress when $f_c = 69 N/mm^2$	CB unit failure stress when $f_c = 87 N/mm^2$	CSB unit failure stress when $f_c = 15 N/mm^2$	CSB unit failure stress when $f_c = 22 N/mm^2$	CSB unit failure stress when $f_c = 28 N/mm^2$
215	65	65	60	78	90	18	26	32
215	100	65	60	78	90	18	26	32
215	150	65	60	78	90	18	26	32
215	200	65	60	78	90	18	26	32
215	240	65	60	78	90	18	26	32
215	65	100	60	78	90	18	26	32
215	100	100	60	78	90	18	26	32
215	150	100	60	78	90	18	26	32
215	200	100	60	78	90	18	26	32
215	240	100	60	78	90	18	26	32
215	65	150	54	72	90	16	24	30
215	100	150	54	72	90	16	24	30
215	150	150	54	72	90	16	24	30
215	200	150	54	72	90	16	24	30
215	240	150	54	72	90	16	24	30
215	65	200	54	72	90	16	22	28
215	100	200	54	72	90	16	22	28
215	150	200	54	72	90	16	22	28
215	200	200	54	72	90	16	22	28
215	240	200	54	72	90	16	22	28
215	65	240	48	72	90	16	22	28
215	100	240	48	72	90	16	22	28
215	150	240	48	72	90	16	22	28
215	200	240	48	72	90	16	22	28
215	240	240	48	72	90	16	22	28

analytical predictions, the single under-integrated 3-D element will be chosen to model the structure analysed on the basis of partial symmetry (i.e. with two, rather than three, planes of symmetry used). Full frictional restraint by the platens is imposed by specifying that all the nodes of the top surface of the element shown in Fig. 4.87(b) are constrained to experience zero displacement in the x and y directions.

4.8.1.4. Theoretical results

Table 4.13 contains the results of the FE study of the brick unit compressed to failure between steel platens which provide full frictional restraint on the two surfaces of the unit with which they are in contact. As mentioned previously, in addition to the calculated mean strengths, the 90% confidence limits were also included as input f_c values. This step was deemed to be essential if sensible conclusions were to be drawn on material(s) exhibiting a (potentially) large scatter. In addition, it permitted study of the effect of the strength parameter itself on the degree of enhancement provided by relative shape size under conditions of full platen friction (a parameter, incidentally, that is apparently not allowed for in the present EC6 proposals). The length (L) parameter was kept constant at 215 mm, whereas both the width (T) and the height (H) of the specimen were varied within the limits $65 \text{ mm} \leq T, H \leq 240 \text{ mm}$. The load steps adopted in the nonlinear FE analysis were 6 N/mm^2 (CB) and 2 N/mm^2 (CSB), both values constituting about 10% of the corresponding mean strength, and thus ensuring, in general, reliable accuracy.

Now, it will be recalled that the EC6 calls for the brick strength to be adjusted by a shape factor with a 200 mm wide unit taken as the reference for strength. Therefore, the enhancement to strength provided by the various shapes (always under assumed full frictional restraint) may be defined by the factor e_1 which is obtained by dividing the relevant strength by the strength of the reference unit of $H = T = 200 \text{ mm}$. (For such a 'normalization' of results with respect to the reference brick size, see reference 189.) Conversely, in the course of testing an arbitrary brick size, a larger strength than that of the reference strength value for $H = T = 200 \text{ mm}$ implies that the tested shape is relatively more prone to frictional effects than the standard one (as is evident by noting that the strengths of the more friction-affected shorter specimens, i.e. $H < 200 \text{ mm}$, are larger than those for the reference case $H = 200 \text{ mm}$), and hence the recorded test result should be *reduced*. Therefore, the shape factor referred to in the EC6 proposal (and implicit in expression (4.6)), termed here δ , is simply

$$\delta = \frac{1}{e_1} \quad (4.7)$$

The relevant δ values are listed in Table 4.14.

Table 4.14. Theoretical shape factors $\delta^{189,190}$

L: mm	T: mm	H: mm	CB unit $\frac{\delta}{\delta}$ when $f_c = 50 \text{ N/mm}^2$	CB unit $\frac{\delta}{\delta}$ when $f_c = 69 \text{ N/mm}^2$	CB unit $\frac{\delta}{\delta}$ when $f_c = 87 \text{ N/mm}^2$	CSB unit $\frac{\delta}{\delta}$ when $f_c = 15 \text{ N/mm}^2$	CSB unit $\frac{\delta}{\delta}$ when $f_c = 22 \text{ N/mm}^2$	CSB unit $\frac{\delta}{\delta}$ when $f_c = 28 \text{ N/mm}^2$
215	65	65	0.9	0.92	1	0.89	0.85	0.88
215	100	65	0.9	0.92	1	0.89	0.85	0.88
215	150	65	0.9	0.92	1	0.89	0.85	0.88
215	200	65	0.9	0.92	1	0.89	0.85	0.88
215	240	65	0.9	0.92	1	0.89	0.85	0.88
215	65	100	0.9	0.92	1	0.89	0.85	0.88
215	100	100	0.9	0.92	1	0.89	0.85	0.88
215	150	100	0.9	0.92	1	0.89	0.85	0.88
215	200	100	0.9	0.92	1	0.89	0.85	0.88
215	240	100	0.9	0.92	1	0.89	0.85	0.88
215	65	150	1	1	1	1	0.92	0.93
215	100	150	1	1	1	1	0.92	0.93
215	150	150	1	1	1	1	0.92	0.93
215	200	150	1	1	1	1	0.92	0.93
215	240	150	1	1	1	1	0.92	0.93
215	65	200	1	1	1	1	1	1
215	100	200	1	1	1	1	1	1
215	150	200	1	1	1	1	1	1
215	200	200	1	1	1	1	1	1
215	240	200	1	1	1	1	1	1
215	65	240	(J-13) 1	1	1	1	1	1
215	100	240	(J-13) 1	1	1	1	1	1
215	150	240	(J-13) 1	1	1	1	1	1
215	200	240	(J-13) 1	1	1	1	1	1
215	240	240	(J-13) 1	1	1	1	1	1

Hidden page

Hidden page

Hidden page

Hidden page

Hidden page

throughout the FE mesh, an unrealistic task as it would not be known *a priori* which regions would correspond to the weaker material. In practice, however, material testing is not usually carried out by 'coupons' cut out of, or cored from, brick units, but these are tested directly. Fortunately, and as mentioned previously, such tests exhibit considerably less scatter than the 'coupons' tested here, this scatter being typically of the order of 14–21%, which implies that the application to such data of F factors is justifiable as these can account for a comparable degree of change in brick-strength values (according to the present study, up to about 15%).

It will be seen that the conclusions emerging from the present analytical study differ considerably from the EC6 draft recommendations, namely values of δ that are significantly closer to unity, a height (i.e. size) — rather than shape — effect (below a certain height) as δ does not seem to vary with length and width, and the influence of brick type/strength. The opinion among experimentalists appears divided, some backing the EC6 proposals and others confirming the present findings, but there is an overall lack of readily-available published data to make more definitive objective judgement. The Authors did, however, manage to see test data — as yet unpublished — from a laboratory which purported to back the EC6 approach, i.e. larger δ variation and effects of all three brick dimensions. On viewing the plots for H , T , L versus δ , two points became immediately obvious. First, the scatter of results was so large that, while the EC6 proposal could fit the test data, so also could, easily, the present analytical findings. Secondly, a comparison of the plots for T and L revealed that the variation of δ for one was a fraction of the corresponding values for the other, as if a brick could 'distinguish' between its lateral dimensions (i.e. 'length' and 'width')! (Such a bizarre result is probably a consequence of the large experimental scatter and possible preferential orientation of the experimental platen set-up.) Therefore, in the absence of more fundamental theoretical investigations and/or more reliable experimental evidence, it does not seem unreasonable to accept tentatively the presently proposed modest heightwise *size* (instead of *shape*) effect for the δ factor, at least for concrete brick units.

4.8.2. Effect of the number of mortar joints on the strength of a masonry wall

4.8.2.1. Problem formulation

This section describes the results of a numerical parametric study aimed at establishing the effect of the number of mortar joints on the load-carrying capacity of brick walls of constant height.^{191,192}

The masonry unit under consideration has dimensions 100 mm × 215 mm × 510 mm. The entire wall, of constant height $h = 510$ mm, has been analysed by setting the number of mortar joints equal to 25, 19, 13, 7 and 1 in turn. Denoting by N the number of mortar joints, the thickness of each of the brick units, t_b , is

Hidden page

Hidden page

using 25 HX20A elements each having 10 mm thickness (CS5c). A careful appraisal of the principal stresses in the various elements and the displacements of the nodes for these three investigations uncovered the fact that, when the size of the elements adopted for representing the brick unit becomes very large in comparison to the adjacent element representing the mortar joint, the effect of the dilation of the weak mortar becomes less prominent and, as a result, the structural member sustains more load as the tensile stresses caused by the mortar are localized. In such cases, the Gauss points of the large-sized brick elements remain outside the zone of influence of the element(s) representing the mortar. However, when the size of the two adjacent elements is comparable, the dilation in the low-strength mortar and its induced tension reach the Gauss points in the neighbouring high-strength brick elements representing part of the whole brick unit, and the brick fails in tension at a load much lower than its own failure load, as it should. This seems to be a rational explanation of the currently observed numerical phenomenon. Thus, the excessive increase in the load-carrying capacity of the brick wall as observed in the first two FE runs (CS5a, CS5b) is due to numerical rather than factual reasons, stemming from the use of coarse meshes for the brick units. In the latter instances, the mortar at loads near to failure was subjected to a lateral confining stress equal to more than 50% of its ultimate capacity and this enabled the mortar to sustain loads in excess of twice its actual failure load. It is obvious that, in reality, the failure load is dictated by the incapacity of the high-strength brick elements to undergo expansion of similar magnitude to the readily expanding mortar. This observation points to the need, in FE modelling, to use elements of consistent size, since the adoption of incompatibly sized elements, *especially in conjunction with structural elements consisting of highly different material properties*, can lead to results which may not portray the real behaviour of the structure. It can also be seen from Table 4.17 that, for the case studies with seven mortar joints (CS4a and CS4b), the effect of mesh size on the load-carrying capacity was much less significant (in fact, the discrepancy is of the order of the load-step increment, i.e. of the order of magnitude of the uncertainty inherent in the analysis). This suggests that only the presence of an isolated low-strength element in an FE mesh consisting of predominantly high-strength elements (for example, case studies CS5a, CS5b and CS5c) demands more care in the discretization process.

4.8.2.3. Results and discussion

The results obtained from the various FE runs, with mortar strength constant at 20 N/mm^2 , are shown in Table 4.18. (Only the case studies which are not affected by the size of the elements will henceforth be reported and discussed.) It is evident from the table

Table 4.18. Masonry wall: case studies with mortar strength constant ($f_m = 20 \text{ N/mm}^2$)/91.192

Case study	Number of mortar joints	Mesh configuration ($x \times y \times z$)	Configuration of elements along z axis	Maximum sustained failure stress: N/mm^2
CS1	25	$1 \times 1 \times 26$	13 B+13 M	22
CS2	19	$1 \times 1 \times 20$	10 B+10 M	22
CS3	13	$1 \times 1 \times 14$	7 B+7 M	22
CS4	7	$1 \times 1 \times 24$	20 B+4 M	28
CS5	1	$1 \times 1 \times 26$	25 B+1 M	28

that, with the decrease in the number of mortar joints, the load-carrying capacity of the brick wall increases. When the number of joints is large, mortar strength practically determines the strength of the wall. The contents of Table 4.18 show that, for walls with 25, 19 or 13 mortar joints, the MSL was 10% above the ultimate strength of the mortar. On the other hand, in walls with seven or one mortar joints, the MSL was 40% above the mortar strength. The explanation for this effect is quite simple. Keeping the size of the wall fixed, the increase in the number of mortar joints results in a corresponding increase in the lateral expansion and thereby lateral tension in the abutting bricks, which eventually give in. However, for walls with a smaller number of mortar joints, the total amount of dilation undergone by all the weak mortar is relatively less. This results in a reduced amount of lateral expansion in the 'constraining' bricks. As a result, the wall sustains more load. What is interesting is that the reduction in structural strength with the number of mortar joints does not appear to be a continuous process; instead, there appear to be two distinct types of behaviour (one above $N = 13$ and the other below $N = 7$).

From the above study, therefore, it becomes clear that the effect of a reduced number of mortar joints is to increase the overall load-carrying capacity of a brick wall unit, the cause of this finding having been explained with reference to the differing triaxiality of the various components of the wall. A more extensive parametric study was subsequently conducted to validate further such observations. All the case studies have been repeated using different values of mortar strength. Thus, in Table 4.19, the load-carrying capacities of brick walls with mortar strengths of 20, 15, 10, 5 and 1 N/mm^2 are reported. In all the runs listed in Table 4.19, 10% of the relevant mortar strength has been used in the input as the uniformly distributed load step.

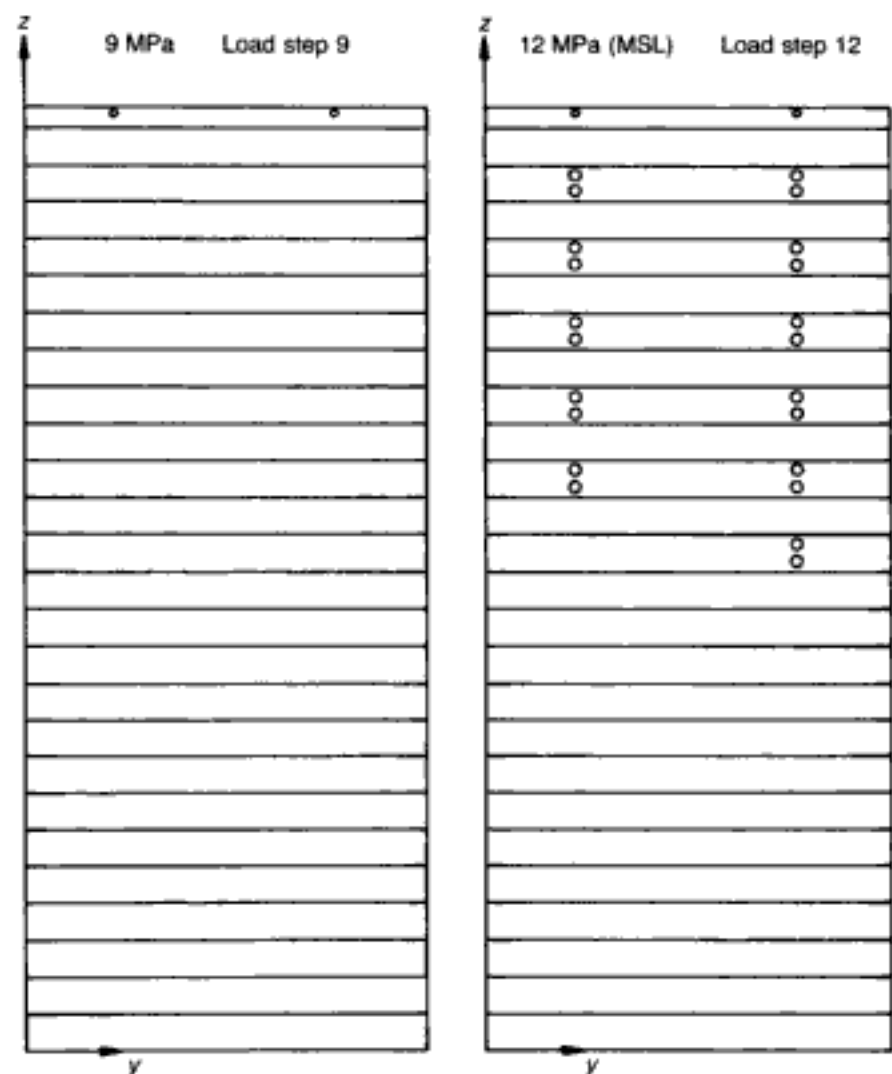
It is evident from Table 4.19 that the basic trend showing the effect of the number of mortar joints in a brick wall, as exhibited in Table 4.18, remains unchanged with variation in the strength of the mortar (i.e. two basic wall-strength values for each mortar strength are apparent, on either side of the intermediate range $7 < N < 13$). A quantitative difference is, however, apparent. While

Hidden page

vertical cracks portray the presence of triaxial stresses perpendicular to the direction of loading, which subject the abutting brick elements to tensile forces. As a result, in the subsequent load step, these vertical cracks propagated suddenly into the adjacent elements representing brick units and the structure failed so abruptly that a suitable plotting file (of load step '777') could not be recovered. With a decrease in the number of mortar joints, the resultant pull exerted by the expanding mortar on the structure also decreases. Thus, for example, in CS5 (with the same mortar strength of 10 N/mm^2), the brick wall (now with only one mortar joint) sustained a load up to the MSL step of 16 N/mm^2 , after which the brick wall suffered sudden fracture and collapse without any early warning of cracking.

It is interesting to note that the general finding of the present analytical exercise is very much in line with the limited experimental evidence available. For example, in reference 194 the effect of the number of mortar joints has been observed experimentally by reference to tests on 9 in ($\sim 230 \text{ mm}$) cubes of brickwork consisting of zero (by placing properly ground bricks

Fig. 4.89. Masonry wall. Crack patterns and deformed shapes ($D.M. = 1$) for CS1 with mortar strength at 10 N/mm^2 ¹⁹²



one upon another to form the brickwork) to four mortar joints. It was concluded that the compressive strength of brickwork cubes decreased gradually as the number of mortar joints increased — a trend also observed in the present study, but not in the range of the number of mortar joints tested (1 to 4) where analysis predicts constant strength. However, a careful study of the data reported in reference 194 provides a timely reminder that experimental scatter in brickwork tests may well make it impossible to correlate experiments with analytically predicted trends: nevertheless, excluding the single-cube test result ('ground bricks') in reference 194, a plot of constant compressive strength throughout the range of 1 to 4 mortar joints can readily be proposed from the test data in view of such scatter, which is more compatible with present numerical findings. (A quantitative comparison between the experimental findings of reference 194 and observations made in the present analytical study cannot, of course, be accomplished directly because of the difference in strength and dimension parameters of the wall units investigated.)

Another correlation of the above test results¹⁹⁴ with the analytical trends reported here refers to the relative values of brick and mortar strengths: thus, the ratio of the wall-to-mortar strengths attains small values for high-strength mortars and, conversely, large values for low-strength mortars. Finally, other workers¹⁹⁵ have found that, with an increase in the thickness of conventional mortar joints, brickwork strength is lowered. The effect of mortar thickness, although not studied here, can also be explained by reference to triaxial stress conditions — a phenomenon which is central to the present analytical study — in the mortar joint in the proximity of failure. The effect of a thicker mortar joint should indeed be very much similar to the effect of additional mortar joints in the brickwork. Accordingly, an increase in the thickness of the mortar joint means a corresponding increase in the amount of lateral expansion (i.e. lateral tension in the neighbouring brick units) due to an increased amount of dilation in the weak mortar, as already explained earlier.

It is, of course, unwise to draw all-embracing conclusions on the basis of the above single wall example despite the parametric variation in both number of mortar joints and mortar strength. Nevertheless, the following remarks, specific to the case studies covered, might, tentatively, point to more general conclusions.

- (a) The load-carrying capacity of the brick wall increases with a decrease in the number of mortar joints. Mortar strength practically determines the strength of the wall when the number of joints is large.
- (b) The basic trend showing the effect of the number of mortar joints in a brick wall remains unchanged with variation in the strength of the mortar. Two basic strength values

- of the brick wall for each mortar strength are apparent, on either side of the intermediate range $7 < N < 13$.
- (c) The rate of increase in the load-carrying capacity of a masonry unit of constant dimensions with respect to the strength of the mortar, as the number of mortar joint decreases, becomes higher with a lowering of mortar strength.

4.9. Concluding remarks

As in the case of the 2-D version of the FE model used in Chapter 3, the 3-D option has been shown to perform reliably in a very wide range of problems encompassing plain concrete, reinforced concrete and prestressed concrete, as well as structural brickwork. While the 3-D package should not be seen as an automatic replacement for the more economical 2-D model — as, indeed, a comparative study of 2-D and 3-D analyses of shear walls has illustrated — there is no doubt that it generally provides a more powerful tool which, in some cases (such as, for instance, complex geometry or when full triaxial effects are relevant even when the problem might *appear* to be amenable to 2-D analysis) becomes, in fact, mandatory.

It is important, at this point, to emphasize once again the main features of the philosophy behind the FE model developed in this book. It is this philosophy, in fact, which has enabled a generally applicable analytical methodology to be developed for arbitrary structures instead of the usual 'tuning' of a model to specific structural types and/or experimental data, with 'retuning' of parameters necessary as soon as other problems are tackled. Accordingly, in the past, studies of the general validity of proposed nonlinear models for concrete structures have rarely been reported, the reason for this, usually, being their limited success. Instead, most published work has focused on the role of various factors believed to affect analytical predictions (such as, for example, various material 'characteristics' (which, in actual fact, are either unimportant or non-existent), the FE mesh, etc.), with the result that a large number of these factors are regarded as key parameters for the FE modelling of concrete. What is surprising is that such factors have received much more attention than the inclusion of the feature that is actually of paramount importance in the successful modelling of concrete structures, namely the triaxial properties of concrete at the material level, which invariably occur and govern collapse.

Moreover, even when triaxial data appear to have been implemented in some of the existing FE packages, such data seem to be based on material models that do not provide an adequate description of volume dilation, which, although rarely mentioned, is the *key* feature exhibited by concrete just before the peak stress level, and is the feature that gives rise to triaxial stress states in that *zone* of the structure which governs its (overall) strength. In

fact, it is this sudden volumetric dilation which leads inevitably to tensile — never compressive — material failure in a structure, and relegates the notion of ‘strain softening’ to one of (doubtful) academic interest, since the peak compressive strength can never be exceeded anywhere in the structure. Without a proper allowance for, and description of, volume dilation, any so-called ‘triaxial’ data are meaningless, for the simple reason that, before volume dilation, three-dimensional effects are relatively unimportant, while, near the peak-stress level, the ignoring of volume dilation fails to recognize the fundamental feature and failure mode of concrete. The concurrent existence of volume dilation and strain softening is incompatible with a *meaningful* set of triaxial data; and yet, to the Authors’ knowledge, even when analysts claim to have implemented triaxial material properties, they still use these in conjunction with strain-softening branches.¹⁰⁸

The failure to understand the importance of a *proper* triaxial description of concrete at the material level forces analysts and investigators to adopt (to varying degree) one or all of the following three courses of action. First, in order to compensate for the lack of the few really fundamental features stemming from realistic triaxial data, it is essential to resort to various secondary (or imaginary) concepts such as strain softening, tension stiffening, aggregate interlock, dowel action, bond-slip relations, etc. Secondly, instead of using a small number of simple and readily definable variables, all sorts of complex parameters are introduced, the number and values of which must be adjusted (*a posteriori*) from problem to problem.¹⁰⁸ Thirdly — and this is one of the more bizarre aspects of the current way of thinking — tests are conducted on what could aptly be described as (specialist) structural members in the hope of extracting (pseudo) material data, which are then to be fed into the structural-analysis program that purports to predict the behaviour of the (presumably larger) specialist structure to be investigated! It is, therefore, not an exaggeration to state that, by concentrating on the primary features of concrete behaviour and ignoring secondary effects, the present model follows precisely the opposite approach to other FE models proposed to date.

Throughout this book, emphasis has been placed on a proper quantitative formulation — based on meaningful and definable triaxial test data — of the stress-strain relationships and of the failure envelopes under static loading. Therefore, the resulting FE model incorporates the main properties of material concrete: the large effect of the confining stress on both the strength and ductility of the material; the sudden loss of load-carrying capacity beyond peak-stress levels; and the very sharp decrease in shear stiffness as concrete cracks under increasing loading. In addition, the FE model formulation requires only the specification of f_c , which, besides being the only readily available (and understood) parameter in

practical design, avoids the subjectivity of assigning other material parameters which are rarely measured or measurable (e.g. initial Young's modulus, uniaxial tensile strength, fracture energy, etc.) and for which the experimental scatter is large (certainly when compared with that of f_c). Although a second material parameter, β , is also required (its justification in the present model being of a numerical rather than of a physical nature), its value may be fixed safely at 0.1 (despite the usual relative insensitivity of predictions to β values between 0.1 and 0.5). Since most mix-design methods are based on achieving a specific value of f_c , the present numerical procedure may be used to predict the behaviour of structures of unknown experimental response, the actual behaviour of which could, if required, be confirmed *a posteriori* by means of a restricted series of tests. The FE model thus provides a potentially reliable basis for the analysis and design of complex structural members. The minimizing of the risk of numerical instability is greatly aided by physically sound concepts concerning the stiffness of concrete — high in compressive zones and the main contributor to strength, low in cracked regions and therefore not requiring the detailed post-cracking descriptions that seem to dominate other FE models. In this sense, the widespread — but, in the Authors' opinion — misguided notion that cracked zones still contribute significantly to the load-carrying capacity of a structure is not compatible with the present package's immediate loss in stiffness (implicit in the brittle model) and the low value assigned to the shear-retention factor.

Finally, one of the most important conclusions stemming from the problems studied in this chapter (and confirming the 2-D analyses of Chapter 3) concerns the basic mode of failure of structural concrete in that the material failure envelope has always been attained in tension (i.e. at least one principal stress is tensile), with no (fully) compressive failures ever detected for any of the case studies. Therefore, and as repeatedly stated in this book, the inclusion of strain-softening branches in compression is irrelevant from a structural viewpoint, even if these were actually to exist. This finding also suggests that even the formal inclusion of a failure criterion in compression (i.e. all principal stresses are compressive) may be regarded as irrelevant. The reason for this failure type becomes clear on recalling the extremely rapid increase in lateral expansion of a concrete specimen as the peak compressive stress is approached, as was explained in detail in Chapter 1. A direct consequence is the setting up of tensile stresses in regions of a structure which are immediately adjacent to regions of maximum compressive stresses. As a result, the latter (compressive) stresses (usually deemed to be critical in compression zones) can never, in fact, reach their peak ('ultimate') values since earlier tensile failure in the orthogonal direction occurs. This explains, for example, the sudden horizontal cracking in the compressive region

of flexural members thought to exhibit '(compressive) concrete failure'. More generally, it provides the theoretical basis for the well-known observation, often made by experienced designers, that *concrete* (in compressive zones) *always fails in tension*, despite the universal adoption in codes of practice of the *uniaxial* strength in compression as the failure criterion in these (critical) zones.

Appendix A. Octahedral formulation of stresses and strains

A.1. Octahedral coordinates

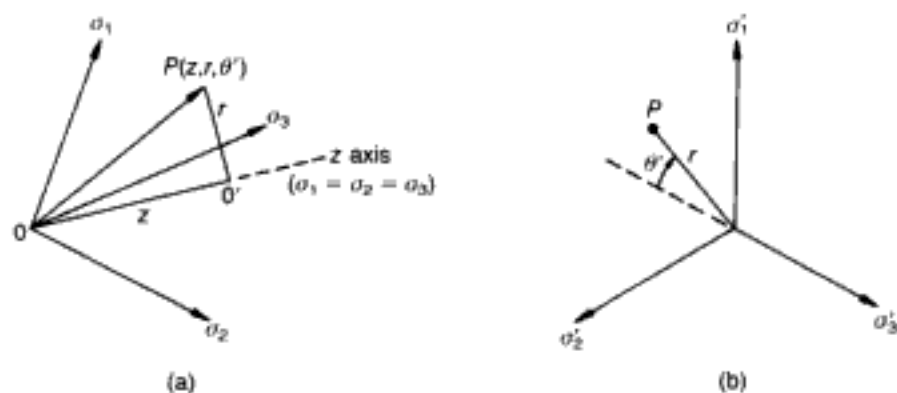
Consider the Cartesian stress space depicted in Fig. A.1(a), the coordinate axes of which are the principal stresses ($\sigma_1, \sigma_2, \sigma_3$), these being used to define any given state of stress as indicated generally by point P. The octahedral coordinates (z, r, θ'), on the other hand, refer to a cylindrical coordinate system having its z axis coincide with the space diagonal ($\sigma_1 = \sigma_2 = \sigma_3$) while r and θ' represent the radius and rotational variable respectively: such a system is also shown in Fig. A.1(a). In addition, the cylindrical system may be viewed more clearly along the space diagonal or z axis, as in Fig. A.1(b) which thus lies in the plane normal to z (the deviatoric plane). Basic vector algebra enables the following relationships between octahedral and Cartesian coordinates to be established

$$z = \frac{1}{\sqrt{3}}(\sigma_1 + \sigma_2 + \sigma_3) \tag{A.1a}$$

$$r = \frac{1}{\sqrt{3}}\sqrt{[(\sigma_1 - \sigma_2)^2 + (\sigma_2 - \sigma_3)^2 + (\sigma_3 - \sigma_1)^2]} \tag{A.1b}$$

$$\cos\theta' = \frac{1}{\sqrt{6}r}(\sigma_1 + \sigma_2 - 2\sigma_3) \tag{A.1c}$$

Fig. A.1. Stress space: (a) Cartesian ($\sigma_1, \sigma_2, \sigma_3$) and cylindrical (z, r, θ') coordinates; (b) view from the deviatoric plane



A.2. Octahedral stresses

The octahedral stress, σ_{oct} , acts on a plane orthogonal to the line that trisects equally the sets of axes defined by the principal stress directions. As stated above, such a plane is known as the deviatoric plane: in Fig. A.2(a), it is shown in the form of a triangle. With u_z (the unit vector along z) given by $(\sqrt{3})^{-1}(1, 1, 1)$, the octahedral stress is obtained through the following product

$$\sigma_{oct} = \begin{bmatrix} \sigma_1 & 0 & 0 \\ 0 & \sigma_2 & 0 \\ 0 & 0 & \sigma_3 \end{bmatrix} \frac{1}{\sqrt{3}} \begin{bmatrix} 1 \\ 1 \\ 1 \end{bmatrix} = \frac{1}{\sqrt{3}} \begin{bmatrix} \sigma_1 \\ \sigma_2 \\ \sigma_3 \end{bmatrix} \tag{A.2}$$

Hidden page

$$I_1 = \sigma_x + \sigma_y + \sigma_z = \sigma_1 + \sigma_2 + \sigma_3 \quad (\text{A.5a})$$

$$I_2 = \sigma_x \sigma_y + \sigma_y \sigma_z + \sigma_z \sigma_x - (\tau_{xy}^2 + \tau_{yz}^2 + \tau_{zx}^2) \\ = \sigma_1 \sigma_2 + \sigma_2 \sigma_3 + \sigma_3 \sigma_1 \quad (\text{A.5b})$$

$$I_3 = \sigma_x \sigma_y \sigma_z + 2\tau_{xy} \tau_{yz} \tau_{zx} - (\sigma_x \tau_{yz}^2 + \sigma_y \tau_{zx}^2 + \sigma_z \tau_{xy}^2) \\ = \sigma_1 \sigma_2 \sigma_3 \quad (\text{A.5c})$$

Of interest here are the relations between octahedral quantities (σ_0 , τ_0 , θ) and the stress invariants, so that the former may be computed directly from the given stress state σ_{ij} in arbitrary Cartesian coordinates x_i , without the necessity to calculate the principal stresses as an intermediate step. It is easily verified that the relevant expressions are

$$\sigma_0 = \frac{1}{3} I_1 \quad (\text{A.6a})$$

$$\tau_0 = \sqrt{\left(2\sigma_0^2 - \frac{2}{3} I_2\right)} \quad (\text{A.6b})$$

$$\cos 3\theta = -\frac{\sqrt{2}}{\tau_0^3} J_3 \quad (\text{A.6c})$$

where J_3 is the third invariant of the deviatoric stress tensor $s_{ij} = \sigma_{ij} - \sigma_0 \delta_{ij}$ (and the use was made of the trigonometric relation $\cos 3\theta = 4 \cos^3 \theta - 3 \cos \theta$).

A.4. Octahedral strains

All the preceding definitions relating to the octahedral stress and its component quantities (σ_0 , τ_0 , θ) apply equally to their strain counterparts, as would be expected on account of the essentially identical mathematical nature of stresses and strains. Therefore, denoting the three principal strains by $(\epsilon_1, \epsilon_2, \epsilon_3)$, the following definitions for the hydrostatic and deviatoric strains (ϵ_0 and γ_0 respectively), as well as the angle between the vector γ_0 and the projection of the ϵ_3 axis (δ), hold

$$\epsilon_0 = \frac{1}{3} (\epsilon_1 + \epsilon_2 + \epsilon_3) \quad (\text{A.7a})$$

$$\gamma_0 = \frac{1}{3} \sqrt{[(\epsilon_1 - \epsilon_2)^2 + (\epsilon_2 - \epsilon_3)^2 + (\epsilon_3 - \epsilon_1)^2]} \quad (\text{A.7b})$$

$$\cos \delta = \frac{1}{\sqrt{2} \gamma_0} (\epsilon_0 - \epsilon_3) \quad (\text{A.7c})$$

A.5. Elastic constitutive relations in terms of octahedral stresses and strains

Since all the octahedral parameters may be expressed in terms of principal stresses/strains, only three of the six constitutive relations linking strains and stresses need to be invoked, namely those dealing with normal, or direct, quantities. These are

$$\epsilon_1 = \frac{1}{E} [\sigma_1 - \nu (\sigma_2 + \sigma_3)] \quad (\text{A.8a})$$

$$\epsilon_2 = \frac{1}{E} [\sigma_2 - \nu (\sigma_3 + \sigma_1)] \quad (\text{A.8b})$$

$$\epsilon_3 = \frac{1}{E} [\sigma_3 - \nu (\sigma_1 + \sigma_2)] \quad (\text{A.8c})$$

Combining the above gives

$$\epsilon_0 = \frac{1 - 2\nu}{E} \sigma_0 = \frac{\sigma_0}{3K} \quad (\text{A.9a})$$

$$\gamma_0 = \frac{1 + \nu}{E} \tau_0 = \frac{\tau_0}{2G} \quad (\text{A.9b})$$

where K and G are the bulk and shear moduli respectively, defined in the usual way

$$K = \frac{E}{3(1 - 2\nu)} \quad (\text{A.10a})$$

$$G = \frac{E}{2(1 + \nu)} \quad (\text{A.10b})$$

Appendix B. Coordinate transformations

Transformation of stresses and strains from one coordinate system to another is a recurrent operation in assessing the critical stress/strain state in a structure, one of its familiar forms being the well-known Mohr-circle construction. In FE analysis, transformations of constitutive ($[D]$) and/or stiffness ($[k]$) matrices occur repeatedly as, for example, in expressing stiffness properties from local to global coordinates, or the imposition of constraints which do not coincide with global axes. As indicated in section 2.3.2, coordinate transformation is implicit in the isoparametric formulation of stiffness matrices; however, an explicit transformation is required for purposes of expressing cracked D -matrices — set up initially in temporary local axes that follow the direction of cracking — in (overall) structure coordinates.

B.1. Strain transformations

Consider two sets of Cartesian axes ($x, y, z \equiv x_i$) and ($x', y', z' \equiv x'_i$) sketched in Fig. B.1, with the direction cosines that define their relative orientations given by (l_1, m_1, n_1) (for x' relative to x, y, z respectively), (l_2, m_2, n_2) (for y') and (l_3, m_3, n_3) (for z'). Through the use of these direction cosines, the relations linking displacements in the two coordinate systems can readily be formulated, and then, in combination with the chain-rule of differentiation and the strain-displacement expressions of 3-D elasticity (with the engineering definition of shear strains applicable), the transformation of strains ϵ (in the x_i system) into strains ϵ' (in the x'_i system) follows

$$\begin{bmatrix} \epsilon'_x \\ \epsilon'_y \\ \epsilon'_z \\ \gamma'_{xy} \\ \gamma'_{xz} \\ \gamma'_{yz} \end{bmatrix} = \begin{bmatrix} l_1^2 & m_1^2 & n_1^2 & l_1 m_1 & m_1 n_1 & n_1 l_1 \\ l_2^2 & m_2^2 & n_2^2 & l_2 m_2 & m_2 n_2 & n_2 l_2 \\ l_3^2 & m_3^2 & n_3^2 & l_3 m_3 & m_3 n_3 & n_3 l_3 \\ 2l_1 l_2 & 2m_1 m_2 & 2n_1 n_2 & l_1 m_2 + l_2 m_1 & m_1 n_2 + m_2 n_1 & n_1 l_2 + n_2 l_1 \\ 2l_3 l_1 & 2m_3 m_1 & 2n_3 n_1 & l_3 m_1 + l_1 m_3 & m_3 n_1 + m_1 n_3 & n_3 l_1 + n_1 l_3 \\ 2l_2 l_3 & 2m_2 m_3 & 2n_2 n_3 & l_2 m_3 + l_3 m_2 & m_2 n_3 + m_3 n_2 & n_2 l_3 + n_3 l_2 \end{bmatrix} \begin{bmatrix} \epsilon_x \\ \epsilon_y \\ \epsilon_z \\ \gamma_{xy} \\ \gamma_{xz} \\ \gamma_{yz} \end{bmatrix} \quad (\text{B.1a})$$



Fig. B.1. Two sets of Cartesian coordinate systems arbitrarily oriented with respect to each other

i.e.

$$\epsilon' = [T_\epsilon] \epsilon \quad (\text{B.1b})$$

For 2-D problems, Fig. B.1 may be visualized with axes z and z' (now coincident) pointing out of the page and the rotation (in the plane of the page) of x', y' with respect to x, y defined by the angle $\bar{\theta}$. Then, $n_1 = n_2 = l_3 = m_3 = 0$, whereas $l_1 = m_2 = \cos \bar{\theta} (= c)$, $m_1 = -l_2 = \sin \bar{\theta} (= s)$, $n_3 = 1$, so that (B.1a) reduces to

$$\begin{bmatrix} \epsilon'_x \\ \epsilon'_y \\ \gamma'_{xy} \end{bmatrix} = \begin{bmatrix} c^2 & s^2 & cs \\ s^2 & c^2 & -cs \\ -2cs & 2cs & c^2 - s^2 \end{bmatrix} \begin{bmatrix} \epsilon_x \\ \epsilon_y \\ \gamma_{xy} \end{bmatrix} \quad (\text{B.1c})$$

B.2. Stress transformations

The relations governing the transformations of stresses σ (system x_i) into stresses σ' (system x'_i) are derived by straightforward equilibrium considerations, and may be written as

$$\sigma' = [T_\sigma] \sigma \quad (\text{B.2})$$

where the ordering of the elements of the stress vectors is compatible with that of their strain counterparts as listed in (B.1a). It is interesting that $[T_\sigma]$ may be obtained from $[T_\epsilon]$ by simply moving the factors 2 symmetrically with respect to the diagonal. It may also be shown that

$$[T_\epsilon]^{-1} = [T_\sigma]^T \quad (\text{B.3a})$$

$$[T_\sigma]^{-1} = [T_\epsilon]^T \quad (\text{B.3b})$$

B.3. Transformations of material properties

Consider the constitutive matrices $[D]$ and $[D']$ in the two coordinate systems x_i and x'_i respectively. Their relationship can be established by invoking the invariance of the strain energy stored (as a result of strains caused by the application of virtual displacements) in either system of axes. Here, however, a more direct derivation may be achieved through expressions such as (B.3). Thus, in the system x'_i

$$\sigma' = [D'] \epsilon' \quad (\text{B.4})$$

which, upon use of (B.2) and (B.1b), may be written as

$$[T_\sigma] \sigma = [D'] [T_\epsilon] \epsilon$$

so that

$$\sigma = [T_\sigma]^{-1} [D'] [T_\epsilon] \epsilon$$

On account of (B.3b),

$$\sigma = [T_\epsilon]^T [D'] [T_\epsilon] \epsilon$$

and hence finally

$$[D] = [T_\epsilon]^T [D'] [T_\epsilon] \quad (\text{B.5})$$

References

1. Pavlović, M.N. (Duffield, C.F., Hutchinson, G.L. and Mansell, D.S. (eds)) Structural concrete and ultimate-strength philosophy: towards a more rational approach to analysis and design. *The art of structural engineering (A conference in honour of Professor Emeritus Leonard Kelman Stevens) (Proc. Invited Papers for the International Conference, Melbourne University, May 1991)*. The University of Melbourne, Melbourne, 1991, 171–195.
2. Pavlović, M.N. and Poulton, S.M. On the computation of slab effective widths. *J. Struct. Engng, Proc. ASCE*, 1985, **111**, 363–377.
3. Kotsovos, M.D. and Lefas, I.D. Behavior of reinforced concrete beams designed in compliance with the concept of the compressive-force path. *ACI Struct. Journal*, 1990, **87**, 127–139.
4. Maier, J. and Thürlimann, B. *Bruchversuche an Stahlbetonscheiben. Bericht Nr. 8003-1*, Institut für Baustatik und Konstruktion (Eidgenössische Technische Hochschule), Zurich, 1985.
5. Schlaich, J., Schäfer, K. and Jennewein, M. Towards a consistent design of structural concrete. *PCI Journal*, 1987, **32**, 74–150.
6. Newman, J.B. (Lydon, F.D. (ed.)) Concrete under complex stress. *Developments in concrete technology—1*, Applied Science Publishers, London, 1979, 151–219.
7. Timoshenko, S.P. *History of strength of materials*, McGraw-Hill, New York, 1953.
8. Gerstle, K.H., Linse, D., Bertacchi, P., Kotsovos, M.D., Ko, H-Y., Newman, J.B., Rossi, P., Schickert, G., Taylor, M.A., Traina, L.A., Zimmerman, R.M. and Bellotti, R. Strength of concrete under multiaxial stress states. *Proc. Douglas McHenry International Symposium on Concrete and Concrete Structures, SP-55*, American Concrete Institute, Detroit, 1978, 103–131.
9. Gerstle, K.H., Aschl, H., Bellotti, R., Bertacchi, P., Kotsovos, M.D., Ko, H-Y., Linse, D., Newman, J.B., Rossi, P., Schickert, G., Taylor, M.A., Traina, L.A., Winkler, H. and Zimmerman, R.M. Behavior of concrete under multiaxial stress states. *J. Engng Mech. Div., Proc. ASCE*, 1980, **106**, 1383–1403.
10. Newman, J.B. *Deformational behaviour, failure mechanisms and design criteria for concretes under combinations of stress*, University of London, 1973, PhD Thesis.
11. Drucker, D.C. *Introduction to mechanics of deformable solids*, McGraw-Hill, New York, 1967.
12. Kotsovos, M.D. and Newman, J.B. Generalized stress–strain relations for concrete. *J. Engng Mech. Div., Proc. ASCE*, 1978, **104**, 845–856.
13. Kotsovos, M.D. and Newman, J.B. Plain concrete under load — a new interpretation. *Proc. IABSE Colloquium on Advanced Mechanics of Reinforced Concrete*, Delft, June 1981, 143–158.
14. Kotsovos, M.D. Effect of testing techniques on the post-ultimate behaviour of concrete in compression. *Mat. & Struct., RILEM*, 1983, **16**, 3–12.
15. Barnard, P.R. Researches into the complete stress–strain curve for concrete. *Mag. Concr. Res.*, 1964, **16**, 203–210.
16. Ahmad, S.H. and Shah, S.P. Complete stress–strain curve of concrete and nonlinear design. *Proc. CSCE–ASCE–ACI–CEB International Symposium on Nonlinear Design of Concrete Structures*, University of Waterloo (Ontario), August 1979, 61–81.

17. Wang, P.T., Shah, S.P. and Naaman, A.E. Stress-strain curves of normal and lightweight concrete in compression. *ACI Journal*, 1978, **75**, 603-611.
18. Newman, K. and Lachance, L. The testing of brittle materials under uniform uniaxial compressive stress. *Proc. ASTM*, 1964, **64**, 1044-1067.
19. Shah, S.P. and Sankar, R. Internal cracking and strain-softening response of concrete under multiaxial compression. *ACI Mat. Journal*, 1987, **84**, 200-212.
20. Kotsovos, M.D. *Failure criteria for concrete under generalised stress states*, University of London, 1974, PhD Thesis.
21. Evans, R.H. and Marathe, M.S. Microcracking and stress-strain curves for concrete in tension. *Mat. & Struct., RILEM*, 1968, **1**, 61-64.
22. Kotsovos, M.D. A fundamental explanation of the behaviour of reinforced concrete beams in flexure based on the properties of concrete under multiaxial stress. *Mat. & Struct., RILEM*, 1982, **15**, 529-537.
23. Kotsovos, M.D. and Cheong, H-K. Applicability of test specimen results for the description of the behavior of concrete in a structure. *ACI Journal*, 1984, **81**, 358-363.
24. Heyman, J. *The masonry arch*, Ellis Horwood, Chichester, 1982.
25. Kotsovos, M.D. Fracture processes of concrete under generalised stress states. *Mat. & Struct., RILEM*, 1979, **12**, 431-437.
26. Griffith, A.A. The phenomena of rupture and flow in solids. *Phil. Trans. Roy. Soc. (London), Series A*, 1921, **221**, 163-198.
27. Brace, W.F. and Bombolakis, E.G. A note on brittle crack growth in compression. *J. Geophys. Res.*, 1960, **68**, 3709-3713.
28. Hoek, E. and Bieniawski, Z.T. Brittle fracture propagation in rock under compression. *Int. J. Fract. Mech.*, 1965, **1**, 137-155.
29. Kotsovos, M.D. and Newman, J.B. Fracture mechanics and concrete behaviour. *Mag. Concr. Res.*, 1981, **33**, 103-112.
30. Kotsovos, M.D. and Newman, J.B. Behavior of concrete under multiaxial stress. *ACI Journal*, 1977, **74**, 443-446.
31. Kotsovos, M.D. Effect of stress path on the behavior of concrete under triaxial stress states. *ACI Journal*, 1979, **76**, 213-223.
32. Cook, J. and Gordon, J.E. A mechanism for the control of crack propagation in all-brittle systems. *Proc. Roy. Soc. (London), Series A*, 1964, **282**, 508-520.
33. Bažant, Z.P. and Bhat, P.D. Endochronic theory of inelasticity and failure of concrete. *J. Engng Mech. Div., Proc. ASCE*, 1976, **102**, 701-722.
34. Bažant, Z.P. and Kim, S.S. Plastic-fracturing theory for concrete. *J. Engng Mech. Div., Proc. ASCE*, 1979, **105**, 407-428.
35. Bažant, Z.P. and Tsubaki, T. Total strain theory and path-dependence of concrete. *J. Engng Mech. Div., Proc. ASCE*, 1980, **106**, 1151-1173.
36. Fardis, M.N., Alibe, B. and Tassoulas, J.L. Monotonic and cyclic constitutive law for concrete. *J. Engng Mech., Proc. ASCE*, 1983, **109**, 516-536.
37. Newman, J.B. Apparatus for testing concrete under multiaxial states of stress. *Mag. Concr. Res.*, 1974, **26**, 229-238.
38. Kotsovos, M.D. and Newman, J.B. A mathematical description of the deformational behaviour of concrete under complex loading. *Mag. Concr. Res.*, 1979, **31**, 77-90.
39. Spooner, D.C. and Dougill, J.W. A quantitative assessment of damage sustained in concrete during compressive loading. *Mag. Concr. Res.*, 1975, **27**, 151-160.
40. Kotsovos, M.D. Concrete. A brittle fracturing material. *Mat. & Struct., RILEM*, 1984, **17**, 107-115.
41. Kotsovos, M.D. A mathematical model of the deformational behavior of concrete under generalised stress based on fundamental material properties. *Mat. & Struct., RILEM*, 1980, **13**, 289-298.

42. Kupfer, H., Hilsdorf, H.K. and Rüsç, H. Behavior of concrete under triaxial stresses. *ACI Journal*, 1969, **66**, 656–666.
43. Popovics, S. A numerical approach to the complete stress–strain curve of concrete. *Cement & Concr. Res.*, 1973, **3**, 583–599.
44. Kotsovos, M.D. A mathematical description of the strength properties of concrete under generalized stress. *Mag. Concr. Res.*, 1979, **31**, 151–158.
45. Hannant, D.J. Nomograms for the failure of plain concrete subjected to short-term multi-axial stresses. *Struct. Engr.*, 1974, **52**, 151–165.
46. Hobbs, D.W., Pomeroy, C.D. and Newman, J.B. Design stresses for concrete structures subject to multi-axial stresses. *Struct. Engr.*, 1977, **55**, 151–164.
47. Lowe, P.G. Deformation and fracture of plain concrete. *Mag. Concr. Res.*, 1978, **30**, 200–204.
48. Newman, J.B. and Newman, K. *Development of design criteria for concrete under combined states of stress. Technical Note 93*, CIRIA, London, 1978.
49. Willam, K.J. and Warnke, E.P. Constitutive model for the triaxial behaviour of concrete. *Seminar on Concrete Structures Subjected to Triaxial Stresses*. Istituto Sperimentale Modelli e Strutture, Bergamo, May 1974, Paper III-1.
50. Franklin, J.A. *Classification of rock according to its mechanical properties. Rock Mechanics Research Report No. T.1*, Imperial College, London, 1970.
51. Kotsovos, M.D. and Pavlović, M.N. Non-linear finite element modelling of concrete structures: basic analysis, phenomenological insight, and design implications. *Engng Computations*, 1986, **3**, 243–250.
52. Kotsovos, M.D., Bobrowski, J. and Eibl, J. Behaviour of reinforced concrete T-beams in shear. *Struct. Engr.*, 1987, **65B**, 1–10.
53. British Standards Institution. *Code of practice for the structural use of concrete, CP 110 (Part 1. Design, materials and workmanship)*, British Standards Institution, London, 1972.
54. Bédard, C. (1983) *Non-linear finite element analysis of concrete structures*, University of London, 1983, PhD Thesis.
55. British Standards Institution. *British Standard. Structural use of concrete, BS 8110 (Part 1. Code of practice for design and construction)*, British Standards Institution, London, 1985.
56. González Vidosa, F. *Three-dimensional finite element analysis of structural concrete under static loading*, University of London, 1989, PhD Thesis.
57. Kotsovos, M.D. Consideration of triaxial stress conditions in design: a necessity. *ACI Struct. Journal*, 1987, **84**, 266–273.
58. British Standards Institution. *British Standard. Structural use of concrete, BS 8110 (Part 2. Code of practice for special circumstances)*, British Standards Institution, London, 1985.
59. Taylor, R. and Al-Najmi, A.Q.S. The strength of concrete in composite reinforced concrete beams in hogging bending. *Mag. Concr. Res.*, 1980, **32**, 156–163.
60. Kotsovos, M.D. An analytical investigation of the behaviour of concrete under concentrations of load. *Mat. & Struct., RILEM*, 1981, **14**, 341–348.
61. Zienkiewicz, O.C. *The finite element method*, McGraw-Hill, London, 1977, 3rd edn.
62. Cook, R.D. *Concepts and applications of finite element analysis*, J. Wiley, New York, 1981, 2nd edn.
63. Cook, R.D., Malkus, D.S. and Plesha, M.E. *Concepts and applications of finite element analysis*, J. Wiley, New York, 1989, 3rd edn.
64. Owen, D.R.J. and Hinton, E. *Finite elements in plasticity. Theory and practice*, Pineridge Press, Swansea, 1980.

65. Hitchings, D. *FINEL user's manual*, Imperial College, London, 1972.
66. Hitchings, D. *FINEL programming manual*, Imperial College, London, 1980.
67. Phillips, D.V. and Zienkiewicz, O.C. Finite element non-linear analysis of concrete structures. *Proc. Instn Civ. Engrs, Part 2*, 1976, **61**, 59–88.
68. Irons, B. and Ahmad, S. *Techniques of finite elements*, Ellis Horwood, Chichester, 1980.
69. Timoshenko, S.P. and Goodier, J.N. *Theory of elasticity*, McGraw-Hill, New York, 1970, 3rd edn.
70. Bergan, P.G. and Clough, R.W. Convergence criteria for iterative processes. *AIAA Journal*, 1972, **10**, 1107–1108.
71. Lin, C.S. and Scordelis, A.C. Nonlinear analysis of reinforced concrete shells of general form. *J. Struct. Div., Proc. ASCE*, 1975, **101**, 523–538.
72. Suidan, M.S. and Schnobrich, W.C. Finite element analysis of reinforced concrete. *J. Struct. Div., Proc. ASCE*, 1973, **99**, 2109–2122.
73. Cedolin, L. and Dei Poli, S. Finite element studies of shear-critical R/C beams. *J. Engng Mech. Div., Proc. ASCE*, 1977, **103**, 395–410.
74. Crisfield, M.A. Local instabilities in the non-linear analysis of reinforced concrete beams and slabs. *Proc. Instn Civ. Engrs, Part 2*, 1982, **73**, 135–145.
75. Cedolin, L. and Nilson, A.H. A convergence study of iterative methods applied to finite element analysis of reinforced concrete. *Int. J. Num. Meth. Engng*, 1978, **12**, 437–451.
76. Burns, N.H. and Siess, C.P. Plastic hinging in reinforced concrete. *J. Struct. Div., Proc. ASCE*, 1966 (October), **92** (ST5), 45–64.
77. Ngo, D. and Scordelis, A.C. Finite element analysis of reinforced concrete beams. *ACI Journal*, 1967, **64**, 152–163.
78. Saouma, V.E. and Ingraffea, A.R. Fracture mechanics analysis of discrete cracking. *Proc. IABSE Colloquium on Advanced Mechanics of Reinforced Concrete*, Delft, June 1981, 413–436.
79. Tassios, T.P. and Scarpas, A. A model for local crack behaviour. *Proc. IABSE Colloquium on Computational Mechanics of Concrete Structures — Advances and Applications*, Delft, August 1987, 35–42.
80. Shenglin, D., Qigen S. and Bingzi, S. A finite element simulation model for cracks in reinforced concrete. *Proc. IABSE Colloquium on Computational Mechanics of Concrete Structures — Advances and Applications*, Delft, August 1987, 209–214.
81. Rashid, Y.M. Ultimate strength analysis of prestressed concrete pressure vessels. *Nuclear Engng & Design*, 1968, **7**, 334–344.
82. González Vidosa, F., Kotsovos, M.D. and Pavlović, M.N. On the numerical instability of the smeared-crack approach in the non-linear modelling of concrete structures. *Commun. Appl. Num. Meth.*, 1988, **4**, 799–806.
83. Zienkiewicz, O.C., Taylor, R.L. and Too, J.M. Reduced integration technique in general analysis of plates and shells. *Int. J. Num. Meth. Engng*, 1971, **3**, 275–290.
84. Hand, F.R., Pecknold, D.A. and Schnobrich, W.C. Nonlinear layered analysis of reinforced concrete plates and shells. *J. Struct. Div., Proc. ASCE*, 1973, **99**, 1491–1505.
85. Bédard, C. and Kotsovos, M.D. Fracture processes of concrete for NLFEA methods. *J. Struct. Engng, Proc. ASCE*, 1986, **112**, 573–587.
86. Pavlović, M.N. and Stevens, L.K. The effect of prior flexural prestrain on the stability of structural steel columns. *Engng Struct.*, 1981, **3**, 66–70.
87. Nilson, A.H. Nonlinear analysis of reinforced concrete by the finite element method. *ACI Journal*, 1968, **65**, 757–766.
88. Edwards, A.D. and Yannopoulos, P.J. Local bond-stress–slip relationships under repeated loading. *Mag. Concr. Res.*, 1978, **30**, 62–72.
89. ASCE Task Committee on Finite Element Analysis of Reinforced

- Concrete Structures. *Finite element analysis of reinforced concrete*. ASCE Special Publication, New York, 1982.
90. Labib, F. and Edwards, A.D. An analytical investigation of cracking in concentric and eccentric reinforced concrete tension members. *Proc. Instn Civ. Engrs, Part 2*, 1978, **65**, 53–70.
 91. Labib, F. *Non-linear analysis of the bond and crack distribution in reinforced concrete members*, University of London, 1976, PhD Thesis.
 92. Kollegger, J. and Mehlhorn, G. Material model for cracked reinforced concrete. *Proc. IABSE Colloquium on Computational Mechanics of Concrete Structures — Advances and Applications*, Delft, August 1987, 63–74.
 93. Greunen, J. *Nonlinear geometric, material and time dependent analysis of reinforced and prestressed concrete slabs and panels*. Report No. UC-SESM 79-3, University of California (Berkeley), 1979.
 94. Clough, R.W. The finite element method after twenty-five years: a personal view. *Comp. & Struct.*, 1980, **12**, 361–370.
 95. ASCE Task Committee on Finite Element Analysis of Reinforced Concrete Structures. *Constitutive relations and failure theories*. CE — STR — 81 — 21, New York, 1981.
 96. Fried, I. Basic computational problems in the finite element analysis of shells. *Int. J. Sol. & Struct.*, 1971, **7**, 1705–1715.
 97. Bazant, Z.P. and Oh, B.H. Crack band theory for fracture of concrete. *Mat. & Struct., RILEM*, 1963, **16**, 155–177.
 98. Bédard, C. and Kotsovos, M.D. Application of NLFEA to concrete structures. *J. Struct. Engng, Proc. ASCE*, 1985, **111**, 2691–2707.
 99. Kotsovos, M.D., Pavlović, M.N. and Arnaout, S. (Middleton, J. and Pande, G.N. (eds)). Nonlinear finite element analysis of concrete structures: a model based on fundamental material properties. *NUMETA 85. Numerical methods in engineering: theory and applications (Proc. International Conference on Numerical Methods, Swansea, January 1985)*. A.A. Balkema, Rotterdam, 1985, **2**, 565–575.
 100. Niyogi, S.K. Concrete bearing strength — support, mix, size effect. *J. Struct. Div., Proc. ASCE*, 1974, **100**, 1685–1702.
 101. Hawkins, N.M. The bearing strength of concrete loaded through rigid plates. *Mag. Concr. Res.*, 1968, **20**, 31–40.
 102. Neville, A.M. *Properties of concrete*, Pitman, London, 1973, 2nd edn.
 103. Kotsovos, M.D. and Newman, J.B. Effect of boundary conditions upon the behaviour of concrete under concentrations of load. *Mag. Concr. Res.*, 1981, **33**, 161–170.
 104. Williams, A. *The bearing capacity of concrete loaded over a limited area*. Technical Report 526 (Publication 42.526), Cement and Concrete Association, Wexham Springs, 1979.
 105. Haynes, H.H. *Concrete spherical structures subjected to rapid loading by external pressure — an exploratory investigation*. Technical Memorandum No. 44-80-6, Civil Engineering Laboratory, Port Hueneme (California), 1980.
 106. Kong, F.K. and Evans, R.H. *Reinforced and prestressed concrete*, Nelson, Walton-on-Thames, 1980.
 107. Fenwick, R.C. and Paulay, T. Mechanisms of shear resistance of concrete beams. *J. Struct. Div., Proc. ASCE*, 1968, **94**, 2325–2350.
 108. González Vidosa, F., Kotsovos, M.D. and Pavlović, M.N. Discussion (L.J. Pakianathan, D.V. Phillips) and Authors' Closure of: Three-dimensional non-linear finite-element model for structural concrete: parts 1 and 2 (*Proc. Instn Civ. Engrs*, 1991 **91**, 517–560), *Proc. Instn Civ. Engrs Structs & Bldgs*, 1992, **94**, 365–374.
 109. Kotsovos, M.D. Compressive force path concept: basis for reinforced concrete ultimate limit state design. *ACI Struct. Journal*, 1988, **85**, 68–75.

110. Kotsovos, M.D. Mechanisms of 'shear' failure. *Mag. Concr. Res.*, 1983, **35**, 99–106.
111. Kotsovos, M.D. Shear failure of reinforced concrete beams. *Engng Struct.*, 1987, **9**, 32–38.
112. Kotsovos, M.D. Behavior of reinforced concrete beams with a shear span to depth ratio between 1.0 and 2.5. *ACI Journal*, 1984, **81**, 279–286.
113. Kotsovos, M.D. Behavior of beams with shear span-to-depth ratios greater than 2.5. *ACI Journal*, 1986, **83**, 1026–1034.
114. ACI Committee 318. *Building code requirements for reinforced concrete, ACI 318-77*, American Concrete Institute, Detroit, 1977.
115. Kani, G.N.J. The riddle of shear and its solution. *ACI Journal*, 1964, **61**, 441–467.
116. Bresler, B. and Scordelis, A.C. Shear strength of reinforced concrete beams. *ACI Journal*, 1963, **60**, 51–74.
117. Ramakrishnan, V. and Ananthanarayana, Y. Ultimate strength of deep beams in shear. *ACI Journal*, 1968, **65**, 87–98.
118. Kotsovos, M.D. Design of reinforced concrete deep beams. *Struct. Engr.*, 1988, **66**, 28–32.
119. Kong, F.K., Sharp, G.R., Appleton, S.C., Beaumont, C.J. and Kubik, L.A. Structural idealization for deep beams with web openings: further evidence. *Mag. Concr. Res.*, 1978, **30**, 89–95.
120. Taner, N., Fazio, P.P. and Zielinski, Z.A. Strength and behavior of beam-panels — tests and analysis. *ACI Journal*, 1977, **74**, 511–520.
121. Cardenas, A.E., Russell, H.G. and Corley, W.G. Strength of low rise structural walls. *Reinforced concrete structures subjected to wind and earthquake forces, SP-63*, American Concrete Institute, Detroit, 1980, 221–241.
122. Lefas, I.D. and Kotsovos, M.D. Behaviour of reinforced concrete structural walls: a new interpretation. *Proc. IABSE Colloquium on Computational Mechanics of Concrete Structures — Advances and Applications*, Delft, August 1987, 455–462.
123. Lefas, I.D. and Kotsovos, M.D. (Carlomagno, G.M. and Brebbia, C.A. (eds)). Nonlinear finite element analysis of reinforced concrete structural walls. *Computers and experiments in stress analysis (Proc. Fourth International Conference on Computational Methods and Experimental Measurements, Capri, May 1989)*. Computational Mechanics Publications, Southampton, 1989, 25–34.
124. Barda, F., Hanson, J.M. and Corley, W.G. Shear strength of low-rise walls with boundary elements. *Reinforced concrete structures in seismic zones, SP-53*, American Concrete Institute, Detroit, 1977, 149–202.
125. Oesterle, R.G., Fiorato, A.E., Aristizabal-Ochoa, J.D. and Corley, W.G. Hysteretic response of reinforced concrete structural walls. *Reinforced concrete structures subjected to wind and earthquake forces, SP-63*, American Concrete Institute, Detroit, 1980, 243–273.
126. Wiradinata, S. and Saatcioglou, M. Tests of squat shear walls under lateral load reversals. *Proc. Third U.S. National Conference in Earthquake Engineering*, Charleston (South Carolina), August 1986, Earthquake Engineering Research Institute, El Cerrito (California), 1986, **2**, 1395–1406.
127. Lefas, I.D. *Behaviour of reinforced concrete walls and its implication for ultimate limit state design*, University of London, 1988, PhD Thesis.
128. Lefas, I.D. Kotsovos, M.D. and Ambraseys, N.N. Behavior of reinforced concrete structural walls: strength, deformation characteristics, and failure mechanism. *ACI Journal*, 1990, **87**, 23–31.
129. Lefas, I.D. and Kotsovos, M.D. NLFE analysis of RC structural walls and design implications. *J. Struct. Engrng, Proc. ASCE*, 1990, **116**, 146–164.

130. ACI Committee 318. *Building code requirements for reinforced concrete, ACI 318-83*, American Concrete Institute, Detroit, 1983.
131. Cardenas, A.E., Hanson, J.M., Corley, W.G. and Hognestad, E. Design provisions for shear walls. *ACI Journal*, 1973, **70**, 221–230.
132. Kani, G.N.J. Basic facts concerning shear failure. *ACI Journal*, 1966, **63**, 675–692.
133. Ritter, W. Die Bauweise Hennebique. *Schweizerische Bauzeitung*, 1899, **33**(7), 59–61.
134. Mörsch, E. *Concrete steel construction*, McGraw-Hill, New York, 1909.
135. Oesterle, R.G., Aristizábal-Ochoa, J.D., Shiu, K.N. and Corley, W.G. Web crushing of reinforced concrete structural walls. *ACI Journal*, 1984, **81**, 231–241.
136. Bennett, D.F.H. *Advances in concrete construction technology (A review of construction techniques to maximize speed and economy of in situ concrete frame construction)*, British Cement Association, Slough, 1989.
137. González Vidosa, F., Kotsovos, M.D. and Pavlović, M.N. Symmetrical punching of reinforced concrete slabs: an analytical investigation based on nonlinear finite element modeling. *ACI Journal*, 1988, **85**, 241–250.
138. Kinnunen, S., Nylander, H. and Tolf, P. Undersökningar rörande genomstansning vid Institutionen för Byggnadsstatik, KTH. *Nordisk Betong*, 1978, **3**, 25–37.
139. Elstner, R.C. and Hognestad, E. Shearing strength of reinforced concrete slabs. *ACI Journal*, 1956, **53**, 29–58.
140. Regan, P.E. Symmetric punching of reinforced concrete slabs. *Mag. Concr. Res.*, 1986, **38**, 115–128.
141. Anis, N.N. *Shear strength of reinforced concrete flat slabs without shear reinforcement*. University of London, 1970, PhD Thesis.
142. Regan, P.E. and Braestrup, M.W. *Punching shear in reinforced concrete: a state of art report. Bulletin d'Information No. 168*, Comité Euro-International du Béton, Lausanne, 1985.
143. Loo, Y.C. and Chiang, C.L. Methods of punching shear strength analysis of reinforced concrete flat slabs — a comparative study. *Struct. Engng & Mech.*, 1993, **1**, 75–86.
144. González Vidosa, F. Análisis del punzonamiento de placas de hormigón armado por elementos finitos con fisuración distribuida. *Anales de Ingeniería Mecánica*, 1988, **6**(3), 305–310.
145. Ghali, A., Sargjions, M.A. and Huizer, A. Vertical prestressing of flat plates around columns. *Shear in reinforced concrete, SP-42*, American Concrete Institute, Detroit, 1974, **2**, 905–920.
146. Vecchio, F. and Collins, M.P. Stress-strain characteristics of reinforced concrete in pure shear. *Proc. IABSE Colloquium on Advanced Mechanics of Reinforced Concrete*, Delft, June 1981, 211–225.
147. Collins, M.P., Vecchio, F. and Mehlhorn, G. An international competition to predict the response of reinforced concrete panels. *Festschrift Prof. Dr. Bruno Thürlimann zum 60 Geburtstag*, Eidgenössische Technische Hochschule, Zurich, 1983, 471–491.
148. Somerville, G. The behaviour and design of reinforced concrete corbels. *Shear in reinforced concrete, SP-42*, American Concrete Institute, Detroit, 1974, **2**, 477–502.
149. Kriz, L.B. and Rath, C.H. Connections in precast concrete structures — strength of corbels. *PCI Journal*, 1965, **10**, 16–61.
150. Kinoshita, M. *Constitutive relations of concrete under passive confinement and their use in structural analysis*, University of London, 1992, PhD Thesis.
151. Kinoshita, M., Kotsovos, M.D. and Pavlović, M.N. Behaviour of concrete under passive confinement. *J. Mat., Concr. Struct. & Pavements, Proc. JSCE*, 1994, **25**, 131–142.

152. Kinoshita, M., Pavlović, M.N. and Kotsovos, M.D. Constitutive models of concrete under passive confinement and their use in structural analysis. *J. Mat., Concr. Struct. & Pavements, Proc. JSCE*, 1994, **25**, 143–154.
153. Goode, C.D. and Fatheldin, Y.T. Sandwich cylinders (steel-concrete-steel) subjected to external pressure. *ACI Journal*, 1980, **77**, 109–115.
154. Pavlović, M.N. and Zingoni, A. On the elastic design of concrete domes. *Struct. Engng Review*, 1994, **6**, 57–69.
155. González Vidosa, F., Kotsovos, M.D. and Pavlović, M.N. Non-linear finite element analysis of cellular and composite concrete structures. *Concrete offshore in the nineties — COIN (A summary Report/OTH 90 320)*, HMSO, London, 1990, 51–67.
156. González Vidosa, F., Kotsovos, M.D. and Pavlović, M.N. Discussion (R. de Borst) and Authors' Closure of: On the numerical instability of the smeared-crack approach in the non-linear modelling of concrete structures (*Commun. Appl. Num. Meth.*, 1988, **4**, 799–806), *Commun. Appl. Num. Meth.*, 1989, **5**, 489–493.
157. Shimodaira, H. Equivalence between mixed models and displacement models using reduced integration. *Int. J. Num. Meth. Engng*, 1985, **21**, 89–104.
158. de Borst, R. and Nauta, P. Non-orthogonal cracks in a smeared finite element model. *Engng Computations*, 1985, **2**, 35–46.
159. Crisfield, M. A. Snap-through and snap-back response in concrete structures and the dangers of underintegration. *Int. J. Num. Meth. Engng*, 1986, **22**, 751–767.
160. Rots, J.G. and de Borst, R. Analysis of mixed-mode fracture in concrete. *J. Engng Mech., Proc. ASCE*, 1987, **113**, 1739–1758.
161. González Vidosa, F., Kotsovos, M.D. and Pavlović, M.N. Three-dimensional nonlinear finite-element model for structural concrete. Part 1: main features and objectivity study. *Proc. Instn Civ. Engrs, Part 2*, 1991, **91**, 517–544.
162. Fernández, M.A. *Un modelo por el método de los elementos finitos para el análisis no lineal de estructuras de hormigón en tensión plana con representación real de la fisura*. Universidad Politécnica de Valencia, 1988, Dr. Ing. Thesis.
163. González Vidosa, F., Kotsovos, M.D. and Pavlović, M.N. (Bićanić, N. and Mang, H. (eds)). Three-dimensional finite element analysis of structural concrete. *Computer aided analysis and design of concrete structures (Proc. SCI-C 1990, Second International Conference, Zell am See, Austria, April 1990)*, Pineridge Press, Swansea, **2**, 1029–1040.
164. González Vidosa, F., Kotsovos, M.D. and Pavlović, M.N. Three-dimensional nonlinear finite-element model for structural concrete. Part 2: generality study. *Proc. Instn Civ. Engrs, Part 2*, 1991, **91**, 565–560.
165. González Vidosa, F., Kotsovos, M.D. and Pavlović, M.N. Nonlinear finite-element analysis of concrete structures: performance of a fully three-dimensional brittle model. *Comp. & Struct.*, 1991, **40**, 1287–1306.
166. Irons, B.M. Quadrature rules for brick based finite elements. *Int. J. Num. Meth. Engng*, 1971, **3**, 293–294.
167. Hellen, T.K. Effective quadrature rules for quadratic solid isoparametric finite elements. *Int. J. Num. Meth. Engng*, 1972, **4**, 597–600.
168. Bažant, Z.P. and Cedolin, L. Blunt crack band propagation in finite element analysis. *J. Engng Mech. Div., Proc. ASCE*, 1979, **105**, 297–315.
169. Comité Euro-International du Béton. *Model code for concrete structures* (English edition). *CEB-FIB 78*, Cement and Concrete Association, London, 1978.
170. Ottosen, N.S. 2-D finite element analysis of massive RC structures. *J. Struct. Div., Proc. ASCE*, 1982, **108**, 1874–1883.
171. Balakrishnam, S. and Murray, D.W. Prediction of response of concrete

- beams and panels by nonlinear finite element analysis. *Proc. IABSE Colloquium on Computational Mechanics of Concrete Structures — Advances and Applications*, Delft, August 1987, 393–404.
172. Kotsovos, M.D., Pavlović, M.N. and Lefas, I.D. (Fajfar, P. and Krawinkler, H. (eds)). Two- and three-dimensional nonlinear finite-element analysis of structural walls. *Nonlinear seismic analysis and design of reinforced concrete buildings*, Elsevier Applied Science, London, 1992, 215–227.
173. Seraj, S.M., Kotsovos, M.D. and Pavlović, M.N. Three-dimensional finite-element modelling of normal- and high-strength reinforced concrete members, with special reference to T-beams. *Comp. & Struct.*, 1992, **44**, 699–716.
174. Seraj, S.M. *Reinforced and prestressed concrete members designed in accordance to the compressive-force path concept and fundamental material properties*, University of London, 1991, PhD Thesis.
175. Seraj, S.M., Kotsovos, M.D. and Pavlović, M.N. Behaviour of high-strength mix reinforced concrete beams. *Arch. Civ. Engng (Polish Acad. Sciences)*, 1995, **41**, 31–67.
176. Mphonde, A.G. and Frantz, G.C. *Shear strength of high-strength concrete beams. Report No. CE 84-157*, Department of Civil Engineering, University of Connecticut, 1984.
177. Mphonde, A.G. and Frantz, G.C. Shear tests of high- and low-strength concrete beams with stirrups. *High-strength concrete, SP-87*, American Concrete Institute, Detroit, 1985, 179–196.
178. Seraj, S.M., Kotsovos, M.D. and Pavlović, M.N. Non-linear finite-element analysis of prestressed concrete members. *Proc. Instn Civ. Engrs Structs & Bldgs*, 1992, **94**, 403–418.
179. Elzanaty, A.H., Nilson, A.H. and Slate, F.O. *Shear critical high-strength concrete beams. Research Report No. 85-1*, Department of Structural Engineering, Cornell University, 1985.
180. Elzanaty, A.H., Nilson, A.H. and Slate, F.O. Shear capacity of prestressed concrete beams using high-strength concrete. *ACI Struct. Journal*, 1986, **83**, 359–368.
181. Seraj, S.M., Kotsovos, M.D. and Pavlović, M.N. Compressive-force path and behaviour of prestressed concrete beams. *Mat. & Struct., RILEM*, 1993, **26**, 74–89.
182. Seraj, S.M., Kotsovos, M.D. and Pavlović, M.N. Experimental study of the compressive-force path concept in prestressed concrete beams. *Engng Struct.*, 1993, **15**, 439–451.
183. Hillerborg, A. The theoretical basis of a method to determine the fracture energy G_f of concrete. *Mat. & Struct., RILEM*, 1985, **18**, 291–296.
184. Gustafsson, P.J. and Hillerborg, A. Sensitivity in shear strength of longitudinally reinforced concrete beams to fracture energy of concrete. *ACI Struct. Journal*, 1988, **85**, 286–294.
185. Kotsovos, M.D. and Pavlović, M.N. A possible explanation for size effects in structural concrete. *Arch. Civ. Engng (Polish Acad. Sciences)*, 1994, **40**, 243–261.
186. Kotsovos, M.D. and Pavlović, M.N. (Topping, B.H.V. and Papadrakakis, M. (eds)). Size effects in structural concrete: a numerical experiment. *Advances in non-linear finite element methods (Proc. Second International Conference on Computational Structures Technology, Athens, August–September 1994)*. Civil-Comp Press, Edinburgh, 1994, 109–118 (To be reprinted in *Comp. & Struct.*).
187. Leonhardt, F. and Walther, R. *The Stuttgart shear tests, 1961. Contributions to the treatment of the problems of shear in reinforced concrete construction*. (A translation (made by C.V. Amerongen) of the articles that appeared in *Beton- und Stahlbetonbau*, Vol. 56, No. 12, 1961

- and Vol. 57, Nos 2, 3 7 & 8, 1962.) *Translation No. 111*, Cement and Concrete Association, London, 1964.
188. Allen, A.H. *Reinforced concrete design to CP 110 — simply explained*, Cement and Concrete Association, London, 1974.
189. Kotsovos, M.D., Pavlović, M.N. and Seraj, S.M. *An appraisal of shape factors for masonry units with reference to the proposed Eurocode 6 approach. Report BDA-1*, Department of Civil Engineering, Imperial College, 1990.
190. Morton, J., Kotsovos, M.D., Pavlović, M.N. and Seraj, S.M. An initial investigation of the shape factor platen effects when testing masonry units to determine the material compressive strength. *Proc. Ninth International Brick/Block Masonry Conference*, Berlin, October 1991, Deutsche Gesellschaft für Mauerwerksbau, Bonn, 1991, 1, 653–661.
191. Kotsovos, M.D., Pavlović, M.N. and Seraj, S.M. *An investigation into the effect of the number of mortar joints on the strength of a masonry wall. Report BDA-2*, Department of Civil Engineering, Imperial College, 1991.
192. Morton, J., Kotsovos, M.D., Pavlović, M.N. and Seraj, S.M. (Topping, B.H.V. (ed.)). The effect of the number of mortar joints on the strength of masonry walls: an analytical investigation. *Developments in structural engineering computing (Proc. Fifth International Conference on Civil and Structural Engineering Computing /CIVIL-COMP 93*, Heriot-Watt University, August 1993). Civil-Comp Press, Edinburgh, 1993, 391–396.
193. Haseltine, B.A., Kirtschig, K. and Macchi, G. *Eurocode No. 6: common unified rules for masonry structures, Report EUR 9588 EN*, Commission of the European Communities, Luxembourg, 1988.
194. West, H.W.H., Everill, J.B. and Beech, D.G. The testing of bricks and blocks for loadbearing brickwork. *Proc. Tenth International Ceramic Congress*, Stockholm, June 1966, 559–565.
195. Prasan, S., Hendry, A.W. and Bradshaw, R.E. Crushing tests on storey height panels $4\frac{1}{2}$ in. thick. *Proc. Brit. Ceram. Soc.*, No. 4, July 1965.

Index

- aggregate interlock 172, 184, 185, 193, 194, 244, 248, 249, 250, 328, 346, 361, 377, 525
anchor plates in PSC structures 222
anchoring forces 420
anisotropy 52, 64, 174, 504
'anti-friction' media 29, 30
axial (vertical) load in structural walls 286, 293, 296, 305–306, 417
axisymmetric analysis 222, 231, 233, 337, 407
axisymmetric stress states 88, 89, 99–100
- βG term 176, 179
B-matrices 128, 201
sparsity 159, 160
beams
effective depth 369, 375, 392, 397
end block 397, 452, 467
high-strength concrete (HSC) 418, 452
ductility 452
prestressed concrete (PSC) 347, 453–483
reinforced concrete (RC) 244–275
beam failing in flexure (CS2) 367, 373
beam failing in shear (CS3) 374–385
(CS5) 389–391
bearing blocks 222
bearing strength 223, 224, 228, 229, 230, 231, 232, 233, 234, 235, 236, 241, 242, 367
bearing stress 223, 224, 236, 239, 243, 319, 388
biaxial compression data 83
biaxial strength data 78, 101
biaxial strength envelope 96, 98, 123
biaxial stress states 82, 96, 307, 322, 324
biaxial tests 18
bond action 191
bond failure 270, 271, 463, 464, 476
bond-slip law 187
bond-slip models 187, 189
bond-slip relations 525
bond stress 188, 189, 271
boundary conditions, influence on PC components 222, 232, 241, 386–387
boundary restraints 30
branch in stress–strain plot
ascending 20, 23, 61, 65, 69, 70, 103, 107, 108
descending 20, 23, 37, 103, 108, 191, 194
post-peak 111
post-ultimate 119
strain softening 194
branching 48, 49, 50, 52, 250, 257
brick unit 505, 506, 518, 519
normalized strength 503, 511, 512
brickwork *see* masonry
bridge bearings over piers 222
brittle nature of concrete 28, 37, 39, 40, 42, 43, 44, 58, 123, 124, 165, 183, 184, 194, 268, 348, 349, 351, 355, 356, 359, 360, 363, 366, 408, 451, 473, 525
brittle (punching) behaviour of slabs 319–322
effect of stirrups 322
brush-bearing platens (BR) 9, 10, 29, 30, 83, 98
bulk modulus (K) 68, 531
tangent 79, 158
- C_0 -elements 144, 149
Cartesian coordinates 528, 530
cement paste matrix 43, 48
characteristic compressive strength of masonry 503
codes of practice 1, 2, 119, 164, 192, 293, 306, 431, 527
ACI 318-77 261, 287, 293
ACI 318-83 297, 306, 368, 375
BS 8110 101, 108, 164, 297, 368, 375, 439, 463, 464, 469, 478, 500
CEB-FIB 78 368, 375, 500
CP 110 101, 164, 265, 266, 268
design procedures 305, 308
errors in 1–3, 325
predictions 297, 302
provisions 249, 294, 300, 304, 305, 306, 307, 389, 391, 395
collapse mechanism 209
composite construction 336
compression reinforcement 254, 441
compressive failure 334
compressive-force path (CFP) concept 250, 256, 257, 266, 268, 271, 304, 307, 344, 377, 383, 391, 395, 411, 431, 433, 439, 452, 463, 464, 469, 473, 478, 482, 484
computer-based methods 83
concrete
brittle nature 28, 37, 39, 40, 42, 43, 44, 58, 123, 124, 165, 183, 184, 194, 268, 348, 349, 351, 355, 356, 359, 360, 363, 366, 408, 451, 473, 525
constitutive law 20, 22, 23, 61, 66, 68, 80, 81, 123, 152, 164, 192, 337, 362
failure envelope 51
failure initiation 103
failure mechanism 50, 51, 59, 250
fatigue strength 50
heterogeneity 47, 105, 173, 304, 500
high-strength 188, 190, 306, 414, 418, 478
local failure 247
long-term strength 50
multiaxial properties 361
normal strength 418
strength 232, 286, 294, 297, 306
effect on structural walls 301
strength envelope 83, 85, 88, 93, 96, 121
stress–strain curve 59
uniaxial tensile strength 96, 188, 191
concrete blocks 502
concrete columns, steel encased 336

- concrete cover 245, 247, 258, 265, 275, 276, 285, 368, 375, 380, 389, 391, 441
- concrete dilation 106
- concrete hinges 222
- concrete-steel bond 169, 172, 185, 187, 193, 194, 361
- concrete structures
- ductile behaviour 114
 - failure mechanisms [103](#), [107](#), 121, 124, 125
 - crushing [107](#), 113, 125
 - splitting [107](#), 113, 125
- confinement
- active 336
 - passive 336
- confinement reinforcement 294, 304, 307, 308
- confining pressure (σ_c) 38, 39, 40, 83, 105, 106, 113, 117, [119](#), 460, 483, 519
- confining (triaxial) stress state 27, 525
- constant-stiffness strategy 205
- constitutive laws 20, 22, 23, 61, 66, 68, 80, 81, [123](#), 152, 164, 192, 337, 362
- constitutive matrix 152, 158
- convergence 132, 133, 134, 135, 152, 154, 155, 156, 161–163, 206, 246, 359, 370
- conversion factor (F) for brick strength 513, 515, 516
- convexity principle 19, 84, 88
- coordinate transformation 177, 178, [542](#)
- corbels 334–336
- failure mechanisms 336
- coupling 69, 70, 78, 81
- between hydrostatic and deviatoric components of stress and strain states 66, 124
 - between stress deviation and volume change 69, 77
- coupling modulus (H) 69
- coupon-type tests 504, 505, 506, 512, 515, 516
- crack closure 175
- crack implementation 204
- crack initiation 169, 196
- crack propagation 38, 39, 44, 45, 47, 49, 51, 52, 53, 55, 57, 58, 62, 66, 164, 165, 169, 170, 171, 204, 357
- crack propagation 'inhibitor' 53, 55, 73
- crack propagation procedures 182, 198, 209, 211, 213, 364, 366, 367, 369
- crack tips 45, 48, 59, 61, 62, 66, 81, 124, 173
- cracked concrete regions, contribution to structural strength 180, 194, 249, 360, 421, 525
- cracking 59, 81, 163, 193, 195, 206
- circumferential 176, 177, 178, 209, 315, 318, 321, 407
 - compressive 168
 - non-symmetrical 489, 490, 493–495, 500, 501, 502
 - radial 176, 177, 178, 209, 315, 318, 321, 407
 - symmetrical 490, 493–495, 500, 501, 502
 - tensile 168
- critical cross-section 244, 250, 256, 265, 266, 271, 345
- shear capacity 254, 268
- crushing 263
- crushing failure mode 256, 257
- current design procedures 256
- cyclic tests 58, 66
- cylinder test (CYL) 9
- cylinders under load 214
- cylindrical coordinate system 88
- D-matrix 128, 152, 158, 175, 177
- sparsity 159
- deep beams 274–282
- deformational and yield characteristics of reinforcing steel 101–103, 183
- degrees of freedom (DOF) 126, 150, 195, 363, 369
- description of reinforcing steel 185–192
- design 105, 106, [107](#), 108, 117, [119](#), 192, 244, 245, 284, 344, 346, 386, 427, 453, 463, 482, 483, 526
- guidelines 275
 - philosophies 345
 - procedures 294
- deviatoric loading 77
- deviatoric plane 100, 528, 529
- deviatoric shear 19
- see also octahedral shear
- deviatoric strain 20, 61, 62, 530
- deviatoric stress 20, 47, 48, 53, 55, 58, 61, 62, 63, 66, 77, 88, 323, 324, 529
- direct iteration [131](#), 132, 134
- direction cosines 532
- discrete crack approach 169, 171, 173, 174, 193, 357
- displacement field 126
- displacement magnification (DM) factor 209, 348, 490
- divergence 156, 162–164, 246, 270, 358, 359, 363, 371, 377, 383, 385
- domes 343
- double-precision accuracy 490, 494, 500, 502
- dowel action 172, 193, 194, 328, 361, 525
- in shear transfer mechanisms 101
- drop-head columns 309
- dry or unlubricated metal platens (DP) 9, 23
- ductile failure 408, 476
- ductile (flexural) behaviour of slabs 316
- ductility 1, 42, 262, 263, 268, 325, 328, 433, 438, 445, 451, 476, 481
- earthquake-resistant wall design 300
- eccentricity of applied load 489
- unintended 500
- effect of FE mesh 209, 210, 362, 364, 369, 380, 492
- effect of FE type 362, 364, 365, 369, 373
- effect of number of mortar joints on masonry wall strength 503, 516
- effective depth, of beam 369, 375, 392, 423, 441
- effective-width ratio 1
- eigenvalue formulation 529
- eigenvalue test 150, 183
- elastic concepts 3
- elastic constitutive relations, in terms of octahedral stresses and strains 530–531
- elastic moduli 72
- elastic recovery 34, 72
- elastic working-stress approach 1
- elasticity 156

- elastoplasticity [58](#)
 element stiffness matrix (k) [129](#), [130](#), [149](#), [151](#), [182](#), [183](#)
 end blocks of T-beam [400](#), [419](#), [420](#), [423](#), [427](#)
 end effects [23](#), [25](#)
 end zones [27](#), [36](#), [37](#), [38](#)
 engineering strain deformations [157](#)

 failure criteria for concrete [50](#), [51](#), [54](#), [55](#), [56](#), [85–86](#), [95](#), [96](#), [152](#), [164](#), [204](#), [324](#), [362](#), [525](#)
 failure laws [192](#)
 failure mechanisms [42](#), [105](#), [108](#), [164](#), [216](#), [250](#), [257](#), [271](#), [307–309](#), [323–325](#), [354](#), [402](#), [411](#), [415](#), [504](#)
 in concrete structures [103](#), [119](#), [525](#)
 failure mode [485](#)
 failure surfaces [83](#), [88](#), [96](#)
 FINEL [136](#), [138](#), [140](#), [151](#), [198](#), [202](#)
 Z FILE [140](#), [203](#)
 FINEL libraries [138](#)
 finite element
 choice [193](#), [195](#), [361](#)
 isoparametric [130](#), [141](#), [142](#), [144](#), [195](#), [209](#), [490](#), [506](#)
 Lagrangian [142](#), [143](#), [144](#), [183](#), [195](#), [362](#), [363](#), [367](#), [407](#)
 mesh configuration [195](#), [209](#), [210](#), [361](#), [362](#), [364](#), [369](#), [380](#), [404](#), [492](#)
 mesh size [193](#), [210](#), [358](#), [366](#), [373](#), [517](#), [518](#)
 mesh stiffening [196](#), [210](#), [271](#), [273](#), [276](#)
 serendipity [142](#), [143](#), [144](#), [145](#), [149](#), [150](#), [151](#), [183](#), [195](#), [348](#), [362](#), [363](#), [375](#), [385](#), [408](#), [454](#)
 shape ratio [197](#)
 size [195](#)
 lower bound limit [196](#), [197](#)
 upper bound limit [197](#), [210](#)
 type [362](#), [364](#), [365](#), [369](#), [373](#)
 finite-element method (FEM) [3](#), [126](#), [136](#), [192](#)
 finite-element (FE) model [3](#), [5](#), [6](#), [125](#), [164](#), [168](#), [171](#), [173](#), [187](#), [192](#), [193](#), [386](#), [489](#), [500](#), [524](#), [525](#)
 comparison of 2D and 3D analysis [412–418](#)
 three-dimensional [347](#), [361–411](#), [524](#)
 generality [385](#)
 two-dimensional [208](#), [209](#), [344](#), [524](#)
 generality [208](#)
 finite-element (FE) modules [138](#), [140](#), [201](#)
 ASMB [201](#), [202](#)
 BNCN [202](#)
 CHOL [202](#)
 LOAD [202](#), [203](#)
 SLVE [203](#)
 STRS [201](#), [202](#), [203](#), [204](#), [206](#)
 first stress invariant [81](#), [96](#)
 flange reinforcement
 in HSC members [453](#)
 effectiveness [445–452](#)
 in PSC members [463](#), [464](#), [465](#), [476](#), [479](#)
 flat-floor slabs [1](#)
 flat-slab construction [309](#)
 flaws [43](#), [44](#)
 flexible platens [222](#), [387](#)
 flexural capacity [254](#), [261](#), [265](#), [268](#), [269](#), [294](#), [299](#), [302](#), [305](#), [306](#), [394](#), [398](#), [451](#), [501](#)
 flexural failure [244](#), [368](#), [369](#), [375](#), [389](#), [400](#), [433](#), [463](#), [469](#), [473](#), [479](#), [500](#)
 fluid cushion (FC) [9](#), [10](#)
 formwork [309](#)
 fracture energy [362](#), [526](#)
 fracture extension [124](#)
 fracture initiation [59](#), [123](#)
 fracture processes [38](#), [39](#), [43](#), [44](#), [45](#), [47](#), [48–50](#), [52](#), [53](#), [54](#), [55](#), [57](#), [58](#), [59](#), [60](#), [62](#), [67](#), [68](#), [71](#), [73](#), [105](#), [108](#), [164](#), [165](#), [168](#), [169](#), [173](#), [257](#)
 friction between loading platens and specimens [10](#), [25](#), [165](#), [236](#)
 friction enhancement factor e_2 [513](#)
 frictional effects [25](#), [39](#), [509](#), [512](#), [513](#)
 frictional interaction [123](#)
 frictional restraint [23](#), [26](#), [27](#), [28](#), [29](#), [30](#), [31](#), [32](#), [33](#), [37](#), [38](#), [39](#), [96](#), [98](#), [105](#), [228](#), [230](#)
 full integration *see* integration, full
 functional iteration [131](#)
 fundamental failure mechanism in a structure [526](#)

 G3 matrix [181](#), [194](#), [362](#), [367](#), [380](#), [386](#), [389](#), [409](#)
 Gauss's method of numerical integration or quadrature [148](#), [358](#)
 Gauss points [149](#), [173](#), [182](#), [347](#), [358](#), [427](#), [469](#), [492](#), [506](#), [519](#)
 Gaussian integration [187](#), [362](#)
 generality of FE models [193](#), [348](#), [356](#), [386–411](#), [418](#)
 geometric imperfections [243](#), [343](#)
 geometric nonlinearity [343](#)

 height effect in brick units [516](#)
 height parameter in brick units [511](#)
 height-to-width ratio in walls [286](#), [293](#), [294](#), [302](#), [417](#)
 heterogeneity of concrete [47](#), [57](#), [105](#), [173](#), [304](#), [486](#), [489](#), [500](#), [502](#)
 high-strength concrete (HSC) prestressed T-beams [482](#), [483](#)
 high-strength concrete (HSC) rectangular beam [439–445](#)
 effective depth [441](#)
 high-strength concrete (HSC) T-beams (HSB) [427–452](#)
 HSB1 [427](#)
 HSB2 [433](#)
 HSB3 [438](#)
 HSB4 [445](#)
 HSB5 [445](#)
 hollow sphere [243](#), [343](#)
 under hydrostatic pressure [243](#)
 homogeneity [196](#)
 Hooke, generalized law [68](#), [71](#), [72](#), [131](#)
 hoop reinforcement [119](#)
 horizontal reinforcement in structural walls [302–305](#)
 hourglass mechanism [348](#), [358](#), [359](#), [377](#)
 truncated [351](#)
 see also spurious mechanism
 hydrostatic axis [51](#), [58](#), [86](#), [88](#), [93](#), [528](#)
 hydrostatic correction [79](#), [81](#)
 hydrostatic loading [77](#)

- hydrostatic pressure [69](#)
 on hollow sphere [243](#)
- hydrostatic strain [20](#), [61](#), [62](#), [96](#), [530](#)
- hydrostatic stress [19](#), [20](#), [47](#), [53](#), [54](#), [55](#), [56](#), [57](#),
[58](#), [61](#), [73](#), [77](#), [89](#), [529](#)
- hysteresis loop [66](#)
- ill-conditioning [154](#), [164](#), [183](#), [185](#), [202](#), [245](#), [246](#),
[358](#)
 matrix [334](#)
- implosion pressure [243](#)
- incremental force–displacement relationship [158](#)
- incremental methods [131](#), [135](#), [136](#), [152](#), [197](#)
- incremental mixed NR method (MIXNR) [205](#), [206](#),
[207](#), [355](#), [356](#), [359](#), [363](#), [370](#), [376](#), [377](#), [385](#)
- incremental modified (initial stiffness) NR method
 (INITK) [363](#), [375](#), [385](#)
- incremental (pure) NR method (INRM) [136](#), [153](#),
[155](#), [195](#), [204](#), [205](#), [363](#)
- incremental strain–displacement relationship [156](#),
[157](#)
- incremental stress–strain relationship
 cracked concrete [174](#)
 uncracked concrete [157](#), [158](#)
- initial/constant stiffness method [134](#), [206](#)
- initial elastic moduli [71](#)
- initial strain technique [161](#), [162](#)
- initial stress technique [162](#), [185](#), [205](#)
- integration
 full [149](#), [151](#), [195](#), [348](#), [354–356](#), [359](#), [383](#),
[407](#), [490](#), [506](#)
 reduced [149](#), [150](#), [151](#), [195](#), [348](#), [354](#), [355](#), [356](#),
[358](#), [359](#), [361](#), [407](#)
- integration points [173](#), [182](#), [183](#)
- interface friction [37](#), [503](#), [513](#)
- internal stress [53](#), [60](#), [61](#), [62](#), [66](#), [68](#), [70](#), [71](#), [72](#),
[73](#), [74](#), [75](#), [77](#), [78](#), [81](#), [124](#)
- interpolation functions [144](#), [145](#), [146](#)
- invariants of the stress tensor [529–530](#)
- isoparametric elements [130](#), [141](#), [142](#), [144](#), [146](#),
[147](#), [148](#), [173](#), [186](#), [195](#), [209](#), [490](#), [506](#)
- isotropic model [69](#)
- isotropy [52](#), [54](#), [68](#), [69](#), [71](#), [88](#), [158](#), [174](#), [196](#),
[505](#)
- iteration
 number of cracks allowed [193](#), [361](#)
- iterative procedures [131](#), [135](#), [193](#), [204](#), [356](#), [361](#),
[362](#), [370](#), [375](#), [385](#)
 premature divergence [348](#)
- Jacobian matrix [J] [130](#), [147](#), [157](#), [159](#), [201](#)
 determinant [147](#)
- kinematic mechanisms [150](#)
- Lagrangian element [142](#), [143](#), [144](#), [183](#), [195](#), [362](#),
[363](#), [367](#), [407](#)
see also finite element
- Lamé's expressions [68](#), [158](#)
- lateral expansion [234](#)
- linear elasticity [80](#)
- load–deflection curve [411](#)
- load path dependency [198](#)
- load step '777' [347](#), [358](#), [522](#)
- load step size [198](#)
- loading history [57](#), [65](#), [89](#), [135](#)
- loading path [193](#), [197](#), [209](#), [211](#)
- local failure criterion [179](#), [334](#)
- local fracture initiation (LFI) [48](#), [50](#), [51](#), [52](#)
- low-order or reduced integration [149](#), [150](#), [151](#),
[195](#), [348](#), [354](#), [355](#), [356](#), [358](#), [359](#), [361](#), [407](#)
- lubricated metal platens (LP) [9](#)
- macrocracking [51](#), [59](#), [124](#), [152](#), [164](#), [165](#)
 simulation [362](#)
see also cracking
- mapping transformation [146](#)
- masonry
 brittleness [502](#)
 characteristic strength [511](#)
 shape factors [503–516](#)
 strength [505](#), [509](#), [512](#), [515](#), [516](#), [517](#)
 structural [502–524](#)
- masonry walls [518](#), [522](#)
 strength [520](#), [522](#), [523](#)
- material factors [42](#), [51](#), [83](#), [192](#), [193](#), [209](#), [271](#),
[348](#), [349](#), [361](#)
- matrix of constitutive relations [128](#)
see also D-matrix
- matrix ill-conditioning [334](#)
- maximum sustained load (MSL) [164](#), [209](#), [411](#)
- membrane action [343](#)
 in flexural members [343–344](#)
- MGA pad [29](#)
- microconcrete [337](#)
- microcracking [43](#), [44](#), [47](#), [48](#), [49](#), [50](#), [51](#), [53](#), [59](#),
[61](#), [68](#), [71](#), [73](#), [124](#), [152](#), [154](#), [155](#), [158](#), [165](#)
see also cracking
- minimum volume level [49](#), [61](#), [65](#), [105](#), [106](#), [110](#)
- modelling of reinforcing steel [101–103](#)
 trilinear σ - ϵ diagram [371](#)
- Mohr-circle construction [532](#)
- monotonic loading [175](#)
- mortar [9](#), [15](#), [502](#), [519](#)
 failure envelope [337](#)
 strength [512](#), [517](#), [518](#), [519](#), [520](#), [521](#), [522](#), [523](#)
 stress–strain characteristics [517](#)
- mortar joints
 number, effect on masonry wall strength
[516–524](#)
 in masonry wall of constant height [516](#), [520](#),
[523](#)
- mortar joint thickness [517](#), [523](#)
- mortar mix [517](#)
- mortar units [518](#)
- multiaxial stress state [9](#), [37](#), [47](#), [48](#), [59](#), [85](#), [114](#),
[115](#), [117](#), [123](#), [193](#), [234](#), [241](#), [257](#), [306](#), [308](#)
see also triaxial stress state
- mushroom columns [309](#)
- Newton-Raphson (NR) method [132](#), [133](#), [134](#), [135](#)
 incremental mixed (MIXNR) [205](#), [206](#), [207](#), [355](#),
[356](#), [359](#), [363](#), [370](#), [376](#), [377](#), [385](#)
 incremental modified (INITK) [363](#), [375](#), [385](#)
 incremental (pure) (INRM) [136](#), [153](#), [155](#), [195](#),
[204](#), [205](#), [363](#)
 plus [206](#), [363](#), [370](#), [377](#), [380](#), [385](#), [386](#)
 non-convergent solutions [205](#)

- nonlinear analysis [59](#), [61](#), [130](#), [136](#)
 nonlinear finite-element analysis (NLFEA) [126](#)
 nonlinearities
 concrete [43](#)
 material [42](#)
 normal stresses [19](#), [61](#)
 numerical instability [3](#), [132](#), [149](#), [150](#), [198](#), [213](#),
[214](#), [355](#), [356](#), [359](#), [360](#), [363](#), [526](#)
 numerical integration techniques [148](#), [149](#), [155](#),
[159](#), [162](#), [195](#), [202](#), [361](#), [375](#)
 low-order [150](#), [151](#)
 numerical stability [164](#), [176](#), [183](#), [185](#), [196](#), [207](#),
[210](#), [211](#), [348](#), [349](#), [356](#), [362](#), [370](#)

 objectivity of FE models [192](#), [193](#), [194](#), [195](#), [209](#),
[348](#), [356](#), [361](#), [362](#), [367](#), [374](#), [375](#), [385](#), [386](#),
[407](#)
 objectivity study [361–386](#), [409](#)
 octahedral coordinates [528](#), [529](#)
 octahedral normal strain [22](#), [61](#), [62](#), [69](#), [78](#), [540](#)
 see also hydrostatic strain, volumetric strain
 octahedral normal stress [18](#), [19](#), [22](#), [61](#), [80](#), [89](#), [96](#),
[100](#), [528–529](#)
 see also hydrostatic stress, volumetric stress
 octahedral planes [65](#), [77](#), [88](#)
 octahedral shear [19](#), [529](#)
 octahedral strains [530](#)
 octahedral stresses [528–530](#)
 offshore structures [343](#), [344](#)
 onset of stable fracture propagation (OSFP) [49](#), [50](#),
[51](#), [52](#), [60](#)
 onset of unstable fracture propagation (OUFP) [49](#),
[50](#), [51](#), [52](#), [53](#), [54](#), [55](#), [56](#), [57](#), [58](#), [60](#), [62](#),
[65](#), [66](#), [69](#), [81](#), [89](#), [105](#), [106](#), [107](#), [108](#), [124](#),
[152](#), [164](#), [165](#)
 orthogonal coordinate system [88](#)
 out-of-plane effects [274](#), [483](#), [484](#)
 unintended [488](#), [489](#), [501](#)
 see also size effects

 parametric studies [208](#), [209](#), [214](#), [222](#), [228](#), [239](#),
[293](#), [294](#), [296](#), [297](#), [307](#), [345](#), [346](#), [361](#), [445](#),
[506](#), [516](#), [520](#)
 path dependency [58](#), [89](#)
 perfect bond [187–189](#), [194](#), [369](#)
 phenomenological insight [244](#), [248–271](#), [296](#), [346](#)
 photoelastic studies [334](#)
 plain concrete (PC) members [208](#)
 plane-stress analysis [222](#), [226](#), [233](#)
 plasticity [1](#), [3](#), [42](#), [58](#), [108](#), [116](#)
 plastification [101](#)
 platens
 brush-bearing [9](#), [10](#), [29](#), [30](#)
 steel [9](#), [10](#), [29](#), [222](#), [236](#), [387](#), [388](#), [504](#)
 platen-effect factor (p) [512](#), [513](#), [515](#)
 plotting [199](#), [201](#), [205](#), [209](#), [347](#), [358](#), [367](#)
 Poisson's ratio [23](#), [24](#), [25](#), [29](#), [32](#), [68](#), [80](#), [201](#),
[504](#)
 post-failure phenomena [113](#), [239](#), [346](#)
 post-ultimate behaviour [58](#)
 post-ultimate branch [32](#), [36](#), [37](#), [39](#), [103](#), [119](#)
 post-ultimate characteristics [25](#)
 in tension [166](#)
 post-ultimate stress–strain relationship [27](#), [114](#), [115](#)
 preformed cracks [248](#), [249](#)

 premature divergence [350](#), [355](#)
 prestressed concrete (PSC) beams [453–483](#)
 PSC I-beam, failing in shear [455–461](#)
 effective depth [455](#), [456](#)
 PSC T-beam (PCB1) [461](#)
 PCB3 [469](#)
 PCB6 [473](#)
 PCB7 [478](#)
 prestressed concrete (PSC) structures [232](#), [347](#)
 prestressing force [453](#), [454](#), [456](#), [458](#), [461](#), [467](#)
 prestressing operation [454](#), [461](#), [467](#), [482](#)
 prestressing tendon [454](#), [467](#)
 profile [467](#)
 principal directions [529](#)
 principal stresses [86](#), [96](#), [528](#), [529](#), [530](#)
 prism
 CS1 [364–367](#)
 CS4 [386–389](#)
 under load [214](#)
 procedural factors [192](#), [193](#), [194](#), [195](#), [197](#), [209](#),
[271](#), [348](#), [349](#), [385](#), [386](#)
 punching in slabs [309–328](#), [404–408](#)
 failure mechanism [328](#)

 quadrature points [150](#)

 reinforced concrete (RC) beams
 with stirrups, size effects [485](#), [486](#), [488](#), [490](#),
[492](#), [495](#), [500](#), [501](#), [502](#)
 without stirrups, size effects [484](#), [487](#), [488](#), [490](#),
[492](#), [495](#), [499](#), [500](#), [501](#), [502](#)
 reinforced concrete (RC) components [208](#)
 reinforced concrete (RC) slabs
 size effects [485](#), [486](#), [488](#)
 reinforced concrete (RC) structures
 beams [244–275](#)
 deep beam design [277](#)
 deep beams [274–282](#)
 reinforcement [294](#), [296](#), [410](#)
 characteristics [404](#)
 details [294](#), [306](#)
 flange [397](#)
 high-strength steel [453](#)
 mild steel [101](#), [185](#), [453](#)
 web [397](#)
 reinforcement detailing [245](#), [281](#), [286](#), [413](#), [415](#),
[461](#)
 residual force [135](#), [153](#), [154](#), [156](#), [161](#), [162](#), [169](#),
[173](#), [174](#), [187](#), [193](#), [205](#), [206](#), [213](#), [351](#), [356](#),
[361](#), [363](#), [367](#), [380](#)
 divergence [154](#), [163](#)
 residual shear stiffness [180](#), [181](#)
 residual strain [162](#)
 residual stress [161](#)
 residual stress criteria [162](#), [375](#)
 Ritz technique [126](#)
 rotational variable (θ) [63](#), [88](#), [96](#), [528](#), [529](#)
 round-off errors [196](#), [363](#)
 rubber layer [29](#), [30](#)

 sampling-point locations, optimal [148](#)
 sandwich cylinders [336](#)
 effect of imperfections [337](#)
 in sub-sea oil production [337](#)
 under external pressure [337](#)

- scatter [8](#), [22](#), [56](#), [58](#), [73](#), [83](#), [89](#), [95](#), [96](#), [165](#), [187](#), [362](#), [388](#), [486](#), [500](#), [505](#), [506](#), [509](#), [514](#), [516](#), [523](#), [526](#)
- secant-modulus approach [69](#), [78](#), [79](#), [132](#)
see also variable stiffness approach
- second stress invariant [81](#), [96](#)
- secondary stresses [114](#), [119](#), [367](#), [483](#), [484](#), [489](#)
 caused by eccentricity of load [484](#)
- seismic action [3](#), [283](#)
- serendipity element [142](#), [143](#), [144](#), [145](#), [149](#), [150](#), [151](#), [183](#), [195](#), [348](#), [362](#), [363](#), [375](#), [385](#), [408](#), [454](#)
see also finite element
- serviceability [L](#), [50](#)
- shape factor (δ) [503](#), [504](#), [509](#), [511](#), [512](#), [515](#), [516](#)
- shape functions [126](#), [127](#), [129](#), [144](#), [145](#), [146](#), [147](#), [156](#)
- shear capacity [261](#), [292](#), [293](#), [294](#), [299](#), [300](#), [303](#), [304](#), [305](#), [500](#)
- shear connectors [337](#)
- shear design [256](#), [262](#), [263](#), [299](#)
- shear failure [244](#), [250](#), [254](#), [256](#), [262](#), [263](#), [269](#), [271](#), [287](#), [293](#), [303](#), [305](#), [307](#), [346](#), [368](#), [375](#), [389](#), [432](#), [439](#), [463](#), [489](#), [500](#), [502](#)
- shear modulus (G) [68](#), [78](#), [79](#), [158](#), [531](#)
- shear panels [328](#)–[334](#)
 failure mechanism [334](#)
- shear reinforcement [254](#), [256](#), [257](#), [258](#), [261](#), [262](#), [274](#)
 confining effect [261](#), [262](#)
- shear resistance [248](#), [249](#)
- shear-retention factor (SRF) [169](#), [175](#), [182](#), [184](#), [185](#), [194](#), [209](#), [248](#), [349](#), [359](#), [360](#), [362](#), [371](#), [377](#), [380](#), [526](#)
- shear stiffness, residual [175](#)
- shear strength [297](#), [305](#), [306](#)
- shear stress (τ_0) [18](#)
- shear walls [293](#), [347](#)
- shearheads [328](#)
- shells [336](#)–[342](#)
- similitude, geometrical/reinforcement similarity of structural members [485](#), [486](#), [487](#), [490](#)
- similitude index [485](#)
- single crack approach (SCA) [211](#), [213](#), [351](#), [356](#), [357](#), [363](#), [366](#), [367](#), [370](#), [375](#), [385](#), [386](#), [389](#), [406](#), [409](#)
- size effects [483](#)–[502](#)
- slabs [347](#)
 brittle (punching) behaviour [319](#)–[322](#)
 ductile (flexural) behaviour [316](#)
 exhibiting punching failure (CS8) [404](#)–[408](#)
- smear-crack approach [169](#), [171](#), [173](#), [174](#), [185](#), [187](#), [193](#), [194](#), [201](#), [348](#)–[361](#), [411](#)
- 'softening' branch [23](#)
- space diagonal
see hydrostatic axis
- splitting [293](#), [307](#), [354](#), [373](#), [389](#), [390](#), [391](#), [402](#), [407](#), [411](#), [415](#)
- spurious cracking [383](#)
- spurious mechanism [184](#), [348](#), [349](#), [358](#), [362](#), [363](#), [377](#), [380](#)
- standard cylinder test [20](#)
- steel
 deformational characteristics [101](#)–[103](#), [185](#)
 high-strength [102](#)
 incremental relations [185](#)
 plastification [101](#)
 stress-strain characteristics [101](#)
 yield criteria [59](#), [101](#), [185](#)
- steel piston-flexible cushion system (FP) [9](#)
- steel reinforcement, FE modelling [185](#)
- stiffness matrix
 element [129](#), [130](#), [146](#), [147](#)
 structure [130](#)
- stiffness method [206](#)
- stiffness-updating strategies [182](#), [195](#)
- stirrups [264](#), [266](#), [268](#), [269](#), [271](#), [273](#), [287](#), [312](#), [323](#), [325](#), [328](#), [389](#), [391](#), [393](#), [400](#), [445](#), [455](#), [458](#), [460](#), [488](#), [489](#), [490](#), [500](#), [501](#)
 effect of brittle-type behaviour [322](#)
- stirrup confinement [305](#), [390](#), [391](#), [402](#), [404](#), [415](#), [445](#), [453](#), [460](#)
- strain
 deviatoric [20](#)
 hydrostatic [20](#)
 octahedral [22](#)
- strain energy [533](#)
- strain-energy concentration [44](#)
- strain softening [37](#), [39](#), [42](#), [103](#), [107](#), [108](#), [165](#), [166](#), [192](#), [194](#), [350](#), [351](#), [355](#), [357](#), [359](#), [360](#), [365](#), [373](#), [377](#), [525](#)
 in tension [166](#)
- strain transformations [532](#)–[533](#)
- strength envelope [22](#), [121](#), [169](#), [193](#), [230](#), [234](#), [247](#)
- strength surfaces [18](#), [89](#), [124](#)
- stress
 deviatoric [20](#)
 hydrostatic [20](#)
 octahedral [22](#)
 secondary [105](#), [106](#), [107](#), [115](#), [118](#), [119](#)
- stress block [108](#), [117](#), [118](#), [119](#)
- stress computation modules [201](#)
 ASMB [201](#), [202](#)
 BNCN [202](#)
 CHOL [202](#), [203](#)
 LOAD [202](#), [203](#)
 SLVE [203](#)
 STRS [201](#), [202](#), [204](#), [206](#)
- stress path [54](#), [55](#), [56](#), [57](#), [63](#), [64](#), [81](#), [82](#), [89](#), [119](#)
- stress path influence [56](#)
- stress redistribution [42](#)
- stress space [55](#), [63](#), [86](#), [89](#), [95](#), [528](#)
- stress-space diagonal [63](#)–[64](#)
- stress-strain curve
 ascending branch [123](#), [124](#)
 descending branch [123](#)
- stress-strain relations [193](#), [525](#)
 ascending range [71](#)
 biaxial [83](#)
 post-peak characteristics [193](#), [361](#)
 uniaxial [83](#)
- stress transformations [533](#)
- structural masonry [502](#)–[524](#)
- structural walls [283](#)–[309](#)
 comparison of 2D and 3D analysis [412](#)–[418](#)
 failing in flexure (CS7) [400](#)–[404](#)
 tests [412](#)
- structure stiffness matrix (K) [130](#)
- successive substitution/approximation [131](#)–[132](#)

- T-beams [347](#)
 economic modelling [418–427](#)
 effective depth [423](#)
 end blocks [397](#), [400](#), [419](#), [420](#), [423](#), [427](#)
 flange stirrup [419](#)
 HSC T-beam (HSB) [427–452](#)
 HSB1 [427](#)
 HSB2 [433](#)
 HSB3 [438](#)
 HSB4 [445](#)
 HSB5 [445](#)
 under four-point loading (CS6) [391–400](#)
 tangent modulus [79](#)
 tangential stiffness matrix [133](#)
 tendon profile [463](#)
 tensile testing [39](#)
 tension failure [189](#), [526](#), [527](#)
 tension stiffening [185](#), [190](#), [191](#), [192](#), [193](#), [194](#),
 [361](#), [362](#), [380](#), [411](#), [525](#)
 testing methods [9](#), [19](#), [20](#), [22](#), [23](#), [28](#), [30](#), [37](#), [58](#),
 [83](#), [85](#), [96](#), [232](#), [236](#), [241](#)
 effect on strength data [19](#), [20](#)
 third stress invariant [96](#)
 three-moduli approach [68](#), [78](#)
 threshold angles [359](#), [383](#)
 'tie effect' [191](#)
 tied-arch response [250](#)
 tied frame with inclined legs model [277](#), [282](#)
 time-dependent effects [165](#), [208](#), [292](#), [404](#), [412](#),
 [413](#), [415](#)
 torsional effects [488](#)
 total crack approach (TCA) [211](#), [213](#), [226](#), [351](#),
 [357](#), [363](#), [366](#), [367](#), [385](#)
 transformation coordinates [181](#), [532](#)
 transformation of material properties [533](#)
 transformation matrix [130](#), [175](#), [177](#)
 transverse expansion [113](#), [116](#), [121](#)
 transverse reinforcement [324](#), [369](#), [397](#), [400](#), [420](#),
 [423](#), [427](#), [430](#), [442](#), [455](#), [463](#), [464](#), [476](#), [483](#)
 triaxial compression (C-C-C) [18](#), [38](#), [39](#), [50](#), [52](#),
 [63](#), [64](#), [79](#), [82](#), [89](#)
 triaxial effects [356](#), [411](#), [415](#), [503](#), [524](#)
 triaxial extension [18](#), [38](#), [39](#), [50](#), [52](#), [63](#), [64](#), [79](#),
 [82](#), [88](#)
 triaxial strength data [8](#), [42](#), [78](#), [81](#), [100](#), [101](#)
 triaxial strength envelope [99](#), [123](#), [124](#)
 triaxial stress state [42](#), [82](#), [105](#), [113](#), [192](#), [261](#),
 [268](#), [291](#), [293](#), [309](#), [319](#), [322](#), [323](#), [325](#), [328](#),
 [413](#), [450–451](#), [522](#), [523](#), [524](#)
 triaxial tension (C-C-T) [40](#), [50](#), [89](#), [95](#)
 zones [52](#)
 triaxial tests [18](#), [37](#), [59](#), [88](#), [89](#), [99](#)
 triaxiality [119](#), [124](#), [228](#), [271](#), [346](#), [414](#), [445](#), [453](#),
 [511](#), [520](#), [521](#), [525](#)
 and failure initiation [108](#)
 truss-analogy concept [283](#), [284](#), [293](#), [304](#), [306](#)
 truss model [271](#), [303](#)
 ultimate deviatoric stress [96](#)
 ultimate load conditions [192](#)
 ultimate strain [102](#), [185](#)
 ultimate-strength concept [1](#), [51](#), [53](#), [81](#), [88](#), [89](#), [93](#)
 ultimate-strength envelope [52](#), [54](#), [55](#), [56](#), [57](#), [58](#),
 [89](#), [96](#), [119](#), [165](#)
 ultimate-strength surface [93](#), [100](#)
 under-integration *see* integration, reduced
 uniaxial compression [25](#), [30](#)
 uniaxial compression data [78](#), [83](#)
 uniaxial compression test [12](#), [13](#), [26](#)
 uniaxial (cylinder) compressive strength [13](#), [20](#), [37](#),
 [61](#), [89](#), [95](#), [105](#), [110](#), [123](#), [223](#), [230](#), [293](#),
 [306](#), [362](#), [367](#), [444](#), [461](#), [525](#), [526](#), [527](#)
 updating technique [155](#), [204](#)
 variable stiffness approach [132](#)
 vertical force [294](#)
 vertical prestressing [328](#)
 vertical reinforcement in structural walls [297–302](#)
 virtual displacement [533](#)
 viscoplasticity [58](#)
 void formation [45](#), [49](#), [60](#), [61](#), [65](#), [81](#), [82](#), [105](#),
 [124](#)
 voids [27](#), [43](#), [45](#), [58](#), [59](#), [81](#)
 volume reduction [81](#)
 volumetric dilation [81](#), [105](#), [106](#), [113](#), [119](#), [124](#),
 [270](#), [307](#), [309](#), [328](#), [346](#), [520](#), [523](#), [524](#), [525](#)
 volumetric strain [61](#), [62](#), [75](#)
 variation [103](#)
 wall shear capacity [283](#)
 'weakest-link' theory [15](#)
 wet bricks [504](#)
 wet-to-dry conversion factor [504](#), [512](#)
 working loads [334](#)
 'working' or 'serviceability' conditions [131](#), [328](#),
 [336](#)
 yielding criteria [163](#), [206](#)
 yield-line theory [405](#)
 yield stress [102](#)
 Young's modulus [68](#), [80](#), [186](#), [201](#), [362](#), [370](#), [504](#),
 [526](#)
 Z3 matrix [181](#), [194](#), [362](#), [367](#), [380](#), [381](#)
 zero-energy deformation modes [150](#), [151](#)
 ZFILE [140](#), [203](#)

Hidden page

Hidden page

Hidden page

STRUCTURAL CONCRETE


Finite-element analysis for limit-state design

A review of available experimental data on the behaviour of concrete at both the material and structural levels reveals the unavoidable development of triaxial stress conditions prior to failure which dictate the collapse and ductility of structural concrete members; moreover — and in contrast with widely-accepted tenets — it can be shown that the post peak-stress behaviour of concrete as a material is realistically described by a complete and immediate loss of load-carrying capacity. Therefore, rational analysis and design of concrete components in accordance with the currently prevailing limit-state philosophy requires the use of triaxial material data consistent with the notion of a fully-brittle material, and such an approach is implemented in the book by outlining a finite-element method for the prediction of the strength, deformation and cracking patterns of arbitrary structural forms encompassing plain, reinforced, and prestressed concrete members. Numerous examples are given that show both the unifying generality of the proposed approach and the reliability of the ensuing computer package for which the sole input is the specified cylinder strength of concrete and the yield stress of steel. The book not only offers a better phenomenological understanding of structural concrete behaviour but also illustrates, by means of suitable examples, the type of revision required for improving design methods in terms of both safety and economy.

The Authors

After conducting extensive research into the triaxial behaviour of concrete materials, **Dr M. D. Kotsovov** has pioneered its application to the analysis and design of structural concrete members. He has authored about 100 papers in these fields, and has been engaged on various consultancies covering the design of concrete structures and their safety and repair under earthquake conditions. He is currently a professor at the National Technical University of Athens.

While maintaining a wide interest in the fields of structural engineering and mechanics, with over 100 publications in various fields of analysis and design, **Dr M. N. Pavlović** has been active in the numerical modelling of concrete structures and its application to rational design practice. His consultancy work includes several large concrete dams and domes. He is currently a reader at the University of London, Imperial College of Science, Technology and Medicine.

 Thomas Telford

ISBN 0-7277-2027-9



9 780727 720276